Springer Proceedings in Physics 156

Olena Fesenko
Leonid Yatsenko *Editors*

Nanocomposites, Nanophotonics, Nanobiotechnology, and Applications

Selected Proceedings of the Second FP7 Conference and International Summer School Nanotechnology: From Fundamental Research to Innovations, August 25–September 1, 2013, Bukovel, Ukraine

Springer

Springer Proceedings in Physics

Volume 156

For further volumes:
http://www.springer.com/series/361

Olena Fesenko • Leonid Yatsenko
Editors

Nanocomposites, Nanophotonics, Nanobiotechnology, and Applications

Selected Proceedings of the Second FP7 Conference and International Summer School Nanotechnology: From Fundamental Research to Innovations, August 25–September 1, 2013, Bukovel, Ukraine

Springer

Editors
Olena Fesenko
National Academy of Sciences of Ukraine
Institute of Physics
Kiev
Ukraine

Leonid Yatsenko
National Academy of Sciences of Ukraine
Institute of Physics
Kiev
Ukraine

ISSN 0930-8989 ISSN 1867-4941 (electronic)
ISBN 978-3-319-06610-3 ISBN 978-3-319-06611-0 (eBook)
DOI 10.1007/978-3-319-06611-0
Springer Cham Heidelberg New York Dordrecht London

Library of Congress Control Number: 2014945121

Printed on acid-free paper

Springer is part of Springer Science+Business Media (www.springer.com)

Preface

This book presents a selection of the latest developments in nanotechnology and nanomaterials. It features articles written by lecturers and young scientists from Europe, in particular from Ukraine, who participated in the Second International Summer School "Nanotechnology: From Fundamental Research to Innovations," held in Bukovel, Ukraine from August 25 to September 1, 2013 within the framework of the FP7 project Nanotwinning. This International Summer School provided early-career scientists the opportunity to participate in a series of lectures on the emerging fields of nanoscience and nanotechnology. The goal of the Second International Summer School was to familiarize young scientists with actual research and problems of application in this area and to promote the future implementation of nanotechnology in innovative development to meet public needs. The First Summer School, held in 2012, received positive feedback from international experts and sparked interest in the media, with mentions on the Ukrainian Channel 5 programs "Window to Europe" and "Intellect.UA," the TBi Ukrainian TV program "Today," and on the Tonis national TV Channel program "Social Pulse," as well as in Viche magazine and the scientific journal World of Physics. International Summer School was hosted by the Institute of Physics of NAS of Ukraine in conjunction with its Nanotwinning project partners: University of Tartu (Estonia), European Profiles A.E. (Greece), University of Turin (Italy), and Pierre and Marie Curie University (France).

The beginning of the twenty-first century witnessed tremendous breakthroughs in nanoscience and nanotechnology. Today, nanotechnology is used in computer technology and electronics; the aerospace, chemical, and construction industries; medicine and pharmacology; and in the manufacture of new unprecedented materials. The present volume surveys some of the latest advances in the field and points the way to exciting future investigations and applications. The book chapters cover such currently important topics as microscopy of nanostructures; nanocomposites; nanostructured interfaces and surfaces; nanooptics; nanoplasmonics; and enhanced vibrational spectroscopy. The book demonstrates that researching nanocarbons, nanosilicon, biomolecular nanostructures, and their applications is a very interesting and exciting area of modern science, which will certainly attract the attention of scientists and engineers for many years to come.

The book is divided into four sections: Part I: Nanocomposites and Nanostructures; Part II: Nanophotonics; Part III: Nanobiotechnology; and Part IV: Application.

An overview of the chapters is provided below. The reader is recommended to read the following descriptions first, as they provide insights into the book's contents and the results presented.

Part I: Nanocomposites and Nanostructures

In Chap. 1 (Dodziuk) endohedral fullerene complexes involving C_{60}, C_{70}, and $C_{50}H_{10}$ nanotubes, especially those containing small molecular guests, are reviewed and calculations of their stability presented. Chapter 2 (Nykyforchyn) focuses on the improvement of certain physical and mechanical properties of surface layers of engineering steels by severe thermal–plastic deformation treatment using high-speed friction and simultaneous rapid cooling in a special medium. The authors of Chap. 3 (Korol) consider a gapped graphene superlattice (SL) constructed in accordance with the Fibonacci rule. Chapter 4 (Cravanzola) focuses on the characteristics and electrical conductivity mechanisms of carbon nanotubes and expanded graphite. Chapter 5 (Beresnev) presents nanocomposite (Zr-Ti-Cr-Nb)N coatings with high hardness and thickness around 8.5 μm which allows their use as protective coatings for cutting tools. In Chap. 6 (Savchenko), the luminescent spectra of obtained metallocomplexes in solid state are investigated and analyzed. In Chap. 7 (Vretik) possible morphological changes on a poly(methacrylamidoaryl methacrylate) surface before and after irradiation with polarized UV-light were investigated. Chapter 8 (Orel) presents research into the nonlinear magnetic properties magneto-mechano-chemical nanocomplex synthesized from magnetite and antitumor antibiotic doxorubicin. Chapter 9 (Bellel) describes the electrochemical preparation process of magnesium-based nanocomposites on a metallic cathode. Chapter 10 (Ulyanova) focuses on preparation processes of SiO_2–Al_2O_3–TiO_2 composite materials doped with nanostructured fibrous powders γ- and α-Al_2O_3.

Part II: Nanophotonics

Chapter 11 (Donets) presents technological aspects of corrosion resistant steels surfacing by intense relativistic electron beams. Chapter 12 (Chrzanowska) reviews the consequences of the presence and amount of water on the silicon based parts of nanodevices such as AFM tips. Chapter 13 (Uklein) examines the structural and optical characterization of the ($Y_3Al_5O_{12}$, YAG) ceramics prepared by high-pressure low-temperature technique. The authors of Chap. 14 (Raczyński) interpret the behavior of homocysteine molecules in the pure clusters and in the clusters with carbon nanotube, by qualitative interpretation of physical observables and snapshots of instantaneous configurations. Chapter 15 (Sumarokov) examines the heat capacity of 1D chains of atom/molecule adsorbates in the grooves of c-SWNT bundles.

Part III: Nanobiotechnology

Chapter 16 (Martseniuk) is devoted to the analysis of properties of water, diffused in the layered compounds $SrFe_2As_2$ and $FeTe_{0,8}S_{0,2}$. The aim of Chap. 17 (Pavlovich) is to study the effect of gold nanoparticles on morphological and functional characteristics of SPEV cells. Chapter 18 (Shcherbak) focuses applications of nanomaterials in rational gene pool preservation technology. In Chap. 19 (Christophorov) the author describes the basis and development of the concept of dynamic molecular self-organization, a model he first introduced more than 20 years ago when searching the most adequate approach to analyzing the functioning of biomolecules, in particular, proteins–enzymes. Chapter 20 (Burlaka) presents applications of CNT-based strategies for improved efficacy, reproducibility, accuracy, and speed in gene transfer in plants. In Chap. 21 (Chevichalova) the authors present the result of investigations on the effect of platinum nanoparticle aggregations on the vital activity of a variety of cancer cells.

Part IV: Applications

Chapter 22 (Kucherenko) describes urease-based conductometric biosensors that were created using a non-typical method of urease immobilization via adsorption on micro- and nanoporous particles. Chapter 23 (Bażela) presents the results of investigations into the effect of particle size on the magnetic properties of $RMnO_3$ (R = Pr, Nd and Tb) using magnetometric and X-ray and neutron diffraction methods. Chapter 24 (Nichkalo) reviews investigations of silicon nanowire formation via a combination of LPCVD and wet etching methods on Si substrate using gold films as mask. In Chap. 25 (Draidi) the authors develop a precision MESFET model for transconductance variation based on gate length and voltage and resistance and voltage. Chapter 26 (Shalaeva) discusses the nanocrystalline structure formation mechanism of quasi-one-dimensional nanostructured aggregates ZnO and Zn–O–C used as photocatalysts and the effect of thermolysis condition on the formation of textured structure in these aggregates. Chapter 27 (Boudine) focuses on the study of spin-polarized transport in semiconductors as new type of current transmission in semiconductor devices. In the chapter, the authors present a two-degree model for a so-called SPINFET transistor. Chapter 28 (Protsenko) is devoted to the strain properties of multilayer thin-film materials based on metals. Chapter 29 (Gudyma) is devoted to an analysis of spin-crossover system dynamics using both an Ising-like mechanoelastic model and a macroscopic phenomenological model.

Contents

Contributors

M. I. Bagatskii B.Verkin Institute for Low Temperature Physics and Engineering of the National Academy of Sciences of Ukraine, Kharkov, Ukraine

I. V. Baklanova Institute of Solid State Chemistry UB RAS, Ekaterinburg, Russian Federation

M. S. Barabashko B.Verkin Institute for Low Temperature Physics and Engineering of the National Academy of Sciences of Ukraine, Kharkov, Ukraine

Stanisław Baran M. Smoluchowski Institute of Physics, Jagiellonian University, Kraków, Poland

Wiesława Bażela Institute of Physics, Cracow University of Technology, Kraków, Poland

N. Bellel Physics Energy Laboratory, Physics Department, Constantine University, Constantine, Algeria

V. V. Belozerov National Technical University "KhPI", Ministry of Education and Science of Ukraine, Kharkiv, Ukraine

A. Benaboud Active Devices and Materials Laboratory, Faculty of Exact Sciences and Nature and Life Sciences, Larbi Ben M'hidi University, Oum El Bouaghi, Algeria

K. Benhizia Université Constantine, Constantine, Algérie

V. M. Beresnev Karazin Kharkiv National University, Kharkiv, Ukraine

A. S. Berezhnytska V. I. Vernadsky Institute of General and Inorganic Chemistry NASU, Kiev, Ukraine

M. Bilokur Sumy National University, Sumy, Ukraine

Yaroslav B. Blume Institute of Food Biotechnology and Genomics, National Academy of Sciences of Ukraine, Kyiv, Ukraine

O. V. Bondar Sumy National University, Sumy, Ukraine

A. Boudine Faculty of Exact Sciences and Natural and Life Sciences, Active Devices and Materials Laboratory, Larbi Ben M'hidi University, Oum El Bouaghi, Algeria

M. S. Brodyn Institute of Physics NASU, Kiev, Ukraine

L. Yu. Buldakova Institute of Solid State Chemistry UB RAS, Ekaterinburg, Russian Federation

A. P. Burlaka R.E. Kavetsky Institute of Experimental Pathology, Oncology and Radiobiology/45, Kyiv, Ukraine

Olga M. Burlaka Institute of Food Biotechnology and Genomics, National Academy of Sciences of Ukraine, Kyiv, Ukraine

Federico Cesano Department of Chemistry, NIS (Nanostructured Interfaces and Surfaces), Centre of Excellence and INSTM Centro di Riferimento, University of Torino, Torino, Italy

A. V. Chevichalova F. D. Ovcharenko Institute of Biocolloid Chemistry, Ukrainian National Academy of Sciences, Kyiv, Ukraine

Leonid N. Christophorov Bogolyubov Institute for Theoretical Physics, NAS Ukraine, Kiev, Ukraine

Agnieszka Chrzanowska Institute of Physics, Kraków University of Technology, Kraków, Poland

Sara Cravanzola Department of Chemistry, NIS (Nanostructured Interfaces and Surfaces), Centre of Excellence and INSTM Centro di Riferimento, University of Torino, Torino, Italy

Helena Dodziuk Institute of Physical Chemistry, Polish Academy of Sciences, Warsaw, Poland

S. E. Donets Institute of Electrophysics and Radiation Technologies, National Academy of Sciences of Ukraine, Kharkiv, Ukraine

M. Draidi Faculty of Exact Sciences and Natural and Life Sciences, Active Devices and Materials Laboratory, Larbi Ben M'hidi University, Oum El Bouaghi, Algeria

Anatoly Druzhinin Lviv Polytechnic National University, Lviv, Ukraine

Marcin Dul Institute of Physics, Cracow University of Technology, Kraków, Poland

Ryszard Duraj Institute of Physics, Cracow University of Technology, Kraków, Poland

Stanislav Dvornytskyi Lviv Polytechnic National University, Lviv, Ukraine

Konstantin Dyakonov A. F. Ioffe Physico-Technical Institute RAN, St.-Petersburg, Russia

Volodymyr Dyakonov A. A. Galkin Donetsk Physico-Technical Institute, National Academy of Sciences of Ukraine, Donetsk, Ukraine

Institute of Physics, PAS, Warszawa, Poland

Sergei V. Dzyadevych Laboratory of Biomolecular Electronics, Institute of Molecular Biology and Genetics, National Academy of Sciences of Ukraine, Kyiv, Ukraine

Institute of High Technologies, Taras Shevchenko National University of Kyiv, Kyiv, Ukraine

Cristian Enachescu Alexandru Ioan Cuza University of Iasi, Iasi, Romania

V. R. Estrela-Llopis F. D. Ovcharenko Institute of Biocolloid Chemistry, Ukrainian National Academy of Sciences, Kyiv, Ukraine

Anatoly Evtukh V.E. Lashkaryov Institute of Semiconductor Physics NAS of Ukraine, Kyiv, Ukraine

Piotr Fornal Institute of Physics, Kraków University of Technology, Kraków, Poland

N. P. Galagan O.O. Chuiko Institute of Surface Chemistry, National Academy of Science of Ukraine, Kiev, Ukraine

V. Ya. Gayvoronsky Institute of Physics NASU, Kiev, Ukraine

Zygmunt Gburski Institute of Physics, University of Silesia, Katowice, Poland

Krzysztof Górny Institute of Physics, University of Silesia, Katowice, Poland

Iurii Gudyma Chernivtsi National University, Chernivtsi, Ukraine

O. I. Gyrdasova Institute of Solid State Chemistry UB RAS, Ekaterinburg, Russian Federation

Jens-Uwe Hoffmann Helmholtz-ZentrumBerlin für Materialien und Energie GmbH, Berlin, Germany

Tommy Hofmann Helmholtz-ZentrumBerlin für Materialien und Energie GmbH, Berlin, Germany

Andreas Hoser Helmholtz-ZentrumBerlin für Materialien und Energie GmbH, Berlin, Germany

V. M. Isai National University for Food Technologies, Kiev, Ukraine

N. B. Ivakha V. I. Vernadsky Institute of General and Inorganic Chemistry NASU, Kiev, Ukraine

L. Kalla Active Devices and Materials Laboratory, Faculty of Exact Sciences and Nature and Life Sciences, Larbi Ben M'hidi University, Oum El Bouaghi, Algeria

Berna Ozansoy Kasap Central Laboratory, Middle East Technical University, Ankara, Turkey

Yuriy Khoverko Lviv Polytechnic National University, Lviv, Ukraine

V. F. Kivshik Institute of Electrophysics and Radiation Technologies, National Academy of Sciences of Ukraine, Kharkiv, Ukraine

V. F. Klepikov Institute of Electrophysics and Radiation Technologies, National Academy of Sciences of Ukraine, Kharkiv, Ukraine

N. Y. Klymenko O.O. Chuiko Institute of Surface Chemistry, National Academy of Science of Ukraine, Kiev, Ukraine

D. A. Kolesnikov Belgorod State National University, Belgorod, Russia

A. M. Korol National University for Food Technologies, Kiev, Ukraine

Laboratory on Quantum Theory, Linköping, Sweden

S. I. Kovtun Biotechnology laboratory, Institute of Animal Breeding and Genetics, National Academy of Agrarian Science of Ukraine, Kiev, Ukraine

V. N. Krasilnikov Institute of Solid State Chemistry UB RAS, Ekaterinburg, Russian Federation

Zinaiida Kravchenko A. A. Galkin Donetsk Physico-Technical Institute, National Academy of Sciences of Ukraine, Donetsk, Ukraine

N. P. Krutko Institute of General and Inorganic Chemistry of NAS of Belarus, Republic of Belarus

Ivan S. Kucherenko Laboratory of Biomolecular Electronics, Institute of Molecular Biology and Genetics, National Academy of Sciences of Ukraine, Kyiv, Ukraine

Institute of Biology, Taras Shevchenko National University of Kyiv, Kyiv, Ukraine

Burcu Akata Kurç Central Laboratory, Middle East Technical University, Ankara, Turkey

Micro and Nanotechnology Department, Middle East Technical University, Ankara, Turkey

Michail Vasilievich Kurik Institute of physics NAS Ukraine, Kiev, Ukraine

Volodymyr Kyryliv Karpenko Physico-Mechanical Institute of NASU, Ukraine

Gabriela Lewińska Institute of Physics, Kraków University of Technology, Kraków, Poland

P. M. Litvin V. E. Lashkarev Institute of Semiconductor Physics, Ukrainian National Academy of Sciences, Kyiv, Ukraine

Yu. F. Lonin National Science Center Kharkov, Institute of Physics and Technology, National Academy of Sciences of Ukraine, Kharkov, Ukraine

S. N. Lukin R.E. Kavetsky Institute of Experimental Pathology, Oncology and Radiobiology/45, Kyiv, Ukraine

S. V. Lytovchenko Karazin Kharkiv National University, Kharkiv, Ukraine

V. V. Lytvynenko Institute of Electrophysics and Radiation Technologies, National Academy of Sciences of Ukraine, Kharkiv, Ukraine

Olga Maksymiv Karpenko Physico-Mechanical Institute of NASU, Ukraine

Artur Maksymov Chernivtsi National University, Chernivtsi, Ukraine

Aleksandr Stepanovich Martseniuk National University of Food Technology, Kiev, Ukraine

Ludmila Stepanovna Martseniuk Institute of Nuclear Researches NAS Ukraine, Kiev, Ukraine

M. A. Melkozerova Institute of Solid State Chemistry UB RAS, Ekaterinburg, Russian Federation

Volodymir G. Melnyk Department of Electrical and Magnetic Measurements, Institute of Electrodynamics, National Academy of Sciences of Ukraine, Kyiv, Ukraine

V. V. Multian Institute of Physics NASU, Kiev, Ukraine

Lucia Muscuso Department of Chemistry, NIS (Nanostructured Interfaces and Surfaces), Centre of Excellence and INSTM Centro di Riferimento, University of Torino, Torino, Italy

Stepan Nichkalo Lviv Polytechnic National University, Lviv, Ukraine

Olena A. Nikolaeva Macromolecular Chemistry Department, Taras Shevchenko National University of Kyiv, Kyiv, Ukraine

Natalia Nosidlak Institute of Physics, Kraków University of Technology, Kraków, Poland

Hryhoriy Nykyforchyn Karpenko Physico-Mechanical Institute of NASU, Ukraine

Larysa V. Odnodvorets Department of Applied Physics, Sumy State University, Sumy, Ukraine

V. E. Orel National Cancer Institute/33/43, Kyiv, Ukraine

Ihor Ostrovskii Lviv Polytechnic National University, Lviv, Ukraine

O. S. Osypchuk Biotechnology laboratory, Institute of Animal Breeding and Genetics, National Academy of Agrarian Science of Ukraine, Kiev, Ukraine

L. V. Ovseenko Institute of General and Inorganic Chemistry of NAS of Belarus, Republic of Belarus

Edyta Oziębło Institute of Physics, Kraków University of Technology, Kraków, Poland

E. V. Pavlovich Department for Cryobiology of Reproduction System, Institute for Problems of Cryobiology and Cryomedicine, Natl. Acad. of Sci. of Ukraine, Kharkiv, Ukraine

Bogusław Penc M. Smoluchowski Institute of Physics, Jagiellonian University, Kraków, Poland

Yaroslav V. Pirko Institute of Food Biotechnology and Genomics, National Academy of Sciences of Ukraine, Kyiv, Ukraine

A. D. Pogrebnjak Sumy National University, Sumy, Ukraine

A. G. Ponomarev National Science Center Kharkov, Institute of Physics and Technology, National Academy of Sciences of Ukraine, Kharkov, Ukraine

A. S. Popov Institute of Physics NASU, Kiev, Ukraine

Ivan Yu. Protsenko Department of Applied Physics, Sumy State University, Sumy, Ukraine

Serhyi I. Protsenko Department of Applied Physics, Sumy State University, Sumy, Ukraine

Przemysław Raczyński Institute of Physics, University of Silesia, Katowice, Poland

A. Y. Rykhalskiy National Cancer Institute/33/43, Kyiv, Ukraine

M. Sahli Physics Energy Laboratory, Physics Department, Constantine University, Constantine, Algeria

Jerzy Sanetra Institute of Physics, Kraków University of Technology, Kraków, Poland

I. A. Savchenko National Taras Shevchenko University of Kyiv, Kyiv, Ukraine

Domenica Scarano Department of Chemistry, NIS (Nanostructured Interfaces and Surfaces), Centre of Excellence and INSTM Centro di Riferimento, University of Torino, Torino, Italy

I. B. Schepotin National Cancer Institute/33/43, Kyiv, Ukraine

Lyudmila M. Semenycheva Department of Electrical and Magnetic Measurements, Institute of Electrodynamics, National Academy of Sciences of Ukraine, Kyiv, Ukraine

E. V. Shalaeva Institute of Solid State Chemistry UB RAS, Ekaterinburg, Russian Federation

O. V. Shcherbak Biotechnology laboratory, Institute of Animal Breeding and Genetics, National Academy of Agrarian Science of Ukraine, Kiev, Ukraine

A. D. Shevchenko G.V. KurdyumovInstitute for Metal Physics/36, Kyiv, Ukraine

E. D. Shishko R. E. Kavetsky Institute of Experimental Pathology, Oncology and Radiobiology, Ukrainian National Academy of Sciences, Kyiv, Ukraine

O. O. Shul'zhenko V. N. Bakul Institute for Superhard Materials NASU, Kiev, Ukraine

O. V. Sobol Kharkiv polytechnical institute, National Technical University, Kharkiv, Ukraine

Alexei P. Soldatkin Laboratory of Biomolecular Electronics, Institute of Molecular Biology and Genetics, National Academy of Sciences of Ukraine, Kyiv, Ukraine

Institute of High Technologies, Taras Shevchenko National University of Kyiv, Kyiv, Ukraine

Oleksandr O. Soldatkin Laboratory of Biomolecular Electronics, Institute of Molecular Biology and Genetics, National Academy of Sciences of Ukraine, Kyiv, Ukraine

Institute of High Technologies, Taras Shevchenko National University of Kyiv, Kyiv, Ukraine

V. V. Sumarokov B.Verkin Institute for Low Temperature Physics and Engineering of the National Academy of Sciences of Ukraine, Kharkov, Ukraine

Volodymyr G. Syromyatnikov Macromolecular Chemistry Department, Taras Shevchenko National University of Kyiv, Kyiv, Ukraine

Andrzej Szytuła M. Smoluchowski Institute of Physics, Jagiellonian University, Kraków, Poland

L. V. Titova Institute of General and Inorganic Chemistry of NAS of Belarus, Republic of Belarus

I. N. Torianyk Karazin Kharkiv National University, Kharkiv, Ukraine

N. A. Tregubova R. E. Kavetsky Institute of Experimental Pathology, Oncology and Radiobiology, Ukrainian National Academy of Sciences, Kyiv, Ukraine

E. K. Trunova V. I. Vernadsky Institute of General and Inorganic Chemistry NASU, Kiev, Ukraine

P. V. Turbin Karazin Kharkiv National University, Kharkiv, Ukraine

A. V. Uklein Institute of Physics NASU, Kiev, Ukraine

T. M. Ulyanova Institute of General and Inorganic Chemistry of NAS of Belarus, Republic of Belarus

V. T. Uvarov National Science Center Kharkov, Institute of Physics and Technology, National Academy of Sciences of Ukraine, Kharkov, Ukraine

Polina V. Vakuliuk Nature Department, Institute of Chemistry, National University "Kyiv-Mohyla Acadamy", Kyiv, Ukraine

P. A. Vitiaz Institute of General and Inorganic Chemistry of NAS of Belarus, Republic of Belarus

N. A. Volkova Department for Cryobiology of Reproduction System, Institute for Problems of Cryobiology and Cryomedicine, Natl. Acad. of Sci. of Ukraine, Kharkiv, Ukraine

Lyudmyla O. Vretik Macromolecular Chemistry Department, Taras Shevchenko National University of Kyiv, Kyiv, Ukraine

Alla I. Yemets Institute of Food Biotechnology and Genomics, National Academy of Sciences of Ukraine, Kyiv, Ukraine

M. Zaabat Faculty of Exact Sciences and Natural and Life Sciences, Active Devices and Materials Laboratory, Larbi Ben M'hidi University, Oum El Bouaghi, Algeria

Valentyna V. Zagniy Macromolecular Chemistry Department, Taras Shevchenko National University of Kyiv, Kyiv, Ukraine

Adriano Zecchina Department of Chemistry, NIS (Nanostructured Interfaces and Surfaces), Centre of Excellence and INSTM Centro di Riferimento, University of Torino, Torino, Italy

Eduard Zubov A. A. Galkin Donetsk Physico-Technical Institute, National Academy of Sciences of Ukraine, Donetsk, Ukraine

Part I
Nanocomposites and Nanostructures

Chapter 1
Endohedral Fullerene Complexes. Which and How Many Small Molecules Can Be Inserted into Fullerenes and a Carbon Nanotube?

Helena Dodziuk

1.1 Introduction

The discovery of C_{60} **1** [1–3] (Fig. 1.1) and its studies abound in sudden twists like a detective story. The first fullerene endohedral complexes were observed in the same year when C_{60} was discovered [4]. Few years later, an "application rush" begun with proposals of exciting, strange, and unrealized fullerene applications [5] until today. In spite of the lack of massive commercialized applications of endohedral fullerene complexes, this is a rapidly developing domain, which was recently reviewed by the groups of Cong [6], Lu [7], and Popov [8]. These reviews were almost exclusively devoted to a very specific type of the complexes, i.e., endohedral metallofullerenes (EMFs). On the other hand, our review on the endohedral fullerene complexes involving small guests and in-out isomerism in perhydrogenated fullerenes [9] published three years ago calls for an update although one of its main conclusions that, in spite of numerous claims (see, for instance, [10–14]) fullerene cages cannot serve for hydrogen storage, is valid. Therefore, this report is devoted mainly to the recent results in the modeling of the endohedral fullerenes stability.

Predicting properties of the endohedral fullerene complexes is a difficult task in view of their size and complexity. Taking into account properly dispersive interactions (describing nonbonding attraction) is a difficult task. In addition, for the polar guests there is a strong interaction of the guest with electrons of the host. Numerous calculations on the endohedral complexes involving hydrogen were published with the number of the molecules inserted into the cage ranging from 0 [15] to 28 [11, 12]. The first Cioslowski's work of 1991 [15] yielded instability of one hydrogen molecule inside C_{60} since the simple Hartree–Fock model with a very small basis set which could be applied at that time did not describe properly small but numerous stabilizing nonbonding interactions. On the other hand, simple model considerations taking into account the C_{60} diameter, van der Waals radii of the hydrogen and

H. Dodziuk (✉)
Institute of Physical Chemistry, Polish Academy of Sciences, Kasprzaka 44/52,
01-224 Warsaw, Poland
e-mail: dodziuk10@vp.pl

O. Fesenko, L. Yatsenko (eds.), *Nanocomposites, Nanophotonics, Nanobiotechnology, and Applications,* Springer Proceedings in Physics 156,
DOI 10.1007/978-3-319-06611-0_1,

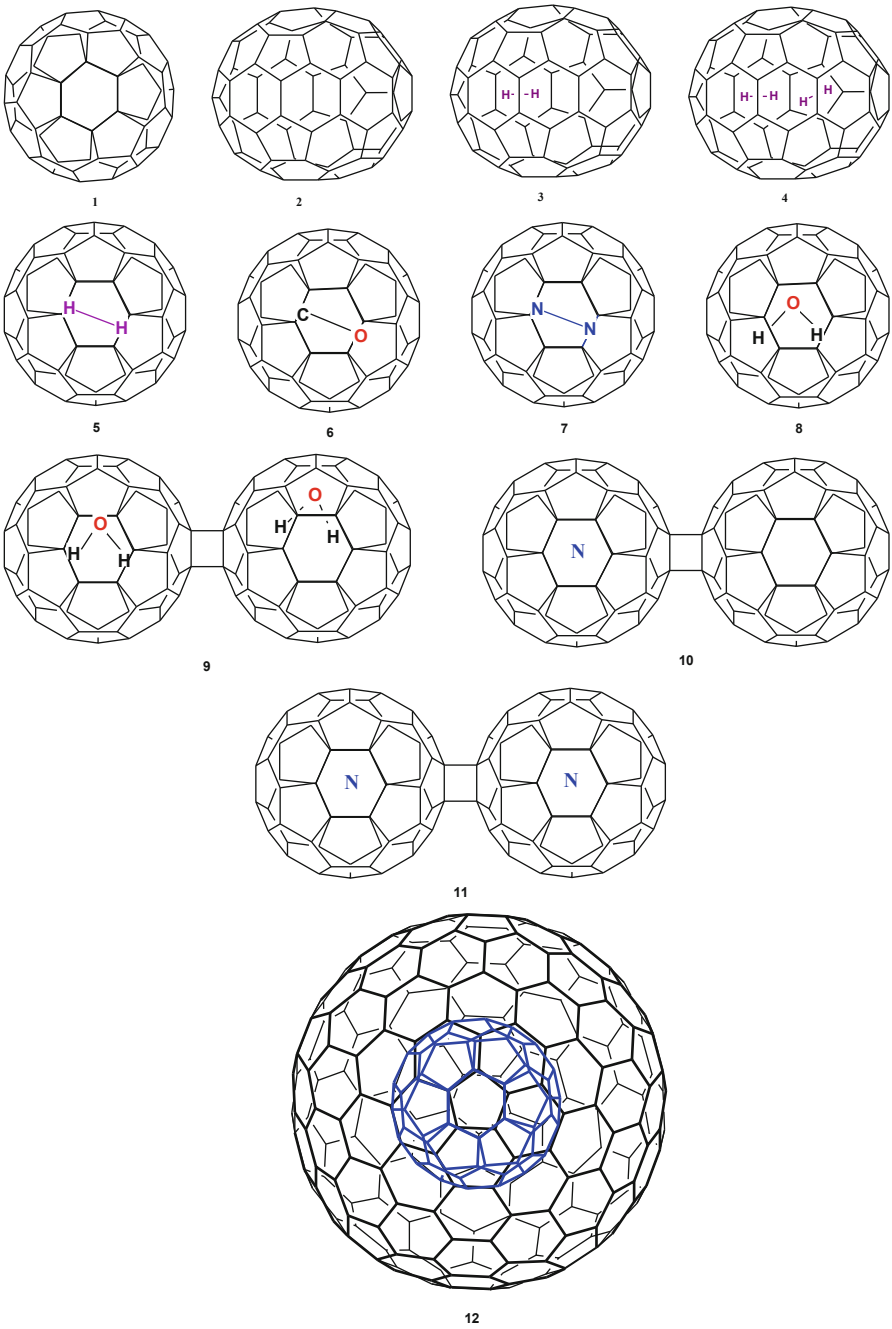

Fig. 1.1 Formulae 1–12

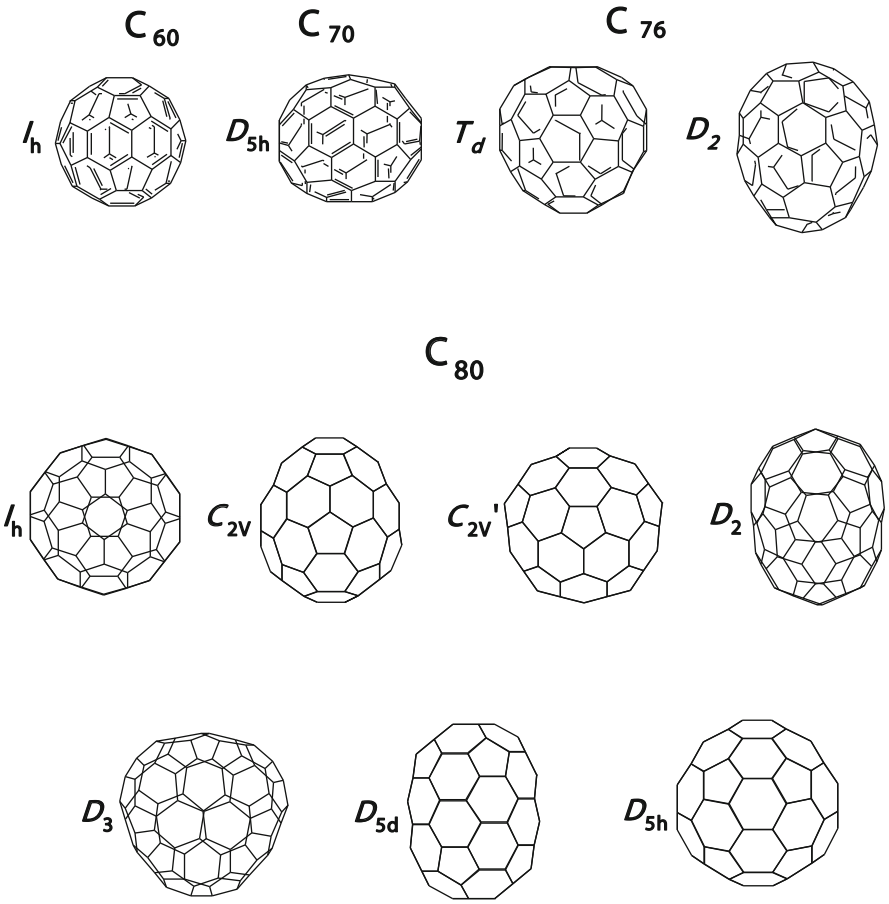

Fig. 1.2 IPR isomers of C_{60}, C_{70}, C_{76} and C_{80}

carbon atoms and H–H bond length show unequivocally that the complexes with two or more H_2 molecules inside the fullerene cannot be stabilized. On the other hand, our simple molecular mechanics calculations on the complexes formed by C_{60} **1**, C_{70} **2**, two isomers of C_{76}, five isomers of C_{78}, and 7 isomers of C_{80} [16] (see Fig. 1.2 for the formulae) with one to four hydrogen molecules inside revealed in an agreement with a later experimental finding [17] that $H_2@C_{70}$ **3** prevails in the mixture with $2H_2@C_{70}$ **4**; interestingly although partially accidentally, and experimentally determined **3**:**4** as 96:4 [17] corresponds to the earlier calculated difference of 1.8 kcal/mol [18]). The prediction of the same study that $3H_2$ molecules should be stable inside some isomers of C_{80} has not yet been proven experimentally. The symmetry adapted perturbation theory (SAPT) calculations [19, 20] for complexes involving one or two H_2 **5**, CO **6**, N_2 **7**, HCN, H_2O **8**, H_2S, CO_2, NH_3, CH_4, C_2H_2, H_2CO, and CH_3OH guest molecules in C_{60} and C_{70}, of which only few have been

detected, will be discussed and those on the recently synthesized $C_{50}H_{10}$ chair nanotube and its complexes with H_2, N_2, CO, HCN, H_2O, CO_2, CS_2, H_2S, NH_3, C_2H_2, CH_4, CH_3CN, CH_3OH, CH_3CCN, 2–butyne, methyl halides, or noble gas atoms inside [21]. In addition, the molecular dynamics simulations on the $C_{50}H_{10}$ nanotube complexes will be presented. Both methods yielded a very good agreement between the results obtained and a few available experimental data.

1.2 Nontrivial Fullerene Discovery

Science is often presented to students as a fully logical structure, impersonal, and devoid of emotions. Among other, centuries-long discussion on the nature of light, whether it consists of waves or particles in which not the facts but Newton authority was decisive for more than one hundred years, is a good example of the serendipitous development of this domain. Fullerene history is of course much shorter but it also abounds in exciting moments. A structure of such a high, I_h, symmetry was drawn by Leonardo da Vinci and Dürer ([22] and the references cited therein). Interestingly, a possibility of existence of a molecule of such a high symmetry was denied in 1945 by Herzberg [23] who was later awarded the Nobel Prize. Then, C_{60} was predicted independently in 1970 by Japanese scientists [23] and in 1973 by Russian computational chemists [24]. Next, the MS signal of C_{60} was observed and even published, but went unnoticed [25] in 1984, and a year later, Kroto, Smalley, and Curl with collaborators published their correctly interpreted observation of the strong MS C_{60} signal [3]. For this discovery, they were honoured with the Nobel Prize in 1996. Interestingly, until the Krätschmer et al. paper on fullerene purification [26], very small amount of the fullerene available for studies did not enable to prove its proposed structure. The proof came from the single ^{13}C NMR signal which was only possible for the very high symmetry of the molecule [27]. Similarly, the NMR study enabled first, although not very accurate determination of the fullerene bond lengths [28], since, in view of the tumbling of the almost spherical C_{60} at room temperature, X-ray analysis yielded only the molecular radius and the distance between the molecules in the crystal. Of course, the full X-ray structure determination at 110 K [29] yielded much more accurate values than the NMR one.

The first endohedral fullerene complex was observed very soon after the C_{60} discovery [4] (a compendium of atoms that have been inserted until 2007 is given in http://homepage.mac.com/jschrier/endofullerenes_table.html). However, similar to catenanes **13**, rotaxanes **14**, knots **15**, and Möbious strips **16** shown in Fig. 1.3, the endohedral fullerene complexes have been analyzed as objects of nontrivial topology only in the works of our group [9, 18, 30–32]. For this, the definition of molecules with nontrivial topological properties had to be extended allowing for a bond deformation only to such an extent that it does not break [30]. The endohedral fullerene complexes are the fullerenes that have atoms, ions, and molecules inside the cage. In the nomenclature used in supramolecular chemistry, the fullerene cage plays a role of the host, H, while what is inside is treated as a guest, G, and the complex is denoted as G@H. The detected complexes include not only $H_2@C_{70}$ **3**, $2H_2@C_{70}$ **4** [17], $H_2@C_{60}$ **5** [33], $HD@C_{60}$ [34], $D_2@C_{60}$ [35], $CO@C_{60}$ **6** [36], $^{13}CO@C_{60}$

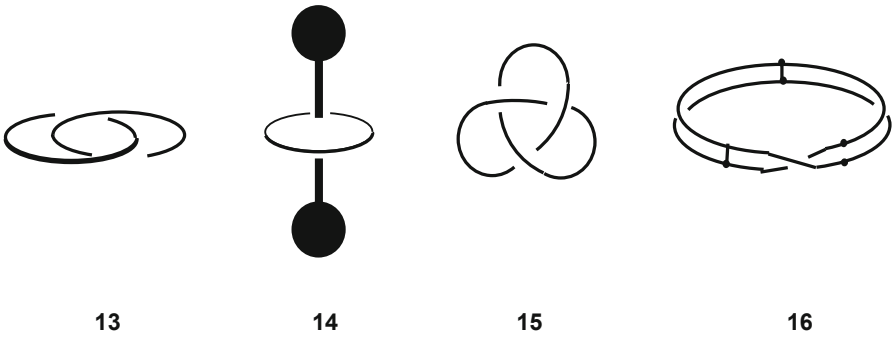

Fig. 1.3 Schematic formulae of catenane *13*, rotaxane *14*, knot *15*, and Möbius strip *16*

[37], $N_2@C_{60}$ **7** [37, 38], and $N_2@C_{70}$ [37], $H_2O@C_{60}$ **8** [39] but also $2H_2O@C_{120}$ **9** [40], two C_{60}–C_{60} dimers containing an isolated nitrogen atom like **10** [41, 42], the dimer in which each cage contains an isolated nitrogen atom have also been reported **11** [43], and an analog containing nitrogen isotopomers [44]. Specific nested (onion-like) fullerenes reported $C_{60}@C_{240}$**12**, $C_{240}@C_{540}$ and $C_{60}@C_{240}@C_{540}$ (the outer shell of the latter two were most probably incorrectly described as C_{560}) [45], while nested fullerenes with hundreds of fullerene layers were reported long before the fullerene discovery [46].

As briefly discussed in Sect. 1.5, inserting an atom, a molecule or an ion into a molecular cage can lead to spectacular changes of the host and/or guest properties. It can even stabilize a nonisolated pentagon rule (IPR) fullerene isomer [47–52] or another short-lived species [53] or change the fullerene symmetry upon the guest inclusion [54], as shown in case of $Y@C_{82}$.

It should be stressed that although C_{60} is the most common fullerene, it does not form numerous endohedral complexes because of its small internal cavity. As pointed out independently by Patchkovskii and Thiel [55] and Dodziuk et al. [16], to obtain endohedral complexes with fairly large guest molecules suitable for applications one has to master the synthesis and purification of much larger fullerenes.

The stupendous isolation of atomic nitrogen in the C_{60} cage [38, 56, 57] and in one [41, 42] or two [43] cages of the C_{60}–C_{60} dimer, H_2O without any hydrogen bonds in one C_{60} cage [39] and in each cage of the C_{60}–C_{60} dimer [40], diatomic van der Waals molecules of noble gases He_2 in the C_{60} [58] and C_{70} [58, 59] cages as well as Ne_2 in C_{70} **1** [60] and simultaneous insertion of helium and nitrogen atoms inside C_{60} and C_{70} [61] or helium and neon atoms inside C_{70} [37] illustrate radical changes in the guests' properties due to its encapsulation into the fullerene cage. Other examples of exotic, short-lived species stabilized in "molecular flasks" are briefly reviewed by Dodziuk [62, 63].

Today, the endohedral fullerene complexes are studied by several groups not only because of their exciting properties but also in view of their future applications. The applications in medicine have been reviewed by Dellinger et al. [64], Nitta group [65], and Bakry and coworkers [66]. With a metal guest, so called EMFs can be metal, small-gap semiconductors, or insulators depending upon the fullerene

size and the kind and number of encapsulated metal atoms. Interestingly, they form unusual salts since the metallic guest transfers its electron(s) to the cage. Thus, one has to destroy the cage for the salt decomposition. EMFs are applied in medicine, (among others as radiotracers [67], MRI contrast agents [68, 69], drugs [70] (in particular, HIV-1 protease inhibitors [71])) in electronics [72–76], (in particular, as single-molecule transistor for quantum computing [77–79]), in photovoltaics [80], and in the solar cells [80, 81]. Noteworthy, the application of so-called peapods that is carbon nanotubes filled with endohedral fullerenes encapsulating metal atoms in the latter devices seems promising [82].

1.3 Types of Endohedral Fullerene Complexes

As mentioned above, due to its small size only few endohedral complexes of C_{60} are known. The first observation of fullerene complexes was published as early as in 1985 [4], the same year in which C_{60} itself has been detected. Depending on the guest character, the endohedral fullerenes can have an atom(s) or molecule(s) inside their cages and the guest can be metal or not. It can even be tritium [53] or muonium [83]. A special class of the complexes are multishell-nested fullerenes that span the structures having from two [45] to even hundreds of fullerene cages buried inside one another [46].

The complexes are often so stable that they undergo several chemical reactions and their numerous derivatives have been synthesized [81, 84–88]. Noteworthy, the guest can influence the shape of the host cage. To our best knowledge, no endohedral fullerene complex with an isolated hydrogen atom as the guest has been detected. However, as mentioned earlier, Cross et al. reported a tritium guest inside C_{60} [53].

Contrary to organic molecules with distinct topological properties such as catenanes **13**, rotaxanes **14**, knots **15** and Möbius strip **16** (schematically shown in Fig. 1.2), the endohedral fullerene complexes **3–12** are not obtained by taking advantage of the preorganization phenomenon [9, 89] or dynamic covalent chemistry [90–92]. They are manufactured by applying completely different procedures. Those having metal cations inside are obtained in an arc reactor or via laser evaporation during the process of fullerene formation [93, 94], while the ones with noble gas guests are produced by heating fullerenes in the nobel gas atmosphere at high pressure using Krätschmer–Huffmann procedure [95]. The endohedral fullerene complexes of few simple molecules inside the fullerene cage were obtained mainly by so-called molecular surgery approach consisting in making a hole in the cage chemically, inserting a guest inside the cage (for instance, one [96] or two [17] hydrogen molecules), and closing the hole chemically. On the other hand, different nitride cluster fullerenes, like $Sc_3N@C_{80}$ [97], were obtained by a reactive gas addition to the cooling gas of the arc burning process [98]. It should be stressed that the main effort in studying endohedral fullerene complexes seems to be focused on group 2 and 3 metallofullerenes involving Sc, Y, La, Ca, Sr, Ba, and lanthanide (Ce–Lu) metallofullerenes [99] for which exciting applications are expected.

Few, but very exciting, proposals of application of endohedral complexes have been published soon after the C_{60} discovery [5]. One of them consisted in using

an endohedral fullerene with a door enabling the guest drug escape in appropriately controlled conditions, another in using the perfluorinated $C_{60}F_{60}$ as an ideal lubricant or the solid C_{60} with intercalated alkali metals as superconductors. None of them have been realized until now. The fall of the perfluorinated fullerene proposal was spectacular. The molecule was synthesized [100] but was unstable and on air it decomposed with the HF, the strongest acid, formation.

Few studies were devoted to the degree of isolation of the endohedral guest by the fullerene cage. Measurements of the triplet lifetime or EPR indicated that the interaction of the H_2 molecular guest with the cage walls is too weak to be determined but, on the other hand, there is a significant interaction between singlet molecular oxygen ($^1O_2$) and the incarcerated H_2 or D_2 guest [101]. A quantum chemical study by Varadvaj and Varadvaj [102] indicates that, although the guest water molecule inside the C_{60} cage does not form usual O–H. . . H hydrogen bonds, its hydrogen and oxygen atoms interact with the host carbon atoms, thus it is not fully isolated in $H_2O@C_{60}$ **8**. The recent obtaining of the latter complex [39] and that of two H_2O in both cages of the C_{60}–C_{60} dimer **9** [40] resulted in several physicochemical studies of these systems [86, 103–105]. Similarly, availability not only of the C_{60} and C_{70} complexes with H_2 but also of those with HD and D_2 allowed one to study their subtle properties [34, 106, 107]. In addition, interconversion of *para* and *ortho* H_2 inside fullerenes was demonstrated [108, 109].

Until now, very few fullerenes applications have been commercialized. The idea of using fullerenes for hydrogen storage also looked promising. However, as mentioned above placing H_2 molecules inside the cage seems impractical for such a purpose since, even if we do not bother for a moment how to put hydrogen inside, one has to destroy the cage irreversibly to release it. Some other possibilities, e.g., enhancing exohedral hydrogen binding electrochemically, or by forming composites either by placing a metal cation inside the fullerene cavity, or by coating fullerene with Ca have been proposed [110–114] but their feasibility for practical uses is still unclear.

1.3.1 Fullerenes with Noble Gas Atoms and Molecules as Guests

Individual He, Ne, Ar, and Kr atoms are inserted into C_{60} and C_{70} cages by the fullerene manufacturing in the nobel gas atmosphere [95, 115]. Interestingly, He and Kr were also detected in higher fullerenes having up to 400 carbon atoms [116]. Cross et al. studied a possibility of inserting another noble gas atom into $He@C_{60}$ [58]. The observation of two He atoms [117] inside C_{60} and two He or two Ne atoms [59] or a mixed guest $^3He^{22}Ne$ inside C_{70} at a close distance [37] raised the question of the possibility of the existence of a noble gas two-atomic molecule, Ng_2. Krapp and Frenking carried out elaborated analysis of the $Ng_2@C_{60}$ [118] using density functional theory (DFT) with BP86 functional, ab initio methods at MP2 and SCS-MP2 levels topped with the charge and energy partitioning and topological analysis of the electron density using Atoms in Molecules (AIM) method. They concluded that He_2 and Ne_2 guests in C_{60} form weakly bound van der Waals complexes and stated "The Ng–Ng and Ng–C interactions interactions could also be considered as

genuine chemical bonds". Similarly, in $Xe_2@C_{60}$ both Xe–Xe distance lower than that in Xe_2 (2.494 Å versus 2.746 Å) and the charge transfer from xenon to the cage $Xe_2^{q+}@C_{60}^{q-}$ (typical for the strong electron acceptors) indicate that the Xe–Xe bond is genuine. It remains to wait to be able to observe complexes of higher noble gases with C_{60} and study their properties.

Simultaneous insertion of helium and nitrogen atoms inside C_{60} and C_{70} [61] raises the question on the character of He to nitrogen bonding in these systems.

In addition to studies of $Ar@C_{60}$ and $Xe@C_{60}$, Amusia et al. carried out calculations of generalized oscillator strength for nested endohedral fullerenes $A@C_{N1}@C_{N2}$ with $N2 \gg N1$[119].

In general with very few exceptions, this mini review is devoted to studies of small molecules inside fullerene cages in which only stabilization energies, that is, the enthalpic increment to the complex stability is calculated. The results obtained for the complexes of noble gas atoms with the $C_{50}H_{10}$ nanotube on the basis of the SAPT calculations will be given here since they include also the entropic term and allowed Dodziuk and Korona [21] to estimate the temperature at which the complexes decompose. The negative values of interaction energy showed stabilization at $T = 0$ K due to the attractive E^2_{disp}, E^2_{ind}, and E^1_{elst} terms (Table 1.1). Further analysis including zero-point vibrational energies and entropic terms allowed them to estimate temperature for which the complex $Ng@C_{50}H_{10}$ becomes stable at 1 atm showing that the complexes with the Kr and Xe atoms as guests should be stable at room temperature. In the Scott group [120], the work is in progress to check this prediction.

1.3.2 Endohedral Metallofullerenes

EMF are endohedral fullerene complexes with metals as molecular guests. In these complexes, the metal atom looses electrons which are accepted by the fullerene cage. Thus, they represent a quite unusual group of salts since their decomposition into the cation and anion requires the cage destruction. As mentioned earlier, EMFs are most thoroughly studied endohedral fullerene complexes since they are relatively easily obtained and promise applications, among other in medicine [67–70], photovoltaic [75, 80], and electronics [72–79]. Several reviews of EMFs [6–8, 121–124] appeared. Thus, an extension covering EMF with molecular guests requires only brief update. Combining Echegoyen and coworkers [124] and Popov et al. [8] works, we divide endohedral metallofullerenes into four groups:

a. Mono–di, and trimetallic classical EMFs ($M@C_{2n}$, $M_2@C_{2n}$, $M_3@C_{2n}$, M = metal and $60 \leq 2n \geq 138$) including mainly alkali metal and alkali earth metal atom(s), transition metals, lantanides, iron, cobalt, and uranium. The largest endohedral fullerenes involved include $M@C_{94}$–C_{3v}(134) (M = Ca, Tm, Sm) [125, 126], $Sm_2@C_{104}$-D_{3d}(822) [127], the second largest dimetallofullerenes isolated to date $La_2@C_{138}$ [128] and Dy_2C_{100} and trimetallic Dy_3C_{100} [98]. Rare trimetallic EMF of $Sm_3@I_h$-C_{80} was recently detected [129].

Table 1.1 SAPT interaction energy E_{int} and its components, zero-point vibrational energies ΔZPVE, free Gibbs energy for standard conditions for the encapsulation reaction $Ng + C_{50}H_{10} \rightarrow Ng@C_{50}H_{10}$, $\Delta G_{298.15}$, thermal vibrational correction $\Delta u_{298.15}$, and estimated temperature $T_{\Delta G=0}$ for which the complex $Ng@C_{50}H_{10}$ becomes thermodynamically stable at 1 atm for the complexes of $C_{50}H_{10}$ nanotube with the noble gas guest Ng atoms at minimum geometry

Guest	E_{int}	E^1_{elst}	E^1_{exch}	E^2_{ind}	$E^2_{exch-ind}$	E^2_{disp}	$E^2_{exch-disp}$	δE_{HF}	ΔZPVE	$\Delta G_{298.15}$	$\Delta u_{298.15}$	$T_{\Delta G=0}$
He	−1.14	−0.57	2.45	−0.20	0.19	−3.07	0.20	−0.16	0.60	4.70	1.25	40
Ne	−1.83	−1.89	5.98	−2.41	2.61	−6.60	0.68	−0.20	0.25	3.69	1.54	90
Ar	−6.79	−4.01	11.12	−4.78	4.65	−15.20	1.84	−0.41	0.32	0.56	1.48	270
Kr	−8.23	−11.41	26.52	−16.96	15.46	−27.61	4.73	1.03	0.33	0.03	1.47	300
Xe	−8.72	−17.43	38.47	−30.10	26.23	−35.72	7.03	2.80	0.31	−0.32	1.49	310

All energies expressed in kcal/mol

b. Metallic carbides EMFs ($M_2C_2@C_{2n}$, and $M_3C_2@C_{2n}$, M = metal and $68 \leq 2n \geq 124$) [130–132]. Several members of the series of $Gd_2@C_{90}$ to $Gd_2@C_{124}$ were detected by mass spectrometry [133]. A carbide structure of one of them have been proven by X-ray also for $Gd_2C_2@C_{92}$-D_3(85) with non-IPR structure [133]. As with numerous other endohedral fullerenes, also in this case the guest can stabilize a non-IPR structure.
c. Metallic nitrides EMFs ($M_3N@C_{2n}$, M = metal and $68 \leq 2n \geq 96$) [124, 134–136], $Er_xSc_{3-x}N@C_{80}$ (x = 0–3) [137, 138], mixed lutetium/yttrium nitride metallofullerenes [139] and several other [140–142]. Some of them also have been proven to have non-IPR structures. Interestingly, the X-ray study of $Sc_3N@C_{78}$–D_{3h}(5) revealed that the distances between scandium and nitrogen atoms of the guest and the carbon atoms are smaller than the sums of their van der Waals radii and those of the closest cage atoms indicating that in this case there is no endohedral complex but the molecule [137]. Contrary to such a behavior, $Sc_3N@C_{80}$ forms a standard EMF with the guest rotating almost freely inside the host cage. Supramolecular structures of higher order involving fullerenes such as $Er_3N@C_{80}$ and $Sc_3N@C_{80}$ forming monolayers are very rare [143].
d. EMF metal cyanides (like $Sc_3NC@C_{80}$-I_h complex having a planar Sc_3NC endohedral cluster with a $(NC)^{3-}$trianion [144] and the $Sc_3NC@C_{78}$–C_2 complex with a non-IPR structure having adjacent five membered rings with a common bond [145]), oxides (like $M_4O_2@C_{80}$ or $M_4O_3@C_{80}$ [146], and sulfides (like large $Sc_2S@C_{2n}$ (n = 40–50 [121, 147]).
e. Methano cluster EMF $Sc_3CH@C_{80}$ [148].
f. Hetero EMFs are the endohedral complexes having one or more carbon atoms of the cage replaced by noncarbon atom, e.g., nitrogen like $M_2@C_{79}N$ (M = Y, Tb, Gd) [149, 150].

1.3.3 Fullerenes with Neutral or Slightly Polar Molecules as Guests

1.3.3.1 Simple Fullerenes with Small Non-metal Molecular Guests

In this subchapter, under simple we understand monolayer fullerenes as opposed to multilayered onion-like ones buried inside one another like **9** and **10**. As mentioned above, only few endohedral fullerenes with neutral or slightly polar small molecules (other than noble gases) as guests have been reported. They encompass $H_2@C_{60}$ **5** [96], $HD@C_{60}$ [34], $D_2@C_{60}$ [35], $H_2@C_{70}$ **3**, $2H_2@C_{70}$ **4** [17], $CO@C_{60}$ **6** [36] and $^{13}CO@C_{60}$ [37], $N_2@C_{60}$ **7** [37, 38], and $N_2@C_{70}$ [37], $H_2O@C_{60}$ **8** [39] but also $2H_2O@C_{120}$ **9** [40], two C_{60}–C_{60} dimers containing an isolated nitrogen atom like **10** [41, 42] and the dimer in which each cage contains an isolated nitrogen atom **12** [43] as well as an analog containing nitrogen isotopomers [44] and nested fullerenes like **11** discussed in Sect. 3.3.2.

On the other hand, N_2 inserted into one of the C_{60} cages of the dimer as well as two nitrogen molecules inserted into two C_{60} cages of C_{120} still await their synthesis. It should be stressed that CO and N_2 molecules have been inserted into the fullerene

cages by more standard procedures during the fullerene manufacturing while hydrogen and water [17, 39] have been put into the fullerene cages by so-called molecular surgery, that is, by chemically opening the cage, carrying out the guest insertion and chemically closing the cage. As mentioned before, this method of obtaining fullerene complexes with molecular guests has been proposed earlier independently by Patchkovskii and Thiel [55] and Dodziuk et. al. [16].

H_2 [151], HD [152] and D_2 [35, 101, 152], H_2O [153–155], CO [156, 157], N_2 [156], NH_3 [158], and CH_4 [159] have been inserted inside an "opened" fullerene, mainly C_{60}. Whether those involving ammonia and methane inside an "opened" C_{60} can be closed without losing the guest remains to be seen. The model calculations carried out in our group long ago suggested that ammonia could be slightly stabilized inside C_{60} while methane could not [16]. However, it should be stressed that once a guest "sits" inside the fullerene cavity, it can be relieved by the host bonds breaking only if the associated strain is very high.

Recently, we have carried out the SAPT [160, 161] calculations for the complexes involving one H_2 (and two H_2 molecules in C_{60} and C_{70} [20]), N_2, CO, HCN, H_2O, H_2S, CO_2, NH_3, C_2H_2, H_2CO, CH_4, and CH_3OH guest molecules in C_{60} and C_{70} [19] of which, as mentioned above, only those involving H_2, N_2, CO, and H_2O are known. Contrary to the standard DFT and some other approaches, the method applied correctly describes the dispersion contribution of the host–guest interactions. In this approach, the interaction energy between host H and guest G is defined as a difference between the calculated energy of the complex G@H and the sum of the energies of the host and guest with an additional assumption that the geometry of the host and guest do not change upon complexation.

$$E_{\text{int}} = E\,(\text{G@H}) - [E\,(\text{H}) + E\,(\text{G})] \tag{1.1}$$

In the SAPT approach, the interaction is calculated as a sum [160–163]:

$$E_{\text{int}}^{\text{SAPT}} = E_{\text{elst}}^{(1)} + E_{\text{ind}}^{(2)} + E_{\text{disp}}^{(2)} + E_{\text{exch}}^{(1)} + E_{\text{exch-ind}}^{(2)} + E_{\text{exch-ind}}^{(2)} + \delta E_{\text{HF}} \tag{1.2}$$

of the first-order electrostatics ($E_{\text{elst}}^{(1)}$), second-order induction ($E_{\text{ind}}^{(2)}$) and dispersion ($E_{\text{disp}}^{(2)}$) energies, and their exchange counterparts: first-order exchange ($E_{\text{exch}}^{(1)}$), second-order exchange-induction ($E_{\text{exch-ind}}^{(2)}$), and exchange-dispersion ($E_{\text{exch-disp}}^{(2)}$), accounting for the electron tunneling between the interacting constituent molecules and δE_{HF} describing intramolecular electron correlation accounted for by the DFT method.

As described earlier [9], the SAPT calculations for the complexes involving one [20] or two H_2 guest molecules in C_{60} and C_{70} in agreement with expectations revealed that there is place for only one hydrogen molecule inside the former fullerene cage and that, although there is place for two of them inside the latter larger cage, $H_2@C_{70}$ is considerably more stable than $2H_2@C_{70}$.

The calculated SAPT(DFT) interaction energies for a large series of C_{60} and C_{70} complexes with small molecules, parts of which have been obtained earlier either for opened or intact host cages, are given in Table 1.2, respectively. The data collected in the Table 1.2 indicate that all guests under study, except probably H_2CO, should

Table 1.2 Calculated SAPT(DFT) interaction energies in the TZVP basis set[a] for the complexes of linear, planar, and three-dimensional guests in C_{60} and C_{70} (in kcal/mol)

Guest	C_{60} host	C_{70} host
Linear guests		
H_2	−3.2[b]	−3.1
N_2	−3.8	−7.2
CO	−5.1	−7.5
HCN[c]	2.4	−9.6
HCN[d]	−1.5	Not calculated
CO_2	28.3	−7.7
C_2H_2	17.5	−5.3
Planar guests		
H_2O	−7.4	−6.7
H_2S	−7.7	−7.9
H_2CO[c]	15.6	0.4
H_2CO[d]	Not calculated	−2.1
Non-planar guests		
NH_3	−5.4	−7.4
CH_4[c]	−1.5	−5.7
CH_4[d]	−4.0	Not calculated
CH_3OH	47.8	−7.1

[a] For a few cases, the calculations were repeated in the larger def2-TZVPP basis
[b] In [18], where the better TZVPP basis has been used for this complex, the interaction energy was equal to (−4.6)–(−4.7) kcal/mol for three orientations studied, while for one orientation (the hydrogen molecule parallel to one hexagon), it was higher by 0.18 kcal/mol
[c] Calculated using TZVP basis set
[d] Calculated using def2-TZVPP basis set

be stable inside the larger cage while four complexes involving HCN, CO_2, H_2CO, and CH_3OH were not stabilized inside the smaller cage. It should be stressed that the stability of the H_2O molecule inserted into the C_{60} cage was predicted [19] before the complex was reported [39].

Typically for supramolecular complexes, the stabilization energy for some larger guests (e.g., H_2, H_2O, and N_2 or H_2O and H_2S series) is larger than for the smaller ones. Similarly for the H_2 and H_2O guests, the stabilization inside the smaller cage is larger than the larger one. The effect is easily understood by analyzing in which complexes the distances between host and guest atoms are closer to the sum of their van der Waals radii. The larger value of the stabilization energy obtained for the larger basis set (TZVP versus def2-TZVPP) is attributed to a better description of the dispersion component of the host–guest interaction. Interestingly, most complexes with the larger C_{70} cage exhibit close values of the interaction energy (-7.2 ± 0.7 kcal/mol).

At present, no reliable quantum calculations for the known endohedral complexes of the C_{60}–C_{60} dimer can be carried out. Therefore, it is not clear why the dimer with two water molecules situated in two cages could be obtained while for the nitrogen only two paramagnetic atoms [43, 44, 85], not more usual two diamagnetic N_2 molecules were observed separately in the dimer C_{60} cages.

A decomposition of the interaction energy in the complexes calculated using the SAPT method (Eq. 2) presented in Tables 1.3 and 1.4 for the complexes with C_{60} and

Table 1.3 Decomposition of the SAPT interaction energies E_{int} into components (in kcal/mol) for the complexes with C_{60}

Guest	$E_{elst}^{(1)}$	$E_{exch}^{(1)}$	$E_{ind}^{(2)}$	$E_{exch-ind}^{(2)}$	$E_{disp}^{(2)}$	$E_{exch-disp}^{(2)}$	E_1	E_2	E_{int}	E_{int}^{c}
H_2	−1.8	5.2	−0.3	1.1	−7.4	1.0	3.4	−6.6	−3.2	−3.9
N_2	−4.3	12.3	−1.0	3.7	−13.2	1.8	8.0	−11.8	−3.8	−5.1
CO	−5.7	14.7	−1.6	5.8	−15.7	2.5	9.0	−14.1	−5.1	−6.7
HCN[a]	−21.9	55.9	−23.9	20.7	−36.3	7.8	34.1	−31.7	2.4	−1.3
HCN[b]	−21.7	56.2	−26.1	21.9	−39.8	8.0	34.5	−36.0	−1.5	–
CO_2	−40.5	108.2	−45.4	43.5	−48.6	11.2	67.7	−39.4	28.3	23.4
C_2H_2	−39.9	106.5	−53.0	45.1	−53.8	12.6	66.6	−49.8	17.5	12.1
H_2O	−3.2	8.5	−4.4	2.6	−12.6	1.7	5.3	−12.7	−7.4	−8.6
H_2S	−16.8	38.4	−22.2	20.1	−34.4	7.2	21.6	−29.3	−7.7	−11.1
H_2CO	−35.5	88.6	−42.8	9.3	−43.6	10.2	53.1	−37.5	3.7	11.2
NH_3	−15.0	35.8	−20.6	18.0	−29.8	6.3	20.8	−26.2	−5.4	−8.4
CH_4[a]	−18.1	45.7	−19.9	18.8	−35.3	7.2	27.6	−29.1	−1.5	−5.0
CH_4[b]	−17.8	45.7	−19.5	18.3	−38.2	7.5	27.9	−31.9	−4.0	–
CH_3OH	−64.6	170.9	−89.4	77.3	−65.6	16.5	106.3	−58.5	47.8	41.5

E_1 and E_2 are the sums of the first-order and the second-order components, respectively

[a] calculated using the TZVP basis set,

[b] calculated using the def2-TZVPP basis set,

[c] obtained by adding 10 % of $E_{disp}^{(2)}$ to E_{int} calculated in the TZVP basis

Table 1.4 SAPT interactions energy components (in kcal/mol) for the complexes with C_{70}

Guest	$E_{elst}^{(1)}$	$E_{exch}^{(1)}$	$E_{ind}^{(2)}$	$E_{exch-ind}^{(2)}$	$E_{disp}^{(2)}$	$E_{exch-disp}^{(2)}$	E_1	E_2	E_{int}	E_{int}^{c}
H_2	−1.1	3.1	−0.78	0.6	−5.7	0.6	2.0	−5.1	−3.1	−3.7
N_2	−5.7	15.2	−4.7	4.5	−19.1	2.5	9.6	−16.8	−7.2	−9.1
CO	−6.9	17.6	−6.3	6.0	−20.8	3.0	10.7	−18.1	−7.5	−9.6
HCN	−12.6	31.5	−15.5	12.9	−31.8	5.8	18.9	−28.5	−9.6	−12.8
CO_2	−9.8	25.5	−8.9	8.2	−26.6	3.8	15.7	−23.4	−7.7	−10.4
C_2H_2	−15.3	40.1	−19.6	17.7	−34.9	6.7	24.8	−30.1	−5.3	−8.8
H_2O	−2.9	8.4	−4.5	2.8	−12.2	1.7	5.5	−12.2	−6.7	−7.9
H_2S	−15.9	36.3	−23.3	21.4	−33.5	7.0	20.4	−28.3	−7.9	−11.3
H_2CO[a]	−15.2	39.2	−22.8	21.9	−28.3	5.6	24.0	−23.6	0.4	−2.4
H_2CO[b]	−15.1	39.5	−17.5	16.2	−30.6	5.5	24.4	−26.4	−2.1	–
NH_3	−8.9	21.8	−13.0	11.1	−22.6	4.2	−20.3	−16.8	−7.4	−9.6
CH_4	−10.5	27.6	−10.8	10.3	−26.9	4.7	17.1	−22.8	−5.7	−8.4
CH_3OH	−16.6	42.6	−18.2	15.7	−37.4	6.7	26.0	−33.1	−7.1	−10.9

E_1 and E_2 are the sums of the first-order and the second-order components, respectively

[a] calculated using TZVP basis set

[b] calculated using def2-TZVPP basis set

[c] obtained by adding 10 % of $E_{disp}^{(2)}$ to E_{int} calculated in the TZVP basis

C_{70}, respectively, allowed Korona and Dodziuk to analyze the factors influencing the complexes stability. The largest stabilizing effect is due to $E^{(2)}_{\text{disp}}$ followed by $E^{(2)}_{\text{ind}}$ and $E^{(1)}{}_{\text{elst}}$ while the largest destabilization was the result of $E^{(1)}_{\text{exch}}$ followed by the $E^{(2)}_{\text{exch-ind}}$ and/or $E^{(2)}_{\text{exch-disp}}$ terms.

1.3.3.2 Nested Fullerenes and Analogous Structures

As mentioned above, nested or onion-like fullerenes are built of two or more fullerene cages buried inside one another. The number of fullerene layers in such complexes can reach several hundreds [164]. Interestingly, such structures have been discovered long before C_{60} itself [46]. Nonspheroidal nested fullerenes have also been detected [165]. On the basis of model calculations, the driving force for the formation of nested fullerenes was found to be due to small but numerous nonbonding attractions [166]. Mordkovitch reported obtaining two- and three-layered $C_{60}@C_{240}$, $C_{240}@C_{560}$ and $C_{80}@C_{240}@C_{560}$ [45]. We believe that what he really had observed were complexes **9**, **10** and $C_{80}@C_{240}@C_{540}$ involving the C_{540} cage not the C_{560} one [166].

A different, interesting type of clusters were reported in which fullerene forms the core containing multilayered metal (Ca, Sr, Ba) structures grown over a fullerene such as $C_{60}@M_{32}$, $C_{60}@M_{32}@M_{72}$, $C_{60}@M_{32}@M_{72}@M_{132}$, and $C_{60}@M_{32}@M_{72}@M_{132}@M_{212}$ [167]. In $C_{60}@M_{32}$ and $C_{70}@Ba_{37}$, in the first layer one metal atom is placed over each of the 12 pentagonal faces and 20 (or 25 for the larger cage) over the hexagonal faces.

1.4 Complexes with the $C_{50}H_{10}$ Nanotube as the Host

Recently, Scott group obtained the $C_{50}H_{10}$ nanotube [120] using a more standard synthetic method than those usually applied in fullerene and nanotube manufacturing [168, 169] and found that it forms a complex with the CS_2 molecule inside. The group was interested in finding which other molecules can be complexed with the nanotube. Therefore, we carried the SAPT calculations for the complexes with a large series of guests including H_2, N_2, CO, HCN, H_2O, CO_2, CS_2, H_2S, NH_3, C_2H_2, CH_4, CH_3CN, CH_3OH, CH_3CCN, 2–butyne, methyl halides, or noble gas atoms inside [21]. For the unsymmetrical guests, two orientations with a guest inside the cage were taken into account. For molecules with the methyl group, one such orientation has been denoted as “out”, if the methyl group is inside the hole, while the reverse orientation has been called “in”. For hydrogen cyanide and carbon monoxide, the “in” orientation has the nitrogen or carbon atom, respectively, in the $C_{50}H_{10}$ hole.

The results of the SAPT calculations for the complexes of the nanotube with noble gases have been presented in Sect. 3.1 while those with other molecular guests have been collected in Table 1.5. Interestingly, all complexes under study have been found stable at 0 K but most of them should dissociate into constituent parts at room temperature. In agreement with expectation, the largest (in absolute value) stabilizing

Table 1.5 SAPT interactions energy and its components (in kcal/mol) for the complexes with $C_{50}H_{10}$ at minimum geometries

Guest	E_{int}	$E^{(1)}_{elst}$	$E^{(1)}_{exch}$	$E^{(2)}_{ind}$	$E^{(2)}_{exch-ind}$	$E^{(2)}_{disp}$	$E^{(2)}_{exch-disp}$	ΔE_{HF}	$\Delta ZPVE$	$\Delta G_{298.15}$	$\Delta u_{298.15}$	$T_{\Delta G=0}$
H_2	−2.96	−1.31	3.93	−0.96	0.86	−6.07	0.72	−0.13	0.87	1.37	2.20	180
N_2	−6.90	−3.72	10.39	−3.43	3.28	−14.32	1.59	−0.70	0.64	2.09	2.37	220
CO (in)	−7.22	−4.52	11.49	−4.39	4.14	−15.18	1.91	−0.68	0.68	1.75	2.35	230
CO (out)	−7.18	−4.08	11.19	−3.61	3.40	−15.09	1.76	−0.75	–	–	–	–
HCN (in)	−10.19	−6.57	14.50	−6.44	5.21	−18.57	2.61	−0.93	0.72	−0.30	2.30	310
HCN (out)	−6.87	−3.14	12.53	−5.55	4.27	−16.29	2.15	−0.83	–	–	–	–
H_2O	−6.20	−2.84	8.64	−4.23	2.83	−11.96	1.66	−0.30	1.10	1.98	1.10	210
H_2S	−5.46	−11.48	29.21	−16.94	15.84	−26.30	5.15	−0.94	1.10	3.70	2.59	160
CO_2	−9.79	−5.66	12.43	−5.32	4.84	−17.52	1.94	−0.50	0.54	−0.01	2.46	300
CS_2	−12.36	−17.33	42.04	−26.15	25.45	−41.71	7.62	−1.85	0.59	−1.50	2.43	340
C_2H_2	−7.32	−6.83	20.38	−9.83	9.14	−23.34	3.95	−0.80	0.88 (0.40)	2.80 (1.63)	2.18	210
NH_3	−6.61	−6.50	16.01	−8.82	7.48	−17.26	3.00	−0.52	1.08	1.72	2.60	230
CH_4	−3.28	−6.67	19.81	−6.24	6.03	−18.14	2.92	–	−(1.26)	−(4.70)	–	–
CH_3CN (in)	−12.76	−8.88	21.17	−10.42	8.42	−25.58	3.70	−1.17	–	–	–	–
CH_3CN (out)	−10.17	−10.78	31.85	−12.81	10.53	−31.73	4.76	−2.00	–	–	–	–
CH_3OH (in)	−7.54	−6.26	17.94	−6.91	5.78	−19.60	2.73	−1.22	–	–	–	–
CH_3OH (out)	−6.32	−8.34	23.94	−9.45	8.41	−23.07	3.61	−1.44	–	–	–	–
CH_3C_2H (in)	−9.89	−7.87	23.06	−12.05	11.34	−27.98	4.56	−0.94	0.76	0.44	2.87	280
CH_3C_2H (out)	−8.94	−8.86	24.19	−9.06	8.24	−25.68	3.86	−1.62	–	–	–	–
$CH_3C_2CH_3$	−9.90	−8.34	27.06	−10.90	9.98	−30.82	4.73	−1.61	–	–	–	–
CH_3F (in)	−8.52	−6.51	15.69	−4.89	4.11	−18.34	2.28	−0.87	–	–	–	–
CH_3F (out)	−4.19	−7.70	22.45	−8.635	7.99	−19.85	3.02	−1.47	–	–	–	–
CH_3Cl (in)	−9.37	−8.36	21.07	−10.33	9.67	−24.34	3.75	−0.83	–	–	–	–
CH_3Cl (out)	−8.16	−6.81	17.30	−7.00	6.28	−19.36	2.60	−1.17	–	–	–	–
CH_3Br (in)	−9.67	−14.35	34.27	−22.08	21.21	−33.90	6.32	−1.14	0.76	0.44	2.87	280
CH_3Br (out)	−9.52	−7.37	18.78	−8.44	7.59	−21.73	2.91	−1.26	–	–	–	–
CH_3I (in)	−14.90	−13.76	26.72	−23.71	21.06	−31.56	5.93	0.42	–	–	–	–
CH_3I (out)	−10.87	−8.46	20.55	−10.68	8.72	−24.32	3.32	0.00	–	–	–	–

term is $E^{(2)}_{disp}$ and the largest destabilizing one is $E^{(1)}_{exch}$. The estimation of temperature at which the Gibbs free energy G = 0 revealed that only the complexes with CS_2, HCN, Xe, and CO_2 are stable at room temperature. The former recently obtained complex, $CS_2@C_{50}H_{10}$ [120], is the most stable "surviving" up to 340 K, while the corresponding complexes with HCN and Xe guests should decompose at ca. 310 K and the one with CO_2 at ca. 300 K.

The molecular dynamics (MD) simulations (described in [21]) showed the complex decomposition at ca. 350 K. The calculations in $CHCl_3$ solution yielded an energy minimum of −12.7 kcal/mol at about 3 Å separation between the CS_2 and the nanotube centers of mass indicates that the guest molecule should have a definite tendency to remain inside the nanocage. It should be stressed that the MD value is in a very good agreement with −12.36 kcal/mol one obtained by the SAPT(DFT) calculations (Table 1.5). The simulations showed that the presence of $CHCl_3$ solvent stabilizes the $CS_2@C_{50}H_{10}$ complex in comparison to vacuum. Thus, for the complexes obtained in solution the CO_2 gas responsible for the greenhouse effect could probably be stored in the $C_{50}H_{10}$ nanotube.

1.5 Exciting Properties of Endohedral Fullerene Complexes

Inserting one or more guests into a fullerene can significantly change their properties. For instance, in nature, noble gases exist as a single atom species but He_2 in C_{60} [170] and Ne_2 in C_{70} [60] have been reported as the weakly bonded van der Waals diatomic molecules of noble gases. On the other hand, nitrogen usually present in the form of a diatomic molecule was found as a monoatomic nitrogen radical inside C_{60}, C_{70},and C_{120} dimers [38, 41, 56, 171, 172] and in the $C_{61}(COOC_2H_5)_2$, $C_{66}(COOC_2H_5)_{12}$, $C_{66}(COOC_2D_5)_{12}$, $C_{61}(COOC_2D_5)_2$ cages [171].

The complexes involving an isolated, paramagnetic nitrogen atom inside a fullerene cage are so exotic that they will be mentioned here, in spite of the fact that the guests in these cases are not molecular. The nitrogen atom as monoatomic radical has been found in both C_{60} and C_{70} as well as in four C_{60} adducts [38, 56, 57, 171–174]. Interestingly, the $N@C_{60}$ complex is so stable at ambient conditions that it does not decompose during exohedral addition reactions. Proving its radical character, it produces so characteristic, very clear hyperfine split EPR signal with sharp lines even in the solid state that it has been proposed as an ideal probe for monitoring chemical reactions of C_{60} via changes of the signal [56]. The effect of cage variation in the series $N@C_{60}$, $N@C_{61}(COOC_2H_5)_2$, $N@C_{66}(COOC_2H_5)_{12}$, $N@C_{66}(COOC_2D_5)_{12}$, $N@C_{61}(COOC_2D_5)_2$ [171], and $N@C_{70}$ exemplifies this. The nanomagnet formed by an isolated nitrogen atom and fullerene was proposed to be applied in novel devices for high-density information storage and quantum-state control [175]. Similarly, due to the spin to charge conversion in thin $N@C_{60}$ films at room temperature, the possibility of application of these endohedral fullerene spin qubits has been proposed [176]. In addition, two C_{60}–C_{60} dimers containing an isolated nitrogen atom were also detected [41, 42] in which only one of the connected C_{60} cages is filled. The dimer **11** in which both cages contain isotopomers of an isolated nitrogen atom have also been reported [43, 44, 85]).

"Empty" C_{2n} fullerenes are known to obey the IPR stating that the most stable are those in which pentagons do not share any common atom. This rule holds for empty fullerene cages larger than C_{60} since there are no IPR structures for fullerenes smaller than this cage. There is only one IPR isomer for C_{60} and C_{70}, but the number of isomers increases rapidly with the increase of the cage. The IPR rule limits the number of fullerene structures. It can be shown that there are only 450 IPR isomers of C_{100} while the number of all possible isomers (enantiomers excluded) for this cage molecule equals 285,913 [177]. However, a guest can invalidate this rule and several stable non-IPR endohedral fullerene isomers [47–51, 99] have been observed. Interestingly, as shown, for instance, in case of $Y@C_{82}$ the cage symmetry can change upon the guest inclusion [54].

In agreement with the "induced fit" mechanism [178], not only are the non-IPR isomers $Sc_2@C_{66}$ [50] and $Sc_3N@C_{68}$ [99] stable but they were also isolated although neither the C_{66} and C_{68} hosts nor the scandium guests are stable molecules.

One of the most interesting problems in the structure of fullerene complexes is whether there is a bonding of included atom(s) or molecule(s) to the cage. A covalent bond between the C_{66} cage and the endohedral scandium dimer creates a molecule with exciting but topologically trivial structure [50]. Similarly, $Sc_3N@C_{78}$ does not represent a "real" endohedral complex since there is a considerable bonding between three Sc and cage carbon atoms [137], whereas in the $Sc_3N@C_{80}$ complex, the nonbonded guest rotates freely inside the cage. Analogously, in $La_2@I_h$–C_{80} [179] and $Ce_2@I_h$–C_{80} complexes, the guests do not occupy specific positions but circulate three-dimentionally executing large amplitude movements [123]. Such a movement was also documented in $Sc_3N@C_{80}$ and in $Yb@C_{74}$ [180].

Fullerenes act as the Faraday cage isolating the guest from the outside and/or suppressing the influence of the guest on the whole system [181–183]. The DFT calculations of the electronic structure and static dipole polarizability of $C_{60}@C_{240}$ **12** have shown practically identical values of dipole polarizability of the complex and that of the isolated C_{240} (449 $Å^3$ versus 441 $Å^3$). This means that the outer cage effectively shields the inner one [183].

Interestingly, at low temperatures, hydrogen molecules can exist in form of *para*- and *ortho*-allotropes, which interconvert when H_2 is immersed inside C_{60} [108].

Formation of a topological nontrivial system can change its properties as compared with the nontrivial one. These changes are less pronounced for catenanes **13**, rotaxanes **14**, and knots **15** than for molecules that are endohedral complexes of cage compounds such as endohedral fullerene complexes. The former ones are characterized by a considerable restriction of molecular dynamics characterized by worm-like movement of knots [184] or dynamical behaviour of catenanes and rotaxanes [185]. Such properties and their manifestations in NMR spectra are presented in a very detailed review, mainly based on the Stoddart group works [186].

Endohedral fullerene complexes exhibit a very strong sensitivity of the NMR signals of their host and guest to the charge distribution enabling isomers identification [187], probing fullerene reactivity [188] and internal magnetic field in the cage [170] or its aromaticity [189].

1.6 Conclusions

Endohedral fullerene complexes are fascinating objects promising at long-run numerous applications. The results presented in this mini review indicate that the modeling of endohedral fullerene complexes, when applied cautiously, can provide valuable information on their stability. On the other hand, the literature data [10–14] show several examples of erroneous results on the stability of the complexes, especially those with the hydrogen guest.

References

1. Kroto HW (1997) Symmetry, space, stars, and C_{60} (Nobel lecture). Angew Chem Int Ed 36:1579–1593
2. Kroto HW (1992) C_{60}: buckminsterfullerene, the celestial sphere that fell to earth. Angew Chem Int Ed 31:111–129
3. Kroto HW, Heath JR, O'Brien SC, Curl RF, Smalley RE (1985) C_{60}: buckminsterfullerene. Nature 318:162–163 doi:10.1038/318162a0
4. Heath JR, O'Brien SC, Zhang Q, Liu Y, Curl RF, Kroto HW, Tittel FK, Smalley RE (1985) Lanthanum complexes of spheroidal carbon shells. J Am Chem Soc 107:7779–7780
5. Stoddart JF (1991) The third allotropic form of carbon. Angew Chem Int Ed Engl 30:70–71
6. Cong H, Yu B, Akasaka T, Lu X. (2013) Endohedral metallofullerenes: an unconventional core -shell coordination union. Coord Chem Rev 257:2880–2898
7. Lu X, Feng L, Akasaka T, Nagase S (2012) Current status and future developments of endohedral metallofullerenes. Chem Soc Rev 41:7723–7760
8. Popov AA, Yang S, Dunsch L (2013) Endohedral fullerenes. Chem Rev 113:5989–6113
9. Dodziuk H (2011) Endohedral fullerene complexes and in-out isomerism in perhydrogenated fullerenes. Why the carbon cages cannot be used as the hydrogen containers? In: Graovac A, Ori O, Cataldo F (eds) Mathematics and topology of fullerenes. Springer, Hamburg, pp 117–151
10. Pupysheva OV, Farajian AA, Yakobson BI (2008) Fullerene nanocage capacity for hydrogen storage. Nano Lett 8:767–774
11. Yang C-K (2007) Density functional calculation of hydrogen-filled C_{60} molecules. Carbon 45:2451–2453
12. Yang C-K (2008) Reply to the commentary on "density functional calculation of hydrogen-filled C_{60} molecules". Carbon 46:705–705
13. Turker L, Erkoc S (2003) AM1 treatment of endohedrally hydrogen doped fullerene, $nH_2@C_{60}$. J Mol Struct 638:37–40
14. Turker L, Erkoc S (2006) Comment on "Modeling complexes of H2 molecules in fullerenes" by H. Dodziuk. Chem Phys Lett 426:222–223
15. Cioslowski J (1991) Endohedral chemistry: electronic structures of molecules trapped inside the C_{60} cage. J Am Chem Soc 113:4139–4141
16. Dodziuk H, Dolgonos G, Lukin O (2001) Molecular mechanics study of endohedral fullerene complexes with small molecules. Carbon 39:1907–1911
17. Murata M, Maeda S, Morinaka Y, Murata Y, Komatsu K (2008) Synthesis and reaction of fullerene C_{70} encapsulating two molecules of H_2. J Am Chem Soc 130:15800–15801
18. Dodziuk H. (2005) Modeling complexes of H_2 molecules in fullerenes. Chem Phys Lett 410:39–41
19. Korona T, Dodziuk H (2011) Small molecules in C_{60} and C_{70}. Which complexes could be stabilized? J Chem Theory Comp 7:1476-1483. dx.doi.org/10.1021/ct200111a

20. Korona T, Hesselmann M, Dodziuk H (2009) Symmetry-adapted perturbation theory applied to endohedral fullerene complexes: a stability study of $H_2@C_{60}$ and $2H_2@C_{60}$. J Chem Theory Comp 5:1585–1596
21. Dodziuk H, Korona T, Lomba E, Bores CJ (2012) A carbon nanotube container: complexes of C50H10 with small molecules. Chem. Theor. Comp. 8:4546–4555
22. Dresselhaus MS, Dresselhaus G, Eklund PC, P. C (1995) Science of fullerenes and carbon nanotubes. Academic, San Diego, pp. 1–2
23. Herzberg G (1945) Infrared and Raman spectra of polyatomic molecules. Lancaster Press, Lancaster, p. 12
24. Botchvar DE, Galpern EG (1973) About hypothetical systems: carbododecahedron, s-icosaedron and carbo-s-icosaedron (in Russian). Dokl. AN SSSR 209:610
25. Rohlfing EA, Cox DM, Kaldor A (1984) Production and characterization of supersonic carbon cluster beams. J Chem Phys 81:3322
26. Krätschmer W, Fostiropoulos K, Huffmann DR (1990) The infrared and ultraviolet absorption spectra of laboratory-produced carbon dust: evidence for the presence of the C_{60} molecule. Chem Phys Lett 170:167
27. Taylor R, Hare JP, Abdul-Sada AK, Kroto HW (1990) Isolation, separation and characterisation of the fullerenes C_{60} and C_{70}: the third form of carbon. Chem Commun 20:1423–1425
28. Yannoni CS, Bernier PP, Meier G, Salem JR (1991) NMR determination of the bond lengths in C_{60}. J Am Chem Soc 113:3190–3192
29. Liu S, Lu YJ, Kappes MM, Ibers JA (1991) The structure of the C_{60} molecule-X-ray crystal structure determination of a twin at 110K. Science 254(5030):408–410
30. Dodziuk H, Nowinski KS (1998) 'In'-'out' topological isomerism. Should rotaxanes and endohedral fullerene complexes be involved? Tetrahedron 54:2917–2930
31. Dodziuk H, Nowinski KS (1996) Horror vacui or topological in-out isomerism in perhydrogenated fullerenes. Part 1. $C_{60}H60$ and monoalkylated perhydrogenated fullerenes. Chem Phys Lett 249:406–412
32. Dodziuk H (2007) Modeling the structure of fullerenes and their endohedral complexes involving small molecules with nontrivial topological properties. J Nanosci Nanotechnol 7:1102–1110
33. Komatsu K, Murata M, Murata Y (2005) Encapsulation of molecular hydrogen in fullerene C_{60} by organic synthesis. Science 307:238–240
34. Ge M, Nagel U, Hüvonen D, Room T, Mamone S, Levitt MH, Carravetta M, Murata Y, Komatsu K, Lei X, Turro NJ (2011) Interaction potential and infrared absorption of endohedral H_2 in C_{60}. J Chem Phys 135:114511
35. Tanabe F, Murata M, Murata Y, Komatsu K (2006) Nippon Kagakkai Koen Yokoshu 86:1282
36. Holleman I, Robyr P, Kentgens APM, Meier BH, Meijer G (1999) Motion of CO molecules in solid C_{60} probed by solid-state NMR. J Am Chem Soc 121:199–207
37. Peres T, Cao BP, Cui WD, Lifshitz C, Khong A, Cross RJ, Saunders M (2001) Some new diatomic molecule containing endohedral fullerenes. Int J Mass Spectr 210:241–247
38. Suetsuna T, Dragoe N, Harneit W, Weidinger A, Shimotani S, Ito S, Takagi H, Kitazawa K (2002) Separation of $N_2@C_{60}$ and $N@C_{60}$. Chem Eur J 8:5079–5083
39. Kurotobi K, Murata Y (2011) A single molecule of water encapsulated in fullerene C_{60}. Science 333:613–616
40. Zhang R, Murata M, Wakamiya A, Murata Y (2013) Synthesis and X-ray structure of endohedral fullerene C_{60} dimer encapsulating a water molecule in each C_{60} cage. Chem Lett 42:879–881
41. Goedde B, Waiblinger M, Jakes P, Weiden N, Dinse KP, Weidinger A (2001) "Nitrogen doped" C_{60} dimers ($N@C_{60}$ -C_{60}). Chem Phys Lett 334:12–17
42. Zhang J, Porfyrakis K, Morton JJL, Sambrook MR, Harmer J, Xiao L, Ardavan A, Briggs GAD (2008) Photoisomerization of a fullerene dimer. J Phys Chem C 112:2802–2804
43. Farrington BJ, Jevric M, Rance GA, Ardavan A, Khlobystov AN, Briggs GAD, Porfyrakis K (2012)Chemistry at the nanoscale: synthesis of an $N@C_{60}$-$N@C_{60}$ endohedral fullerene dimer. Angew Chem Int Ed 51:3587–3590

44. Plant SR, Jevric M, Morton JJL, Ardavan A, Khlobystov AN, Briggs GAD, Porfyrakis K (2013) A two-step approach to the synthesis of N@C_{60} fullerene dimers for molecular qubits. Chem Sci 4 :2971–2975
45. Mordkovich VZ (2000) The observation of large concentric shell fullerenes and fullerene-like nanoparticles in laser pyrolysis carbon blacks. Chem Mater 12:2813
46. Iijima S (1980) Direct observation of the tetrahedral bonding in graphitized carbon black by high resolution electron microscopy. J Cryst Growth 50:675
47. Tan Y-Z, Xie ST, Huang RB, Zheng LS (2009) The stabilization of fused-pentagon fullerene molecules. Nature Chem 1:450–460
48. Shustova NB, Popov AA, Newell BS, Miller SM, Anderson OP, Seppelt K, Bolskar RD, Boltalina OV, Strauss SH (2007) Discovering and verifying elusive fullerene cage isomers: structures of C_2-p^{11}-(C_{74}-D_{3h})(CF_3)$_{12}$ and C_2-p^{11}-(C_{78}-D_{3h})(CF_3)$_{12}$. Angew Chem Int Ed 46:4111–4114
49. Rapta P, Popov AA, Yang S, Dunsch L (2008) Charged states of $Sc_3N@C_{68}$: an in situ spectroelectrochemical study of the radical cation and radical anion of a non-IPR fullerene. J Phys Chem A 112:5858–5865
50. Takata M, Nishibori E, Sakata M, Wang CR, Shinohara H (2003) Sc_2 dimer in IPR-violated C_{66} fullerene: a covalent bonded metallofullerene. Chem Phys Lett 372:512–518
51. Shi ZQ, Wu X, Wang CR, Lu X, Shinohara H (2006) Isolation and characterization of $Sc_2C_2@C_{68}$: a metal-carbide endofullerene with a non-IPR carbon cage. Angew Chem Int Ed 45:2107–2111
52. Yang SF, Popov AA, Dunsch L (2007) Violating the isolated pentagon rule (IPR): the endohedral non-IPR C_{70} cage of $Sc_3N@C_{70}$. Angew Chem Int Ed 46:1256–1259
53. Jimenez-Vazquez HA, Cross RJ, Saunders M, Poreda RJ (1994) Hot-atom incorporation of tritium atoms into fullerenes. Chem Phys Lett 229:111–114
54. Takata M, Umeda B, Nishibori E, Sakata M, Saito Z, Ohno M, Shinohara H (1995) Confirmation by X-ray diffraction of the endohedral nature of the metallofullerene Y@C_{82}. Nature 377:46
55. Patchkovskii S, Thiel WJ (1996) How does helium get into buckminsterfullerene? Am Chem Soc 118:7164
56. Pietzak B, Waiblinger M, Murphy TA, Weidinger A, Hohne M, Dietel E, Hirsch A (1998) Properties of endohedral N@C_{60} carbon. Carbon 36:613–615
57. Jakes P, Weiden N, Eichel RA, Gembus A, Dinse KP, Meyer C, Harneit W, Weidinger AJ (2002) Electron paramagnetic resonance investigation of endohedral fullerenes N@C_{70} in a liquid crystal. Magn Res 156:303–308
58. Giblin DE, Gross ML, Saunders M, Jiménez-Vázquez H, Cross RJ (1997) Incorporation of helium into endohedral complexes of C_{60} and C_{70} containing noble-gas atoms: a tandem mass spectrometry study. J Am Chem Soc 119:9883–9890 doi: 10.1021/ja9711041
59. Khong A, Jiménez-Vázquez HA, Saunders M, Cross RJ, Laskin J, Peres T, Lifshitz C, Strongin R, Smith AB (1998) An NMR study of He_2 inside C_{70}. J Am Chem Soc 120:6380–6383
60. Laskin J, Peres T, Lifshitz C, Saunders M, Cross RJ, Khong A (1998) An artificial molecule of Ne_2 inside C_{70}. Chem Phys Lett 285:7
61. Morinaka Y, Sato S, Wakamiya A, Nikawa H, Mizorogi N, Fumiyuki T, Murata M, Komatsu K, Furukawa K, Kato T, Nagase S, Akasaka T, Murata Y (2013) X-ray observation of a helium atom and placing a nitrogen atom inside He@ C_{60} and He@C_{70}. Nat Commun 4 art:1554, doi:10.1038/ncomms2574
62. Dodziuk H (2002) Among synthetic, supramolecular and theoretical chemistry: stabilization of short-lived species in "molecular" or "supramolecular flasks". Int J Molec Sci 3:814–821
63. Dodziuk H (2009) Strained hydrocarbons: beyond the van't Hoff and Le Bel hypothesis. Wiley-VCH, Weinheim, pp 449–458
64. Dellinger A, Zhou ZG, Connor J, Madhankumar AB, Pamujula S, Sayes CM, Kepley CL (2013) Application of fullerenes in nanomedicine: an update. Nanomedicine 8:1191–1208
65. Nitta N, Seko A, Sonoda A, Ohta S, Tanaka T, Takahashi M, Murata K, Takemura S, Sakamoto T, Tabata Y (2008) Is the use of fullerene in photodynamic therapy effective for atherosclerosis? Cardiovasc Intervent Rad 31:359–366

66. Bakry R, Vallant RM, Najam-ul-Haq M, Rainer M, Szabo Z, Huck CW, Bonn GK (2007) Medicinal applications of fullerenes. Int J Nanomed 2:639–649
67. Cagle DW, Kennel SJ, Mirzadeh S, Alford JM, Wilson LJ (1999) In vivo studies of fullerene-based materials using endohedral metallofullerene radiotracers. Proc Natl Acad Sci U S A 96:5182–5187
68. Bolskar RD (2008) Medicinal applications of fullerenes. Nanomedicine 3:201–213
69. MacFarland DK, Walker KL, Lenk RP, Wilson SR, Kumar K, Kepley CL, Garbow JR (2008) Hydrochalarones: a novel endohedral metallofullerene platform for enhancing magnetic resonance imaging contrast. J Med Chem 51:3681–3683
70. Wilson LJ, Cagle DW, Thrash TP, Kennel SJ, Mirzadeh S, Alford JM, Ehrhardt GJ (1999) Metallofullerene drug design. Coord Chem Rev 192:199–207
71. Ibrahim M, Saleh NA, Elshemey WM, Elsayed AA (2010) Computational notes on fullerene based system as HIV-1 protease inhibitors. J Comput Theor Nanos 7:224–227
72. Kobayashi S, Mori S, Iida S, Ando H, Takenobu T, Taguchi Y, Fujiwara A, Taninaka A, Shinohara H, Yoshihiro IJ (2003) Conductivity and field effect transistor of $La_2@C_{80}$ metallofullerene. Am Chem Soc 125:8116–8117
73. Shibata K, Kubozono Y, Kanbara T, Hosokawa T, Fujiwara A, Ito. Y, Shinohara H (2004) Fabrication and characteristics of C_{84} fullerene field-effect transistor. Appl Phys Lett 84:2572–2574
74. Yasutake Y, Shi ZJ, Okazaki T, Shinohara H, Majima Y (2005) Single molecular orientation switching of an endohedral metallofullerene. Nano Lett 5:1057–1060
75. Ross RB, Cardona CM, Swain FB, Guldi DM, Sankaranarayanan SG, Van Keuren E, Holloway BC, Drees M (2009) Tuning conversion efficiency in metallo endohedral fullerene-based organic photovoltaic devices. Adv Funct Mat 19:2332–2337
76. Dao TT, Matsushima T, Murata H (2012) Highly stable fullerene memory transistors with an electron-trapping polymer. Org Electronics 2012 13:2709–2715
77. Benjamin SC, Ardavan AQ, Briggs GAD, Britz DA, Gunlycke D, Jefferson JH, Jones MAG, Leigh DF, Lovett BW, Khlobystov AN, Lyon S, Morton JJL, Porfyrakis K, Sambrook MR, Tyryshkin AM (2006) Towards a fullerene-based quantum computer. J Phys Condens Matter 18:S867–S883
78. Harneit W, Meyer C, Weidinger A, Suter D, Twamley J (2002) Quantum computer based on endohedral fullerenes. Phys. Stat. Solid. B 233:453
79. Twamley J (2003) Quantum-cellular-automata quantum computing with endohedral fullerenes. Phys Rev A 67 art no. 052318
80. Morinaka Y, Nobori M, Murata M, Wakamiya A, Sagawa T, Yoshikawa S, Murata Y (2013) Synthesis and photovoltaic properties of acceptor materials based on the dimerization of fullerene C_{60} for use in efficient polymer solar cells. Chem Commun 49:3670–3672
81. Li X, Zhang W, Wu Y, Mina C, Fang J (2013) Controllable threshold voltage of a pentacene field-effect transistor based on a double-dielectric structure. J Mater Chem1:12413–12416
82. Kurokawa Y, Ohno Y, Shimada T, Ishida M, Kishimoto S, Okazaki T, Shinohara H, Mizutani T, Jap J (2005) Fabrication and characterization of peapod field-effect transistors using peapods synthesized directly on Si substrate. Appl Phys Part 2 44:L1341–L1343
83. Prassides K, Dennis TJS, Christides C, Roduner E, Kroto HW, Taylor R, Walton DMR (1992) $Mu@C_{70}$: monitoring the dynamics of fullerenes from inside the cage. J Phys Chem 96:10600
84. Komatsu K, Murata YJ (2004) Synthesis of fullerene derivatives with novel structures -liquid-phase versus solid-state reactions. Synth Org Chem Jpn 62:1138–1147
85. Hormann F, Hirsch A, Porfyrakis K, Briggs GAD (2011) Synthesis and magnetic properties of a nitrogen-containing fullerene dimer. Eur J Org Chem 117–121.
86. Li Y, Chen JY-C, Lei X, Lawler RG, Murata Y, Komatsu K, Turro NJ (2012) Comparison of nuclear spin relaxation of $H_2O@C_{60}$ and $H_2@C_{60}$ and their nitroxide derivatives. J Phys Chem Lett 3:1165–1168
87. Li Y, Lei X, Lawler RG, Murata Y, Komatsu K, Turro NJ (2011) Synthesis and characterization of bispyrrolidine derivatives of $H_2@C_{60}$: differentiation of isomers using ^{1}H NMR spectroscopy of endohedral H_2. Chem Commun 47:2282–2284

88. Cardona CM, Kitaygorodskiy A, Ortiz AL, Herranz MA, Echegoyen L (2005) The first fulleropyrrolidine derivative of $Sc_3N@C_{80}$: pronounced chemical shift differences of the geminal protons on the pyrrolidine ring. J Org Chem 70:5092–5097
89. Dodziuk H (2002) In Introduction to supramolecular chemistry; Kluwer: Dordrecht, pp 27-39, 275–284
90. Haussmann PC, Stoddart JF (2009) Synthesizing interlocked molecules dynamically. Chem Rec 9:136–154
91. Stoddart JF (2009) The chemistry of the mechanical bond. Chem Soc Rev 38:1802–1820
92. Rowan SJ, Cantrill SJ, Cousins GRL, Sanders JKM, Stoddart JF (2002) Dynamic covalent chemistry. Angew Chem Int Ed Engl 41:898–952
93. Nishibori E, Narioka S, Takata M, Sakata M, Inoue T, Shinohara H Jap J (2006) A C_2 molecule entrapped in the pentagonal-dodecahedral Y_2 cage in $Y_2C_2@C_{82}$(III). Appl Phys Part 1 46:881–891
94. Nishibori E, Narioka S, Takata M, Sakata M, Inoue T, Shinohara H (2006) A C_2 molecule entrapped in the pentagonal-dodecahedral Y_2 cage in $Y_2C_2@C_{82}$(III). ChemPhysChem 7:345–348
95. Saunders M, Cross RJ, Shimshi R, Jimenez-Vazquez HA, Khong A (1996) Noble gas atoms inside fullerenes. Science 271:1693–1697
96. Komatsu K, Murata M, Murata Y (2005) In: Kuzmany H (ed) XIX international winterschool on electronic properties of novel materials. Kirchberg, Tirol
97. Cai T, Xu L, Gibson HW, Dorn HC, Chancellor CJ, Olmstead MM, Balch AL (2007) $Sc_3N@C_{78}$: encapsulated cluster regio-control of adduct docking on an ellipsoidal metallofullerene sphere. J Am Chem Soc 129:10795–10800
98. Yang SF, Dunsch L (2006) Di- and tridysprosium endohedral metallofullerenes with cages from C_{94} to C_{100}. Angew Chem Int Ed 45:1299–1302
99. Stevenson S, Fowler PW, Heine T, Duchamp JC, Rice G, Glass T, Harich K, Hajdu E, Bible R, Dorn HC (2000) A stable non-classical metallofullerene family. Nature 408:427–428
100. Taylor R, Avent AG, Dennis TJ, Hare JP, Kroto HW, Holloway JH, Hope EG, Langley GJ (1992) No lubricants from fluorinated C_{60}. Nature 355:27
101. Lopez-Gejo J, Marti AA, Ruzzi M, Jockush S, Komatsu K, Tanabe F, Murata Y, Turro NJ (2007) Can H_2 inside C_{60} communicate with the outside world? J Am Chem Soc 129:14554
102. Varadwaj AVaradwaj PR (2012) Can a single molecule of water be completely isolated within the subnano-space inside the fullerene C_{60} cage? A quantum chemical prospective. Chem Eur J 18:15345–15360
103. Beduz C, Carravetta M, Chen J, Concistre M, Denning M, Frunzi M, Horsewill AJ, Johannessen O, Lawler R, Lei X, Levitt MH, Li Y, Mamone S, Murata Y, Nagel U, Nishida T, Ollivier J, Rols S, Room T, Sarkar R, Turro NJ, Yang Y (2012) Quantum rotation of ortho and para-water encapsulated in a fullerene cage. Proc Natl Acad Sci U S A 109:12894–12898
104. Concistre M, Mamone S, Denning M, Pileo G, Lei S, Li Y, Carravetta M, Turro NJ, Levitt MH (2013) Anisotropic nuclear spin interactions in $H_2O@C_{60}$ determined by solid-state NMR. Phil Trans R Soc A 371:20120102
105. Chen JY-C, Li Y, Frunzi M, Lei X, Murata Y, Lawler RG, Turro NJ (2013) Phil Trans R Soc A 371:20110628
106. Room T, Peedu L, Ge M, Hüvonen D, Nagel U, Ye S, Xu M, Bacic Z, Mamone S, Levitt MH, Carravetta M, Chen J, Lei X, Turro NJ, Murata Y, Komatsu K (2013) Recognition of hydrogen isotopomers by an open-cage fullerene. Phil Trans R Soc A 371:20110631
107. Horsewill AJ, Panesar KS, Rols S, Ollivier J, Johnson MR, Carravetta M, Mamone S, Levitt MH, Murata Y, Komatsu K, Chen JY-C, Johnson JA, Lei X, Turro NJ (2012) Inelastic neutron scattering investigations of the quantum molecular dynamics of a H_2 molecule entrapped inside a fullerene cage. Phys Rev B 85:205440
108. Turro NJ, Mart AA, Chen JY-C, Jockusch S, Lawler RG, Ruzzi M, Sartori E, Chuang S-C, Komatsu K, Murata Y (2008) Demonstration of a chemical transformation inside a fullerene. The reversible conversion of the allotropes of $H_2@C_{60}$. J Am Chem Soc 130:10506

109. Frunzi M, Jockusch S, Chen JY-C, Calderon RMK, Lei X, Murata Y, Komatsu K, Guldi DM, Lawler RG, Turro NJ (2011) A photochemical on-off switch for tuning the equilibrium mixture of H_2 nuclear spin isomers as a function of temperature. J Am Chem Soc 133:14232–14235
110. Yoon M, Yang SY, Wang E, Zhang ZY (2007) Charged fullerenes as high-capacity hydrogen storage media. Nano Lett 7:2578–2583
111. Yoon M, Yang SY, Zhang ZY (2009) Interaction between hydrogen molecules and metallofullerenes. J Chem Phys 131 art 64707
112. Arai M, Utsumi S, Kanamaru M, Urita K, Fujimori T, Yoshizawa N, Noguchi D, Nishiyama K, Hattori Y, Okino F, Ohba T, Tanaka H, Kanoh H, Kaneko K (2009) Enhanced hydrogen adsorptivity of single-wall carbon nanotube bundles by one-step C_{60}-pillaring method. Nano Lett 9:3694–3698
113. Lan JH, Cao DP, Wang WC (2009) $Li_{12}Si_{60}H_{60}$ fullerene composite: a promising hydrogen storage medium. ACS Nano 3:3294–3300
114. Liu W, Zhao YH, Li Y, Lavernia EJ, Jiang Q (2009) A reversible switch for hydrogen adsorption and desorption: electric fields. PhysChemChemPhys 11:9233–9240
115. Saunders M, Jimenez-Vazquez HA, Cross RJ, Poreda RJ (1993) Stable compounds of helium and neon: He@C_{60} and Ne@C_{60}. Science 259:1428
116. Becker L, Poreda RJ, Bunch TE (2000) Fullerenes: an extraterrestrial carbon carrier phase for noble gases. Proc Natl Acad Sci U S A 97:2979–2983
117. Peng RF, Chu SJ, Huang YM, Yu HJ, Wang TS, Jin B, Fu YB, Wang CR (2009) Preparation of He@C_{60} and He_2@C_{60} by an explosive method. J Mat Sci 19:3602–3605
118. Krapp A, Frenking G (2007) Is this a chemical bond? A theoretical study of Ng_2@C_{60} (Ng=He, Ne, Ar, Kr, Xe). Chem Eur J 13:8256–8270
119. Amusia MY, Chernysheva LV, Liverts EZ (1912) Generalized oscillator strength of endohedral molecules. Int J Quant Chem 112:3119–3130
120. Scott LT, Jackson EA, Zhang Q, Steinberg BD, Bancu M, Li BJ (2011) A short, rigid, structurally pure carbon nanotube by stepwise chemical synthesis. Am Chem Soc 134:107–110
121. Mercado BQ, Chen N, Rodriguez-Fortea NA, Mackey MA, Stevenson S, Echegoyen L, Poblet JM, Olmstead MM, Balch AL (2011) The shape of the $Sc_2(\mu 2\text{-S})$ unit trapped in C_{82}: crystallographic, computational, and electrochemical studies of the isomers, $Sc_2(\mu_2\text{-S})$@C_s(6)-C_{82} and $Sc_2(\mu_2\text{-S})$@C_{3v}(8)-C_{82}. J Am Chem Soc 133:6752–6760, 10.1021/ja200289w
122. Akasaka T, Nagase S (eds) (2002) Endofullerenes: a new family of carbon clusters. Kluwer, Dordrecht
123. Yamada M, Akasaka T, Nagase S (2010) Endohedral metal atoms in pristine and functionalized fullerenes cages. Acc Chem Res 43:92–102
124. Chaur MN, Melin F, Ortiz AL, Echegoyen L (2009) Chemical, electrochemical, and structural properties of endohedral metallofullerenes. Angew Chem Int Ed 48:7514–7538
125. Che Y, Yang H, Wang Z, Jin H, Liu Z, Lu C, Zuo T, Dorn HC, Beavers CM, Olmstead MM, Balch AL (2009) Isolation and structural characterization of two very large, and largely empty, endohedral fullerenes: Tm@C_{3v}-C_{94} and Ca@C_{3v}-C_{94}. Inorg Chem 6004–6010
126. Jin H, Yang H, Yu M, Liu Z, Beavers CM, Olmstead MM, Balch AL, Dorn HC (2012) Single samarium atoms in large fullerene cages. Characterization of two isomers of Sm@C_{92} and four isomers of Sm@C_{94} with the X-ray crystallographic identification of Sm@C_1(42)-C_{92}, Sm@C_s(24)-C_{92}, and Sm@C_{3v}(134)-C_{94}. J Am Chem Soc 134:10933–10941 doi: 10.1021/ja302859r
127. Mercado BQ, Jiang A, Yang H, Wang Z, Jin H, Liu Z, Olmstead MM, Balch AL (2009) Isolation and structural characterization of the molecular nanocapsule Sm_2@D_{3d}(822)-C_{104}. Angew Chem Int Ed 130:9114–9116. doi: 10.1002/anie.200904662
128. Beavers CM, Jin H, Yang H, Wang Z, Wang X, Ge H, Liu Z, Mercado BQ, Olmstead MM, Balch AL (2011) Very large, soluble endohedral fullerenes in the series La_2C_{90} to La_2C_{138}: isolation and crystallographic characterization of La_2@D_5(450)-C_{100}. J Am Chem Soc 133:15338–15341. doi: 10.1021/ja207090e
129. Xu W, Feng L, Calvaresi M, Liu J, Liu Y, Niu B, Shi Z, Lian Y Zerbetto F (2013) An experimentally observed trimetallofullerene Sm_3@I_h-C_{80}: encapsulation of three metal atoms in a cage without a nonmetallic mediator. J Am Chem Soc 135:4187–4190

130. Wang CR, Kai T, Tomiyama T, Yoshida T, Kobayashi Y, Nishibori E, Takata M, Sakata M, Shinohara H (2001) A scandium carbide endohedral metallofullerene $Sc_2C_2@C_{84}$. Angew Chem Int Ed 40:397–399
131. Wakahara T, Sakuraba A, Iiduka Y, Okamura M, Tsuchiya T, Maeda Y, Akasaka T, Okubo S, Kato T, Kobayashi K, Nagase S, Kadish KM (2004) Chem Phys Lett 398:553–556
132. Iiduka Y, Wakahara T, Nakahodo T, Tsuchiya T, Sakuraba A, Maeda Y, Akasaka T, Yoza K, Horn E, Kato T, Liu MTH, Mizorogi N, Kobayashi K (2005) $Sc_3@C_{82}$ structural determination of metallofullerene $Sc_3@C_{82}$ revisited: a surprising finding. J Am Chem Soc 127:12500–12505
133. Yang H, Lu CX, Liu ZY, Che YL, Olmstead MM, Balch AL (2008) Detection of a family of gadolinium-containing endohedral fullerenes and the isolation and crystallographic characterization of one member as a metal-carbide encapsulated inside a large fullerene cage. J Am Chem Soc 130:17296–17300
134. Chaur MN, Anthans AJ, Echegoyen L (2008) Lantanide nitrides in C_{84}, C_{88}, C_{92} and C_{96}. Tetrahedron 64:11387–11393
135. Chaur MN, Melin F, Elliott B, Kumbhar A, Athans AJ, Echegoyen L (2008) New $M_3N@C_{2n}$ endohedral metallofullerene families (M = Nd, Pr, Ce; n=40-53): Expanding the preferential templating of the C_{88} cage and approaching the C_{96} cage. Chem Eur J 14:4594–4599
136. Chaur MN, Valencia R, Rodríguez-Fortea A, Poblet JM, Echegoyen L (2008) Trimetallic nitride endohedral fullerenes: experimental and theoretical evidence for the $M_3N_{6+}@C^{6-}{}_{2n}$ model. Angew Chem Int Ed 48:1425–1428
137. Campanera JM, Bo C, Olmstead MM, Balch AL, Poblet JM (2002) Bonding within the endohedral fullerenes $Sc_3N@C_{78}$ and $Sc_3N@C_{80}$ as determined by density functional calculations and reexamination of the crystal structure of $\{Sc_3N@C_{78}\}$center dot Co(OEP)center dot 1.5(C_6H_6)center dot 0.3($CHCl_3$). J Phys Chem A 106:12356–12364
138. Stevenson S, Rice G, Glass T, Harich K, Cromer F, Jordan MR, Craft J, Hadju E, Bible R, Olmstead MM, Maitra K, Balch AL, Dorn HC (1999) Small-bandgap endohedral metallofullerenes in high yield and purity. Nature 401:55–57
139. Tarabek J, Yang S, Dunsch L (2009) Redox properties of mixed lutetium/yttrium nitride custerfullerenes: endohedral $Lu_xY_{3-x}N@C_{80}$(I) (x=0-3) compounds.ChemPhysChem 10:1037–1043
140. Wang CR, Zuo TM, Olmstead MM, Duchamp JC, Glass TE, Cromer F, Balch AL, Dorn HC (2006) Preparation and structure of $CeSc_2N@C_{80}$: An icosahedral carbon cage enclosing an acentric CeSc2N unit with buried f electron spin. J Am Chem Soc 128, art. no. JA061434I
141. Stevenson S, Mackey MA, Stuart MA, Phillips JP, Easterling ML, Chancellor CJ, Olmstead MM, Balch AL (2008) A distorted tetrahedral metal oxide cluster inside an icosaedral carbon cage. Synthesis, isolation, and structural characterization of $Sc_4(m_3\text{-}O)2@I_h\text{-}C_{80}$. J Am Chem Soc 130:11844–11845
142. Beavers CM, Chaur MN, Olmstead MM, Echegoyen L, Balch AL (2009) Non-IPR C_{78} large metal ions in a relatively small fullerene cage: the structure of $Gd_3N@C_2(22010)\text{-}C_{78}$ departs from the isolated pentagon rule. J Am Chem Soc 131:11519–11524
143. Gimenez-Lopez MD, Gardener JA, Shaw AQ, Iwasiewicz-Wabnig A, Porfyrakis K, Balmer C, Dantelle G, Hadjipanayi M, Crossley A, Champness NR, Castell MR, Briggs GAD, Khlobystov AN (2010) Endohedral metallofullerenes in self-assembled monolayers. Phys Chem Chem Phys 12:123–131
144. Wang T, Feng L, Wu J, Xu W, Xiang J, Tan K, Ma Y, Zheng J, Jiang L, Lu X, Shu C, Wang C (2010) Planar quinary cluster inside a fullerene cage: synthesis and structural characterizations of $Sc_3NC@C_{80}\text{-}I_h$. J Am Chem Soc 132:16362–16364
145. Wu J, Wang T, Ma Y, Jiang L, Shu C, Wang C (2011) Synthesis, Isolation, Characterization, and Theoretical Studies of Sc3NC@C78-C_2. J Phys Chem C 115:23755–23759. doi:10.1021/jp2081929
146. Mercado BQ, Olmstead MM, Beavers CM, Easterling ML, Stevenson S, Mackey MA, Coumbe CE, Phillips JD, Phillips JP, Poblet JM, Balch AL (2010) A seven atom cluster in a carbon cage, the crystallographically determined structure of $Sc_4(m_3\text{-}O)_2@I_h\text{-}C_{80}$. Chem Commun 279–281

147. Chen N, Chaur MN, Moore C, Pinzon JR, Valencia R, Fortea AR, Poblet JM, Echegoyen L (2010) Synthesis of a new endohedral fullerene family, $Sc_2S@C_2n$ (n = 40 -50) by the introduction of SO_2. Chem Commun 46:4818–4820
148. Krause M, Ziegs. F, Popov AA, Dunsch L (2007) Entrapped bonded hydrogen in a fullerene: the five-atom cluster Sc_3CH in C_{80}. ChemPhysChem 8:537–540
149. Fu W, Zhang J, Fuhrer T, Champion H, Furukawa K, Kato T, Mahaney JE, Burke BG, Williams KA, Walker K, Dixon C, Ge JC, Shu CY, Harich K, Dorn HC (2011) $Gd_2@C_{79}N$: isolation, characterization, and monoadduct formation of a very stable heterofullerene with a magnetic spin state of S = 15/2. J Am Chem Soc 133:9741–9750. doi:10.1021/ja202011u
150. Zuo TM, Xu LS, Beavers CM, Olmstead MM, Fu WJ, Crawford D, Balch AL, Dorn HC (2008) $M_2@C_{79}N$ (M = Y, Tb): Isolation and characterization of stable endohedral metallofullerenes exhibiting M-M bonding interactions inside aza[80]fullerene cages. J Am Chem Soc 130:12992–12997
151. Rubin Y, Jarrosson T, Wang W, Bartberger MD, Houk KN, Schick G, Saunders M, Cross RJ (2001) First opened fullerene with H_2 and He. Angew Chem Int Ed 40:1543–1546
152. Murata Y, Chuang SC, Tanabe F, Murata M, Komatsu K (2013) Recognition of hydrogen isotopomers by an open-cage fullerene. Philos Trans A Math Phys Eng Sci. doi:10.1098/rsta.2011.0629
153. Xiao Z, Yao JY, Yang DZ, Wang FD, Huang SH, Gan LB, Jia ZS, Jiang ZP, Yang XB, Zheng B, Yuan G, Zhang SW, Wang ZM (2007) Synthesis of [59]fullerenones through peroxide-mediated stepwise cleavage of fullerene skeleton bonds and X-ray structures of their water-encapsulated open-cage complexes. J Am Chem Soc 129:16149–16162
154. Iwamatsu S-I, Uozaki T, Kobayashi K, Re S, Nagase S, Murata S (2004) Bowl-shaped fullerene encapsulates a water into the cage. J Am Chem Soc 126:2668–2669
155. Iwamatsu S, Murata S (2004) $H_2O@$open-cage fullerene C_{60}: control of encapsulation property and the first mass spectroscopic identification. Tetrah Lett 45:6391–6394
156. Stanisky CM, Cross RJ, Saunders M (2009) Putting atoms and molecules into chemically opened fullerenes. J Am Chem Soc 131:3392–3395
157. Iwamatsu SI, Stanisky CM, Cross RJ, Saunders M, Mizorogi N, Nagase S, Murata S (2006) CO in opened fullerene. Angew Chem Int Ed 45:5337–5340
158. Whitener Jr KE, Frunzi M, Iwamatsu S-I, Murata S, Cross RJ, Saunders M (2008) Ammonia in an open-cage [60]fullerene. J Am Chem Soc 13996–13999
159. Whitener Jr KE, Cross RJ, Saunders M, Iwamatsu S-I, Murata S, Mizorogi N, Nagase S (2009) Methane in an open-cage [60]fullerene. J Am Chem Soc 131:6338–6339
160. Jeziorski B, Moszynski R, Szalewicz K (1994) SAPT perturbation theory approach to intermolecular potential energy surfaces of van der Waals complexes. Chem Rev 94:1887–1930
161. Szalewicz K, Patkowski K, Jeziorski B (2005) Intermolecular interactions via perturbation theory: from diatoms to biomolecules. Structure and Bonding 116:43–117
162. Jansen G (2013) Symmetry-adapted perturbation theory based on density functional theory for noncovalent interactions. Wiley Interdisc Rev: Comp Mol Sci. doi: 10.1002/wcms.1164
163. Szalewicz K, Jeziorski B (2007) Symmetry-adapted perturbation theory of intermolecular interactions. In: Schreiner S (ed) Molecular interactions —from van derWaals to strongly Bound complexes. Wiley, Chichester, pp 3–43
164. Ugarte D (1992) Curling and closure of graphitic networks under electron beam irradiation. Nature 359:707
165. Terrones H, Terrones M (1997) (Tetrahedral $C_{264}@C_{660}@C_{1248}$) The transformation of polyhedral particles into graphitic onions. J Phys Chem Solids 38:1789–1796
166. Dodziuk H, Dolgonos G, Lukin O (2000) Ease of formation of nested fullerenes. Chem Phys Lett 329:351–356
167. Zimmermann U, Malinowski N, Näher U, Frank S, Martin TP (1994) Multilayer metal coverage of fullerene molecules. Phys Rev Lett 72:3542–3545
168. Rafique MMA, Iqbal JJ (2011) Production of carbon nanotubes by different routes—-a review. Encaps Adsorption Scie 1:29–34

169. Bystrzejewski M, Rümmeli MH, Lange H, Huczko A, Baranowski P, Gemming T, Pichler T (2008) Single-walled carbon nanotubes synthesis: a direct comparison of laser ablation and carbon arc routes. J Nanosci Nanotechnol 8:6178–6186
170. Sternfeld T, Hoffman RE, Saunders M, Cross RJ, Syamala MS, Rabinovitz M (2002) Two helium atoms inside fullerenes: probing the internal magnetic field in C_{60}^6- and C_{70}^6. J Am Chem Soc 124:8786–8787
171. Dietel E, Hirsch A, Pietzak B, Waiblinger R, Lips K, Weidinger A, Gruss A, Dinse KP (1999) Atomic nitrogen encapsulated in fullerenes: effects of cage variations. J Am Chem Soc 121:2432–2437
172. Naydenov B, Spudat C, Harneit W, Süss HI, Hulliger J, Nuss J, Jansen M (2006) Ordered inclusion of endohedral fullerenes N@C_{60} and P@C_{60} in a crystalline matrix. Chem Phys Lett 424:327–332
173. Mauser H, Hommes NJRV, Clark T, Hirsch A, Pietzak B, Weidinger A, Dunsch L (1997) Stabilization of atomic nitrogen inside C_{60}. Angew Chem Int Ed 36:2835–2838
174. Cao BP, Peres T, Lifshitz C, Cross RJ, Saunders M (2006) Kinetic energy release of C_{70}^+ and its endohedral cation N@C_{70}^+: Activation energy for N extrusion. Chem Eur J 12:2113–2221
175. Grose JE, Tam ES, Timm C, Scheloske M, Ulgut B, Parks JJ, Abruna HD, Harneit W, Ralph DC (2008) Tunnelling spectra of individual magnetic endofullerene molecules. Nature Mat 7:884–889
176. Scheloske M, Naydenov B, Meyer C, Harneit W (2006) Synthesis and functionalization of fullerenes encapsulating atomic phosphorus. Isr J Chem 46:407–412
177. Fowler PW, Manolopoulos DE (1995) An atlas of fullerenes. Clarendon, Oxford
178. Koshland DE Jr (1994) The key-lock theory and the induced fit theory. Angew Chem Int Ed 33:2375–2378
179. Akasaka T, Nagase S, Kobayashi K, Waelchli M, Yamamoto K, Funasaka H, Kako M, Hoshino T, Erata T (1997)^{13}C and^{139}La NMR studies of La_2@C_{80}: first evidence for circular motion of metal atoms in endohedral dimetallofullerenes. Angew Chem Int Ed Engl 36:1643
180. Xu J, Tsuchiya T, Hao C, Wakahara T, Mi W, Gu Z, Akasaka T (2006) Dynamics structure determination of a missing-caged metallofullerene: Yb@C_{74} (II) and the dynamic motion of the encaged ytterbium ion. Chem Phys Lett 419:44–47
181. Delaney P, Greer JC (2004) C_{60} as a Faraday cage. Appl Phys Lett 84:431–433
182. Lips K, Waiblinger M, Pietzak B, Weidinger A (2000) Atomic nitrogen encapsulated in fullerenes: proof of an ideal chemical Faraday cage. Mol Mater 13:217–224
183. Zope RR (2008) Electronic structure and static dipole polarizability of C_{60}@C_{240}. J Phys B 41 art no. 085101
184. Sauvage J-P, Dietrich-Buchecker CO (1999) Molecular catenanes, rotaxanes and knots. A journey through the world of molecular topology. Wiley-VCH, Weinheim, pp 107–142
185. Watanabe N, Furusho Y, Kihara N, Takata T, Kinbara K, Saigo K (2001) Chemical modification of amide-based catenanes and rotaxanes II. Synthesis of tertiary amine [2]catenanes and [2] rotaxanes via N-methylation followed by borane reduction of secondary amide. Bull Chem Soc Japan 74:149–155
186. Vignon SA, Stoddart JF (2005) Exploring dynamics and stereochemistry in mechanically-interlocked compounds. Collect Czech Chem Commun 70:1493–1576
187. Peera A, Saini RK, Alemany LB, Billups WE, Saunders M, Khong A, Syamala MS, Cross RJ (2003) Formation, isolation, and spectroscopic properties of some isomers of $C_{60}H_{38}$, $C_{60}H_{40}$, $C_{60}H_{42}$, and $C_{60}H_{44}$ —Analysis of the effect of the different shapes of various helium-containing hydrogenated fullerenes on their^{3}He chemical shifts. Eur J Org Chem 21:4140–4145
188. Rosenthal J, Schuster DI, Cross RJ, Khong A (2006)^{3}He NMR as a sensitive probe of fullerene reactivity: [2+2] Photocycloaddition of 3-methyl-2-cyclohexenone to C_{70}. J Org Chem 71:1191–1199
189. Sternfeld T, Saunders M, Cross RJ, Rabinovitz M (2003) The inside story of fullerene anions: a^{3}He NMR aromaticity probe. Angew Chem Int Ed 42:3136–3139

Chapter 2
Physical and Mechanical Properties of Surface Nanocrystalline Structures Generated by Severe Thermal-Plastic Deformation

Hryhoriy Nykyforchyn, Volodymyr Kyryliv and Olga Maksymiv

2.1 Introduction

Improvement of mechanical properties of engineering steels due to the formation of nanocrystalline structures (NCS) is generally done by severe plastic deformation. Both volume and surface NCS can be achieved by this type of treatment [8, 13, 14, 23, 25, 26]. One method for the creation of surface NCS consists in severe thermal-plastic deformation by high-speed friction. A technology for the formation of surface gradient NCS is developed on this base by mechanical-pulse treatment (MPT) [11, 17] which is based on the principles of grinding process (Fig. 2.1). A special metal tool is installed instead of a grinding ring.

A lathe equipped by the special device similar to spindle mandrel of a grinder can be used for the treatment of cylindrical surfaces. This tool rotates with velocity V_1 of 50–70 m/s and the treated component rotates at $V_2 = 0.03$–0.18 m/s. The tool pressure on treated component surface in the friction contact zone reaches 1 GPa at a depth of run of $t = 0.25$–0.35 mm and the longitudinal feed of $S = 0.3$–4 mm/rev. The coolant is brought up into the friction area. Its role consists not only in rapid cooling of thermal-plastic-deformed surface layer but also in its alloying. The surface temperature in the friction contact area depends on the treatment regimes and varies between 1100 and 1600 K.

The applied coolants are oil or water based with different polymer additives. The thermal and mechanical destruction of the additives in the contact area under high pressure and temperature create active carbon, hydrogen, oxygen and other alloying elements [10, 12]. The rapid plastic deformation and high temperature promote a mass transfer at abnormally high diffusion velocity of $D = 10^{-6}$–10^{-7} m^2/s [12]. In particular, a special oil-base coolant with low molecular weight polyethylene

H. Nykyforchyn (✉) · V. Kyryliv · O. Maksymiv
Karpenko Physico-Mechanical Institute of NASU, 5 Naukova Str.,
79060 Lviv, Ukraine

H. Nykyforchyn
+38 (032) 2632133
e-mail: nykyfor@ipm.lviv.ua

O. Fesenko, L. Yatsenko (eds.), *Nanocomposites, Nanophotonics, Nanobiotechnology, and Applications,* Springer Proceedings in Physics 156,
DOI 10.1007/978-3-319-06611-0_2,

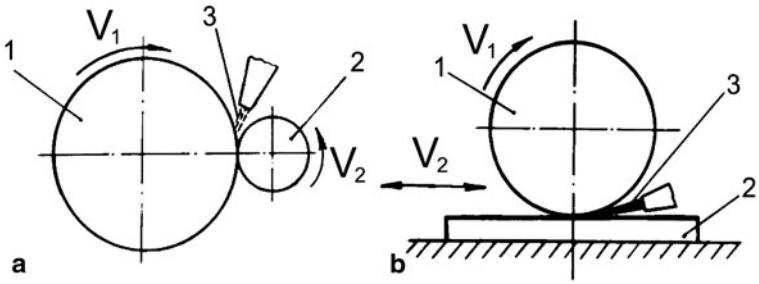

Fig. 2.1 The scheme of MPT of **a** cylindrical and **b** plane surfaces: *1*—strengthening tool; *2*—treated component; *3*—coolant

additives was developed for saturation of surface layers with carbon [10]. This is especially useful for the treatment of low carbon steels.

The contact zone is the area with high shear deformation. Phase transformations occur in the surface layers due to high-speed heating above the phase transformation temperature and the subsequent cooling by heat sink in the coolant, the tool and the component.

The achieved nanostructure of the surface layer with a different phase composition and a modified chemical composition has different physical and mechanical properties, which are discussed in this chapter.

2.2 Investigation Methods

Armco iron and carbon steels 45 (0.45C), 40Kh (0.40 C-1Cr) and 65G (0.65 C-1Mn) with a ferrite-pearlite structure in as-received state (after annealing) were investigated. Three coolant types were used for MPT: mineral oil U-12 A (GOST 20799-88 standard), 10 % aqueous solution of emulsol and a special coolant for carbonization [11]. MPT was carried out on specimens of two geometries: (a) cylindrical specimens strengthened by a lathe and (b) flat specimens, which were strengthened by a flat grinding machine.

The cylindrical specimens were of two sizes:

a. Specimens with net diameter of 20 mm and a length of 100 mm were used for chemical and phase analysis as well as microhardness measurements.
b. Ring specimens with a diameter of 40 mm were used for ring-insert wear-resistance tests [11].

The counter body was a specimen of the high carbon martensite ball-bearing steel ShKh15 (1.0 C-1.5Cr). The GOST TAP-30 oil with an addition of 0.1 wt% of fine quartz sand with grain size up to 40 μm was used. The tests were performed at the loading of 4.0 MPa and the sliding velocity of 0.9 m/s. The specimens were preloaded at 0.8 MPa within 2 h.

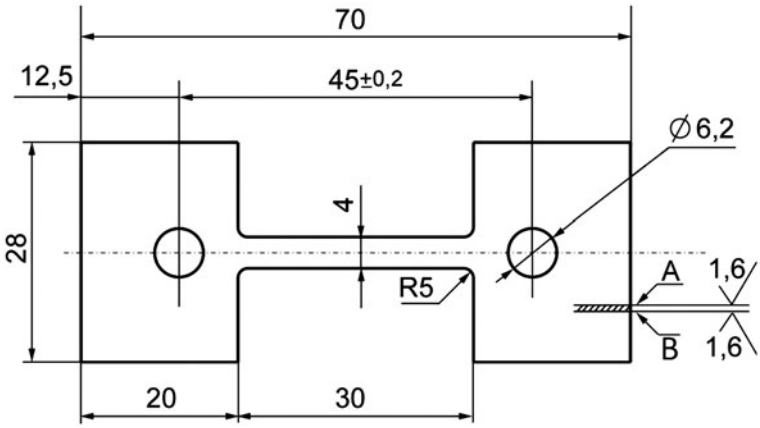

Fig. 2.2 Specimen for an evaluation of mechanical properties of tension

Two sizes of flat specimens were used as well. The tensile properties were determined using 1.6-mm thick specimens (Fig. 2.2). However, the hardening effect of the surface treatment is localized in the surface layer. To decrease the hardness gradient in the specimen cross section, they were preliminary quenched and tempered at 500°C, grinded, treated by MPT and tempered again at the same temperature. Fatigue crack growth was determined on 6 × 19 × 150-mm single-notched beam specimens under the cycle bending load with the frequency of 26 Hz and the load ratio $R = 0$.

The phase analyses were carried out metallographically and with the transmission electron microscope JEM-CX. The diffractometry analyses were performed with the diffractometer DRON-3 to measure the average grain size and the dislocation density. The dislocation density was calculated on the basis of widening of the lines (220)k_α. Phase analyses of the surface layers were carried out with the CuK_α radiation method ($U = 30$ kV, $I = 20$ mA) with a step of 0.05 and the exposition of 4 s. The diffractograms were post processed using the software Powder Cell [5]. The X-ray pictures were analysed after the Joint Committee on Powder Diffraction Standards/American Society for Testing and Materials (JCPDS-ASTM) index [19].

The carbon content in surface layers of the strengthened Armco iron was determined layer by layer by the chemical analysis. For this purpose, three layers 0.05 mm thick were cut off the specimen.

2.3 Results of Investigations and Discussion

The metallographic examination showed the presence of unetched surface area (Fig. 2.3a) with a high dislocation density, which is maximal on the surface (Fig. 2.3b, curve 1). Two types of deformation occur during friction: pressure and shear, both

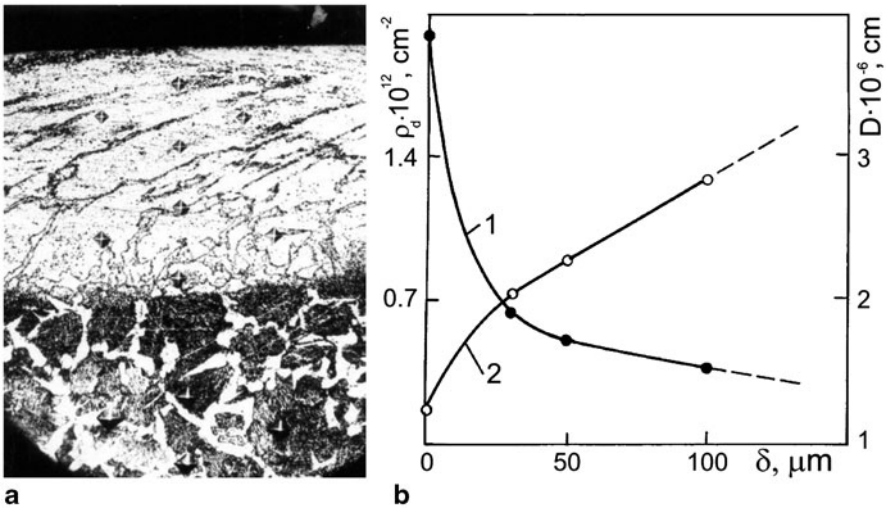

Fig. 2.3 Steel 45 after MPT ($V_2 = 1.0$ m/min; $S = 0.5$ mm/double motion; $t = 0.3$ mm) in mineral oil. **a** Microstructure (× 300). **b** Dislocation density (*1*) and grain size (*2*) in a depth of strengthened layer δ

of which decrease with increasing depth δ. Shear deformation causes a particular texture, which can be distinguished by the inclination of grain groups (Fig. 2.3a).

With increasing depth from the surface, the deformation grade decreases and thus the grain size decreases (Fig. 2.3b, curve 2). The calculated average grain size d on the surface is 12 nm, which is in good agreement with the literature data [24]. The obtained data of d and ρ are comparable with those for powder iron milled in a ball mill [20]. Therefore, it can be argued that MPT and the ball milling decrease the grain size to nearly the same extent.

The phase composition changes were caused by rapid heat treatment during MPT with material temperature rising above the phase transformation point and subsequently dropping below this point. The resulting martensite–austenite microstructure includes rest of cementite that have not fully transformed during the deformation process (Fig. 2.4). The phase composition and parameters of the nanocrystalline-hardened surface layer depend on the coolant type, process parameters and the chemical compositions of the material [6].

The electron microscopy images of the microstructure of the hardened surface layer are presented in Fig. 2.5. The grain size on the surface of 10–15 nm is achieved and it grows gradually with the distance from the surface.

The grains look strongly distorted. The probable reason for it is the far field stresses in non-equilibrium grain boundaries due to high dislocation density. A cellular structure with low degrees of lattice disorientation of grains is typical at the distance from the surface of 200 μm and above. Randomly distributed dislocation clews are observed in the grains. The microstructure is strongly fragmented in the surface layer at a depth of 5 μm. Arrays of parallel nanocrystals 10–15 nm are observed in dark-field images, which is in good agreement with the diffractometry

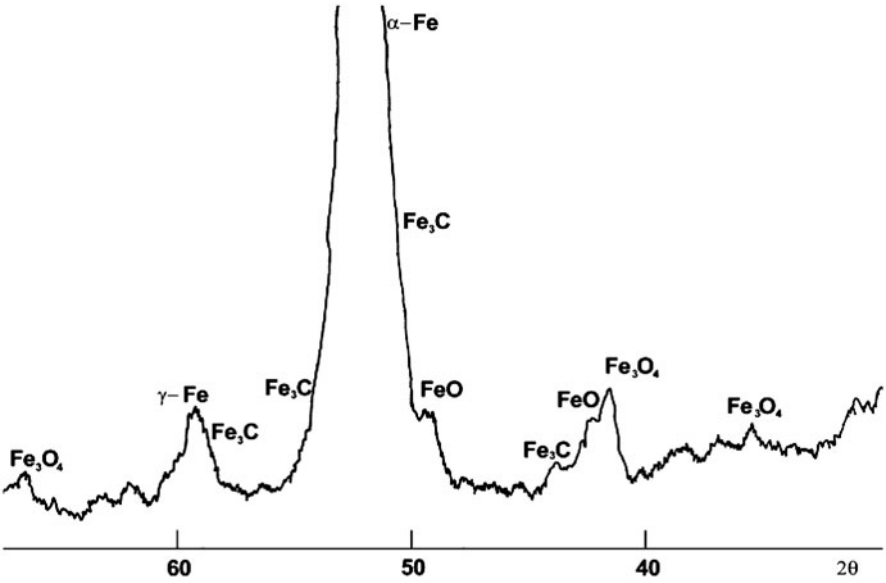

Fig. 2.4 The fragment of diffractogram of the surface layer on 45 steel after MPT in a mineral oil

(X-ray) examinations. The observed washed out rings on diffractograms are indications of a quasi-amorphous structure. The absence of the typical amorphous halo ([3]; Fig. 2.4) can be explained by deep penetration of X-rays (over 10 μm). The observed circular distribution of grains signifies big disorientation (over 10) between adjacent grains, and the azimuthal blurring is particular for large strains. With the depth increasing to 20–30 μm, the grain boundary stresses gradually decrease, the grain size increases and diffraction picture corresponds to a fine-grain microstructure. The deformation velocity $\varepsilon = 2 \times 10^3\ s^{-1}$ was calculated by using the dislocation density $\rho \approx 10^9$(Fig. 2.3b) and the Jonston–Hilman law [4]. This means that the deformation velocity $10^3\ s^{-1}$ is required for the nanocrystalline structure formation in surface layers.

For the Armco iron, the effectiveness of carbon enrichment of surface layers by MPT with a special coolant is shown (Fig. 2.6). Carbon concentration *C* on the surface can reach 1 % and depend on not only the treatment process parameters [9, 12] but also the surface roughness; for polished surfaces, higher carbon enrichment can be obtained. According to Fisher [2], a linear decrease of carbon content lg C versus δ^2 occurs for volumetric diffusion and linear decrease of lg C versus δ is typical for grain-boundary diffusion. The analysis of concentration curves after MPT showed that carbon is distributed mainly on grain boundaries (Fig. 2.7).

The percentage of coolant additives in the chemical composition of the surface layers is presented in Table 2.1. The most differences were obtained for carbon and oxygen. It is known [16] that the presence of carbon at grain boundaries increases material strength, while the presence of oxygen, nitrogen and hydrogen deteriorates

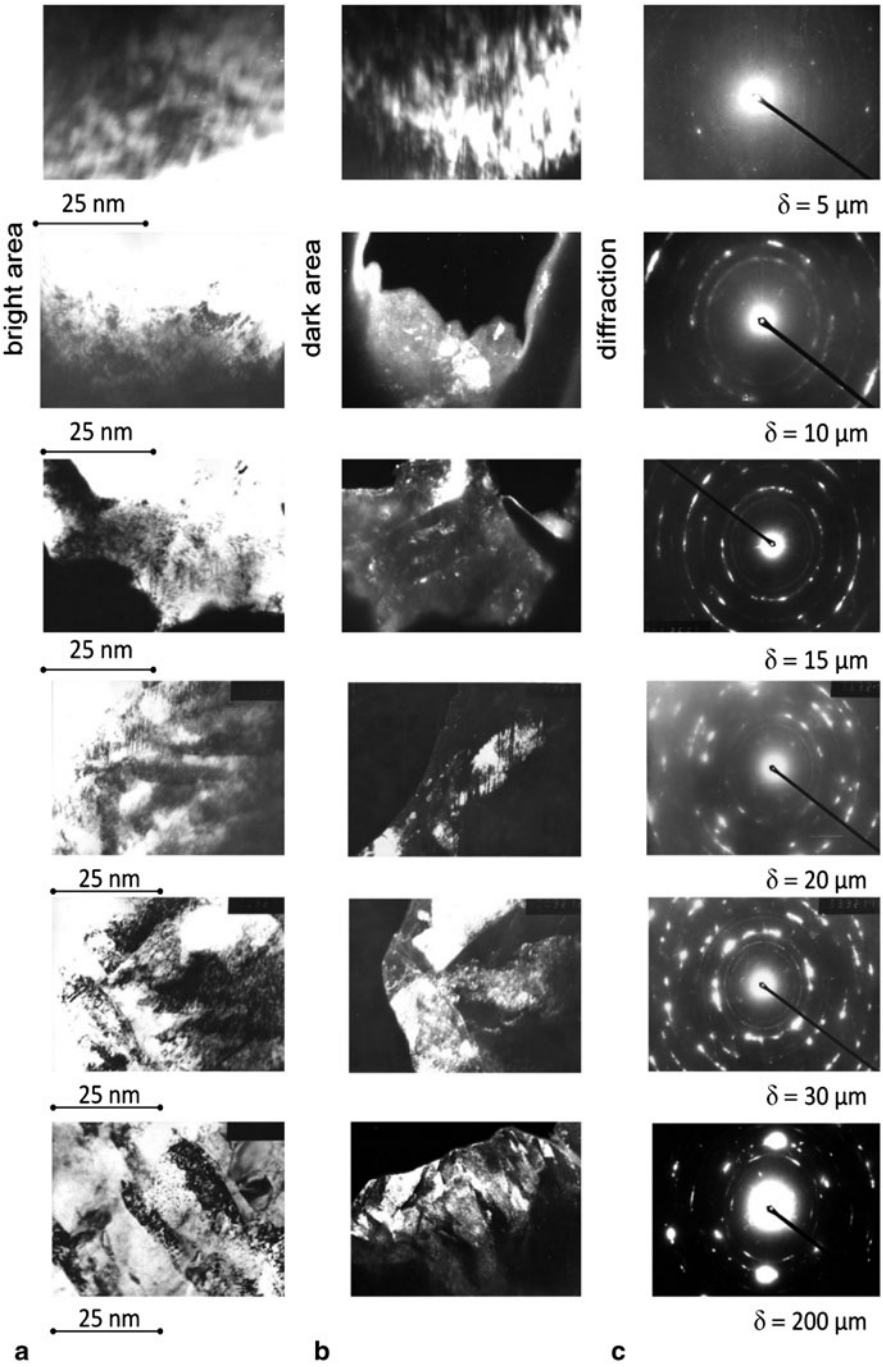

Fig. 2.5 Electron-microscope images: **a** light field, **b** dark field and **c** electrongrams of nanocrystalline structures of 45 steel surface layers from the different depth δ after MPT

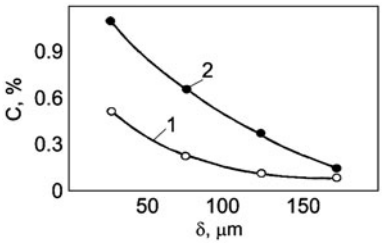

Fig. 2.6 Distribution of carbon in Armco iron during MPT using the special coolant for carbonization: *1*—polishing, *2*—grinding

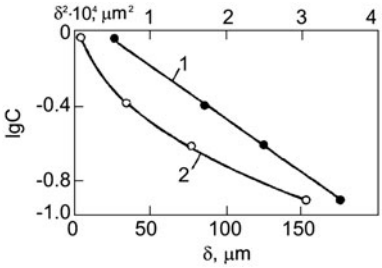

Fig. 2.7 Dependence of lgC on δ (*1*) and δ^2 (*2*) for saturation of the surface by carbon during MPT

Table 2.1 Mass-spectral analysis of surface nanocrystalline layer, obtained by MPT on 40Kh steel in different coolants

Type of TE	Amount of elements on surface, in relative units			
	H_2	N_2	O_2	C
Without MPT	1.0	1.0	1.0	1.0
MPT in mineral oil	3.0	1.7	1.2	2.3
MPT in aqueous environment	2.3	1.0	2.2	1.1

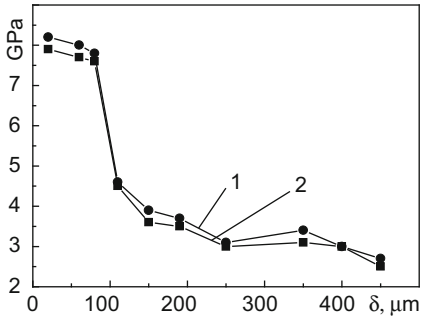

Fig. 2.8 Microhardness distribution of 45 steel in depth from surface after MPT in the special coolant for carburization (*1*) and mineral oil (*2*)

mechanical properties of steels. Useful additives while diffusing into grain boundaries increase the grain boundary energy, which results in increase of intergranular fracture energy. Therefore, the chemical composition of coolants affects the mechanical properties of surface NCS.

It is generally acknowledged that NCS in the bulk material improves its mechanical properties [15, 21, 22, 25, 26]. This was proved also for the surface NCS [7, 18]. It is shown in the example of strengthening by MPT (Fig. 2.8) that the surface

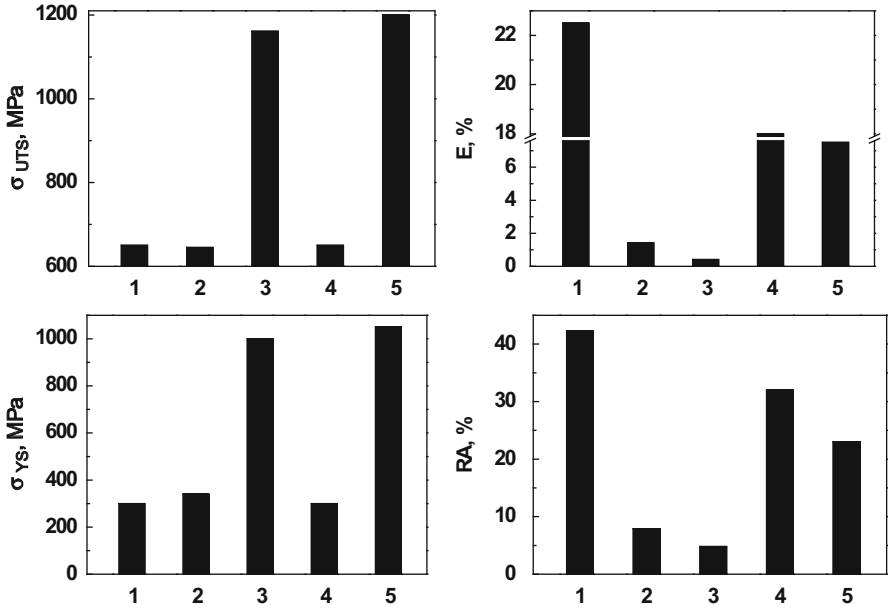

Fig. 2.9 A change of the mechanical properties of 65G steel specimens (Fig. 2.2) after MPT in the different coolants: *1*—as-received state; *2, 3*—MPT in aqueous TE; *4, 5*—MPT in mineral oil; *2, 4*—as received state + MPT; *3, 5*—quenching + tempering at 500°C + MPT + tempering at 500°C

microhardness of the 45 steel reaches 8–8.5 GPa after the MPT, which is three times higher than for the original material.

Changes in the mechanical properties of the high-carbon 65G steel after MPT ($V_2 = 1.0$ m/min; $S = 0.5$ mm/double motion; $t = 0.3$ mm) are presented in Fig. 2.9. The tensile strength changed insignificantly and independent of the coolant type. However, the plastic

behaviour, the elongation in particular, varies with the coolant type. Such behaviour is caused due to carbon, oxygen and hydrogen, which are segregated mainly at grain boundaries and affect the grain boundary strength. The surfaces of flat specimens pretreated by MPT with different coolants and then subjected to tensile loading are presented in Fig. 2.10. Numerous microcracks can be observed in the case of aqueous coolant.

Wear-resistance tests of the 40Kh steel showed (Fig. 2.11) a positive effect of MPT in comparison with quenching and low tempering. The wear resistance was increased for both hardened rings and not-hardened inserts. It is caused by a substantial decrease of the friction.

The applied MPT also had a positive effect on the fatigue crack growth resistance of the 40Kh steel (Fig. 2.12). The fatigue test results show the lowest crack growth rate dA/dN for the specimens treated in mineral oil (curve 3) and the highest crack growth rate dA/dN for the untreated specimens (curve 1). This is in good agreement with the X-ray examinations showing a lower-surface grain size of 19 nm for the

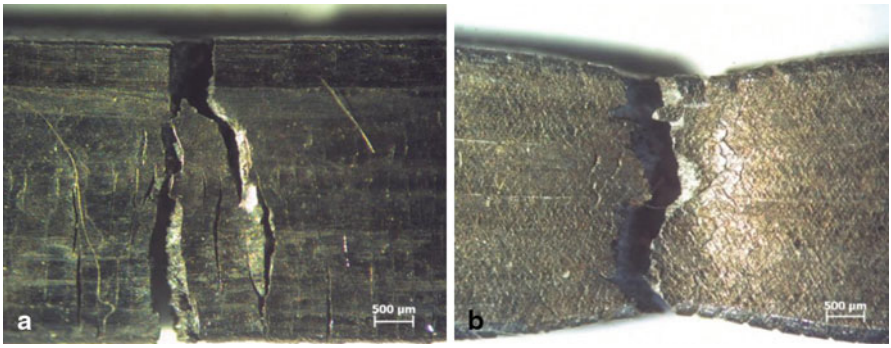

Fig. 2.10 Treated by MPT, the 65G steel specimens after the tension test: **a** in aqeueos MPT and **b** mineral oil coefficient from 0.14–0.16 at quenched state to 0.04–0.06 after the MPT in mineral oil [11]. Such effects can be explained by a change of contribution of electrons of *d*-orbitals in metallic bonding [1].

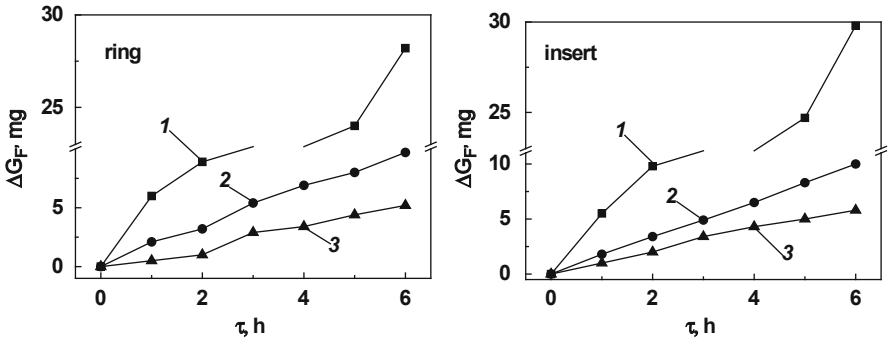

Fig. 2.11 Wear kinetic of the couple 40Kh–ShKh15 in the oil-abrasive environment (MPT regimes, $V_2 = 1.0$ m/min, $S = 0.5$ mm/double motion, $t = 0.3$ mm): *1*—quenching and low tempering; *2*—MPT in aqeuous coolant; *3*—MPT in mineral oil

specimen treated in mineral oil than for the specimen treated in the aqueous coolant (24 nm).

2.4 Conclusions

The surface gradient nanocrystalline structure is formed during MPT by severe thermal-plastic deformation. The phase transformations and the changes of the chemical composition of surface layers take place due to the very fast heating and cooling as well as due to alloying by the coolant additives. The mechanical properties of the hardened layers substantially depend on the coolant type, which affects the grain

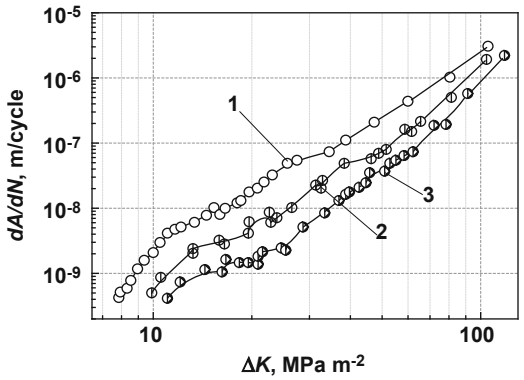

Fig. 2.12 Fatigue crack growth rate *dA*/*dN* in 40Kh steel: *1*—without MPT, *2*—MPT in aqueous coolant, *3*—MPT in mineral oil

boundary strength by segregation of carbon, oxygen and hydrogen. Such structures are characterized by improved mechanical properties: higher tensile strength and yield stress, higher microhardness, wear resistance and fatigue crack growth resistance.

References

1. Buckley DH (1981) Surface effects in adhesion, friction, wear, and lubrication. Elsevier, New York
2. Fisher JC (1951) Calculation of diffusion penetration curves for surface and grain boundary diffusion. J Appl Phys 22:74
3. Hunger H-J et al (1983) Ausgewelte Untersuchungverfaren in der Metalkunde. VEB Deutscher Verlag für Grundstoffindustrie. Leipzig
4. Hull D, Bacon DJ (2011) Introduction to dislocations. Elsevier, New York
5. Krous W, Nolze G (1996) Powder cell—a program for the representation and manipulation of crystal structures and calculation of the resulting x-ray powder patterns. J Appl Cryst 29:301–303
6. Kalichak TN, Kyryliv VI, Fenchin S (1989) Mechanopulsed hardening of long components of the hydraulic cylinder rod type. Sov Mater Sci 25(1):96–99
7. Kocanda D, Hutsaylyuk V, Slezak T, Torzewski J, Nykyforchyn H, Kyryliv V (2012) Fatigue crack growth rates of S235 and S355 steels after friction stir processing. Mater Sci Forum 726:203–210
8. Kuzydlowski KJ (2006) Physical, chemical, and mechanical properties of nanostructured materials. Mater Sci 42(1):85–94
9. Kyryliv VI (1998) Surface alloying of steels in the process of mechanical pulse treatment. Mater Sci 34(3):416–419
10. Kyryliv VI (1999) Surface saturation of steel with carbon during mechanikel-pulse treatment. Mater Sci 35(6):853–858
11. Kyryliv VI (2012) Improvement of the wear resistance of medium-carbon steel by nanodispersion of surface layers. Mater Sci 48(1):119–123
12. Kyryliv VI, Koval' YuM (2001) Surface alloying of steels from special process media. Mater Sci 37(5):816–819
13. Liu G, Lu J, Lu K (2000) Surface nanocrystallization of 316 Lstainless steel induced by ultrasonic shot peening. Mater Sci Eng A 286:91–95

14. Lu K, Lu J (1999) Surface nanocrystallization (SNC) of metallic materials-presentation of the concept behind a new approach. Mater Sci Technol 15:193
15. Morris DG (1998) Mechanical behaviour of nanostrured materials. Trans Tech, Uetikon-Zurich
16. Meuers MA, Mishra A, Benson DJ (2006) Mechanical properties of nanocrystalline materials. Prog Mater Sci 51:427–556
17. Nykyforchyn HM, Kyryliv VI, Slobodjan DzV et al (1998) Structural steels surface modification by mechanical pulse treatment for corrosion protection and wear resistance. Surf Coat Technol 100–101: 125–127
18. Nykyforchyn HM, Kyryliv VI, Bassarab AI (2002) Wear resistance of the mechanical-pulse treatment 40X steel during abrasive friction and cavitation. Mater Sci 38(6):860–864
19. Powder Diffraction File (1973) Search manual alphabetical listing and search section of frequently encountered phases (1974) Inorganic, Philadelphia
20. Takaki S (2003) Thermodynamics of nitrogen absorption into solid solution in Fe-Cr-Mn ternary alloys. Mater Sci Forum 215:426–432
21. Takaki S (2010) Review on the hall-petch relation in ferritic steel. Mater Sci Forum Vols. 654–656: pp. 11–16
22. Takaki S, Kawasaki K, Kimura Y (2001) Mechanical properties of ultra fine grained steels. J Mater Technol 117(3):359–363
23. Tao NR, Sui ML, Lu J, Lu K (1999) Surface nanocrystallization of iron induced by ultrasonic shot peening. NanoStruct Mater 11:433–440
24. Tao NR, Wang ZN, Tong WP (2003) An investigation of surface nanocrystallization mechanism in Fe induced by surface mechanical attrition treatment. Acta Mater 50:215
25. Valiev RZ, Islamgaliev RK, Aleksandrov IV (2000) Bulk nanostructured materials from severe plastic deformation. Progress Mat Sci 45:103
26. Valiev RZ, Islamgaliev RK, Alexandrov IV (2000) Nanostructured materials from severe plastic deformation. Prog Mater Sci 45:103–189

Chapter 3
Energy Spectra of the Fibonacci Superlattice Based on the Gapped Graphene

A. M. Korol and V. M. Isai

3.1 Introduction

It is known that semiconductor superlattices (SLs) can play an essential role in controlling the electron processes in various devices of modern electronics (see, e.g., [1]). Therefore, great attention is paid to the investigation of physical properties of SLs. The SLs of various types are considered, namely, strictly periodic, disordered, lattices with defects, etc. The structures intermediate between the periodic and disordered structures of quasi-periodic lattices, e.g., the Fibonacci and the Thue-Morse SLs, occupy a special place among the SLs. This is associated with their unusual properties such as self-similarity, the Cantor nature of the energy spectrum, etc. (see, e.g., [2]).

However, starting from 2004, graphene-based structures attracted great attention, which is naturally explained by nontrivial properties of graphene, including electron ones. It is sufficient to call the analogy of π electrons of graphene with the Dirac massless fermions at low energies (which are formally described by the Dirac massless equation), the linear dispersion law, the chirality property, the Klein tunneling, the high mobility, the ballistic transport, the unusual Hall quantum effect, etc. [3–6]. It should be also taken into account that graphene is a promising material in modern electronics from the viewpoint of the substitution of the silicon technology, the development of which has come to its limit, by the graphene technology. It is evident that by virtue of the mentioned properties, the investigation of physical properties of graphene-based SLs is an urgent problem [7–16]. Particularly, it is shown in [9, 10, 13] that a new Dirac point and the corresponding forbidden band manifest

A. M. Korol (✉) · V. M. Isai
National University for Food Technologies, Kiev, Ukraine

A. M. Korol
Laboratory on Quantum Theory, Linköping, Sweden
e-mail: korolam@ukr.net

V. M. Isai
e-mail: ivn@edu.nuft.ua

O. Fesenko, L. Yatsenko (eds.), *Nanocomposites, Nanophotonics, Nanobiotechnology, and Applications,* Springer Proceedings in Physics 156,
DOI 10.1007/978-3-319-06611-0_3,

themselves in graphene SLs; it is determined through the zero value of the averaged wave number [9]. In new studies, the properties of this new gap in various graphene SLs are investigated in detail. (For brevity, we will call this forbidden band an "SL Dirac" band, and we will call other gaps in the energy spectrum of the strictly periodic SL as well as the gaps in the Fibonacci SLs similar to them as the Bragg gaps [9, 10, 13, 14].)

A series of methods to form graphene structures is suggested and implemented in practice [17–20]. We note that among other ones, it is important to obtain such graphene-based structures, in which the forbidden band exists in the energy spectrum since just its presence plays the key role in the development of transistor-type semiconductor devices. Therefore, developers apply the efforts to the formation of graphene structures with a sufficiently wide gap. Here, using various methods, such as the use of graphene nanoribbons, the interaction with the substrate, etc., essential results are already attained [21–25]. Particularly, developers succeeded to obtain the gap several tenth of electron-volt wide by chemical methods [24].

3.2 Concretization of the Statement of the Problem and the Method for Calculating the Spectra

In this study, we investigate the energy spectrum of the graphene-based Fibonacci SLs in a continual model. We assume that there is an energy gap of equal value Δ in both elements of the SL a and b and the quasi-periodic modulation along axis Ox is formed due to a difference in barrier height values in different elements of the SL, so that $V = V_a$ in elements a and $V = V_b$ in elements b; the barrier height accepts one of two different values in different elements in the SL chain according to the Fibonacci rule.

Thus, we have the SL constructed according to the Fibonacci inflation rule: $S_n = S_{n-1} + S_{n-2}$ and therefore, for example, for the fourth Fibonacci generation (sequence) we have $S_4 = abaab$. Transmission conditions for the electron wave through the SL constructed for the n-th Fibonacci generation are determined by the period of this generation. Energy ranges E, for which the transmission coefficient of electrons though the lattice $T(E)$ is close to unity, form the allowed bands in the energy spectrum, while forbidden bands correspond to energy segments with $T << 1$. Coefficient T can be calculated by the transfer matrix method expressing it either via the Green's functions or via the wave functions. The latter can be found from the Dirac-type equation corresponding to the problem:

$$[V_F(p,\sigma) + m \cdot V_F^2 \cdot \sigma_z + V(x) \cdot I] \cdot \Psi = E \cdot \Psi, \tag{3.1}$$

where $V_F \approx 10^6$ m/s is the Fermi velocity; $p = (p_x, p_y)$ is the momentum operator; $\sigma = (\sigma_x, \sigma_y)$, σ_z are the Pauli matrices for the pseudospin; $V(x)$ is the external potential, which depends on the coordinate x; I is the unity two-dimensional matrix; we denote the mass summand by symbol Δ as it is accepted in publications. Function Ψ is a two-component pseudospinor. $\Psi = [\Psi_A, \Psi_B]^T, \Psi_A, \Psi_B$. are the envelope

functions for graphene sublattices A and B, and T is the transposition. Let us assume that potential $V(x)$ consists of periodically repeating rectangular barriers along axis Ox, and inside each j-th barrier, $V_j(x) = \text{const}$. In this case, using the translational invariance of the solution over axis Oy, we can write $\Psi_{A,B} = \Psi_{A,B} e^{ik_y y}$ and we can derive for $\Psi_{A,B}$ from Eq. (3.1):

$$\frac{d^2\Psi_{A,B}}{dx^2} + (k_j^2 - k_y^2) \cdot \Psi_{A,B} = 0 \tag{3.2}$$

where $q_j = sign(S_{j+})[(E - V_j)^2 - \Delta^2]^{1/2}$, $S_\pm \equiv E - V(x) \pm \Delta$; here and below, measurement units $\hbar = e = V_F = 1$ are adopted. If we represent the solutions for eigenfunctions in the form of the sum of planar waves moving in the direct and inverse directions along axis Ox, we derive:

$$\Psi(x) = \left[a_j \cdot e^{i \cdot q_j \cdot x} \begin{pmatrix} 1 \\ g_j^+ \end{pmatrix} + b_j \cdot e^{-i \cdot q_j \cdot x} \begin{pmatrix} 1 \\ g_j^- \end{pmatrix} \right], \tag{3.3}$$

where $q_j = sgn(S_{j+})\sqrt{k_j^2 - k_y^2}$, if $k_j^2 > k_y^2$ and $q_j = i\sqrt{k_j^2 - k_y^2}$; in the opposite case, $g_j^\pm = \frac{\pm q_j + i k_y}{k_y}$, the upper line in (3.3) is referred to sublattice A and the lower one is referred to B. The transmission coefficient of electrons through the SL can be expressed via the transfer matrix and the last can be evaluated using the boundary conditions for the eigenfunctions. Since this procedure has been reported for many times, we can proceed here with the results obtained.

3.3 The Analysis of the Results Obtained

In Fig. 3.1 the trace map is presented for the SL considered with the following parameters: $k_y = 0$, $d = w = 0.5$, $\Delta = 1$, $V_b = 4$, and $V_a = 1$ (except for the first generation, in that $V_b = V_a = 1$; we will also note, that $k_y = 0$ for all figures, i.e., we examine only the case of the normal incidence of the electron wave on a lattice) and d and w are barrier and the well width, respectively.

This one and other figures make it evident that under the act of the quasi-periodical factor, namely differences in values of the potential barrier heights in the elements of SL a and b there is the effective splitting of the allowed bands, and it takes place at the normal incidence of an electronic wave on a lattice. The first Fibonacci generation is related to the strictly periodic SL with the values $V_b = V_a = V = 1$. In a corresponding spectrum, there are two basic gaps D and B that play an important role in spectra of the next generations.

The first one relates to the so-called new Dirac point (see [9, 10, 13, 14]), and we will name it the SL Dirac band, the second is the Bragg band. The position of the middle of the SL Dirac band is determined by the parameters of SL and as per the values taken here the indicated middle is located at a point $V/2 = 0.5$ [9, 10, 13, 14].

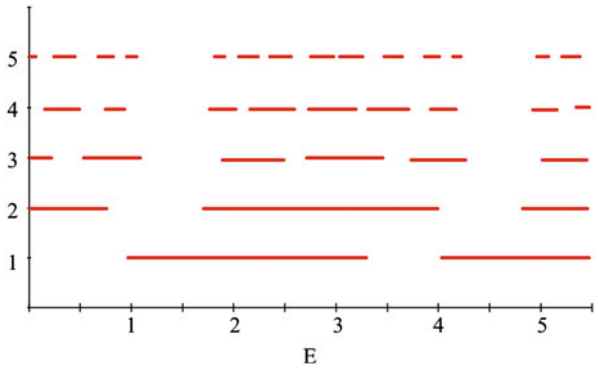

Fig. 3.1 Trace map of the energy spectra for the SL considered; n denotes the Fibonacci generation number

This one and other bands can be substantially moved with the change of barrier height, which is obvious from the figures presented.

In an interval between the bands D and B, under the act of the quasi-periodical factor, there is splitting of the allowed bands with the formation of several gaps. The widths and the number of bands and their location in the energy interval of D and B depends, on the one hand, on the parameters of the problem considered, and on the other, on the number of Fibonacci generation. This number of the allowed bands submits to the inflation Fibonacci rule $Z_n = Z_{n-1} + Z_{n-2}$ and in this case beginning from the third generation we have the following set of numbers: 3, 5, 8, 13...

As the quasi-periodical modulation in our problem is realized due to the different heights of potential barriers, it is important to see what changes are observed in spectra with the increase of difference between values V_a and V_b. First, it is necessary to notice that most gaps in spectra appear in the vicinity of energy $E = V_a$, or $E = V_b$, nearby a border between subbarrier and overbarrier regions, i.e., at energies with the strongest electronic wave perturbation. If barriers are near a size, then the strong perturbation of wave results in especially wide gaps. On the other hand, the closeness of values V_a and V_b means the weakness of the quasi-periodical factor. Thus, spectra are formed under the action of two counteractive tendencies. The above said is illustrated in Fig. 3.2 with values $d = w = 0.5$, $\Delta = 1$, $V_a = 1$, and $V_b = 3$, 5, 8, and 10 for Fig. 3.2a, b, c, d, respectively. The narrowing of the main gaps is observed with the simultaneous widening of the gaps which arise as a result of the effect of the quasi-periodical factor. This process is not monotonous; so with increasing of $\Delta V = | V_a - V_a |$ the P gap broadens and becomes larger than the Q gap, and then P gap becomes smaller than Q gap once again. An increase in difference between V_a and V_b results in narrowing of all gaps being not in a vicinity of V_a or V_b. Basic gaps can become narrower than, e.g., the P band (Fig. 3.2d).

It is interesting also to note that at certain parameters spectra have a structure that periodically recurs with the change of E. So, e.g., the high-symmetric, in relation to points R and S, spectra of Fig. 3.3 repeat their configuration in an interval approximately equal to 1.6.

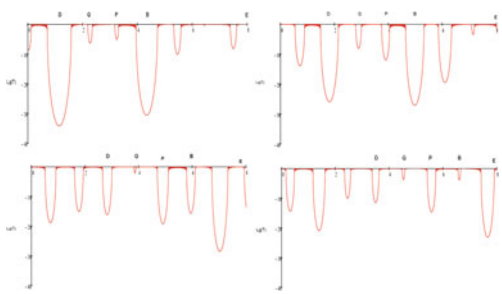

Fig. 3.2 Energy spectra of the third Fibonacci generation with different values of the barrier heights V_a and V_b

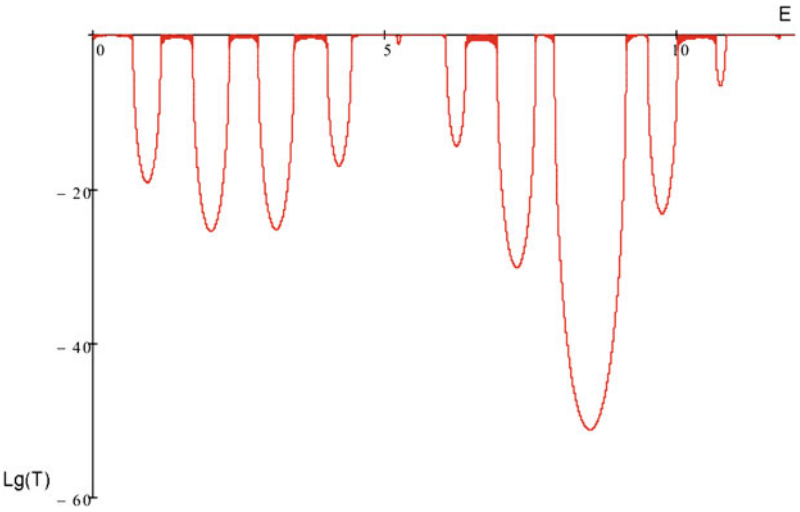

Fig. 3.3 Energy spectra of the third Fibonacci generation with the parameters: $\Delta = 1$, $V_a = 2$, $V_b = 8$, $w = 0.5$, $d = 1$

It is here appropriate to represent Fig. 3.4, in which the spectrum of the fifth Fibonacci generation is given for the wide enough range of energies. This figure shows that the investigated Fibonacci spectra of quasi-particles subjected to Eq. (3.1) expose a periodic character depending on the energy of E. In the spectrum, it is possible to distinguish the different areas of energies, less and large energy intervals, that can be considered the spectrum periods (more precisely the conventional periods), and each of them has a certain number of the allowed (forbidden) bands. The regions of energies between D and B gaps can be considered the least period of spectrum.

We would also like to note that the change of widths of bands has not the monotonous but the oscillating character—with an increase in E we see the alternating widening and narrowing of the forbidden (allowed) bands. As a result, broader periods are formed (conventionally superperiods). In other words, this wave-like variation in the bandwidth results in grouping of smaller separate units into larger ones with the formation of the additional structural order, and the self-similarity

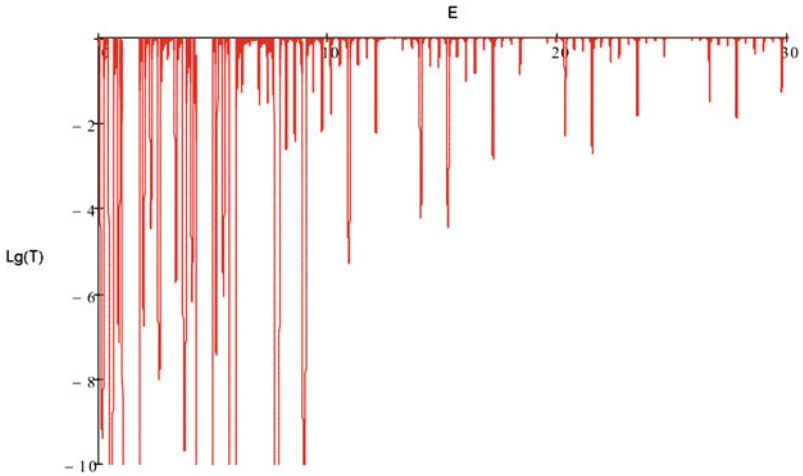

Fig. 3.4 Energy spectra of the 5th Fibonacci generation with the parameters: $\Delta = 1$, $V_a = 1$, $V_b = 4$, $w = d = 0.5$

property is manifested itself in this fact in our problem. The nonmonotonous change of widths of gaps, discussed above, is just explained by the fact that the spectrum on the axis of energies consists of totality of different sized periods, and it is necessary for providing of such complicated periodicity, that the widths of gaps changed on a corresponding complicated law.

References

1. Tsu R (2011) Superlattice to nanoelectronics, 2nd edn. Elsevier, Oxford327 p
2. Cheng Z, Savit R, Merlin R (1988) Structure and electronic properties of Thue-Morse lattices. Phys Rev B 37:4375
3. Geim AK, Novoselov KS (2007) The rise of graphene. Nat Materials 6:183
4. Castro Neto AN, Guinea F, Peres NMR, Novoselov KS, Geim AK (2009) The electronic properties of graphene Rev Mod Phys 81:109
5. Pereira JM, Peeters FM, Chaves A, Farias, GA (2010) Klein tunneling in single and multiple barriers in graphene Semicond Sci Tech 25:033002
6. Cheianov VV, Falko VI (2006) Selective transmission of Dirac electrons and ballistic magnetoresistance of n-p junctions in graphene Phys Rev B 74:041403
7. Zhao Q, Gong J, Muller CA (2012) Localization behavior of Dirac particles in disordered graphene superlattices Phys Rev B 85:104201
8. Barbier M, Vasilopoulos P, Peeters FM (2011) Single-layer and bilayer graphene superlattices: collimation, additional Dirac points and Dirac lines E-print archives, cond-mat/1101.4117 V 1
9. Wang L, Chen X (2010) Robust zero-averaged wave-number gap inside gapped graphene superlattices E-print archives, cond-mat. Mes-hall/1008. 0504, V 1
10. Wang L, Zhu S (2010) Electronic band gaps and transport properties in graphene superlattices with one-dimensional periodic potentials of square barriers Phys Rev B 81:205444
11. Nhuyen VH, Bournel A, Dollfus P (2011) Resonant tunneling structures based on epitaxial graphene on SiC Semicond Sci Technol 26:125012

12. Barbier M, Vasilopoulos P, Peeters FM (2009) Dirac electrons in a Kronig-Penney potential: Dispersion relation and transmission periodic in the strength of the barriers Phys Rev B 80:205415
13. Zhao P, Chen X (2011) Electronic band gap and transport in Fibonacci quasi-periodic graphene superlattice E-print archives, cond-mat. Mes-hall/1111. 1754 V 1
14. Ma T, Liang C, Wang L, Chen X (2011) E-print archives, cond-mat. 1754 V 1
15. Bliokh YuP, Freilikher V, Savel'ev S, Nori F (2009) Transport and localization in periodic and disordered graphene superlattices Phys Rev B 79:075123
16. Ratnikov PV (2009) Superlattice based on graphene on a strip substrate JETP Lett 90(6):469
17. Meyer JC, Girit CO, Crommie MF, Zetti A Hydrocarbon lithography on graphene membranes (2008) Appl Phys Lett 92:123110
18. Sutter PW, Flege J, Sutter EA (2008) Epitaxial graphene on ruthenium. Nat Materials 7:406
19. Coraux J, N'Diaye AT, Busse C, Micheli T (2008) Structural coherency of graphene on Ir(111). Nano Lett 8:565
20. Son YW, Cohen ML, Louie SG (2006) Energy gaps in graphene nanoribbons. Phys Rev Lett 97:216803
21. Han MY, Ozyilmaz B, Zhang Y, Kim F (2007) Energy band-gap engineering of graphene nanoribbons. Phys Rev Lett 98:206805
22. Giovanetti G, Khomyakov PA, Brocks G, Kelly P, van der Brink J (2007) Substrate-induced band gap in graphene on hexagonal boron nitride: *Ab initio* density functional calculations Phys Rev B 76:073103
23. Zhou SY, Gweon G, Fedorov AV, Guinea F, Castro Neto AH, Lanzara A, First P, de Heer W, Lee D-H (2007) Substrate-induced bandgap opening in epitaxial graphene. Nat Materials 6:770
24. Balog R, Jorgensen B, Nilsson L, Anderson M, Rienks E, Bianchi M (2010) Bandgap opening in graphene induced by patterned hydrogen adsorption. Nat Materials 9:315
25. Casolo S, Martinazzo R, Tantardini GF (2011) Band Engineering in Graphene with Superlattices of Substitutional Defects J Phys Chem C 115(8):3250

Chapter 4
Carbon-Based Piezoresistive Polymer Composites

Sara Cravanzola, Federico Cesano, Lucia Muscuso, Domenica Scarano and Adriano Zecchina

4.1 Polymeric Composites

The field of nanostructure science and technology has been growing very rapidly in the past few years, since the realization of new materials and devices from nanoscale building blocks could access new and improved properties and functionalities. As a result of these developments, a wide range of new opportunities for research and applications in the field of nanotechnology now present themselves. Some examples of potential applications with significant technological impact can be identified, such as dispersions and coatings and synthesis of high surface area materials with ultra-high strength and conduction properties. Considerable resources are being expended around the world for research and development aimed at realizing these and a variety of other promising applications [59].

Polymers represent a class of materials which, due to their well-known electrical insulating properties, are widely used in many electronic fields.

In recent years, the interest in obtaining polymers with new characteristics has considerably increased, trying to combine them with conductive nanomaterials, such as metals or carbon-based systems. Thus, the so-called polymeric conductive composites belong to the wide class of the composite materials, which attracts scientific,

S. Cravanzola (✉) · F. Cesano · L. Muscuso · D. Scarano · A. Zecchina
Department of Chemistry, NIS (Nanostructured Interfaces and Surfaces), Centre of Excellence and INSTM Centro di Riferimento, University of Torino, Via P. Giuria, 7, 10125 Torino, Italy, Tel.: 0039 011670 8372
e-mail: sara.cravanzola@unito.it

F. Cesano
e-mail: federico.cesano@unito.it

L. Muscuso
e-mail: lucia.muscuso@unito.it

D. Scarano
e-mail: domenica.scarano@unito.it

A. Zecchina
e-mail: adriano.zecchina@unito.it

O. Fesenko, L. Yatsenko (eds.), *Nanocomposites, Nanophotonics, Nanobiotechnology, and Applications,* Springer Proceedings in Physics 156,
DOI 10.1007/978-3-319-06611-0_4,

industrial and commercial interest, with an annual production which goes beyond 10 tons [81].

Generally, a composite is a system made up of the combination of two or more phases with different structure and chemical composition, which brings about an enhancement of physical, chemical or mechanical properties.

Therefore, from a technological point of view, the combination of two materials is particularly useful to integrate the properties of the two components in a hybrid material. Thus, they can be used in catalysis, nanoelectronics, energy storage, gas sensors and solar cells, to name but a few [56].

Many materials are used as fillers; among those, inorganic materials such as semiconductors PbS, CdSe, CdTe, ZnS [40] and SnO_2 [54] can be used in high-refractive-index materials, light-emitting diodes, photocatalysts, photovoltaic solar cells and non-linear optical devices. Other possibilities are represented by conventional fibres made from alumina, glass, boron, silicon carbide and conductor carbon [47]. All these cited materials are fillers of special interest because, depending on the polymer matrix structure and on the peculiar treatments (UV-Vis, γ-ray or moderate temperature curing), they allow to obtain composites characterized by novel properties [8, 25, 40, 54, 71].

As far as conductive polymeric composites are concerned, the combination of the peculiar electrical and mechanical properties of the fillers, together with some typical characteristics of polymers, resistance to chemical corrosion, simplicity of production and manufacturing, low costs, low density and lightweight if compared to metals [83], offers new and interesting opportunities.

In particular, the polymer nanocomposites are made up of a polymeric matrix (i.e. polypropylene, polyethylene, polyvinylchloride) and nanostructured materials, known as nanofillers.

Nowadays, concerning nanofillers, carbon nanofibres, nanographite, graphene and single-wall carbon nanotubes (SWCNTs) or multiwall carbon nanotubes (MWCNTs) are the most promising materials [7, 9, 18, 37, 52] due to their excellent electrical and mechanical properties.

The reason for this is that carbon particles, mainly carbon fibres and CNTs, have a much greater tendency to form a conductive network due to their chain-like aggregate structures compared with other conducting additives such as metal powder [81].

Focusing on the electrical properties of carbon/polymer nanocomposites, the conductivity of such composites is usually discussed in terms of percolation theory [56]. Following this, the material exhibits an abrupt insulator-to-conductor transition at a specific concentration of the conductive filler (percolation threshold) due to the formation of a continuous conductive network. A detailed description will be given in the following paragraphs.

A further element of interest in this kind of composites is piezoresistivity. It means that electrical conductivity is stress–strain dependent, that is to say that it changes because of a deformation applied to the material, which causes the mechanical properties of the composite to change. This implies that these composites can be used for deformation and pressure sensing. This property has been observed in reinforced polymer matrices or wearable textiles [29, 39] as well as for carbon

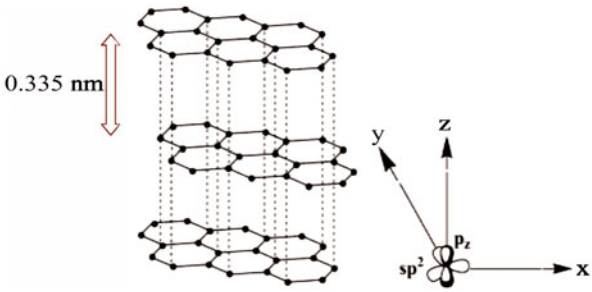

Fig. 4.1 Layered graphene structure of graphite and hybridation of *p* orbitals

nanofibre/polypropylene [55], multiwalled nanotubes/polyimide, multiwalled nanotubes/rubber composites [16, 24, 50] and in hybrid CNTs/expanded graphite (EG) sheets [31].

4.1.1 EG: Synthesis and Properties

EG is an important carbon material for the industrial production of graphite sheets, which are flexible, compactable and resilient [80]. As graphite, its structure is composed of layers of stacked graphene sheets.

Graphene is a two-dimensional, crystalline allotrope of carbon. In graphene, carbon atoms are densely packed in a regular sp^2-bonded atomic-scale hexagonal pattern. Graphene can be described as a one-atom-thick layer of graphite. It is the basic structural element of other allotropes, including graphite, CNTs and fullerenes.

Carbon atomic orbitals *s,* p_x and p_y are hybridized and generate strong sp^2 covalent bonds. The atomic orbital p_z is overlapped with the three adjacent carbon atoms, creating a π (valence band) and a π^* orbitals band (conductance band) (Fig. 4.1).

Usually, EG is prepared by rapid heating of expandable graphite to a high temperature, obtaining the thermally expanded graphite (TEG) [3, 80]. Expandable graphite includes the so-called graphite intercalation compounds (GICs).

Similarly to graphite, TEG is chemically inert and heat resistant. Its electrical and thermal conductivities are determined by the porous structure of the material. Thanks to a unique combination of properties of the material and to the possibility of their purposeful modification, catalysts, adsorbents, fireproofing, composites, flexible heaters and many other TEG-based articles are widely used in modern high-tech industry. The high chemical and thermal stability, combined with controllable electrical and thermal conductivity, porosity and developed specific surface area, create prerequisites for the development of multifunctional materials [78].

The general principle for production of TEG is the intercalation of substances or compounds, which either are themselves converted into gas upon rapid heating or give gaseous decomposition products, into the interlayer spaces of graphite. Many methods have been developed for GIC synthesis: they are subdivided into *chemical* methods and *electrochemical* methods [78]. The chemical model of GIC formation

presumes occurrence of conjugated reactions of oxidation and acid intercalation. The necessity for presence of an oxidizing agent is due to the low redox potential of the systems containing most of the acids being introduced, which cannot withdraw electrons from the graphite network. An exception is provided by nitric and perchloric acids, which are self-intercalating agents. As oxidizing agents a wide variety of compounds can serve: CrO_3, $K_2Cr_2O_7$, $(NH_4)_2S_2O_8$, HNO_3, $KMnO_4$, H_2O_2, O_3, etc.

A particular place among GICs is occupied by compounds with sulphuric and nitric acids, i.e. graphite bisulphate and graphite nitrate. For example, the chemical method for synthesis of graphite bisulphate consists in oxidation of graphite with an H_2SO_4 solution additionally containing an oxidizing agent. The rate of formation and stage of the resulting graphite bisulphate is dependent on the H_2SO_4 concentration and on the nature and content of the oxidizing agent in the solution.

The chemical method is rather technologically and instrumentally simple. However, changes in the concentration of an acid and of the oxidizing agent in the course of the intercalation predetermine inhomogeneity of the GIC composition. In addition, the compounds obtained are contaminated with the oxidizing agent and products of its reduction. This, combined with the high concentration of the acids, requires a large expenditure of water for hydrolysis and washing of the final product [78].

The electrochemical method has a number of advantages over the chemical technique: it is environmentally safer, the compound obtained is not contaminated with the oxidizing agent and products of its reaction and synthesis can be performed in a controlled mode, which makes it possible to obtain with high precision a product of the required composition and diminishes the expenditure of the acid. The electrochemical synthesis is used to produce GICs with inorganic and organic acids such as H_2SO_4, HNO_3, $HClO_4$, $HSeO_4$, CF_3COOH and HCOOH. For example, the electrochemical synthesis of graphite bisulphate is based on anodic oxidation of graphite in H_2SO_4 solutions of sufficient concentration [78].

As regards the thermal expansion of GICs, its mechanism is still a matter of discussion. Some studies assume that carbon networks break down after fast removal of a certain amount of intercalating particles from the interlayer space of the graphite host, with neighbouring planes disintegrated. In other works [2], the process of thermal expansion of graphite is regarded as a phase transition caused by the removal of the intercalating agents from GIC. The degree of foaming depends on the synthesis conditions and the composition of the resulting GIC, as well as on the structure and size of the particles of the starting carbon raw material. Most frequently, it is assumed that the fast heating of GIC gives rise to a pressure between layers of carbon networks of graphite, and this pressure has a dispersing effect.

The basic and technological characteristic of TEG is its low bulk density, which largely depends on preparation conditions.

Owing to their high inertness towards corrosive media and thermal stability, combined with elasticity and plasticity, TEG-based materials can replace such conventional sealing and laying materials such as fluoroplastic, copper and lead. Their use is especially effective in chemical and oil-and-gas machine building, fuel-and-energy complex, as electrically and structuring additives in electrodes of lithium chemical power cells to improve their specific characteristics and in conductive composites.

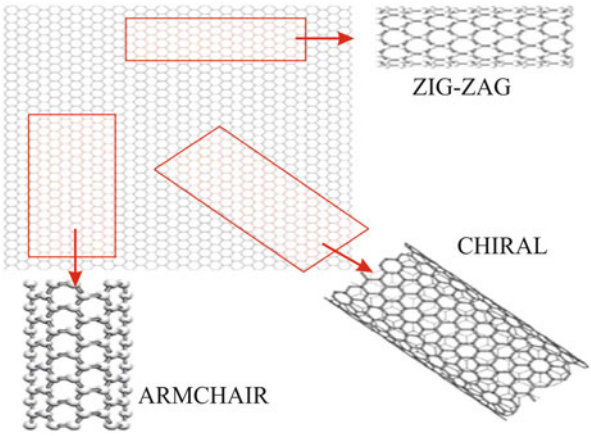

Fig. 4.2 A schematic image of a graphene layer and SWCNTs formed by rolling up of rectangular strips of a hexagonal graphite monolayer. The short side of the rectangle becomes the tube diameter. The rectangle must be properly oriented with respect to the flat hexagonal lattice, which allows only a finite number of roll-up choices, leading to different tube structures such as zig-zag, chiral or armchair

4.1.2 CNTs: Synthesis and Properties

CNTs represent one of the best examples of novel nanostructures derived by bottom-up chemical synthesis approaches. Nanotubes have a simple chemical composition and atomic-bonding configuration but exhibit perhaps the most extreme diversity and richness among nanomaterials in structures and structure–property relations.

CNTs can be visualized as graphene layers rolled into cylinders consisting of a planar hexagonal arrangement of carbon–carbon bonds. Their outstanding properties are a consequence of this unique bonding arrangement combined with the topological defects required for rolling up the sheets of graphene into cylinders.

Nanotubes are classified into two types, namely MWCNTs and SWCNTs [17]. Their diameters range from a few nanometres to tens of nanometres with lengths ranging from several micrometers to millimetres or even centimetres. MWCNTs contain several concentric, coaxial graphene cylinders with interlayer spacing of 0.34 nm. Note that this spacing is larger than for single crystal graphite (0.335 nm). The intershell spacing ranging from 0.34 to 0.39 nm decreases with increasing the CNT diameter [67]. The geometrical constraints in forming the seamless honeycomb graphene cylinders cause the layers to be uncorrelated with respect to each other, which is in contrast to crystalline graphite that exhibits a perfect 'ABAB' layer stacking. In the case of SWCNTs, the structure consists of a single cylinder and special properties emerge from the strong one-dimensionality and crystalline perfection of the structure. SWCNTs can be metallic or semiconducting depending on the geometrical characteristics of their structure, that is the orientation of the hexagons with respect to the nanotube axis (chirality). In fact, a SWCNT can be represented as a single sheet of graphene rolled into a cylinder along a (m, n) lattice vector $\mathbf{C}_h = n \times a_1 + m \times a_2$ in the graphene plane. The (m, n) indices determine the diameter and the chirality, which are key parameters of a nanotube [15]. Depending on n and m values, armchair, zig-zag and chiral tubes are obtained (Fig. 4.2).

$$n = m : armchair \text{ structure.}$$

$$m = 0 : zig\ zag \text{ structure.}$$

$$n \neq m \neq 0 : chiral \text{ structure}$$

Armchair nanotubes are always metallic, while zig-zag and chiral nanotubes can be either metallic or semiconducting. For $(n - m)/3 =$ whole number, the nanotube is metallic. For $(n - m)/3 =$ fractional number, the nanotube is semiconducting [23].

For same-chirality semiconducting nanotubes, the band gap is inversely proportional to the diameter. Thus, there are infinite possibilities in the type of carbon tube 'molecules', and each nanotube could exhibit distinct physical properties.

In the case of MWCNT where conduction occurs through the outermost shell, the large diameter of the outer nanotube causes the structure to be essentially non-semiconducting [67].

Arc discharge, laser ablation and chemical vapour deposition (CVD) have been the three main methods used for CNT synthesis [4, 15, 67]. The first two employ solid-state carbon precursors to provide carbon sources needed for nanotube growth and involve carbon vaporization at high temperature (thousands degrees Celsius). These methods are well established to produce high-quality and nearly perfect nanotube structures, despite large amounts of by-products associated with them. CVD utilizes hydrocarbon gases as sources for carbon atoms and metal catalyst particles as 'seeds' for nanotube growth that takes place at relatively lower temperatures ($500 - 1000\,^{\circ}C$).

Arc discharge: An electric arc is generated between two graphite electrodes under a helium or argon atmosphere, which causes the graphite to vaporize and condense on the cathode. The deposit contains the nanotubes and also fullerenes, amorphous carbon materials and catalyst particles. This technique requires further purification to separate the CNTs from the by-products present in the crude material. The electrodes of graphite are doped with catalytic metal atoms (Ni, Co) for the production of SWCNTs.

Laser ablation: A laser ablates a graphite target in flowing argon at a temperature near 1200 °C. The graphite target contains a small amount of a metal catalyst such as nickel, cobalt, iron and platinum. It has been shown that bimetallic catalysts are more productive than single metals. Various configurations of laser ablation experiments were developed for the production of SWCNTs. They range from a single- or dual-pulsed laser to a continuous laser. The yield, mean diameter and diameter distribution can be changed by varying the growth temperature, gas pressure, catalyst composition and laser pulse.

CVD: It consists in the pyrolysis of a carbon source such as carbon monoxide, hydrocarbon gases (acetylene, ethylene, methane) or liquid aliphatic saturated hydrocarbons over metal catalyst-supported silica, alumina or zeolite at temperatures between 500 and 1000 °C. The catalyst consists of nano-sized particles of a single metal (Fe, Co or Ni) or a mixture of metals.

Small amounts of CNTs can be formed by arc discharge and laser ablation which is really a limitation to scale up the production to the industrial level. Larger quantities of nanotubes can be obtained by CVD.

4.1.3 Composite Processing and Fabrication

Fabrication methods have focused on improving carbon-filler dispersion. In fact, a better filler dispersion in the polymer matrices has been found to improve the properties because of the enhanced interfacial interaction with the matrix itself. For example, a functionalization of CNTs can improve nanotube dispersion in solvents and polymers [49]. Solution blending, melt blending and in situ polymerization [11, 46, 60] are the most widely applied methods to produce carbon-based polymer composites.

Solution processing: The most common method for preparing composites implies the mixing of conductive filler and polymer matrix into a certain solvent and evaporating the latter to form a composite film. All the solution-processing methods are variations on a general theme which includes the dispersion of carbon filler powder in a liquid medium by vigorous stirring and/or sonication, mixing the dispersion with a polymer in solution by energetic agitation and controlled evaporation of the solvent with or without vacuum conditions. Agitation is usually provided by magnetic stirring, reflux or ultrasonication. Sonication can be provided in two forms: mild sonication in a bath or high-power sonication using a tip or horn [27]. The choice of solvent is generally made based on the solubility of the polymer.

An advantage of this method is that agitation of the filler in a solvent facilitates particle de-aggregation and dispersion. However, it must be pointed that pristine nanotubes cannot be well dispersed in most solvents. To get around this problem, additives are used, such as surfactants (e.g. sodium dodecylsulphate), to disperse the nanotubes before mixing with the polymer solution [75].

Melt mixing: Due to the fact that thermoplastic semi-crystalline polymers soften when heated above their melting point, melt processing has been a very valuable technique and it is most compatible with current industrial practices. In fact, melt mixing uses high temperatures and high shear forces to disperse carbon fillers in a polymer matrix. Depending on the final morphology and shape of the composites, samples can then be processed by several techniques, such as extrusion [13, 14, 75]. The method is suitable for polymers that cannot be processed with solution techniques due to their insolubility in common solvents.

However, relative to solution-blending methods, melt mixing is generally less effective for dispersing carbon fillers in polymers and it is limited to lower concentration due to the high viscosities of the composites at higher filler loadings.

In situ polymerization: This fabrication strategy starts by dispersing the carbon filler in a monomer, followed by polymerizing the monomer. The main advantage of this method is that it produces polymer-grafted filler particles, mixed with free polymer chains, and enables covalent bonding between the carbon filler and the polymer matrix using covalent reactions. Moreover, due to the small size of monomeric molecules, the homogeneity of the resulting composite adducts is much higher than mixing filler and polymer chains in solution. In this sense, the method allows the preparation of composites with high-conducting filler weight fraction. This technique is particularly important for the preparation of insoluble and thermally unstable polymers, which cannot be processed by solution or melt blending.

Depending on required molecular weight and molecular weight distribution of polymers, chain transfer, radical anionic, ring-opening metathesis and catalysed (Ziegler–Natta) [30, 63] polymerization reactions can be used.

4.2 Electrical Conductivity Percolation Threshold

Concerning the properties of polymeric conductive composites, the fundamental one is, of course, electrical conductivity.

Electrical conductivity is the measure of a material's ability to accommodate the transport of an electric charge. In a polymeric composite, the transport of electrons is guaranteed by the filler nanoparticles that can establish a conductive network of contacts, creating a pathway for the transfer of electrons within the polymer matrix.

Depending on the type and the concentration of the nanofiller, several conduction mechanisms have been suggested: the tunnelling effect and the conduction path theory [81].

The tunnelling effect describes the electrical conductivity not only as a consequence of a direct contact between conducting particles but also as the ability of electrons to 'jump' across energetic barriers, gaps or tunnels between the conductive elements within the polymeric matrix. It is a quantomechanical process occurring when the distance between the conductive components lies in the order of few nanometres. The tunnelling effect takes place according to the type, the concentration and the dispersion degree of the nanofiller. It is promoted at high temperatures because the thermal fluctuations cause the potential barrier of carbon aggregates to decrease. In particular, for temperatures in the 45–298 K range, conduction strongly depends on the thermal fluctuations, while below 45 K, temperature does not influence the conduction anymore [12].

On the other hand, according to the conduction path theory the electron motion within the conductive material occurs through a continuous chain (network) established by the physical contact between the filler particles.

The significant difference between the two described mechanisms lies in the amount of conductive material. For the conduction path theory, the physical contact between carbon aggregates is essential, making the formation of the continuous network more probable for higher concentrations of filler.

For the tunnelling effect, otherwise, a lower amount of filler is sufficient.

Many factors affect the conductive properties of polymeric composites [12, 21]; in particular, the operative conditions adopted during the mixing of the polymer and nanofiller to prepare the composite are crucial. On one hand, long mixing times guarantee a homogeneous dispersion of nanoparticles within the polymer matrix. On the other hand, too much extended times can lead to the fracture of the carbon aggregates or to the formation of very short carbon fibres, unfavouring the formation of the conductive network. In fact, during mixing operations, when new filler–polymer bonds form, some pre-existing filler–filler bonds are broken.

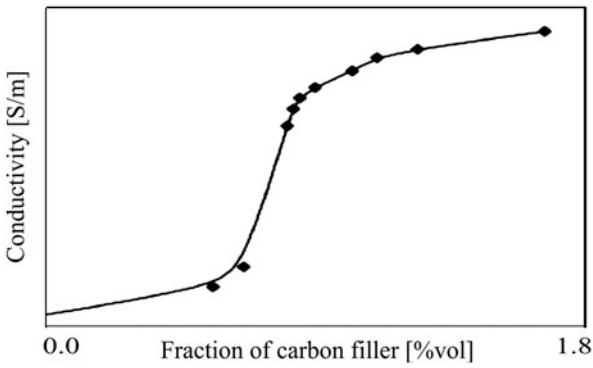

Fig. 4.3 Typical S curve representing the electrical behaviour and percolation threshold for a carbon-based polymer composite at 298 K

Conductivity is strongly affected by the type of the filler in terms of geometrical and morphological characteristics, particle dimensions and porosity and by the nature of the polymer. It is a matter of fact that polymers with different properties influence in a different way the conductivity of the composite.

The polymeric matrix–conductive nanofiller compatibility is also very important. To this purpose, it is essential to evaluate the ideal operative conditions for the preparation of a composite to obtain a product with high properties.

On the basis of data which correlate the conductivity of a composite to the fraction of its conducting nanofiller, it can be shown that in a narrow range, a small increase of the filler can bring a drastic change in the value of electrical conductivity.

This behaviour is shown in Fig. 4.3 for a carbon fibre/silica rubber composite [79].

The graph shows a typical S-shaped curve representing the electrical conductivity of the composite as a function of the content of nanofiller. Within the small range in which the volume fraction of carbon fibre changes from 0.78 to 0.84 %, the electrical conductivity drastically increases. This is due to a sudden change in the dispersion of the carbon nanoparticles and then in their mutual structural interaction.

The volume fraction of a filler at which an insulator-to-conductor transition is shown is called percolation threshold. It is the limit amount of the conductive phase that is necessary to create a conductive network within the material. This makes electron transfer suitable to give electrical conductivity to the polymer.

Many factors can influence the value of the percolation threshold. It rises when the polarity [45] and the viscosity [57] of the polymer increase. The crystallization degree of the polymer is also important: Narkis and Vaxman [48], studying the electrical resistance of high-density polyethylene added with carbon black particles, observed a tendency of the smallest carbon aggregates to concentrate in the amorphous regions of the polymer. Therefore, the percolation threshold in semi-crystalline systems is lower than in amorphous systems.

Otherwise, the type and the amount of the conductive filler are crucial. In fact, the fraction of the conductive phase has to be sufficient to give to the composite the desired electrical characteristics, but not too high, in such a way to avoid problems during the production phase and then to decrease the quality of the mechanical properties of the composite.

Various theoretical approaches have been applied to describe the electrical conductivity of composites. For example, Stankovich et al. [61] described the percolation threshold as a rapid increase in the direct current electrical conductivity of the composite materials, taking place when the conductive filler forms an infinite network of connected paths through the insulating matrix. When the filler particles are rigid bodies, the conductivity of such media is typically described with a bond percolation model [62]. The conductivity of the composite σ_c above the percolation threshold is then treated with a power law [43].

$$\sigma_c = \sigma_f[(\phi - \phi_c) / (1 - \phi_c)]^t$$

where σ_f is the conductivity of the filler, ϕ the filler volume fraction, ϕ_c the percolation threshold (the onset of the transition) and t is the 'universal critical exponent'.

In the classical percolation theory, the conductivity of a composite has been expressed as [27]:

$$\sigma_c = \sigma_0(\phi - \phi_c)^t$$

where ϕ is the volume fraction of the filler, ϕ_c is the volume fraction of the filler at the percolation threshold and σ_0 is the conductivity of the filler.

The critical exponent (t) is universal; it depends only on the type of percolation model [81] and on the dimensionality of the system, t values being comprised between 1–1.3 and 1.6–2 for two-dimensional and three-dimensional networks, respectively [27].

The classical percolation theory is valid for spherical, monodispersed, isotropically conductive particles. Otherwise, the obtained theoretical value deviates from the real one.

4.2.1 Percolation for Two Fillers

The use of a combination of different carbon fillers (1D, 2D, 3D) can help to obtain composites with enhanced properties, getting a balance of properties and costs of the different fillers [42, 76]. In fact, each type of carbon filler has its own characteristics. For example, graphite is cheap but its percolation threshold is very high, which could lead to distortion of mechanical properties. On the contrary, CNTs have a very low percolation threshold but high costs.

It has been proved that combinations of fillers further improve the electrical conductivity of the composite material because additional pathways for electron transport are formed between the different fillers. Combinations of different carbon particles do have a positive synergistic effect [20, 42, 65] for conductive properties. For example, carbon fibres or CNTs [82] can act as long-distance charge transporters, while particulate carbon black [10], graphite [69] or graphene/expanded graphite [33] act as an interconnection between the fibres by forming a dense conducting network [77, 82].

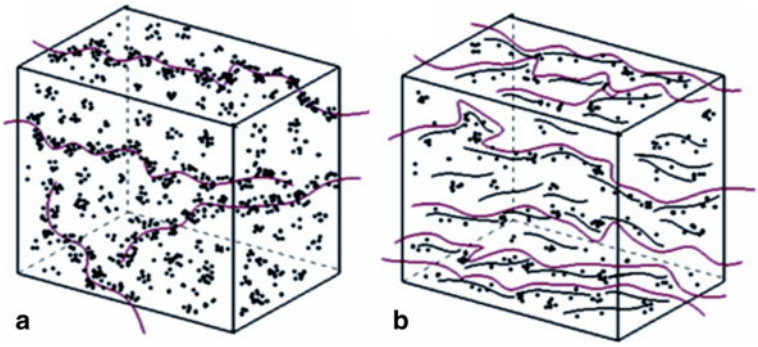

Fig. 4.4 In violet, conductive pathways are represented for composites containing **a** carbon black and **b** carbon black and CNTs as conducting fillers

The co-presence of conducting fillers of different dimensionality (1D and 2D) able to enhance the conductivity of the composite gives rise to the well-known synergistic effect, shown in Fig. 4.4.

For example, 1D MWCNTs are flexible and can promote the formation of new conducting pathways by bridging adjacent 2D graphite platelets or carbon black, with the generation of conductive structures [14].

Moreover, it has also been demonstrated that the incorporation of binary combinations of nanocarbons results in extraordinary synergy in mechanical properties (hardness and elastic modulus [53]).

A model of the electrical conductivity for the evaluation of the percolation threshold for mixed-carbon-filler-filled systems can be proposed on the basis of the excluded volume theory [66]. In polymer science, excluded volume refers to the idea that one part of a long chain molecule cannot occupy space that is already occupied by another part of the same molecule [28]. In other words, the excluded volume of a molecule is the volume that is inaccessible to other molecules in the system as a result of the presence of the first molecule [28].

According to the excluded volume theory, the number of objects per unit volume at percolation q_p is inversely proportional to the excluded volume $V<_{ex}>$ of one of the objects.

$$q_p \sim 1/(V_{<ex>})$$

It is possible to define V_{unit} as the unit volume, N_c as the number of objects in the unit volume V_{unit} at percolation and k as the proportionality constant:

$$N_c = k\,(V_{unit}/V_{<ex>})$$

That is to say, $V_{unit} = (N_c V_{<ex>})/k$, where k shows the relationship between N_c/V_{unit} and $1/V_{<ex>}$.

k becomes unity when the aspect ratio of the object is long and randomly oriented [6].

If there is only one type of conductive filler, then we may assume that the unit volume V_{unit} is divided into N_c with much smaller equivalent volumes (called small volumes thereafter), and each small volume is $V_{<ex>}/k$.

Therefore, if there is only CNT-type filler and the averaged excluded volume of one CNT object is $V_{<CNT>}$ and the corresponding constant is $k_{CNT,}$ then the small volume is $V_{<CNT>}/k_{CNT}$, and when one CNT object occupies one small volume ($V_{<CNT>}/k_{CNT}$), percolation occurs [66].

For a system containing two types of conductive fillers *a* and *b,* the unit volume can be divided into two types of small volumes, $V_a/k_a and V_b/k_b$:

$$\mathrm{V_{unit}} = \mathrm{N'_a}\,(\mathrm{V_a/k_a}) + \mathrm{N'_b}\,(\mathrm{V_b/k_b})$$

where N_a and N'_b are the numbers of *a* and *b* objects, respectively.

When all of the small volumes are filled, percolation occurs.

It is possible to explain V_{unit} as follows:

$$\mathrm{V_{unit}} = \left(\mathrm{V_a}/\phi_{\mathrm{c,a}}\right)\mathrm{V_{unit}} + \left(\mathrm{V_b}/\phi_{\mathrm{c,b}}\right)\mathrm{V_{unit}}$$

where V_a and V_b are the actual volume fractions of *a* and *b* objects and $\phi_{c,a}$ and $\phi_{c,b}$ are the percolation concentrations of *a* and *b* expressed in volume fraction if the unit volume is filled with *a* or *b* alone.

$$\left(\mathrm{V_a}/\phi_{\mathrm{c,a}} + \mathrm{V_b}/\phi_{\mathrm{c,b}}\right) = 1$$

It means that when $\left(\mathrm{V_a}/\phi_{\mathrm{c,a}} + \mathrm{V_b}/\phi_{\mathrm{c,b}}\right) = 1$, the conductive fillers begin to percolate in the polymer matrix; when $\left(V_a/\phi_{c,a} + V_b/\phi_{c,b}\right) > 1$, the conductive fillers connect to each other, and the material is conductive; when $\left(V_a/\phi_{c,a} + V_b/\phi_{c,b}\right) < 1$, the conductive fillers separately disperse in the polymer matrix, and the electrical resistivity is high. It should be noted that the condition of using this last equation is that the dispersion of one type of filler is not affected by the presence of the other.

Furthermore, the volume fraction ϕ_c can be generalized like weight fraction for the convenience of practical use and the avoidance of the uncertainty of the fillers' density.

$$\left(\mathrm{M_a}/\mathrm{P_{c,a}}\right) + \left(\mathrm{M_b}/\mathrm{P_{c,b}}\right) = 1$$

where M*a* and M*b* are the weight fractions of fillers *a* and *b,* respectively, and $P_{c,a}$ and $P_{c,b}$ are the corresponding percolation concentrations when *a* and *b* are used alone.

4.3 Piezoresistivity

One of the most important properties of carbon-based polymer composites is piezoresistivity, which is a common sensing principle for sensors.

The piezoresistive effect describes a variation of the value of electrical resistivity of a material when it is subjected to an external mechanical deformation.

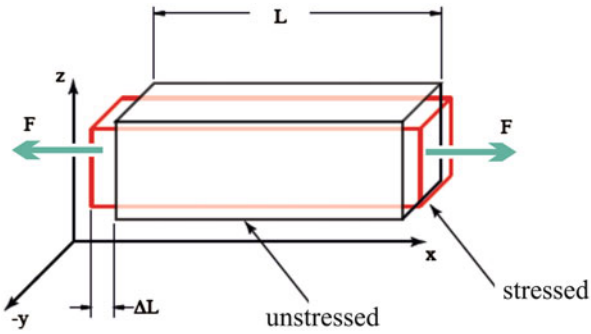

Fig. 4.5 Mechanical deformation of a composite

This property can be used for a large variety of sensing applications, including pressure sensors [64], tactile sensors [32], flow sensors, sensors for monitoring structural integrity of mechanical elements [26] and chemical and biological sensors.

The piezoresistive effect was first discovered by Lord Kelvin in 1856. An electrical resistor may change its resistance when it experiences strains and deformations. This effect provides an easy and direct energy/signal transduction mechanism between the mechanical and the electrical domains [38].

The resistivity r is the aptitude of a material to impede the transition of electrons. Usually, the value of resistance R is reported, that is determined by both the bulk resistivity and the dimensions:

$$\mathrm{R} = \rho \cdot (l/\mathrm{A})$$

where l is the length and A is the cross-sectional area of the resistor.

Consequently, there are two modes of resistance change when a device is deformed or strained. First, the physical changes in dimensions, including the length and cross section, are considered. It recalls the Poisson's ratio, which states that if we elongate a 'member', the dimensions change in all three axes x, y and z; that is to say, transverse strains may be developed in response to longitudinal loading, as shown in Fig. 4.5.

Assuming that the material is stretched or compressed along the axial direction (the x axis in Fig. 4.5):

$$\nu = -\left(\varepsilon_{\mathrm{trans}}/\varepsilon_{\mathrm{axial}}\right) = \left|\varepsilon_{\mathrm{y}}/\varepsilon_{\mathrm{x}}\right| = \left|\varepsilon_{\mathrm{z}}/\varepsilon_{\mathrm{x}}\right|$$

where ν is the resulting Poisson's ratio, $\varepsilon_{\mathrm{trans}}$ is transverse strain (negative for axial tension, positive for axial compression) and$\varepsilon_{\mathrm{axial}}$ is axial strain (positive for axial tension, negative for axial compression).

Second, the resistivity ρ of certain materials can change as a function of strain ε.

By strict definition, piezoresistors refer to resistors whose resistivity changes with applied strain [38]. Therefore, it is possible to establish a linear relation between the change in resistance and the applied strain:

$$(\Delta\mathrm{R}/\mathrm{R}) = \mathrm{G}(\Delta\mathrm{L}/\mathrm{L})$$

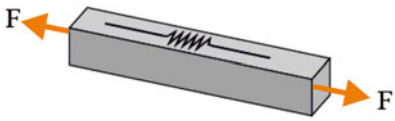

Fig. 4.6 Example of a longitudinal strain

where G is the so-called Gauge factor of a transistor. It is possible to explicitly express G as follows:

$$G = (\Delta R/R)/(\Delta L/L) = \Delta R/\varepsilon R$$

The resistance of a resistor is customarily measured along its longitudinal axis. However, for 2D, the total resistance change is the summation of changes due to longitudinal and transverse strain components [38]:

$$(\Delta R/R) = (\Delta R/R)_{\text{longitudinal}} + (\Delta R/R)_{\text{transverse}}$$

that is to say:

$$(\Delta R/R) = G_{\text{longitudinal}} \cdot \varepsilon_{\text{longitudinal}} + G_{\text{transverse}} \cdot \varepsilon_{\text{transverse}}$$

For any given piezoresistive material, the longitudinal and transverse gauge factors are different. The change of measured resistance under the longitudinal stress component is called longitudinal piezoresistivity (Fig. 4.6) The relative change of the measured resistance to the longitudinal strain is called the longitudinal gauge factor.

The change of resistance under transverse strain components is called transverse piezoresistivity (Fig. 4.7). The relative change of measured resistance to the transverse strain is called the transverse gauge factor [38].

Carbon-based polymer composites show high piezoresistive properties even under low deformations. Their piezoresistive behaviour is due to the deformation of the conductive network of filler particles within the polymeric matrix. In particular, during a mechanical deformation (e.g. compression) three main phenomena can occur [41]:

1. *Change in gap size in existing effective conductive path:* The compression makes the gaps between two adjacent conductive particles smaller, leading to the decrease of the electrical resistance of existing effective conductive paths.
2. *Formation of new effective conductive paths:* The compression makes the gaps between carbon particles smaller, leading to the formation of new effective conductive paths, then contributing to the increase of their number.
3. *Destruction of effective conductive paths:* The transverse slippage of carbon black, caused by compression, leads to the destruction of effective conductive paths. This effect contributes to the decrease of the number of effective conductive paths.

The changes in (1) and (2) contribute to the decreasing of the resistance. The change in (3) contributes to the increasing of the resistance.

Obviously, piezoresistivity properties of a composite strongly depend on the kind and the concentration of filler and on the type and strength of the mechanical deformation imposed [74].

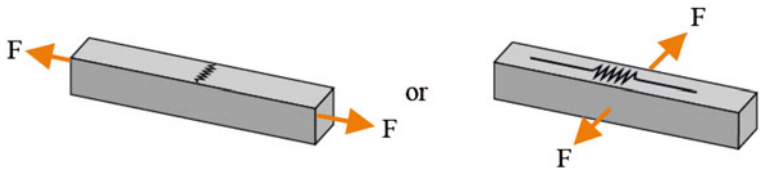

Fig. 4.7 Examples of transversal strains

Also, the type of polymer matrix can affect the piezoresistive behaviour. It has been demonstrated that, with the same content and structure of filler, the composite shows an enhanced piezoresistive response if the Young modulus of the polymer is lower. In fact, Young modulus represents the deformability of the material [73].

Piezoresistivity of graphene has been investigated by Medvedyeva et al. [44]. Usually, mechanical properties of graphene have been measured on suspended graphene flakes mechanically deposited over a hole. By indentation in an atomic force microscope (AFM), it can be shown that graphene is incredibly stiff [22, 36].

Recent experiments combine mechanical and electrical properties of graphene by measuring conductivity of suspended graphene flakes, which exhibit much higher mobility than graphene on substrate due to much weaker disorder [5, 19, 72]. Suspension of graphene flakes always leads to their deformation, which in turn affects the conduction properties of graphene. Deformation creates inhomogeneous elongation of the lattice constant which locally affects the electron spectrum of graphene. In some experiments, graphene flakes are typically suspended over a back gate, which redistributes the electron density in the flake due to the spatial variation of the capacitance. Medvedyeva considers two situations [44]: graphene deformed homogeneously by interaction with a gate and graphene deformed locally by an AFM tip. Experiments conclude that deformation of graphene can change the conductivity by inducing changes in the band structure as well as by changing the electron density over the flake. The two effects provide functionally different contributions to the conductivity. For small deformations, the correction due to the charge redistribution dominates and leads to the enhancement of the conductivity. For stronger deformations, the effect of the lattice distortion becomes more important and eventually leads to the suppression of the conductivity.

As for CNTs, piezoresistive characteristics can be evaluated under local-probe manipulation. In particular, Tombler et al. [68] prepared individual SWCNTs bridging metal electrodes on SiO_2/Si substrates, with part of the SWCNT length suspended over the trenches fabricated on the SiO_2 surface. The AFM tip was positioned above the centre of the suspended nanotubes. The nanotubes suspension was pushed towards the bottom of the trench by moving the sample stage upward. The stage was the retracted. The pushing–retracting cycle was repeated many times in which then AFM cantilever deflection and the resistance of the SWCNT sample were simultaneously recorded as a function of the time. Analysis revealed that strong local bonding deformation induced by the AFM tip is responsible for the conductance decrease of the SWCNT. When pushed by an AFM tip, the nanotube region proximal

to the tip exhibits significant changes in atomic-bonding configuration. For small bending angles, the nanotube retains sp^2 bonding throughout its structure. The nanotubes respond elastically but exhibit a larger bond distortion for the atoms in the region underneath the tip than the global strain [70]. This distortion accounts for an initial conductance decrease at small bending angles where the overall structure remains sp^2. As tip pushing proceeds, the tube structure progressively evolves and larger structural changes occur underneath the tip. The local bonding configuration changes from sp^2 to nearly sp^3. Away from the tip region, the nanotubes remain essentially in an sp^2-bonding configuration. Analysis in the tip vicinity reveals the onset of an increase in σ-electrons contributing to the local density. This is accompanied by a significant decrease of the π-electron density. As the π-electrons are delocalized and therefore mainly responsible for electrical conduction, a drastic reduction in the π-electron density is responsible for the substantial decrease in conductance [70].

Moreover, the length, the concentration of CNTs and the matrix elastic modulus influence the geometric piezoresistive sensitivity of a composite. The contribution of CNTs deformation on the piezoresistivity of polymer composites increases with increased CNT length and matrix elastic modulus [51]. The main factor responsible for a measured piezoresistive behaviour of CNTs/polymer composite is the change in the configuration of the CNTs network, rather than the changes in length and diameter of the CNTs themselves.

4.4 Piezoresistive Sensors

Over the years, piezoresistive sensing has been used for many categories of sensor applications, for example, inertia, pressure, tactile and flow sensors [38].

In inertia sensors, under an applied acceleration, a proof mass experiences an inertial force, which in turn deforms the mechanical support elements connected to the proof mass and introduces stress and strain. By measuring the magnitude of the stress, the value of the acceleration can be inferred. This is the basic principle of piezoresistive accelerometers.

The pressure sensor consists of a membrane suspended from the substrate by a small gap, where piezoresistive sensors experience tension when the membrane is deflected downward.

Tactile sensors are used to measure contact forces and to characterize surface profiles and roughness.

In flow sensors, fluid flow around a microstructure can impart a lifting force, drag force or momentum transfer on a floating element. These forces can cause the microstructure to deform, producing minute changes of stress in the floating element or its supporting structures. Piezoresistors located strategically on these structures can therefore infer the bending by measuring the resistance.

Piezoresistive materials find their main application in strain-sensing field. The applications of strain sensors are mainly used in engineering fields for structural

health monitoring of aerospace systems, wind turbines and civil structures among others. Some examples of these emerging sensing technologies include infrared thermography, shape-memory alloys, fibre optics, ultrasonics and acoustic emissions [39]. Strain measurements by the traditional sensors (metal and semiconductor strain gauges) have shown high sensitivities and are less expensive. However, despite these advantages, there are drawbacks. They are fixed directional sensors, meaning that strain can only be measured in a specific direction; they have low resolution at nanoscale and cannot be embedded in structural materials. The optical fibre sensors, mostly used as trunk lines for the transmission of information, have been attracting special interest recently due to their strain-sensing characteristics. Optical fibre strain sensors match quite well with other composite materials like glass and carbon fibre composites. They can be embedded into composites or can be fixed on the surface of the structural materials. They can measure very high strains and are well suited to highly stressed composite constructions. One of the major disadvantages of optical fibre strain sensors is the insensitivity to strain on a nanoscale [39].

Thin film piezoresistive strain sensors of single-walled/multiwalled CNTs and graphite serve as good alternatives for developing new sensors because of their outstanding properties.

CNTs thin film strain sensors can be embedded into structural materials and operate as both multidirectional and multifunctional sensors with high strain resolution on nanoscale. The electromechanical properties of CNTs thin film strain sensors exhibit excellent characteristics compared to the traditional sensors due to a combination of high elastic moduli and outstanding electrical properties [50].

4.4.1 Carbon-Based Polymer Piezoresistive Composite Strain Sensors

The strain sensing of CNTs-polymer composites is mainly due to the piezoresistive properties of the conductive network of CNTs in the polymer matrices.

When the network of CNTs is altered due to a mechanical deformation, there is an increase in the resistivity. This difference in the resistivity is associated with the modification of contact arrangements and the tunnelling distance between CNTs [50].

In general, this kind of polymer composites is produced in the shape of films or filament/fibres. CNTs films composed of randomly oriented single-walled or multiwalled CNTs make their electronic properties independent of direction. Hence, taking measurements along these different directions provides corresponding strains. CNTs films can also act as strong structural materials and sensors in composites.

Many types of polymers can be used for the production of composite sensors: polypropylene [14], polyethylene, epoxy matrices [39], poly(dimethylsiloxane) [35], polyether sulphone [58] and so on. Usually, piezoresistive characterizations are performed by conducting cyclic tension and compression tests on composite specimens (Fig. 4.8).

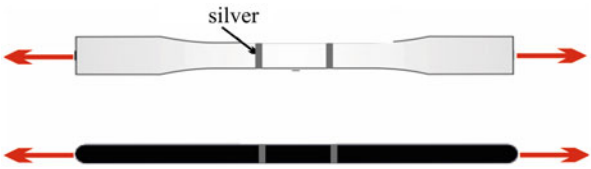

Fig. 4.8 Two different possible shapes for a composite specimen for tension and compression tests

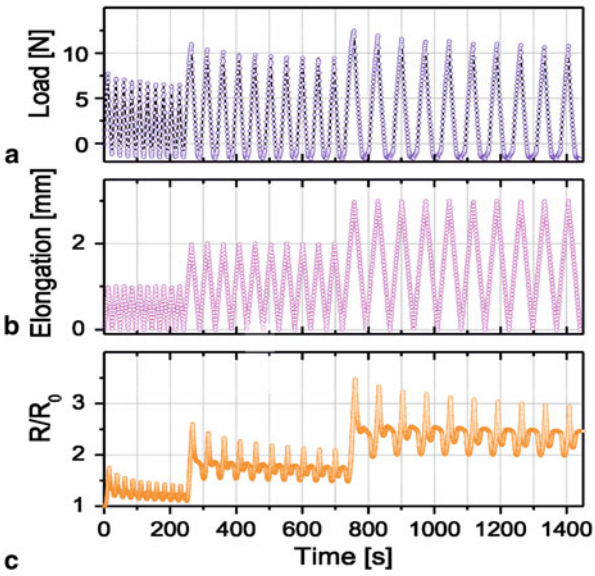

Fig. 4.9 **a** Load imposed on a conductive polymer composite fibre, **b** deformation (% elongation of the fibre) upon the cyclic loading cycles; **c** piezoresistive variations (R/R_0) upon tensile loading

Upon several cycles of mechanical deformation, (for example, traction) stress–strain curves and piezoresistive properties of samples are investigated by evaluating how the value of R/R_0 changes as a function of the imposed stress or strain. R represents the value of electrical resistance after the deformation and R_0 is the initial value of the electrical resistance [14].

Figure 4.9 shows the trend of the piezoresistive behaviour for a MWCNTs + EG/polypropylene composite fibre (1.5 mm in diameter).

It is inferred that under repeated elongation of the fibre, R/R_0 slightly drifts downward but abruptly increases for increased loadings. In other words, the R/R_0 changes are proportional to the tensile stress with synchronous variations and a good signal/noise ratio.

The reduction of R/R_0 amplitude, which occurs by applying several numbers of deformation cycles for each elongation percentage, can be due to the rearrangements of the MWCNTs conductive network. In fact, after each cycle, R/R_0 does not go back to its initial value, probably because some phenomena, occurring in the viscoelastic polymer matrix, permanently modifies the morphology of MWCNTs network [34].

To explain the non-specular signal in loading/unloading cycles, some considerations can be drawn. First of all, for piezoresistive CNT-based polymer composites a

linear piezoresistivity is usually obtained under low strains ($\varepsilon \leq 1\ \%$) [1], followed by non-linearity at larger strains. In addition, at the end of each cycle of the release step, a rebound peak of R/R_0 is obtained. It is an effect very common in carbon-based composite fibres upon cyclic tensile loading–unloading cycles and tensile–compressive cycles. Bumps were ascribed to the fibre buckling occurring in return steps [58]. Moreover, the electric conductivity in conductive polymer composites above the percolation threshold is a complex phenomenon, which can be explained as resistor networks among conductive nanofillers, with tunnelling resistances in neighbouring EG flakes and/or MWCNTs. Although at microscopic level, the electric conductivity of the nanocomposites can be deeply affected from aggregation phenomena; nevertheless, variations of conductive networks due to loss of contacts among nanofillers upon deformation and the intrinsic piezoresistivity of MWCNTs and of EG flakes cannot be inferred.

This kind of piezoresistive composite filament can be used in some real applications. A piezoresistive sensor device can be made by integrating two piezoresistive fibres into two sandwiched polymer panels. Each conductive fibre inside the device is able to monitor different areas of the panel. By monitoring the changes in electrical resistance of each fibre compared to the initial value, it is possible to evaluate the effect of an applied load in damaging the mechanical properties of the tested portion of the panel. Actually, it is possible to evaluate 'in situ' the structural integrity of a material examining the electrical resistance behaviour of the sensing polymer panel as a function of time without analysing the stress–strain curves [14].

Filaments, made by piezoresistive composites, can be also used to develop textiles which can detect environmental conditions and then react and adapt to environmental changes. These smart textiles can measure and monitor the physiological conditions of the wearer. Thus, they could be applied in health-care systems. Many applications based on this kind of sensing fabrics can be developed. One typical application is to capture posture or motion. The others are related to measuring biomechanical signals for health care, especially for respiration detections [29].

4.5 Conclusion

It is a matter of fact that carbon-based polymer composites are attracting more and more interest due to their distinct properties and their importance is expected to increase in the years to come.

When used as conductive materials, they possess the merits of lightweight, ease of manufacturing and chemical resistance.

These outstanding properties are given both by the polymeric nature of the matrix and by the carbon allotropes used as conducting fillers. CNTs, EG and graphene are nowadays challenging due to their special electrical and mechanical characteristics.

One of the most important properties of this kind of materials is piezoresistivity, which makes carbon-based polymer composites the best candidates for the development of piezoresistive sensors for many applications.

Many applications of CNTs and graphite for strain sensors will be explored in future works due to increasing importance of the nanotechnology research in strain-sensing fields.

References

1. Alamusi, Hu N, Fukunaga H, Atobe S, Liu Y, Li J (2011) Piezoresistive strain sensors made from carbon nanotubes based polymer nanocomposites. Sensors 11:10691–10723
2. Anderson SH, Chung DDL (1984) Exfoliation of intercalated graphite. Carbon 22(3):253–263
3. Bian J, Xiao M, Wang SJ, Lu YX, Meng YZ (2009) Novel application of thermally expanded graphite as support of catalysts for direct synthesis of DMC from CH_3OH and CO_2. J Colloid Interface Sci 334:50–57
4. Bokobza L (2007) Multiwall carbon nanotube elastomeric composites: a review. Polymer 48:4907–4920
5. Bolotin KI, Sikes KJ, Jiang Z, Klima M, Fudenberg G, Hone J, Kim P, Stormer HL (2008) Ultrahigh electron mobility in suspended graphene. Solid State Commun 146:351
6. Bug ALR, Safran SA, Webman I (1985) Continuum percolation rods. Phys Rev Lett 54(13):1412–1415
7. Cesano F, Bertarione S, Scarano D, Zecchina A (2005) Connecting carbon fibers by means of catalytically grown nanofilaments: Formation of carbon-carbon composites. Chem Mater 17(20):5119–5123
8. Cesano F, Pellerej D, Scarano D, Ricchiardi G, Zecchina A (2012) Radially organized pillars of TiO2 nanoparticles: synthesis, characterization and photocatalytic tests. J Photochem Photobiol a-Chem 242:51–58
9. Ci L, Suhr J, Pushparaj V, Zhang X, Ajayan PM (2008) Continuous carbon nanotube reinforced composites. Nano Lett 8(9):2762–2766
10. Clingerman ML, Weber EH, King JA (2002) Synergistic effects of carbon fillers in electrically conductive nylon 6, 6 and polycarbonate based resins. Polym Compos 23(5):911–924
11. Coleman JN, Khan U, Blau WJ, Gun'ko YK (2006) Small but strong: a review of the mechanical properties of carbon nanotube-polymer composites. Carbon 44:1624–1652
12. Connor MT, Roy S, Ezquerra TA, Balta' Calleja FJ (1998) Broadband ac conductivity of conductor-polymer composites. Phys Rev B 57(4):2286–2294
13. Cooper CA, Ravich D, Lips D, Mayer J, Wagner HD (2002) Distribution and alignment of carbon nanotubes and nanofibrils in a polymer matrix. Compos Sci 62:1105–1112
14. Cravanzola S, Haznedar G, Scarano D, Zecchina A, Cesano F (2013) Carbon-based piezoresistive polymer composites: Structure and electrical properties. Carbon 62:270–277
15. Dai H (2002) Caron nanotube: synthesis, integration and properties. Acc Chem Res 35:1035–1044
16. Dang Z-M, Jiang M-J, Xie D, Yao S-H, Zhang L-Q, Bai J (2008) Supersensitive linear piezoresistive property in carbon nanotubes/silicone rubber nanocomposites. J Appl Phys 104(2):024114
17. Das S (2013) A review on carbon nano-tubes—a new era of nanotechnology. Int J Emer Tech Adv Eng 3(3):774–783
18. Du J, Cheng H-M (2012) The fabrication, properties, and uses of graphene/polymer composites. Macromol Chem Phys 2013(10–11):1060–1077
19. Du X, Skachko I, Duerr F, Luican A, Andrei EY (2009) Fractional quantum Hall effect and insulating phase of Dirac electrons in graphene. Nature 462:192–195
20. Etika KC, Liu L, Hess LA, Grunlan JC (2009) The influence of synergistic stabilization of carbon black and clay on the electrical and mechanical properties of epoxy composites. Carbon 47(13):3128–3136

21. Foulger S (1999) Electrical properties of composites in the vicinity of the percolation threshold. J Appl Polym Sci 72:1573–1582
22. Frank IW, Tanenbaum DM, Van der Zande AM, McEuen PL (2007) Mechanical properties of suspended graphene sheets. JVacSciTechnol B 25(6):2558
23. Gao G, Cagin T, Goddard WA (1997) Energetics, structure, mechanical and vibrational properties of Single Walled Carbon Nanotubes (SWNT). Paper presented at the fifth foresight conference on molecular nanotechnology, Palo Alto, CA
24. Gau C, Ko SH, Chen HT (2009) Piezoresistive characteristics of MWCNT nanocomposites and fabrication as a polymer pressure sensor. Nanotechnology 20(18):185503
25. Ha HJ, Kwon YH, Kim JY, Lee S-Y (2011) A self-standing, UV-cured polymer networks-reinforced plastic crystal composite electrolyte for a lithium-ion battery. Electrochim Acta 57:40–45
26. Hautamaki C, Zurn S, Mantell SC, Polla D (1999) Microelectromechanical Systems (MEMS) as embedded sensors in composites. J Microelectromech Syst 8(3):272–279
27. Haznedar G, Cravanzola S, Zanetti M, Scarano D, Zecchina A, Cesano F (2013) Graphite nanoplatelets and carbon nanotubes based polyethylene composites: electrical conductivity and morphology. Mater Chem Phys 143:47–52
28. Hill TL (1986) An introduction to statistical thermodynamics. Dover, New York
29. Huang C-T, Shen C-L, Tang CF, Chang S (2008) A wearable yarn-based piezo-resistive sensor. Sensor Actuat A-Phys 141:396–403
30. Huang Y, Qin Y, Zhou Y, Niu H, Yu Z-Z, Dong J-Y (2010) Polypropylene/graphene oxide nanocomposites prepared by in situ Ziegler−Natta polymerization. Chem Mater 22(13):4096–4102
31. Hwang S-H, Park H, Park Y-B (2013) Piezoresistive behavior and multi-directional strain sensing ability of carbon nanotube-graphene nanoplatelet hybrid sheets. Smart Mater Struct 22(1):015013
32. Kane BJ, Cutkosky MR, Kovacs GTA (2000) A traction stress sensor array for use in high-resolution robotic tactile imaging. J Microelectromech Syst 9(4):425–434
33. Kostagiannakopoulou C, Maroutsos G, Sotiriadis G, Vavouliotis A, Kostopoulos V (2012) Study on the synergistic effects of graphene/carbon nanotubes polymer nanocomposites. Proc SPIE 8409, third international conference on smart materials and nanotechnology in engineering, 8409
34. Ku-Herrera JJ, Avilés F (2012) Cyclic tension and compression piezoresistivity of carbon nanotube/vinyl ester composites in the elastic and plastic regimes. Carbon 50:2592–2598
35. Kwon SY, Park YK, Kim MS (2012) Piezoresistive properties of multi-walled carbon nanotube-poly(dimethylsiloxane) composites for low-pressure-sensing applications. NANO: Brief Rep Rev 7(1):1250005
36. Lee C, Wei X, Kysar JW, Hone J (2008) Measurement of the elastic properties and intrinsic strength of monolayer graphene. Science 328(5887):385–388
37. Lin W, Zhang R, Wong CP (2010) Modeling of thermal conductivity of graphite nanosheet composites. J Electron Mater 39(3):268–272
38. LiuCh06v3.qxd (2005) Piezoresisitve sensors: Chap. 6
39. Loyola BR, La Saponara V, Loh KJ (2010) In situ strain monitoring of fiber-reinforced polymers using embedded piezoresistive nanocomposites. J Mater Sci 45:6786–6798
40. Lü C, Cheng Y, Liu Y, Liu F, Yang B (2006) A facile route to ZnS-polymer nanocomposite optical materials with high nanophase content via gamma-ray irradiation initiated bulk polymerization. Adv Mater 18(9):1188–1192
41. Luheng W, Tianhuai D, Peng W (2009) Influence of carbon black concentration on piezoresistivity for carbon-black-filled silicone rubber composite. Carbon 47:14
42. Ma P-C, Liu M-Y, Zhang H, Wang S-Q, Wang R, Wang K, Wong Y-K, Tang B-Z, Hong S-H, Paik K-W, Kim J-K (2009) Enhanced electrical conductivity of nanocomposites containing hybrid fillers of carbon nanotubes and carbon black. Appl Mater Interfaces 1(5):1090–1096
43. McLachlan DS, Chiteme C, Park C, Wise KE, Lowther SE, Lillehei PT, Siochi EJ, Harrison JS (2005) AC and DC percolative conductivity of single wall carbon nanotube polymer composites. J Polym Sci 43:3273–3287

44. Medvedyeva MV, Blanter YM (2011) Piezoconductivity of gated suspended graphene. Phys Rev B 83:045426
45. Miyasaka K, Watanabe K, Jojima E, Aida H, Sumita M, Ishikawa K (1982) Electrical conductivity of carbon-polymer composites as a function of carbon content. J Mater Sci 17:1601–1616
46. Moniruzzaman M, Winey KI (2006) Polymer nanocomposites containing carbon nanotubes. Macromolecules 39:5194–5205
47. Mylvaganam K, Zhang LC (2007) Fabrication and application of polymer composites comprising carbon nanotubes. Recent Pat Nanotechnol 1:59–65
48. Narkis M, Waxman A (1984) Resistivity behavior of filled electrically conductive crosslinked polyethylene. J Appl Polym Sci 29(5):1639–1652
49. Niyogi S, Hamon MA, Hu H, Zhao B, Bhowmik P, Sen R, Itkis ME, Haddon RC (2002) Chemistry of single-walled carbon nanotubes. Acc Chem Res 35(12):1105–1113
50. Obitayo W, Liu T (2012) A review: carbon nanotube-based piezoresistive strain sensors. J Sens 2012:1–15
51. Oliva AAI, Avilès F, Seidel GD, Sosa V (2013) On the contribution of carbon nanotube deformation to piezoresistivity of carbon nanotube/polymer composites. Compos Part B 47:200–206
52. Potts JR, Dreyer DR, Bielawski CW, Ruoff RS (2011) Graphene-based polymer nanocomposites. Polymer 52:5–25
53. Prasad KE, Das B, Maitra U, Ramamurty U, Rao CNR (2009) Extraordinary synergy in the mechanical properties of polymer matrix composites reinforced with 2 nanocarbons. Proc Nat Acad Sci U S A 106(32):13186–13189
54. Rahman MM, Cesano F, Bardelli F, Scarano D, Zecchina A (2010) Hybrid SnO_2/carbon composites: from foams to films by playing with the reaction conditions. Catal Today 150(1):84–90
55. Rocha JG, Paleo AJ, Hattum FWJ van, Lanceros-Méndez S (2012) Piezoresistive polypropylene-carbon nanofiber composites as mechanical transducers. Microsystem Technology 18(5):591–597
56. Sanjinés R, Abad MD, Vâ ju C, Smajda R, Mionić M, Magrez A (2011) Electrical properties and applications of carbon based nanocomposite materials: an overview. Surf Coat Technol 206:727–733
57. Sau KP, Chaki TK, Khastgir D (1997) Conductive rubber composites from different blends of ethylene-propylene-diene rubber and nitrile rubber. J Mater Sci 32(21):5717–5724
58. Shui X, Chung DDL (1996) A piezoresistive carbon filament polymer-matrix composite strain sensor. Smart Mater Struct 5:243–246
59. Siegel RW, Hu Evelyn H, Roco MC, Cox Donald M, Herb G (1999) Nanostructure science and technology: a worldwide study. Prepared under the guidance of the National Science and Technology Council (NSTC) Committee on Technology and the Interagency Working Group on NanoScience, Engineering and Technology (IWGN), Executive Summary: p xix
60. Spitalskya Z, Tasis D, Papagelis K, Galiotis C (2010) Carbon nanotube-polymer composites: chemistry, processing, mechanical and electrical properties. Prog Polym Sci 35(3):357–401
61. Stankovich S, Dikin D, Dommett G, Kevin M, Kohlhaas KM, Zimney EJ, Stach EA, Piner RD, Nguyen ST, Ruoff RS (2006) Graphene-based composite materials. Nature 442:282–286
62. Stauffer D, Aharnoy A (1991) Introduction to percolation theory. Taylor & Francis, London
63. Steinmetz J, Lee H-J, Kwon S, Lee D-S, Goze-Bac C, Abou-Hamad E, Kim H, Park Y-W (2007) Routes to the synthesis of carbon nanotube-polyacetylene composites by Ziegler-Natta polymerization of acetylene inside carbon nanotubes. Curr Appl Phys 7(1):39–41
64. Sugiyama S, Takigawa M, Igarashi I (1983) Integrated piezoresistive pressure sensor with both voltage and frequency output. Sens Actuators 4:113–120
65. Sumfleth J, Adroher XC, Schulte K (2009) Synergistic effects in network formation and electrical properties of hybrid epoxy nanocomposites containing multi-wall carbon nanotubes and carbon black. J Mater Sci 44(12):3241–3247

66. Sun Y, Bao H-D, Guo Z-X, Yu J (2009) Modeling of the electrical percolation of mixed carbon fillers in polymer-based composites. Macromolecules 42:459–463
67. Teo KBK, Singh C, Chhowalla M, Milne WI (2004) Catalytic synthesis of carbon nanotubes and nanofibres. Encycl Nanosci Nanotechnol 1:1–22
68. Thomas WT, Chongwu Z, Leo A, Jing K, Hongjie D, Lei L, Jayanthi CS, Meijie T, Wu S-Y (2000) Reversible electromechanical characteristics of carbon nanotubes under local-probe manipulation. Nature 405:769–772
69. Thongruang W, Spontak RJ, Balik CM (2002) Bridged double percolation in conductive polymer composites: an electrical conductivity, morphology and mechanical property study. Polymer 43(13):3717–3725
70. Tombler TW, Zhou C, Alexseyev L, Kong J, Dai H, Liu L, Jayanthi CS, Meijie T, Shi-Yu W (2000) Reversible electromechanical characteristics of carbon nanotubes under local-probe manipulation. Nature 405:769–772
71. Tsitsilianis C, Gotzamanis G, Iatridi Z (2010) Design of "smart" segmented polymers by incorporating random copolymers as building blocks. Eur Polym J 47(4):497–510
72. Velasco J Jr, Liu G, Bao W, Lau CN (2009) Electrical transport in high-quality graphene pnp junctions. New J Phys 11 (095008)
73. Wang P, Ding T (2009) Conductivity and piezoresistivity of conductive carbon black filled polymer composite. J Appl Polym Sci 116(4):2035–2039
74. Wang L, Ding T, Wang P (2008) Effects of instantaneous compression pressure on electrical resistance of carbon black filled silicone rubber composite during compressive stress relaxation. Compos Sci 68(15-16):3448–3450
75. Watts PCP, Hsu WK (2003) Behaviours of embedded carbon nanotubes during film cracking. Nanotechnology 14(5):L7–L10
76. Wei Z, Abbas ADehghani-Sanij, Blackburn RS (2007) Carbon based conductive polymer composites. J Mater Sci 42:3408–3418
77. Wen M, Sun X, Su L, Shen J, Li J, Guo S (2012) The electrical conductivity of carbon nanotube/carbon black/polypropylene composites prepared through multistage stretching extrusion. Polymer 53(7):1602–1610
78. Yakovlev AV, Finaenov AI, Zabud'kov SL, Yakovleva EV (2006) Thermally expanded graphite: synthesis, properties, and prospect for use. Russ J App Chem 79(11):1741–1751
79. Yang L, Ge Y, Zhu Q, Zhang C, Wang Z, Liu P (2012) Experimental and numerical studies on the sensitivity of carbon fibre/silicone rubber composite sensors. Smart Mater Struct 21:035011
80. Yue X, Li L, Zhang R, Zhang F (2009) Effect of expansion temperature of expandable graphite on microstructure evolution of expanded graphite during high-energy ball-milling. Mater Charact 60:1541–1544
81. Zhang W, Dehghani-Sanij AA, Blackburn RS (2007) Carbon based conductive polymer composites. J Mate Sci 42:3408–3418
82. Zhang SM, Lin L, Deng H, Gao X, Bilotti E, Peijs T, Zhang Q, Fu Q (2012) Synergistic effect in conductive networks constructed with carbon nanofillers in different dimensions. Polym Lett 6(2):159–168
83. Zhihua L, Yihu S, Yonggang S, Zheng Q (2007) Conductive behavior of composites composed of carbon black-filled ethylene-tetrafluoroethylene copolymer. J Mater Sci 42:2903–2906

Chapter 5
Structure and Physical and Mechanical Properties of Nanocomposite (Zr-Ti-Cr-Nb)N and (Ti-Zr-Al-Nb-Y)N Coatings, Obtained by Vacuum-Arc Evaporation Method

V. M. Beresnev, I. N. Torianyk, A. D. Pogrebnjak, O. V. Bondar, M. Bilokur, O. V. Sobol, D. A. Kolesnikov, S. V. Lytovchenko and P. V. Turbin

We obtained nanocomposite (Zr-Ti-Cr-Nb)N coatings using the method of cathode vacuum-arc evaporation under pulse stimulation. The structure of the coatings is characterized by (5–10 nm) the crystallite's size. Bias potential increasing leads to more intensive formation of nitrides, to increasing of relative concentration of Ti and Cr, and to increasing of hardness up to 4500 $HV_{0,1}$ GPa. Sklerometrical investigations showed high adhesion strength and high hardness. Also, we studied nanostructured (Ti-Zr-Al-Nb-Y)N coatings, fabricated from high-entropy alloys. Face-centered cubic (FCC) phases with average lattice parameter $<a> = 4.3$ are formed in such coatings. Hardness of such coatings is very high and equals to 4220 kg/mm^2, thickness is around 8.5 μm. All these physical properties allow us to use such coatings as protective coatings for cutting tools.

5.1 Introduction

Protective coatings are an effective means of increasing the productivity and durability of functional materials. Due to the high mechanical properties and thermal stability, the protective layer can maintain the functionality of tools in severe operating conditions for a long time. Protective coatings were designed for providing high hardness of material on its surface, low friction coefficient, oxidation resistance, and wear resistance [1–3].

V. M. Beresnev (✉) · I. N. Torianyk · S. V. Lytovchenko · P. V. Turbin
Karazin Kharkiv National University, Kharkiv, Ukraine
e-mail: beresnev-scpt@yandex.ua

A. D. Pogrebnjak · O. V. Bondar · M. Bilokur
Sumy National University, Sumy, Ukraine

O. V. Sobol
Kharkiv polytechnical institute, National Technical University, Kharkiv, Ukraine

D. A. Kolesnikov
Belgorod State National University, Belgorod, Russia

O. Fesenko, L. Yatsenko (eds.), *Nanocomposites, Nanophotonics, Nanobiotechnology, and Applications,* Springer Proceedings in Physics 156,
DOI 10.1007/978-3-319-06611-0_5,

One of the most called-for materials among those which are widely used for the formation of protective coatings are nitrides of transition metals which perform one of the best complexes of their properties. Among the binary systems of the nitrides, titanium nitride (TiN) is the most widely used material due to its high mechanical properties and corrosion resistance [4].

In the last decade, the titanium-aluminum nitride ($Ti_{1-x}Al_xN$) has got a wide application. It increases hardness and durability of the cutting tool in high-speed machining. Besides, the addition of aluminum in the coating composition leads to the increased oxidation resistance in the temperature interval of 500–800 °C, due to the formation of a resistant layer of aluminum oxide on the surface [5]. Adding such elements as chromium or zirconium in order to form a ternary system leads to the positive effects in improving the functional properties of the coatings [6, 7]. Thus, the transition from the two-element coatings to the more complex ones by means of doping by the elements of the transition metals is the effective way to significantly change the functional properties of the coating.

The next step in the universalization of properties of the obtained nitride materials is the use of four- and five-component coating systems in which there are three and four transition metal components, respectively, and nitrogen as a component of the filling, stimulating strong covalent bonds [8]. The most frequently used vacuum-plasma methods, used for obtaining the mentioned systems of coatings, are the following: vacuum-arc deposition, and magnetron sputtering [8, 9].

The aim of this chapter is to study the regularities of the structure formation of multi-component coating of the system (Zr-Ti-Cr-Nb)N and the investigation of their physical and mechanical characteristics.

5.2 Equipment and Methods of Investigation

As a method of obtaining coatings of (Zr-Ti-Cr-Nb)N system, the vacuum-arc evaporation method was used. The unit-cast cathode Zr+Ti+Cr+Nb with the composition: Ti—12.32 at. %, Zr—27.99 at. %, Cr—37.39 at. %, and Nb—22.30 at. % was used as a vaporized material. The cathode was made by electron-beam-melting method. Coatings were deposited in the installation "BULAT-6" in the atmosphere of molecular nitrogen on the polished surface of the steel 45 substrate as well as on the surface of the silicon substrate.

Table 5.1 shows the physical and technological parameters of obtaining the coatings based on (Zr-Ti-Cr-Nb)N system

The thickness of the coatings, the state of the boundaries between the substrate, and the coating and the surface morphology were investigated by means of scanning electron microscope FEI Nova NanoSEM 450. The X-ray diffraction studies of the coated samples were held using DRON-4 diffractometer in Cu-k_α radiation. The analysis of the surface topography of the coatings was performed additionally by means of atomic force microscope NT-MDT, Russia, in the atmosphere of air. Si-cantilevers NSG10/W2C with solid current-conductive W_2C coatings with a thickness of 30 nm

Table 5.1 Physical and technological parameters obtaining the coatings based on (Zr-Ti-Cr-Nb)N system

Evaporated material	Coatings	I_a, A	P_N, Pa	U_{CM}, V	Series no.
Zr+Ti + Cr+Nb	(Zr-Ti-Cr-Nb)N	110	0.3	− 100	1
Zr+Ti + Cr+Nb	(Zr-Ti-Cr-Nb)N	110	0.7	− 100	2
Zr+Ti + Cr+Nb	(Zr-Ti-Cr-Nb)N	110	0.3	− 200	3
Zr+Ti + Cr+Nb	(Zr-Ti-Cr-Nb)N	110	0.7	− 200	4
Zr+Ti + Cr+Nb	(Zr-Ti-Cr-Nb)N	110	0.7	− 200	5[a]

[a]Pulse stimulation was used

Table 5.2 The results of energy dispersion analysis for the coatings based on the system (Zr-Ti-Cr-Nb)N

Series No.	Elemental composition of the coatings at. %			
	Zr	Ti	Cr	Nb
	Elemental composition of the cathode before deposition			
	27.99	12.32	37.39	22.30
1	27.87	13.47	14.89	43.77
2	23.55	12.07	14.82	49.56
3	18.54	25.73	36.95	18.78
4	20.74	28.15	31.27	19.84

were used. The thickness of the coatings was ∼ 7.0 microns. Studying of mechanical characteristics (hardness) of the layers of the coatings was carried out on DM-8 hardness tester.

5.3 Experimental Results and Discussion of (Zr-Ti-Cr-Nb)N Systems

The results of research of elemental composition of the coatings based on the system (Zr-Ti-Cr-Nb)N as a function of the physical and technological deposition parameters that are given in Table 5.2.

Figure 5.1 shows the XRD spectra of the coatings. The lattice is cubic, structure-type NaCl. The results of the structural conditions of the obtained coatings are shown in Table 5.3.

As can be seen from the Table 5.3, increasing the values of the bias potential applied to the substrate, the size of the crystallites (L) increases.

The analysis held on the basis of the data from the Table 5.2 indicates a significant dependence of the composition of the coatings on the bias potential applied to the substrate, i.e., due to the bias potential the energy of the sputtered particles increases, which leads to higher radiation component during the formation of structure of the coatings. Thus, the increase of the bias potential to − 200 V leads to an increase of the strong nitride formatting components of Ti and Cr, as well as to an increase of the content of the nitrogen atoms.

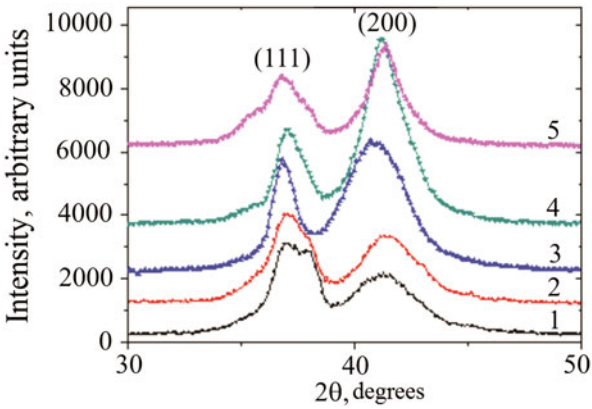

Fig. 5.1 Parts of diffraction spectra of the condensate (Zr-Ti-Cr-Nb)N, deposited by vacuum-arc method: *1*—P = 0.3 Pa, $U_b = -100$ V; *2*—P = 0.7 Pa, $U_b = -100$ V; *3*—P = 0.3 Pa, $U_b = -200$ V; *4*—P = 0.7 Pa, $U_b = -200$ V; *5*—P = 0.7 Pa, $U_b = -200$ V (pulse stimulation)

Table 5.3 The crystallite size (L) and the lattice constant (a) of the coatings based on the system (Zr-Ti-Cr-Nb)N

Parameters	Series no.				
	1	2	3	4	5
L, nm	4.5	5.2	5.1	6.9	7.3
a, nm	0.4359	0.4365	0.441	0.4381	0.4371

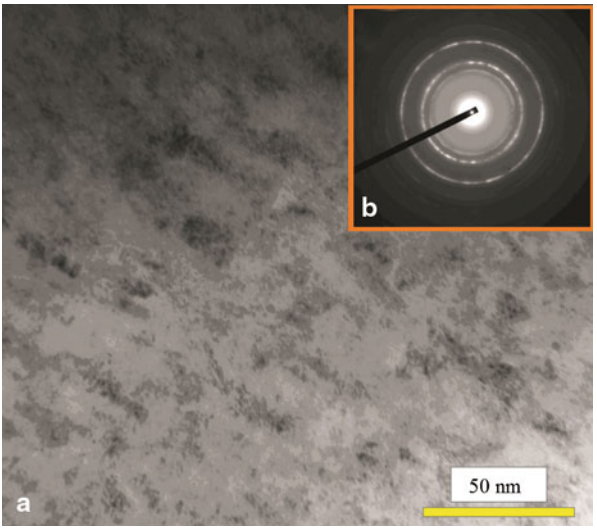

Fig. 5.2 Electron microscopy image of the coatings of the system (Zr-Ti-Cr-Nb)N. **a** Bright field image of the microstructure of the coating. **b** Microdiffraction image

The direct studies of the structure of the obtained coatings based on (Zr-Ti-Cr-Nb)N system were carried out by using an electron microscope Jeol Jem-2100. Figure 5.2 shows an electron microscopic image of the coatings based on (Zr-Ti-Cr-Nb)N system. It can be seen that the formed crystal structure is very finely dispersed, which corresponds to the results presented in Table 5.3

Hardness, as the most revealing mechanical characteristic of the coatings based on (Zr-Ti-Cr-Nb)N system, is given in Table 5.4. The imprints were made at the distance

Table 5.4 The results of hardness measuring for the coatings based on the system (Zr-Ti-Cr-Nb)N

Series no.	Hardness, $HV_{0.1}$ GPa	Note
1	3093	Coatings were not polished
1	3652	Coatings were polished
2	3478	Coatings were not polished
3	3886	Coatings were not polished
3	3996	Coatings were polished
4	4393	Coatings were polished
5	4457	Coatings were polished

Table 5.5 Comparative results of adhesion testing for the coatings based on the system (Zr-Ti-Cr-Nb)N and on the system TiN

Critical load	Series no.					
	1	2	3	4	5	TiN
L_{C1}	10.94	11.8	10.35	15.21	9.49	21.31
L_{C2}	18.69	20.93	18.42	24.29	30.37	30.91
L_{C3}	26.95	30.35	23.12	33.45	34.38	40.28
L_{C4}	39.15	45.94	45.12	40.97	40.49	48.84
L_{C5}	49.09	56.17	61.08	62.06	58.23	–

of 1.0 mm between each other; ten measurements were held for each sample. In order to reduce the impact of droplet component and in order to measure the hardness of the coatings more accurately, part of the coatings had been polished after deposition.

The adhesive properties of the coatings were determined by the scratch tester REVETEST (CSM Instruments). For this, the scratches were made on the surface of the coated samples at continuously increasing loads by means of the diamond spherical indenter "Rockwell C" type with a radius of curvature of 200 mm and the following physical parameters were registered: acoustic emission, coefficient of friction, and the depth of penetration of the indenter. To obtain the reliable results, two scratches on the surface of the coating were made. The substrates for the deposition of the coatings were steel 18Cr10NiTi cylinders with a diameter of 30.0 mm and height of 5.0 mm. The coatings of (Zr-Ti-Cr-Nb)N system were deposited on their polished surface. The thickness of the coatings was 6.2 μm.

The following are the critical loads changing the coefficient of friction and acoustic emission curves from the scribing load: L_{C1}—characterizes the time of occurrence of the first chevron crack, L_{C2}—the moment of the appearance of chevron cracks, L_{C3}—the destruction has a cohesive and adhesive nature, L_{C4}—local flaking of the areas of the coating, and L_{C5}—plastic abrasion of the coating to the substrate.

Table 5.5 shows the results of adhesion tests of the coated samples obtained at different technological deposition parameters. After the deposition of the coatings in order to reduce the influence of the droplet constituents, the coatings were polished. For comparison, the samples coated by TiN, obtained by the vacuum-arc deposition method with the hardness of $H = 28.0$ GPa, were taken.

Figure 5.3 shows the curve of the change of the coefficient of friction (μ) when moving the diamond indenter on the surface of the coating of the (Zr-Ti-Cr-Nb)N system (sample 4) and the curve of change of the acoustic emission (AE).

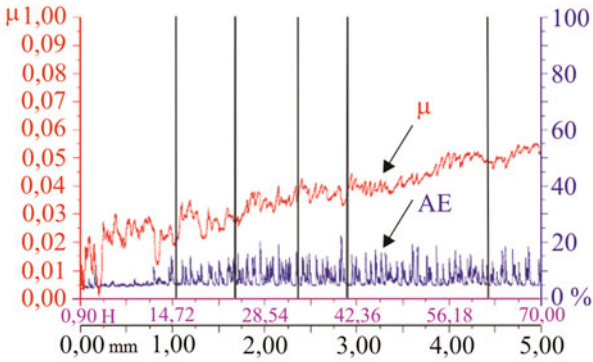

Fig. 5.3 The results of measurement of the friction coefficient and acoustic emission (sample 4), the length of the scribing path is represented in millimeters

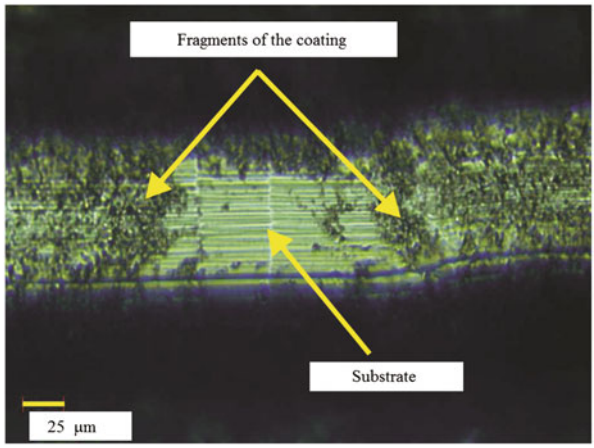

Fig. 5.4 Image of the remaining fragments of the coating on the bottom of the scratch after the influence of the diamond indenter

As seen from the results shown in Fig. 5.3, the process of destruction of the coating when scratched by the diamond indenter can be conventionally divided into several stages. In the beginning, the monotonous penetration of the indenter into the coating takes place and the first cracks appear (load up to 15.21 N); the coefficient of friction (μ) is increasing, but the acoustic emission signal remains unchanged. Subsequently, with the increased load, the appearance of chevron and diagonal cracks takes place [11, 12], which leads to the increase of coefficient of friction to a value of 0.3. At a load of up to 14 N, the amplitude of the acoustic emission signal dramatically increases, and its value remains at the same level until the end of the test. After this, with the increase of the load reaching 62 N, there is a local abrasion of the coating down to the substrate material (see Fig. 5.4).

Comparative analysis shows that the coatings wear away when scratched, but no chalking takes place, i.e., they are destroyed following the cohesive mechanism which is associated with the plastic deformation and the formation of fatigue cracks in the coating material.

The work was performed by the authors in the framework of complex state-funded research works 0112U006974 and 0113U001079, funded by the Ministry of

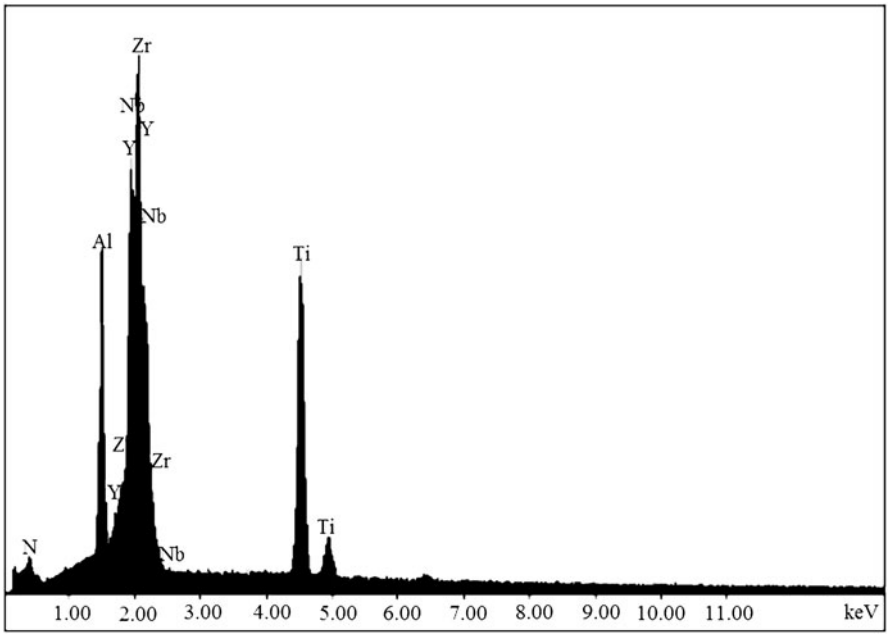

Fig. 5.5 X-ray spectra of the (Ti-Zr-Al-Nb-Y)N coating, which was obtained using EDX

Table 5.6 Integral concentration of elements in the (Ti-Zr-Al-Nb-Y)N coating

Element	wt.%	at.%	K-ratio
N_K	10.77	35.62	0.0155
Al_K	8.32	14.27	0.0516
Y_L	24.18	12.59	0.2014
Zr_L	23.69	12.03	0.2047
Nb_L	13.79	6.87	0.0903
Ti_K	19.25	18.61	0.1636
Total	100.00	100.00	

Education and Science of Ukraine. Part of the work is performed using the diagnostic equipment of the Center for collective use of scientific equipment of Belgorod State National Research University "Diagnostics of the structure and the properties of nanomaterials" of the Ministry of Education and Science of the Russian Federation.

5.4 Experimental Results and Discussion of (Ti-Zr-Al-Nb-Y)N Systems

Another sample of high-entropy nitride (HEAN) (Ti-Zr-Al-Nb-Y)N coatings was fabricated under the same conditions as the previous one.

In Fig. 5.5, we present the X-ray spectra of the coating, which was obtained using EDX. We can see all elements, which form the coating. Integral concentration of elements in atomic and weight percents are presented in Table 5.6. Nitrogen

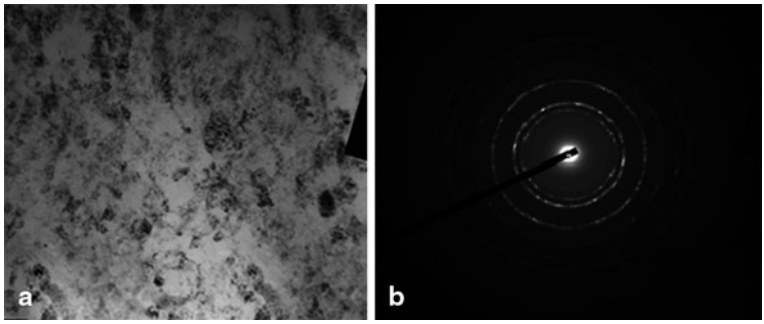

Fig. 5.6 Results of the TEM analysis of the (Ti-Zr-Al-Nb-Y)N coating. **a** Microstructure of the coating. **b** Microdiffraction image

Table 5.7 Lattice parameters of the (Ti-Zr-Al-Nb-Y)N coating

circle	r, sm	d, Å	$Q = r_i^2/r_1^2$	HKL	$H^2+K^2+L^2$	a, Å	<a>, Å	Δa, ±Å
1	1	2.51	1	111	3	4.347448	4.305811	0.061903
2	1.15	2.182609	1.3225	200	4	4.365217		
3	1.65	1.521212	2.7225	220	8	4.302638		
5	2.05	1.22439	4.2025	222	12	4.241412		
6	2.35	1.068085	5.5225	400	16	4.27234		
Type of the lattice: FCC								

concentration is rather high and equals to 35 at.%, Ti ≈ 18.25 at.%, Al ≈ 14.27 at.%, Y ≈ 12.59 at.%, Zr ≈ 12.03 at.%, and Nb ≈ 6.87 at.%.

In Fig. 5.6, we present the results of Transmission Electron Microscopy (TEM) analysis, Fig. 5.6a corresponds to the coating's structure and Fig. 5.6b shows the diffraction of the selected region of the coating. We can claim that type of the crystal lattice is face-centered cubic (FCC), with an average lattice parameter $<a> = 4.305811$, $\Delta a = 0.061903$ C°, which is normal for such nitrides of high-entropy alloys, fabricated by vacuum-arc deposition method. Lattice parameters and its evaluation are presented in the Table 5.7

In Fig. 5.7, the diffraction image of the (Ti-Zr-Al-Nb-Y)N coating's fracture is shown. As we can see from this figure, the thickness of the coating equals 8.534 μm, hardness is $Hv_{0.1} = 4220\,kg/mm^2$ (the loading was applied using Vickers pyramid under the pressure 0.1 N).

Investigations of hardness of such rather thick nanostructured coatings showed that due to the deposition conditions, such as bias potential and residual pressure, dispersion of the hardness' values was high. For example, we have coatings with the hardness of $5358\,kg/mm^2$ and higher, but, at the same time, minimal value of hardness is $3627\,kg/mm^2$ under adverse deposition conditions.

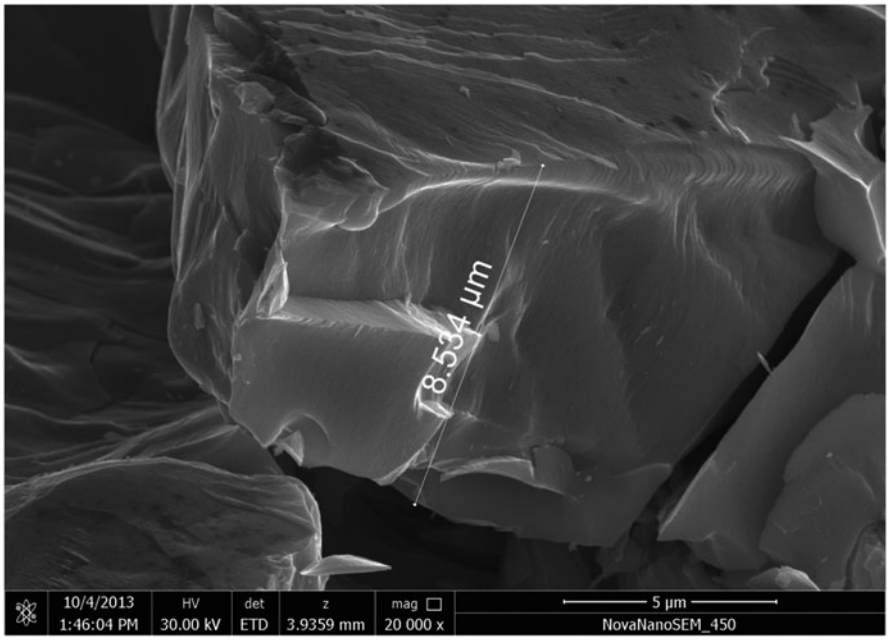

Fig. 5.7 The cross-section image of the (Ti-Zr-Al-Nb-Y)N coating's fracture

5.5 Summary

1. The coatings of the systems (Zr-Ti-Cr-Nb)N and (Ti-Zr-Al-Nb-Y)N were obtained by means of evaporation of the unit-cast cathode in the nitrogen atmosphere using the vacuum-arc method.
2. Crystallites of the coatings based on (Zr-Ti-Cr-Nb)N system are characterized by an average size of 5–10 nm, depending on the deposition parameters.
3. The hardness of the obtained coatings reaches the value of 4457 $HV_{0,1}$ GPa.
4. The coatings demonstrate high adhesion strength and are characterized by cohesion mechanism of destruction during the testing.
5. By physical and mechanical properties, the obtained coatings of the systems (Zr-Ti-Cr-Nb)N and (Ti-Zr-Al-Nb-Y)N have shown themselves as promising for using them as protective coatings for cutting tools.

Acknowledgment The authors are grateful to the collaborators from the National Science Center "Kharkov institute of physics and technology": to Professor A.A. Andriyiv and to senior researcher V.A. Stolbovoy for the assistance in preparing and carrying out the experiments and informative discussion of the results obtained.

References

1. Kavaleiro A, de Hossona D (2011) Nanostructured coatings. Technosphere, Moscow, p 792
2. Azarenkov NA, Sobol OV, Pogrebnjak AD, Lytovchenko SV, Ivanov ON (2012) Material science of nonequilibrium state of the modified surface. Sumy State University, Sumy, p 683
3. Azarenkov NA, Sobol OV, Beresnev VM, Pogrebnjak AD, Kolesnikov DA, Turbin PV, Toryanik IN (2013) Vacuum-plasma coatings based on multicomponent nitrides. Metalllofiz Noveishie Technol 35(8):1061–1084
4. Azarenkov NA, Sobol OV, Pogrebnjak AD, Beresnev VM (2011) Vacuum-plasma coatings engineering. Karazin Kharkiv National University, Kharkiv, p 344
5. Pogrebnjak AD, Shpak AP, Azarenkov NA, Beresnev VM (2009) Structure and properties of hard and superhard nanocomposite coatings. Phys Usp 52:29–54
6. Pogrebnjak AD, Shpak AP, Beresnev VM et al (2012) Effect of thermal annealing in vacuum and air on nanograin sizes in hard and superhard coatings Zr-Ti-Si-N. J Nanosci Nanotech 12:9213–9219
7. Pogrebnjak AD, Beresnev VM, Demjanenko AA et al (2012) Adhesive strength, superhardness and the phase and elemental composition of nanostructuted coatings based on Ti-Hf-Si-N. Phys Solid State 54(9):1882–1890
8. Pogrebnjak AD, Sobol OV, Beresnev VM et al (2010) Phase composition, thermal stability, physical and mechanical properties of superhard on base Zr-Ti-Si-N nanocomposite coatings. Nanostructured Mater Nanotechnol IV Ceramic Eng Sci Proc 31(7):127–138
9. Krause-Rehberg R, Pogrebnjak AD, Borisyk VN et al (2013) Analysis of local regions near interfaces in nanostructured multicomponent (Ti-Zr-Hf-V-Nb)N coatings produced by cathodic-arc-vapor deposition from arc of an evaporating cathode. Phys Met Metallogr 114(8):672–680

Chapter 6
New Nanosized Systems Based Lanthanide Diketonate Complexes for OLEDs

I. A. Savchenko, A. S. Berezhnytska, N. B. Ivakha and E. K. Trunova

6.1 Introduction

Over the last decade, organic light-emitting devices (OLEDs) have attracted great interest for their manifold applications in different areas, varying from white lighting, such as light bulbs replacement, to multicolor displays for televisions and cell phones [1–4]. OLEDs are considered the next generation of technology for flexible flat-panel displays and low-cost solid state lighting [5–8].

Light emitting diodes (LEDs) will probably become the most important type of light source for artificial lighting in the twenty-first century and will probably replace the incandescent lamps and even the mercury-containing discharge lamps. Typically, a LED consists of inorganic *p*- and *n*-type semiconductors. The holes and electrons are driven to the *p*–*n* junction by the applied electric field. The electrons and holes recombine at this *p*–*n* junction, and the excess of energy is emitted as visible or infrared radiation. In an LED, electrical energy is transformed into light (electroluminescence).

In OLEDs, the active components are organic molecules instead of inorganic semiconductors. OLEDs are mainly developed for display applications. One hopes to use OLEDs for the design of large flat-panel displays with very wide viewing angles.

The advantages of OLEDs are that they are easier and cheaper to fabricate than their inorganic counterparts, that they can be made very large (luminescent sheets), and that they can be deposited on almost every substrate including flexible ones, like plastics, to yield flexible displays [9–10].

An OLED consists of very thin layers sandwiched by two electrodes. These layers can be deposited by various techniques such as chemical vapor deposition, plasma

I. A. Savchenko (✉)
National Taras Shevchenko University of Kyiv, 60, Volodymyrska str.,
Kyiv 01601, Ukraine, Tel.: +380667336633
e-mail: iras@univ.kiev.ua

A. S. Berezhnytska · N. B. Ivakha · E. K. Trunova
V. I. Vernadsky Institute of General and Inorganic Chemistry NASU,
32/34 Palladina prosp., Kiev 03680, Ukraine

O. Fesenko, L. Yatsenko (eds.), *Nanocomposites, Nanophotonics, Nanobiotechnology, and Applications,* Springer Proceedings in Physics 156,
DOI 10.1007/978-3-319-06611-0_6,

deposition, or spin coating from a solution. Electrons are injected into the emitting layer from the cathode, and holes are injected from the anode. The cathode is typically a layer of a metal with a low work function such as aluminum, magnesium, or calcium or a magnesium/aluminum alloy to guarantee efficient injection of electrons. The anode is typically a transparent layer of indium tin oxide (ITO). ITO is a nonstoichiometric composition consisting of In_2O_3 (80–90 %) and SnO_2 (10–20 %). The recombination of the injected holes with the injected electrons allows the formation of singlet and triplet excitons. Because of spin statistics, 75 % of the recombinations give rise to triplet excitons and 25 % to singlet excitons. Only singlet excitons can produce electroluminescence. The triplet excitons decay nonradiatively and do not generate electroluminescence. For this reason, the maximum internal quantum efficiency of an OLED is limited to 25 %.

The study of luminescent lanthanide compounds in hybrid materials is not only of fundamental interest because these materials have also a high potential for different applications (optical amplifiers, optical waveguides, OLEDs, etc.).

There has been a large research activity on coordination compounds of the lanthanide ions with organic ligands including β-diketones, which can act as light-emitting diodes and electroluminescent devices.

Lanthanide β-diketonates are the most popular and the most intensively investigated luminescent lanthanide coordination compounds. Their popularity is partially because many different β-diketones are commercially available and the synthesis of the corresponding lanthanide complexes is relatively easy but also because of their excellent luminescence properties [11–15]. Weak visible or near-infrared emission is possible for the complexes of praseodymium(III), neodymium(III), holmium(III), erbium(III), thulium(III), and ytterbium(III).

However, sometimes it is difficult to disperse the organic low-molecular-weight lanthanide complexes uniformly in a polymer matrix. Compared to guest–host systems, the polymers with covalently bonded lanthanide chromophores can be used in pure forms without doping into other matrixes because of their own film-forming ability, enhanced solubility in solvents, better homogeneity, and higher stability.

There are different methods for incorporating lanthanide complexes into polymers. First of all, one has to distinguish between host–guest systems and systems in which the lanthanide complexes are an integral part of the polymer.

In a host–guest system, the lanthanide complex is dissolved in the polymer matrix or blended with the polymer matrix. To prepare host–guest systems, two techniques can be used. The first technique involves dissolution of the lanthanide complex directly into the monomer or into the monomer solution. After addition of an appropriate initiator, the monomer solution is polymerized by thermal polymerization of photopolymerization to form a uniformly doped polymer. In the second technique, the lanthanide complex and the pure polymer are both dissolved in a cosolvent. The solvent is then evaporated, and a uniformly doped polymer is obtained. There is a limit to the amount of dopant that can be incorporated in the polymer host. This limit is determined by the solubility of the lanthanide complex in the host polymer. Beyond this limit, aggregation of the complexes occurs, and this ruins the optical quality of the doped polymer. Lanthanide complexes that contain polymerizable groups can be

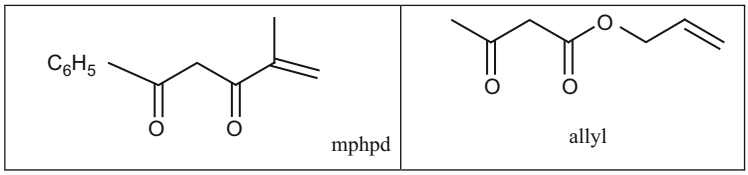

Fig. 6.1 Structures of investigated monomers

copolymerized together with another monomer. This results in a copolymer in which the lanthanide complex is part of the polymer backbone or of the side chain.

The aim of this chapter is the synthesis of Er complexes with 2-methyl-5-phenylpentene-1-dione-3,5 and allyl-3-oxo-butanoate as well as polymers based on them and investigations of properties of metal-containing polymeric systems depending on influence of the nature of organic ligand (Fig. 6.1).

6.2 Experimental

6.2.1 Samples

We synthesized two kinds of monomeric ligands: allyl-3-oxo-butanoate and 2-methyl-5-phenylpentene-1-3,5-dione. NMR (mphpd):^{1}H (D_2O) δ (ppm): 3.27 (singlet, 3H, CH_3); 3.47(singlet, 1H, =CH-); 5.27 (singlet, 1H, $=CH_2$); 5.58 (singlet, 1H, $=CH_2$); 7.15–7.60 (multiplet, 5H, Ph).

Complexes obtained by an exchange reaction between equimolar amounts of lanthanide acetate and sodium 2-methyl-5-phenylpentene-1-3,5-dione salt or allyl-3-oxo-butanoate in a water-alcohol solution at pH 9–9.5 with a slight excess of the ligand.

The polymerization was carried out at 80 °C in the thermostat in dimethylformamide solution with monomer concentration 0.03 mol/l and initiator 2,2′-azobisisobutyronitrile concentration 0.003 mol/l. Thus obtained metal polymers precipitate out from propanol-2 solution. $[Er(mphpd)_3]_n$ GPC (eluent DMF, polystyrene standarts): $M_n = 1918$ $M_w = 2009$ $M_w/M_n = 1.05$.

6.2.2 Observation and Measurements

The synthesized compounds have been studied by NMR, IR-, electronic absorption, and diffuse reflectance spectroscopy. The infrared spectra were recorded in KBr tablets at a range of 4000–400 cm^{-1} with Spectrum BX II FT-IR manufactured by Perkin Elmer. The electronic absorption spectra were recorded using spectrophotometer Shimadzu "UV-VIS-NIR Shimadzu UV-3600" and the diffuse reflectance

Table 6.1 Some distinctive absorption band of metallic complexes and metallopolymers

Complex	ν(M-O)	ν_{as}(C-O)	ν_{as}(C-C)	ν_{s}(C-O)	ν_{s}(C = C)
$Er(mphpd)_3 \cdot 2H_2O$	420	1465	1557	1594	1676
$[Er(mphpd)_3]_n$	425	1470	1575	1575	–
$[Er(OH)(allyl)_2] \cdot H_2O$	416	1420	1518	1640	1720
$[Er(OH)(allyl)_2]_n$	418	1412	1518	1638	–

spectra were obtained using the Specord M-40 spectrophotometer in the range of 30000–12000 cm^{-1}. The excitation and luminescence spectra of solid samples were recorded on a spectrofluorometer "Fluorolog FL 3-22", "Horiba Jobin Yvon" (Xe-lamp 450 W) with the filter OS11. The InGaAs photoresistor (DSS-IGA020L Electro-Optical Systems, Inc, USA) cooled to the temperature of liquid nitrogen was used as a radiation detector for infrared region. The excitation and luminescence spectra were adjusted to a distribution of a xenon lamp reflection and the photomultiplier sensitivity. The particle size studying was performed at 25 °C using the equipment from "Zeta Sizer Nano by Malvern." Photomicrographs were obtained by a scanning electron microscope "Hitachi H-800" (SEM).

6.3 Results and Discussion

The monomeric complexes of $Er(mphpd)_3 \cdot 2H_2O$ and $Er(OH)(allyl)_2 \cdot H_2O$ were prepared in an aqueous alcohol solution at pH 8–10.

The monomeric and polymeric complexes of erbium with 2-methyl-5-phenylpenten-1-3,5-dion (mphpd), $Er(mphpd)_3 \cdot 2H_2O$, and allyl-3-oxo-butanoate (allyl) $Er(OH)(allyl)_2 \cdot H_2O$ were synthesized at the first instance. The metallopolymers $[Er(mphpd)_3]_n$ and $[Er(OH)(allyl)_2]_n$were obtained by free-radical polymerization with the initiator AIBN and the kinetics of polymerization was studied by dilatometric method.

Kinetic parameters of radical polymerization of complexes $Er(mphpd)_3$ and $Er(OH)(allyl)_2$ were calculated: the rate of polymerization is 0.46×10^{-4} (0.97×10^{-4}) mol/L·s, the reduced rate of polymerization is 1.52×10^{-4} (3.36×10^{-4})s^{-1}, and the total rate constant is 2.57×10^{-3} (5.14×10^{-3}) $dm^{1.5}/(mol^{0.5}\ s)^1$, respectively. The influence of the nature of organic ligand on polymerization rate are deduced in case *allyl* the polymerization rate above *mphpd* are observed owing to steric restrictions under polymerization of $Er(mphpd)_3 \cdot 2H_2O$.

With the aim of the identification of ligand functional groups coordination methods to metal ions were studied the IR spectra of synthesized compounds (Table 6.1).

In the IR spectra of the synthesized complexes and metallopolymers in 1500–1600 cm^{-1}, there are bands corresponding to stretching vibrations of the ν (C-O) and ν (C-C), which confirms the bidentate cyclic coordination of the ligand to the metal ions (Table 6.1). At the same time, a higher frequency band should be attributed to the stretching vibrations ν (CC) and a lower frequency to the stretching vibrations

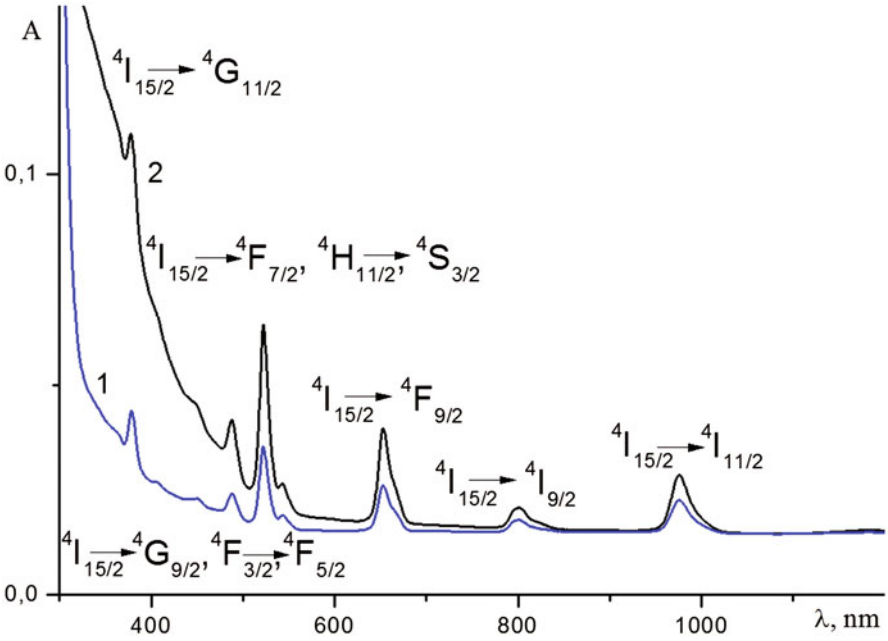

Fig. 6.2 Electronic absorption spectra *1*—Er(OH)(allyl)$_2$, *2*—[Er(OH)(allyl)$_2$]$_n$

of the ν (CO). The region of 1640–1680 cm^{-1} contains stretching vibrations ν (C = C) [14]. In the case of metallopolymers, this band disappears or is significantly reduced in intensity, indicating the presence of only the terminal unsaturated groups. Fairly broad band of coordinated water molecules is observed in the region 3300–3500 cm^{-1}.

In IR spectra of the metallopolymers [Er(mphpd)$_3$]$_n$ and [Er(OH)(allyl)$_2$]$_n$, comparatively with monomeric metallocomplexes, the location of main absorption bands are shifted in short-wave spectrum region, their intensity is significantly lower, and the intensity is decreased especially which corresponds to vibration of the double bond. Presented results are confirmed of the polymer complex formation.

In the case of erbium complexes, a band pattern of the Er^{3+} ion transition with the $^4I_{15/2}$ main (quantum) state is observed (Table 6.2, Fig. 6.2).

Electronic absorption spectra (EAS) of Er(OH)(allyl)$_2$ demonstrate transitions that are shifted at the short-wave region of spectrum relatively with aqua-ion which are indicated about the complex formation with less coordination number of central atom and enhancement of ionic component in bond erbium-oxygen.

Electronic absorption spectra of metallopolymers are analogous to EAS of monomeric complexes. But, main absorption bands of polycomplexes undergo the long-wavelength shift 10–100 cm^{-1} that is indicated about the decay of the metal bond with ligand in the polymer. The decrease of the intensity of all absorption bands for metallopolymers and their bathochromic shift in comparison with monomeric

Table 6.2 Energy transition in Er electronic absorbtion spectrum

Transition	Er(III), cm^{-1}	$Er(mphpd)_3$, cm^{-1}	$[Er(mphpd)_3]_n$, cm^{-1}	$Er(OH)(allyl)_2$, cm^{-1}	$[Er(OH)(allyl)_2]$, cm^{-1}
$^4I_{15/2} \rightarrow {}^4D_{7/2}$	39215	–	–	38,834	38,460
$^4I_{15/2} \rightarrow {}^4G_{11/2}$	26370	26,350	26,350	26,420	26,490
$^4I_{15/2} \rightarrow {}^4F_{7/2}$	20480	20,470	20,450	20,480	20,480
$^4I_{15/2} \rightarrow {}^4H_{11/2}$	19160	19,120	19,120	19,160	19,160
$^4I_{15/2} \rightarrow {}^4S_{3/2}$	18400	18,385	18,385	18,420	18,420
$^4I_{15/2} \rightarrow {}^4F_{9/2}$	15320	15,270	15,290	15,320	15,320
$^4I_{15/2} \rightarrow {}^4I_{9/2}$	12480	12,450	12,470	12,500	12,500

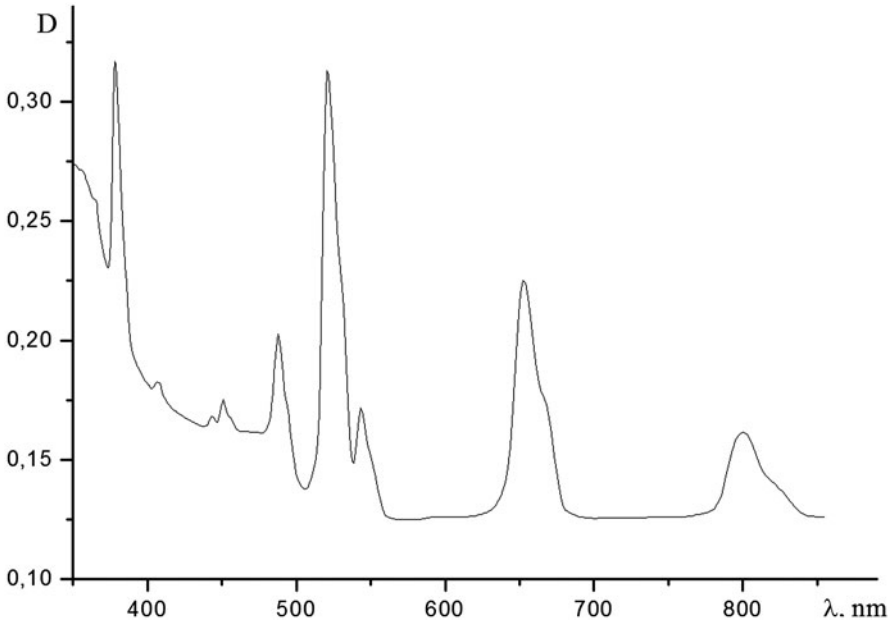

Fig. 6.3 Diffuse reflection spectrum of $Er(OH)(allyl)_2$

spectra indicates about polymer structure formation. The similarity of monomers EAS with polymer spectra confirms of the identical coordinative environment of lanthanide ions in both cases.

Thus, coordination number is 8 for $Er(mphpd)_3 \cdot 2H_2O$ and $[Er(mphpd)_3]_n$, and coordination number is 7 for $Er(OH)(allyl)_2 \cdot H_2O$ and $[Er(OH)(allyl)_2]_n$.

Diffuse reflection spectra (Fig. 6.3) and electronic absorption spectra (Fig. 6.2) of all samples do not differ much, suggesting a similar structure in solution and polycrystalline state.

The mass loss is 5.3 % ($\Delta m_{theor} = 4.7$ %) for the erbium complex $Er(mphpd)_3$ $2H_2O$ at 125 °C, which corresponds to the decoupling of two coordinative water molecules accordingly. The small exoeffect in the region 190 °C can be conditioned

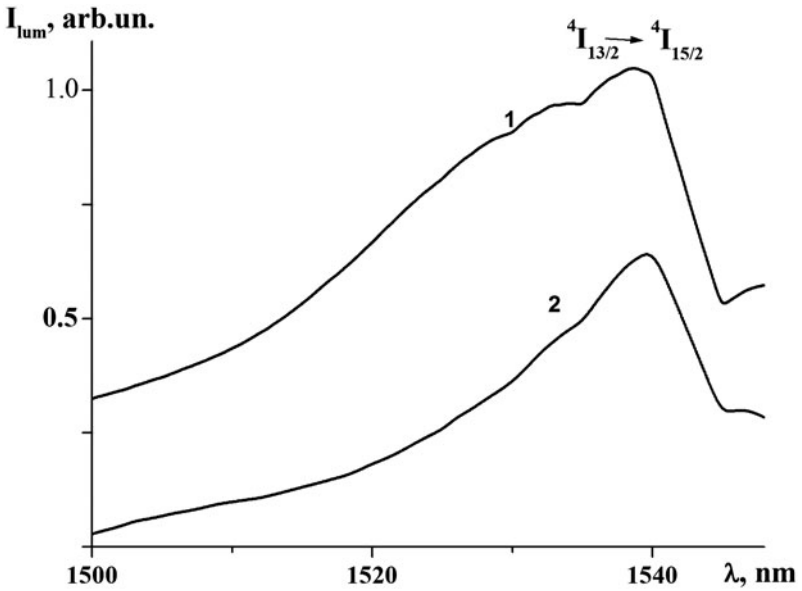

Fig. 6.4 Luminescence spectra of $Er(mphpd)_3 \cdot 2H_2O$ (1) and $[Er(mphpd)_3]_n$ (2) in solid state (λ_{ex} = 362 nm, 298 K)

by the polymerization process of complex melting. The process of the complex decomposition begins with the removal of one ligand molecule, which corresponds of the exoeffect at 248 °C and the mass loss 28 % ($\Delta m_{theor} = 24.5$). The following heating is attended by exoeffects at temperature 337, 384, 419, 460, 484 °C and results in the total complex decomposition $\Delta m = 15$ %. The total weight loss is 66 % for the erbium complex.

The presented results allow to assume that the complexes composition corresponds to the formula, $Er(mphpd)_3 \cdot 2H_2O$, $Er(OH)(allyl)_2 \cdot H_2O$.

The luminescent spectra of the erbium complex $Er(mphpd)_3 \cdot 2H_2O$ and metallopolymer are analogous; the band, which corresponds $^4I_{13/2} \rightarrow {}^4I_{15/2}$ transition, is observed. The luminescence intensity of the present samples do not differ practically that is testified about the low polymerization degree of the obtained metallopolymer (Fig. 6.4).

The 4 f luminescence of erbium is weak relatively and is detected in the range 1450–1560 nm, which corresponds to the bandwidth (the maximum half-height) for $Er(mphpd)_3 \cdot 2H_2O$—18 FWHM, and $[Er(mphpd)_3]_n$—19 FWHM; therefore, the luminescence quantum yield of its complexes is not established definitely.

Investigations of a particle size were performed at 25 °C on the Zeta Sizer Malvern instrument. The results showed (Figs. 6.5, 6.6) that the systems obtained are polydisperse with a predominance of particles 6–12 nm for $Er(mphpd)_3 \cdot 2H_2O$, 10–170 nm for $Er(OH)(allyl)_2$, and 10–50 nm for metallopolymer $[Er(mphpd)_3]_n$, 20–200 nm for $[Er(OH)(allyl)_2]_n$.

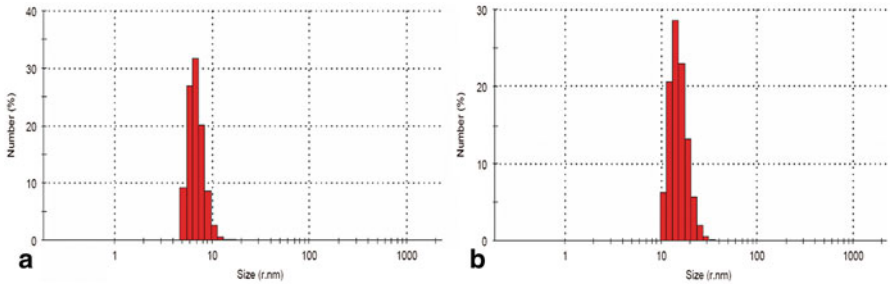

Fig. 6.5 The polydisperse assignment of particles in system **a**—Er(mphpd)$_3$, **b**—[Er(mphpd)$_3$]$_n$

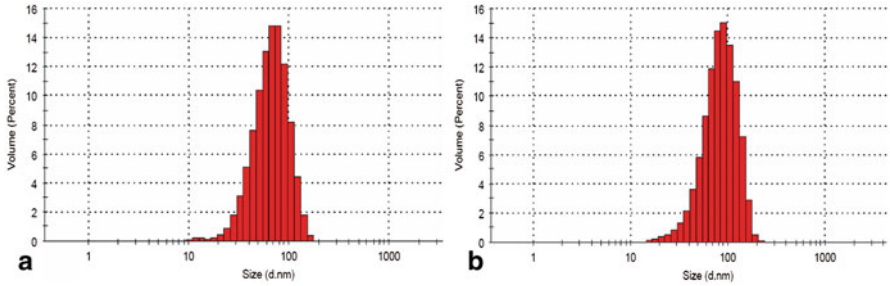

Fig. 6.6 The polydisperse assignment of particles in system **a**—Er(OH)(allyl)$_2$, **b**—[Er(OH)(allyl)$_2$]n

Monomeric complex Er(OH)(allyl)$_2$ and metallopolymers based on them were fixed in chloroform what the large size of particles of these compounds explained.

Since the primary purpose of these studies is associated with obtaining of new nanomaterials which can be used as layers in the organic light emitting diodes, it is necessary to choose a solvent which promotes good spreading, and therefore high adhesion of the complex to the substrate surface, allowing to obtain homogeneous films by deposition from solutions. Studies of particle size of the monomeric and polymeric complexes (25 °C) in the dimethylformamide, chloroform, and ethyl alcohol were conducted. The results showed that the smallest particle size observed in the chloroform solution.

The system is homogeneous in terms of uniform distribution of metal throughout the polymer matrix as seen from the micrographs of powdered samples (Fig. 6.7).

The method of dynamic light scattering and the results of electronic microscopy showed that the obtained polymer systems are nanoscale.

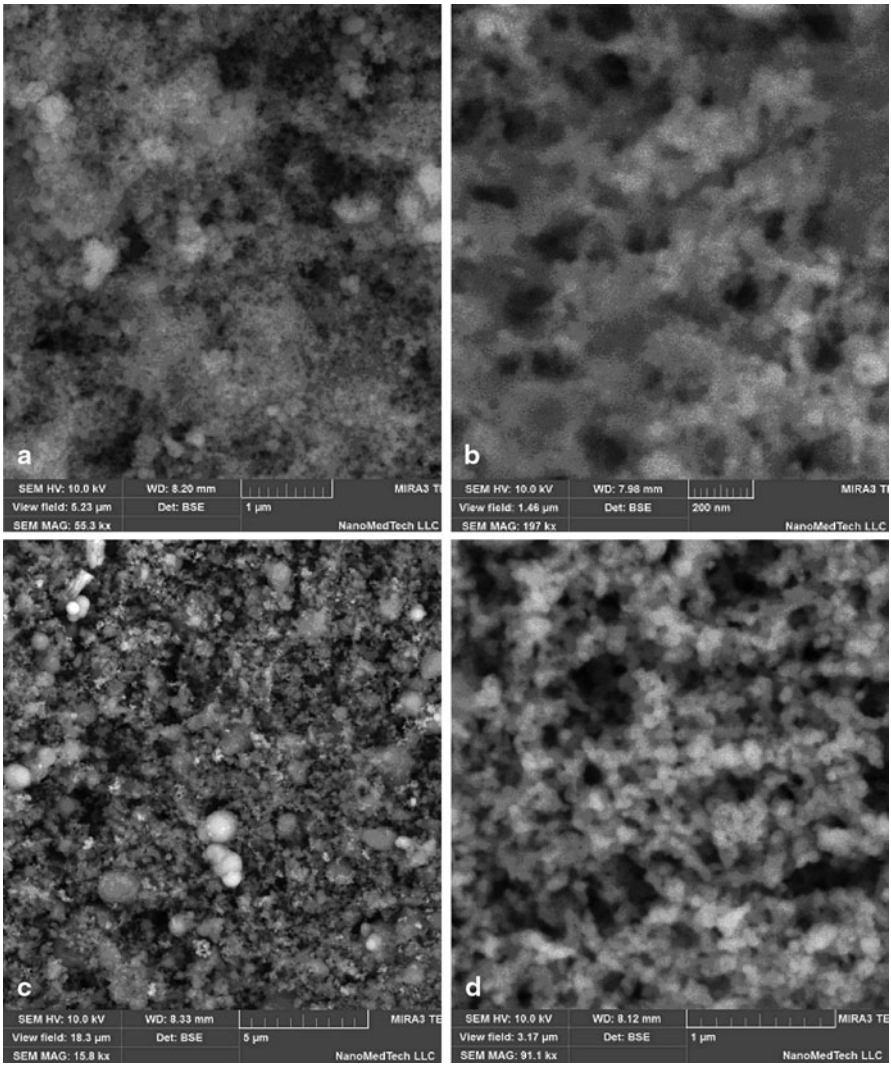

Fig. 6.7 SEM microphoto of metallopolymers powders **a**—$Er(mphpd)_3$, **b**—$[Er(mphpd)_3]_n$, **c**—$Er(OH)(allyl)_2$, **d**—$[Er(OH)(allyl)_2]_n$

6.4 Conclusions

The investigations conducted in the present chapter allowed to determine the composition, structure, and properties of the complexes and metallopolymers on their basis obtained for the first time. The results of the above study showed that the configuration of the chelate unit is unchanged during the polymerization.

It was shown that all synthesized compounds are nano systems. Using electron microscopy confirmed the homogeneity of metal distribution in the polymer matrix of synthesized metallopolymers.

The similarity of monomers electronic absorption spectra with polymers spectra confirms of identical coordinative environment of lanthanide ions in both cases.

The obtained polymetallocomplexes can be used as potential materials for organic light-emitting devices.

References

1. Wang Z, Helander M, Qiu J et al (2011) Highly simplified phosphorescent organic light emitting diode with $> 20\,\%$ external quantum efficiency at $> 10{,}000$ cd/m^2. Appl Phys Lett 98:073310
2. Chen Z, Ding F, Hao F et al (2009) A highly efficient OLED based on terbium complexes. Org Electron 10:939–947
3. Pekka H, Harri H (2011) Lanthanide luminescence: Photophysical, analytical and biological aspects. Springer, Berlin, p. 385
4. Sastri V et al (2003) Modern aspects of rare earths and their complexes. Elsevier, Amsterdam
5. Quirino W, Legnani C, Dos Santos R et al (2008) Electroluminescent devices based on rare earth tetrakis beta-diketonate complexes. Thin Solid Films 517:1096–1100
6. Jiu H, Liu G, Zhang Z et al (2011) Fluorescence enhancement of Tb(III) complex with a new β-diketone ligand by 1,10-phenanthroline. J Rare Earth 29:741–745
7. Kuo Y, Chi-Chou L (2013) A light emitting device made from thin zirconium-doped hafnium oxide high-k dielectric film with or without an embedded nanocrystal layer. Appl Phys Lett 102:031117 (1–7)
8. Sun M, Xin H, Wang K et al (2003) Bright and monochromic red light-emitting electroluminescence devices based on a new multifunctional europium ternary complex. Chem Commun 6:702–703
9. Stathatos E, Lianos P, Evgeniou E et al (2003) Electroluminescence by a Sm^{3+}-diketonate-phenanthroline complex. Synth Met 139(2):433–437
10. Sun J, Zhang X, Xia Z et al (2012) Luminescent properties of LiBaPO4:RE (RE=Eu3+, Tb3+, Sm3+) phosphors for white light-emitting diodes. J Appl Phys 11:013101 (1–7)
11. Savchenko I, Bereznitskaya A, Smola S et al (2012) Novel electroluminescent materials on polymer metal complexes. Funct mater 19(4):541–547
12. Neng-Jun X, Louis M, Shu-Kong S et al (2006) Preparation and photoluminescence of a novel β-diketone ligand containing electro-transporting group and its europium(III) ternary complex. Spectrochim Acta A Mol and Biomol Spectrosc 65:907–911
13. Zeng L, Yang M, Wu P et al (2004) Tb-containing electroluminescent polymer with both electron- and hole-transporting side groups for single layer light emitting diodes. Synth Met 144(3):259–263
14. Savchenko I, Bereznitskaya A, Fedorov Y et al (2013) Structural organization of polymer metal complexes with water or phenanthroline and their influence on luminescence properties. Chem Chem Technol 7(4):423–428
15. Semenov V, Zolotareva N, Klapshina L et al (2009) Synthesis of C-functionalized acetylacetone and its europium complex. Preparation and study of luminescence of europium-containing Sol-Gel films. Rus J General Chem 79(9):1802–1810

Chapter 7
Poly(Methacrylamidoaryl Methacrylate)'s Surface Morphology

Lyudmyla O. Vretik, Valentyna V. Zagniy, Olena A. Nikolaeva, Volodymyr G. Syromyatnikov and Polina V. Vakuliuk

7.1 Introduction

Surface-mediated photoalignment of liquid crystals (LCs) arises on adjacent surfaces treated with light. The photoalignment effect was firstly described in 1988 by Ichimura et al. [1]. Actual applications of photoalignment provide new incentives for research in this field. Development of advanced photoalignment processes, synthesis of new photoalignment materials, and fundamental studies of the mechanisms of photoalignment continue to be a focus of interest of researchers and engineers dealing with LCs. The photoalignment phenomenon was observed for materials with photosensitive species undergoing *trans-cis* photoisomerization; cycloaddition-type photo-cross-linking as well as materials susceptible to photodestruction [2–5].

Recently, we have proposed poly(methacrylamidoaryl methacrylates) as efficient LC photoalignment materials [6–8]. In contrast to widely used C = C groups capable of [2 + 2] cycloaddition, in our materials, photoalignment effect is caused by one

L. O. Vretik (✉) · V. V. Zagniy · O. A. Nikolaeva · V. G. Syromyatnikov
Macromolecular Chemistry Department, Taras Shevchenko National University of Kyiv, Volodymyrs'ka Str. 60, Kyiv 01033, Ukraine
e-mail: vretik@list.ru

L. O. Vretik
Tel.: +380 97 541 0888

V. V. Zagniy
e-mail: zagnij@gmail.com

O. A. Nikolaeva
e-mail: avealokin.anel@gmail.com

V. G. Syromyatnikov
e-mail: svg@univ.kiev.ua

P. V. Vakuliuk
Nature Department, Institute of Chemistry, National University "Kyiv-Mohyla Acadamy", Skovorody Str. 4, Kyiv 04655, Ukraine
e-mail: polina_vakuliuk@mail.ru

O. Fesenko, L. Yatsenko (eds.), *Nanocomposites, Nanophotonics, Nanobiotechnology, and Applications,* Springer Proceedings in Physics 156,
DOI 10.1007/978-3-319-06611-0_7,

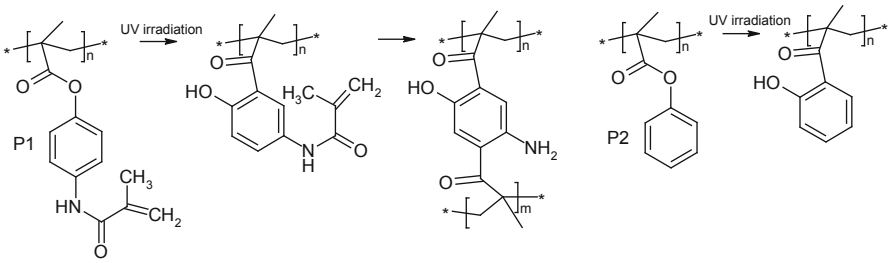

Fig. 7.1 Structures of investigated polymers and scheme of photo-Fries rearrangement in poly(methacrylamidoaryl methacrylate) P1 and model polymer poly(phenyl methacrylate) P2

or several photo-Fries rearrangements (see Fig. 7.1) combining with thermo- or photo-induced cross-linking of C = C groups [9, 10].

The photoaligning effect occurs due to anisotropic interaction of an LC with the orientationally ordered aligning film. As commonly believed, the major mechanism of this interaction is a short-range anisotropic interaction of LC molecules with the anisotropic orientationally ordered species on the photoaligning surface. Van der Waals, dipole–dipole, p–p stacking, hydrogen bonding, or steric interactions may contribute to the anchoring, depending on the molecular structure of LC and the photoaligning material. Due to the long-range interaction in mesophases, the surface-induced alignment extends to the LC bulk resulting in homogeneous alignment of the whole LC [5].

Taking into account that some authors support the view that the alignment direction is determined mainly by the morphological anisotropy of the polymer layer [11, 12], in the presented study, we discuss a possible morphological changing onto poly(methacrylamidoaryl methacrylate) P1 (see Fig. 7.1) surface before and after irradiation with polarized ultraviolet (UV) light. In parallel, the water contact angle was measured as a function of irradiation time and compared with infrared (IR) spectroscopy data. The same comparisons were made for model polymer P2 bearing only one type of photoactive group.

7.2 Experimental

7.2.1 Samples

We examined two kinds of polymer films: P1 and P2. Corresponding monomers were synthesized with a procedure similar to the procedures described in our earlier works [7–10]. The polymerization was carried out in N,N-dimethylformamide (DMF) solutions (at 10 wt. % concentration of monomer) at 80°C with AIBN as initiator. For P1 and P2, gel permeation chromatography (GPC) analysis (eluent DMF, polystyrene standards) gave the following molecular weights: $M_n = 12{,}600$, $M_w = 29{,}400$, $M_w/M_n = 2.30$ and $M_n = 10{,}000$, $M_w = 17{,}000$, $M_w/M_n = 1.7$.

The P1 and P2 thin films were prepared by spin coating from 1 wt. % DMF solution onto 100 × 150 mm glass plates at 3000 rpm. Before spin coating, the DMF solution was filtered via 0.20-μm pore filter. Subsequently, the films were baked at 100°C for 30 min and then at 40°C for 72 h to complete evaporation of solvent that remained after the coating procedure. For the LC cells, 1 wt. % solution of photoaligning polymer in DMF was spin-coated at 3000 rpm onto ITO-covered glass plates. The films were subsequently baked at 120°C for more than 30 min.

The intensity of the UV light after passing through the polarizer (a Glan-Thompson prism) was 12 mW/cm^2, illumination time was 40 min. The intensity of the non-polarized UV light was 40 mW/cm^2, illumination time was 20 min.

7.2.2 Observations and Measurements

The polymer surface morphology was monitored using atomic force microscopy (AFM). AFM images obtained for nonirradiated, irradiated with non-polarized UV light (40 mW/cm^2, time of irradiation 20 min) as well as irradiated with linearly polarized UV light (12 mW/cm^2, time of irradiation 40 min). The AFM observations have been done with AFM (NTEGRA Probe Nano Laboratory) along with Fourier analysis and estimation of surface roughness. For each sample, 1 × 1 μm and 10 × 10 μm scans were performed using single crystal silicon N-type cantilevers with sharpened pyramidal tips, nominal tip radius of 6 nm, and nominal apex angle of 18°C.

The LC cells for orientation capability evaluations have been made in a standard way [7]. The photoalignment processing was realized by using the high-pressure mercury lamp DRS-500, whose irradiation was linearly polarized by a Glan-Thompson prism. The intensity of the UV light after passing through the polarizer was approximately12 mW/cm^2, illumination time was 40 min. The cells were filled at room temperature with nematic LCs from Merck with positive (ZLI2293) dielectric anisotropy. We judged the alignment quality by cell observations in a light box and polarizing microscope using an evaluation scale with five grades: (1) excellent; (2) good (single alignment faults); (3) satisfactory (minor alignment faults); (4) bad (big number of alignment faults in a form of inversion walls, flowing patterns, etc.), and (5) no alignment.

The room temperature Fourier transform IR (FTIR) absorption spectra of the polymer films obtained by spin coating of the polymer solutions on the KBr plates were measured in the spectral range 400–4000 cm^{-1} with a resolution of 1 cm^{-1} with Perkin Elmer Spectrum BX FTIR spectrometer. As a reference, the KBr window was used. All spectral manipulations, such as baseline correction, smoothing, and normalization, were performed using the standard "Spectra" spectroscopy software package.

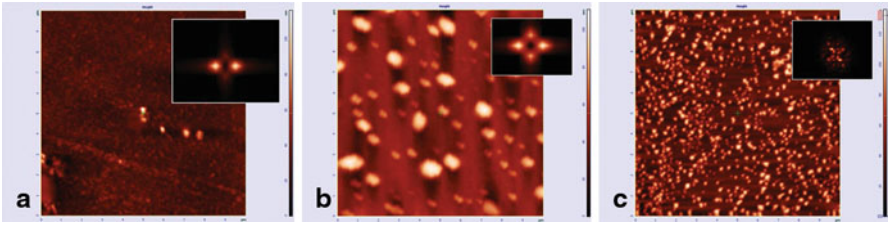

Fig. 7.2 AFM images with 10 × 10 μm scan area of **a** uncoated glass substrate and **b** coated with nonirradiated P1, and **c** nonirradiated P2 films. The inserts show the two-dimensional fast Fourier transform (2D FFT) power spectra

7.3 Results and Discussion

The LC alignment is believed to be influenced by (1) the chemical interactions between the alignment layer and the LC and (2) the interplay between LC anisotropic elastic properties and the substrate's topography [13].

In our previous investigations, Fries rearrangement was considered as an order-generating photochemical reaction. The angularly selective photo-Fries conversion, occurring in polarized light, results in orientational ordering, which manifests itself in optical birefringence and dichroism [14]. We demonstrated that this ordering results in LC photoalignment by means of UV/Vis and FTIR spectroscopy analysis as well as null-ellipsometry method [9, 10].

Since the LC alignment occurs at the substrate surface, it is very important to understand the role of surface morphology in LC alignment. Taking into account a number of publications that demonstrated that surface topology contributes to the alignment, the morphology of the films together with that of the uncoated glass substrate were measured with an atomic force microscope (NTEGRA Probe NanoLaboratory) along with Fourier analysis and estimation of surface roughness.

An excellent alignment capability of poly(methacrylamidoaryl methacrylates) was illustrated in [7, 8]; sample P1 was prepared in identical conditions as described in these publications, and its LC photoaligning properties that were tested in a standard way were classified as "excellent." Sample P2 was used as an analog of P1 with a more simple structure of photoactive aromatic side-chain groups, but they are unable to form cross-linked polymer spices during syntheses.

The surface morphologies in air at room temperature of uncoated glass substrate and coated with P1 and P2 thin films as well as their power spectra (Fourier transforms) are shown in Fig. 7.2a, b, and c, respectively. Figure 7.3 shows the surface morphologies of P1 films determined by AFM before and after irradiation by unpolarized ($I = 40\ mW/cm^2$, 20 min; a) and linearly polarized UV (LPUV; $I = 12\ mW/cm^2$, 40 min; b) light. In addition, Fig. 7.3 shows the two-dimensional fast Fourier transformations (2DFFT) from AFM images, too.

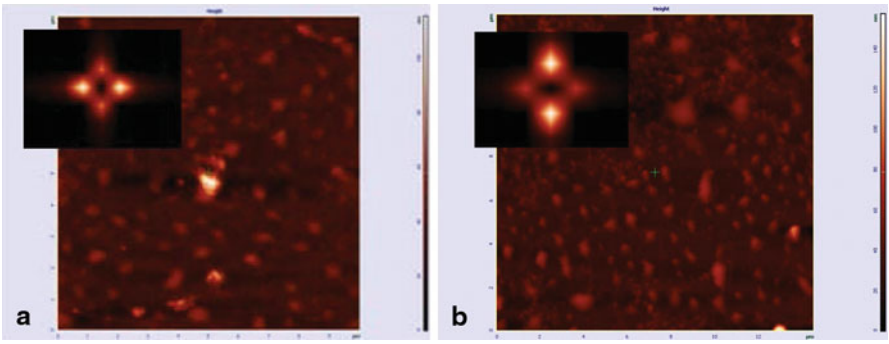

Fig. 7.3 10 × 10 μm AFM surface images of glass substrate coated with P1 **a** irradiated with non-polarized UV light and **b** irradiated with LPUV light. The inserts show the two-dimensional fast Fourier transform (2D FFT) power spectra

The most popular parameter characterizing the morphology of surfaces is the rms roughness, which represents the root mean square height of a surface around its mean value [15]. The rms roughness values for different P1 samples in comparison with P2 and uncoated glass substrate were computed for the 1 × 1 μm scans in order to avoid the influence of the large casual defects which appear in the 10 × 10 μm images (e.g., on Fig. 7.2a).

The surface of nonexposed P1 film shown in Fig. 7.2b is not flat, but hillocks are observable in the case of P1 and its analog P2. The values of rms roughness for uncoated glass, non-illuminated P1 and P2 are 4.11 nm, 25.46 nm and 21.34 nm, respectively. The difference between P1 and P2 is apparently associated with higher molecular weight of P1 in comparison with P2.

The roughness value of P1 increases by ~5 nm up to 29.60 nm when irradiated with non-polarized UV light. This observation is in good agreement with data of contact angle of water θ_{water} for P1 irradiated samples. Values of θ_{water} on P1 films were found to be 70 ± 2° before and 75 ± 2° after UV illumination. Our findings are consistent with the date of [16] which also notes that the increase of the contact angle may be caused by enhanced roughness of the films.

At the next stage, FTIR spectra of P1 as well as model polymer P2 before and after UV irradiation were compared. Due to the complicated structure of P1, most pronounced changes in the absorption bands related to Fries photoreaction in the ester Ar-O-C = O group (see Fig. 7.1) were detected in spectra of model polymer P2. As one can see from Fig. 7.4, significant weakening and broadening of ν(C = O) stretching vibration band centered at 1,748 cm^{-1} could be recognized after irradiation and could be employed as direct evidence for Fries photorearrangement [10, 17]. A comparison of IR spectroscopy data with the contact angle and roughness enhancement on irradiated P1 and P2 films gives a reason to believe that the main photochemical reaction responsible for their surface modification is Fries rearrangement.

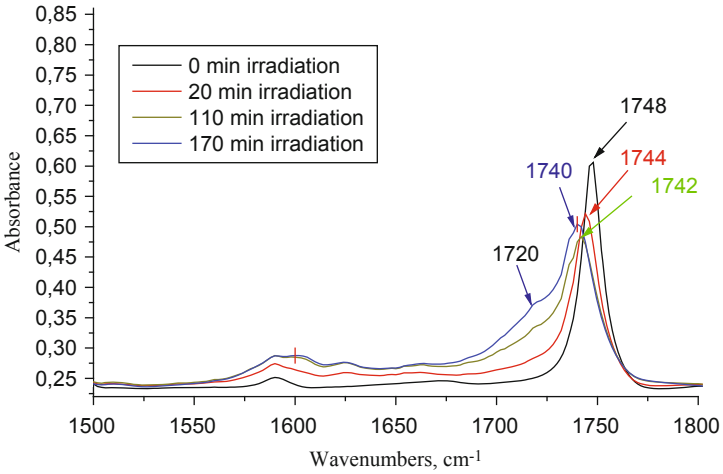

Fig. 7.4 Fragments of IR spectra of P2 films before irradiation and irradiated with non-polarized UV- light (40 mW/cm^2)

The nonirradiated sample of P1, the sample irradiated with unpolarized UV light (40 mW/cm^2) as well as the sample irradiated with polarized UV light (12 mW/cm^2) have no directional difference in polymer morphology. No grooves were observed on the surface of LPUV-illuminated P1 film as shown in Fig. 7.3b. The resultant 2D power spectra obtained by Fourier analysis of Fig. 7.2b, 7.2c calculated for nonirradiated surfaces of P1 as well as for LPUV-irradiated surfaces are not directional. Morphological anisotropy in 2DFFT power spectrum for the P1 sample irradiated with polarized UV light was not detected. Thus, no physical modification of surface during LPUV light irradiation of poly(methacrylaminophenyl methacrylate) P1 was observed. Our results, obtained for a new class of photoaligning materials are in contrast with the findings of [11, 12] where it was proved that morphological changes are directly responsible for the alignment in poly(vinyl cinnamate)-type polymers.

7.4 Concluding Remarks

We examined the possibility of that the polymer alignment occurred through grooves induced on the photoactive polymer surface by the linearly polarized UV (LPUV) illumination. While such a mechanism may be applicable to some situations, we find it to be an unsuitable explanation in the case of poly(methacrylamidoaryl methacrylates).

References

1. Ichimura K, Suzuki Y, Seki T et al (1988) Reversible changes in alignment mode of nematic liquid crystals regulated photo-chemically by command surfaces modified with an azobenzene monolayer. Langmuir 4:1214–1216
2. Ichimura K (2000) Photoalignment of liquid-crystal systems. Chem Rev 100(5):1847–1874
3. Neill MO, Kelly SM (2000) Photoinduced surface alignment for liquid crystal displays. J Phys D Appl Phys 33:R67–R84
4. Chigrinov VG, Kozenkov VM, Kwok HS (2008) Photoalignment of liquid crystalline materials: physics and applications. Wiley, New York
5. Yaroshchuk O, Yu R (2012) Photoalignment of liquid crystals: basics and current trends. J Mater Chem 22:286–300
6. Syromyatnikov V, Vretik L, Yaroshchuk O et al (2001) Naphthalene containing polymers as new photoaligning materials for LCs. Mol Cryst Liq Cryst 368:543–549
7. Vretik L, Yaroshchuk O, Zagniy V et al (2011) New strategy in development of liquid crystal photoaligning materials with reactive C = C bonds. In: Iwan A (ed) Liquid crystalline organic compounds and polymers as materials of the XXI century: from synthesis to applications. Transworld Research Network, Kerala, pp 153–190
8. Vretik L, Syromyatnikov V, Zagniy V et al (2008) Problem of photoalignment the LCD's development: synthetic routes in its solving. Mol Cryst Liq Cryst 486:57(1099)–65(1107).
9. Kyrychenko V, Smolyakov G, Zagniy V et al (2008) Photochemistry of bis-methacrylic polymers and alignment of liquid crystals. Mol Cryst Liq Cryst 496:278–292
10. Vretik L, Kyrychenko V, Smolyakov G et al (2011) Photochemical transformations in bis-methacrylic polymers for liquid crystal photoalignment: IR spectroscopy studies. Mol Cryst Liq Cryst 536:224–235
11. Kumar S, Kim JH, Shi Y (2005) What aligns liquid crystals on solid substrates? The role of surface roughness anisotropy. Phys Rev Let 94:077803(1)–077803(4)
12. Cull B, Shi Y, Kumar S et al (1996) Anisotropic surface morphology of poly(vinyl 4-methoxy-cinnamate) and 12 − 8(poly)diacetylene thin films induced by linear photopolymerization. Phys Rev E: Stat Phys Plasmas Fluids Relat Interdiscip Top 53:3777–3781
13. Patrício P, Telo da Gama MM, Dietrich S (2002) Geometrically-controlled twist transitions in nematic cells. Phys Rev Let 88:245502–245505
14. Kawatsuki N, Takatsuka H, Yamamoto T (2001) Thermally stable photoalignment layer of a novel photo-crosslinkable polymethacrylate for liquid crystal display. Jpn J Appl Phys 40:L209
15. Raposo M, Ferreira Q, Ribeiro PA (2007) A guide for atomic force microscopy analysis of soft-condensed matter Modern research and educational topics in microscopy. In: Mendez-Vilas A, Diaz J (eds) Modern research and educational topics in microscopy, vol 2. Formatex Research Institute, Spain, pp 758–769
16. Ma J, Bartels JW, Li Zh et al (2010) Synthesis and solution-state assembly or bulk statethiol-ene crosslinking of pyrrolidinone- and alkene-functionalized amphiphilic block fluorocopolymers: From functional nanoparticles to anti-fouling coatings. Aust J Chem 63:1159–1163
17. Gunzler H, Gremlich HU (2002) IR spectroscopy. An introduction. Wiley, Weinheim

Chapter 8
Investigation of Nonlinear Magnetic Properties Magneto-Mechano-Chemical Synthesized Nanocomplex from Magnetite and Antitumor Antibiotic Doxorubicin

V. E. Orel, A. D. Shevchenko, A. Y. Rykhalskiy, A. P. Burlaka, S. N. Lukin and I. B. Schepotin

8.1 Introduction

Nanotechnology became one of the most promising areas of research in the recent years. High interest in nanomaterials is motivated by the fact that the transition to the nanoscale changes a number of fundamental properties of materials. One of the main factors that determine the physical properties of nanoscale objects is the active surface. As a result, new physical phenomena and properties can be observed in solids that did not exist before and that could not be predicted from the structure and properties of the material. Also, material magnetic properties could differ from magnetic properties of nanoparticles from the same material and they may acquire ferromagnetic and superparamagnetic properties. Currently, a wide range of magnetic nanoparticles of metals (Co, Fe, Ni etc.), iron oxides, and ferrites have been synthesized [1, 2].

Oxide nanoparticles have smaller magnetic moments than the metal nanoparticles, but they have higher oxidation resistance. That is why iron oxide nanoparticles have currently become the most widely used nanoparticles in medicine due to their low toxicity and stability of magnetic properties. They consist of a metal oxide core enclosed in a shell of organic material. This makes the nanoparticles more stable when used in biology and medicine [3, 4].

V. E. Orel (✉) · A. Y. Rykhalskiy · I. B. Schepotin
National Cancer Institute/33/43, Lomonosova Str., 03022 Kyiv, Ukraine
e-mail: v-orel@voliacable.com

A. D. Shevchenko
G.V. KurdyumovInstitute for Metal Physics/36, AcademicanVernadsky Blvd.,
03680 Kyiv, Ukraine
e-mail: admit@imp.kiev.ua

A. P. Burlaka · S. N. Lukin
R.E. Kavetsky Institute of Experimental Pathology, Oncology and Radiobiology/45,
Vasilkovsky Str., 03022 Kyiv, Ukraine

S. N. Lukin
e-mail: s.lukin@mail.ru

O. Fesenko, L. Yatsenko (eds.), *Nanocomposites, Nanophotonics, Nanobiotechnology, and Applications,* Springer Proceedings in Physics 156,
DOI 10.1007/978-3-319-06611-0_8,

Magneto-mechano-chemical technology of synthesis in nanoreactors is a new method based on the integration of two well-known technologies: mechanochemical synthesis [5] and synthesis in the microreactor with magnetic elements [6]. Mechanochemical synthesis includes the fragmentation of separate elements and the initiation of paramagnetic centers (free radicals) in the nanocomplex (NC) structure [7]. Simultaneous exposure of nonhomogeneous constant magnetic field (CMF) and electromagnetic field (EMF) causes eddy currents and magnetic vortices in the areas of contact between nanoparticles of iron oxides and organic compounds [8, 9].

Magneto-mechano-chemical synthesized (MMCS) antitumor NC, consisting of magnetite Fe_3O_4 and anthracycline antitumor antibiotic doxorubicin (DOXO) is the most investigated NC. Under normal conditions, iron ions get inside of cells bounded to the protein ferritin and can neutralize or initiate hydroxyl radicals depending on various factors of influence [10]. Magnetite is a soft ferromagnetic material with a high-saturation magnetic moment in a wide temperature range. During magneto-mechano-chemical activation (MMCA), its magnetic properties are changing. DOXO is a cytotoxic drug that is widely used to treat various types of malignant tumors. Influence of external magnetic and EMF on chemical reactions is caused by magnetic spin effects that may occur in radical reactions involving compounds with paramagnetic and ferromagnetic properties. These are the radical recombination reactions that occur with the formation of biradicals, reactions of radicals with triplet molecules, paramagnetic complexes, etc. Therefore, the natural formation of the DOXO, iron oxide complex during combined therapy with chemotherapy, and electromagnetic irradiation (EI) triggers cytotoxicity effect as a result of the formation of hydroxyl radicals in a malignant tumor. A local antitumor effect of the drug is a treatment factor; however, side effects are possible in other organs (for example, cardiotoxicity) [11]. DOXO in the normal state is diamagnetic and dielectric. MMCA of DOXO causes a controlled appearance of additional charge carriers and additional growth of the number of paramagnetic centers (free radicals). This raises the possibility of artificial control on the effect of the drug cytotoxicity due to external EI.

During EI in metal nanoparticles and on their surface, the nonlinear electromagnetic effects are triggered. Nonlinearity occurs due to the major role of the magnetic component of the EMF. The magnetic component of the EMF can significantly change the trajectory of the electron. If the length of the free electrons path exceeds the typical size of electron trajectories in a magnetic field, then the conductivity of the metal becomes a function of the spatial distribution of the field, which is causing nonlinearity [12].

Nonlinear magnetic properties play an important role for the ability of the remote control of CMF, EMF, and antitumor activity of NC, its ferromagnetic core (magnetite), and the outer shell of DOXO with paramagnetic properties [13]. Therefore, the aim of this chapter is to study the nonlinear magnetic characteristics of MMCS NC of Fe_3O_4 and DOXO with different values of CMF and EMF during MMCS.

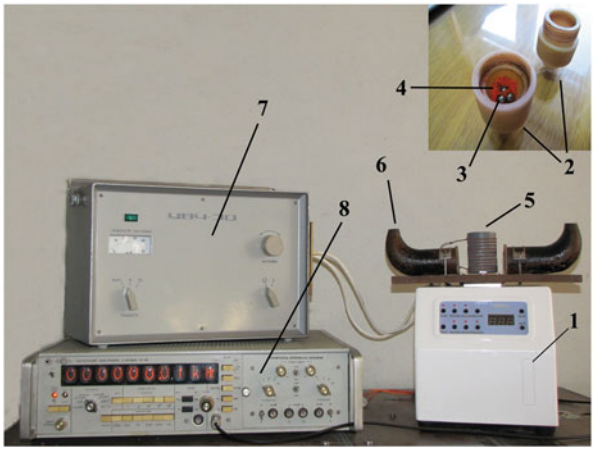

Fig. 8.1 Magneto-mechanical nanoreactor: *1* mechanical nanoreactor; *2* diamagnetic chamber; *3* metallic balls; *4* Fe_3O_4 and DOXO; *5* inductor; *6* permanent magnets; *7* generator; *8* frequency meter

8.2 Materials and Methods

8.2.1 Magneto-Mechano-Chemical Synthesis

In this work, we used nanoparticles of Fe_3O_4 (produced by International Center for Electron Beam Technologies of E. O. Paton Electric Welding Institute, Ukraine) with diameters in the range 20–40 nm and DOXO (from Pfizer, Italy). Mass concentration of DOXO in NC was 65 %. MMCA and MMCS with simultaneous disintegration of particles and electromagnetic radiation in a dry powder form was performed in magneto-mechanical nanoreactor (NCI, Ukraine) [14].

The nanoreactor picture is shown in Fig. 8.1 The samples with Fe_3O_4 and DOXO were placed in the diamagnetic chamber (2) together with metallic balls (3) and Fe_3O_4 and DOXO (4). Mechanical processing was performed by vertical oscillation of the mechanical nanoreactor (1) at a frequency of 36 Hz and amplitude of 9 mm for 5 min with intensity of a supply of mechanical energy 20 W/g. Simultaneously, El was applied at 42 MHz by an induction coil (5) from the master generator (7) and constant magnetic field from permanent magnets (6). Generator frequency was measured with magnetic flux sensor (8).

8.2.2 Magnetic Studies

The magnetic properties were studied by magnetometry using a "Vibrating Magnetometer 7404 VSM" ("Lake Shore Cryotronics," Inc., USA) with magnetic fields up to 13 kOe. The magnetometer sensitivity is 10^{-7} emu and this allowed the measurement of magnetic moment of samples weighting milligrams. The mass was determined by an electronic microbalance AB135-S/FACT ("Mettler Toledo," Switzerland) with auto-identification which has a sensitivity of 10^{-5} g.

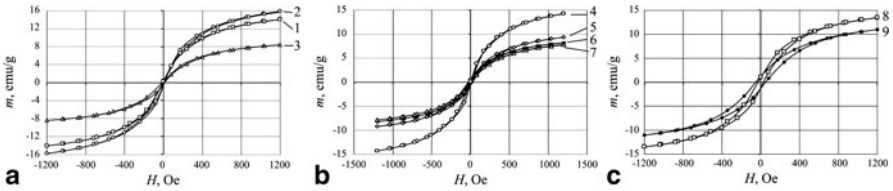

Fig. 8.2 Hysteresis loops. W—EMF generator output power. B—induction of CMF. T—MMCS environment temperature. **a** W=2 W; T=293 K; B=0 mT (1); B=8 mT (2); B=5 mT (3). **b** B=12 mT; T=293 K; W = 2 W (4), W=50 W (5), W=160 W (6), W=270 W (7). **c** W=2 W; B=30 mT; T=293 K (8), T ≈ 77 K (9)

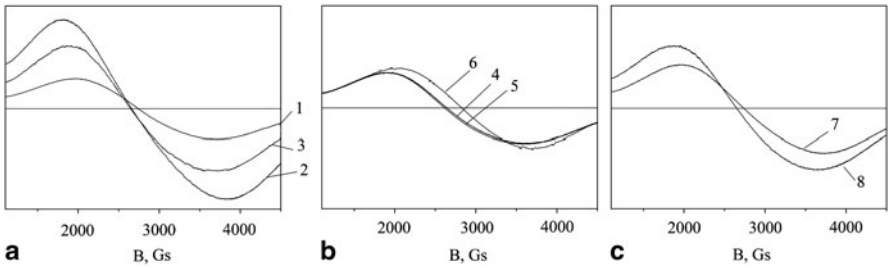

Fig. 8.3 EPR spectra. W—EMF generator output power. B—induction of CMF. T—MMCS environment temperature. **a** W=2 W; T=293 K; B=0 mT (1); B=8 mT (2); B=5 mT (3). **b** B=0 mT; T=293 K; W=160 W (4), W=270 W (5), W=50 W (6). **c** W=2 W; B=30 mT; T=293 K (7), T ≈ 77 K (8)

8.2.3 Electron Paramagnetic Resonance Spectroscopy

In order to measure the *g*-factor and the concentration of paramagnetic centers in the samples, electron paramagnetic resonance (EPR) spectra were recorded with the spectrometer RE1307 at liquid nitrogen temperatures (77 K) in a cylinder resonator with the mode H_{011}, with frequency 9.15 ± 0.1 GHz. The power microwave radiation was 40 mW and the magnetic field modulation frequency 100 kHz.

The samples were placed in a quartz Dewar with an inner diameter of 4.5 mm. The *g-factor* was calculated according to the formula of the resonance condition [15]:

$$h\nu = g\beta B$$

where $h\nu = 9.15$ GHz is microwave frequency, $\beta = 1.39968 GHz/kGs$ is Bohr magneton, and B is magnetic induction.

8.3 Results and Discussion

The analysis presented in the magnetic characteristics in Fig. 8.2 and EPR spectra in Fig. 8.3 show that all the samples of NC were soft ferromagnetic.

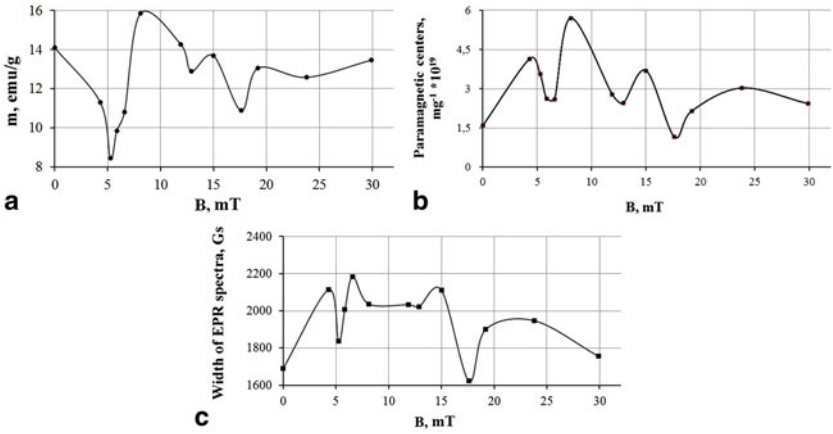

Fig. 8.4 Nonlinear magnetic properties of NC in conditions of 2 W EMF generator output power and their polynomial approximation, R—correlation with data in experiment; B—induction of CMF. **a** Magnetic moment: $m = 227.5B^6 - 222.2B^5 + 6.1B^4 + 44B^3 - 8.1B^2 - 1.3B + 0.2$; $R = 0.76$. **b** Number of paramagnetic centers: $C = -121.5B^6 - 0.12B^5 + 39.8B^4 - 11.7B^3 - 4.14B^2 - 1.48B + 0.1$; R=0.66. **c** Width of EPR spectra: $w = -340.7B^6 + 79B^5 + 105.4B^4 - 2.7B^3 - 10B^2 - 1.1B + 0.2$; $R = 0.76$

Combined effects of CMF and EMF with 2 W output power of the EMF generator increased coercivity in all studies in comparison with experiments where NCs were examined without the influence of CMF. The number of paramagnetic centers in the samples also increased except in the experiment at 18 mT CMF. The saturation magnetic moment value decreased in all experiments except at 8 mT CMF and 2 W of output power of EMF during constant mechanical vibration. In the last experiment to measure saturation magnetic moment, the number of paramagnetic centers and EPR line width reached maximum values (Fig. 8.4). Increase in these parameters at 8mT CMF and 2W output power EMF, expectedly, has been caused by the influence of CMF, mechanical vibration, and EMFs on the spin dynamics of spin-correlated pairs and have a resonant character. Therefore, amplification of recorded magnetic parameters, probably, could be caused by the effect of magneto-mechano-chemical resonance.

We can see that the magnetic properties of MMCS NC inherent nonlinear effects. It is well known that even small perturbations can cause large effects in nonlinear systems. This confirms the previously developed theoretical models and experimental studies concerning magnetodynamic nonlinearity [16]. The mechanisms of this process can be based on the effects of electron transfer between magnetite nanoparticles and DOXO influenced by CMF and EMF. One of the possible mechanisms of electron transfer is the emergence of eddy currents and magnetic vortices compatible with CMF and EMF exposure due to nonuniform magnetization of the NC material [17]. Another mechanism of electron transfer called spintronics mechanism is associated with phenomena of giant and colossal magnetoresistive effects [18]. The

source of spin-polarized electrons in Fe_3O_4–DOXO heterostructure is magnetite. In the presence of a CMF, the Zeeman splitting of the conduction band with the formation of two Zeeman energy sublevels arises. With joint action of CMF and EMF, the injection of spin-polarized electrons occurs, which makes it possible to implement managed electron transitions on the upper and lower levels in NC and create inversions of their settlement. In the number of experiments after MMCS, *g*-factor was varied from 2.3 to 2.46. This fact shows the increase of unpaired electron spin contribution to magnetic moment, which is indirect evidence of the increasing number of paramagnetic centers (free radicals).

Increased output power of the EMF generator from 50 to 160 W at 12 mT CMF reduced saturation magnetic moment to the lowest in the entire series of experiments value—7.82 emu/g. It is connected with effects of when MMCS simultaneous action of mechanical factors, CMF, and EMF resulted in degaussing magnetic domains, but the number of paramagnetic centers in the investigated samples increased to 2.02×10^{19} mg^{-1}. Based on the fact that Fe_3O_4 nanoparticles include in its composition ions with unpaired electrons in the inner shell (3d shell of Fe ions in Fe_3O_4), which determine the magnetic properties of magnetite [19], we can suggest the existence of conditions for electron transition during MMCS between internal and partially filled outer orbitals, which leads to the increase of paramagnetic number in the Fe_3O_4–DOXO heterostructure.

In experiments where NC MMCS were performed in liquid nitrogen temperature (≈ 77 K), the saturation magnetic moment decreased by 22 % but increased coercive force and the number of paramagnetic centers by 43 and 28 %, respectively, in comparison with experiments when synthesis was carried under room temperature. EMF and CMF parameters were the same in both experiments. These data agree well with known facts according to coercivity of ferromagnets from the effects of deformation of the structure during cooling [20].

Analyzing Fig. 8.4, dependences of saturation magnetic moment, line width of the EPR spectrum, and the number of paramagnetic centers on the magnitude of induction of CMF at 2 W output power of the EMF generator and constant mechanical vibration indicates that they are not linear and can be approximated by sixth-order polynomials.

In the graphs can be observed a pronounced maximum saturation magnetic moment, concentration of paramagnetic centers, and EPR line width at 8 mT induction CMF and EMF generator output power 2 W. Minims are not coincided. Thus, the smallest saturation magnetic moment (8.44 emu/g) was observed at 5 mT induction of CMF, the minimum concentration of free radicals (1.17×10^{19} mg^{-1}), and the line width of the EPR spectrum at 18 mT of CMF.

On the graph of saturation magnetic moment with increasing induction CMF from 8 to 30 mT, we can see a pronounced oscillatory process. Dependences of the magnetic moment and the concentration of paramagnetic centers are not correlated with each other.

In known technologies, the antitumor effect of drugs is initiated as a result of ablation (evaporation) tumors at 50–60 °C or synergistic effects with 42–46 °C [21], but the treatment of cancer patients in these temperatures has several problems. In

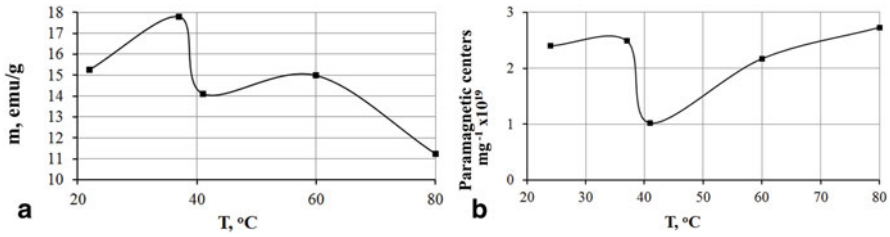

Fig. 8.5 Temperature influence on MMCS NC: **a**—magnetic moment; **b**—number of paramagnetic centers

our alternative technology of magnetic nanotherapy, the antitumor magnetothermal effect is initiated by free radical reactions under mild hyperthermia at 37–39 °C. Based on the Curie law, we conducted a study of the temperature effect on the magnetic moment and the number of paramagnetic centers in MMCS NC (Fig. 8.5).

These results show that at a temperature of 37 °C, magnetic moment and the number of paramagnetic centers are larger than at 41 °C. With further increase in temperature to 80 °C, magnetic moment decreased and the number of paramagnetic centers increased. This indicates that moderate physiological magnetic inductothermy is a better condition for the magnetic nanotherapy.

8.4 Conclusion

In this chapter was observed that the coercivity increased in all experiments. The number of paramagnetic centers, the magnetic moment, and the EPR line width demonstrated nonlinear properties change. In the experiment with 8 mT CMF and 2 W output power, EMF saturation magnetic moment, the number of paramagnetic centers, and EPR line width were the biggest in the entire series of experiments. The studies of temperature influence on sample magnetic properties have shown that moderate physiological magnetic hyperthermia is a better condition for cancer treatment.

Our results have two promising possibilities of practical use in oncology. First, this can be a basis for the nonlinear dynamics of magnetic properties of NC and polynomial approximations for the next opportunity in development of computer models and programs in order to obtain the required magnetic properties of anticancer drugs at MMCS according to CMF and EMF parameters. The second is the possibility to remotely control cytotoxic and antioxidant properties of the NC into a malignant tumor by generating nonlinear effects with CMF and EMF based on the theory of dynamical chaos malignant processes [13]. So, the results of the study are promising for practical application of magnetic nanotherapy in cancer treatment.

References

1. Shenoi MM, Shah NB, Griffin RJ et al (2011) Nanoparticle pre-conditioning for enhanced thermal therapies in Cancer. Nanomedicine (Lond) 6(3):545–563
2. Xiang-Hong P, Ximei Q, Hui M et al (2008) Targeted magnetic iron oxide nanoparticles for tumor imaging and therapy. Int J Nanomed 3(3):311–321
3. Roca AG, Costa R, Rebolledo AF, Veintemillas-Verdaguer S et al (2009) Progress in preparation of magnetic nanoparticles for applications in biomedicine. J Phys D Appl Phys 42:1–11;
4. Fisher JK, Vicci L, Cribb J et al (2006). Superfine magnetic force micromanipulation systems for the biological sciences. NANO Br Rep Rev 1(3):191–205
5. Gutman EM (1998) Mechanochemistry of materials. Int Science Publishing, Cambridge
6. Kuramitz H (2009) Magnetic microbead-based electrochemical immunoassays. Anal Bioanal Chem 394(1):61–69
7. Baláž P (2008) Mechanochemistry in nanoscience and minerals engineering. Springer, Berlin
8. Cohen AE (2009) Nanomagnetic control of intersystem crossing. J Phys Chem 113:11084–11084
9. Wang H, Yu Y, Sun Y, Chen Q (2011) Magnetic nanochains: a review. NANO Br Rep Rev 6(1):1–17
10. Britigan BE, Serody JS, Cohen MS (1994) The role of lactoferrin as an anti-inflammatory molecule. Adv Exp Med Biol 357:143–156
11. Gille L, Kleiter M, Willmann M, Nohl H (2002) Paramagnetic species in the plasma of dogs with lymphoma prior to and after treatment with doxorubicin. An ESR study. Biochem Pharmacol 64(12):1737–1744
12. Kosevich AM, Ivanov VA, K ovalev AS (1983) Nonlinear waves of magnetization. Dynamic and topological solitons, Kiev (in Russian)
13. Orel VE, Shchepotin IB, Smolanka II et al (2012) Radiofrequency hyperthermia of malignant neoplasm, nanotechnology and dynamic chaos. Ukrmedbook (in Russian)
14. Orel VE, Romanov AV, Dzyatkovska NN et al (2013) Magnenic nanotherapy of cancer. LAP Lambert Academic Publishing, Saarbrücken (in Russian)
15. Schweiger A, Jeschke G (2001) Principles of pulse electron paramagnetic resonance. Oxford University Press, Oxford
16. Kosevich AM, Ivanov BA, Kovalev AS (1990) Magnetic solitons. Phys Rep 194(3–4):117–238
17. Stoll RL (1974) The analysis of eddy currents. Oxford University Press, Oxford
18. Fert A (2008) The origin, development and future of spintronics. Phys Usp 178(12):1336–1348
19. Symons M, Gutteridge J (1998) Free radicals and iron: chemistry, biology, and medicine. Oxford University Press, Oxford
20. Livingston JD (1981) A review of coercivity mechanisms. J Appl Phys 52(3):2541–2545
21. Maier-Hauff K, Ulrich F, Nestler D, Niehoff H et al (2010) Efficacy and safety of intratumoral thermotherapy using magnetic iron-oxide nanoparticles combined with external beam radiotherapy on patients with recurrent glioblastomamultiforme. J Neurooncol 103(2):317–324

Chapter 9
Electrochemical Elaboration of Nano Powders Based on Magnesium and Lithium for Solid Hydrogen Storage

M. Sahli and N. Bellel

9.1 Introduction

Currently, there exist three modes of hydrogen storage:

- Gaseous state storage: compressed by pressures of about 350–700 bar with a volume density of 39 kg m^{-3}, however, the compression is consumer energy (5–20 − compression is consumerenergy) [1], in heavy and large bottles composed of a metallic or thermoplastic envelope to ensure the sealing and a shell for continuous fiber resin impregnated to provide mechanical rigidity [2].
- Liquid storage: requires very low temperatures of cooling (20 K with 1 bar). The volume density of hydrogen under these conditions is equal to 71 kg m^{-3} [3]. This method induces important costs of liquefaction (pressure composition isotherm, PCI, of H_2 stored between 30 and 40 %) [1] and an evaporation phenomenon called boil-off (warming up evaporation).
- Solid storage: hydrogen interacts via strong connections (chemisorption: Molecular hydrogen absorbs by reversible chemical combination with atoms which compose the metallic material) or weak connections (physical absorption: hydrogen adsorption at the solid surface level under the effect of intermolecular forces) by solids [4].

Every mode has advantages and disadvantages trying to achieve the wanted application. The two first modes of storage (gaseous and liquid) are ineffective because they are affected by a weak volume density and by safety problems [5]. On the other hand, the solid storage presents an enormous advantage in terms of safety and volume capacity which are represented in Table 9.1.

We can distinguish three processes in order to store hydrogen in a solid state:

M. Sahli (✉) · N. Bellel
Physics Energy Laboratory, Physics Department, Constantine University, Constantine, Algeria
e-mail: bellelnadir@yahoo.fr

O. Fesenko, L. Yatsenko (eds.), *Nanocomposites, Nanophotonics, Nanobiotechnology, and Applications,* Springer Proceedings in Physics 156,
DOI 10.1007/978-3-319-06611-0_9,

Table 9.1 Comparison of the various modes of hydrogen storage [6]

	Density (kg m^{-3})	Mass capacity (%)	Energy cost (% PCI H_2 stored)	Remarks
H_2 700 bar	62	100	15	Low volume density
H_2 liquid	70	100	30	Evaporation, energy cost
MgH_2	106	7.6	31	$T > 300\,°C$
$2LiBH_4 + MgH_2$	96	11.6	17	Partial reversibility

- The insertion of hydrogen's atoms within a metallic network (hydride metal formation)
- The adsorption of gas on the porous material surfaces
- The reversible decomposition of chemicals hydrides (iono-covalent bonds)

Studies had shown that hydride of magnesium has a high thermodynamic stability ($\Delta H = -75\,\text{kJ/mol}H_2$) and consequently a high desorption temperature (573–673 K) [7, 8].

MgH_2 remains the most agreeable because of its high mass capacity (7.6 % in mass), the abundance, and the weak cost [9], but sorption/desorption kinetic and the high operating temperature (300 °C) limit the use of materials which contain magnesium in the applications based on hydrogen [10, 11].

Two principle approaches are considered now in order to solve these problems. The first one is magnesium particle scale reduction [12] and the second is adding catalytic elements in the solid magnesium solution or introducing catalytic additives with composites containing magnesium [11].

The objective of our work resides in hydrogen desorption temperature reduction by structural modification of materials in order to promote hydrogen desorption.

9.2 Experimental

The experiment shows that hydride elaboration is done by the electrochemical way and it is too useful because it produced hydrides without any need for gaseous hydrogen or any high temperatures. Consequently, magnesium alloys electrochemical elaboration have been widely used in order to improve batteries performances [13].

The electrodeposition occurs at the electrolyte/electrode interface which implies electron transfer toward or from the electrode surface. The deposit is the result of ion reduction in the solution on a negatively charged electrode (cathode).

Several parameters have an influence on the process:

- Metallic ion concentrations
- Electrolytic bath temperature
- pH solution
- Current density
- Additives

The electrolyte is a solution which contains mobile ions (so it leads to an electrical current) and has a mixture of two aqueous solutions that had been prepared in ultra-pure water with the following commercial products: magnesium chloride ($MgCl_2$ $6H_2O$) and lithium hydroxide monohydrate (LiOH. plate H_2O).

During all the electrolysis manipulation, the used cathode is a plate of aluminum. All experiments were realized in ambient temperature and in a potentiometric.

The experimental device is presented in the following figure:

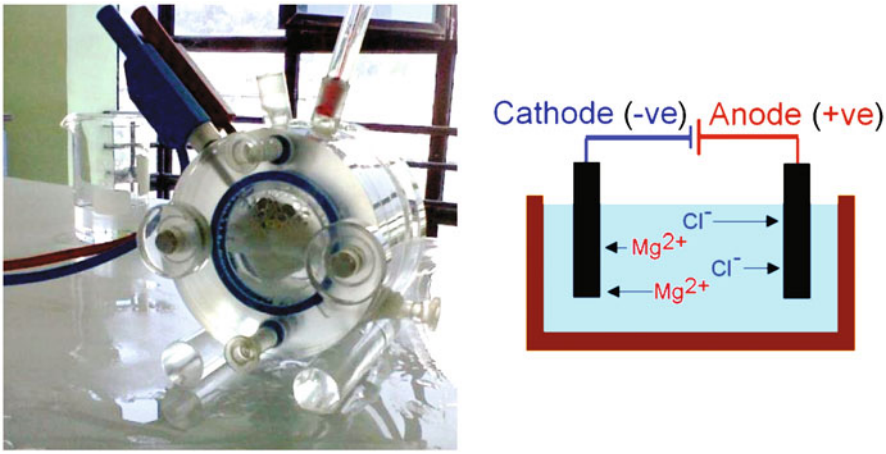

Experimental device diagram

9.3 Results

The electro-deposed powder on the aluminum cathode was analyzed in order to obtain information related to its chemical composition and its structure.

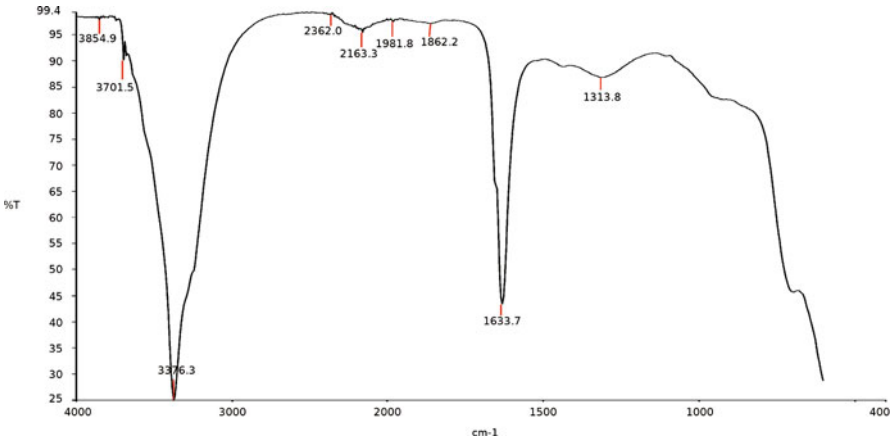

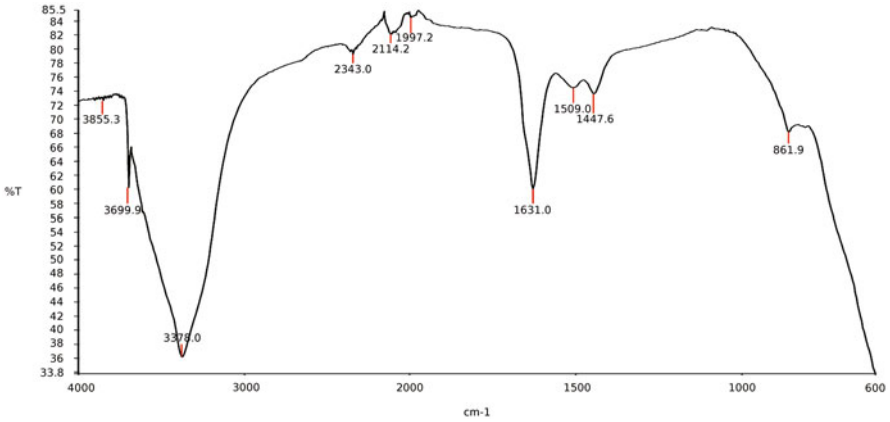

Fourier transform infrared spectroscopy (FTIR) spectrum of the powders was obtained from various experiments.

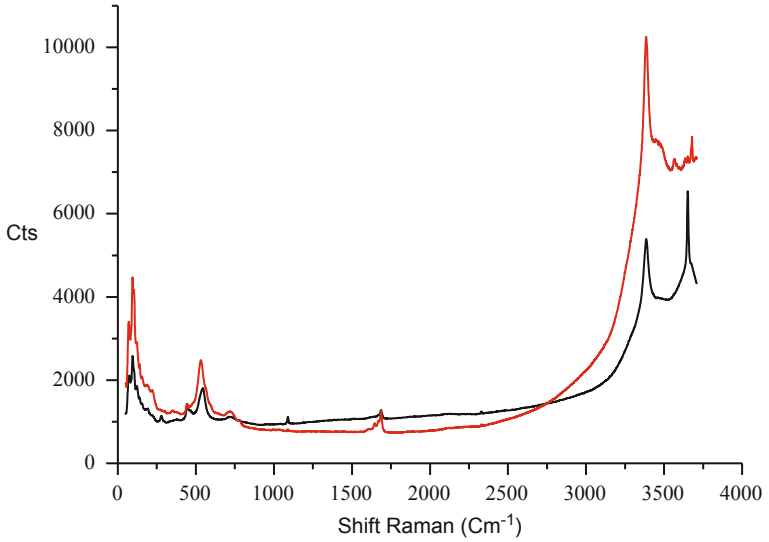

Raman spectrum of the powders was obtained from various experiments.

The electro-deposed powder on copper cathode was analyzed in order to obtain information related to its chemical composition and its structure.

Figures 9.1, 9.2, and 9.3 have the results of analysis by X-ray diffraction, Raman spectroscopy, and Fourier transform infrared spectroscopy obtained for all the powders with the various parameters of development.

The Mg alloy phases indentified for the Ech2 sample are presented in Fig. 9.4, which will be tested under hydrogen to study the kinetics of absorption and desorption at different temperatures and pressures. Similar to those obtained for Ech1, Ech X, Ech X1 (the peaks corresponding to MgH_2, LaH_3, La_2Mg_{17}, $AlMg_3$ and Mg_2Cu).

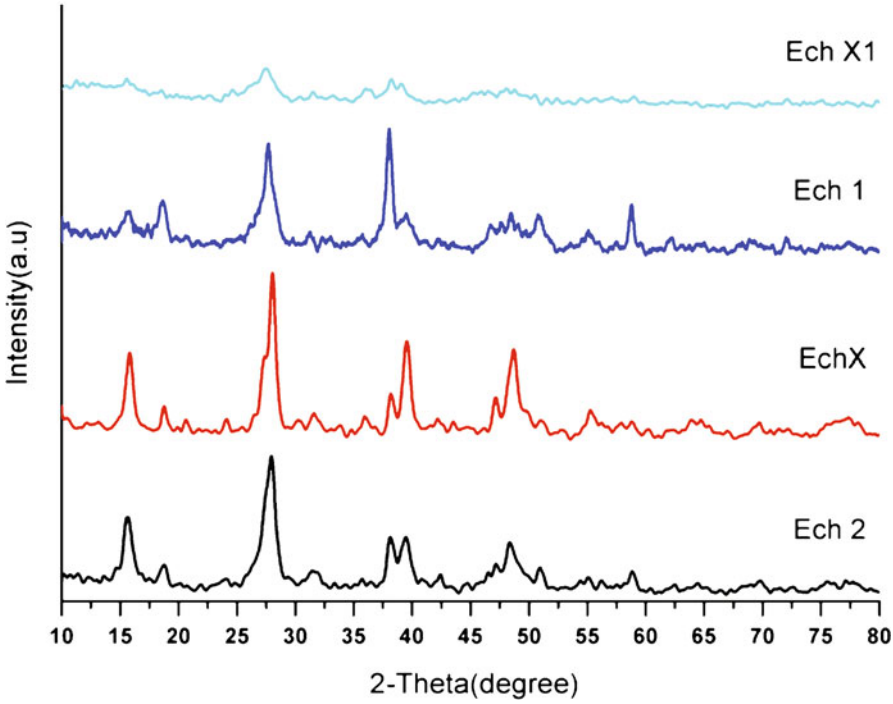

Fig. 9.1 X-ray diffraction spectrum of the powders obtained from the various experiments

9.4 Conclusion

This study shows the possibility of development of magnesium-based nanocomposites on a metallic cathode for solid storage of hydrogen by electrochemical preparation process. The powders obtained will be tested under hydrogen to study the kinetics of absorption and desorption at different temperatures and pressures.

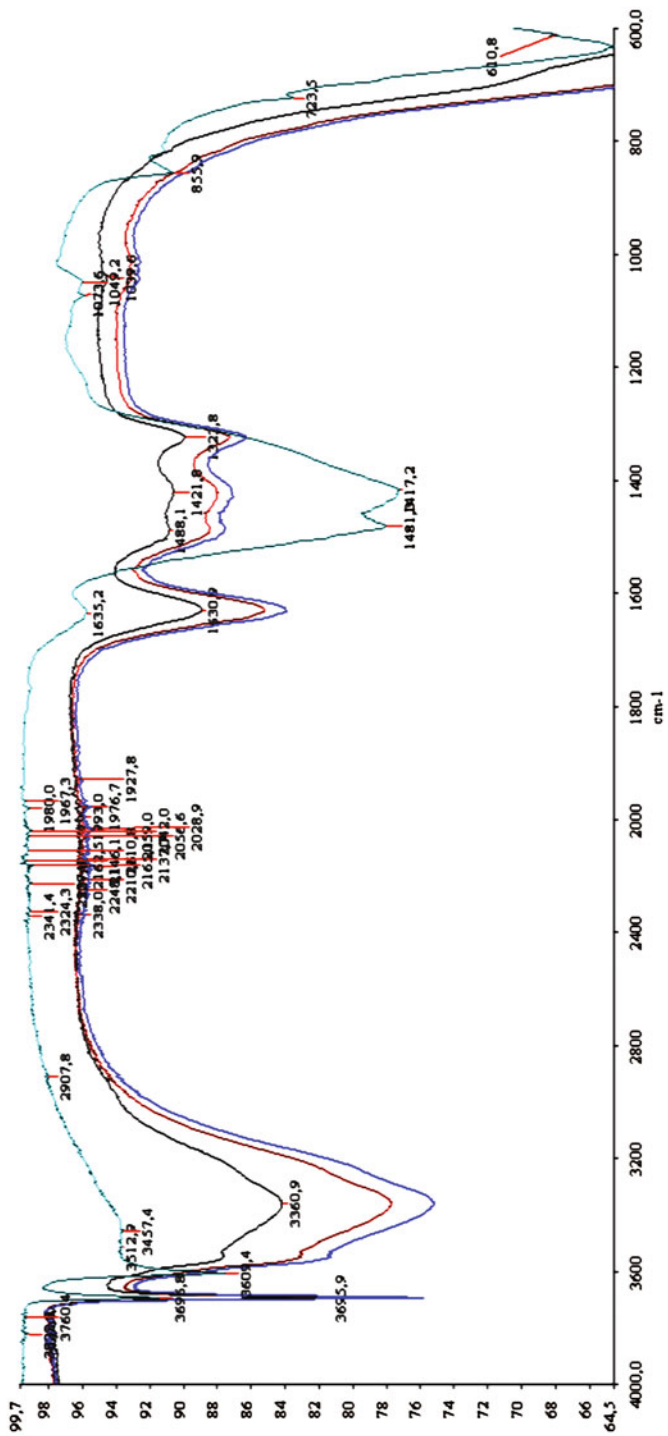

Fig. 9.2 FTIR spectrum of the powders obtained from the various experiments

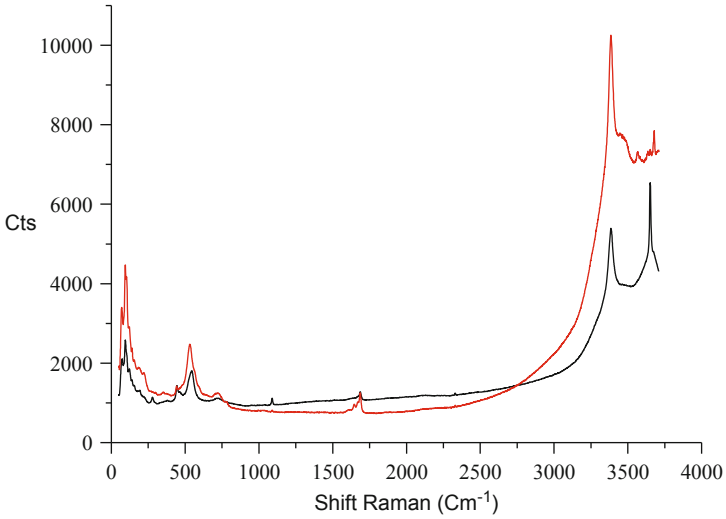

Fig. 9.3 Raman spectrum of the powders obtained from the various experiments

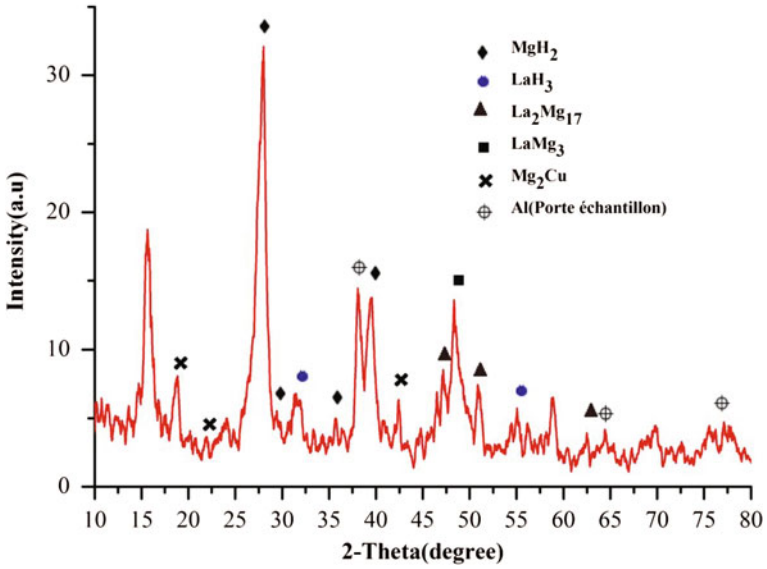

Fig. 9.4 Phase identification by XRD in Ech2 powder

References

1. Jinyang Z, Xianxin L, Ping X, Pengfei L, Yongzhi Z, Jian Y (2012) Development of high pressure gaseous hydrogen storage technologies. Int J Hydrogen Energy 37:1048–1057
2. Patricia K Réservoirs haute pression en composites. Techniques de l'ingénieur, AM 5 530
3. Jean G Liquéfaction de l'hydrogène. Technique de l'ingénieur, J3603
4. Christophe B Hydrogène. Technique de l'ingénieur, J6368
5. Ross DK (2006) Hydrogen storage: the major technological barrier to the development of hydrogen fuel cell cars. Vacuum 80:1084 – 1089
6. Baptiste D (2012) Couplage d'un réservoir d'hydrure de magnésium et d'une source externe de chaleur, Université de Grenoble, Thèse doctorat soutenue le 21 juin 2012
7. Sandra K, Zeljka R, Nikola N, Bojana PM, Zoran J, Zvezdana B, Jasmina GN, Ljiljana M (2011) Hydrogen storage properties of MgH_2 mechanically milled with α and β SiC. Int J hydrogen energy 36:549–554
8. Sakintuna B, Lamari-Darkrim F, Hirscher M (2007) Metal hydride materials for solid hydrogen storage: a review. Int J Hydrogen Energy 32:1121 – 1140
9. Tong L, Chenggong Q, Mu Z, Yurong C, Hailong S, Xingguo L (2012) Synthesis and hydrogen storage properties of Mg-La-Al nanoparticles. J Power Sources 219:100–105
10. Schlapbach L, Züttel A (2001) Hydrogen-storage materials for mobile applications. Nature 414:353 – 358
11. Jianxin Z, Xiaoqin Z, Yanjun Y, Xi C, Hao G, Si Z, Wenjiang D (2012) Study on the hydrogen storage properties of core-shell structured Mg-RE (RE [Nd, Gd, Er) nano-composites synthesized through arc plasma method. Int J Hydrogen Energy 36:1–10
12. Cheng FY, Tao ZL, Liang J, Chen J (2012) Efficient hydrogen storage with the combination of lightweight Mg/MgH_2 and nanostructures. Chem Commun 48:7334 – 7343
13. Knotek V, Vojtech D (2013) Electrochemical hydriding of Mg-Ni-Mm (Mm = mischmetal) alloys as an effective method for hydrogen storage. Int J Hydrogen Energy xxx:1–11

Chapter 10
Heat-Resistant SiO_2–Al_2O_3–TiO_2 Ceramics with Nanostructured Alumina Filler and Their Properties

T. M. Ulyanova, N. P. Krutko, P. A. Vitiaz, L. V. Ovseenko and L. V. Titova

10.1 Introduction

Developing designs of new vehicles, chemical reactors, and kilns, as well as diagnostic and ecological equipment, requires the use of new composite materials, among which is refractory heat-resistant ceramics with high-performance characteristics. Of special interest is the use of nanocrystalline powders and nanostructured fibers in the technology of ceramic processes. At present, the technologies, which allow one to manufacture molded hot forging parts from such materials without additional machining, are under development. The study of mechanical properties shows that such products have substantial compression ductility. This phenomenon is associated with diffusion of nanograins in the vicinity of intergrain boundaries, not destructing ceramic products. Based on such ceramics, cutting and drilling tools for metal working, bearings of friction pairs, parts of stop valves, and also constructional and heat-insulating heat-resistant materials [1] can be designed.

Heat-resistant ceramics are composed as follows: structure, composition, and availability of certain material porosity. By varying the size of crystals, the composition and mutual distribution of crystalline and glassy phases, and the size and configuration of pores, it is possible to a certain extent to control the value of thermal stresses and the dynamics of cracks to appear in ceramics at temperature drops, i.e., their heat resistance. This increases the ceramic durability under the conditions of cyclic changing of temperatures and thermal shocks.

There exist several ways of solving such a problem: to make fundamentally new products, for example, refractory products based on fibrous, powder, composite, and other materials, as well as to improve the quality of conventional refractory materials by changing their composition and structure. The third way is also possible—to develop high-temperature composite materials with improved structural, mechanical, and thermal-physical characteristics [2].

T. M. Ulyanova (✉) · N. P. Krutko · P. A. Vitiaz · L. V. Ovseenko · L. V. Titova
Institute of General and Inorganic Chemistry of NAS of Belarus,
9/1 Surganov St., 220072 Minsk, Republic of Belarus
e-mail: ulya@igic.bas-net.by

O. Fesenko, L. Yatsenko (eds.), *Nanocomposites, Nanophotonics, Nanobiotechnology, and Applications,* Springer Proceedings in Physics 156,
DOI 10.1007/978-3-319-06611-0_10,

It should be noted that the relationship between the structure, the composition, solid-phase processes, and heat resistance is quite complex. As a rule, it is calculated preliminarily and then checked experimentally for each particular material. As a result, to establish general relationships: composition–structure–property is a necessary condition both for gaining new knowledge in the field of solid physics and chemistry and material science and for synthesizing new ceramic materials with improved thermal and mechanical characteristics.

The objective of the present work was to prepare compositions with the use of natural and commercial powders and to create ceramic composite materials with improved physical-mechanical and thermal-physical properties. At that, it is assumed to use natural materials, commercial powders, and reactive–active nanostructured fibrous aluminum oxide additives to study the structural, mechanical, and thermal-physical characteristics of the ceramic composites synthesized.

10.2 Experiment

To make studies, the silicate system Al_2O_3–SiO_2–TiO_2 has been chosen, in which at heating there occur solid-phase reactions. The products formed are substantially different in their properties from the initial components. To produce inexpensive products, quartz sand—SiO_2, commercial alumina powder—α-corundum, and titanium oxide powder, as well as the nanostructured filler—fibrous powder α-Al_2O_3, were used as initial components. Charge compositions for ceramic materials were made by analyzing the system SiO_2–TiO_2–Al_2O_3 in the crystallization field of the mixture of mullite and tialite phases. To conduct the experiment, two basic compositions with the component ratio: Al_2O_3-SiO_2-TiO_2—35:35:30 mass %—matrix 1 (M1) and 35:40:25 mass %—matrix 2 (M2) were prepared. Aluminum oxide was represented by commercial powder—GK technical grade alumina, titanium oxide by the pure-grade chemical reagent, and quartz sand by grade 00BC-015-1 (GOST 22551-77). Usually, this sand was used for manufacturing crystal glass, its iron oxide content not exceeding 0.015 mass %. Prior to experiment, quartz sand was carefully ground in a planetary-type mill in agate drums and was bolted on sieves and a 0.1-mm fraction was used. Powder mixtures were thoroughly mixed in a ball mill for 4 h. After that, from the matrices 1 and 2 obtained, mixtures were prepared for making composite samples with nanostructured aluminum oxide. The crystalline structure of the initial powders was: alumina—α-corundum, silica—α-quartz, and titanium oxide—rutile. The active fibrous filler had a crystalline structure α-Al_2O_3. Based on the previous studies, the content of the active filler was chosen as equal to 15 mass % [3].

The nanostructured filler was formed from cellulose hydrate filaments that were impregnated with the aqueous solution of aluminum chloride. They were then dried and subjected to heat treatment within a special regime. Cellulose hydrate is a complex-architecture polysaccharide: its macromolecule contains (3–36) × 10^3 of elementary links formed from anhydro-D-glucose [4]. In some other natural polymers, the cellulose microstructure is a system of crystallites—microfibrils

surrounded by semicrystalline and amorphous regions. This develops a large inner surface in the fiber that plays a decisive role in the processes both of filling capillaries and pores and of smelling cellulose hydrate in the solution. When cellulose fibers come in contact with the aqueous aluminum salt solution, first they penetrate into loose disordered parts of microfibrils. Then liquid absorption takes place in polysaccharide crystallites [5]. This structure and properties of polymer allow one to introduce solutions of different metal salts and, after the organic component has been removed, to obtain inorganic fibrous materials that follow the macrostructure of the initial polysaccharide [6].

During heating of aluminum chloride salt-impregnated cellulose hydrate material, complex physical-chemical processes accompanied by substantial weight loss took place. As a result, the entire organic component of polymer fiber was removed and hydrolysis and dissociation of aluminum chloride occurred. Hydrated oxide grains were formed and then, aluminum oxide grains fixed in the carbon skeleton of the matrix at thermolysis. Carbon was burnt off and fibers imitating the initial shape and architectonics of polymer reduced to 10–20 times were formed. The process came to an end with the temperature up to 600 °C; the nanostructured fibers were composed of X-ray aluminum oxide amorphous grains 1–5 nm in size. Crystalline aluminum oxide started forming at an annealing temperature of 700–800 °C in the form of γ-alumina. As the temperature was increased up to 900 °C, the reflexes of the θ-phase appeared on the X-ray diffraction patterns, whereas at 1150–1200 °C there occurred the diffusionless conversion of γ and θ-alumina to the α-Al_2O_3 that did not change with a further temperature increase of up to 1600 °C [7] (Fig. 10.1a–c). The fibers formed were easily ground into a powder with 0.5–1-μm-long particles, the size of α-Al_2O_3 nanograins being 45.0–50.0 nm; open porosity, 65 %; packed density, 0.54 g/cm^3; pictometric density, 3.75 g/cm^3; specific surface, 35 m^2/g; macropores, 100–500 nm; and nanopores, 5–10 nm. The microstructure of aluminum oxide monofiber and its nanostructure are shown in Fig. 10.2. Crystalline lattice parameters of the different-phase fibrous aluminum oxide powder were determined by the X-ray structural method and are summarized in Table 10.1.

Samples of matrices M1 and M2 with the SiO_2–Al_2O_3–TiO_2 composition and composites (MC1) and (MC2) with the active filler were prepared according to the standard ceramic technology by the method of dry pressing from the moistened slip mass of the powder mixture. The samples were dried at 120 °C and heated in the electric stove, first up to 900–1100 °C, and then isothermal annealing was performed at temperatures 1350 and 1400 °C and 1450 and 1500 °C for a period of 2 h.

The fibrous powder and ceramics were investigated by the method of physical–chemical analysis. The crystalline structure and microstructure of the fibrous powder synthesized and the ceramic samples prepared were examined. Density, porosity, moisture absorption, and compression strength of the ceramic samples were determined. The structure was investigated using the methods of X-ray phase and X-ray structure analysis (DRON 3, Advance 8) during *CuKα* monochromated radiation. Sizes of different-structure alumina oxide crystallites were calculated by Sherrer formula [8]. The microstructure of powders and ceramics was studied by the electron microscopy

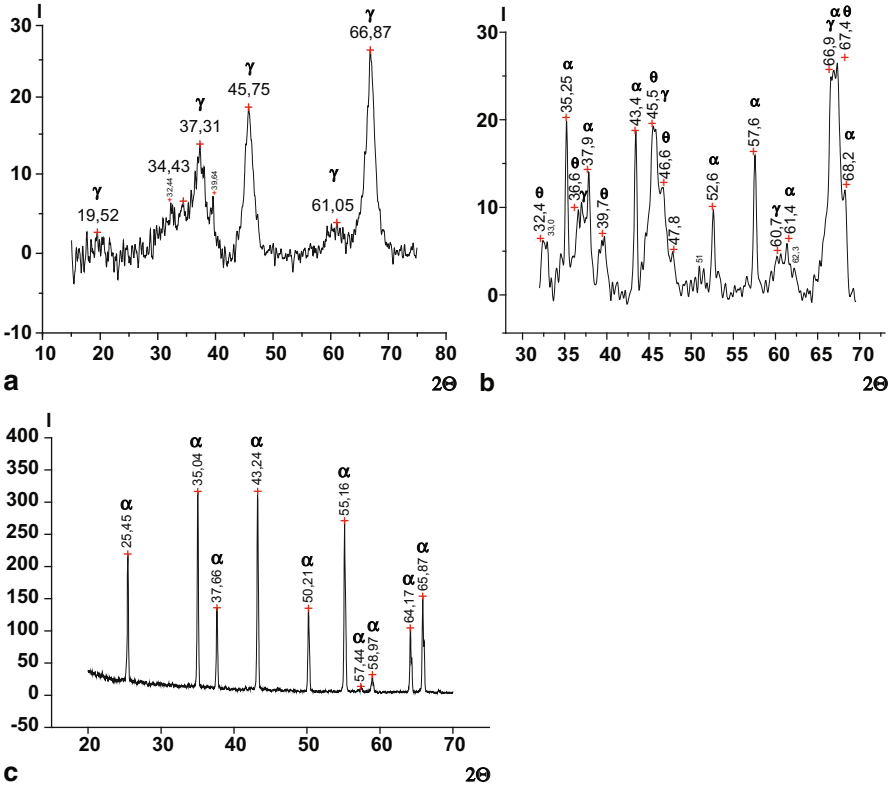

Fig. 10.1 X-ray grams of fibrous alumina samples, annealed at the temperatures. **a** 700 °C. **b** 1000 °C. **c** 1600 °C

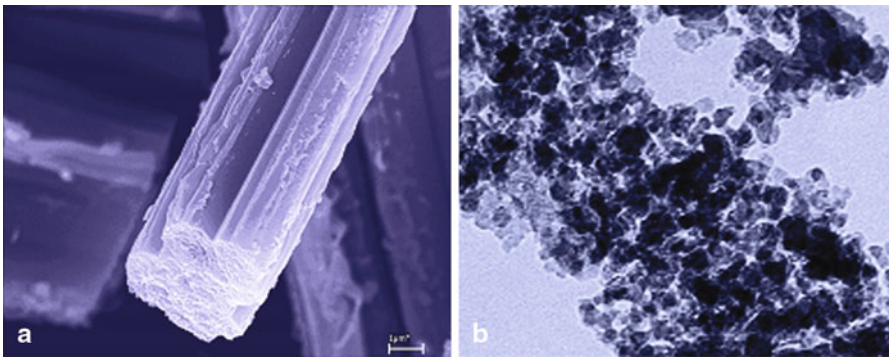

Fig. 10.2 Photographs of α-Al_2O_3 fiber microstructure (x10,000—SEM) (**a**) and its nanostructure (x100,000—TEM) (**b**)

Table 10.1 Parameters of fibrous nanostructured alumina phases lattice

Composition	Temperature,°C	Crystalline phase	Parameters of lattice, Å		
			a	b	c
Al_2O_3	500	Amorphous	–	–	–
	700	γ–	7.93	7.93	7.93
	900	Θ–	11.81	2.91	5.63
	1100	A–	4.73	4.73	12.94
	1300	α–	4.75	4.75	12.98

method on a scanning electron microscope (SEM) "Mira" of the Firm "Tescan" (Czechia) within the reflected electron regime at an accelerating voltage of 20 kV. The error of geometric sizes determined by the SEM method was 5 %. The nanostructure of the fibrous powder was examined by the transmission electron microscopy method (TEM) (microscope JSM—200 A at an accelerating voltage of 200 kV with × 100,000–120,000).

The properties of fibrous powders: packed and pycnometric densities, were found according to GOST 27801–93 and GOST 24409–80 and the specific surface by the Brunauer, Emmett and Teller (BET) method (analyzer of surface and porosity ASAP 2020 of the Firm "Micromeritics," USA). Apparent, pycnometric density and open porosity of annealed ceramic samples were determined by the method of hydrostatic weighing according to GOST 24409–80. Compression strength was tested by a universal test machine Instron 1195 (UK) at a loading of 50 kg, with a loading rate of 1 mm/min; the measuring error was 1 %.

The temperature coefficient of linear dimensions of the matrix and the composite was examined by a quartz dilatometer in the temperature range 50–600 °C.

The thermal stability was estimated by a number of heat changes at a temperature difference of 900 °C/10 °C. This method consisted in defining a number of the cycles, including the heating of samples at 900 °C for 30 min and their subsequent cooling in running water.

10.3 Results and Discussion

The study of the shrinkage of the samples of the system Al_2O_3–SiO_2–TiO_2 in the process of consolidating powders has shown that the changes in linear dimensions and weight loss of samples within 1350–1500 °C was insignificant and was, on an average, 1–5 rel. %. This is due to the use of low-shrinkage quartz sand as alumina. In what follows, the sintering processes in ceramics were accompanied by melting glass masses in the range of temperatures above 1400 °C. The shrinkage was determined both through the temperature, at which the melting started, and through the amount of the liquid phase to be formed in material and reached 2 %. In this case, the weight loss did not exceed 1–1.5 mass %. The samples annealed at 1500 °C had somewhat increased shrinkage when the melting process intensified.

The introduction of the nanostructured filler slowed down the process of melting glass masses, because with its participation new high-temperature phases of mullite and tialite were formed. As a whole, the synthesized composite material was characteristic for low shrinkage and weight loss. This was the important technological quality, since practically the machining of the blanks sintered was not needed. To determine the refractoriness, the samples of the matrices M1 and M2 and composites MC1 and MC2 were annealed at 1580 °C. The silicate matrices M1 and M2 were completely melted and spread, whereas the composites were partially melted near the ends of the cylinders, but they fully preserved their shape.

The investigation of the structure of the composites sintered made it possible to discover the mechanism and dynamics of solid-phase processes in the multicomponent silicate system and to assess the influence of the nanostructured filler α-Al_2O_3. The X-ray phase analysis of the initial components and the M1 samples after heat treatment at 1350 and 1400 °C is evident of the fact that chemical reactions are absent and new compounds are formed in material. Within this temperature range, α-quartz partially turns to α-cristobalite. Moreover, the mullite reflexes appeared on the X-ray photograph. While introducing the nanostructured filler, quartz completely turned to α-cristobalite and the mullite content increased. As the heat-treatment temperature of M1 samples was increased up to 1450 °C, the aluminum titanite phase appeared in small amount and α-quartz transformed to α-cristobalite. After 1500 °C isothermal annealing, the composition of the matrix M1 was a multiphase mixture of initial and newly formed products: alumina, rutile, α-cristobalite, mullite, and tialite impurities. The introduced nanocrystalline filler α-Al_2O_3 caused a complete interaction of the initial components. As a result, at 1450 °C mullite was the basic phase, whereas at 1500 °C, tialite, silica, and alumina were absent and the rutile content did not exceed 5–10 mass %. The same influence on solid-phase processes was also exerted by the nanostructured filler in the composite MC2 with the increased silica content. The SiO_2 excess prevented the formation of chemical compounds at heating up to 1500 °C (Fig. 10.3a). The influence of the nanostructured filler α- Al_2O_3 on solid-phase reactions in silicate matrices of variable composition was practically the same. The noncompensated energy of the surface of particles and their agglomerates decreased the Gibbs energy ΔG and initiated the interaction between the initial components. In what follows, at 1400–1450 °C the process of forming mullite became more intense and at 1500 °C, tialite.

The filler–matrix particle interaction and the formation of glass masses were also investigated with the use of an electron microscope. The analysis of the microstructure of the M1 samples enables one to define the process of consolidating powder particles into ceramic material as nonequilibrium and the structure of a ceramic sample as heterogeneous and chaotic. In the process of sintering, the particles did not form symmetric layers but were located in all directions at different angles. Owing to this, the porosity of the material was nonuniform and the material contained small and mean pores as well as large pores and capillaries. When the M1 samples were heated up to 1450–1500 °C, aluminum silicate was partially melted and the melt filled large pores and bonded matrix particles (Fig. 10.4a, b).

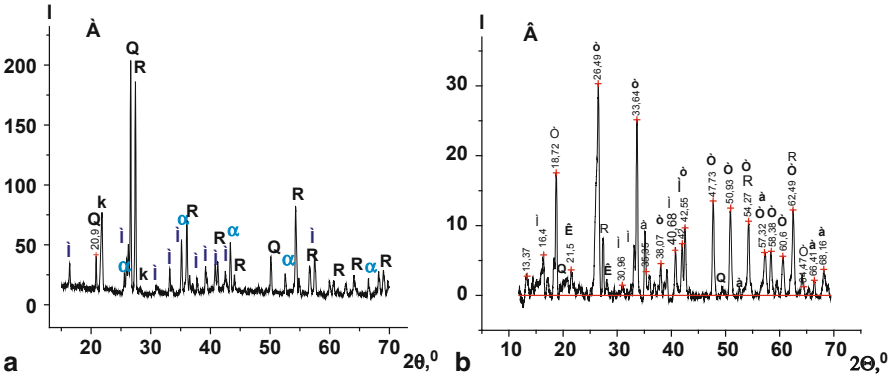

Fig. 10.3 X-ray grams of the SiO_2–Al_2O_3–TiO_2 ceramics samples annealed at a temperature of 1500 °C with nanocrystalline filler α-Al_2O_3. **a** Matrix M2. **b** Composite MC2. *M* mullite, *R* rutile, *α* α-Al_2O_3, *K* α-crystobalite, *Q* quartz, *T* tialite

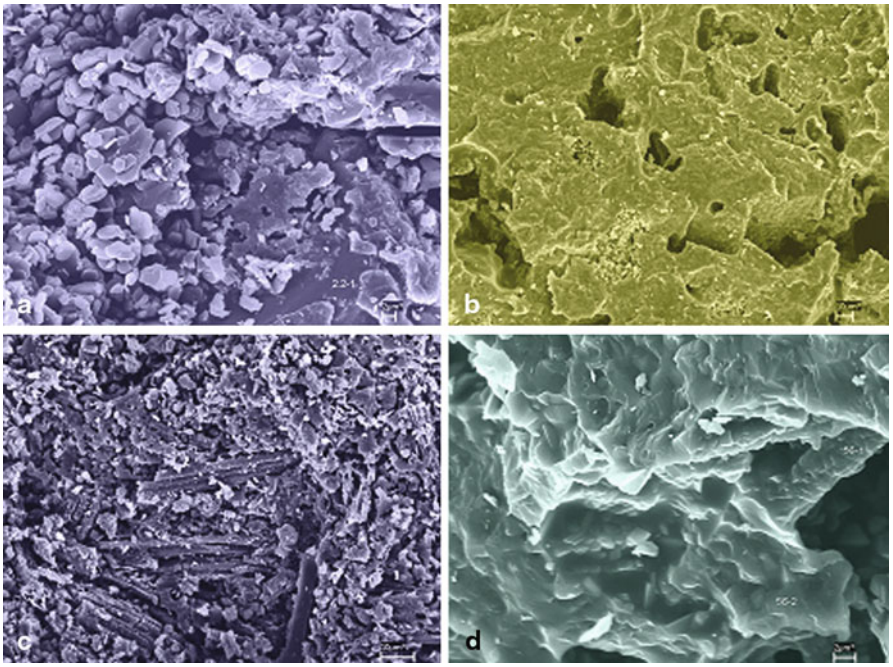

Fig. 10.4 Photographs of the microstructure matrix M2 (**a**) and (**b**) and composite MC2 (**c**) and (**d**) annealed at temperatures 1350 °C (**a**) and (**c**) and 1500 °C (**b**) and (**d**)

The introduction of the nanostructured filler favored a more uniform distribution of the small particles of the matrix and the skeleton of fibrous particles was formed in the composite material (Fig. 10.4c, d). The glass masses fully covered the particles of the fiber α-Al_2O_3, thereby forming a close contact with them. This gave rise to solid-phase reactions at the phase boundary and material strengthening.

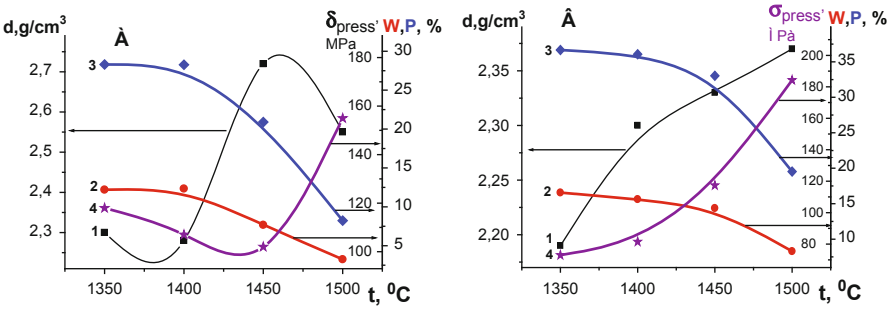

Fig. 10.5 Dependence of *1*—apparent density, *2*—water absorption, *3*—porosity, *4*—compression strength of matrix M1 (**a**) and composite MC1 (**b**) on heat treatment temperature

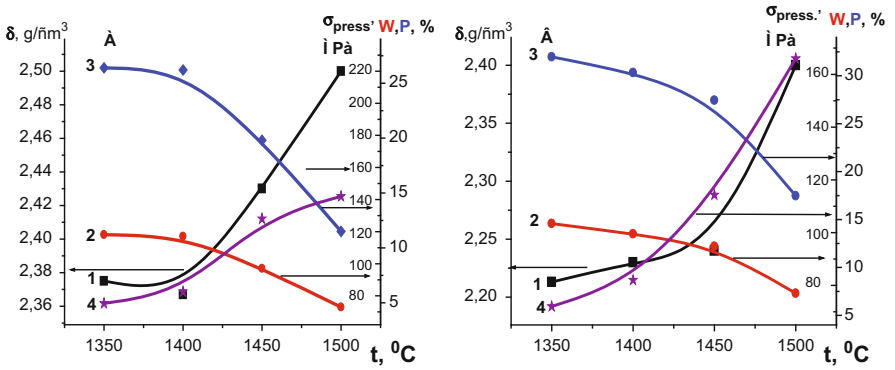

Fig. 10.6 Dependence of *1*—apparent density, *2*—water absorption, *3*—porosity, *4*—compression strength of matrix M2 (**a**) and composite MC2 (**b**) on heat treatment temperature

For the influence of the filler on the physical-mechanical properties of composites to be assessed, apparent density, open porosity, and moisture absorption, as well as the bending and compression strength of the samples of the matrix and the composites annealed at assigned temperatures: 1350, 1400, 1450 and 1500 °C, were determined. The averaged measurement results of the properties of the samples of the matrices M1 and M2 and composites MC1 and MC2 are plotted graphically in Figs. 10.5 and 10.6.

It was found that as the temperature was increased, the porosity and moisture absorption of the matrix and the composite decreased differently. The porosity of the matrix M1 sintered at 1500 °C was preserved at a level of 6–7 %, whereas that of the composite MC1 was 17 %. The moisture absorption value decreased up to 1–2 %. The density of the matrix samples annealed at 1350–1400 °C almost did not change, sharply increased with melting glass masses (1450 °C), and again decreased in the samples annealed at 1500 °C. This is due to forming new macropores at cooling of the melt of glass masses in samples. The strength of the composite samples changed

similarly, and its value was maximum after heat treatment at 1450 °C. The viscous melt of silicate masses filled macropores and enveloped small particles, thus forming closed pores. The total material porosity was then about 20 %. It should be taken into account that the cooled-down mass was brittle. So, the strength of such a material at deformation is not high.

The introduction of the nanostructured filler gave rise to a new structure in the composite–elastic skeleton that was in contact with different matrix particles. At heating, it interacted in the solid phase with silica. As a result of this interaction, mullite was formed. The reaction of the nanostructured filler with the melt of glass masses resulted in the formation of tialite. The formation of the mullite–tialite composite increased the density and strength of ceramic material (Fig. 10.5).

The similar dependences of physical-mechanical properties, when the heat treatment temperature is increased, are seen for the matrix M2 and the composite MC2. When introducing the filler, a higher material porosity was preserved, but this did not reduce the strength since between the filler surface and the matrix particles a great number of contacts were formed because of the generation of new phases. The latter strengthened the material. The dependences of porosity and moisture absorption as well as of density and strength of M2 and MC2 materials on the heating temperature are similar in character. However, the silica content in the matrix M2 is higher, which decreased the temperature of forming the melt of glass masses and also caused some decrease in the composite material strength as compared to the matrix M1 and the composite MC1 (Fig. 10.6).

The material density of the obtained composite samples was higher than that of the matrix. The material porosity was higher; however, the strength characteristics were also higher.

The influence of the nanostructured filler α-Al_2O_3 on the thermal coefficient of linear expansion (TCLE) was studied in the case of the matrix and composite samples at heating from 50 to 600 °C. The analysis of the measurement results has shown that for the ceramic samples annealed at 1350–1450 °C, the coefficient of linear expansion of material first increased by growing the heating temperature to 300 °C and then decreased. The availability of a small maximum in the curves is caused by a reversible phase conversion $\alpha \leftrightarrow \beta$ of cristobalite that occurred at 250–300 °C [9]. The TCLE values of the samples annealed above 1450 °C smoothly increased from 2.5×10^{-6} to 3.7×10^{-6} K^{-1}. According the X-ray analysis data, at 1500 °C tialite with low TCLE was formed. TCLE of the materials heat treated at 1500 °C decreased by a factor of 2 in comparison with ceramic samples annealed at 1350–1400 °C. The heat resistance of the samples of the system SiO_2–Al_2O_3–TiO_2 as well as of the composites MC1 and MC2, was investigated within the thermal shock regime. First, the ceramic samples preliminarily sintered at 900 °C for 35–40 min were kept to achieve thermal equilibrium. Then, they were removed and placed into cold running water with a temperature of +10 °C. After each temperature-changing cycle, the samples were visually examined in effort to reveal cracks and defects. After each 10 cycles, the changes in the mass and sizes of the samples were assessed. The testing of the materials has shown that 70 % of the M1 samples and 72 % of the M2 samples stood more than 50 temperature-changing cycles and 98 % of the samples

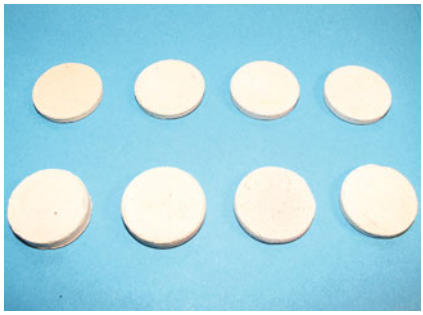

Fig. 10.7 Photographs of the composite samples MC1 and MC2 after thermal shock tests

of nanostructured-filler-containing composite materials—more than 70 temperature-changing cycles. Figure 10.7 illustrates the photographs of the composite ceramic samples after their testing for heat resistance.

Thus, using fibrous nanostructured aluminum oxide as the active filler in the system Al_2O_3–SiO_2–TiO_2, it became possible to prepare lightweight porous heat-resistant ceramic materials with improved mechanical and thermal characteristics at 1450–1500 °C. The use of nanostructured oxide modifiers—fillers enables one not only to improve their reliability and durability but also to create new ceramic composites with required properties.

Acknowledgment Research was realized by the support of State Scientific Program of NAS of Belarus.

References

1. Kats SM (1981) High-temperature and heat-insulating materials. Metallurgia, Moscow
2. Krasulin Yul, Barinov SM, Ivanov VS (1985) Structure and destruction of materials made of refractory compound powders. Nauka, Moscow
3. Ulyanova TM, Krutko NP, Dyatlova EM, Paemurd ES, Podbolotov KB (2010) Solid-phase processes in a ceramic matrix in the system SiO_2-Al_2O_3-TiO_2 with addition of fibrous nanostructured alumina. J Glass Ceram 67(1–2):47–51
4. Rogovin ZA (1972) Chemistry of cellulose. Khimiya, Moscow
5. Ermolenko IN, Ulyanova TM, Vityaz PA, Fyodorova IL (1991) Fibrous high-temperature ceramic materials. Nauka i Tekhnika, Minsk
6. Ulyanova TM, Krutko NP, Vityaz PA, Titova LV (2011) Investigation of nanostructured oxides: Synthesis, structure and properties. J Nanosci Nanotechnol 11:2107–2112
7. Ulyanova TM, Krutko NP, Titova LV, Zub EM (2002) Radiographical investigation of phase transitions and components interaction in system ZrO_2-Al_2O_3. J Surf Radiogr Synchrotron Neutron Investig. 7:49–52
8. Umansky YaS (1969) Radiography of metals and semiconductors. Metallurgia, Moscow
9. Eitel V (1962) Physical chemistry of silicates. Foreign Literature Publishing House, Moscow

Part II
Nanophotonics

Chapter 11
Technological Aspects of Corrosion-Resistant Steels Surfacing by Intense Relativistic Electron Beams

V. V. Belozerov, S. E. Donets, V. F. Klepikov, V. F. Kivshik, V. V. Lytvynenko, Yu. F. Lonin, A. G. Ponomarev and V. T. Uvarov

11.1 Introduction

Intense tubular relativistic electron beams are a promising tool for a number of practical applications, such as obtaining nanodispersed powder materials, surface properties modification of products, remote surfacing, etc. In current technologies for obtaining of nanopowder materials, one of the leading techniques is one based on the materials handling concentrated flows of energy. Using the various technological equipment (pulse current generators, accelerators), energy is inputted into the material in the form of intense impulse current [1], the plasma flows of charged particle beams. Each of the specified types of impact is characterized by a certain decomposition mechanism of processed materials to micro- and nano-sized state. Thus, the action of intense pulsed currents based on the thermal evaporation of a melt conductor with its subsequent condensation in liquid [2], the use of plasma flows and charged particle beams also involves evaporation and condensation of a material in a vacuum or in a special atmosphere [3]. Specified ways of using these beams are mentioned due to the fact that the irradiation of metals and alloys by intense relativistic electron beams (IREB) in the ablation mode is accompanied by the ejection of material from the surface [4] and change of properties of the target material. It is known [5] that the modified properties area of the inhomogeneous modified target by volume significantly exceeds the limits of penetration of the beam particles. The irregularity factor is significantly enhanced with the irradiation by tubular beam. Understanding of the

S. E. Donets (✉) · V. F. Klepikov · V. F. Kivshik · V. V. Lytvynenko
Institute of Electrophysics and Radiation Technologies, National Academy of Sciences of Ukraine, Kharkiv, Ukraine
e-mail: s.j.donets@gmail.com

V. V. Belozerov
National Technical University "KhPI", Ministry of Education and Science of Ukraine, Kharkiv, Ukraine

Yu. F. Lonin · A. G. Ponomarev · V. T. Uvarov
National Science Center Kharkov, Institute of Physics and Technology, National Academy of Sciences of Ukraine, Kharkov, Ukraine

O. Fesenko, L. Yatsenko (eds.), *Nanocomposites, Nanophotonics, Nanobiotechnology, and Applications,* Springer Proceedings in Physics 156,
DOI 10.1007/978-3-319-06611-0_11,

features' change in the state of the target irradiated by tubular IREB (structural phase transitions, the redistribution of the elemental composition, microhardness) seems to be important to create new scientific fundamentals of radiation nanotechnology.

11.2 The Experimental Technique and Problem Statement

As test samples, we used the two grades of corrosion-resistant steels 12Cr21Ni5Ti and 08Cr18Ni10Ti since their radiation modification is of practical interest as well as scientific and model objects. The first grade containing 5 % Ni and 21 % Cr is characterized except α and γ phases by the presence of σ-phase (intermetallic compound type FeCr). The second grade contains to about 10 % Ni and 18 % Cr has a typical austenitic structure [6].

Experiments were made on the accelerator MIG-1 [7] (NSC "Kharkov Institute of Physics and Technology" NASU, Kharkov) with the following parameters: electron energy 0.5 MeV beam current ≤ 2 kA and pulse duration of about 5 ms. In order to increase the density of the energy released at the target surface and increase the nonuniformity of the irradiation field, tubular electron beam was formed. The external beam diameter was about 40 mm, wall thickness of the beam 2–3 mm, and the density of the released energy at the surface of the irradiated target in the ablation mode reached 1 kJ/cm^2. The targets were irradiated in a vacuum chamber at booster pressure 10^{-4}–10^{-5} torr with three pulses of irradiation.

The aim was to study the fracture of targets in the area of the beam influence and metallographic studies to estimate the change of the phase composition and microhardness.

The surface and cross section of the samples were investigated with an optical microscope MIM-7; electrolytic etching was made in a solution of acetic acid. For a phase analysis of the samples, X-ray diffractometer DRON-3 was used with the radiation of λ-Cu with monochromator on diffracted beam. An analysis of fractures was carried out with a scanning electron microscope JEOL JSM-840. Microhardness was measured on a PMT-3 durometer. The beam current on the target is measured using a Rogowski coil and shunt [8].

11.3 Results and Discussion

The influence of a series of tubular IREB pulses on the target surface forms an annular crater with the bottom, shores, and overlays, formed due to the explosive ejection of the target substance. The remelted surface layer consists of numerous macrolugs. Figures 11.1 and 11.2 show a cross section of the steel target samples 12Cr21Ni5Ti and 08Cr18Ni10Ti, respectively, at the same magnification. The average thickness of the remelted layer is about 15 microns and its structure differs significantly from the rest of the material.

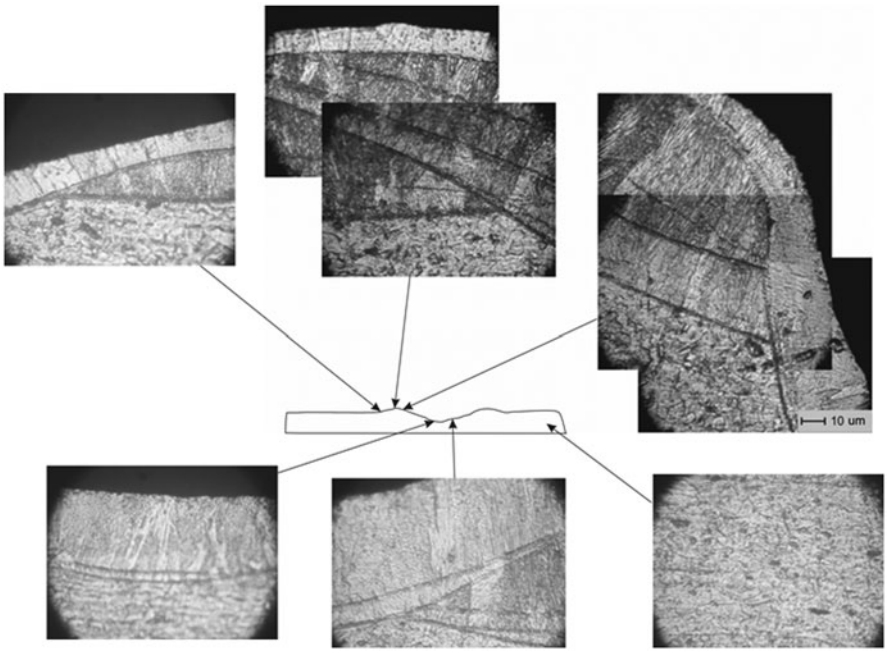

Fig. 11.1 Panorama microsection of steel grade 12Cr21Ni5Ti

There is a distinction in the thickness of the heat-affected zone, depending on the part of the crater. In the area of the crater, the shores and overlays remelting zone is thick enough, and the zone of thermal effects (transition zone) is very small. At the bottom of the crater from which the material was ejected, the remelting zone is fairly shallow and outstrip zone of thermal influence. This is encompassed to both the studied materials (Figs. 11.1 and 11.2). It is obvious that the remelting zone corresponds to a region maximum energy absorption of the beam, whereas in the neighboring areas the specific value of the absorbed energy is sufficient only to initiate solid phase recrystallization, which provided a wider monitored zone of the heat-affected area. The observed bands reproducing curves that delineate the boundaries of the crater are of interest. The nature of these bands can be explained as superposition of impacted areas of the previous pulse (in this experiment, there were only three pulses whereas bands number significantly greater) as the segregation [9] to the boundary contour temperature values corresponding to the solubility limit of the alloying elements. The possibility of observing the effects of electroplastic effect [10], which exhibits itself in a dynamic impact of current pulses on the target material, cannot be excluded.

Since the modifying effect of the electron beam on the target lies not only in radiation-thermal mechanism but also in the shock wave, whose influence spreads deeper heat-affected zone, we measured the microhardness in different areas, as shown in Fig. 11.3, its values presented in Table 11.1.

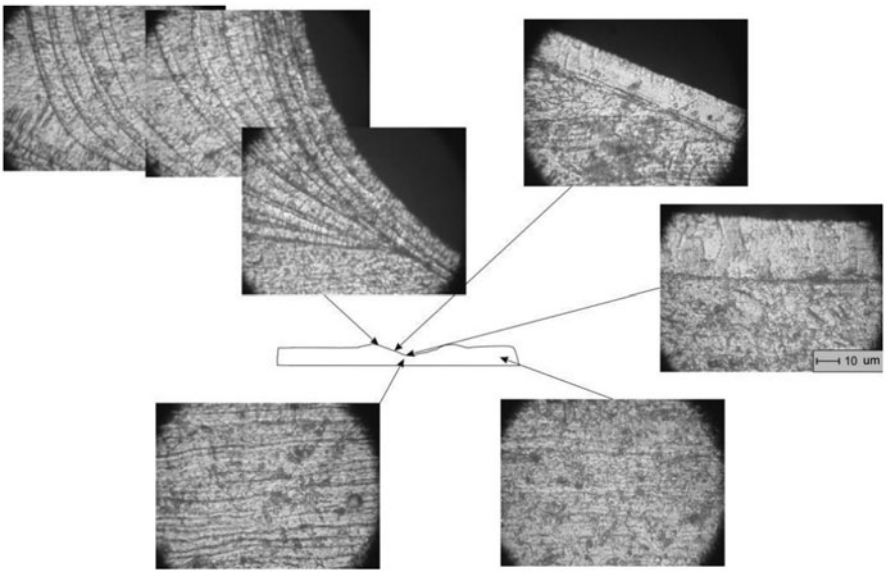

Fig. 11.2 Panorama microsection of steel grade 08Cr18Ni10Ti

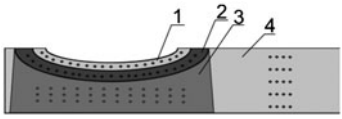

Fig. 11.3 Scheme for measuring in the cross section of the sample (*1*—remelting zone, *2*—zone of thermal influence, *3*—zone of integrated influence, *4*—not treated zone)

Table 11.1 Microhardness values for different zones of the samples

Zone	Microhardness 12Cr21Ni5Ti, MPa	Microhardness 08Cr18Ni10Ti, MPa
Zone of integrated influence	2530	1900
Zone of thermal influence	3450	2280
Remelting zone	2900	2120
Initial sample	3200	2200

As can be seen from Table 11.1, the zone of thermal influence is slightly hardened, whereas in the remelting zone and in the zone of integrated influence the microhardness decreases. For the remelting zone, it can be interpreted by preferential evaporation of alloying elements. For the zone of shock-wave impact, it can be interpreted by loss of strength due to the movement of the rarefaction wave front.

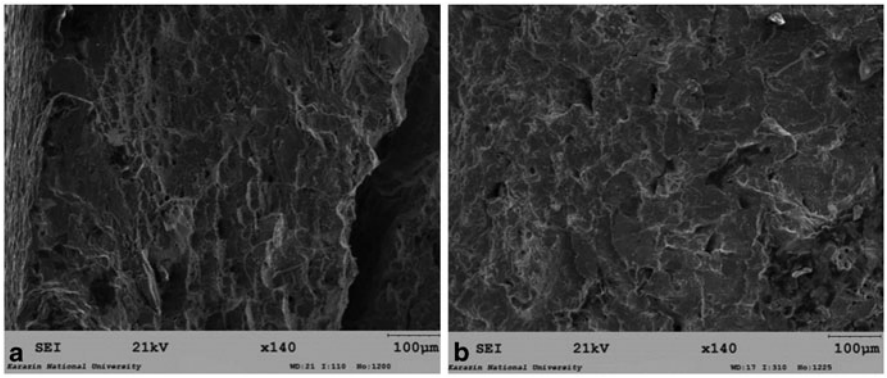

Fig. 11.4 Fracture of steel grade 12Cr21Ni5Ti (a—initial sample, **b**—irradiated sample)

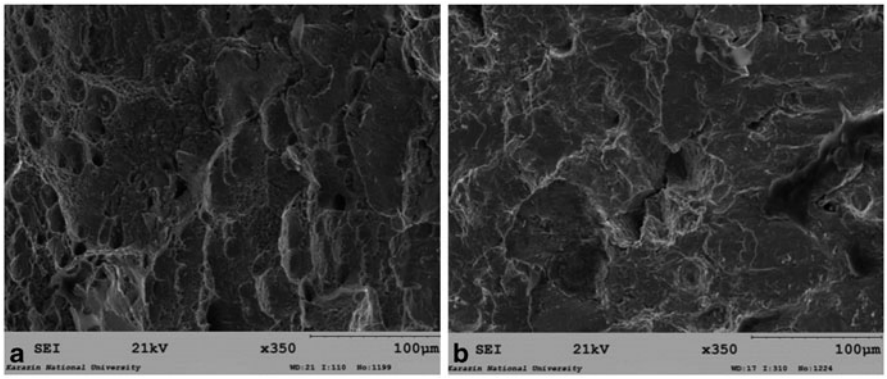

Fig. 11.5 Fracture of steel grade 08Cr18Ni10Ti (**a**—initial sample, **b**—irradiated sample)

Fracture images are shown in Figs. 11.4 and 11.5. For fracture samples were subjected to cyclic loading. The remelted layer has a columnar structure, indicating that there occurred crystallization of the melt. In the heat-affected zone, facets with an average size of 1 micron are visible, while in the initial sample size of facets on the order more for both grades.

In order to clarify the content of alloying elements in the remelted area, we carried out elemental analysis of microsections of the irradiated samples. An elemental analysis in Fig. 11.6 shows a tendency to reduce the content in the surface region of the chromium and nickel.

For initial samples of two grades of steel was found occurrence of two phases (α-Fe and γ-Fe) using quantitative phase analysis Fig. 11.7. After irradiation of the samples, the α-Fe decrease (Table 11.2) is also confirmed by examination of the microstructure of the surface with a much smaller number of α-phase crystallites.

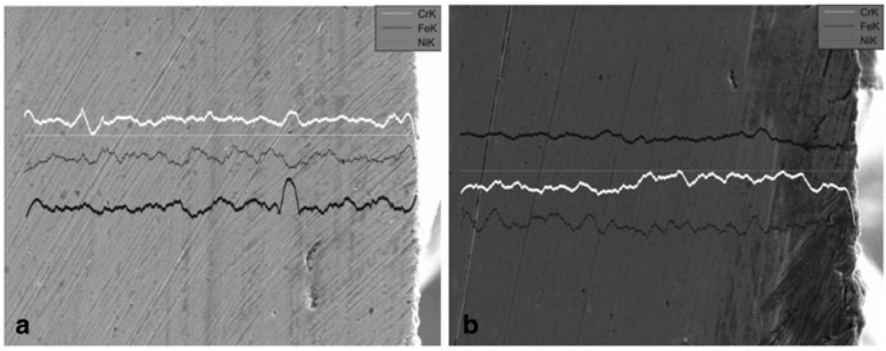

Fig. 11.6 Changing element composition of subsurface area of the treated steels 12Cr21Ni5Ti (**a**) and 08Cr18Ni10Ti (**b**)

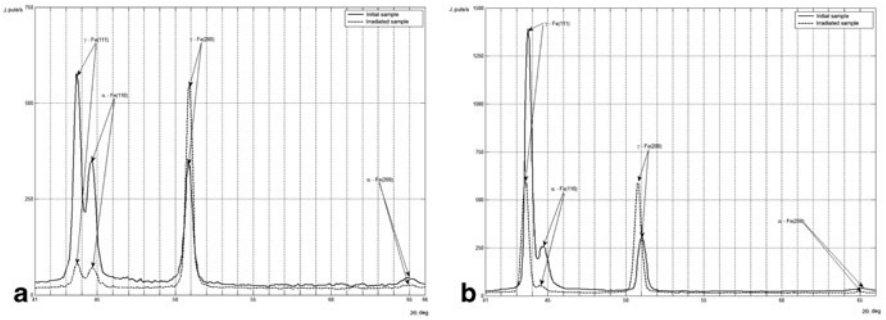

Fig. 11.7 Diffraction pattern of steel grades 12Cr21Ni5Ti (**a**) and 08Cr18Ni10Ti (**b**)

Table 11.2 Quantitative phase analysis

Grade	Initial sample		Irradiated sample	
	Austenite, %	Ferrite, %	Austenite, %	Ferrite, %
12Cr21Ni5Ti	85	15	93	7
08Cr18Ni10Ti	87	13	97	3

Phase composition of the remelted layer is composed mainly of austenite but in the same is very small observed quantity δ- and α-iron. For sample of 12Cr21Ni5Ti in the heat-affected zone on projecting parts martensite structure is formed with clearly seen acicular structure. Due to the high cooling rates in the remelting zone, the alloying elements are superseded to solidification front.

Microhardness in the integrated impact zone is lower than the value for the same depth as observed in the initial sample for both grades of steel.

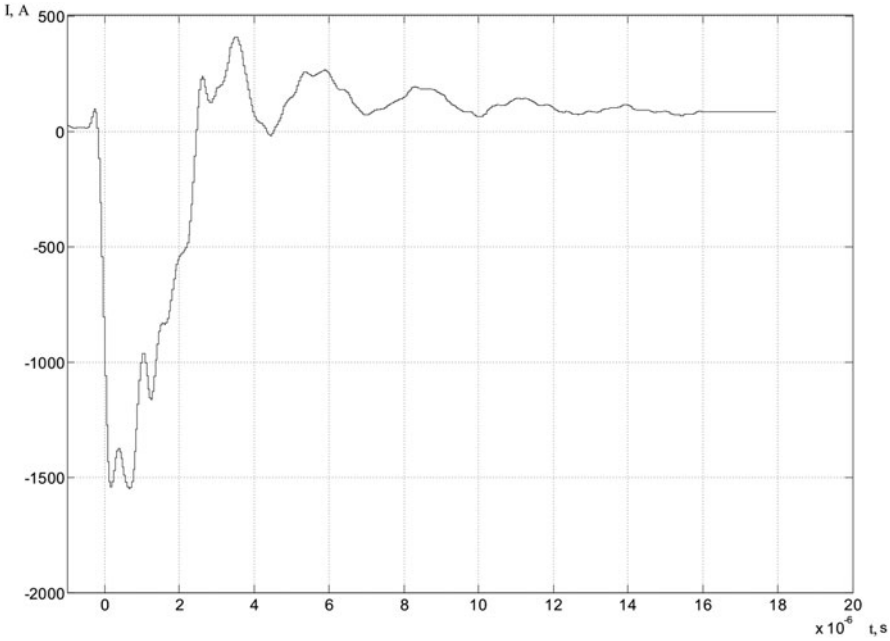

Fig. 11.8 IREB current oscillogram through target

As the pulsed electron beam current with a peak value of 1.5 kA (beam current oscillogram is shown in Fig. 11.8) passes through the target, one of the possible factors affecting the structural and phase transformations mentioned above is electroplastic effect accompanying the spread deformation (shock) waves in the target material. Due to the occurrence of this effect deceleration γ-α transformation is observed, which caused of increasing the plasticity of austenite [11, 12]. The last fact can also explain microhardness values in the area of integrated influence.

11.4 Conclusions

The impact of tubular IREB on stainless steel in the ablation mode leads to the depletion of the surface layer by alloying elements, the formation of the surface layer structures (martensite) with increased microhardness, as well as affecting mechanism and kinetics of the γ-α transformation. In the heat-affected zone of the beam adjacent to remelting area, segregation bands directions corresponds to the location of lines of constant temperature.

References

1. Dorovskoj VM, Elesin LA, Stoliarov VI et al (2006) Research of yields of an electrical explosion of titanium foils by an electron microscope. Appl Phys 4(28): 28–34
2. Naugolnykh KA, Roy NA (1971) Elektricheskiye razryady v vode (M.: Nauka)
3. Muller G, Schultheiss C (1994) Proc Beams II, p 833
4. Donets SE, Kivshik VF, Klepikov VF, Lytvynenko VV, Ponomarev AG, Uvarov VT (2011) Fizika i khimiya obrabotki materialov 2(8)
5. Bazaleev NI, Donets SE, Klepikov VF et al (2005) In Tezisy 7-oy Mezhd. konf. Fizicheskiye yavleniya v tverdykh telakh, Kharkov
6. Gulyayev AP (1986) Metallovedeniye (M.: Metallurgiya)
7. Uvarov VT, Tkach JV, Gadetskiy NP, Skachek GV, Ponomarev AG, Kivshik VF, Gaponenko NI, Kozachek AS, Prasol YA (1984) Preprint KhPTI 84–30, (M.:TSNIIatominform)
8. Donets SE, Ledenev VV, Lytvynenko VV (2008) Vestnik NTU KHPI. Tekhnika i elektrofizika vysokih napryazeniy 44: 39–44
9. Winegard WC (1964) An introduction to the solidification of metals (London)
10. Kaganov MI, Kravchenko YV, Natsik VD (1974) Physics-Uspekhi 6:878
11. Spitsyn VI, Trotskiy OA (1985) Elektroplasticheskaya deformatsiya metallov (M.: Nauka)
12. Belozerov VV, Donets SE, Klepikov VF, Kivshik VF, Lytvynenko VV, Lonin JuF, Ponomarev AG, Uvarov VT (2011) Physical and mechanical properties of steels 12H21N5T and 08H18N10T irradiated by the highcurrent tubular relativistic electron beam under ablation. Phys Surf Eng 9(2):170

Chapter 12
An Ellipsometric Model for Establishing Thickness of Thin Water Nanolayers on the Silicon Wafers

Agnieszka Chrzanowska, Piotr Fornal, Natalia Nosidlak, Gabriela Lewińska, Edyta Oziębło and Jerzy Sanetra

12.1 Introduction

Electromagnetic field interacts with matter in different ways. Depending on the energy of the incident wave this interaction may concern electronic properties and structure properties of the molecules themselves or the whole organization of the particles. The ability of decoding information from the reflected rays is an undeniably useful source of information about matter properties.

A special chance to study optical properties of materials offers the technique of ellipsometry which has been grounded within the field of semiconductor metrology as a quantitative method for obtaining thin-film properties. Generally, this method is based on polarization changes that occur when the light is reflected from the sample. In case of existence of thin films, the reflected light contains contribution from the light that also travels through the thin films.

The basic quantity measured in an ellipsometric experiment [2] is the complex reflectance ratio equation

$$\rho = \frac{R_p}{R_s} = tan\Psi e^{i\Delta} \tag{12.1}$$

where R_p and R_s are the complex reflection coefficients for the light polarized parallel and perpendicular to the plane of incidence, respectively (p and s polarizations). The two parameters—the so called ellipsometric angles—Ψ and Δ are experimentally determined. The data obtained within the ellipsometric experiment show a very high sensitivity of Δ parameter to nanometer scale films. Such an effect is not observable within, for example, the intensity measurements. As a result one can obtain very reliable data of the thin layer properties.

The aim of the present work is to obtain a quick and reliable assessment of the water layer thickness on the silicon origin substrates. This information is needed for

A. Chrzanowska (✉) · P. Fornal · N. Nosidlak · G. Lewińska · E. Oziębło · J. Sanetra
Institute of Physics, Kraków University of Technology, ul. Podchorążych 1,
Kraków 30-084, Poland, Tel:. 0048 12 6370666
e-mail: achrzano@usk.pk.edu.pl

O. Fesenko, L. Yatsenko (eds.), *Nanocomposites, Nanophotonics, Nanobiotechnology, and Applications,* Springer Proceedings in Physics 156,
DOI 10.1007/978-3-319-06611-0_12,

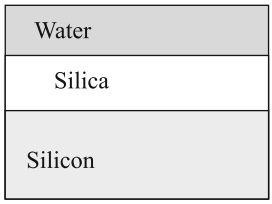

Fig. 12.1 Geometry of the sample studied

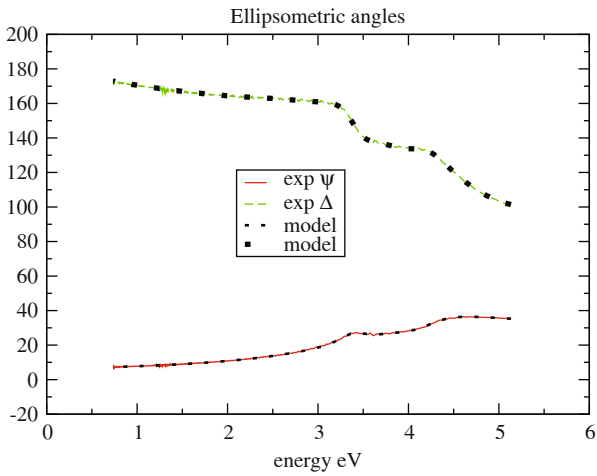

Fig. 12.2 Ellipsometric data and fit for the range of 1 eV-5 eV for the two layers model of the silicon wafer. The model of Si is according to the data from Table 12.2 and the thickness 3.07 nm of the water layer

several reasons—the field of interest here includes adsorption studies, biomedical and electronic applications, soil science aspects, or colloidal materials.

Different methods to study water adsorption on silica has been reviewed in [7]. In this chapter, we also show that ellipsometry measurements, which are quick and nondestructive, may lead to reliable assessments.

Figure 12.1 presents the geometry of the sample studied. A simple silicon (Si) wafer is considered here as covered by the thin layer of silica ($Si\,O_2$), which is present due to its exposure to air. If the experiment is carried out at room temperature on top of the surface, a thin layer of the adsorbed water should be considered. Ellipsometric data for this sample were acquired using J. A. Woolam Company VASE ellipsometer. Optical modeling and data analysis were done using CompleteEASE™ software package which also contains the database of optical properties of different materials. Ellipsometric properties Ψ and Δ were obtained at different wavelengths 180–1800 nm (or energies corresponding to them.)

12.2 Results

In Fig. 12.2 measurements of the ellipsometric angles Ψ and Δ vs. energy are presented together with the resulting model of two thin layers on the silicon substrate—silica and water. The agreement of the model and experimental data is indeed very good. Yet, because of quite a large number of the material data parameters,

Table 12.1 The parameters of the oscillators used to model the silicon experimental data of Aspnes

Oscillator type	A	B_r	E_0	E_g
'Tauc-Lorentz'	555.63	0.258	3.381	3.028
'Tauc-Lorentz'	21.534	0.429	4.255	0.938
'Tauc-Lorentz'	7.9493	1.037	5.394	1.084
'Tauc-Lorentz'	79.290	0.869	3.803	2.049

obtaining a reliable model was not an easy task. In order to successfully model these data the following properties are needed: the refraction and extinction coefficients (n and k) of water, silica, and silicon and the thickness of water and silica layers.

We start our analysis from modeling of the silicon optical properties of our sample. Refraction and extinction coefficients for silica and water have been taken from the database of the Woolam software. In the case of silicon it is possible that such properties can be different from the reference data due to the peculiar polycrystalline structure or defects; hence, modeling is needed. As a springboard we consider the data of n and k due to Aspnes. On the basis of that, a model is constructed composed of four Tauc–Lorentz oscillators. The Tauc Lorentz model [5] assumes that the imaginary part of the dielectric constant is given according to the formula

$$\begin{aligned} \epsilon_2(E) = &\quad A\frac{1}{E}\frac{E_0 B_r (E - E_g)^2}{(E^2 - E_0^2)^2 + B_r^2 E^2} && E > E_g \\ \epsilon_2(E) = &\quad 0 && E \leq E_g \end{aligned} \tag{12.2}$$

where A denotes the amplitude of the oscillator, E_g is the so-called optical band gap (the Tauc gap), B_r is the broadening coefficient of the oscillator, and E_0 is the peak transition energy of the oscillator. The above parameters obtained for the sample studied are given in Table 12.1.

As a next step, we have tried to assess the thickness of the silica (SiO_2) layer. According to Vedam [10] the spontaneously created silica layer on top of the silicon surface is about 2.5 nm (see Fig. 12.2 in [10]). This information has been obtained there as well by ellipsometric modeling as by cross-section electron transmission microscopy.

Performing fit to the experimental data obtained by us without considering water layer one obtains the layer of silica about 5 nm thickness. Unless obtaining additional information or basing solely on the ellipsometric technique results it would be impossible now to judge which model is more reliable: the one with a water layer or without a water layer. Fortunately, there exists vast evidence from chemical research about hydrophilic character of silica due to the presence of surface hydroxyl groups [1]. Moreover, the model without considering the water layer to the data obtained after heating of the sample shows that the possible silica layer has shrunk almost as twice, which is a nonphysical result, giving at the same time a strong argument for the model with the water layer. Silica is also known as the material with a very small temperature expansion coefficient thus its thickness should remain practically unchanged during the fittings.

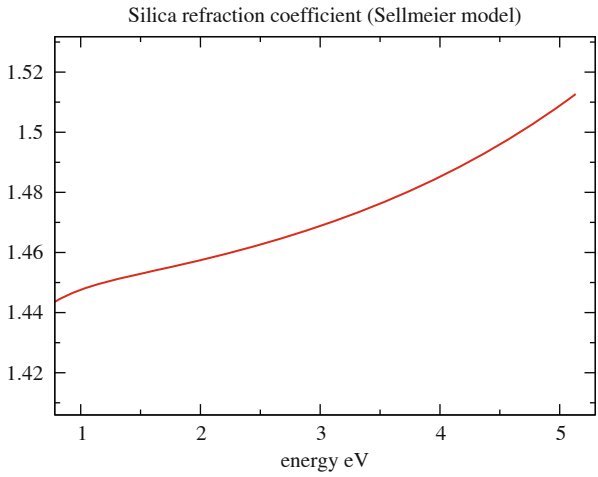

Fig. 12.3 Refractive coefficient of silicon dioxide (Sellmeier model)

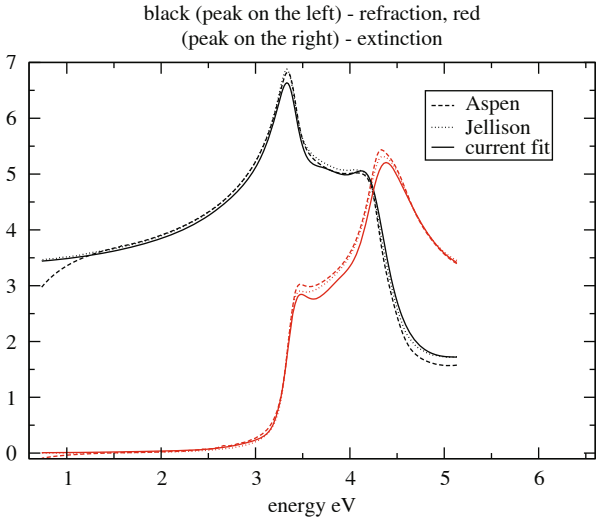

Fig. 12.4 Refractive and extinction coefficients of silicon

The procedure to find appropriate layers thicknesses we have used is as follows. First, we have found the thickness of the silica layer at the temperature of 300 °C from the one layer model on the silicon substrate. The found value, 2.32 nm, together with the optical properties from the Woolam reference material data (the Sellmeier model for the refraction and the extinction coefficient, see Fig. 12.3) has been used as fixed values for the fittings of the silicon wafer measurements at room temperature. By doing so, the only fitting parameter left is the water thickness. The needed refraction coefficient of water is due to Palik (also from the reference data collected in the Woolam database).

Using exactly the profiles of the refractive and extinction coefficient adjusted to Aspnes data (solid lines in Fig. 12.4 and in Fig. 12.5) the water layer is obtained as

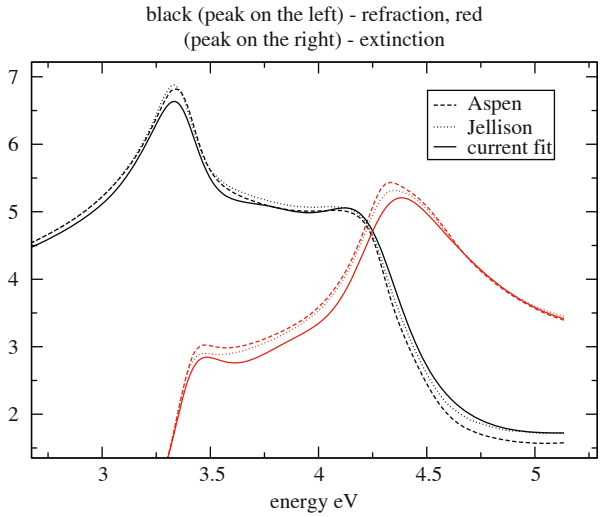

Fig. 12.5 Magnified view of the refractive and extinction coefficients of silicon

2.96 nm, whereas using directly the Aspnes data—2.71 nm. We have also checked the silicon data due to Jellison. The obtained value of the water thickness is now 3.06 nm. As already mentioned before, the data from the database may slightly differ from the silicon material we actually used, because of the possible influence of the defects.

Since the precise values of the thin layer thickness depend strongly on the accuracy of the refractive index used in the calculations, at the end we have allowed the oscillator parameters to be adjustable parameters. The starting values for fittings were chosen to correspond to the Aspnes data. After calculations, a silicon model adjusted to our sample provided parameters that are given in Table 12.2. The value of water thickness obtained happens to be very close to the Jellison data based model – 3.07 nm.

The optical properties of silicon from different models and measurements have been given in Figs. 12.4 and 12.5. The fittings of the optical properties of our silicon sample give slightly smaller values to the known in literature, especially at the areas with the peak structures. This property is attributed to the influence of defects and their consequences. Yet all the data are still very close to each other.

A summary of the water layer thicknesses obtained on the basis of different silicon data is provided in Table 12.3.

12.3 Discussion and Conclusions

As it is given in Table 12.3 the water layer is relatively thick, about 3 nm (with humidity about 50 %), which corresponds approximately to the stack of 10 water molecules. This result leads to very nontrivial conclusions. First of all one should

Table 12.2 The parameters of the oscillators (of the Tauc-Lorentz type [5]) used to model the silicon sample studied

Oscillator type	A	B_r	E_0	E_g
'Tauc-Lorentz'	565.86	0.276	3.373	3.026
'Tauc-Lorentz'	22.6	0.461	4.279	0.981
'Tauc-Lorentz'	8.20	1.386	5.537	0.0
'Tauc-Lorentz'	89.52	0.872	3.814	2.291

Table 12.3 Thickness of the water layer on the top of silicon wafer

Model of the silicon	Water thickness
Jellison	3.06
Aspnes	2.71
Aspnes: Tauc-Lorentz	2.96
Tauc-Lorentz current sample	3.07

remember that AFM tips are made of silicon, unless they are metalized their operation undergoes within the water—on the nanoscale the tips are wet. If the sample studied by AFM is also of silicon, as, for instance, for nanotribology purposes [8, 9], then this feature is even more enhanced. Also, substrates that are of other kind but still contain silicon molecules like silicon nitride surfaces [4] or silicon-containing diamond-like carbon (DLC-Si) films are covered with adsorbed water [6], yet not because of silica but rather due to the larger content of silanol groups(Si-OH) which are expected to exist if silicon molecules are present at the surface interface. In fact, these are free silanol aggregates and hydrogen-bonded silanol aggregates which play a crucial role in the adsorption of water molecules. Any rearrangement or change in concentration of silanol groups is expected to change the adsorption properties of any material containing silica [12]. These groups are found to be thermally stable up to 900 K [11]. In [6], on the basis of the ellipsometry modeling, it has been given that the water layer thickness is, like here, also large, between 1 nm and 4 nm. In this chapter, it has been also shown using different diamond-like carbon samples enriched with silicon atoms that the absence of silanol groups (because of no silicon atoms in the sample) leads to no adsorbed water.

The amount of silanol groups and water adsorption have also been investigated in detail, in the case of a bilayer silica by Yang et al. [11] under vacuum conditions using infrared reflection–absorption spectroscopy (IRAS) and temperature-programmed desorption. Although the experiment conditions there were performed at vacuum, thus far from room-like conditions, there is a notion of already five layers of heavy water D_2O at the temperature as low as 100 K from temperature-programmed desorption method.

Knowledge of the water layer thickness is also indispensable in studying biological samples. In [3], for instance, the estimated thicknesses of the associated water in the presence of the biological membrane used in the model was assumed as 0.9 nm; no information has been, however, given about the substrate without attached biomolecules, whether it was still on the level of 1 nm, or it was thicker but the presence of biomolecules made it thinner. No details of ellipsometric calculations have been given in this paper. A more popular tool in studying biological samples is

the AFM microscope, which gives even more opportunity to obtain important data, like elastic properties. Here also the knowledge about nanowater amount is of crucial importance. In the case of softer samples like, for instance, compressible fluid lipid membranes, the AFM tips may induce molecular rearrangements and bilayer deformations. Tip-induced perturbations together with the thin layer water influence as yet remain incompletely understood.

Acknowledgments This work has been partly supported by Polish Grant No. F-1/18/DS/13 and F-1/541/DS/13.

References

1. Christy AA (2011) Effect of hydrothermal treatment on adsorption properties of Silica Gel. Ind Eng Chem Res 50(9):5543; Christy AA (2010) New insights into the surface functionalities and adsorption evolution of water molecules on silica gel surface: a study by second derivative near infrared spectroscopy. Vibr Spect 54:42; Bobok M, Christy AA, Kluvanec D, Illásová L (2011) State of water molecules and silanol groups in opal minerals: a near infrared spectroscopic study of opals from Slovakia. Phys Chem Minerals 38:809; Christy AA (2012) Effect of heat on the adsorption properties of silica gel. IACSIT Int J Eng Tech 4:(4)
2. Fujiwara H (2007) Spectroscopic ellipsometry: principles and applications. Wiley, Hoboken
3. Howland MC, Szmodis AW, Sanii B, Parikh AN (2007) Characterization of physical properties of supported phospholipid membranes using imaging ellipsometry at optical wavelengths. Biophys J 92(4):1306
4. Ishigaki H, Nagata R, Iwasa M (1988) Effect of adsorbed water on friction of hot-pressed silicon nitride and silicon carbide at slow speed sliding. Wear 121:107
5. Jellison GE Jr, Modine FA (1996) Parameterization of the optical functions of amorphous materials in the interband region. Appl Phys Lett 371 (1996) (Erratum, Appl Phys Lett 2137)
6. Kato N, Mori H, Takahashi N (2008) Spectroscopic ellipsometry of silicon-containing diamond-like carbon (DLC-Si) films. Phys Status Solidi (c) 5:1117
7. Rimola A, Costa D, Sodupe M, Lambert J-F, Ugliengo P (2013) Silica surface features and their role in the adsorption of biomolecules: computational modeling and experiments. Chem Rev 113(6):4216
8. Rymuza Z (2010) Advanced techniques for na notribological studies. Sci Probl Mach Oper Main 1(161):33
9. Szlufarska I, Chandross M, Carpick RW (2008) Recent advances in single-asperity nanotribology. J Phys D Appl Phys 41:123001
10. Vedam K (1998) Spectroscopic ellipsometry: a historical overview. Thin Solid Films 313:1
11. Yang B, Emmez E, Kaden WE, Yu X, Boscoboinik JA, Sterrer M, Shaikhutdinov S, Freund H-J (2013) Hydroxylation of metal-supported sheet-like silica films. J Phys Chem C 117(16):8336
12. Zhuravlev LT (2000) The surface chemistry of amorphous silica. Zhuravlev model. Coll Surf A Physicochem Eng Asp 173:1

Chapter 13
The Effect of Sintering Temperature on Linear and Nonlinear Optical Properties of YAG Nanoceramics

V. Ya. Gayvoronsky, A. S. Popov, M. S. Brodyn, A. V. Uklein, V. V. Multian and O. O. Shul'zhenko

13.1 Introduction

In the early 1960s, translucent alumina ceramics (Lucalox) were first developed by General Electric Co. [1] which is now widely used as tube material for high-pressure sodium lamps. Since then, other transparent (or translucent) ceramic systems such as SiAlON, AlON, MgO, AlN, SiC, Si_3N_4, ZrO_2, PLZT [2] were developed. Recent improvements in powder synthesis and ceramics sintering made it possible to fabricate high-quality materials. Besides good transparency, these ceramics have main advantages of structural ceramics, e.g. high strength, hardness, corrosion resistance, and high- temperature resistance. It became possible at the first time to prepare active elements from such media of high temperature melting points as sesquioxides like lutetium (Lu_2O_3), scandium (Sc_2O_3), and yttrium (Y_2O_3) [3, 4]. Nowadays, transparent ceramics have attracted much attention due to numerous advantages over single crystals (SCs). The use of ceramics can solve some technological and economical issues associated with the production of SCs [5, 6, 7]. It is possible to produce heavily and homogeneously doped ceramics with composite structure [8, 9] and complex shape [10]. Besides, ceramics can provide highly efficient laser generation comparable or superior to those of SCs [11, 12].

Currently, yttrium aluminum garnet ($Y_3Al_5O_{12}$, YAG) co-doped with rare-earth elements is one of the most extensively studied and widely used material for applications. During the 1980s, translucent YAG ceramics were fabricated [13, 14]; however, poor optical quality and relatively large scattering losses resulted in low laser generation efficiency. In 1995, Ikesue et al. showed the possibility of fabricating transparent Nd:YAG ceramics with reasonable efficiency for solid-state laser applications [15]. Continuous wave (CW) lasing was observed at 1064 nm with generation efficiency of 28 % using diode pumping at 808 nm. The efficiency was

V. Ya. Gayvoronsky (✉) · A. S. Popov · M. S. Brodyn · A. V. Uklein · V. V. Multian
Institute of Physics NASU, Prospect Nauki 46, Kiev 03680, Ukraine
e-mail: vlad@iop.kiev.ua

O. O. Shul'zhenko
V. N. Bakul Institute for Superhard Materials NASU, Avtozavodskaya 2, Kiev 04074, Ukraine

O. Fesenko, L. Yatsenko (eds.), *Nanocomposites, Nanophotonics, Nanobiotechnology, and Applications,* Springer Proceedings in Physics 156,
DOI 10.1007/978-3-319-06611-0_13,

similar to the obtained for the single crystal one. Since then, the development of this technology has led to the achievement of highly efficient laser oscillation in both compact devices and powerful laser setups. J. Dong et al. [16] have studied heavily Yb-doped YAG ceramics. They achieved a generation efficiency of 52 % for 1-mm-thick YAG ceramic doped with 20 atomic percent ytterbium ions. In 2002, a group led by Ueda, in collaboration with Toshiba and Konoshima Co. (Osaka, Japan), reached 1.46 kW using a Nd:YAG ceramic rod with the size of 8 mm in diameter and 203 mm in length [17]. In application to medical diagnostics imaging, dosimetry, nuclear medicine etc., scintillation optical ceramic materials have become comprehensive as single crystal ones. Transparent Ce:YAG demonstrates significant advantages against SC [18, 19]. Luminescent and scintillation characteristics of the scintillation ceramics based on Ce-doped YAG (Ce:YAG) and rare-earth ion-doped lutetium aluminium garnet (LuAG) have been reported in [18] and [19] respectively.

Dense ceramics with nano grain size may display new structural, magnetic, electronic, and optical properties with large application potential. There are three main methods to prevent grain growth during sintering: addition of dopant that modifies atoms diffusion process, application of hot-pressing, and sintering powders in metastable crystallographic phases. Also, there is an alternative method to produce optical ceramics like microwave sintering, field assisted sintering, shock consolidation, slip casting in a strong magnetic field, and high-pressure low-temperature sintering (HPLT) [2].

Sintering at high pressures and low temperatures has several advantages in comparison with traditional methods, namely: (1) inhibition or grain growth; (2) lower sintering temperature; (3) shorter sintering time; (4) ease of fabrication, etc. The pronounced advantages forced more detailed study of the high pressure sintering techniques performed by several research groups.

It was found that sintering mechanism under high pressure is quite different from that under ambient pressure [20]. It was stated that pressure can restrain grain growth and initiate plastic deformation to eliminate pores and additional phases that can exist in triple junction of grains. With increase in pressure of up to 1.0 GPa, the average grain size was about 55 nm. At this initial stage of high-pressure sintering, high pressure accelerates particle flow and reduces the distance between the particles. However, sintering stress increase and grain growth promotion was observed. At the middle and high pressure range, between 2.0 and 5.0 GPa, grain growth is modest. It indicates that even high pressure can restrain grain growth resulting in obtaining nanostructured ceramics. When loading pressure is equal to 4.0 GPa, the local high-stress concentration is expected to diminish due to the increase of the total contact area between individual particles, i.e., the yield strength that the sample reaches.

Recently, Liu et al. [21] has reported about synthesis of the near totally dense transparent nanostructured YAG ceramics. It was proposed a high pressure sintering mechanism based on analysis of grain size and residual stresses in nanoceramics. It has been found that increase of sintering temperature from 300 to 500 °C at 5.0 GPa causes nonmonotonic variations of residual microstrains while average grain size increases.

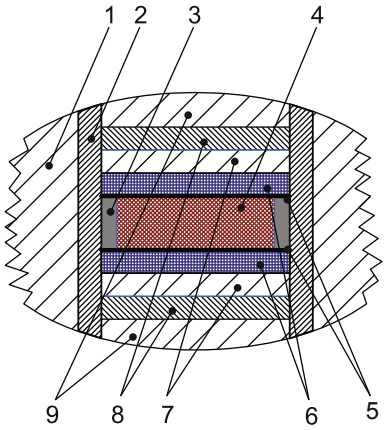

Fig. 13.1 Scheme of high-pressure cell setup: *1* container made from calcium carbonate; *2* graphite heater; *3* tantalum foil cover; *4* YAG nanopowder; *5* molybdenum disks; *6* hard alloy disks; *7* hexagonal boron nitride; *8* graphite disks; *9* pyrophyllite insulator

In the present work we study the effect of sintering temperature on structural and optical properties of YAG nanoceramics fabricated by HPLT pressure technique. The object of present research is optical nanoceramics produced from nanopowders sintered under high pressures ~7.5 GPa using relatively low temperatures 400–500 °C. The impact of the structure on the NLO response of the studied ceramics was analyzed.

13.2 Sample Preparation

All samples were consolidated under thermobaric static conditions at high-pressure toroid-type apparatus [22]. The scheme of pressure cell setup is presented in Fig. 13.1. Before placing into the high pressure cell at the initial YAG, powder was uniaxially compressed in a steel mold at a pressure of 450 MPa into pellets 15 mm in diameter and 1 mm in height. Pressed precursor powder covered by protective tantalum foil (3) placed between two molybdenum disks (5). Such construction allows chemical purity of nanoceramics to remain unchanged. After sintering, in order to prevent concavity, the nanoceramics were placed between two disks made from hard alloy (6). The pellet was placed in a capsule of chemically inert hexagonal boron nitride (7), which was used to ensure the quasi hydrostatic compression of a sample and to prevent its contact with a graphite heater (2).

The consolidation was conducted at pressures of ~7.5 GPa and temperatures in the range from 400 to 500 °C. The isothermal holding time during hot isostatic pressing was 2.5 min. The main preparation parameters for fabricated samples and notation used in this work are summarized in Table 13.1. Average density ρ of sintered samples was measured using gravimetric method. The porosity P was estimated from measured average density according to formula $P = 1 - \rho/\rho_{sc}$, where $\rho_{sc} = 4.55$ g/cm^3 is the density of the YAG single crystal [23].

Table 13.1 Preparation parameters and notation of the ceramic YAG samples including scintering pressure/temperature, sintering time and resultant thickness, density and porosity

Notation	Pressure, GPa	Temperature, °C	Time, min	Thickness, mm	Density, g/cm^3	Porosity, %
S1	7.5	400	2.5	0.180	3.94	13
S2	7.5	450	2.5	0.178	3.98	13
S3	7.5	475	2.5	0.180	4.10	10
S4	7.5	500	2.5	0.180	4.01	12

The mean size of the YAG powder particles was found out by transmission electron microscopy. It was shown that the precursor powder mostly consist of the particles with the size range 30–100 nm, being agglomerated in aggregates with the size about 1–5 μm. The aggregates are tough and in the form of plates. Probably, the aggregates follow the form of the synthesized primary YAG nanoparticles. The diffraction patterns were measured in 2θ range from 10 to 80 degrees with step size of 0.01 degrees and step time of 5 s at room temperature. The diffraction patterns were evaluated using MAUD 2.3 open-source software. Reference diffraction patterns were collected using Crystallography Open Database (COD) [24]. Both experimental and reference (COD # 4312143) diffraction patterns are presented at Fig. 13.2. Experimental X-ray diffraction peaks in the patterns (solid and dashed lines) match well with reference data for YAG (red vertical lines). This result indicates that the composition of the ceramics is $Y_3Al_5O_{12}$ with garnet structure. The stated in other works structural decomposition [25] of YAG ceramics or partial amorphization [26] was not observed. Nevertheless, the diffraction peaks from the different phase may not be clearly seen due to their low intensity or large width.

The X-ray diffraction peaks are asymmetric and their width increase with 2θ. This fact indicates presence of microstrains. The intensities of the diffraction peaks increase with growth of sintering temperature due to decrease of the vacancy concentration [27]. The background intensities increase with higher vacancy concentration. It can be seen from difference curve (difference between S4 and S2 diffraction patterns) that with the increase of sintering temperature diffraction peaks exhibit shift to the low angles side (Fig. 13.2).

13.3 Experimental Techniques

The scheme of experimental setup for spatial distribution of the cross-section analysis of the optical scattering is presented in Fig. 13.3a [28]. The measurement system is based on the goniometer G-5. The DPSS laser ($\lambda = 532$ nm, P = 50 mW) and sample were mounted on fixed arm of goniometer. The light was registered by CCD array AMKO LTI MuLTIray (1024 pixels with $25 \times 200\mu m^2$ pixel size, 12-bit digital resolution) that was positioned on the movable arm at a distance of $L = 200$ mm from the sample. The optical scattering indicatrix measured for ceramic samples characterize spatial distribution of the power of the scattering radiation $\Delta P_{scat}(\theta)$, which propagated along the direction θ (Fig. 13.3a).

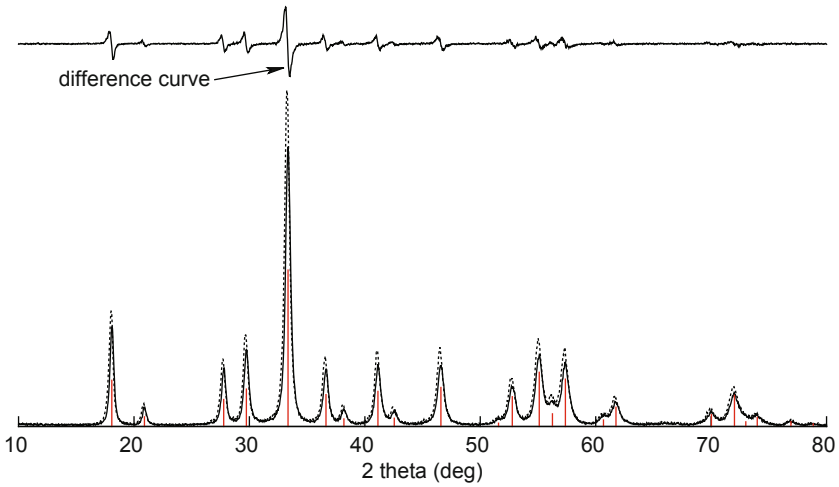

Fig. 13.2 X-ray diffraction patterns for nanoceramics sintered at different temperatures: 450 °C (*S2—solid line*), 500 °C (*S4—dashed line*). The patterns are compared with the YAG reference (COD # 4312143) (red vertical lines). Upper curve corresponds to the difference between the two samples

To estimate the scattering losses in forward hemisphere we calculate the integral coefficient of scattering p_{scat} [29]:

$$p_{scat} = \frac{2\pi}{P_0} \int_{\theta_{min}}^{\pi/2} \frac{\Delta P(\theta)}{\Delta\Omega} \sin\theta d\theta \tag{13.1}$$

where $\Delta\Omega = 4\pi \sin^2 \theta_{lens}/2 = 1.8 \times 10^{-3}$ sr is a solid angle over the part of forward hemisphere, $\theta_{min} \sim 1.8^o$ exceeds the lens angular aperture $\theta_{lens} = \arctan(d/2\ L) \sim 1.4^o$. The data was normalized on total power P_0 transmitted into the forward hemisphere. The scheme of experimental setup for the measurements of spatial laser beam profile transformation is presented in Fig. 13.3b. Two CW DPSS lasers at 532 nm and 1064 nm with the Gaussian spatial profile were used as laser sources. The samples were positioned after the focal point of the focusing lens. The study of spatial beam profile transformation behind ceramic samples was performed with CCD-camera (ATiK 16 IC-HS with pixel size 7.4×7.4 μm^2 and 640×480 image resolution) as in scattering measurements (it was positioned in 6 cm after the sample output face). The high-frequency noise of the spatial profile was removed by moving average filter in combination with Fourier low-pass filter. All statistics including standard deviation, skewness and kurtosis were calculated in order to provide quantitative information about laser beam profile.

13.4 The Total Transmittance Measurements

The measurements of the total transmittance (TT) were performed with three different laser sources at the wavelengths 532 nm, 650 nm and 1064 nm. The spatial beam profile beam quality checkup was performed with a CCD array. The sample was

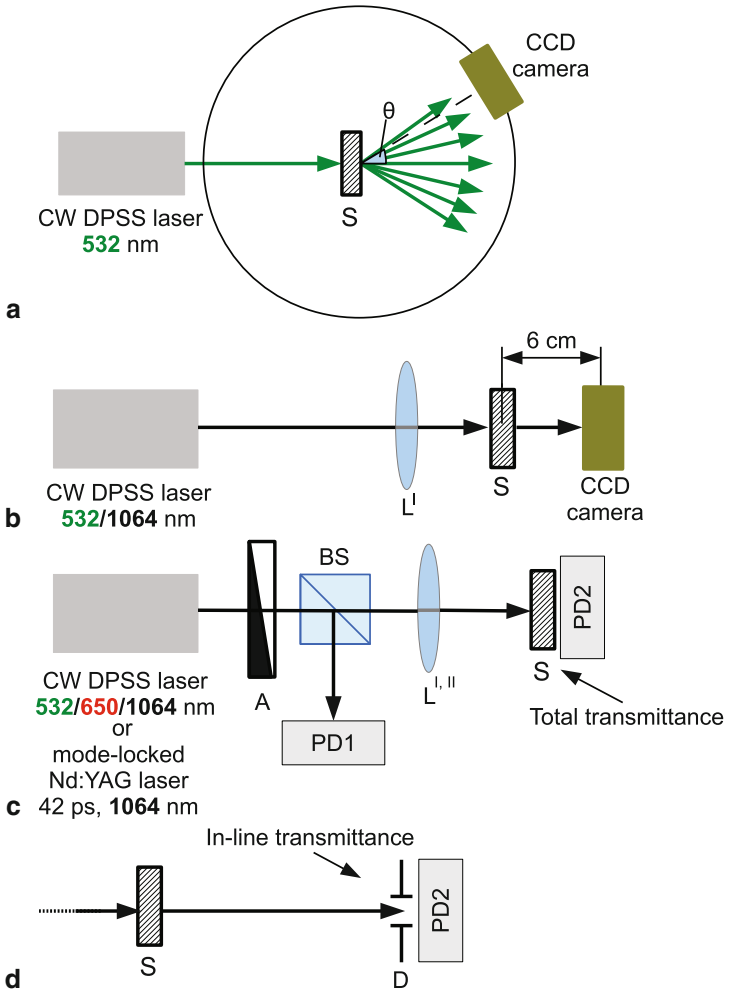

Fig. 13.3 Schemes of the experimental setups: **a** for measurements of angular dependence of scattered light intensity (θ denotes the angle between the incidence laser beam and scattering signal acquisition directions); **b** spatial laser beam profile transformation analysis; **c** laser beam self-action technique (photoinduced variation of total transmittance); **d** in-line transmittance measurements. *A* attenuator, *BS* beam splitter, $L^{I,II}$ lens with focal distance 8 (I) or 11 (II) cm, *S* ceramics sample, *D* diaphragm (Ø = 5 mm), *PD1* and *PD2* – incident and transmitted power/energy registration channels

placed at the fixed distance of 16 cm after the lens, and the intensity was varied with a neutral attenuator that does not deflect the beam. The experimental setup contains two photodiode channels. The first, reference channel (photodiode of this channel is indicated as PD1 in Fig. 13.3c) measures the laser beam power/energy at the input

of the optical system. To measure the TT, the sample was placed at the photodiode (PD2) aperture to avoid energy loss due to the high scattering.

The TT of the studied samples is determined by the signals ratio of the photodiodes PD2 to PD1 corrected to the apparatus function. In the framework of the cubic NLO response, the photoinduced variation of the TT $T(I_0)$ versus the incident intensity I_0 of the plane light wave can be derived analytically $T(I_0) = T_0/(1+q(I_0))$. Typically, the effect is attributed to the two-photon absorption (TPA) process.

In the expression above, T_0 is the linear transmission coefficient and $q(I_0)$ is given by the formula:

$$q(I_0) = \beta I_0 L_{eff} \sim Im(\chi^{(3)})I_0, \tag{13.2}$$

where $L_{eff} = (1 - e^{-\alpha L})/\alpha$ – self-action effective length, α – linear absorption coefficient, L – the thickness of the media, β – TPA coefficient, $\chi^{(3)}$ – cubic NLO susceptibility. Spatial averaging across the Gaussian beam profile transforms $T(I_0)$ into

$$T^{CW}(I_0) = T_0 \cdot \ln(1 + q(I_0))/q(I_0) \tag{13.3}$$

for TEM_{00} CW laser beam excitation [30].

For the pulsed laser excitation regime it is impossible to obtain the exact expression for the spatial and temporal averaging across the beam and pulse Gaussian profiles. We applied the approximate formula

$$T^{P}(I_0) = T^{CW}(I_0)\frac{1 + 0.228q(I_0)}{1 + 0.136q(I_0)} \tag{13.4}$$

where the fraction in brackets provides the proper contribution of the temporal averaging [30].

Thus, the fitting of the experimental TT dependencies by Eq. (13.4) for chosen laser intensity range allows us to obtain the magnitudes of $\Delta\alpha$ as well as $\mathrm{Im}(\chi^{(3)})$.

13.5 The Total and In-Line Transmissions

We measured the absolute in-line and TT in order to determine optical quality at the samples. The in-line transmittance grows from 0.5 to 7 % with wavelength increase (Fig. 13.4). The level of in-line transparency of resultant ceramics is considerably lower than theoretical limit of transmission for YAG single crystal. Such a decrease of in-line transmittance is due to large scattering caused by presence of pores, surface roughness, cracks and light absorption by microdefects in ceramics.

Digital photo of as-prepared YAG ceramic sample sintered at 475 °C is presented in the inset of Fig. 13.4. It is clearly seen that the sample is translucent which is mainly due to relatively large porosity (see Table. 13.1) caused by strong precursor powder agglomeration. Nevertheless, the text on the other side can be distinctly seen. Morphology and dispersity of precursor plays a significant role in sintering process.

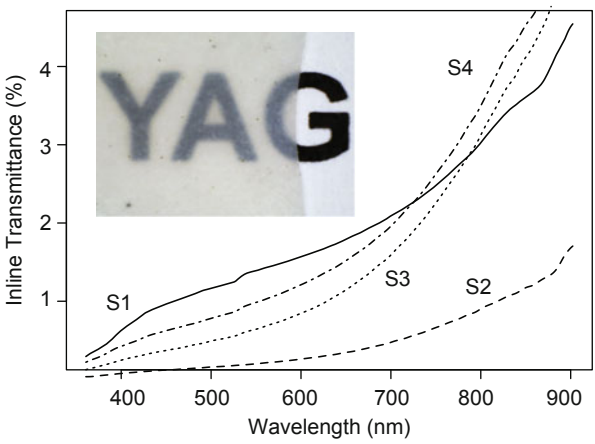

Fig. 13.4 The in-line spectral transmittace dependencies of YAG ceramics samples with different sintering temperature: 400 °C (*S1—solid line*), 450 °C (*S2—dashed line*), 475 °C (*S3—dotted line*), 500 °C (*S4—dash-dot line*). In the inset digital photo of *S3* sample sintered at 475 °C

The capillary pressure in pores that present within particle agglomerates is as high as several GPa. External pressure (∼7.5 GPa) applied to the samples is insufficient to close all the pores. The utilization of plate-shape precursor reduces the optical quality of the ceramics in comparison to the spherical one probably due to more efficient inhomogeneities formation during the sintering process [31].

The in-line spectral transmittance dependencies for the all studied samples are monotonic and rise with wavelength increase. The character of the in-line transmittance for the samples S3 and S4 is similar and in the near IR range it's higher than for the other ceramics. On the contrary, the sample S1 demonstrates the highest in-line transmittance in the visible range (< 700 nm). Whereas, the lowest in-line transmittance was observed for the ceramic S2. In general, the low magnitudes of the in-line transmittance for the studied samples (< 5%) is determined by the efficient scattering that will be discussed in Sect. 13.6.

Spatial laser beam profiles transmitted through the ceramics sample with sintering temperature 475 °C are presented in Fig. 13.5. Colorbar on the right side of the graph shows the appropriate intensity distribution. Image scale is shown as a segment of length 1 mm. The amplitude on the left subplot is three times lower.

No significant sintering temperature effect on spatial laser profile at 532 nm (Fig. 13.5a) for the samples was observed, while at 1064 nm (Fig. 13.5b) a large narrowing (∼15 %) was observed in comparison with incident laser beam. In the case of 532 nm there is a strong scattering of laser radiation and speckle pattern formation. Whereas at 1064 nm only a small distortion of the profile is observed indicating good transparency at this wavelength.

We performed measurements of laser beam profile form transformation transmitted through the samples with different sintering temperature. All laser beam profiles were approximated with Gaussian law. The estimated beam width is presented in Table 13.2. All the samples demonstrate self-focusing effect at moderate laser intensity (Fig. 13.6). This result indicates that the studied ceramic samples are very promising for use as nonlinear optical materials (Table 13.2).

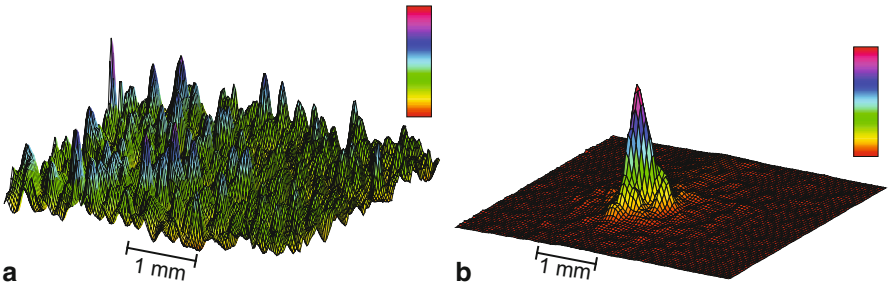

Fig. 13.5 Spatial distribution of laser beam at wavelength of **a** 532 nm and **b** 1064 nm transmitted through the ceramics sample sintered at 475 °C. Amplitude on the left subplot is three times lower

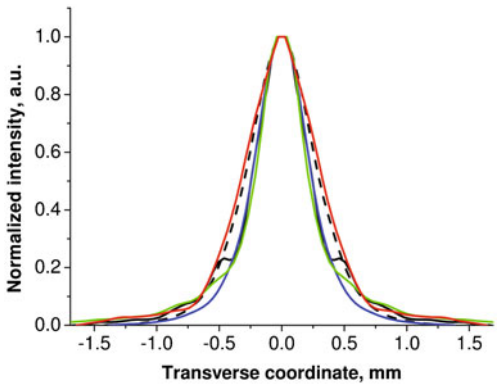

Fig. 13.6 Laser beam profiles transmitted trough the YAG ceramic samples at 1064 nm: laser profile without sample (*dashed line*), 400 °C (*S1—black line*), 450 °C (*S2—red line*), 475 °C (*S3—blue line*), 500 °C (*S4—green line*)

Table 13.2 Comparison of laser beam width transmitted though the YAG ceramic samples at wavelength of 1064 nm. w/w_0 stands for ratio of the laser beam transmitted though the sample to the laser beam without the sample (the laser beam width without the sample $w_0 = 0.54$ mm)

	Gaussian w, mm	w/w_0
S1	0.45	0.83
S2	0.57	1.06
S3	0.44	0.81
S4	0.41	0.76

As stated before, the scattering losses cause a significant decrease of the in-line transmission in visible wavelength region. Further study of the optical properties will concern total transmittance (TT). During the TT measurements, the sample was fixed right on registering device (PD2, see Fig. 13.3c) to neglect scattering losses. Only surface roughness or absorption due to defects in cercamic samples can be considered as factors that reduce TT.

The magnitudes of TT of studied samples at given wavelengths are presented in Table 13.3. The lossless transmission coefficients for single-crystal YAG was calculated using Sellmeier model [32] with parameters found in [23]. TT of samples is approximately 70 % (1064 nm), almost twice the magnitude of the one at 532 nm

Table 13.3 Comparison of measured TT (%) in visible (532 and 650 nm) and near IR (1064 nm) with calculated values from Sellmeier model and experimental data from Ref. [33] for ceramic samples

	Thickness, mm	Temperature, °C	532 nm	650 nm	1064 nm
S1	0.180	400	24	39	68
S2	0.178	450	31	38	76
S3	0.180	475	37	47	82
S4	0.180	500	28	40	73
Ref. [33]	1	350	39	40	40
Ref. [33]	1	450	38	42	47
SC (calc.)	–	–	83	84	84

(Table. 13.3). While at a wavelength of 650 nm the magnitudes of TT for ceramics samples with different sintering temperature is close to each other, sample S3 with sintering temperature 475 °C has the highest magnitudes of TT. The effect of sintering temperature on TT in all three cases (532, 650, and 1064 nm) is unclear. The TT magnitude for S3 sample at a wavelength of 1064 nm is 82 % which is close to theoretical magnitude for the YAG single crystal. The photoinduced transmittance variations are relatively small.

13.6 Scattering Properties

We studied the scattering properties of sintered ceramic samples under the effect of CW laser excitation at wavelength of 532 nm. The choice of wavelength was based on the samples that are transparent in near-IR range and most of the scattering appears at visible wavelength range.

Rigorous solutions of the scattering problem, whether analytical or numerical, are complicated and tend to involve considerable computer time and storage for all but the simplest shapes and smallest particles. For certain ranges of size and refractive index, approximations may be used. Not only are these simplifications more readily computable, but they often provide insight into the scattering process.

The phenomena related to light scattering by particles can be fully described by the solution of the Mie equation [34]. However, the use of this method is cumbersome due to the large required amount of calculation resources. Instead of Mie theory several approximations can be used. In the particular case where the grain size is comparable to the wavelength, the scattering follows a $(a/\lambda)^4$ law known as Rayleigh–Gans–Debye (RGD) approximation [34]. It is valid for small scatters with a refractive index very similar to that of the environment ($|s-1| << 1$ and $2\pi\,|s-1|\,a/\lambda << 1$, where s is the quotient between the refractive index of the scatter and that of the surrounding medium. This model has been well established for isotropic materials [35]. For the present case, i.e., YAG ceramics, in the RGD approximation, the scattering profile of unpolarized light for one sphere with refractive index n and radius r is given by [36].

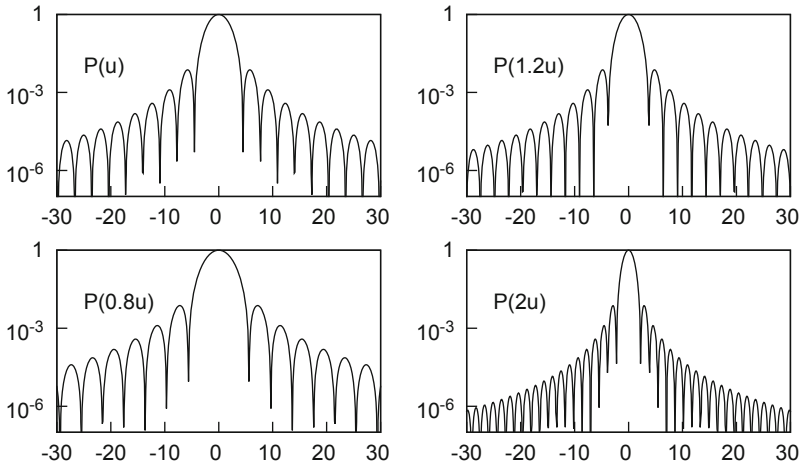

Fig. 13.7 Form factor $P(u)$ for a spherical scattering particle as a function of u (semilogarithmic scale)

$$I(\beta) = I_0 \frac{32\pi^4 r^6}{9\lambda_m^4 \, l^2} \left(\frac{\Delta n}{n}\right)^2 \left(1 + \cos^2 \beta\right) P(u) \tag{13.5}$$

where l is the distance between the sphere and detector, β is the scattering angle, Δn the refractive index difference between the sphere and the surrounding medium, and $P(u)$ is a scattering form factor, which, for a sphere, is given by:

$$P(u) \equiv \left[\frac{3}{u^3}(\sin u - u \cos u)\right]^2, \tag{13.6}$$

where u

$$u \equiv \frac{4\pi r}{\lambda_m} \sin \frac{\beta}{2} \tag{13.7}$$

The total scattering intensity is the sum of all spheres responses in the detected volume V. For monodisperse spheres

$$I_{total}(\beta) = \rho V I_0 \frac{32\pi^4 r^6}{9\lambda_m^4 \, l^2} \left(\frac{\Delta n}{n}\right)^2 \left(1 + \cos^2 \beta\right) P(u) \tag{13.8}$$

where ρ is the number density. The examples of $P(u)$ is drawn in Fig. 13.7 (different values of u argument were taken to show transformations of indicatrix shape with increasing grain size). It is clearly seen that $P(u)$ is oscillating function with well determined maxima and minima. Due to the fact that light is unpolarized, the $(1 + \cos^2 \beta)$ term needs to be taken into account. Thus, $P(u)$ determines the shape of the scattering profile.

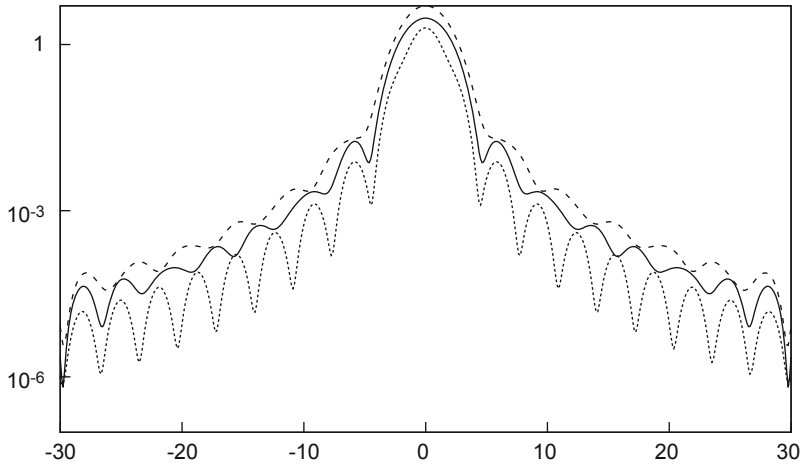

Fig. 13.8 Polydisperse form factor for a trimodal, pentamodal, and bimodal distribution of spherical scattering particles as a function of u (semilogariphmic scale)

To take into account the effect of polydispersity, $P(u)$ should be determined as a sum of all scattering factors from various grain sizes r_j, for example,

$$\sum_V r_j^6 P(u_j) \equiv P_p(u) \tag{13.9}$$

Then, Eq. 13.8 with polydispersity factor

$$I_{total}(\beta) = I_0 \frac{32\pi^4}{9\lambda_m l^2} \left(\frac{\Delta n}{n}\right)^2 (1 + \cos^2\beta) P_p(u) \tag{13.10}$$

where $P_p(u)$ is referred to a polydisperse form factor. For systems with trimodal, pentamodal, and bimodal distribution of the spheres with equal numbers, the polydisperse form factor is plotted at Fig. 13.8.

Because of the polydispersity clear minima and maxima of the form factor vanishes and the shape becomes smooth and concave. Therefore, for very small average grain sizes, the primary minima of the summed form factors are located at high angles. For a sample with an uniform grain size less than 2 μm, the primary minima is located at an angle of 15 °. Therefore, for a sample with an average grain size less than 2 μm, polydispersity leads to the concave shape of the scattering tail.

To perform a more detailed study of the effect of sintering temperatures on optical scattering properties of ceramic samples, scattering indicatrix at wavelength 532 nm was measured. The measurements were carried out only in the forward hemisphere, i.e., in the angle range $0 \leq \theta \leq 180°$. Laser beam propagated along the normal to the sample surface ($\theta = 90°$). To eliminate the effect of possible inhomogeneity of sintered samples, the measurements were performed at three different points and then average signal was taken.

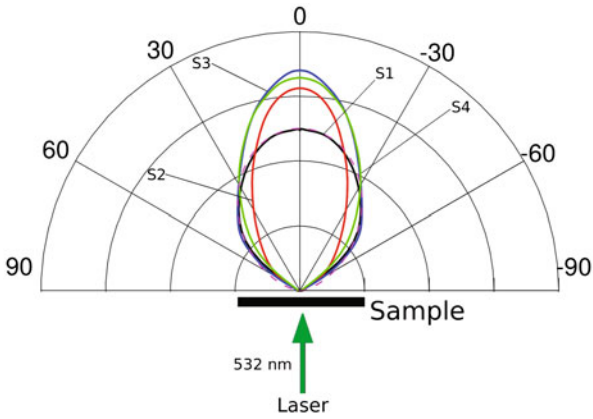

Fig. 13.9 Optical scattering indicatrices ($\lambda = 532$ nm) in forward hemisphere of ceramics samples sintered at different temperature: 400 °C (*S1—black line*), 450 °C (*S2—red line*), 475 °C (*S3—blue line*), 500 °C (*S4—green line*). Lambertian source represented as $\cos\theta$, *magenta dashed line*

Polar plots of optical scattering indicatrices are presented in Fig. 13.9. The green arrow shows the direction of incident laser beam. The indicatrix form changes with the increase of the sintering temperature. S1 sample demonstrates a highly dispersive character which is close to perfect scatterer (so-called Lambertian source represented as $\cos\theta$, magenta dashed line on plot). The indicatrix profiles of samples S3 and S4 are similar. In contrast with lowest in-line transmission, S2 sample has the narrowest indicatrix which points to lowest scattering in this sample. This can be caused by complex internal absorption mechanisms at the visible wavelength range. A possible reason for the asymmetry of indicatrices is the sample inhomogeneity. Calculated scattering losses for all samples are summarized in Table. 13.4. It is clearly seen that S3 sample has the lowest scattering losses, due to the highest density among all studied samples. All samples are strongly dispersive (more than 95 % scattering losses) in visible wavelength region and only a slight ballistic component of laser beam can be observed.

The theoretical approach described in the current section was used to estimate the effective scatterer size $\overline{d}_{scat}$ which can be related either with pressed agglomerate or pore size in ceramics samples. In accordance with electron microscopy of precursor powder, the average particle size from 30 to 100 nm were used as initial parameters in calculations. The refractive index of YAG was equal to $n = 1.838$[23]. Optimal value of average scatterer size was determined by minimum of cost function. Results are shown in Table 13.4. Dependence of average scatterer size $\overline{d}_{scat}$ versus sintering temperature is nonmonotonic with maximum at 475 °C (S3 sample). Samples S2 and S4 with sintering temperatures 450 and 500 °C correspondingly have similar magnitudes $\overline{d}_{scat}$. Such nonmonotonic character can be caused by numerous factors. The theoretical model used in the present work describes scattering caused by single particle averaged over an ensemble of particles of correlation between relative density (or porosity of samples) and magnitudes of $\overline{d}_{scat}$ (Table 13.4).

Table 13.4 Estimated integral scattering losses ($\lambda = 532$ nm) and the effective scatterer size ($\overline{d}_{scat}$) within the RGD approximation for the ceramic samples

	Temperature, °C	Sca. losses, %	$\overline{d}_{scat}$, μm
S1	400	98.7	0.084
S2	450	96.4	0.123
S3	475	97.6	0.178
S4	500	97.9	0.127

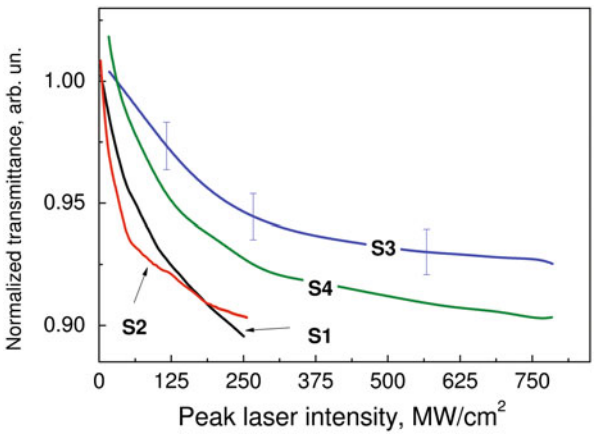

Fig. 13.10 Normalized dependencies of the photoinduced total transmittance versus peak laser intensity ($\lambda = 1064$ nm) for ceramics samples sintered at different temperatures: 400 °C (*S1—black line*), 450 °C (*S2—red line*), 475 °C (*S3—blue line*), 500 °C (*S4—green line*)

13.7 Nonlinear Optical Properties

In order to study the nonlinear optical properties of scintered ceramics, we performed the measurements of photoinduced TT dependencies versus the peak laser intensity under picosecond laser impulses excitation at wavelength of 1064 nm. The normalized dependencies of photoinduced TT versus the peak laser intensity are presented in Fig. 13.10. All samples demonstrate photoinduced darkening with different efficiency that depends on sintering temperature. The TT dependencies of the samples S1 and S2 is similar with the experimental error.

The observed photodarkening character could be due to the efficient TPA in ceramic samples. Ab initio study of vertical transition energies of oxygen vacancy states in YAG crystal revealed four optical transition models [37]. One of them is an electron transition from the top of valence band (VB) to the energy state of positively charged oxygen vacancies.

With the rise of the incident laser peak intensity the slopes of the normalized dependencies of TT get more flatter witch indicates the saturation of TPA processes. The shape of the experimental curves can be described with at least two different mechanisms of the NLO response. The photoinduced variations in absorption can then be written as $\Delta\alpha_{NLO} = \beta_1 I/(1 + 1/I_t) + \beta_2 I$ [38], where $\beta_1 > \beta_2$ and I stands for the peak laser intensity, I_t for the saturation intensity. The first term corresponds to effective photoinduced darkening at the moderate intensities $I < I_t$ which arises

Table 13.5 The effective two-photon absorption coefficient β and the imaginary part of the cubic nonlinear optical susceptibility ($\mathrm{Im}(\chi^{(3)})$) of studied samples under pulsed (ps) laser excitation at wavelength of 1064 nm

	TPA β, 10^{-3} cm/MW	$\mathrm{Im}(\chi^{(3)})$, 10^{-11} esu
S1	11.8	4.9
S2	16.6	6.9
S3	4.4	1.9
S4	10.2	4.3

due to singe- or two-photon resonance at the excitation of either the grain surface defects or the volume associated energy levels. While term $\beta_2 I$ characterizes the contribution of the second mechanism of NLO response for the intensities $I \geq I_t$. The origin of observed TPA is a matter of more detailed study. It is possible that the photoinduced absorption is associated with more complex process.

Calculated magnitudes of the absorption coefficient and imaginary part of the cubic NLO susceptibility $\mathrm{Im}(\chi^{(3)})$ for the initial intensity range are presented in Table. 13.5. S2 sample demonstrates the highest magnitude of $\mathrm{Im}(\chi^{(3)})$. It is clearly seen that $\mathrm{Im}(\chi^{(3)})$ significantly depends on sintering temperature. Even in the case when the difference in sintering temperature between S3 and S2 samples is 25 °C the $\mathrm{Im}(\chi^{(3)})$ differs by ~60 %.

It is known that the origin of the absorptive/refractive NLO response at 1064 nm of the metal oxides nanocomposites is determined by the resonant excitation of the interface defects (O vacancies states) [28, 38]. For the samples S3 and S4 that have demonstrated similar spectral (Fig. 13.4) and NLO (Fig. 13.10) responses, the efficiency of the photoinduced absorption is inversely proportional to the surface of the elementary scatterer: $\beta(500\ ^\circ\mathrm{C})/\beta(475\ ^\circ\mathrm{C}) \sim (\overline{d}_{scat}(475\ ^\circ\mathrm{C})/\ \overline{d}_{scat}(500\ ^\circ\mathrm{C}))^2$. Thus, the applied self-action technique was shown to be sensitive to the sintering temperature of the samples. It can be proposed as noninvasive method of sintering process control and diagnostics of sintered samples.

The dependency of $\mathrm{Im}(\chi^{(3)})$ versus sintering temperature is unclear. At the same time correlation between $\mathrm{Im}(\chi^{(3)})$ values and oxygen vacancies concentration can take place in the studied ceramic samples. It should be noted that the values of $\mathrm{Im}(\chi^{(3)})$ can be further increased/decreased by additional thermal treatment of precursor powder or pressed samples under different gas atmospheres. However, in the case of thermal treatment of pressed samples under high temperatures, it can lead to optical quality, decreased recrystallization, and substantial grain growth.

13.8 Summary

The optical and nonlinear optical properties of the sintered YAG ceramic samples were studied. It was shown that in-line transmittance (in visible range) of ceramics samples sintered at low temperatures with high-pressure is relatively low (~2–5 %) due to high porosity. Measured spatial profile of laser beam transmitted through the

samples at wavelength of 532 nm indicates that all studied samples can be considered as highly diffusive media. Only a small distortion of the profile is observed at 1064 nm, indicating good transparency at this wavelength. The measured value of the TT of samples at wavelength of 1064 nm is about 80 % which is close to theoretical magnitude of YAG single crystal.

The measurements of optical scattering indcatrix were performed with CW laser excitation at wavelength 532 nm. All the samples integral scattering losses are extremely high (> 95 %). The values of d_{scat} was estimated by applying RGD model to measure scattering indicatrix data. It was found that effective scatterer size d_{scat} values do not exceed 200 nm.

Photoinduced variation of TT of ceramic samples was studied under picosecond laser excitation at a wavelength of 1064 nm. All studied samples demonstrate the photoinduced darkening ∼10 %. It was found that imaginary part of the cubic nonlinear optical susceptibility are $\mathrm{Im}(\chi^{(3)}) \sim 10^{-11}$ esu. The magnitude of $\mathrm{Im}(\chi^{(3)})$ is highly dependent on sintering temperature which confirms the sensitivity of proposed self-action technique. It can be used as one of the noninvasive methods of sintering process control and diagnostics of sintered samples.

Acknowledgement The authors acknowledge V. Yu. Timoshenko, G. I. Dovbeshko and T. E. Konstantinova for the assistance in sample characterization and discussions. This work was partially supported by NASU V-166 and VC-157 grants.

References

1. Coble RL (1962) Sintering alumina: effect of atmospheres. J Am Ceram Soc 45(3):123–127
2. Wang S, Zhang J, Luo D et al (2013) Transparent ceramics: processing, materials and applications. Prog Solid State Chem 41:20–54
3. Li J-G, Ikegami T, Mori T (2005) Fabrication of transparent, sintered Sc_2O_3 ceramics. J Am Ceram Soc 88(4):817–821
4. Ikegami T, Li J-G, Mori T, Moriyoshi Y (2002) Fabrication of transparent yttria ceramics by the low-temperature synthesis of yttrium hydroxide. J Am Ceram Soc 85(7):1725–1729
5. Yadegari M, Asadian M, Saeedi H et al (2013) Formation of gaseous cavity defect during growth of Nd:YAG single crystals. J Cryst Growth 367:57–61
6. Brandle C (2004) Czochralski growth of oxides. J Cryst Growth 264:593–604
7. Muller G, Friedrich J (2005) Crystal growth, bulk: methods. In: Bassani F, Liedl LG, Wyder P (eds) Encyclopedia of condensed matter Physics. Elsevier Ltd., Oxford, pp 262–274
8. Tang F, Cao Y, Huang J et al (2012) Fabrication and laser behavior of composite yb:yag ceramic. J Am Ceram Soc 95(1):56–69
9. Ikesue A, Aung YL (2006) Synthesis and performance of advanced ceramic lasers. J Am Ceram Soc 89(6):1936–1944
10. Yagi H, Yanagitani T, Numazawa T, Ueda K (2007) The physical properties of transparent $Y_3Al_5O_{12}$ elastic modulus at high temperature and thermal conductivity at low temperature. Ceram Int 33(5)711–714
11. Yagi H, Yanagitani T, Takaichi K et al (2007) Characterizations and laser performances of highly transparent Nd^3+ :$Y_3Al_5O_{12}$ laser ceramics. Opt Mater 29(10):1258–1262
12. Mezeix L, Green DJ (2006) Comparison of the mechanical properties of single crystal and polycrystalline yttrium aluminum garnet. Int J Appl Ceram Technol 3(2):166–176

13. de With G, van Dijk H (1984) Translucent $Y_3Al_5O_{12}$ ceramics. Mater Res Bull 19(12):1669–1674
14. Mulder C, de With G (1985) Translucent $Y_3Al_5O_{12}$ ceramics: electron microscopy characterization. Solid State Ionics 16:81–86
15. Ikesue A, Kinoshita T, Kamata K, Yoshida K (1995) Fabrication and optical properties of high-performance polycrystalline Nd:YAG ceramics for solid-state lasers. J Am Ceram Soc 78(4):1033–1040
16. Dong J, Shirakawa A, Ueda K et al (2007) Laser-diode pumped heavy-doped Yb:YAG ceramic lasers. Opt Lett 32(13):1890–1892
17. Lu J, Ueda K-i, Yagi H et al (2002) Neodymium doped yttrium aluminum garnet ($Y_3Al_5O_{12}$) nanocrystalline ceramics—a new generation of solid state laser and optical materials. J Alloys Compd 341(1–2):220–225
18. Zych E, Brecher C, Lingertat H (1998) Host-associated luminescence from YAG optical ceramics under gamma and optical excitation. J Lumin 78(2):121–134
19. Nikl M, Mihokov E, Mare J et al (2000) Traps and timing characteristics of LuAG:Ce^3+ scintillator. Phys Status Solidi A 181(1):R10–R12
20. Zou Y, He D (2010) Nanosintering mechanism of $MgAl_2O_4$ transparent ceramics under high pressure. Mater Chem Phys 123:529–533
21. Liu K, He D, Wang H et al (2012) High-pressure sintering mechanism of yttrium aluminum garnet ($Y_3Al_5O_{12}$) transparent nanoceramics. Scr Mater 66:319–322
22. Khvostantsev L, Vereshchagin L, Novikov A (1977) Device of toroid type for high pressure generation. High Temp High Press 9:637–639
23. Bass M, DeCusatis C, Enoch J et al (2009) Handbook of optics, 3rd edn, vol IV: optical properties of materials, nonlinear optics, quantum optics (set). Handbook of optics, McGraw-Hill Education. ISBN: 9780071498920
24. Grazulis S, Daskevic A, Merkys A et al (2012) Crystallography open database (COD): an open-access collection of crystal structures and platform for world-wide collaboration. Nucleic Acids Res 40:D420–D427
25. Hreniak D, Gierlotka S, Lojkowski W et al (2005) High-pressure induced structural decomposition of re-doped YAG nanoceramics. Solid State Phenomena 106:17–22
26. Lukowiak A, Wignusz R, Maczka M et al (2010) IR and Raman spectroscopy study of YAG nanoceramics. Chem Phys Lett 494:279–283
27. Makinson J, Lee J, Magner S et al (2000) X-rat diffraction signatures of defects in nanocrystalline materials. Adv X-Ray Anal 42:407–411
28. Gayvoronsky VYa, Kopylovsky MA, Vishnyakov EA et al (2009) Optical and nonlinear optical characterization of nanostructured oxyhydroxide of aluminium. Func Mat 16:136–140
29. Borshch A, Brodyn M, Gayvoronsky V et al (2004) Simulation of an experimental setup for measurements of light scattering by porous films. Ukr J Phys 49(2):196–202
30. Gayvoronsky V, Timoshenko V, Brodyn M et al (2005) Giant nonlinear optical response of nanoporous anatase layers. Appl Phys B 80:97–100
31. Qin X, Yang H, Zhou G et al (2011) Synthesis of submicron-sized spherical Y_2O_3 powder for transparent YAG ceramics. Mater Res Bull 46:170–174
32. von Sellmeier W (1871) Zur erklarung der abnormen farbenfolge in spectrum einiger substanzen. Ann Phys Chem 219:272–282
33. Vovk E, Deineka T, Doroshenko A et al (2009) Production of the $Y_3Al_5O_{12}$ transparent nanostructured ceramics. J Superhard Mater 31(4):252–259
34. Dmitruk N, Goncharenko A, Venger E (2009) Optics of small particles and composite media. Naukova Dumka Kyiv, ISBN: 978–966-00–0948-8
35. Hulst H, van de Hulst H (1957) Light scattering: by small particles. Dover Books on Physics Series. DOVER PUBN Incorporated, ISBN: 9780486642284
36. Apetz R, van Bruggen MPB (2003) Transparent alumina: a light-scattering model. J Am Ceram Soc 86(3):480–486

37. Chen J, Lu TC, Xu Y et al (2008) Ab initio study of a charged vacancy in yttrium aluminum garnet ($Y_3Al_5O_{12}$). J Phys Condens Matter 20(32):325212
38. Pritula I, Gayvoronsky V, Kolybaeva M et al (2011) Effect of incorporation of titanium dioxide nanocrystals on bulk properties of KDP crystals. Opt Mat 33:623–630

Chapter 14
Impact of Carbon Nanotube on Homocysteine Clusters: MD Simulation

Przemysław Raczyński, Krzysztof Górny and Zygmunt Gburski

14.1 Introduction

Homocysteine is an amino acid produced in the human body by the chemical conversion of methionine, a compound regularly consumed within the diet. It is given by the formula $C_4H_9NO_2S$. The role of homocysteine in a human body is not fully understood and it is a subject of the current debate [1–3]. Recent studies show that high level of homocysteine (homocystinemia) is considered as a risk factor for cardiovascular disease [4–8]. Other studies indicate an increased risk of fractures (in humans) which is related with an elevated level of homocysteine [9–14]. Moreover, higher homocysteine and lower folate concentrations in early pregnancy are associated with lower placental weight and birth weight, and higher risk of adverse pregnancy outcomes [15–18]. Unfortunately, it is not clear yet whether high serum of homocysteine is itself the problem or if it is merely an indicator of other existing problems [19, 20]. Understanding the properties of homocysteine may help, when one considers the role it plays in the complex, biological environment, for example, in the human body.

In this chapter, we present the results of computer simulation (molecular dynamics (MD) technique) of the homocysteine clusters. Two clusters composed of $n = 65$ and 2500 homocysteine molecules have been studied. These clusters with embedded carbon nanotube (CNT) were studied again in order to find the differences between the properties of homocysteine in such various systems. During recent years, many CNT-based systems have been studied, particularly CNTs are considered as potential tools in nanomedicine [21–27]. In this work, the MD of homocysteine was studied for several temperatures (including physiological). Knowledge of the dynamics of homocysteine systems, with and without nanotube, may help when one would consider some applications of CNTs in the biological environment.

P. Raczyński (✉) · K. Górny · Z. Gburski
Institute of Physics, University of Silesia, Uniwersytecka 4, 40–007 Katowice, Poland
e-mail: przemyslaw.raczynski@us.edu.pl

P. Raczyński
Tel.: +48323591832

O. Fesenko, L. Yatsenko (eds.), *Nanocomposites, Nanophotonics, Nanobiotechnology, and Applications,* Springer Proceedings in Physics 156,
DOI 10.1007/978-3-319-06611-0_14,

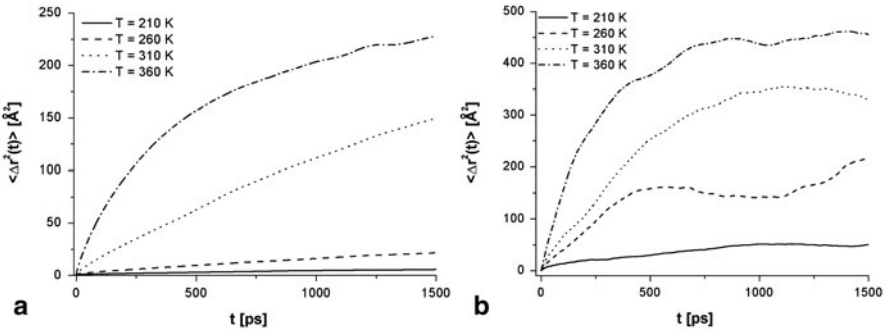

Fig. 14.1 The temperature dependence of the mean square displacement of the center of mass of homocysteine for the clusters consisting of $n = 65$ homocysteine molecules, in the absence (**a**) and presence (**b**) of CNT

14.2 Materials and Methods

Fully atomistic MD simulations were performed with NAMD 2.7b2 simulation code [28, 29] and visualized with VMD 1.9.1 OpenGL Display [30, 31]. In the first part of our work, we studied clusters consisting of finite numbers $n = 65$ and $n = 2500$ homocysteine molecules. Next, we embedded the capped CNT in these clusters (using steered MD) and repeated all MD simulations. The charge distribution in the homocysteine molecule was calculated using *ab initio* method with 6–31G** basis set. Homocysteine molecule was modeled with the Chemistry at Harvard Macromolecular Mechanics (CHARMM)27 [32] force field. The CHARMM-based force field was also employed for CNT [33]. All simulations were performed for four temperatures $T = 210$, 260, 310 (physiological), and 360 K. The initial configurations of the system were obtained from the series of NVT ensemble simulations. All the systems studied were equilibrated for 1×10^6 time steps in the NVT ensemble. The 0.5 fs integration time step was applied in all performed simulations. All results presented in this work were obtained from 0.5 ns production runs.

14.3 Results

The first quantity we discuss is the mean square displacement (MSD) $\langle|\Delta\vec{r}(t)|^2\rangle$ of the center of mass of homocysteine where $\Delta\vec{r}(t) = \vec{r}(t) - \vec{r}(0)$ and $\vec{r}$ is the position of the center of mass of a single molecule. Figure 14.1 shows the $\langle|\Delta\vec{r}(t)|^2\rangle$ plots for the cluster consisting of $n = 65$ homocysteine molecules with the absence (Fig. 14.1a) and with the presence (Fig. 14.1b) of the CNT.

Figure 14.2 shows MSD plots for the cluster containing $n = 2500$ homocysteine molecules.

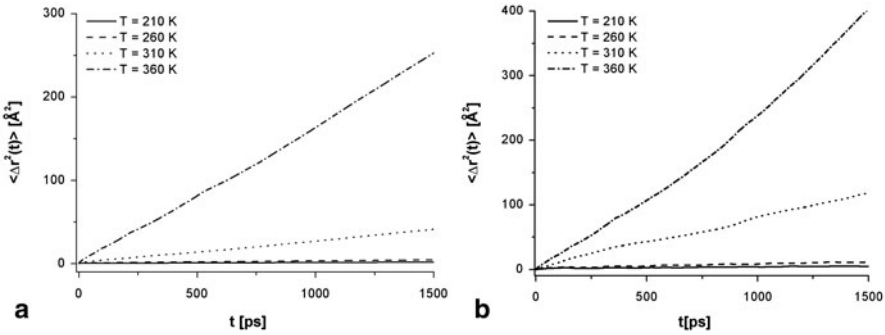

Fig. 14.2 The temperature dependence of the mean square displacement of the center of mass of homocysteine for the clusters consisting of $n = 2500$ homocysteine molecules, in the absence (**a**) and presence (**b**) of CNT

In all samples presented in Figs. 14.1 and 14.2, the slope of $\langle|\Delta\vec{r}(t)|^2\rangle$ increases with an increase in temperature. The MSD slope reflects the mobility of the molecule. In all studied clusters, the mobility of the homocysteine molecules' grows with heating of the cluster. The longtime courses of $\langle|\Delta\vec{r}(t)|^2\rangle$ plots show that at the temperature range studied the clusters do not vaporize; the molecules in clusters keep together. One can see that in clusters with CNT (Figs. 14.1b and 14.2b) the plots are less regular, in comparison with the systems without nanotube. These irregularities reflect the impact of the nanotube on the homocysteine molecules. The small homocysteine molecules skim on the surface of CNT and may even go around it, particularly in the small cluster where the homocysteines do not cover tightly the surface of nanotube. MSD plots at $T = 210$ K and $T = 260$ K (excluding the system with nanotube consisting of $n = 65$ homocysteines at $T = 260$ K) indicate that these systems are in the condensed phase. At the highest temperature $T = 360$ K, one can observe the diffusion, characteristic of the liquid phase. Figure 14.3 shows the MSD of the center of mass of homocysteine with the absence (Fig. 14.3a) and presence (Fig. 14.3b) of the CNT. The small clusters are represented by black lines and the large ones by gray lines. The plots for two temperatures are presented: $T = 210$ K (solid lines) and $T = 310$ K (dashed lines).

Steeper slopes of the $\langle|\Delta\vec{r}(t)|^2\rangle$ in case of all these curves which represent small clusters indicate that these systems are more susceptible to the changes of temperature. With rising temperature, the mobility of the homocysteine molecules in small clusters increases more rapidly than in the bigger ones. This happens because the interiors of the large clusters are formed by many tightly packed homocysteine molecules which have little volume to move.

Figure 14.4 shows the radial distribution function g(r) of the center of mass of homocysteine in a small cluster with presence of the nanotube (Fig. 14.4b) and without it (Fig. 14.4a). Figure 14.5 shows the g(r) function but for the systems consisting of $n = 2500$ homocysteine molecules.

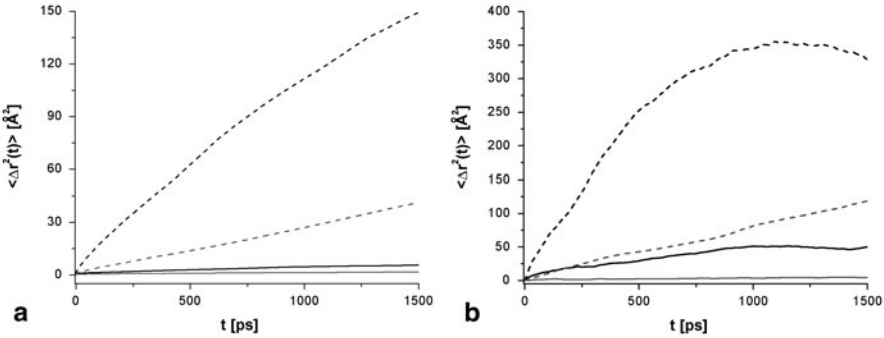

Fig. 14.3 The comparison of the mean square displacement of the center of mass of homocysteine in pure clusters (**a**) and the clusters with embedded nanotube (**b**) for two temperatures: $T = 210$ K (*solid lines*) and $T = 310$ K (*dashed lines*). The clusters consisting of $n = 65$ homocysteine molecules are represented by *black lines* and the clusters consisting of $n = 2500$ homocysteine molecules are represented by *gray lines*

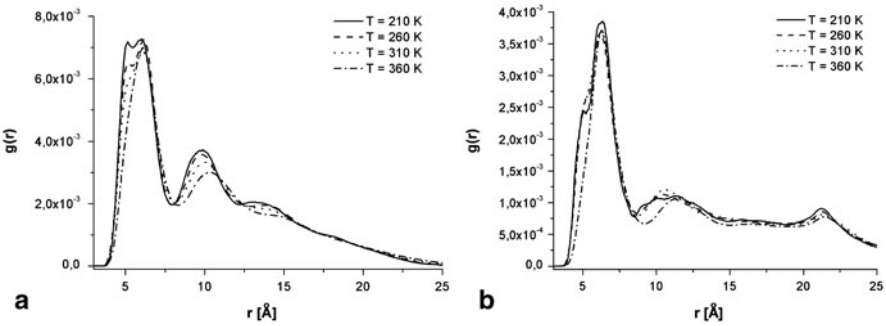

Fig. 14.4 The calculated radial distribution function of the center of mass of homocysteine for the clusters consisting of $n = 65$ homocysteine molecules, in the absence (**a**) and presence (**b**) of CNT

Both figures show that the first homocysteine neighbors are in the distance approximately $r \approx 7$ Å. Next, peaks of g(r) function are connected with the second and third neighbors. These maxima are flatter and they are shifted towards the larger distance when the cluster is heating. In the cluster containing $n = 65$ homocysteines and with the presence of the nanotube (Fig. 14.4b), g(r) plots substantially differ from the others shown in Figs. 14.4 and 14.5. The small peak at the distance of about $r \approx 22$ Å is observed. It is related to the homocysteine neighbors located on the opposite side of the CNT (the diameter of the CNT is $R = 13$ Å). Due to the large number of homocysteines, this peak is not observed for the big cluster. The g(r) allows to estimate the diameter d of the clusters. For the small cluster, the diameter is $d \approx 23$ Å for the pure sample and $d \approx 30$ Å for the system with nanotube. For the large clusters, the diameters are $d \approx 75$ Å for both samples (with and without nanotube). In such a large cluster, the presence of nanotube practically does not affect its diameter.

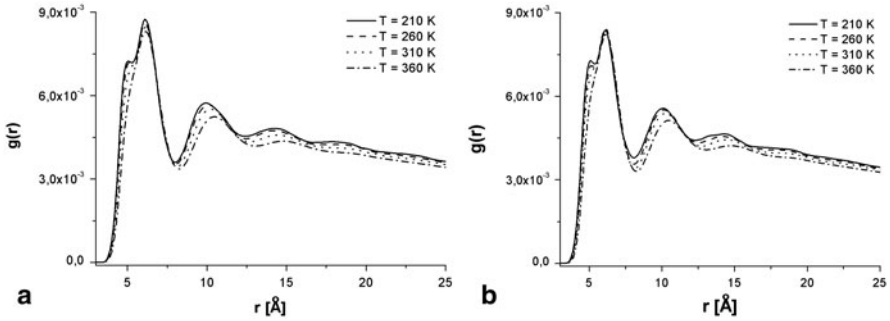

Fig. 14.5 The radial distribution function of the center of mass of homocysteine for the clusters consisting of $n = 2500$ homocysteine molecules, in the absence (**a**) and presence (**b**) of CNT

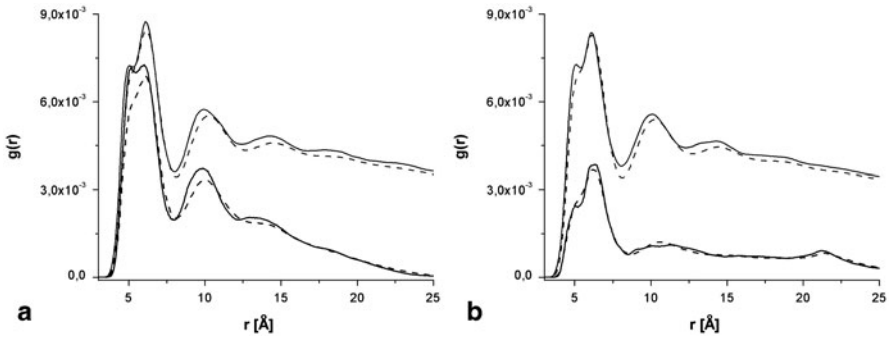

Fig. 14.6 The comparison of the calculated radial distribution function of the center of mass of homocysteine for the pure clusters (**a**) and the clusters with embedded nanotube (**b**) and for two temperatures: $T = 210$ K (*solid lines*) and $T = 310$ K (*dashed lines*). The clusters consisting of $n = 65$ homocysteine molecules are represented by *black lines* and the clusters consisting of $n = 2500$ homocysteine molecules are represented by *gray lines*

In Fig. 14.6, the comparison of g(r) functions for all simulated systems is shown. Figure 14.6a is related to the pure clusters and Fig. 14.1b to the clusters with embedded CNT. The black lines indicate the small clusters and the gray the large ones. The temperatures are $T = 210$ K (solid lines) and $T = 310$ K (physiological, dashed lines).

In the large clusters (with the nanotube and without it), the homocysteine molecules have greater number of the nearest and next neighbors. This indicates that in the large systems the inner cluster core was formed. In this core, the homocysteines are closely tightened and they do not have much space to move. In the small clusters (with CNT and without it), the internal core was not created. The numerous homocysteine molecules are located outside of the clusters and they have a small number of the neighbors. In Fig. 14.6b ($n = 65$ system), one can see practically one

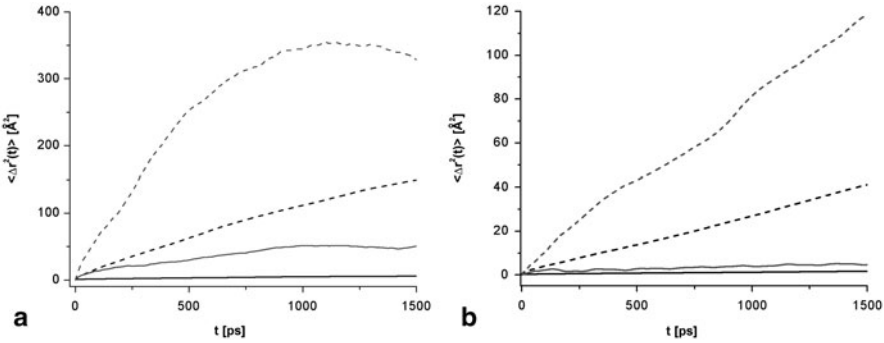

Fig. 14.7 The comparison (with CNT and without it) of the mean square displacement of the center of mass of homocysteine for the clusters consisting of $n = 65$ homocysteine molecules (**a**) and $n = 2500$ homocysteine molecules (**b**) and for two temperatures: $T = 210$ K (*solid lines*) and $T = 310$ K (*dashed lines*). The pure clusters (without CNT) are represented by *black lines* and the clusters with embedded CNT are represented by *gray lines*

distinct peak at $r \approx 7$ Å and two very small (about $r \approx 11$ Å and $r \approx 22$ Å). The value of the first peak is small. It shows that the homocysteine molecule has a very few first neighbors and practically has no next neighbors. The g(r) function in the case of a small cluster and in the presence of nanotube indicates that during the simulations of this system the homocysteines were formed at most one layer surrounding CNT.

In Fig. 14.7, we present the MSD of the center of mass of homocysteine. Figure 14.7a presents the comparison of the systems consisting of $n = 65$ homocysteine molecules (with the presence of nanotube—gray lines and absence of it—black lines). Figure 14.7b presents results for the clusters containing $n = 2500$ molecules.

The greater mobility of the homocysteine molecules with embedded nanotubes can be clearly seen. The homocysteines easily slide over the uniform surface of the nanotube. This is particularly evident for the small cluster. The molecules in system without CNT group in spherical shape while after embedding CNT the homocysteine molecules move over its surface. That the nanotube increases the mobility of the molecules in the clusters is confirmed by the values of the calculated diffusion coefficient D. The MSD is connected with the diffusion coefficient *via* the Einstein relation

$$\left\langle |\Delta\vec{r}(t)|^2 \right\rangle \approx 6Dt, \tag{14.1}$$

where D is the translational diffusion coefficient. Table 14.1 presents the comparison of D for the large clusters with the presence of nanotube and without it. The values of D are higher for the system with embedded CNT, at all temperatures. It confirms that the presence of CNT enhances the mobility of the homocysteine molecules in the cluster volume.

Figure 14.8 shows the radial distribution function of the center of mass of homocysteine. Figure 14.1a presents the comparison of the clusters consisting of $n = 65$

Table 14.1 The comparison of calculated values of D [Å^2/ps] for the pure system and with CNT, in the case of large clusters ($n = 2500$)

	Cluster without CNT	Cluster with CNT
$T = 210$ K	3.8×10^{-4}	4.0×10^{-4}
$T = 260$ K	4.2×10^{-4}	1.0×10^{-3}
$T = 310$ K	4.3×10^{-3}	1.1×10^{-2}
$T = 360$ K	2.8×10^{-2}	5.0×10^{-2}

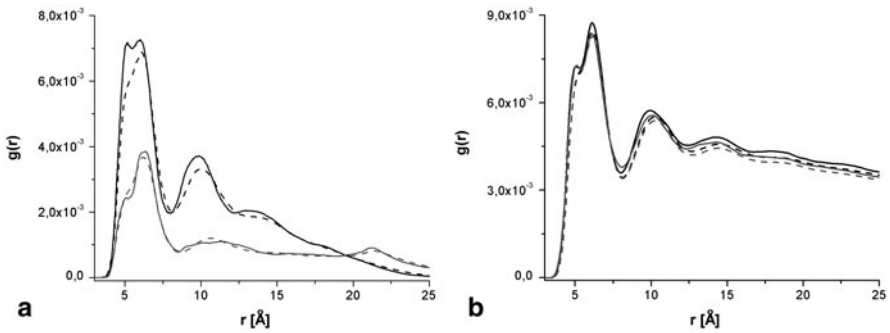

Fig. 14.8 The comparison of the calculated g(r) of the center of mass of homocysteine for the clusters consisting of $n = 65$ homocysteine molecules (**a**) and $n = 2500$ homocysteine molecules (**b**), for two temperatures: $T = 210$ K (*solid lines*) and $T = 310$ K (*dashed lines*). The g(r) for pure clusters (without CNT) is represented by *black lines* and for the clusters with embedded CNT is represented by *gray lines*

homocysteine molecules (with the presence and absence of nanotube). Figure 14.1b presents results for the clusters containing $n = 2500$ molecules.

In Fig. 14.8a, the significant differences between g(r) plots appear. These differences are not observed in case of the large cluster where CNT has no distinct impact on the dynamics of homocysteine molecules. After embedding the nanotube into the cluster, the number and distance of the first and next neighbors practically do not change. This is completely different from the g(r) function in the case of a small cluster, where the impact of CNT on the cluster is clearly visible. The plots of g(r) in Fig. 14.8a confirm that the homocysteine molecules slide on the CNT surface. On the snapshot of the instantaneous configuration ($n = 65$), one can observe (Fig. 14.9a) that the homocysteines do not cover tightly the nanotube surface, only one incomplete layer surrounding CNT was formed. In the case of the large cluster (Fig. 14.9b), CNT is practically not visible in the "sea" of homocysteines. In this case, the impact of the CNT on the homocysteine cluster is small.

In conclusion, the clusters consisting of $n = 65$ and $n = 2500$ homocysteine molecules were simulated. The pure homocysteine clusters (without CNT) form energetically a most favorable spherical shape. The four temperatures including the physiological one ($T = 210$, 260, 310, and 360) were taken into account. In the temperature range studied, the molecules in each sample keep together, and the clusters

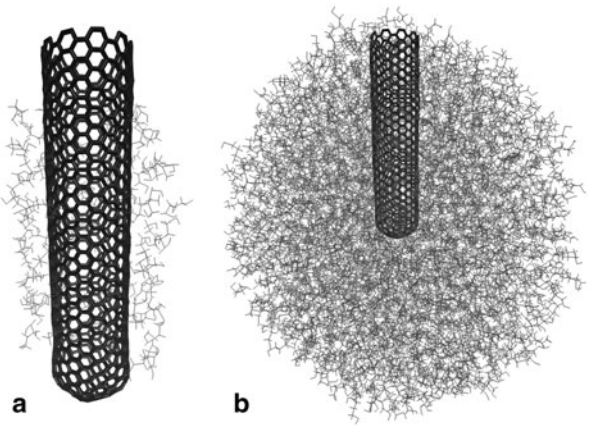

Fig. 14.9 The instantaneous configurations of the cluster consists of $n = 65$ homocysteine molecules (**a**) and $n = 2500$ molecules (**b**). The snapshots are presented for the systems with embedded CNT

do not vaporize. At the lowest temperature studied ($T = 210$ K), the clusters were in the condensed phase. At the highest temperature ($T = 360$ K), the translational diffusion of homocysteine molecules within the clusters' volume appears. The insertion of CNT into molecular cluster leads to the formation of the homocysteine layer surrounding the nanotube surface—that is particularly visible in the case of the small cluster ($n = 65$).

Acknowledgments Calculations were partially performed in ACK CYFRONET AGH on the Rack Server Mars.

References

1. Graham I, Refsum H, Rosenberg IH, Ueland PM, Shuman JM (1997) Homocysteine metabolism: from basic science to clinical medicine. Springer US, Boston
2. McCully KS (1999) The homocysteine revolution: medicine for the new millennium. Keats Pub., Los Angeles
3. Carmel R, Jacobsen DW (2011) Homocysteine in health and disease. Cambridge University, Cambridge
4. Robinson K (2000) Homocysteine and vascular disease. Springer Netherlands, Dordrecht
5. Frayn KN, Stanner S, British NF (2005) Cardiovascular disease: diet, nutrition and emerging risk factors: the report of a British Nutrition Foundation task force. Published by Blackwell Pub. for the British Nutrition Foundation, Oxford, UK; Ames, Iowa, USA
6. Huang C, Zhang L, Wang Z, Pan H, Zhu J (2011) Endothelial progenitor cells are associated with plasma homocysteine in coronary artery disease. Acta Cardiol 66:773–777. doi:10.2143/AC.66.6.2136962
7. Houcher Z, Houcher B, Touabti A, Begag S, Egin Y, Akar N (2012) Nutritional factors, homocysteine and C677T polymorphism of the methylenetetrahydrofolate reductase gene in Algerian subjects with cardiovascular disease. Pteridines 23:14–21
8. Maitland-Van Der Zee AH, Lynch A, Boerwinkle E, Arnett DK, Davis BR, Leiendecker-Foster C, Ford CE, Eckfeldt JH (2008) Interactions between the single nucleotide polymorphisms in the homocysteine pathway (MTHFR 677C > T, MTHFR 1298 A > C, and CBSins) and the efficacy of HMG-CoA reductase inhibitors in preventing cardiovascular disease in high-risk patients of hypertension: the GenHAT study. Pharmacogenet Genomics 18:651–656

9. Fakhrzadeh H, Ghotbi S, Larijani B (2007) The role of homocysteine in health and disease. Iran J Diabetes Lipid Disord 7:135–149
10. Nagele P, Tallchief D, Blood J, Sharma A, Kharasch ED (2011) Nitrous oxide anesthesia and plasma homocysteine in adolescents. Anesth Analg 113:843–848. doi:10.1213/ANE.0b013e31822402f5
11. Haroon NN, Marwaha RK, Godbole MM, Gupta SK (2012) Role of B-12 and homocysteine status in determining BMD and bone turnover in young Indians. J Clin Densitom 15:366–373. doi:10.1016/j.jocd.2012.01.006
12. El Maghraoui A, Ghozlani I, Mounach A, Rezqi A, Oumghar K, Achemlal L, Bezza A, Ouzzif Z (2012) Homocysteine, folate, and vitamin B-12 levels and vertebral fracture risk in postmenopausal women. J Clin Densitom 15:328–333. doi:10.1016/j.jocd.2011.12.001
13. Enneman AW, van der Velde N, de Jonge R, Heil SG, Stolk L, Hofman A, Rivadeneira F, Zillikens MC, Uitterlinden AG, van Meurs JBJ (2012) The association between plasma homocysteine levels, methylation capacity and incident osteoporotic fractures. Bone 50:1401–1405. doi:10.1016/j.bone.2012.03.013
14. Van Meurs JBJ, Dhonukshe-Rutten R a. M, Pluijm SMF, van der Klift M, de Jonge R, Lindemans J, de Groot L, Hofman A, Witteman JCM, van Leeuwen J, Breteler MMB, Lips P, Pols H a. P, Uitterlinden AG (2004) Homocysteine levels and the risk of osteoporotic fracture. N Engl J Med 350:2033–2041. doi:10.1056/NEJMoa032546
15. Bergen NE, Jaddoe VWV, Timmermans S, Hofman A, Lindemans J, Russcher H, Raat H, Steegers-Theunissen RPM, Steegers E a. P (2012) Understanding health behaviours in a cohort of pregnant women at risk of gestational diabetes mellitus: an observational study. BJOG 119:739–751. doi:10.1111/j.1471-0528.2012.03321.x
16. Gadhok AK, Sinha M, Khunteta R, Vardey SK, Upadhyaya C, Sharma TK, Jha M (2011) Serum homocysteine level and its association with folic acid and vitamin B-12 in the third trimester of pregnancies complicated with intrauterine growth restriction. Clin Lab 57:933–938
17. Mansour A, Harb H, Abdelhafeez M (2011) Diagnostic value of homocysteine and other preeclampsia markers: relationship with severity. Int J Biol Chem 5:227–237
18. Reyna-Villasmil E, Mejia-Montilla J, Torres-Cepeda D, Santos-Bolívar J, Aragon-Charrys J, Reyna-Villasmil N, Bravo-Henríquez A (2012) Efecto de las hormonas sexuales sobre las concentraciones de homocisteína en preeclámpticas y embarazadas normales. Prog Obstet Ginecol 55:226–231
19. Brozek W, Hassler N, Varga F, Klaushofer K, Paschalis EP (2012) Effect of bisphosphonates on gene expression of fibroblasts cultured in the presence of homocysteine. Bone 51:S8–S8. doi:10.1016/j.bone.2012.08.021
20. Zoungas S, McGrath BP, Branley P, Kerr PG, Muske C, Wolfe R, Atkins RC, Nicholls K, Fraenkel M, Hutchison BG, Walker R, McNeil JJ (2006) Cardiovascular morbidity and mortality in the atherosclerosis and folic acid supplementation trial (ASFAST) in chronic renal failure. J Am Coll Cardiol 47:1108–1116. doi:10.1016/j.jacc.2005.10.064
21. Wei Shao AP (2013) Carbon nanotube lipid drug approach for targeted delivery of a chemotherapy drug in a human breast cancer xenograft animal model. Biomaterials. doi:10.1016/j.biomaterials.2013.09.007
22. Dawid A, Gburski Z (2007) Dielectric relaxation of 4-cyano-4-n-pentylbiphenyl (5CB) thin layer adsorbed on carbon nanotube—MD simulation. J Non-Cryst Solids 353:4339–4343. doi:10.1016/j.jnoncrysol.2007.02.072
23. Im O, Li J, Wang M, Zhang LG, Keidar M (2012) Biomimetic three-dimensional nanocrystalline hydroxyapatite and magnetically synthesized single-walled carbon nanotube chitosan nanocomposite for bone regeneration. Int J Nanomedicine 7:2087–2099. doi:10.2147/IJN.S29743
24. Raczynski P, Dawid A, Gburski Z (2007) Molecular dynamics (MD) in homocysteine nanosystems—computer simulation. Biomol Eng 24:577–581. doi:10.1016/j.bioeng.2007.08.011
25. Battigelli A, Ménard-Moyon C, Da Ros T, Prato M, Bianco A (2013) Endowing carbon nanotubes with biological and biomedical properties by chemical modifications. Adv Drug Deliv Rev 65:1899–1920. doi:10.1016/j.addr.2013.07.006

26. Gburski Z, Górny K, Raczynski P (2010) The impact of a carbon nanotube on the cholesterol domain localized on a protein surface. Solid State Commun 150:415–418. doi:10.1016/j.ssc.2009.12.005
27. Raczynski P, Gorny K, Pabiszczak M, Gburski Z (2013) Nanoindentation of biomembrane by carbon nanotubes—MD simulation. Comput Mater Sci 70:13–18. doi:10.1016/j.commatsci.2012.12.031
28. Kale L, Skeel R, Bhandarkar M, Brunner R, Gursoy A, Krawetz N, Phillips J, Shinozaki A, Varadarajan K, Schulten K (1999) NAMD2: greater scalability for parallel molecular dynamics. J Comput Phys 151:283–312. doi:10.1006/jcph.1999.6201
29. Phillips JC, Braun R, Wang W, Gumbart J, Tajkhorshid E, Villa E, Chipot C, Skeel RD, Kalé L, Schulten K (2005) Scalable molecular dynamics with NAMD. J Comput Chem 26:1781–1802. doi:10.1002/jcc.20289
30. Humphrey W, Dalke A, Schulten K (1996) VMD: visual molecular dynamics. J Mol Graph Model 14:33–38. doi:10.1016/0263-7855(96)00018-5
31. Nelson M, Humphrey W, Kufrin R, Gursoy A, Dalke A, Kale L, Skeel R, Schulten K (1995) Mdscope—a visual computing environment for structural biology. Comput Phys Commun 91:111–133. doi:10.1016/0010-4655(95)00045-H
32. MacKerell AD Jr, Banavali N, Foloppe N (2000) Development and current status of the CHARMM force field for nucleic acids. Biopolymers 56:257–265. doi:10.1002/1097-0282(2000) 56:43.0.CO;2-W
33. Alexiadis A, Kassinos S (2008) Molecular simulation of water in carbon nanotubes. Chem Rev 108:5014–5034. doi:10.1021/cr078140f

Chapter 15
Heat Capacity of 1D Chains of Atom/Molecule Adsorbates in the Grooves of c-SWNT Bundles

V. V. Sumarokov, M. I. Bagatskii and M. S. Barabashko

15.1 Introduction

Since the discovery of carbon nanotubes in 1991 [1], investigations of the physical properties of these novel materials have been rated as a fundamentally important trend in physics of condensed matter [2, 3]. Of special interest is the study of properties of low-dimensional systems [4–9]. The unique structure of bundles of single-walled carbon nanotubes (SWNTs) permits obtaining quasi-one-dimensional (1D), 2D, and 3D structures formed by adsorbates [5, 10]. Technologically, most of the nanotubes in the prepared bundles have closed ends unless special steps are taken to open them. Figure 15.1 demonstrates the possible sites of adsorption of a relatively small admixture atoms or molecules in a bundle of closed SWNTs (c-SWNTs): interstitial channels (IC), grooves (G) at the outer surface, and the outer surface (OS). These positions differ in geometrical size and energy of adsorbate binding to c-SWNT bundles [11]. At low adsorbate concentrations, quasi-1D chains of admixture atoms/molecules are formed in the IC- and G-sites. One or several layers of atoms/molecules adsorbed at the OS of the c-SWNT bundle form quasi-2D or quasi-3D systems. The 1D, 2D, and 3D systems have different properties at low temperatures [12–19]. Physical properties (adsorption, thermal, and structural) of simple gas admixtures deposited in c-SWNT bundles were investigated in experimental and theoretical works [5, 6, 9–11, 15, 20–39].

The heat capacity of ^{4}He adsorbed on c-SWNT bundles was investigated at temperatures below 6 K [6, 33]. It was observed [6] that the heat capacity of the adsorbed helium exhibited the behavior of 1D and 2D structures depending on the technique of sample preparation (laser evaporation or arc discharge). Structures of ^{4}He adsorbates in the grooves and at the OS of c-SWNT bundles were studied by the neutron diffraction method [18]. At low coverage, the ^{4}He atoms formed a 1D single line lattice along the grooves. As the concentration of the adsorbed helium atoms increased,

V. V. Sumarokov (✉) · M. I. Bagatskii · M. S. Barabashko
B.Verkin Institute for Low Temperature Physics and Engineering of the National Academy of Sciences of Ukraine, 47 Lenin Ave., Kharkov, 61103, Ukraine
e-mail: sumarokov@ilt.kharkov.ua

O. Fesenko, L. Yatsenko (eds.), *Nanocomposites, Nanophotonics, Nanobiotechnology, and Applications,* Springer Proceedings in Physics 156,
DOI 10.1007/978-3-319-06611-0_15,

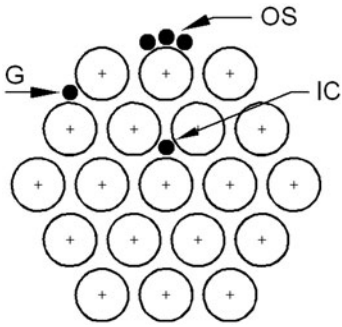

Fig. 15.1 Possible sites of adsorption of relatively small impurity atoms or molecules in a c-SWNT bundle

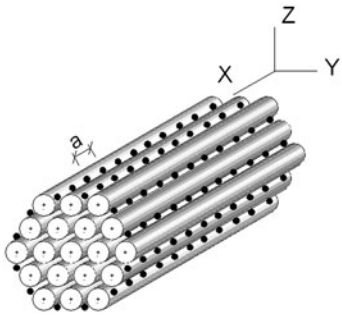

Fig. 15.2 One-dimensional chains of adsorbate in the outer grooves of a c-SWNT bundle; *a* is the distance between the nearest neighboring adatoms/admolecules in the chain

a 2D monolayer was formed, which covered the whole c-SWNT bundle surface [18]. Antsygina et al. [29–31] suggested a rigorous thermodynamic model describing the multilayered atomic adsorbate in grooves, interstitials, and external surface of bundles. The model [30, 31] based on a proper account of the temperature-dependent adsorbate redistribute between 1D, 2D, and 3D subsystems made it possible to explain on a quantitative level the adsorption isotherms and isosteric heat of ^{4}He deposited on the bundles [29, 33]. The thermodynamic research on the neon films adsorbed by HiPCo c-SWNT bundles was carried out experimentally in ref. [40]. However, the behavior of the 1D chains of the adsorbed gas in the grooves on the OS of the bundles has not been given enough attention in this work. The radial thermal expansion coefficient (α_r) of c-SWNT bundles saturated with both Xe atoms and N_2 molecules to a rather high concentration were measured in refs. [32, 38]. Authors [32, 38] observed features in the curves α_r—maxima in the vicinity of 60 K (for Xe) and 28 K (for N_2), which are associated with spatial redistribution of the Xe atoms and N_2 molecules, respectively, at the surface c-SWNT bundles.

The 1D chains of adsorbate in the grooves at the OS of a c-SWNT bundle are shown schematically (one in each groove) in Fig. 15.2.

Low-temperature dynamics of inert gas atoms and methane molecules in c-SWNT bundles were considered in theoretical studies [41–43]. The calculated heat capacities of 1D chains of inert gas atoms and methane molecules adsorbed physically in the

grooves of c-SWNT bundles are reported in refs. [41] (Ar, Kr, Xe) and [42] (Ne, CH_4).

To our knowledge, no experimental investigations of the heat capacity of c-SWNT bundles containing 1D chains of adsorbed both classical inert gas atoms (Ar, Kr, Xe) and simple biatomic molecules have been reported so far.

Our goal was to investigate the low-temperature heat capacity of the quasi-1D chains of atomic and molecular adsorbates in the outer grooves of c-SWNT bundles using xenon atoms and N_2molecules. The choice of the adsorbate was dictated by the following reasons. First, physical adsorption of Xe atoms/N_2 molecules is possible only in the grooves and at the OS of c-SWNT bundles. Adsorption in the IC is prohibited because of the relationship between the geometrical sizes of channels and Xe atoms/N_2 molecules [27]. Second, the binding energy of both Xe atoms and N_2 molecules is higher in the grooves than at the OS [11, 23] and Xe atoms/N_2 molecules are physically adsorbed primarily of all in the grooves where they form 1D chains (see Fig. 15.2).

15.2 Experiment

The heat capacities of quasi-1D chains of Xe atoms and N_2 molecules adsorbed in the outer grooves of c-SWNT bundles have been first measured at a temperature range from 2 to 60 K using an adiabatic calorimeter [44].

A cylindrical sample of c-SWNT bundles (7.2 mm high, 10 mm in diameter, and of 1.27 g/cm^3 density) was prepared by compressing c-SWNT plates under the pressure 1.1 GPa. The plates ($\sim$ 0.4 mm thick) were obtained by compacting a c-SWNT powder ("cheap tubes") under $P = 1.1$ GPa [45]. The powder was prepared by chemical catalytic vapor deposition (CVD). It contained more than 90 wt% of c-SWNT bundles, other allotropic forms of carbon (fullerite, multiwalled nanotubes, and amorphous carbon) and about 2.9 wt% of cobalt catalyst. The average tube diameter in the sample was 1.1 nm; the average length of the c-SWNT bundles was 15 μm [45]. The number of nanotubes in the bundles varied within 100–150 (estimated from high-resolution TEM pictures) and was equal to, on an average, 127. The mass of the c-SWNT bundles sample was equal to 716.00 ± 0.05 mg.

The temperature of the calorimeter was measured with a calibrated CERNOX resistance thermometer (Lake Shore Cryotronics).

First, the addenda heat capacity C_{ad} (the heat capacity of calorimeter with an inserted sample of pure c-SWNT bundles) was measured in a separate experiment. Then the calorimeter with sample was warmed to room temperature. The c-SWNT bundles were saturated with Xe directly in the calorimeter cell. The vacuum cavity of the calorimeter was filled with Xe gas: $3.19 \cdot 10^{-4} \pm 5 \times 10^{-6}$ mole. The ratio is $N_{Xe}/N_C \approx 0.55\,\%$, where N_{Xe}, N_C is the number of Xe and C atoms in the SWNT sample, respectively. The quantity of Xe was estimated by the *PVT* method. The chemical purity of xenon was 99.98 % (0.01 % N_2, 0.01 % Kr).

The calorimeter was cooled from room temperature to 90 K for 8 h. During this period, Xe atoms were being adsorbed in the c-SWNT bundles. For the geometrical reason, Xe atoms cannot penetrate into the IC [27] under low pressure. Since the binding energy of Xe atoms is higher in grooves than at the OS [11, 23], the Xe atoms are physically adsorbed first of all in the grooves where they form 1D chains. After cooling of the calorimeter from 90 K to helium temperatures (during 5–6 h), the sample was thermo cycled (about 1 K heating–cooling) several times and then the heat capacity was measured. The heat capacity measurement runs were made from the lowest temperature of the run up to 60 K. After each measurement series up to 60 K, the sample was heated to 80 K and then, after a slow cooling down to helium temperature and thermo cycling, the measurement was repeated. Several measurement runs were made.

The heat capacity of quasi-1D chains of N_2 molecules adsorbed in the outer grooves of c-SWNT bundles was studied after measuring the heat capacity of c-SWNT bundles with 1D chains of Xe atoms. Before starting the experiment, the vacuum chamber of the calorimeter with a c-SWNT bundle sample at room temperature was washed several times with pure N_2 gas and the sample stayed in dynamic vacuum ($\sim 5 \times 10^{-3}$ Torr) for about 12 h. Then test measurement of the "addenda" heat capacity was performed. The results coincided with previous "addenda" data.

After completing the "addenda" measurement, procedure of saturation of the c-SWNT bundles with N_2 molecules, cooling, and heat capacity measurement was made as an analogical procedure as for Xe case. The c-SWNT bundles were saturated with N_2 directly in the calorimeter cell as in the case with Xe. The vacuum cavity of the calorimeter was filled with N_2 gas: $3.81 \cdot 10^{-4} \pm 6 \times 10^{-6}$ mole. The chemical purity of N_2 was 99.997 % ($O_2 \leq 0.003$ %).

Our estimation of admixture gas quantity shows that both Xe and N_2 gas are sufficient for complete occupancy of the grooves.

The results of different measurement runs for both Xe and N_2 coincided within the measurement error. Other experimental features have been reported elsewhere [44, 46–48].

15.3 Results and Discussion

Figure 15.3 demonstrates low-temperature dependencies of the total heat capacity C_{ad+Xe} and its addenda component C_{ad}. It is interesting that the introduction of only 5–6 Xe atoms per 1000 carbon atoms causes a significant increase in the heat capacity in the whole temperature range of the experiment. For example, the ratio $(C_{ad+Xe}\text{-}C_{ad})/C_{ad} \approx 160$ % and ≈ 20 % at T = 2.6 K and at 30 K, respectively. The contribution C_{Xe} of quasi-1D chains of xenon atoms adsorbed in the outer grooves of c-SWNTs to the total heat capacity C_{ad+Xe} has been separated by subtracting the heat capacity of the addenda from the total heat capacity C_{ad+Xe}.

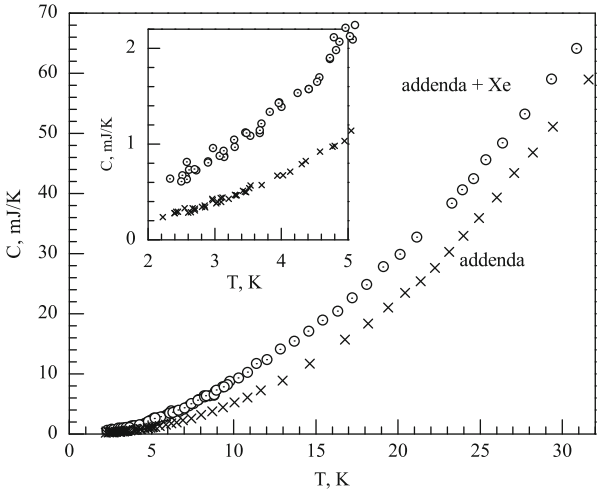

Fig. 15.3 Experimental temperature dependencies of the total heat capacity C_{ad+Xe} and its component C_{ad}

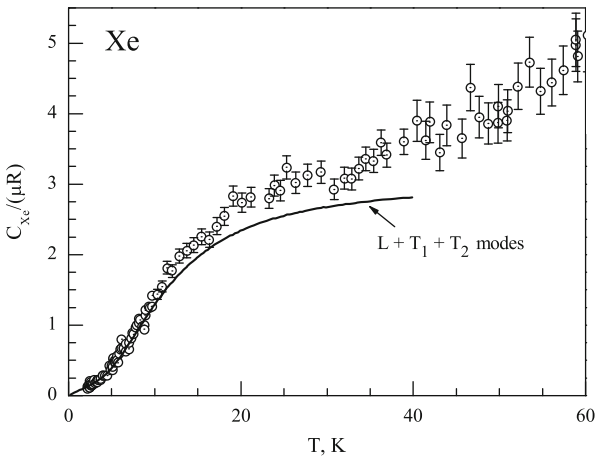

Fig. 15.4 The heat capacity of 1D chains of Xe atoms adsorbed in the outer grooves of c-SWNT bundles. Experiment: *open circles*. Theory [41]: *solid curve* for the L + T_1 + T_2 modes

Random error in the C_{Xe}-value is within 20 % at 2.2 K, 5 % at the temperature region 10–30 K, and about 10 % near 60 K. The systematic error is mainly contributed by inaccuracies concerning the number of SWNTs.

Figure 15.4 demonstrates the $C_{Xe}(T)$ in the coordinates $C_{Xe}(T)/(\mu R)$, where μ is the number of Xe atoms (in moles) and R is the gas constant. For comparison, Fig. 15.4 includes a theoretical temperature dependence of the heat capacity of 1D chains of Xe atoms adsorbed physically in the grooves at the OS of c-SWNT bundles [41].

It is seen in Fig. 15.4 that below 8 K the experimental and theoretical [41] curves of heat capacity C_{Xe} are close. According to the Šiber theory [41], below 4 K the heat capacity is influenced mainly by the longitudinal mode L and is proportional to temperature. Above 4 K, the transverse optical modes T_1, T_2 begin to take effect.

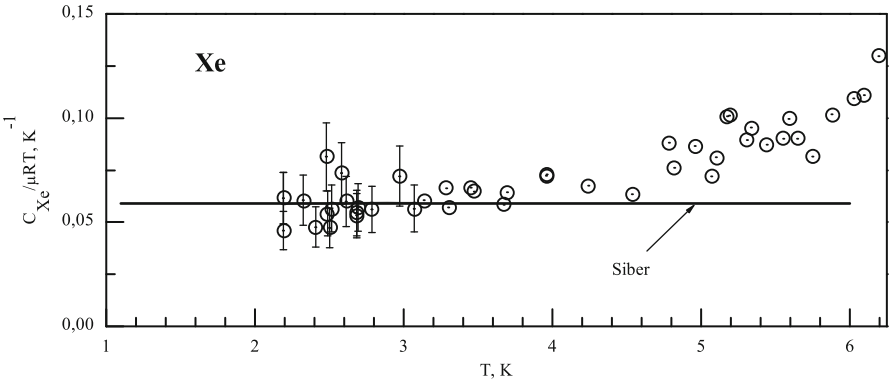

Fig. 15.5 The dependence of $C_{Xe}/\mu RT$ *vs.* T: *circles*—experiment, *straight line*—theoretical low-temperature asymptotics of the heat capacity of the longitudinal mode of the chains of Xe adatoms [41]

Fig. 15.5 illustrates the low-temperature part of heat capacity C_{Xe} in coordinates $C_{Xe}/\mu RT$ *vs.* T. The straight line in Fig. 15.5 shows the theoretical low-temperature heat capacity of the chain of Xe adatoms caused by the longitudinal mode L [41]. It is seen that below ≈ 4 K the experimental dependence of C_{Xe} is close to the predicted straight-line characteristic for the low-temperature heat capacity of 1D chains. Above 4 K, the experimental points start deviating from this line. Using the formula (13) from ref. [41], we estimated both the phonon frequency of the longitudinal mode $\hbar\omega_L \approx 3.1$ meV which is close to the theoretical value 3.06 meV [41] and the Debye temperature $\theta_{D,L} \approx 35.7$ K of 1D chains. There is good agreement between theoretical (35.5 K [41]) and experimental (35.7 K) Debye temperatures of 1D Xe chains.

At $T > 8$ K, the experimental curve $C_{Xe}(T)$ starts to exceed the theoretical one [41] and the excess increases monotonously with the rising temperature. We assume that the excess caused mainly by both the increase of the distance between the nearest neighboring xenon atoms in the chains with increasing temperature and the occurrence of thermal activated vacancies in the 1D chains of the xenon atoms due to spatial redistribution above about 30 K. Analysis of the contribution of thermal activated vacancies in the heat capacity of 1D chains of Xe adatoms will be reported elsewhere.

Šiber [41] suggested that the heat capacity of 1D chains of inert gas atoms adsorbed physically in the grooves of c-SWNT bundles could be calculated using a simple model in which for simplicity author assumes that the substrate is rigid, ignores the discrete structure of the tubes surrounding a groove, and neglects all the interactions between the adsorbates which are not in the same groove. It should be noted that the absolute minimum (-225 meV) of external potential for Xe atom in the groove [41] is higher than the experimental binding energy (-282 ± 11 meV) [11]. These values are an order of magnitude bigger than the binding energy of the adsorbate–adsorbate [41]. He calculated the temperature dependencies of heat capacity of 1D chains of inert gas adsorbates (Ar, Kr, Xe) in interval 2–40 K [41]. Similar results on the heat

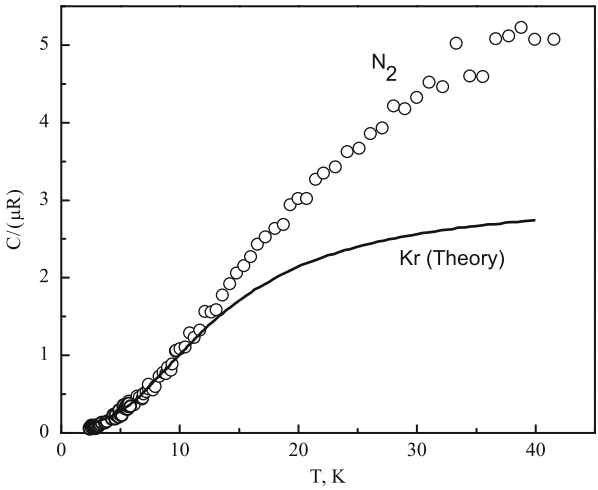

Fig. 15.6 The heat capacity of 1D chains of N_2 molecules adsorbed in the outer grooves of c-SWNT bundles. Experiment: *open circles*. Theory for 1D chains of Kr adatoms [41]: *solid curve* for the $L + T_1 + T_2$ modes

capacity of the chains of Ne atoms and CH_4 molecules adsorbed physically in the grooves of c-SWNT bundles were obtained in a theoretical study [42].

There is surprisingly good agreement between the theoretical predictions and experimental results despite significant simplification in the theoretical model [41] and possible deviations from the ideal object.

The discrete structure of nanotubes has little effect on the transverse modes of Xe atoms beyond the center of the Brillouin zone [43], but the longitudinal mode is more sensitive to the parameters of the models and the chain density.

Notice that saturation of c-SWNT bundles by 5–6 N_2 molecules per 1000 carbon atoms causes a significant increase in the heat capacity over the whole temperature range. The ratio C_{ad+N2}/C_{ad} is equal to about 1.6 at $2\ \mathrm{K} < \mathrm{T} < 15\ \mathrm{K}$ and decreases to ~ 1.2 at 40 K. The contribution C_{N2} of nitrogen 1D chains to the total heat capacity C_{ad+N2} was separated by subtracting C_{ad} from C_{ad+N2}. Figure 15.6 shows the normalized experimental heat capacity ($C_{N2}/(\mu\mathrm{R})$, where μ is the number of the nitrogen moles and R is the gas constant) of the 1D chains of N_2 molecules adsorbed in outer grooves of c-SWNT bundles at $T = 2$–40 K. To our knowledge, no theoretical calculations of the heat capacity of 1D chains of N_2 molecules adsorbed in the outer grooves of c-SWNT bundles have been reported so far. So, for comparison, a theoretical curve of the molar heat capacity $(C_V/R)_{Kr}$ of the 1D chains of Kr atoms adsorbed in grooves of cSWNT bundles [41] is added into Fig. 15.6. It is seen (Fig. 15.6) that the experimental heat capacity of nitrogen 1D chains $C_{N2}/(\mu\mathrm{R})$ and the theoretical phonon heat capacity of krypton $(C_V/\mathrm{R})_{Kr}$ [41] are close below 8 K. Thus, below 8 K the heat capacity of the 1D nitrogen chains in the grooves is influenced predominantly by the phonon modes.

The phonon heat capacity C_V of physically adsorbed 1D chains of Ar, Kr, Xe [41], and Ne [42] atoms and CH_4 molecules [42] in outer grooves is determined by the longitudinal acoustic L and two transverse optical T_1, T_2 modes.

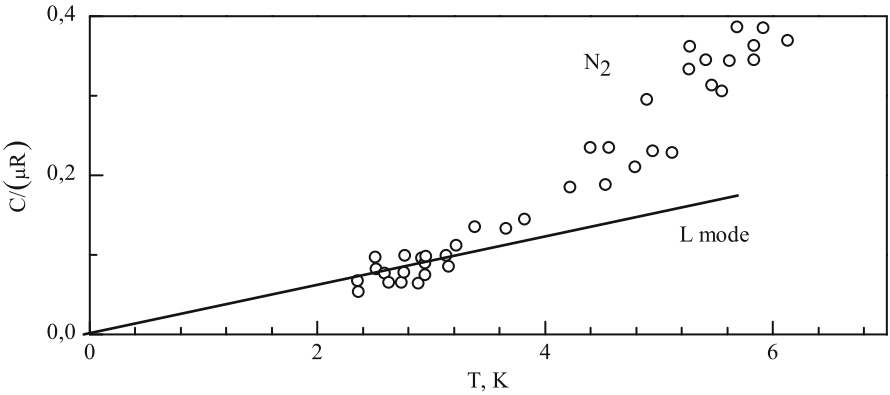

Fig. 15.7 The low-temperature part of the heat capacity of 1D chains of N_2 molecules adsorbed in the outer grooves of c-SWNT bundles. *Open circles*—experiment; the *straight line* shows low-temperature behavior of the heat capacity of the longitudinal mode L of the 1D chains of N_2 admolecules

Figure 15.7 demonstrates the low-temperature part of $C_{N2}/(\mu R)$ below 6 K. The straight line in Fig. 15.7 demonstrates the linear behavior of the specific heat $C_{N2}/(\mu R)$ of 1D chains of N_2 molecules below 4 K. We estimated both the highest Brillouin zone edge frequency of the longitudinal mode $\hbar\omega_L \approx 5.2$ meV and the Debye temperature $\theta_{D,L} \approx 60$ K of 1D chains using the formula (13) from ref. [41] like in the Xe case. The Debye temperature of 1D nitrogen chains is bigger than of Xenon chains.

Above 8 K, the temperature dependence of the heat capacity of chains of N_2 molecules $C_{N2}(T)/(\mu R)$ is steeper than that of Kr atoms $(C_V(T)/R)_{Kr}$[41] (see Fig. 15.6). At higher temperatures, the difference $\Delta C = C_{N2}(T)/(\mu R) - (C_V(T)/R)_{Kr}$ between the heat capacities of the N_2 and Kr chains increases monotonically. It is reasonable to assume that above 8 K the difference ΔC is due to both a contribution of orientational vibrations of the N_2 molecules (librons) and thermal expansion of chains.

The experimental curves of the temperature dependence of heat capacity of Xe atom and N_2 molecule chains adsorbed in the outer grooves are compared in Fig. 15.8. The dependences are qualitatively similar below 12 K. Above 18 K, the experimental curve $C_{N2}(T)$ exceeds the curve C_{Xe}. This difference is caused mainly by the contribution of orientational vibrations of the N_2 molecules.

15.4 Conclusions

The heat capacity of quasi-1D chains of both Xe atoms and N_2 molecules adsorbed in the outer grooves of the c-SWNT bundles has been first investigated in the temperature range 2–60 K. In the case of Xe chains, the experimental and theoretical data

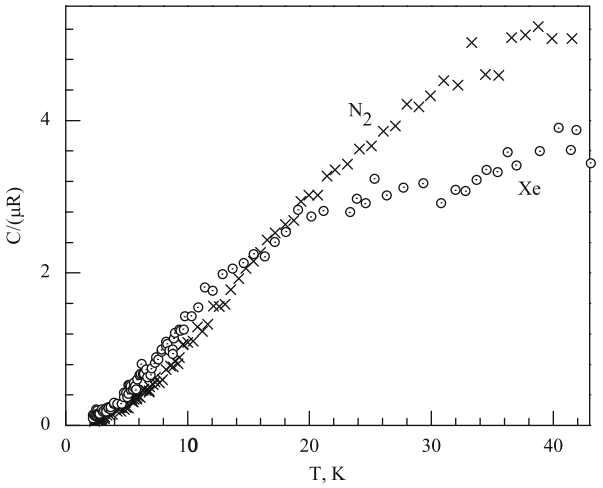

Fig. 15.8 The temperature dependencies of the heat capacity of 1D chains both Xe atoms and N_2 molecules adsorbed in the outer grooves of c-SWNT bundles

are close below 8 K. Observed at higher temperatures, the discrepancy between the experimental and theoretical heat capacities could be mainly due to both the increase of the distance between the nearest neighboring atoms in the chains with increasing temperature and the occurrence of thermal activated vacancies in the 1D chains of the xenon atoms due to spatial redistribution above about 30 K.

Below 8 K, the heat capacity of the 1D nitrogen chains in the grooves is influenced predominantly by the phonon modes. Above 8 K, contribution of orientational vibrations of the N_2 molecules becomes significant.

Above 18 K, the discrepancy between the experimental heat capacities of nitrogen and Xe chains could be mainly due to orientational vibrations of the N_2 molecules.

The Debye temperatures of quasi-1D chains of adsorbates (35.7 K for Xe, 60 K for N_2) were estimated.

Acknowledgments The authors are grateful to V. Manzhelii, Yu. Freiman, M. Strzhemechny, S. Feodosyev, and K. Chishko for helpful discussions.
Electronic address: sumarokov@ilt.kharkov.ua

References

1. Iijima S (1991) Nature 354:56
2. Saito R, Dresselhaus MS, Dresselhaus G (eds) (1998) Physical properties of carbon nanotubes. Imperial College Press, London
3. Dresselhaus MS, Eklund PC (2010) Adv Phys 49:705
4. Trasca RA, Kostov MK, Cole MW (2003) Phys Rev B 67:035410
5. Teizer W, Hallock RB, Dujardin E, Ebbesen TW (1999) Bull Am Phys Soc 44(1):519; Phys Rev Lett 82:5305 (1999);. Phys Rev Lett 84:1844 (2000)
6. Lasjaunias JC, Biljaković K, Sauvajol JL, Monceau P (2003) Phys Rev Lett 91:025901
7. Calbi MM, Toigo F, Cole MW (2001) Phys Rev Lett 86:5062

8. Diallo SO, Fåk B, Adams MA, Vilches OE, Johnson MR, Schober H, Glyde HR (2009) Eur Phys Lett 88:56005
9. Antsygina TN, Poltavsky II, Chishko KA, Wilson TA, Vilches OE (2005) Low Temp Phys 31:1007
10. Ancilloto F, Barranco M, Pi M (2003) Phys Rev Lett 91:105302
11. Zambano AJ, Talapatra S, Migone AD (2001) Phys Rev B 64:075415
12. Bagatskii MI, Barabashko MS, Dolbin AV, Sumarokov VV (2012) Low Temp Phys 38:523
13. Benedict LX, Louie SG, Cohen ML (1996) Solid State Commun 100:177
14. Hone J, Batlogg B, Benes Z, Johnson AT Fischer JE (2000) Science 289:1730
15. Calbi MM, Cole MW (2002) Phys Rev B 66:115413
16. Šiber A (2003) Phys Rev B 67:165426
17. Tu ZC, Ou-Yang ZC (2003) J Phys Condens Matter 15:6759
18. Pearce JV, Adams MA, Vilches OE, Johnson MR, Glyde HR (2005) Phys Rev Lett 95:185302
19. Full SJ, McNutt JP, Cole MW, Mbaye MT, Gatica SM (2010) J Phys Condens Matter 22:334206
20. Šiber A (2002) Phys Rev B 66:205406
21. Simonyan VV, Johnson JK, Kuznetsova A, Yates JT (2001) J Chem Phys 114:4180
22. Hertel T, Kriebel J, Moos G, Fasel R (2001) AIP Conf Proc 590:181
23. Ulbricht H, Kriebel J, Moos G, Hertel T (2002) Chem Phys Lett 363:252
24. Cole MW, Crespi VH, Stan G, Ebner C, Hartman JM, Moroni S, Boninsegni M (2000) Phys Rev Lett 84:3883
25. Stan G, Bojan MJ, Curtarolo S, Gatica SM, Cole MW (2000) Phys Rev B 62:2173
26. Shai DE, Urban NM, Cole MW (2008) Phys Rev B 77:205427
27. Talapatra S, Zambano AZ, Weber SE, Migone AD (2000) Phys Rev Lett 85:138
28. Eletskii AV (2009) Phys Usp 52:209; Phys Usp 50, 225 (2007); Phys Usp 47, 1119 (2004)
29. Antsygina TN, Poltavsky II, Chishko KA (2006) Phys Rev B 74:205429
30. Antsygina TN, Poltavsky II, Chishko KA (2007) J Low Temp Phys 148:821
31. Antsygina TN, Poltavsky II, Chishko KA (2005) J Low Temp Phys 138:223
32. Dolbin AV, Esel'son VB, Gavrilko VG, Manzhelii VG, Popov SN, Vinnikov NA, Danilenko NI, Sundqvist B (2009) Low Temp Phys 35:484
33. Wilson T, Vilches OE (2003) Low Temp Phys 29:732
34. Talapatra S, Migone AD (2001) Phys Rev Lett 87:206106
35. Talapatra S, Migone AD (2002) Phys Rev 65:045416
36. Talapatra S, Krungleviciute V, Migone AD (2002) Phys Rev Lett 89:246106
37. Weber SE, Talapatra S, Journet C, Zambano A, Migone AD (2000) Phys Rev B 61:13150
38. Dolbin AV, Esel'son VB, Gavrilko VG, Manzhelii VG, Popov SN, Vinnikov NA, Sundqvist B (2010) Low Temp Phys 36:365
39. Manzhelii EV, Gospodarev IA, Feodosyev SB, Godovanaja NV (2012) In 9th international conference on cryocrystals and quantum crystals (CC2012), Odessa, p 63
40. Ramachandran S, Vilches OE (2007) Phys Rev B 76:075404
41. Šiber A (2002) Phys Rev B 66:235414
42. Kostov MK, Mercedes Calbi M, Cole MW (2003) Phys Rev B 68:245403
43. Cvitaš MT, Šiber A (2003) Phys Rev B 67:193401
44. Bagatskii MI, Sumarokov VV, Dolbin AV (2011) Low Temp Phys 37:424
45. Dolbin AV, Esel'son VB, Gavrilko VG, Manzhelii VG, Vinnikov NA, Popov SN, Sundqvist B (2008) Low Temp Phys 34:678
46. Bagatskii MI, Barabashko MS, Dolbin AV, Sumarokov VV, Sundqvist B (2012) Low Temp Phys 38:527
47. Bagatskii MI, Manzhelii VG, Sumarokov VV, Barabashko MS (2013) Low Temp Phys 39:618
48. Bagatskii MI, Barabashko MS, Sumarokov VV (2013) Low Temp Phys 39:441

Part III
Nanobiotechnology

Chapter 16
About Some Physical Properties of Water in Nanosystems and the Possible Mechanism of Superconductivity Induction by Water in Compounds $SrFe_2As_2$ and $FeTe_{0,8}S_{0,2}$

Ludmila Stepanovna Martseniuk, Aleksandr Stepanovich Martseniuk and Michail Vasilievich Kurik

16.1 Introduction

The researches of the water which have been carried out in a number of laboratories have shown that usual water is not a homogeneous medium, and will consist of two fractions distinguished on the properties. Rontgen W. K has come to such conclusions while investigating the properties of water with the application of X-ray radiation in the laboratory.

These results deny the standard concepts according to which water represents some intermediate state between solid and gaseous phases. Physical properties of water under the standard concept are determined in a stationary regime by static short-range forces of interaction, whence follows, that water should represent a homogeneous medium. Many researchers still adhere such a point of view.

Essential advance in the development of a new view on essence of the phenomena in the water medium has been carried out due to two remarkable discoveries: to experimental detection of effect SPE (the effect, titled by the name of researchers: Sinitsin NI, Petrosjan VI, Elkin VA for the first time received the spectra of resonant interaction of millimeter waves with water and biological environments) [1] and to a theoretical prediction of existence of coherent regions (coherent domains) in the water system [2]. Results of these works well supplement each other, but differ in theoretical interpretations. A suitable object for verification of the put forward in [1–2] positions is the water in a special state–the nanowater.

Nanowater is present in molecular formations of cellular systems, capillaries, membranes, etc., as an adjoining layer of these systems, finding out surprising properties and determining all vital processes.

L. S. Martseniuk (✉)
Institute of Nuclear Researches NAS Ukraine, 03680, Prospect Nauky 47, Kiev, Ukraine
e-mail: prolisok77@yandex.ua

A. S. Martseniuk
National University of Food Technology, Vladimirskaya, 68, Kiev 601, Ukraine

M. V. Kurik
Institute of physics NAS Ukraine, 03028, Prospect Nauky 46, Kiev, Ukraine

O. Fesenko, L. Yatsenko (eds.), *Nanocomposites, Nanophotonics, Nanobiotechnology, and Applications,* Springer Proceedings in Physics 156,
DOI 10.1007/978-3-319-06611-0_16,

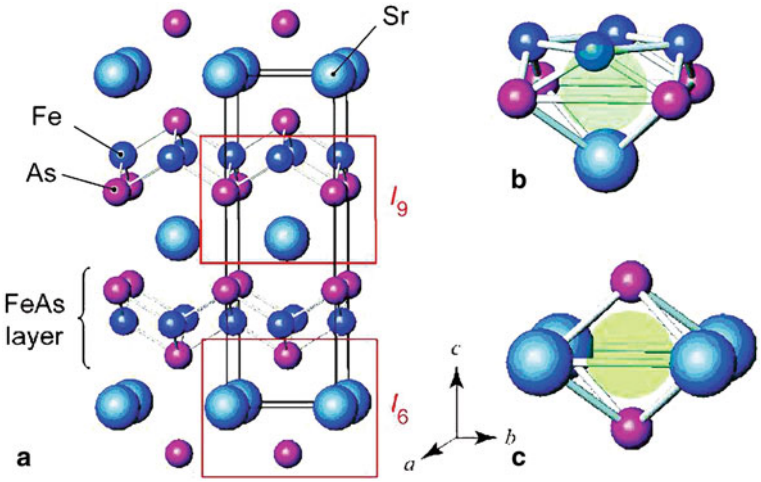

Fig. 16.1 **a** Crystalline structure of $SrFe_2As_2$. The *box* indicates the unit cell. **b**, **c** Expanded views of the interstitial sites I_9, which is surrounded by four As, four Fe and one Sr (**b**), and I_6, which is surrounded by four Sr and two As (**c**). (Taken from [4])

Features of water, adjoining to surfaces of solid systems, so-called exclusion zone (EZ) water, from a position of quantum electrodynamics are investigated in work [3]. It is shown that the positions, developed within the framework of such approach, completely describe experimentally observable phenomena. Therefore, it is of interest to expand this description and on such systems, where water is located as one or several layers (the quasi-two-dimensional systems). We shall note that recent openings of effect of superconductivity induction by water in compounds $SrFe_2As_2$ and $FeTe_{0,8}S_{0,2}$ [4, 5] (where the diffused water takes place the quasi-two-dimensional layers) still do not have satisfactory theoretical interpretation. Revealing the essence of this phenomenon is very important not only for physics of superconductivity but also for understanding of the role of water in functioning living organisms.

16.2 Appearance of Superconductivity in Compounds $SrFe_2As_2$ and $FeTe_{0,8}S_{0,2}$ Under Influence of Water Diffused in them

Compounds $SrFe_2As_2$ and $FeTe_{0,8}S_{0,2}$ [4, 5] belong to layered ferriferous materials, a perspective for creation on their basis of high-temperature superconductors.

In work [4], the data of detection for the first time of superconductivity at diffusion of water in epitaxial thin film of undoped $FeTe_{0,8}S_{0,2}$ (thickness ~ 200 of w are published, the scheme of crystalline structures, Fig. 16.1) are presented.

As it is underlined in [4], $FeAs$-layers of $SrFe_2As_2$, similar to structure layers of other superconducting ferriferous compounds, are formed from $FeAs_4$-tetrahedrons

and play a determining role in the mechanism of formation of a superconducting state. These compounds in the undoped state have the phase transition accompanying structural transition in the antiferromagnetic phase, but in a state of superconductivity without doping or compression do not pass.

The $SrFe_2As_2$-compound, doped with cobalt, attains superconductivity at $T_c = 20$K. Undoped epitaxial thin films pass to an antiferromagnetic phase at $T_{ant} = 204$ K and at exposition in the atmosphere of environment at $T_c = 25$K find out the transition to superconductivity.

Based on the additional researches carried out by them, authors [4] have shown that only the vapors of water, diffused in a film of $SrFe_2As_2$ from an atmosphere, can induce a transition of undoped film to a superconducting state.

Researches of properties of $SrFe_2As_2$-epitaxial films, containing diffused water molecules, have revealed that these films have also other distinctions from the samples doped by cobalt.

First, strong anisotropy properties of these films in a magnetic field are found out, unlike film, doping by cobalt (the last demonstrates almost isotropic behavior). So, the value of temperature of the superconducting transition made $T_c \leq 7$ K for H//C and ≤ 16 K for H//a, at a size of magnetic field H ≈ 9 T.

In the opinion of authors [4] this means that the upper critical field is higher than 9 T and that T_c is more sensitive to H//C than to H//a.

Second, embedding of water in the crystalline structure of a film leads to the compression of a film in a direction of an axis C, instead of an expansion as it would be necessary to expect, proceeding from prospective possibilities of its disposition in crystalline structure.

Authors suppose, that molecules of water can be incorporated in the sites designated as I_6 or I_9, but, proceeding from the sizes of atom of oxygen and geometry of a disposition of sites, the most probable is incorporation of atoms of oxygen in the sites designated as I_9.

On the basis of preliminary calculation, authors indicate that the lattice in a direction of an axis C should have some expansion at such incorporation, instead of compression. However, its thickness has decreased up to 190 nm.

The third difference is an appearance of a certain amount of an impurity Fe_2As-phase which is found out at the X-ray structural analysis. Taking into account that there are no literary data on the existence of transition in a superconducting state for Fe_2As, authors [4] consider that the principal cause of occurrence of superconducting transition is connected to the compression of a lattice, occurring at diffusion of water that is equivalent to exhibit the pressure, instead of appearance of an additional Fe_2As-phase. They come to this conclusion on the basis of the message data that the application of the external pressure leads to the origin of superconductivity with T_c, achieved at 35–38 K. However, achieving superconductivity in such a way a reduction of value $T_{crt.}$ of antiferromagnetic transition at increased pressure is observed. For films $SrFe_2As_2$, containing diffused water, a value $T_{crt.}$ is the same, as well as for the just received samples, and T_c has a smaller value than at application of pressure. It means that the mechanism of occurrence of superconducting transition at embedding of water is another than at external compression.

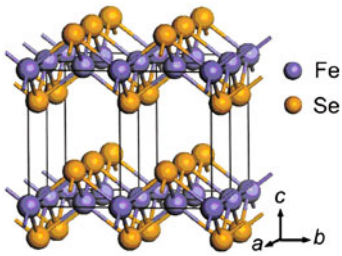

Fig. 16.2 The crystalline structure of $FeSe$. Shown are atoms of iron (*orange colors*) and arsenic (*blue*). (Taken from stonebrakerdesignworks.com)

We shall notice that by virtue of feature of site I_9 structure, molecules of water can occupy both the individual layers, oriented by a disposition of I_9, and double layers (the second layer settles down under the first and it is separated from the first by Sr). The presence of an impurity Fe_2As- of a phase, probably, testifies to such disposition of water layers, since molecules of water incorporated in places, oriented by a site I_9, can displace two molecules of iron from the initial position.

Authors [4] though consider that the main mechanism, resulting in superconductivity, is a compression; however, they do not exclude the other possibilities, for example, the possibility of the origin a subproduct of reactions between $SrFe_2As_2$ and H_2O. It in their opinion, will lead to an interesting discovery, as any other phases except of Fe_2As, $FeAs$, and the amorphous phase has not been fixed by X-ray measurements, but any one of these phases is not a superconductor.

Thus, any of the supposed reasons of origin of superconductivity in the compound $SrFe_2As_2$ are not satisfactory, and authors [4] also could not specify the reason of a lattice compression occurrence.

The induction of superconductivity in $SrFe_2As_2$ did not appear to be a unique phenomenon, such as the effects found out by authors [5] and for compounds $FeTe_{0,8}S_{0,2}$.

The crystalline structure of the compound $FeTe$ is similar to the structure of the compound $FeSe$, shown in Fig. 16.2.

Though the crystal structure $FeSe$ also does not contain intermediate planes, magnetic and superconducting characteristics of this compound are similar to other ferriferous superconductors. It confirms the assumption of researchers of these structures that the basic processes resulting to superconductivity occur in two-dimensional ferriferous planes.

Authors [6] carry out a comparison of properties of not doped $FeSe$ and $FeTe$. The temperature of the superconducting transition T_c of compound $FeSe$ (according to various references) is 8 K and depends on applied pressure.

$FeTe$**,** having as well as $FeSe$ tetragonal structure, passes in an antiferromagnetic state at 70 K and is not superconductor.

Magnetic properties of compound $FeTe$ are suppressed by entering of additives of sulfur or selenium. However, for $FeTe_{0,8}S_{0,2}$ grown by a method of solid-state reaction, the diamagnetism, corresponding to superconductivity, is not found out [5]. On curve dependence of resistance on the temperature, submitted by authors [5] for just-grown samples, the break is found out at 8 K, but zero resistance is not

achieved. As the diamagnetic signal is not found out, authors connect this change of resistance not with origin of total superconductivity but only with origin of filamentary superconductivity. The application of hydrostatic pressure does not lead to the superconducting transition of $FeTe_{0,8}S_{0,2}$ polycrystal.

For the $FeTe_{0,8}S_{0,2}$ samples which have lain on air at room temperatures for more than 20 days, a diamagnetic signal corresponding to total transition of compound to superconductivity was found. With the increase in the time of exposition, the signal increased, and resistance, in comparison with virgin samples, decreased. The reduction of resistance is indicative of an increase in density of carriers with an increase in the time of exposition till day 110.

One more essential change of samples at their exposition on air was the compression of a lattice. The following parameters of compression have been specified in work for virgin samples: $a = 3.8114$ (8) and $c = 6.2421$ (21) Å; for exposing on air at room temperature for 200 days, $a = 3.8097$ (8) and $c = 6.2307$ (20) Å.

Authors [5] had carried out the additional researches, similar described in [4], which have revealed that only molecules of water, diffused in samples $FeTe_{0,8}S_{0,2}$, bring the polycrystals of this compound to superconductivity. Authors [5] have not been able to reveal the exact reason of effect of induction by water of superconductivity; however, they put forward some possible variants, indicating herewith, that the mechanism of such an effect for $FeTe_{0,8}S_{0,2}$ polycrystal should be same, as well as for film $SrFe_2As_2$ and, most likely, is connected to observable reduction of the sizes of a lattice.

16.3 About the Nature of Appearance of Superconductivity in Ferriferous Superconductors

As is known [6], the impurity of magnetic materials negatively influence upon parameters of a superconducting state of usual superconductors. It is stipulated by the fact that magnetic impurity possesses its own magnetic moment, which interacts with the magnetic moment of one of Cooper pair electrons and reorients its direction, which destroys the coupled state of pair.

The existence of high-temperature superconducting ferriferous compounds was revealed in 2008 and, despite a huge number of researches, the mechanism of pairing of electrons in these compounds is not opened. The standard theory BKS, created for the description of processes in earlier known superconductive compounds, is not sufficient as it denies the possibility of origin [6] of superconductivity in magnetic materials. Nevertheless, as follows from references, exactly magnetism can be responsible for the unusual mechanism of superconductivity in these compounds.

As the majority of these compounds have phase transition in an antiferromagnetic state, there is an assumption that the antiferromagnetic state precedes superconducting, and they compete among themselves. Usually to suppress an antiferromagnetic state, doping is applied. Compression changes parameters of a crystalline lattice that influences magnetic ordering and also can suppress antiferromagnetism.

The theoretical development of models of high-temperature superconductivity resulted in the appearance of a wide spectrum of various assumptions; however, the theory of origin of superconductivity in these compounds is far from completion.

At first, in connection with discovering new superconductors, the possibility of using the standard theory of electron–phonon interactions for explaining the mechanism of Cooper pair's formation was researched. So, in work [6] it has been shown theoretically that in using the model of electron–phonon interactions, the temperature of transition in a superconducting state for iron chalcogenides, to which pertains and *FeTe*, will not exceed 1 K. Taking into account that the value of critical temperature is much higher, it means that the given compounds belong to superconductors with the unusual mechanism of pairing. In this work, it is also shown that properties of compounds *FeSe, FeTe* H *FeS* are similar by configuration of a Fermi's surface, phonon spectrum, and magnetism with compounds on a basis *FeAs*. Authors consider that superconductivity is caused by spin fluctuations of spin density waves (SDW) type.

In work [6], calculated data about the structure of the Fermi surface are discussed. It is shown that Fermi's surface has a complicated character and consists of a cylindrical electronic section in corners of Brillouin zone and a section of cylindrical hole surfaces in the center of a zone. Such a structure is caused by a quasi-two-dimensional electronic structure of ferriferous superconductors. The further experimental researches, which have been carried out by various methods, have confirmed these calculations.

For estimating the possibility of the electron–phonon mechanism of coupling researches, the isotopic effect in these compounds [7] has been carried out. If takes place in the electron–phonon mechanism, dependence of the critical temperature on mass of an isotope (at replacement of a superconductor isotope) should be inversely proportional to a square root of an isotope mass m, i.e., $T_c \sim 1/m^{\alpha}$, where α= 0.5.

For an estimation of parameter α, one usually uses a more convenient formula:

$$\alpha = -\frac{m}{\Delta m}\frac{\Delta T_c}{T_c}. \tag{16.1}$$

For the compound $Ba_{1-x}K_xFe_2As_2(x = 0{,}4)$ with $T_c = 37K$, the researches of isotopic effect have been carried out and it appears that at replacement of iron ^{56}Fe by an isotope ^{54}Fe, the value α is approximately equal to 0.35. In the opinion of authors, it means that the electron–phonon mechanism of the formation of Cooper pairs is possible, but it is not described by the standard Bardeen, Cooper, and Schrieffer (BCS) theory

One more work [8], also devoted to research of isotopic effect, has not confirmed results of work [7]. They researched about the same polycrystalline compound $Ba_{1-x}K_xFe_2As_2$, and at the isotopic replacement of atoms of iron, it was revealed that though the exponent α differs from zero, it has a negative sign and consists of $\alpha_{Fe} = -0{,}18$. It means that the heavier an isotope of iron, the higher the value of critical temperature.

Based on the above authors [8], proceeding from the received results, believe, that electron-phonon interaction participates in formation of superconductivity, but character of a display of such interaction is complex and is not described by standard

BCS model. Possibilities also vary, when the mechanism of formation of Cooper pairs represents a mix of exchange and electron–phonon interactions.

Interesting in this respect is the already mentioned work [7]. In this work, authors investigated not only the influence of isotopic replacements on T_c but also investigated the changes of the temperature of transition of not doped compounds $BaFe_2As_2$ and $SmFeAsO$ in a state of spin density wave T_{SDW}. It appeared that $\alpha_{SDW} = -\frac{d \ln T_{SDW}}{d \ln m}$ is 0.05 for oxygen and 0.37 for iron. These data directly specify the presence of strong phonon–magnon interactions. In connection with these results, it is necessary to suppose that an isotopic change of value T_c is also caused by the phonon–magnon interaction.

An important point in the mechanism of superconductivity is the establishment of which mechanisms of behavior electrons in the superconducting system of a compound are realized, the mechanism of strong binding according to which electrons can be distinguished or the mechanism of weak binding, when electrons behave as united integers (so-called strongly correlated the Mott's dielectric).

As follows from review's work [9], the most popular standpoint that $FeAs$-systems are weakly correlated systems. However, there are also a number of experimental works whose results do not agree with such a statement. The author [9] in this connection indicates that though a question on whether $FeAs$ are weakly correlated systems or are strong correlated systems remains open, electronic correlations play a certain role in these systems.

The investigations of properties of iron chalcogenides (FeX) have shown, that as well as for compounds such type as AFe_2As_2 (where A = Ca, Sr, Ba), the transition of chalcogenides to a superconducting state is preceded the phase transition to an antiferromagnetic state.

Suppression of an antiferromagnetic state is possible to achieve by doping or compression due to application of external pressure.

Antiferromagnetic ordering in undoped ferriferous superconductors exists as waves of spin density (SDV), which is possible, in the simplified approach, to associate with periodic reduction and increase in electronic spin density. The period of these waves is determined not by the period of a lattice but by properties of magnetic interaction and this state is distinct from a variety of magnetic excitation—spin waves.

As SDW waves rise as result of magnetism in the system, which is caused by exchange interaction, the mechanism of formation of Cooper pairs in these compounds also can have an exchange character.

In the works, where the dynamics of spin excitation [10, 11] on not doped $SrFe_2As_2$ and $BaFe_2As_2$ by methods of neutron diffraction analysis are investigated, it is informed that at low temperatures antiferromagnetic ordering takes place. For $SrFe_2As_2$ [10], it is revealed that the spectrum of magnetic excitations has a gap $\Delta \leq 6{,}5$ meV, above which spin waves are observed. Magnone spectrum spread up to an energy of order 170 meV, essentially exceeding typical frequencies of phonons (40 meV) [11].

Despite a huge quantity of publications on revealing the mechanism of pairing in high-temperature superconductors, there are some unsolved questions. As it was

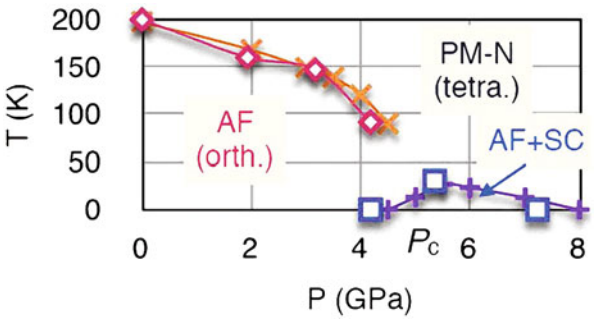

Fig. 16.3 The phase diagram of compound $SrFe_2As_2$ depending on pressure. *Upper curve* divides areas of antiferromagnetic and paramagnetic states; the *bottom curve* outlines area of simultaneous existence of antiferromagnetic and superconducting states. (Taken from [13])

noted in the review [9], there are some unclear questions: "Is 'vicinity' to antiferromagnetism needed for high-temperature superconductivity? Whether antiferromagnetism is a competing phase or does it substantially promote high-temperature superconductivity, for instance, through the replacement of electron–phonon mechanism of pairing by the mechanism, based on spin (antiferromagnetic) fluctuations"? If the author [9] considers that in ferriferous superconductors "a role of electron–phonon interactions, apparently, can be quite significant (isotope effect)," the author of another review [12] asserts "the vicinity to antiferromagnetic ordering in cuprates and $FeAs$-systems stipulates the spin-fluctuating mechanism of the pairing resulting in both cases to high values T_c."

We shall note that for high-temperature superconductors the mechanism of transition to superconducting state can appear even more complex than it was supposed and have a mixed character. This point of view is also confirmed by work [13], where authors investigated influence of pressure on parameters of transition in a superconducting state of $SrFe_2As_2$ monocrystal. This work is interesting and in that relation, that induction by water of superconductivity in $SrFe_2As_2$, as mentioned above, explained by compression of a lattice, which occurs and at application the external pressure.

In this work experimentally by a method of a nuclear magnetic resonance for the first time, the simultaneous existence of two phases—antiferromagnetic and superconducting (Fig. 16.3)—for undoped $SrFe_2As_2$ with the application of external pressure in a diapason 4,2–8 $\Gamma\prod$a has been found.

As can be seen from Fig. 16.3, in the range of 4.2–8 GPa the curves of Neel and phase transition in superconducting state coincide. It means that in this area there is a possible simultaneous existence of superconducting and antiferromagnetic phase.

Such data indicate that antiferromagnetic state and superconducting state can not only compete one with others but also coexist. Besides, these data point to significant role of magnetic interaction (having character of exchange interaction) in realization of the mechanism of superconductivity in this compound.

Authors also note that the effect, observable by them, appears in consequence of formation of nano-dimensional superconducting/antiferromagnetic hybrid structures and this entangled state is a remarkable example of self-organizing of heterogeneous structures in pure systems.

Let us note also that this work [13], to some degree, approximates us and to comprehension of essence of the mechanism induction by water of superconductivity in films $SrFe_2As_2$.

16.4 Modern Physical Views on Properties of Water

According to the theoretical researches described in [2, 3, 14, 15] and other works, usual water in a liquid state is a system consisting of two fractions: the coherent structures, representing individual regions—coherent domains, and not coherent, "classical water," surrounding these regions. Coherent domains are formed owing to resonant interactions of virtual vacuum photons with molecules of water. We shall briefly describe the basic characteristics of these fractions and processes, underlying the basis of their origin, based on the data of works [3, 14, 15] where this description is submitted in the simplified variant.

The condensation of a matter from an ensemble of not coherent molecules of gas from a position of quantum electrodynamics can be related to electromagnetic interaction of these molecules with a vacuum virtual photon. As it is indicated in [3] with reference to [16], the closely packed ensemble of atoms or molecules, which number N, is able to leak out the virtual photons. We shall assume that molecules have only two states, the ground states and excited states; energy of excitation $E = h\nu$ is in the order of 10 эВ. We shall accept a molecule of about 1 Å in size. Then the photon, capable to excite a molecule, should have wavelength $\lambda = c/\nu$ in the order of about 1000 Å. Let the probability of excitation (according to estimations of the authors [3], which have taken for a basis the size of Lamb's shift [3]) be in the order of about 10^{-4}–10^{-5}. The excited molecule can decay, having let out a photon (through a time corresponding to time of decay), which can excite other molecule, or to be the absorbed by vacuum. The relative probability of these two events will depend on the density of the molecules $n = N/\lambda^3$, which are present inside volume λ^3 of a photon. If the density n exceeds the threshold n_{crit} (Equ. 2), the photon will never return in vacuum.

In such a case, the next condition should satisfy:

$$P\lambda^3 n_{crit} = 1, \tag{16.2}$$

where P is the probability of excitation of one molecule by a virtual photon.

Such a process will last until enough amount of photon is trapped and a sizeable electromagnetic field will be built in this region.

This field:

1. Will create attraction among molecules, producing a large increase in density.
2. Will give a common oscillation of all the trapped atoms with common phase for the whole region, named by the author of [3] as coherence domain (CD).

In accordance with the theoretical estimation of the authors of reference [3], made for water, for CD each molecule is coherent oscillated between the ground state,

whose statistical weight is 0.87 and where electrons are closely bound, and the excited state, whose weight is 0.13 and where they are found in a quasi-free state. For $E = 12.06$ эВ, we have, that $\lambda = hc/E = 1000$ Å $= 0.1$ mc and this value corresponds to the size of CD of water.

At formation of coherent domains, there is a reduction of entropy of water system that results to occurrence of such characteristic as energy of transition (energy gap) from a coherent state to not coherent and, according to [3], it means, that energy of a coherent state is lower, than not coherent. As follows from [3], this size becomes 0.26 эВ.

Thermal oscillations in usual water result in the fact that both factions, the coherent and noncoherent, exist in the nonstationary state, but for them, as for superfluid helium, the next expression takes place:

$$F_c(T) + F_{nc}(T) = 1. \tag{16.3}$$

According to [3], Eq. 16.3 determines the total number of molecules in each phase for any time interval, but each molecule passes through two phases continuously. This phenomenon generates a "flickering" regime for the water system. Nevertheless, the situation essentially changed for the water, structured near to solid surfaces (films) [3]; for water, diffused in rocky formation of mountain [17]; for water, bound by biological systems of a living organism; for natural water and for coherency natural water of left and right polarization (where water is close on some parameters to water of living organisms) [18]; for waters in capillaries and in some other cases. For them, the time of existence of the coherent domains is much higher and such domains can form cluster structures in natural water or whole regions of coherence. Memory of water is defined by such properties of water [19]. We shall notice that any external influence on the water environment is fixed by water through change of its internal structure.

As it was specified above, the excited state includes the coherent oscillations with energy 12.06 эВ lying below the energy of the molecule ionization, value of which is at about of 12.60 эВ. Owing to such close disposition of energy of the excited state to energy of ionization in coherent domains, the oscillation of electrons leads to the occurrence of quasi-free electrons in a coherent state. These electrons can easily be released and can participate in chemical transformations and other processes.

The properties of water in both factions, coherent and not coherent, greatly differ.

The SPE effect was described for the first time in work [1] by its authors; they presented the experimental results on the study of water and water-environment of a living organism with using new methods.

The essence of the SPE effect is that the resonance interaction of low intensive (< 10 mcWt/cm^2) of millimeter waves (EHF-diapason) with water and biological environments on frequencies, coincident with frequencies of molecular vibrations of water, is taking place. Such frequencies are named by the authors of the reference as "resonance".

Experimental results of work [1] have confirmed the existence of two phases in the water system.

The water system, as follows from this reference, has in its composition molecular ("ice-like") structures, consisting of cluster's hexagonal formations and the individual water molecules, surrounding these formations. Water molecules in "lusterr's hexagonal" are coupled with hydrogen binding. In a solid phase, as authors [1] indicate, oxygen is tetravalent.

The reveal resonant peaks have a very high quality factor and correspond to the frequency of resonant vibrations of water molecules' hexagonal structures. Peaks of these fluctuations are located in the region of GHz (they correspond to a frequency of 50.3 GHz for radial vibrations and 51.8 GHz for transverse vibrations of chain O-H-hexagonal rings).

The quality factor in a region near to 50 GHz of spectrums, which have been taken off from the water environment of living organisms, is higher than three times, than received at researches of usual water. At treatment of the results authors [12] believe that "the liquid phase of water is not 'the third phase' and represents an associative mix of fragments of molecular structures of its two extreme phases—ice and vapor" though indicated, that water systems of living organisms are in a resonant state. Thus, the "ice-like phase" of waters corresponds in this treatment to a usual solid state.

It is possible to find what the "ice-like phase" is and, to some degree, analyze the behavior of waters in nanosystems.

16.5 About the Reasons of Induction by Water the Superconductivity in Compound $SrFe_2As_2$ and $FeTe_{0,8}S_{0,2}$

As follows from [4, 5], at diffusion of water the compounds $SrFe_2As_2$ and $FeTe_{0,8}S_{0,2}$ essentially change properties and the most substantial change is the transition to the state of superconductivity at low temperatures, which is not found out for just made samples. Besides, as it was indicated above, there are also the structural changes at diffusion of water, one of which is compression of a lattice. Strong anisotropy of properties $SrFe_2As_2$ is found out at applying a magnetic field at low temperatures, which arises for the sample, exposited in air, but does not reveal for doped of cobalt compounds [4]. The reduction of resistance [5] for the samples $FeTe_{0,8}S_{0,2}$, exposed on air for more than 20 days, testifies to the increase in the carrier's density at water diffusion.

A satisfactory explanation of processes, occurring in these compounds, is not found till now; researchers suppose that the main reason of passing to the superconducting state is a compression of lattice, which is equivalent to the application of pressure [4, 5]. But for initial $FeTe_{0,8}S_{0,2}$, the structural transition to a superconducting state is not found out and at application the external pressure, and properties $SrFe_2As_2$ under pressure differ from properties of these compounds at diffusion in their water.

Thus, any explanation put forward, constructed from comparison with properties of other high-temperature ferriferous superconductors, is not satisfactory. One other

possibility remains, to explain the effect of induction on the basis of properties of the water, which are located, as result of diffusion, by single layers, paralleled to basic ferriferous layers.

Unfortunately, it is not known exactly, which one water forms the structures at diffusing in compounds $SrFe_2As_2$ and $FeTe_{0,8}S_{0,2}$, but, nevertheless, the behavior of this two dimension water is possible to predict, having applied to the description of properties of diffusing waters the positions, advanced by J. Preparata in the theory of condensation of water molecules to a liquid state, created by him on the basis of quantum electrodynamics.

In [16], authors have theoretically shown the possibility of leaking out of photons by a closely packed ensemble of atoms or molecules. As it is indicated in this work, it brings to continuous outflow of photons through mirrors of a cavity, even in the absence of an external influence. So, according to the theoretical estimation, resulted in this work, for 104 atoms ^{85}Ru placed in an optical cavity, emission of photons $I = 300\ c^{-1}$ is expected and this settlement value corresponds to experimental data.

Authors [16] also indicated on possible processes of self-organization and the processes of outflow of energy, related to them, which can be caused by the interaction of the system of atoms (molecules) with virtual photons as it occurs in Casimir effect. Pay attention to a possible version of such system behavior in the presence of a dividing barrier and participation of the virtual photons coming from vacuum.

W. Nernst has shown in 1914, that the virtual photon can tune the vibration of identical molecules of the system and that provide arising of common phase of such vibrations in this system. This position is possible to use and for description of the behavior of water molecules, diffusing in crystalline structure of compound $SrFe_2As_2$ and $FeTe_{0,8}S_{0,2}$. Through the diffusing into compounds molecules of water (in accordance with [16]), virtual photons can also leak from a vacuum. At existence of a sufficient transparency of the basic ferriferous layers of compounds in this energy diapason, the molecules of other water layers may be situated in region of interaction with a virtual photon. For this, the probability P of excitation (at a high enough degree of transparency) molecules of water layers, according to the Equ. 2, should be not less than:

$$P_f = 1/\lambda^3 n_w, \tag{16.4}$$

where P_f is the average value of probability of excitation by a photon of water molecule in the volume defined by the size of a photon (~ 1000 Å);

$n_w$is the average density of molecules of water in this volume.

If the ferriferous layer of the basic material (by virtue of some internal processes) greatly absorbs the radiation on frequency of such a virtual photon, then in interaction is included the smaller number of the water layers or it occurs in single water layer only. In the latter case, it does not lead to those effects which, under our assumption, are found out in $SrFe_2As_2$ and $FeTe_{0,8}S_{0,2}$ at diffusion of them in water (partly already at a room temperature, for example, compression of crystalline lattice, the increasing of the concentration of carriers).

The interaction of water molecules with the virtual photon, coming out from vacuum, can lead to the synchronization of vibrations of water molecules and formation

of the coherence regions, similar to coherent domains. According to positions of quantum electrodynamics, it will lead to an attraction between a molecule of water and, accordingly, between the layers of the molecules which have appeared in the field of interaction. The result will be the compression of a crystal lattice of compound.

Any other mechanisms of a lattice compression of compounds at diffusion in water, except the ones specified by us here (connected with the tune of vibrations of water molecules in a uniform by vacuum virtual photon), it has not been put forward till now.

It is interesting to indicate one more publication [20] where it is informed that the effect of induction of superconductivity is found out and at contact of compound $FeTe_{0,8}S_{0,2}$ with the alcohol-containing water solution. While heating the $FeTe_{0,8}S_{0,2}$ compound in various alcoholic beverages, with compound there are the same changes, as well as at an exposition on air, in particular, the compression of lattice. We shall note in this connection that according to [1], the resonant spectra of EHF diapason, which have been taken off from water and alcohol-containing water solution, have a very close location of resonant peaks though the intensity of these peaks are different. Such distinction in [1] explained that for water containing spirit, typically the delaminating of hexagonal planes was higher than for pure water.

Ethanol spirit, as well as usual water, is an associated liquid, i.e., it contains hydrogen bindings. It means [3] that positions quantum electrodynamics, advanced by G. Preparata for water, are suitable for the description of this substance. Probably, exactly these characteristics also cause the possibility of molecules of an ethanol spirit to interact with a virtual photon and induce the superconductivity in a crystalline structure as well as a water molecules.

Though the unique reason of induction, in opinion of authors of the works, which for the first time have fixed the effect, is the compression of a lattice (that equivalently as they consider, to application of external pressure), such explanation as, authors specify, is not sufficient.

In fact, the influence of diffusing waters is not reduced to compression only.

As follows from the above-mentioned works, it is possible to induce the transition to superconductivity in two ways: first, compression and second, doping. Doping can bring us to the next result: to reduce the interaction between layers, to suppress the transition in an antiferromagnetic state, and to increase the concentration of carriers.

Properties of two-dimensional water, being situated between the basic layers, by virtue of features of its formation on some parameters are similar to the so-called EZ water, to water, a thin layer adjoining to any hydrophilic surface.

An adjoining surface shields an EZ layer from destroying the influence of thermal vibrations of external environment, in consequence of which the regions of CD appear substantial anymore. It is typical that for near-surface waters, adjoining to surfaces of living organisms, viscosity is lower than usual water and EZ water. The reasons of such a difference are discussed in detail in [3], and authors connect them with an opportunity of coherent domains to resonate among themselves in living organisms.

Enumerate some differences of EZ water from usual water according to [3].

1. EZ water is considerably more viscous than normal water (on the order).
2. EZ water has a negative electric potential (up to 150 mV).
3. On border between EZ water and usual water protons are concentrated.
4. EZ water blocks penetration of impure molecules.

In the opinion of authors [3], EZ water is formed, basically, from the molecules residing in a coherent state and vibration within a united phase (in area of coherent) between the basic and excited states. The attraction among molecules vibrates in one phase, according to positions of quantum electrodynamics, and causes the higher viscosity, than for not coherent molecules of water. Besides, such water easily gives electrons, since the difference between energy of ionization (12.60 эВ) and energy excitation (12.06 эВ) is insignificant. The ability of easy giving of electron leads to the occurrence of negative electric potential and concentration of protons on border, as it is specified in points 1 and 2.

Let us consider in more detail what occurs with the molecules of water, diffusing in compounds $SrFe_2As_2$ and $FeTe_{0,8}S_{0,2}$.

Water molecules, diffusing in these compounds, in consequence of interaction with a virtual photon and the subsequent passing to coherence, get such quantum characteristic, as a phase, unique for each area of coherence. The further interaction between separate areas can lead to their merging, as well as for EZ water, especially at the decrease in temperature.

Let us note that in the area of interaction with the virtual photon, having the energy $E = 10$ эВ (which length of a wave, accordingly, makes about 1,000 Å) gets enough amount of layers of the water, which are settling down between the basic ferriferous layers. Thus, the condensation of diffusing water molecules in a state, on its properties reminding "ice-like" state, is carried out.

Let us emphasize here that the coherent water in a formations of water layers, as well as usual water in coherent domains, is not the water, which properties correspond to frozen crystallize water, where coherent domains were absent. Here, we have a superposition of the ground state, where molecules closely bond among themselves and the excited, where electrons are "handling" in an electronic cloud and are collectivized for all region of coherence, i.e., are a unit.

The most essential difference of water in two-dimensional layers from "ice-like state" is that: these layers do not couple in a transversal direction by hydrogen binding and have two "external" electrons on one atom of oxygen, because oxygen in "electrons" on is tetravalent.

The second difference will be that in the field of interaction with a virtual photon for all water layers the regime of coherence is established, i.e., all processes occur in a uniform and with a unique phase. The structure of a polycrystal thereof transformed, because the layers of water have a tendency to rapprochement at coherency; the parameters of a lattice can change as result, its compression will be happen.

Let us note that at the usual freezing of water there is, as is known, a process of expansion, instead of compression.

The third difference is that the polycrystal lattice stabilizes processes in water layers in accordance with their own internal process and can appear the resonance

transitions (and it is also possible the processes, similar to some extent to effect of affinity, when superconductivity in one substance induces superconductivity in the other substance).

Diffusing water differs from EZ water as well as from usual water by a two-dimensional character, the absence of hydrogen binding between layers. At the same time inherent to it, as well as for EZ water, higher degree of coherence, ability easily to give of electrons and, probably, number of other properties.

From the enumerated particularities of water in single layers follows that such layer:

1. can shield interaction between layers of the basic material (it is expressed in occurrence of anisotropy of properties, which it was mentioned above for $SrFe_2As_2$),
2. can be suppliers of electrons to the basic ferriferous layers (it is found out for $FeTe_{0,8}S_{0,2}$),
3. can be factors of approaching of ferriferous layers (change of geometrical parameters [4, 5]), and
4. can influence the processes of ordering, than to suppress antiferromagnetic ordering, as compete with a superconducting phase (transition to superconductivity).

All these four listed factors are the factors promoting the transition in a superconducting state.

However, there is also one more factor, related to that at low temperatures the water can be only in the pair-state. For this state, as against from ortho-state, molecules of water cannot rotate and, consequently, to form the binding structures, the type of hexagonal [21].

As for such structures are available of two "external" electrons [1], the opportunity is not excluded, that these electrons also can participate in formation of Cooper pairs: or with others electrons of water layers, or with electrons from the basic ferriferous layers (taking into account, that the processes in individual water layers occur synchronously). We shall note that interaction of water molecules with atoms of iron can lead to the conversion of water protons and transition of water molecules from a pair-state to an ortho-state [21] and thereby to promote the occurrence of processes of electrons pairing.

The synchronization of vibration of the water structures (for usual water is hexagonal structures) and of magnon processes of the basic ferriferous layers are also possible. Really, in [7] the presence of strong phonon–magnon interactions for compound $BaFe_2As_2$, similar to compound $SrFe_2As_2$, is revealed, and authors [1] find out the resonant vibrations of hexagonal water structures in a gigahertz range. Frequency of vibrations of coherence water structures, located by single layers, can be synchronized at low temperatures with the processes, caused by exchange interaction in iron-containing layers.

As there are no reliable literary data on finding correlation interactions of superconducting type for electrons in layers of near-surface waters (some indications on such opportunity for the water, bound by living structures, are available in [22]), the most probable mechanism of stimulation, besides possible processes of pairing

electrons from layers of water and the basic ferriferous layers, apparently, will be a complex manifestation of the factors listed in points 1–4.

16.6 Properties of One-Dimensional Water Chains in Carbon Nanotube

In works [1, 3], two models of a structure of water are stated. Though experimental results of work [1] confirm the theoretical concepts presented in [3], nevertheless, the treatment of experimental results, received by authors [1], does not coincide with positions [3].

If, in opinion of authors [1], "ice-like" phase of water represents a certain crystalline-like structure, in the theory G. Preparata it is the "coherent domain"!

What takes place indeed can show only experiment. It is very important to investigate the behavior of water in such systems, where water steadily keeps the structure, instead of a flickering regime.

Such states arise for water, bounded by living systems, for which very narrow coherent peaks in spectra of resonant interaction with SHF radiation are fixed [1], which specifies a high-degree coherence of such water.

Now there are not enough publications, concerning research of two-dimensional water properties, though it plays an important role in the realization of biological processes in living organisms. Such water is, in quality, similar to near-surface water of living organisms, forms the layers in a few hundred molecule thickness, enveloping molecular structures and surfaces of fabrics of living organisms. All vital processes occur in near-surface water environment. For such water, except of high degree coherence, it is typical also delaminating of water planes, because of what such planes are poorly bound between itself [23].

For this reason, the big interest for physics of water represents the research of effect of induction by water of superconductivity, where diffused water located by single layers, which have not bound by hydrogen bonds between itself.

It is essential that the compounds, in which the effect of induction was showed, are found at low temperatures in a state close to superconductivity [4, 5].

As follows from the above carried-out analysis of mechanism of effect inducing displayed in $SrFe_2As_2$ and $FeTe_{0,8}S_{0,2}$, for the description of diffused waters properties, as well as the mechanism of inducing by water of superconductivity, the treatment of G. Preparata is more acceptable. According to water in the single layers, which settles down in parallel to the basic ferriferous layers of compounds, represents the coherent system, having some characteristics of EZ water. It does not show properties of usual ice, as was expected based on the conclusions of work [1].

The further researches of water properties in nanosystems, carried out for the past decade, have also confirmed the validity of theoretical treatments by G. Preparata.

The most interesting, from our point of view, are the results of researches of water properties in carbon nanotubes, carried out by A. I. Kolesnikov and his colleagues from Argonne National Laboratory [23]. Nanotubes, which were used for researches,

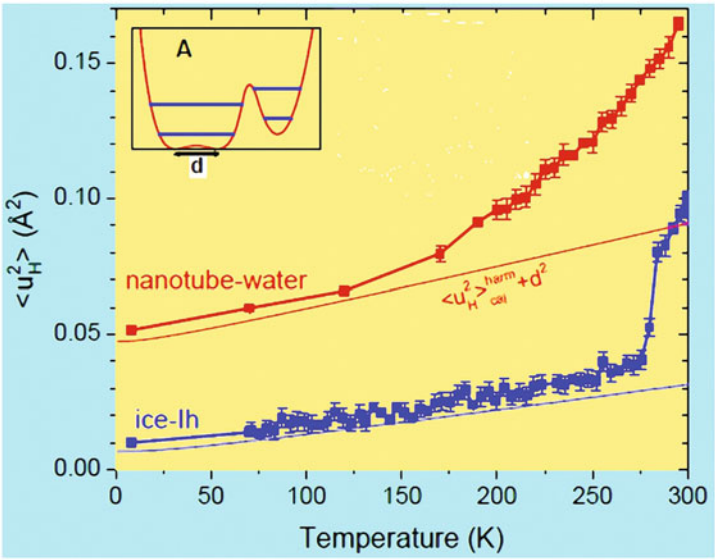

Fig. 16.4 The temperature dependence of the amplitude of root-mean-square fluctuations of water protons in a nanotube and in ice (from experiments on elastic dispersion of neutrons). (Taken from [23])

had a length up to several tens of nanometers and have consisted of one or several rolled up in a tube hexagonal graphite planes (graphene); their diameter ranged from 1.35 up to 1.90 nm. Water in such a nanotube, practically, did not interact with a wall of nanotube and represented one-dimensional structure.

Authors measured elastic dispersion of neutrons in such a system and compared the received data with results of the same measurements on usual ice. In Fig. 16.4, the temperature dependences of root-mean-square fluctuations $\langle u_H^2 \rangle$ of water protons are shown.

As it is visible from Fig. 16.4, root-mean-square fluctuations of water protons in nanotubes in four times exceed those for ice throughout the 8–273 K temperature range.

Authors [23] have also shown that water molecules in nanotubes are found in wide two-well potential (shown on an insert). A low-barrier double-well potential with flattened bottom is presents for hydrogen (as be obvious from an insert). Delocalization of protons makes approximately 0.2 Å.

Authors [23] explain such high values of size by the fact that, according to their results, the average amount of the hydrogen bounds, which bind a molecule of water with its two nearest neighbors (so-called coordinate number), was reduced from 3.8 up to 1.86. In consequence of that, the mobility of molecules has increased. "New water" did not freeze even at temperature, even on eight degrees differing from absolute zero.

In a later work [24], carried out by A. I. Kolesnikov and colleagues, the additional data on properties of nanotubes waters are presented. They added: “We find that at 5 K the kinetic energy of the protons is 35 meV less than that in ice Ih at the same temperature, and the high momentum tail of the distribution, characteristic of the molecular covalent bond, is not present... Our data reveal that the protons in the hydrogen bonds are coherently delocalized and that the low temperature phase is a qualitatively new phase of ice.”.

These works are a direct confirmation that the water in nanosystems is shown the unusual properties and is not the same substance as usual ice.

Unusual properties of water should be shown as in living systems, which the high degree of coherence is peculiar, so and in the some nano objects of the lifeless nature that confirms experiments. Apparently, the positions, advanced J. Preparata, most approach for the description of characteristics of such water systems.

The characteristics of nanowater in layered compounds $SrFe_2As_2$ and $FeTe_{0,8}S_{0,2}$ can appear are close to properties of near-surfaces water of living organisms.

16.7 Conclusions

Now there are two approaches to the description of properties of usual water. According to usual views, water presents a homogeneous medium. However, theoretical and the experimental researches, which have been carried out especially for past decades, have not confirmed such a point of view. The most significant of last achievements in the field of water physics are the discovery of the C∏E effect [1] and theoretical development by G. Preparata [2], which predicted for usual water the existence of separate regions of coherency—coherent domains. Authors of discovery of existence ofon the basis of the results received by them, have drawn a conclusion that water will consist of two extreme phases—vapor and ice. As against them, G. Preparata has shown that processes of condensation of water molecules in a liquid state occur owing to the interaction of water molecules with vacuum virtual photon and the water medium will consist of the separate coherent regions surrounded by individual molecules of water.

As follows from works of the authors, who have opened effect of the inducing by water of superconductivity in $SrFe_2As_2$ and $FeTe_{0,8}S_{0,2}$ [3, 4], it is not possible to explain neither the reason of compression of a lattice of compounds, nor the factors, resulting in superconductivity at diffusion in compounds of water, proceeding from properties of compounds.

For finding such a reason in the present work, the analysis of possible behavior of diffusing waters, situated by single layers parallel to the basic ferriferous layers of compounds, from a position of development, advanced G. Preparata, is carried out for usual water. It is shown that such water can have some properties of EZ water, by virtue of which, layers of diffusing waters:

1. Can shield interaction between layers of the basic material

2. To be effective suppliers of electrons to the basic ferriferous layers
3. To be factors of approaching of ferriferous layers
4. To influence processes of ordering, than to suppress antiferromagnetic ordering as competitive with superconducting phase

As all these four points are factors of induction of the transition to superconductivity, the most probable mechanism of effect of induction, besides arising of the possible processes of pairing of electrons from layers of water and of the basic ferriferous layers, apparently, will be the complex realizing of these factors.

Thus, it appears that the positions, developed by J. Preparata, most befit the description of characteristics of water nanosystems, to which belongs water diffused in $SrFe_2As_2$ and $FeTe_{0,8}S_{0,2}$; such water, on the properties, differs from usual water.

The experimental confirmation that the water in nanosystems can behave in the unusual way is the data of researches on properties of water in nanotubes, where such water does not freeze at temperature up to 8 K.

Thus, nanowater at low temperatures is not usual ice and its properties are expedient to describe from a position of the statement of quantum electrodynamics, advanced by G. Preparata at creation of the theory of a water molecule condensation in a liquid state.

References

1. Sinitsin NI, Petrosjan VI, Elkin VA et al (1999) The special role of system: «millimetric waves—the water environment in the nature». Biomedical radio electronics (in Russian), 1
2. Preparata G (QED) (1995) Coherence in condensed water, (World Sci. Singapore, 1995) 236 p
3. Del Giudice E, Spinetti PR, Tedeschi A (2010) Water dynamics at the root of metamorphosis in living organisms. Water 2:566–586
4. Hiramatsu H, Katase T, Hirano T et al (2009) Water-induced superconductivity in $SrFe_2As_2$. Phys Rev B 80, 052501
5. Mizuguchi Y, Deguchi K, Tsuda S et al (2010) Moisture-induced superconductivity in $FeTe_{0,8}s_{0,2}$. Phys Rev B 81, 214510
6. Subedi AL, Zhang DJ et al (2008) Density functional study of FeS, FeSe, and FeTe: electronic structure, magnetism, phonons, and superconductivity. Phys. Rev. B. 78, 134514
7. Liu RH, Wu T, Chen H et al (2009) A large iron isotope effect in $SmFeAs_{O1-x}F_x$ and $Ba_{1-x}K_x$ Fe_2As_2. Nature 459 arXiv:0810.2694
8. Shirage PM, Kihou K, Miyazawa K et al (2009) Inverse iron isotope effect on the transition temperature of the (Ba, K) Fe_2As_2 superconductor. Phys Rev Lett 103, 257003
9. Sadovsky MI (2008) High-temperature superconductivity in layered compound, on a basis of iron. Success Phys Sci (in Russian). 178 (12):1243–1271
10. Zhao J, Yao D-X, Li S et al (2008) Low energy spin waves and magnetic interactions in $SrFe_2As_2$. Phys Rev Lett 101167203 arXiv:0808.2455
11. Ewings RA, Perring TG, Bewley RI High energy spin excitations in $BaFe_2As_2$. arXiv: 0808.2836
12. Izjumov JA, Kurmaev EZ (2008) New a class of high-temperature superconductors in systems. Success Phys Sci (in Russian). 178 (2):1307–1334
13. Kitagawa K, Katayama N, Gotou H et al (2009) Spontaneous formation of a superconducting and antiferromagnetic hybrid state in $SrFe_2As_2$ under high pressure. Phys Rev Lett 103, 257002

14. Arani R, Bono I, Del Giudice E, Preparata. J (1995) QED coherence and the thermodynamics of water. Int J Mod Phys B 9:1813–1841
15. Del Giudice E, Tedeschi A (2009) Water and the autocatalysis in living matter. Electromagn Med 28:46–54
16. Kurcz A, Capolupo A, Beige A, Del Giudice E et al (2010) Energy concentration in composite quantum. Phys Rev A 81 063821
17. Balk M, Bose M, Ertem G et al (2009) Oxidation of water to hydrogen peroxide at the rock-water interface due to stress-activated electric currents in rocks. Sci Lett 283:87–92
18. Kurik MV, Martsenuyk LS (2012) The physical bases of the life. LAP LAMBERT Academic Publishing, Stuttgart, 174 p
19. Martsenyuk LS, Martsenyuk AS (2008) Questions of interaction of homoeopathic medicinal preparations and electromagnetic radiation of extremely high-frequency range with living organisms. Biomedical radio electronics. (in Russian), 3:56–63
20. Deguchi K, Mizuguchi Y, Ozaki T et al Superconductivity in $FeTe_{1-x}S_x$ induced by alcohol. arXiv:1008.0666
21. Drozdov AV, Nagorskaya TI, Masyukevich SV (2001) The quant-mechanics aspects of effects of the weak magnetic fields on biological objects. Biophysics (in Russian), 5 (4):740–749
22. Pyullman BP, Pyullman AP (1965) Quantum biochemistry (M, «World», 1965) (in Russian), 654 p
23. Gabuda SP (1982) The bounded water. Facts and hypotheses (Novosibirsk: Science. 1982) (in Russian), 99c
24. Kolesnikov AI et al (2004) Neutron spectroscopy of water in carbon nanotubes. Phys Rev Lett 93, 035503
25. Kolesnikov AI et al (2006) Anomalous behavior of proton zero point motion in water confined in carbon nanotubes. Phys Rev Lett 97, 247801

Chapter 17
Effect of Gold Nanoparticles on Proliferative Properties of SPEV Cells

E. V. Pavlovich and N. A. Volkova

The effect of gold NPs on the viability, adhesion capacity, and apoptosis of embryonic porcine kidney epithelial inoculated line (SPEV) cells was studied. We examined the effect of gold NPs on the cell proliferation rate. A stimulating effect of gold NPs under concentration of 6 μg/ml on SPEV cells when cultured for 3 h was seen, the number of adhered cells increased in 1.3 times when compared with the control samples. Adhesion after culturing for an hour in the samples with gold NPs at concentration of 12 μg/ml was slowed down. Cell morphology when culturing with gold NPs within the investigated range of concentrations did not differ from the control at all stages of observation. It was shown that the stimulating effect manifested at low concentrations of gold NPs during 3 and 4 days of culturing. Thus, the number of cells in samples cultured under concentrations of gold NPs of 3 and 6 μg/ml increased if compared with the control samples in 1.15 and 1.24 (the third day) and 1.15 and 1.23 times (the fourth day), respectively.

17.1 Introduction

Nanoparticles (NPs) of metals, especially gold, can stimulate enzymatic activity and have antioxidant properties; they are used for the delivery of drugs and imaging of cells and tissues as well [1]. However, they can have toxic effects on biological objects in high concentrations [2], their interactions with cells and potential health risk are not completely known. Obviously, many in vitro and in vivo studies for a complete description of nanomaterials are required. Information about their potential toxicity and effects on human health is necessary for use of nanomaterials in clinic.

E. V. Pavlovich (✉) · N. A. Volkova
Department for Cryobiology of Reproduction System, Institute for Problems of Cryobiology and Cryomedicine, Natl. Acad. of Sci. of Ukraine, Pereyaslavskaya str., 23, Kharkiv 61015, Ukraine
e-mail: lenapavlovich@gmail.com

N. A. Volkova
e-mail: volkovanatali2006@yandex.ua

O. Fesenko, L. Yatsenko (eds.), *Nanocomposites, Nanophotonics, Nanobiotechnology, and Applications,* Springer Proceedings in Physics 156,
DOI 10.1007/978-3-319-06611-0_17,

We used an inoculated line of SPEV cells, derived in 1959 at the Moscow Scientific Research Institute of Virus Preparations from embryonic porcine kidney. Nowadays, this line has been the object for many researches in the field of cell technologies [3]. Inoculated cell cultures are frequently used as the model for solving many tasks of biology such as cell differentiation, intracellular structures, carcinogenesis, transfer of genetic information, derivation of high-effective vaccines, and antiviral preparations as needed. The advantage of inoculated cell cultures is their specificity to homogeneous cell populations, well growing under standard conditions in semisynthetic media. Moreover, we can study in cell cultures direct responses of cells to some or other influences, whereas there is no integrating effect of an organism of its humoral and nervous systems.

The research aim was to study the interaction of nano-sized compounds with cultured cells. The effect of gold NPs on morphological and functional characteristics of cells and on the cell apoptosis of SPEV cells was investigated.

17.2 Materials and Methods

SPEV cells (embryonic porcine kidney epithelial inoculated line) were cultured in plastic flasks in DMEM (Sigma, USA) with 5 % FBC (v/v; HyClone, USA) supplemented with penicillin/streptomycin (PAA, Austria) and amphotericin B (5 μg/ml) as reported [4]. The total number of the cultured cells was calculated by the traditional method in Goryaev's chamber. Seeding concentration was 5×10^4 cells on Petri dish. The cells were cultured in Sanyo incubator under 37 °C with 5 % CO_2 in humid atmosphere. Culture medium was replaced every 2 days. Cells were passaged at 100 % confluence [5]. SPEV cells had expressed growth properties and during serial passage preserved initial morphological structure of monolayer without evidencences of cell degenaration in the culture.

Gold NPs were obtained at the Institute of Biocolloidal Chemistry of the NAS of Ukraine. Colloidal gold was synthesized by recovery of gold ions from a solution of hydrochloric acid, $HAuCl_4xH_2O$. Initial concentration of gold solution dialyzed with polysaccharides was 44 mg/ml. The adsorption of polysaccharides on the surface of growing crystal is not higher than 40 mg/ml, the average size of NPs was 30 nm. Gold NPs were introduced in cells by passive diffusion at 37 °C.

Adhesive properties of cells were visually evaluated using an inverted microscope, counting the number of adhered and flattened cells on the area of 1.5 mm^2 (square field of view at 150 times magnification). The proliferation dynamics of adhered SPEV cells of 1–4 days was investigated. Apoptotic and necrotic processes in SPEV cells exposed to gold NPs were investigated with fluorescence-activated cell sorter (FACS) analysis. The processes of necrosis/apoptosis were studied with annexin-V (BD, USA), 7-amino-actinomycin (7AAD; BD) and propidium iodide (PI; BD) dyes using FACS Calibur Becton-Dickinson flow cytometer. The cells cultured without gold NPs under the same conditions were the control.

The results were statistically processed using Excel software and Student's *t* test.

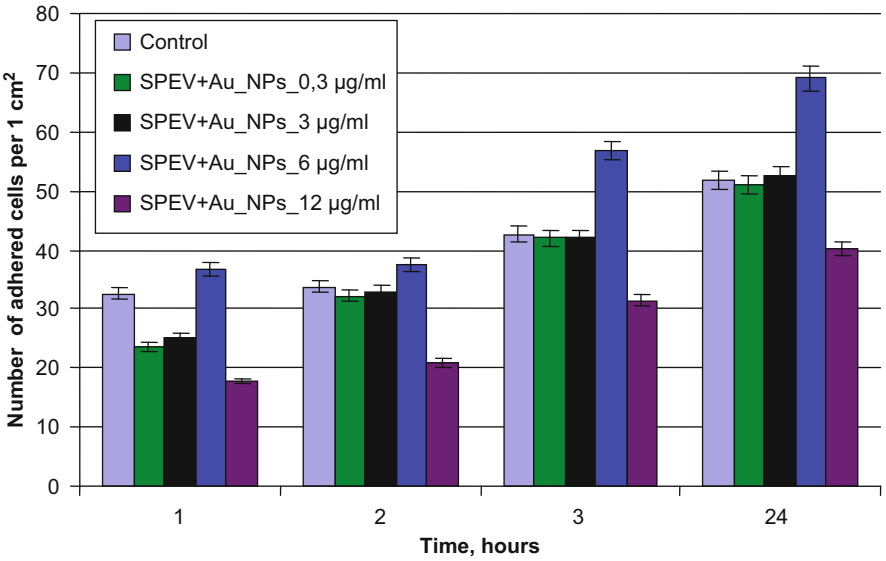

Fig. 17.1 Dynamics of adhesion of SPEV cells after exposure of gold NPs

17.3 Results

The effect of gold NPs on adhesive characteristics of SPEV cultures was studied. Cell adhesion is a requirement for the following growth of the culture and indicates a functional state of cells. Adhesion is known as the start of cell flattening for obtaining of such a morphology. The adhesive properties of SPEV cells are presented in Fig. 17.1. After an hour of SPEV cells culturing with gold NPs of 0.3 and 3 μg/ml, the number of adhered cells was lower if compared with the index of the control samples. Relative number of flattened cells for the samples with NPs for these concentrations did not significantly differ from the control. After 3 h of culturing gold NPs of 6 μg/ml manifested a stimulating effect on SPEV cells, a number of adhered cells increased by 1.3 times, respectively, if compared with the control.

After an hour, culturing supplemented with gold NPs of 12 μg/ml adhesion was slowed down. A number of adhered cells per 1 cm^2 were reduced by 1.8 times if compared with the control. There was also observed a significant slowing of cell flattening with gold NPs in this concentration. After 24 h of observation a number of adhered cells was lower relative to the control in 1.3 times (Fig. 17.1).

We studied the effect of gold NPs within the concentration range of 0.3–12 μg/ml on proliferative processes in SPEV culture cells. The obtained results were presented in Fig. 17.2. At observation time of 1–4 days, there was studied the proliferation dynamics of adhered cells, calculating a number of proliferating cells. Stimulating effect of gold NPs revealed to the third and fourth observation days. To the third day of culturing with gold NPs of 3 and 6 μg/ml a cell number increased by 1.15 and 1.24

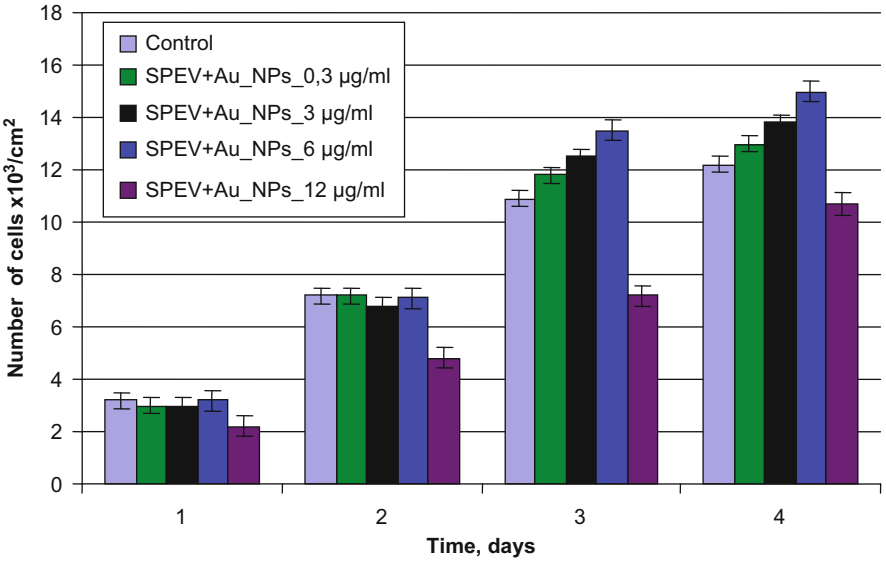

Fig. 17.2 Proliferation dynamics of SPEV cells after exposure of gold NPs

times, respectively, if compared with the control. To the fourth day of culturing with gold NPs of 3 and 6 μg/ml, the investigated index increased by 1.15 and 1.23 times, respectively, if compared with the control. A reduced cell number was observed if compared with the control in 1.5 times (the second and third days) and in 1.15 times by the fourth day of culturing with gold NPs of 12 μg/ml in SPEV culture. Thus, gold NPs of 12 μg/ml result in reduced proliferative activity at the initial stages with the tendency of following recovery at long-term of culturing.

It was shown that gold NPs in concentrations of 3 and 6 μg/ml had a stimulating effect on proliferative capacity of cells. The increase in concentration of NPs up to 12 μg/ml reduces the rate of cell proliferation if compared with control in all observation terms.

The next aim of this research was the assessment of presence/absence of apoptosis in the cells with NPs of gold in the studied concentrations. According to the researchers [6, 7] dendrimers, metal oxides and carbon nanotubes can induce apoptosis in the cultured cells. As it is known, NPs of titanium dioxide and ferrous oxide result in cell death due to the generation of an oxidative stress and the following apoptosis by the activation of caspase-3 [8, 9].

Simultaneous staining with annexin-V and 7AAD enables to reveal both the presence of necrotic cells and the ones at apoptosis. At an early stage of apoptosis, the integrity of cell membrane is preserved; however, there is a recombination of its phospholipid components and phosphatidyl serine appears on cell surface. Annexin has a high affinity to phosphatidyl serine and is binding with the cells on membranes of those it is expressed.

Table 17.1 Cytofluorimetric analysis of SPEV cells suspension after incubation with gold NPs for 1 h, staining with annexin V and 7AAD

Sample/Region	Annexin $V^+/7AAD^-$	Annexin $V^+/7AAD^+$	Annexin $V^-/7AAD^-$	Annexin $V^-/7AAD^+$
Control	1.4 ± 0.5	2.6 ± 0.8	95.7 ± 1.2	0.4 ± 0.2
SPEV + Au_NPs_0,3 μg/ml	2.2 ± 0.5	2.0 ± 0.6	95.7 ± 1.1	0.2 ± 0.1
SPEV + Au_NPs_3 μg/ml	2.2 ± 0.6	1.9 ± 0.6	95.8 ± 1.1	0.2 ± 0.1
SPEV + Au_NPs_6 μg/ml	2.8 ± 0.9	2.0 ± 0.7	95.0 ± 1.4	0.2 ± 0.1
SPEV + Au_NPs_12 μg/ml	1.8 ± 0.7	2.5 ± 0.6	95.2 ± 1.2	0.4 ± 0.2

Table 17.2 Cytofluorimetric analysis of SPEV cells after 3 days culturing with gold NPs, staining with annexin V and 7AAD

Sample/Region	Annexin $V^+/7AAD^-$	Annexin $V^+/7AAD^+$	Annexin $V^-/7AAD^-$	Annexin $V^-/7AAD^+$
Control	3.4 ± 0.5	4.6 ± 0.8	91.7 ± 1.0	0.4 ± 0.2
SPEV + Au_NPs_0,3 μg/ml	3.6 ± 0.6	4.3 ± 0.8	91.5 ± 1.2	0.6 ± 0.2
SPEV + Au_NPs_3 μg/ml	3.7 ± 0.6	3.4 ± 0.6	91.1 ± 1.0	1.8 ± 0.1
SPEV + Au_NPs_6 μg/ml	3.7 ± 0.7	10.1 ± 0.6*	84.8 ± 1.2*	1.3 ± 0.2*
SPEV + Au_NPs_12 μg/ml	5.0 ± 0.8*	12.4 ± 0.7*	81.0 ± 1.3*	1.1 ± 0.1*

* $p \leq 0.05$ is significant if compared with the control

To reveal apoptosis in SPEV cells with gold NPs of the studied concentrations suspended SPEV cells incubated with gold NPs for an hour. As Table 17.1 shows, a number of living cells (annexin $V^-/7AAD^-$) in cell suspensions with gold NPs within 0, 3–12 μg/ml does not significantly differ from the control.

Analysis of the obtained results showed that the incubation of gold NPs within 3–12 μg/ml with cell suspension for an hour did not induce the activation of apoptosis/necrosis.

Further experiments were directed to the studying of gold NP effect of 0.3–12 μg/ml on SPEV cells under culturing. The results of FACS analysis of annexin V and 7AAD stained samples are presented in Table 17.2. SPEV cells with gold NPs were cultured under standard conditions for 3 days. Culturing with gold NPs of 6–12 μg/ml resulted in a decrease of the percentage of living cells contrasted with the increasing of percentage of annexin $V^+/7AAD^+$, annexin $V^-/7AAD^+$, and annexin $V^+/7AAD^-$ cells. Within all the studied range of concentrations of gold NPs, there was a reduction of living cells percentage. In the case of gold NPs of 12 μg/ml, a number of annexin $V^+/7AAD^+$ increased if compared with the control in 7.8 ± 0.7 % ($p \leq 0.05$).

When culturing with gold NPs within the studied range of concentrations, there was a reduction of living cells percentage during growth of cell number at early and late stages of apoptosis and necrotic cells.

17.4 Discussion and Conclusion

Nowadays, scientific interest of many researches has been associated with the application of gold NPs. Due to unique structure and properties the gold NP is a prospective object for usage within the wide range of biological and biomedical studies. However, the results of using the gold NPs when culturing both monolayer and suspension all lines are contradictory [10, 11, 12]. Thus, for example, the approaches to study the toxic effect of gold NPs were described in the report [13]. It was shown that positively charged gold NPs had a medium-toxic effect, while anion particles were nontoxic. In this chapter, the results of the study of gold NPs' effect on the functional state of cells in vitro on the base of accumulating the data on proliferative activity of SPEV cells with the studying of apoptosis and necrosis are presented.

The changes occurring in cells during apoptosis are similar in the majority of cell types. In an apoptotic cell, there are no changes of lipid composition of plasma membrane phosphatidyl serine transfers from cytoplasmic part of bilayer to outer side, causing the activation of caspases' cascade, chromatin condensation, disorder of electron transport chain in mitochondria, and eventually stopping the adenosine triphosphate (ATP) synthesis.

Programmed cell death can be triggered by receptor-mediated physiological stimuli, the result of genetic disorders, exposure to chemical or physical factors of origin, as well as other changes in the cell. In our study, the examined effect is observed when gold NPs were acting under concentration of 12 μg/ml. Finally, mitochondrial death occurs.

Mitochondria play an important role in apoptosis. An initial step for the activation of intrinsic apoptotic pathway is the depolarization of mitochondrial membrane. Depolarization of mitochondria is a result of the formation of mitochondrial permeability transition pores [14]. Mitochondrial permeability transition has been associated with various metabolic consequences such as a halted functioning of the electron transport chain with associated elevation in reactive oxygen species and decreased production of ATP [15]. NPs preferentially are localized in mitochondria and cause oxidative stress as well as potentiate structural damage [16]. A recent article by Pan and colleagues describes that 1.4 nm gold NPs induce necrosis by oxidative stress and mitochondrial damage in Hela cells [17]. The accumulation of NPs in a cell medium under biodegradation is unsafe and may disrupt organelles integrity and even cause genetic mutations [11].

Reduction of proliferative activity of SPEV cells when culturing with gold NPs under concentration of 12 μg/ml could be associated with the accumulation in the culture of C-mitoses, which practically do not occur in the norm. NPs can also cause structural chromosome rearrangements, having a prolonged nature, namely their decondensation. This process may be accompanied by the dissociation or redistribution of minor components of chromatin.

It should be also noted that the effect of gold NPs on SPEV cells is a dose-dependent, reduction of effective concentration of NPs down to 3–6 μg/ml which may cause the stimulation of SPEV cell proliferation activity. There is an increase

in the mitotic index of culture under the action of gold NPs of 6 μg/ml. It is possible that this increase is also due to the accumulation in the culture of C-mitoses and can over time cause the reversion of the level of culture proliferative capacity to the control due to death of C-mitotic cells.

Thus, our experimental study on the effect of gold NPs on SPEV cells is of great practical value to provide their further application in the field of development of new biotechnologies and tissue-engineered constructs.

17.5 Conclusion

- Gold NPs at concentrations of 3 and 6 μg/ml have a stimulating effect on the proliferative capacity of cells.
- The increasing of gold NPs' concentrations up to 12 μg/ml reduces the rate of cell proliferation if compared with the control at all observation time.
- Gold NPs at concentrations of 3–12 μg/ml when incubating with cell suspensions for an hour did not significantly affect the process of apoptosis/necrosis.
- The results obtained by flow cytometric analysis indicate that the presence of gold NPs in culture medium decreases the percentage of living cells due to the increase in cell number at early and late stages of apoptosis and necrosis.

Acknowledgments The work was carried out within the research project of a targeted complex program of basic research NAS "Fundamental problems of nanostructured systems, nanomaterials and nanotechnology."

References

1. Maiti S, Das D, Shome A et al (2010) Influence of gold nanoparticles of varying size in improving the lipase activity within cationic reverse micelles. Chemistry 16(6):1941–1950
2. Chen YS, Hung YC, Liau I, Huang GS (2009) Assessment of the *in vivo* toxicity of gold nanoparticles. Nanoscale Res Lett 4:858–864
3. Kisurina-Evgenieva OP, Onishchenko GE (2004) Organelle redistribution during PK cell spreading in normal conditions and in the presence of Na azide. Tsytologiya 46(11):967–978
4. Freshni R (1989) Culture of animal cells. Methods. Mir, Moscow
5. Birger MO (1982) Manual for microbiological and virological research methods. Medistyna, Moscow
6. Maynard AD, Aitken RJ, Butz T et al (2006) Safe handling of nanotechnology. Nature 444(7117):267–279
7. Kim K, Lee M, Park H (2006) Cell-permeable and biocompatible polymeric nanoparticles for apoptosis imaging. J Am Chem Soc 22(11):3490–3491
8. Park E, Yi J, Chung K (2008) Oxidative stress and apoptosis induced by titanium dioxide nanoparticles in cultured BEAS-2B cells. The FASEB J 22:3358–3369
9. Zhu MT, Wang Y, Feng WY (2010) Oxidative stress and apoptosis induced by iron oxide nanoparticles in cultured human umbilical endothelial cells. J Nanosci Nanotechnol 10(12):8584–8590
10. Lewinski N, Colvin V, Drezek R (2008) Cytotoxicity of nanoparticles. Small 4(1):26–49

11. Bystrzejewska-Piotrowska G, Golimowski J, Urban PL (2009) Nanoparticles: Their potential toxicity, waste and environmental management. Waste Manage 29:2587–2595
12. Mironava T, Hadjiargyrou M, Simon M et al (2010) Gold nanoparticles cellular toxicity and recovery: Effect of size, concentration and exposure time. Nanotoxicology 4(1):120–137
13. Goodman CM, McCusker CD, Yilmaz T, Rotello VM (2004) Toxicity of gold nanoparticles functionalized with cationic and anionic side chains. Bioconjugate Chem 15:897–900
14. Govender R, Phulukdaree A, Gengan MR (2013) Silver nanoparticles of *Albizia adianthifolia*: the induction of apoptosis in human lung carcinoma cell line. J Nanobiotechnol 11:5. doi:10.1186/1477-3155-11-5
15. Wang X (2001) The expanding role of mitochondria in apoptosis. Genes Dev 15(22):2922–2933
16. Derfus AM, Chan WCW, Bhatia SN (2004) Intracellular delivery of quantum dots for live cell labeling and organelle tracking. Adv Mater 16(12):961–966
17. Pan Y, Leifert A, Ruau D, Neuss S, Bornemann J, Schmid G, Brandau W, Simon U, Jahnen-Dechent W (2009) Gold nanoparticles of diameter 1.4 nm trigger necrosis by oxidative stress and mitochondrial damage. Small 5:2067–2076

Chapter 18
Nanobiotechnologies in the System of Farm Animals' Gene Pool Preservation

S. I. Kovtun, N. P. Galagan, O. V. Shcherbak, N. Y. Klymenko and O. S. Osypchuk

18.1 Introduction

Rapid development of nanobiotechnologies and growth of nanomaterial's (NM's) production currently open wide prospects for using them in technology for long-term storage of animal genetic resources. The biological usefulness of sperm that carries valuable genetic information and stays frozen for a long time contributes to solving some practical problems of the modern biotechnology reproduction of farm animals and reproductive medicine [4, 5]. In our experiments with NM, the ultrafine silica (UFS) was used as the carrier, synthesized by high temperature hydrolysis of silica tetrachloride in hydrogen-oxygen flame according to the general scheme [3, 6, 7, 9]:

$SiCl_4 + 2H_2 + O_2 \rightarrow SiO_2 + 4HCl$ [7, 9].

The specific property of such synthesized SiO_2 is a deeply developed surface area covered with a large number of hydroxyl groups [7]. In pharmacy, it is widely and for a long time used in preparation of various drugs [1]. UFS particles (with size of 4–40 nm) have a large specific surface area which provides high absorption effect on different materials. Such SiO_2 is resistant to high temperature and ultraviolet irradiation which allows material sterilization by generally accepted methods. In certain conditions, the hydroxyls on the UFS surface can be replaced by various synthetic or natural molecules allowing obtaining various immobilized preparations [7, 8, 10]. Its specific feature is the ability to prolong and precisely control the concentration of immobilized substance. This allows purposefully to regulate exchange processes in living systems which is important for technologies preservation cells [8, 9, 10].

O. V. Shcherbak (✉) · S. I. Kovtun · O. S. Osypchuk
Biotechnology laboratory, Institute of Animal Breeding and Genetics,
National Academy of Agrarian Science of Ukraine, Pogrebnyaka St.,
v. Chubinske, Borispol District, Kiev, 08321, Ukraine
e-mail: ov19792006@yandex.ru

N. P. Galagan · N. Y. Klymenko
O.O. Chuiko Institute of Surface Chemistry, National Academy of Science of Ukraine,
17 Gen. Naumova St., Kiev, 03164, Ukraine

O. Fesenko, L. Yatsenko (eds.), *Nanocomposites, Nanophotonics, Nanobiotechnology, and Applications,* Springer Proceedings in Physics 156,
DOI 10.1007/978-3-319-06611-0_18,

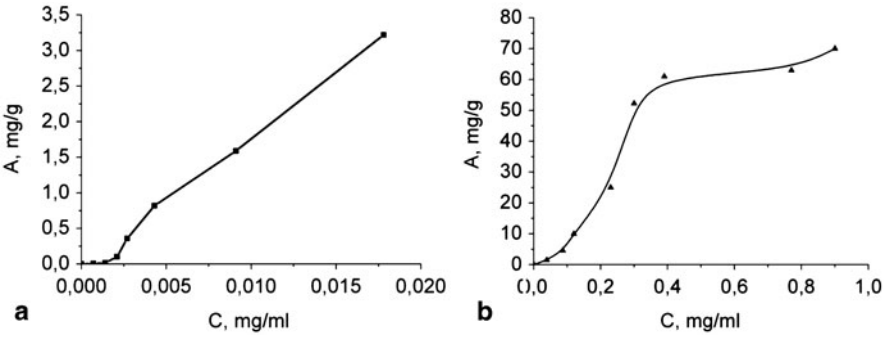

Fig. 18.1 Adsorption isotherms of sucrose (**a**) and D-galactosamine (**b**) on the UFS surface

18.2 Materials and Methods

Thawed ejaculated sperm of Grey Ukrainian bulls (Chudoviy 1276, Barvinok 8247, Inzhir 7927) was used. The choice gametes that are stored in the Bank Animal Genetic Resources of the Institute of Animal Breeding and Genetics National Academy of Agrarian Sciences (NAAS) for more than 40 years have high genetic value for selection. NM UFS + sucrose and UFS + D-galactosamine were obtained by noncovalent adsorption from water solutions of sucrose or D-galactosamine (Aldrich, USA) on the surface of UFS (A-300, $S_{sp} = 285\ M^2/G$; Ukraine, Kalush, Explore Experimental Plant of ISC NAS of Ukraine) after a preliminary thermal treatment (400 °C, 2 h). Adsorption conditions: 1 h for Sucr and 2 h for D-galactosamine, permanent mixing at 22–23 °C.

The adsorbate to adsorbent ratio was 1:10. Concentration of disaccharide solutions was 1.56–50 mcG/mL and for aminosugar—0.2–16 mG/mL. Solid phase was separated by centrifugation (4000 rpm, 10 min); then disaccharide concentration in the liquid was measured by molybdenum method according to [14], aminosugar—by modified Elson–Morgan method [16] using spectrophotometer Lambda-35 (Perkin-Elmer, USA). The residue was dried at 37 °C. Mechanically crushed samples were desorbed and after drying at indicated conditions were used in further experiments. Adsorption parameters were calculated according to [2, 12].

The presence of immobilized biomolecules on the surface of UFS nanoparticles was confirmed with infrared spectroscopy (IR spectroscopy) and mass spectrometry.

IR spectra were obtained using Thermo Nicolet Nexus FTIR in the range of 4000–400 cm^{-1}. Samples were prepared according to [11]. Spectra treatment was done using program "Omnic."

Mass spectrometric measurements were conducted using temperature-programmed desorption mass spectrometry method (TPD MS) at MX-7304A equipment (Ukraine, Sumy). Specific details and features of TPD MS method are revealed in [15].

Isotherms formed according to results of adsorption experiments confirm immobilization of initial substances on the UFS surface (Fig. 18.1, b).

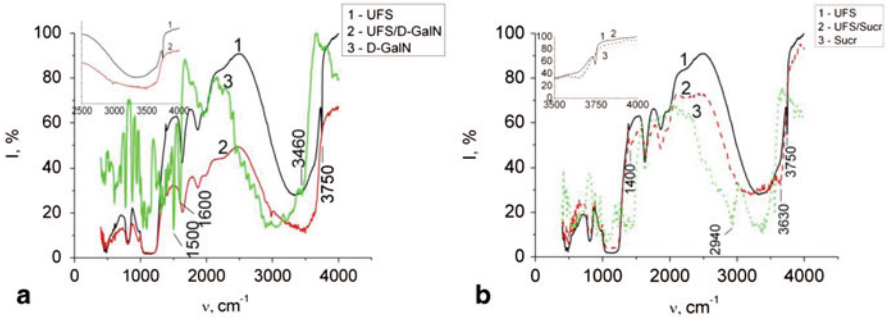

Fig. 18.2 IR spectra of biomolecules adsorbed on the surface of ultrafine silica

Curves formed are described by isotherms of S-type which testifies to intermolecular interaction of the substance in solution and possible formation of associates [13]. Bends of isotherm may be caused either by change in orientation of adsorbed molecules or by formation of polymolecular layers.

At low concentration of sucrose in solution, desorption is almost absent while for aminosugar it reaches 24 %.

In IR spectrum of initial silica (Fig. 18.2a, curve 1), there were detected a stripe of valent OH-vibrations in the 3750 sm^{-1} region, which belongs to isolated OH-groups [6, 8].

Decrease of absorption stripe intensity at $\lambda = 3750\,cm^{-1}$ which was observed after the contact of sucrose or D-galactosamine solution with SiO_2 surface (Fig. 18.2a, 18.2b) testifies to the possibility of formation of hydrogen links with surface layer of hydroxyl groups thus confirming immobilization of biomolecules on the UFS surface.

Specific features of composite surface layer formation, according to adsorption and IR spectroscopy results were confirmed by the TPD MS experiment.

The possibility of sucrose adsorption on UFS was confirmed also by its mass spectra both in condensed and adsorbed states (Fig. 18.3). In a condensed state (Fig. 18.3a, 18.3b), the thermal decomposition of sucrose started at temperature interval 150–250 °C, which resulted in masses 18, 28, and 44 a.u., identified as H_2O^+, C_2H_4, and CO_2, respectively. Also fragments with masses 60 ($C_2H_4O_2^+$), 97 ($C_5H_5O_2^+$), and 126 a.u. ($C_6H_6O_3^+$) were observed. After interaction of sucrose with the UFS surface, essential shift of carbohydrate molecule destruction temperature to higher temperatures was observed (Fig. 18.3c, 18.3d), accompanied by fragments 18, 28 and also 41, 57, and 69 a.u. extraction. The process occurred within a limit of 400–800 °C. The presence of the last three masses probably can be explained by an intermolecular rearrangement of sucrose molecule fixed on the UFS surface. Thus, adsorption interaction of sucrose molecule with UFS surface results in its stabilization on the silica surface.

Thermolysis of aminosugar in a condensed state takes place in the narrow temperature interval from 100 to 200 °C (Fig. 18.4). Revealed that adsorption of aminosugar

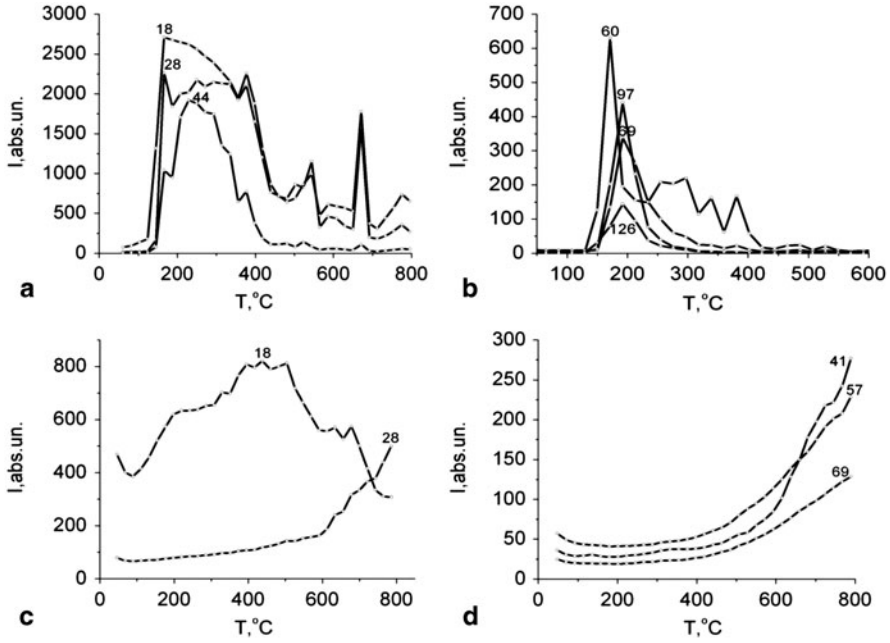

Fig. 18.3 Thermograms of decomposition of sucrose in condensed (**a**, **b**) and adsorbed (**c**, **d**) states

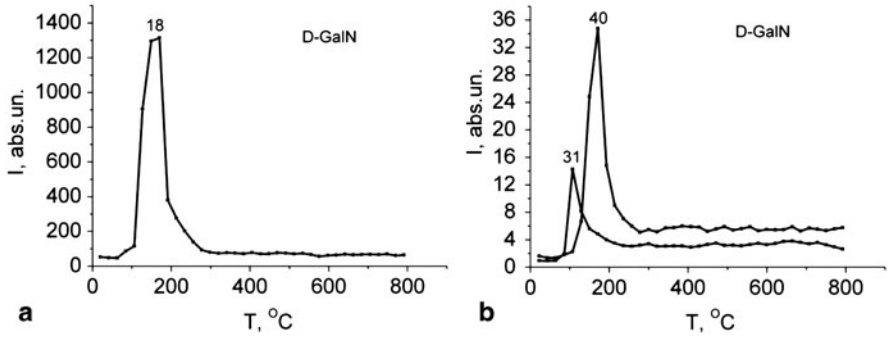

Fig. 18.4 Temperature dependencies of mass spectra components in the course of D-galactosamine thermolysis for mass numbers of 18, 31, and 40 a.u. (the last attributed to CH_2OH^+ and $CH_2{=}C{=}CH_2^+$, correspondingly)

on UFS results in the shift of thermalizes startpoint to low temperature and to widening of thermolysis temperature diapason caused by stabilization of the molecule on the surface of the carrier, similar to thermolysis of the sucrose on the surface of carrier.

Thus, the chosen conditions of experiment allow immobilized the biomolecules under investigation on the surface of UFS.

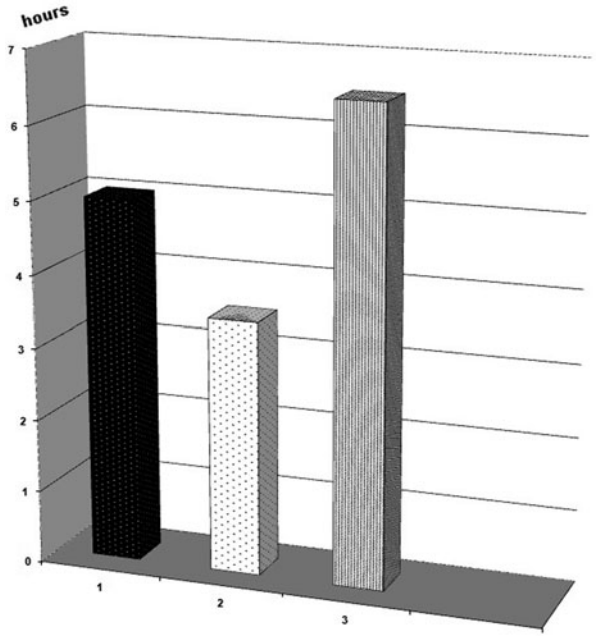

Fig. 18.5 Survival (in hours) thawing ejaculating bulls of sperm in media with NM. *1*—control, *2*—0.001 % UFS + D-galactosamine, *3*—0.001 % UFS + sucrose

18.3 Results and conclusions

We have developed a technological scheme of using NM as ingredients cryomedium for bull ejaculated sperm, the influence of adding NM on the viability of thawed sperm. This technological scheme can be used in reproductive medicine [3, 9]. In our studies, we have shown the possibility of extending survival time of thawed bull sperm. Minimum period of survival had bull gametes added 0.001 % UFS + D-galactosamine and Fig. 18.5 did not exceed 3.5 h.

At that, total survival time of sperm addition of NM was 30 min less than the control. When adding 0.001 % UFS + sucrose were observed extending survival time compared to controls nearly 2 h. The most active was the UFS + sucrose, which provided increased activity of 52 % and overall survival time up to 6 h (Fig. 18.6).

UFS + sucrose capable of adsorption interaction with sperm plasma fructose that provides sperm movement showing. At the expense, the interaction of UFS + sucrose with fructose there is an accumulation of additional energy in the cells, which affects the energy processes in biological systems and prolongs a positive effect on cell viability.

Consequently, we proved the feasibility of adding NM UFS + sucrose at a concentration of 0.001 % to thawed bull sperm that was frozen for a long time. We have improved the efficiency of the gene pool management of local cattle breeds in the system relying on the banks of genetic resources.

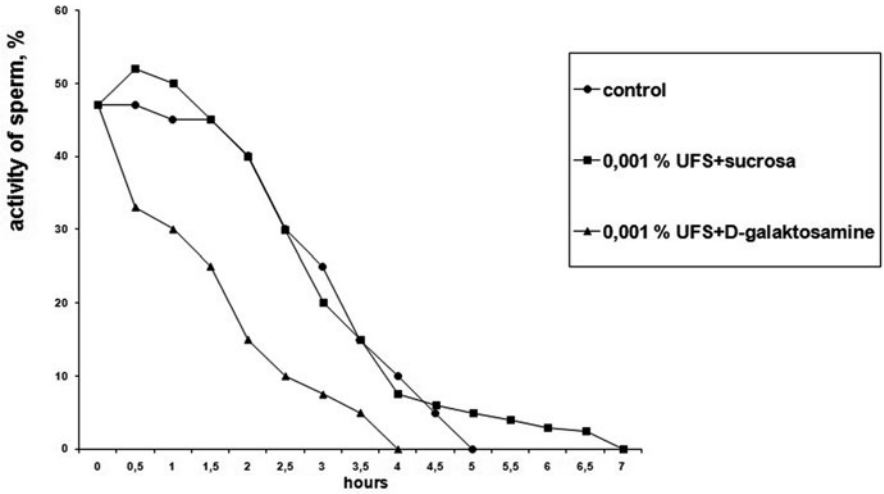

Fig. 18.6 Effect of NM on viability thawing ejaculating bulls of sperm

- Glycoproteins are present in sperm plasma; they can interact with NM due to the presence on the surface of sucrose and release with the UFS, which subsequently interact with the cell. In this case, most likely this process will contribute to the activation of cell surface fragments that activate the movement of gametes.
- But there are significant differences in the concentration and bioactivity. Assumed that UFS + D-galactosamine and UFS + sucrose stimulate the movement of gametes, their common attachment to the consistent media will greatly stimulate motion parameters. However, it appears that immobilization on the surface of galactosamine UFS significantly inhibits bioactivity such as NM. Those results are different to those obtained previously in [17]. A reasonable assumption may be done that this effect may be connected with long-term storage of gametes in liquid nitrogen which may affect the structure elements of cell membranes.

References

1. Aljushin MT, Astrahanova MM (1958) Aerosil and his application in pharmaceutical practice. Pharmacy 17(6):73–77 (in Russian)
2. Ayvazov BV (1973) Practical work for chemistry of surface effects and adsorbtion. Vyschaja shkola 208 p (in Russian)
3. Boehm H, Schneider M (1959) Uber die Hydroxylgruppen an der oberflachendes amorphen siliciumdioxyds “Aerosil” and ihre Reactionen. Z Anorg Allg Chem 301(5–6):326–335
4. Burkat VP, Kovtun SI (Suchasna biotechnologia v tvarynnyctvi) (2008) Modern biotechnology in animal. Biotechnology 3:7–12 (in Ukrainian)
5. Burkat VP, Kovtun SI, Galagan NP (2007) Nanobiotechnology methods to preserve the gene pool. Materials of the international scientific-practical conference. Actual problems of reproductive biology of animals, pp 450–452 (in Russian)

6. Chuiko AA (1993) Silica in medicine and biology. Ed Stavropol Kiev, pp 259 (in Russian)
7. Chuiko AA (2003) Medicinal chemistry and clinical application of dioxide silica. Ed Kiev, Naukova dumka, pp 416–418 (in Russian)
8. Galagan NP (2006) Nanomaterials based on highly dispersed silica and biomolecules in environments with reproductive cells. Materials of the II All-Russian scientific conference with international participation. Sorbents as a factor in the quality of life and health, pp 55–59 (in Russian)
9. Galagan NP, Siora IV, Kovtun SI, Scherbak OV (2007) Nanocomposites in biotechnology for prolonged preservation of gene pool (synthesis and application) IX Polish–Ukrainian symposium. Theoretical and experimental studies of interfacial phenomena and their technological applications, pp 27–29
10. Galagan NP, Klymenko NY, Orel IL, Novikova EA, Turov VV (2010) Biofunctional nanomaterials based on fumed silica, protein and aminocarbohydrates. Biopolym Cell 26(3):205–213 (in Russian)
11. Littl L (1969) Infra-red spectra of adsorbed molecules. Moskow: Mir, 514 p (in Russian)
12. Mitrofanov PP (1950) Praktikum po fizicheskoy i kolloidnoy himii. Practical work for physical and colloidal chemistry. Moskow: Medgis, 183 p (in Russian)
13. Parfitt GD, Rochester CH (1986) Adsorption from solution at the solid liquid interface. Moskow: Mir, 488 p (in Russian)
14. Pochinok HN (1976) Methods of biochemical analyses of plants. Naukova dumka, pp 334–339 (in Russian)
15. Pokrovskiy VA (2000) Temperature-programmed desorbtion mass spectrometry. J Therm Anal Calorim 62:407–415
16. Varbanez LD, Zdorovenko GM, Knirel YA (2006) The methods of analysis of endotoxines. Naukova dumka, 239 p (in Russian)
17. Klymenko NY, Novikova EA, Mischanchuk BH, Galagan NP (2013) Effect of albumin immobilized on the properties of composite systems of cells. In: Kartel NT (ed) "Surface" collect. of scientific works, vol 5, issue 20. pp 291–300 (in Ukrainian)

Chapter 19
Proteins as Nanomachines: Hysteretic Enzymes Revisited

Leonid N. Christophorov

19.1 Introduction

The functioning of proteins, especially enzymes which exemplify natural nanomachines, is inseparably linked with their structural changeability. To successfully perform a specific reaction, it is not sufficient for the protein to have a specially organized active centre. It is also necessary for the whole globule to be in the so-called native conformation—that is, to satisfy a certain pattern of the secondary (mostly hydrogen) bonds defining the secondary and higher structure of the macromolecule. Yet, this is not enough for an effective performance. It has turned out that, first, there is not a single but plenty of those native conformations, and second, much more important, the structure changes in the course of the reaction, and if the enzyme is deprived of this flexibility then its catalytic properties become worse or disappear completely. In view of this, for uncovering sophisticated physicochemical mechanisms of enzymatic reactions the remarkable achievements of X-ray crystallography can mostly serve as reference points only; these beautiful pictures in fact are nothing more than 'platonic images, well removed in its perfection from the kicking and screaming "stochastic" molecule' [1].

And indeed, most of evidences of the multiplicity of conformational (sub)states participating in a given biochemical reaction have been obtained (either in ensemble or single-molecule (SM) experiments) in an indirect way, that is, from the deviations of the observed kinetics from standard (nonexponential time course, non-Arrhenius temperature dependences of rate constants, etc). Nevertheless, it sufficed for revealing and even to some extent classifying a very broad spatial–temporal spectrum of protein structural motions, from times comparable with those of vibrational relaxation down to very low-frequency and long-wave modes and regulatory movements causing global conformational rearrangements (see, e.g. Frauenfelder's concept of the protein energy landscape, glassy character of protein relaxation, so on).

L. N. Christophorov (✉)
Bogolyubov Institute for Theoretical Physics, NAS Ukraine,
14b Metrologichna str., Kiev 03680, Ukraine
e-mail: lchrist@bitp.kiev.ua

O. Fesenko, L. Yatsenko (eds.), *Nanocomposites, Nanophotonics, Nanobiotechnology, and Applications,* Springer Proceedings in Physics 156,
DOI 10.1007/978-3-319-06611-0_19,

The functional roles of these motions which can be conventionally divided into 'fast' and 'slow' are obviously different. Consider a typical expression for the rate constant of a reaction performed by a protein; let it be, for example, the electron transfer between the cofactors of the pigment–protein complex of the photosynthetic reaction centre (RC). For such reactions, a Marcus-type expression (which has deep quantum-mechanical roots) is frequently used:

$$k \sim \frac{2\pi}{h}|V|^2 \mathrm{e}^{-E_\mathrm{a}/k_\mathrm{B}T}, \tag{19.1}$$

where V is the matrix element of electron exchange between the cofactors and E_a is the activation energy which can be written in terms of the fast vibrational subsystem changes caused by the electron transfer (Franck–Condon factor). Defining the form (19.1) of the rate constant, those fast vibrations are usually small amplitude, local, and can be in principle calculated by quantum chemistry methods. The same is not true for the slow and large-scale structural shifts leading sometimes to global conformational changes of the macromolecule. To compute them at the microscopic level seems impossible at present, as well as to monitor them in sufficient detail experimentally. However, let us not be discouraged by that, as it may turn out to be unnecessary, proceeding even from fundamental considerations (cf. a notice in [2] that 'predicting protein functionality or the behaviour of the human brain from these [Schrödinger] equations is patently absurd'). For those aspects of this functionality we speak about here, a statement is sufficient which, like the existence of sound in a solid, does not need a proof [2]. It reads that the slow large-scale structural motions can be represented by some collective generalized coordinates which change on the noticeably slower time scale than the times of single reaction turnovers of the protein–enzyme. Among these coordinates, it is often possible to choose one (or several) playing the decisive role in regulation of the reaction. They may have a transparent (e.g. geometrical) sense; in other cases they can be highly generalized, showing up through, say, energetic parameters which then themselves can be adopted as generalized coordinates. For example, in Eq. (19.1) the matrix element V decreases exponentially with the distance between the electron sites of localization and is thereby very sensitive to changes in this geometrical factor, while the activation energy is sensitive to changes in the electron-free energy difference ('driving force') and reorganization energy which in turn depend on polarization changes caused by the slow relaxation of structural molecular groups. In both cases, under a pronounced temporal hierarchy the rate 'constant' (19.1) holds its form but becomes slowly (but strongly, often exponentially) dependent on the generalized structural coordinate(s).

Due to the regulatory role of these coordinates, they can be called governing modes. In the literature (especially related to systems biology), there exist several analogues of this notion: 'controlling modes', 'slaving modes', or even 'order parameters' (do not confuse with 'control parameters'!) [3]. The last term is closely connected with physics of phase transitions we speak about below. In any case, the existence of such modes reflects the structural and dynamical hierarchy (temporal included) which, in particular, implements Haken's 'slaving principle' and is one

of the necessary conditions of self-organization phenomena [3]. The latter have become customary in the nonlinear approaches to nonequilibrium systems long since, but with an important reservation: the matter always concerned *macroscopic* objects, from many-body physicochemical systems and up to societies. All the expounded below is nothing more than the statement that the same principles are applicable even to SM having at least a single active centre. Moreover, they look much more natural than many of artificial hypothetic models of 'molecular machines' and concern the key biochemical concepts like induced fit, Michaelis–Menten scheme, cooperativity of enzymes, etc.

19.2 The Hysteretic Enzyme Concept

Structural changeability of the macromolecule and the existence of slow governing modes constitute the first necessary condition of our approach. The second, not less important but, strangely, often ignored, are the flow conditions of the functioning, that is, repeated performance of multiple reaction cycles (binding–unbinding of a ligand, turning a substrate into a product, transferring a charge or low-molecular agent, etc). This itself can ensure an essentially nonequilibrium (i.e. far from thermodynamic equilibrium) character of the functioning, even in the stationary states. However, it is the presence of slow degrees of freedom with relaxation times much longer than those of enzymatic turnovers that can add an essentially new element, provided that these degrees of freedom are able to bear the structural memory. In other words, the structural changes introduced by the previous reaction cycle may have no time to totally relax prior to the arrival of the next substrate (beginning of the next cycle). Taking into account the dependences of the characteristics of elementary acts of a turnover like those presented by Eq. (19.1) on the slow structural coordinates, one can easily conclude that this next cycle will be somewhat different from the previous one. This, in turn, will introduce some difference in its footprints on the structural subsystem, so on. Thus, a feedback (and nonlinearity) emerges in the system. Even if a single turnover entails small structural changes only, a series of many consecutive cycles can ensure cumulative effects, eventually able to drastically alter the regime of the functioning. In such in fact nonequilibrium phase transitions [3, 4], the part of the control parameter can be played by first of all the intensity of initialization of the reaction (rate of substrate arrival, actinic light intensity in the case of photochemical reaction, etc). As it is inherent in nonlinear systems, these changes of the functional regimes occur in a sharp, threshold-like manner provided that the control parameter reaches certain critical values.

What is mentioned above may seem trivial—as it really looks for, say, solid-state physicists. All that remains to be done is to correctly formalize these general ideas as applied to biochemical reactions. Most of (bio)chemists, however, still prefer a more traditional approach to deal with those two main conditions listed above. True, it can produce some meaningful results, but to a certain extent only. To clarify this, consider the interpretation of such a central biochemical phenomenon

as cooperativity of enzymes. It implies, generally speaking, a nonhyperbolic (non-Langmuir) dependence of enzymatic reaction rate v (or fractional saturation $\bar{Y}$ of binding sites in sorption processes) on substrate concentration $[S]$. The classical Michaelis–Menten scheme $E + S \underset{k_{-1}}{\overset{k_1[s]}{\rightleftharpoons}} ES \xrightarrow{k_2} E + P$ (where E, S, P stand for enzyme, substrate and product, respectively) gives $v = k_2[S]/([S] + K_M)$, where $K_M = (k_{-1} + k_2)/k_1$, the Michaelis constant. In case of binding (sorption) only, i.e. for $k_2 = 0$, obviously $\bar{Y} = [S]/([S]+k_{-1}/k_1)$. For many vitally important processes, however, such as regulation of the oxygen content in blood and tissues, crucial is a sharper dependence of $\bar{Y}$ on $[S]$, causing saturation drops in a relatively narrow range of concentrations, that is, exhibiting inflections and kinks of the curve $\bar{Y}([S])$. The models that explained such property (first of all, of haemoglobin) involved a discrete set of conformational states of the active centres of the enzyme, see, e.g. [5]. Within the framework of linear equations of standard chemical kinetics, such models did produce the so-called sygmoid dependences, expressing $V([S])$ or $\bar{Y}([S])$ in terms of 'fractional polynomials', that is, the ratio of two polynomials of the second (or higher) power. However, those models inevitably involved two or more (four in the cornerstone case of haemoglobin) binding centres, often implying the quaternary (oligomeric) structure of the protein, i.e. the presence of its several subunits. But in late 1960s the term 'hysteretic enzyme' was introduced for some *monomeric* enzymes possessing a *single* binding site and nevertheless exhibiting cooperative properties [6–8]. In the corresponding models, the key point was the introduction of a state of the free enzyme *after* the release of the product/substrate, structurally different from the initial state and *slowly* relaxing to the latter. The simplest necessary modification of the Michaelis–Menten scheme, as applied to repeatedly cycling enzyme then takes a 'triangular' form

$$E \underset{k_{-1}}{\overset{k_1[S]}{\rightleftharpoons}} ES \underset{k_{-2}[S]}{\overset{k_2}{\rightleftharpoons}} E' \xrightarrow{k_b} E \tag{19.2}$$

for the case of binding (for that of enzymatic reaction, the rate of product release should be added to k_2). It is easy to check that this scheme leads to $\bar{Y}([S])$ as a second power fractional polynomial, and the second derivative $\mathrm{d}^2\bar{Y}/\mathrm{d}[S]^2$ shows that such 'SM cooperativity' (sygmoidicity of $\bar{Y}([S])$) is possible if

$$k_b < k_2[(k_{-2}/k_1) - 1]. \tag{19.3}$$

Condition (19.3) shows that, first, the substrate/ligand binding should be better in the 'active' structural state E', and second, more important, the return of the enzyme to the more stable but less active initial state E should be slow (small k_b) and the direct reaction (k_2) fast. This does reflect the main physical origin of 'monomeric cooperativity': the macromolecule should have no time to return from the active state E' (to which it was sent by the substrate arrival) prior to the arrival of the next substrate. It turns out that the conformational subsystem of the enzyme realizes indirect but effective interaction between the consecutive substrates (but not between different allosteric binding sites) in spite of the fact that only one substrate is involved in each cycle. The sygmoid shape of $\bar{Y}([S])$ can be viewed as a transition between

two hyperbolas with different Michaelis' constants K_M's in the limits of low and high substrate concentrations: the lower hyperbola corresponds to binding in the less active state *E,* and the upper—in the active state E'.

Although such models are on the side-lines of biochemical mainstream (yet the interest in them is periodically returning, see e.g. recent review [9]), they accent the most important aspects of the enzyme functioning: (1) its flow regime (arrival of substrates at maintained concentration) is implied by definition; (2) structural memory of the enzyme macromolecule, ensured precisely by slow conformational relaxation, and thereby the possibility of changes of the working regimes by changing the intensity of the input flow (substrate concentration). However, such enzymes can be hardly called exactly 'hysteretic', since a true hysteresis loop and bistability cannot appear: curves $\bar{Y}([S])$ are always strictly single-valued and never S-like in this kind of models. Besides, their cooperativity is rather poor, as fractional polynomials of low powers do not lead to sharp inflections, i.e. threshold-like effects, and the higher powers would inevitably require more complex schemes with many binding sites, see the case of haemoglobin. The origin of the drawbacks of these models containing *almost* all the necessary prerequisites of dynamical self-organization (temporal hierarchy, flow conditions, even feedback, in a sense) is rather clear: they employ in fact *linear* kinetic equations and *discrete* sets of conformational states. The reaction states of the enzyme and those of its structural subsystem enter such schemes equally, differing in the rates of transitions only. Below we show how to remove these drawbacks and arrive, in a quite natural way, at a richer picture of structure–function coupling.

19.3 Generic Model

The simpler the model, the better the modelling. Let us return to the two-state scheme, *E* and *ES*. Since, however, our model is of very general character beyond the scope of enzymatic reactions, we label these states as **0** and **1**. To ensure the flow conditions, we consider a reversible reaction,

$$\mathbf{0} \underset{r(x)}{\overset{I}{\rightleftharpoons}} \mathbf{1}. \tag{19.4}$$

The rate coefficients in Eq. (19.4) have the following meaning. Rate constant I of the forward reaction stands for intensity of the input flow initiating the reaction. For enzymatic reactions or binding processes $I \sim [S]$; for photochemical reactions I is proportional to actinic light intensity, as it takes place for the electron transfer (charge separation) reactions in isolated photosynthetic RCs [10], etc. The main burden, however, is placed on the rate coefficient of the backward reaction which is supposed to be dependent on the generalized structural coordinate x ('order parameter', see Introduction), thereby making the problem nontrivial. First, instead of a discrete set of prescribed conformations we introduce their continuum. Second, there appears an explicit feedback (and, consequently, nonlinearity), as not only the turnover kinetics ('recombination' rate coefficient r) depends on the state of the structural subsystem

but also the dynamics of the latter is obviously dependent on the reaction state (ligand-free or ligand-bound, charge-separated or neutral/recombined, etc.) occupied by the 'enzyme'. It remains to correctly derive the evolution equations for such a self-consistent (and essentially nonequilibrium!) system.

Begin with the structural subsystem x. Due to the slowness of its motion connected with displacements of heavy atomic groups we can assume this motion overdamped, i.e. suppose that $\dot{x} = -\mathrm{d}V_i(x)/\mathrm{d}x$, where $V_i(x)$ is the structural potential that corresponds to reaction state i ($i = 0$ or 1). Transitions $\mathbf{0} \rightleftharpoons \mathbf{1}$ proceed with the mean rates defined in Eq. (19.4), but each specific transition is a random event causing an instant change of the potential from $V_0(x)$ to $V_1(x)$ or vice versa. Thus, the action of reaction events upon the structural subsystem is in fact a dichotomous noise F_t with its space of states $F_t(x) \in \left\{-V_0'(x),\ -V_1'(x)\right\}$ and master equation

$$\dot{\rho}_0(t|x) = -I\,\rho_0(t|x) + r(x)\rho_1(t|x), \quad \rho_0(t|x) + \rho_1(t|x) = 1 \tag{19.5}$$

for the probabilities of realization of force F_t. Because of the presence of the x-dependent rate coefficient $r(x)$, this noise is certainly non-Markovian; it can be referred to as dichotomous noise with feedback. Besides, the structural subsystem undergoes the action of a standard Langevin force (thermal white noise) F_L, so that the second equation of the model reads:

$$\dot{x} = F_t(x) + F_L. \tag{19.6}$$

As is shown in [11, 12], the set of Eqs. (19.5, 19.6) is equivalent to the forward diffusive evolution equations for probability densities $P_i(x,t)$ of the pair random process $\{i, x\}$:

$$\begin{aligned}
\frac{\partial P_0(x,t)}{\partial t} &= \left[D_0 \frac{\partial}{\partial x}\left(\frac{\mathrm{d}V_0}{\mathrm{d}x} + \frac{\partial}{\partial x}\right) - I\right] P_0(x,t) + r(x)P_1(x,t) \\
\frac{\partial P_1(x,t)}{\partial t} &= \left[D_1 \frac{\partial}{\partial x}\left(\frac{\mathrm{d}V_1}{\mathrm{d}x} + \frac{\partial}{\partial x}\right) - r(x)\right] P_1(x,t) + I\,P_0(x,t),
\end{aligned} \tag{19.7}$$

which can be used as an alternative, avoiding explicit stochastic simulations. In (19.7), the energy is scaled in $k_B T$ units, and D_i's are the corresponding diffusion coefficients.

19.4 Molecular Self-organization in a Nutshell

So far, Eqs. (19.7) are valid for any relationship between the time scale of the reaction acts and that of structural motions caused by the drift and diffusion processes. The effect we are seeking for can be easily seen if we now explicitly exploit the aforementioned temporal hierarchy, applying a proper adiabatic approximation to Eqs. (19.7), i.e. factorization $P_{0,1}(x,t) = \rho_{0,1}(t|x)P(x,t)$. Then, we arrive at an effective Fokker–Planck equation for the probability density of the structural variable $P(x,t) = P_0(x,t) + P_1(x,t)$ [12]:

$$\frac{\partial P(x,t)}{\partial t} = D\frac{\partial}{\partial x}\left[\frac{\mathrm{d}V_I^{eff}(x)}{\mathrm{d}x} + \frac{\partial}{\partial x}\right] P(x,t), \tag{19.8}$$

where

$$\frac{\mathrm{d}V_I^{eff}(x)}{\mathrm{d}x} = \rho_0^{st}(x)\frac{\mathrm{d}V_0(x)}{\mathrm{d}x} + \rho_1^{st}(x)\frac{\mathrm{d}V_1(x)}{\mathrm{d}x} \tag{19.9}$$

and $\rho_{0,1}^{st}(x)$'s are the stationary solutions to Eq. (19.5) at fixed x; for the sake of clarity, here we set $D_0 = D_1 = D$. A peculiar feature of the effective nonequilibrium adiabatic potential consists in its dependence on flow intensity I: it is clear from Eq. (19.9) that $V_I^{eff}(x)$ is close to $V_0(x)$ for low intensities and to $V_1(x)$ for high ones. But what can happen in between?

We illustrated that with the most practical examples of harmonic potentials $V_{0,1}(x) = (\gamma/2)(x - x_{0,1})^2$ and exponential dependence $r(x) = r\exp(-x)$, suitable for many real biochemical reactions like ligand binding to myoglobin, cycling of some enzymes [13] or electron transfer in photosynthetic RCs [14–16], see also comments to Eq. (19.1). Remarkably, it has turned out that under sufficiently strong structure function coupling (here, under the condition $x_m = x_1 - x_0 > 4$, i.e. sufficient displacement of $V_i(x)$'s minima positions), there exists a bistability window $[I_1, I_2]$ where $V_I^{eff}(x)$ acquires a two-well shape, and its extrema positions x_e controlled by intensity I are represented by a truly hysteretic, S-like curve $x_e(I)$ determined by a simple equation

$$I/r = x_e\exp(-x_e)/(x_m - x_e). \tag{19.10}$$

Thus, the whole picture is similar to that described in the previous section but with an important difference: now the transition between the two working regimes—that of, say, low fractional saturation (or weak charge separation, etc.) conditioned by a relatively fast backward reaction ($r(x) \simeq re^{-x_0}$) at low intensities, and that of high fractional saturation ($r(x) \simeq re^{-x_1}$)—proceeds via the bistability window of intensities in which both regimes coexist. After the authors of books [3, 4], we can rightfully classify such a behaviour as nonequilibrium phase transition of the first kind, or as an example of (intra)molecular synergetics phenomena.

Amazingly, even such a simple model has allowed us to give a qualitative and even semi-quantitative account of peculiarities of the reversible photoinduced electron transfer reactions in isolated photosynthetic RCs (see e.g. [15, 16]). In our experiments on this well-known biophysical reference model, we put special emphasis exactly on scanning the RC performance with respect to gradual changes in applied actinic light intensity I. Having elaborated the model with more realistic potentials and performing parallel extensive computer simulations, we have revealed not only bistability/threshold effects in the RC performance originated from its structural rearrangements but also demonstrated rather convincingly the effects of RC structural memory. Those findings clearly showed the vitality of the molecular self-organization concept proposed. Yet, they have been obtained in ensemble experiments; together with the inherent hidden nature of conformational regulation and too high a level of generality of the theory, this can provoke some doubts among sceptics. To this end, it is logical to expect even more convincing evidences of the mentioned synergetic effects in SM experiments. A possible way to register them is outlined in the next section.

19.5 Molecular Self-Organization: Manifestations in Single Molecule Reaction Characteristics

In SM experiments, the serial performance of reaction cycles takes place by definition. For a two-state reaction scheme like (19.4) the corresponding experimental trace is an SM 'trajectory' which looks like a dichotomous process of random flips between states **0** and **1.** One of them, say, **1** is usually referred to as 'on'-state, then the second as 'off'-state. The time spent in state **1** before a flip into state **0** is called 'on-time', and one of the prime statistical characteristics extracted from an SM trajectory is the on-time distribution (OTD). In the absence of structural changeability ($r(x) = r = \text{const}$ in scheme (19.4)) this normalized distribution is a simple time exponential, $f_{\text{on}}(t) = r \exp(-rt)$. Another prime characteristic calculated along such trajectory is the autocorrelation function (ACF) $\langle \xi(t)\xi(0)\rangle$, assuming that $\xi = 1$ in state **1** and $\xi = 0$ in state **0**. Like the OTD, the ACF is also a simple time exponential $\sim \exp[-(I + r)t]$ in the case of constant rate coefficients. However, just the first SM experiments on enzymes revealed pronounced nonexponentiality of both the OTD and ACF [17], thereby explicitly testifying the intercycle memory originated from structural changeability. In order to reproduce the subtle features of this nonexponentiality, a series of models of conformational regulation has been developed, from simple two-conformation schemes, similar to those mentioned in Sect. 19.2, to quite sophisticated ones, involving fractional calculus. This definitely improved our knowledge of protein fluctuations and relaxation but added relatively little to unveiling the mechanisms of protein reactions.

Earlier we showed [18] that the diffusive evolution equations like set (19.7) look most convenient and adequate for calculating the OTD and ACF. The latter obtained from such equations exhibit quite unexpected peculiarities, qualitatively different from those obtained within standard chemical kinetics. Recently [19] we posed a direct question: How do the self-organization effects described show up in the SM characteristics, the OTD and ACF, in particular? To answer it, we have simulated SM trajectories for our system with the two noises based on Eqs. (19.5, 19.6) with subsequent direct calculation of the OTD and ACF. In parallel, we calculated the latter, basing on their analytical expressions in terms of solutions to set (19.7). The system parameters were chosen similar to those in our previous description of the electron transfer in the RC [15], i.e. they admitted S-like curves, bistability, etc. In such a way, we have obtained the OTDs and ACFs in a wide range of intensities *I,* from close to zero, through the bistability window, and up to very high intensities. Both methods, simulation and analytics, have produced practically identical results, but for further processing we used the smoother functions obtained within Eqs. (19.7). Then we expanded the OTDs and ACFs into the relaxation time spectra as $f_{on}(t) = \int_0^\infty \exp(-t/\tau) g(\tau) \mathrm{d}\tau$ with the help of a specially developed version of the maximum entropy method.

The results have turned out to be very eloquent. It could be clearly seen that from low intensities to the left border I_1 of the bistability window all the peaks of $g(\tau)$ were concentrated around short times $\tau < \tau^*$ (where τ^* corresponded to x^*

which divided the attractors of 'weakly' and 'strongly' deformed structural states, $\tau^* = (1/r)\exp(x^*)$), whereas for $I > I_2$ and up to very high values those peaks corresponded to times visibly longer than τ^*. While inside the bistability window, $I_1 < I < I_2$, the short- and long-time components coexisted, showing a gradual transition from 100 %-short to 100 %-long ones with I increasing. As for the ACF, it exhibited quite a sharp splash of long-lived correlations exactly inside the bistability window, witnessing the occurrence of a nonequilibrium phase transition. Thus, these direct indications of intramolecular dynamic self-organization in the functioning of biomolecular machines at the level of prime SM characteristics could serve as a good guidance for real experiments.

19.6 Concluding Remarks

The concept outlined above encompasses quite a wide circle of biochemical processes, as it concerns the core of structure–function coupling. Apart from enzymatic reactions, it may turn out to be fruitful in the analysis of many systems of biological transport like transmembrane ionic channels (see, e.g. the early attempt [20]), electron transport chains in respiration and photosynthesis, ATPase and molecular motors, etc. which function under essentially nonequilibrium conditions. Besides, its merits are obvious for designing various types of biomolecular sensors and other biologically motivated nanodevices. It is promising even in such classical areas as adsorption and surface catalysis (amazingly, the possibility of such type of hysteretic effects to occur in adsorption processes was in fact indicated by Zeldovich as long ago as in 1938 [21] and only recently was theoretically elaborated [22] exactly along the lines of our minimal model presented in Sects. 19.3, 19.4). The clarity and simplicity of the concept models and their computational accessibility allow us to hope for their wide and insightful use in near future.

Acknowledgments Unfortunately, the paper [19] was the last written in coauthorship with recently deceased Professor Valeriy Nikolayevich Kharkyanen, a prominent Ukrainian scientist in theoretical physics and physics of biological systems, whose exciting and productive collaboration I was so privileged to enjoy for so many years. This chapter is dedicated to him.

I also thank my other coauthors of many works in the field, especially A.O. Goushcha and Yu.M. Barabash for performing many high-quality experiments and N.M. Berezetskaya for excellent programming.

References

1. Weber G (1975) Energetics of ligand binding to proteins. Adv Prot Chem 29:1–83
2. Laughlin R, Pines D (2000) Theory of everything. Proc Natl Acad Sci U S A 97:28–31
3. Haken H (1978) Synergetics. Springer, Berlin
4. Horsthemke W, Lefever R (1984) Noise-induced transitions. Springer, Berlin

5. Monod J, Wyman J, Changeux JP (1965) On the nature of allosteric transitions: a plausible model. J Mol Biol 12:88–99
6. Frieden C (1970) Kinetic aspects of regulation of metabolic processes: the hysteretic enzyme concept. J Biol Chem 245:5788–5799
7. Rabin BR (1967) Cooperative effects in enzyme catalysis: a possible kinetic model based on substrate-induced conformational isomerization. Biochem J 102:22c–23c
8. Ricard J, Cornish-Bowden A (1987) Cooperative and allosteric enzymes: 20 years on. Eur J Biochem 166:255–272
9. Qian H (2012) Cooperativity in cellular biochemical processes: noise-enhanced sensitivity, fluctuating enzyme, bistability with nonlinear feedback, and other mechanisms for sygmoidal responses. Annu Rev Biophys 41:179–204
10. Hoff AJ, Deisenhofer J (1997) Photophysics of photosynthesis. Structure and spectroscopy of reaction centers of purple bacteria. Phys Rep 287: 1–247
11. Christophorov LN (1995) Conformation-dependent charge transport: a new stochastic approach. Phys Lett A 205:14–17
12. Christophorov LN, Holzwarth AR, Kharkyanen VN, van Mourik F (2000) Structure-function self-organization in nonequilibrium macromolecular systems. Chem Phys 256:45–60
13. Agmon N (2000) Conformational cycle of a single working enzyme. J Phys Chem B 104:7830–7834
14. McMahon BH, Müller JC, Wraight CA, Nienhaus GU (1998) Electron transfer and protein dynamics in the photosynthetic reaction center. Biophys J 74:2567–2587
15. Barabash YuM, Berezetskaya NM, Christophorov LN, Goushcha AO, Kharkyanen VN (2002) Effects of structural memory in protein reactions. J Chem Phys 116:4339–4352
16. Goushcha AO, Manzo AJ, Scott GW, Christophorov LN, Knox PP, Barabash YuM, Kapoustina MT, Berezetska NM, Kharkyanen VN (2003) Self-regulation phenomena applied to bacterial reaction centers. Nonequilibrium adiabatic potential: dark and light conformations revisited. Biophys J 84:1146–1160
17. Xie XS, Lu HP (1999) Single-molecule enzymology. J Biol Chem 274:15967–15970
18. Christophorov LN, Holzwarth AR, Kharkyanen VN (2003) Conformational regulation in single molecule reactions. Ukr J Phys 48:672–680
19. Christophorov LN, Kharkyanen VN, Berezetskaya NM (2013) Molecular self-organization: a single molecule aspect. Chem Phys Lett 583:170–174
20. Chinarov VA, Gaididei YB, Kharkyanen VN, Sit'ko SP (1992) Ion pores in biological membranes as self-organized bistable systems. Phys Rev A 46:5232–5241
21. Zeldovich YaB (1938) Adsorption on a uniform surface. Acta Physicochim URSS 8:527–530
22. Usenko AS (2012) Adsorption on a surface with varying properties. Phys Scr 85:015601

Chapter 20
Application of Carbon Nanotubes for Plant Genetic Transformation

Olga M. Burlaka, Yaroslav V. Pirko, Alla I. Yemets and Yaroslav B. Blume

20.1 Introduction

Great number of nanotechnology products such as liposome, polymeric and metallic nanoparticles, quantum dots, fullerenes, and carbon nanotubes (CNTs) found their application in biotechnology. Unique properties of CNTs give rise to an increasing interest in their exploitation for the delivery of biomolecules into living cells. They are already designed for imaging [135, 178, 180], biosensing [25, 69, 96, 140, 163], and targeted delivery of molecules into cells [4, 13, 24, 61, 78, 88, 94, 100, 102, 104, 133]. Namely, CNTs have been prepared for delivery of plasmid DNA [100, 131, 160], small interfering RNA (siRNA) [61, 102, 133], proteins [72, 78], and drugs [4, 13, 24, 103, 104]. Exploiting CNTs for the development of novel genetic transformation techniques holds great promises due to expected increased efficiency, applicability, reproducibility, and accuracy of biotransformation compared to existing techniques [27, 143]. CNTs were used in recent approaches for the genetic transformation of bacterial [112, 142, 148, 167] and mammalian [17, 100, 127, 131, 160, 195] cells. Reports also indicate that CNTs loaded with molecular cargoes (labeling molecules, DNA) can enter plant protoplasts [154] and walled plant cells [106, 155]. Having the favor for cell-entering aspect ratio, CNTs exhibit the ability to penetrate through plant cell wall and membrane displaying low cytotoxicity. Despite nano-dimensions,

Y. B. Blume (✉) · O. M. Burlaka · Y. V. Pirko · A. I. Yemets
Institute of Food Biotechnology and Genomics, National Academy of Sciences of Ukraine, Osipovskogo str. 2A, 04123 Kyiv, Ukraine, Tel.: +38 (044) 434-4584
e-mail: cellbio@cellbio.freenet.viaduk.net

O. M. Burlaka
e-mail: burlaka29@gmail.com

Y. V. Pirko
e-mail: yavp@mail.ru

A. I. Yemets
e-mail: yemets.alla@gmail.com

O. Fesenko, L. Yatsenko (eds.), *Nanocomposites, Nanophotonics, Nanobiotechnology, and Applications,* Springer Proceedings in Physics 156,
DOI 10.1007/978-3-319-06611-0_20,

CNTs possess extremely large surface area and are responsible for covalent and non-covalent molecule binding. Biomolecules, in particular DNA, can interact and bind non-covalently to graphitic surface of CNTs through π–π stacking interactions [120]. In this frame, CNTs are considered to be promising for the development of novel approaches in genetic transformation of plants. Comparing to the existing foreign DNA delivery methods for walled plant cells such as the gene gun, electroporation, and microinjection [47, 137, 172], the CNT-based strategy viewed to be advantageous in easy operation, high efficiency, wide applicability, etc. Nevertheless, the lack of CNT dispersibility in aqueous environments has been a major technical barrier for biological and biomedical applications [187]. The recent expansion in methods to chemically modify and functionalize CNTs has made it possible to solubilize and disperse them in water, but existing CNT surface functionalization protocols often involve usage of hazardous chemicals and critical reaction conditions [80]. Therefore, environmentally and biologically friendly functionalization at present is of principal interest in tailoring of CNTs with desired surface properties for biological applications such as genetic engineering of plants.

20.2 CNTs: Features and Properties

Since the time of first observation by Iijima in 1991 [64], CNTs have become increasingly popular in various fields due to the unique combination of dimension, structure, and topology and outstanding mechanical, electronic, and optical properties [151]. Applications of CNTs span composite materials production, nanoelectronics, field-effect emitters, hydrogen storage, biosensors and various electroanalytical devices, bioengineering, cancer therapy, and drug delivery [1, 19, 40, 49, 66, 73, 75, 91, 105, 123, 138, 197]. CNTs are hollow graphitic nanomaterials viewed as rolled-up structures of single or multiple sheets of graphene to give single-walled (SWCNTs) and multi-walled (MWCNTs) CNTs, respectively. CNTs are capped with a hemisphere of a buckyball structure [80]. Carbon atoms in graphene sheets form a hexagonal lattice. The structure of CNTs gives rise to three types of CNTs [12, 55]. Based on the unit cell of a CNT it is possible to identify armchair, zigzag, and chiral nanotubes. The electronic properties of a nanotube are in correspondence to its structure. Thus, armchair nanotubes are metallic, while zigzag and chiral can be either metallic or semiconducting. CNTs have lengths ranging from several hundred nanometers to several micrometers and diameters of few nanometers for SWCNTs and dozens of nanometers for MWCNTs [2, 43, 105, 187].

CNTs are produced by electric arc, laser ablation, chemical vapor deposition (CVD), cyclic oxidation, and modifications of these methods such as plasma-enhanced and thermal CVD [12, 63, 183], etc. Compared with the other conventional methods, CVD is considered as the most promising due to simplicity and economy [8]. Different shapes of CNTs are produced for different applications: straight and waved with regular structure, well-aligned, extremely long, toroidal, coiled, beaded, branched, and bent (kink) CNTs [198], etc. After the growth process, CNTs contain a

large number of impurities such as metal catalyst nanoparticles, amorphous carbon, carbon nanoparticles, and fullerenes, which must be removed [151]. CNT purification techniques include ultrasonication, microfiltration, chromatographic techniques, microwave heating, and gas-phase and acid oxidation [10, 45, 57, 124, 147, 151, 156]. Main current issues in CNT synthesis and processing are ecological safety and maximum economic efficiency (less energy consumption, renewable sources for the synthesis) together with increased variety of end-product properties well designed for different applications.

20.3 Functionalization of CNTs

Despite promising advantages, the use of CNTs for biomedical applications is limited due to their low biocompatibility [28, 145]. Pristine CNTs present highly hydrophobic surfaces, resulting in poor water dispersibility and making them unsuitable for biological applications. They usually occur as close-packed bundles in which tubes are held together by van der Waals forces [12]. To improve the biocompatibility of CNTs, surface modification or functionalization is required to afford dispersing in aqueous media. Towards the functionalization processes, CNTs are differentiated into two zones in terms of their reactivity, i.e., sidewalls and tips (caps) [42, 54, 145]. It has been shown that tips, which have a semifullerene-like structure, as well as sidewall defects appearing due to physical and chemical treatments (pentagone–heptagon pairs, sp^3-hybridized carbon atoms, vacancies in the nanotube lattice, open ends), are more prone for modification than sidewalls [80, 125, 169, 201].

Generally, CNTs can be functionalized by a series of methods, including their functionalization by the aryl diazonium process, use of elemental metals, simple inorganics, acids, esters, aldehydes, amines, aromatics, macrocycles, thiols, biomolecules, polymers, and such techniques as pulsed streamer discharge, microwave or ultrasound treatment, cryogenic crushing, γ-irradiation [83], etc. The main approaches for the functionalization of CNTs can be grouped into two categories: (1) the covalent attachment of chemical groups, through reactions on the conjugated skeleton of CNTs, and (2) the non-covalent supramolecular adsorption or wrapping of various functional molecules onto the tubes [9, 145]. Contrary to covalent functionalization methods, which disrupt the extended π-networks on the CNT surfaces and can modify their mechanical and electronic properties, non-covalent functionalization preserves the desired properties of CNTs [151].

Functionalization may have significant influence on the behavior of CNTs in biological objects [14, 29, 39, 160, 191]. Surface modifications allow tailoring of CNTs with desired properties exhibiting a larger spectrum of biomedical, biotechnological, and pharmaceutical applications for improved accuracy and efficiency of targeted cellular and subcellular delivery, decreased toxicity, and controlled degradation [44, 94, 153, 182, 201].

20.3.1 Covalent Functionalization of CNTs

Covalent functionalization exploits the chemical reactivity of CNTs to form bonds between the CNT surface and a hydrophilic moiety. Covalent bonding of modifying moieties having hydrophilic groups in their structure results in increased water solubility of modified CNTs [145]. Covalent functionalization of CNTs involves disruption of graphitic skeleton, loss of electronic properties, and stable bond formation [80]. It is usually carried out on the sidewalls or tips in way of cyclo- or radical addition reactions, oxidation, esterification, amidation, etc. Among others, currently used functionalization agents include aryl diazonium moieties and halogen-, oxy-, carbon-(alkyl-, alkenyl-, alkynyl-, aryl-, and acyl-), and metal-based radicals [83, 131]. For oxidation, oxidizing acids (nitric, sulfuric, perchloric), ozone, oxygen, hydrogen peroxide, superoxides, and metal oxidants such as osmium tetroxide, potassium permanganate, and chromates are used [26, 28, 34, 60, 117, 161, 165, 184, 188]. Strong acidic media are often used on the first functionalization step with further covalent or non-covalent attachment of various organic moieties to oxidized CNTs [83]. The selective opening at the cap region of nanotubes by oxidants can be used for filling of the inner hollow cavity of CNTs [54]. Reduction reactions are carried out with thiols, carbenes, dienes, etc. Other reactions are based on the use of macrocycles, biomolecules, polymers, radionuclides, irradiation, microwave treatment, and pulsed streamer discharge [83].

For the development of novel genetic transformation methods, covalent-bond approaches of direct DNA attachment onto CNTs surface are nonacceptable since they compromise and spoil biological functions of DNA and prevent releasing DNA in cells. For this aim, covalently grafted chains may function as efficient anchors to non-covalently immobilize molecules of interest, in particular DNA, onto the surface of CNTs [80, 100]. This approach might be exploited to prepare CNT-based DNA sensors or probes and novel gene-delivery systems. Reports indicate that acid-oxidized CNTs can be used to tailor non-covalent protein- or DNA-nanotube conjugates [72, 74, 76, 148]. Different anchoring residues covalently attached onto the CNT surface may differ in DNA non-covalent-binding ability [127, 199]. CNT surface area and charge density are viewed to be critical parameters that determine the interaction and electrostatic complex formation between functionalized CNTs and DNA [160]. Polymers, such as polyallylamine (PAA), polyethylenimine (PEI), polyethylene glycol (PEG), etc., and their mixtures, grafted on CNT surface are often used as anchoring molecules for DNA attachment in the development of novel DNA or siRNA delivery methods [76, 100, 105, 127, 199]. Covalent modification of CNTs may also provide other advantages such as improved CNT-based molecule delivery techniques for walled plant cells [50, 155]. For this, covalent modification of CNT surface with enzymes degrading the components of the plant cell wall is viewed to be a promising approach.

20.3.2 Non-Covalent Functionalization of CNTs

Non-covalent CNT functionalization approaches are of principle interest in recent years since further development of nanotechnology-based approaches is viewed to involve the combination of nanotechnology and green chemistry principles and practices [176]. The latter include the design and development of syntheses using renewable high energy-efficient materials, benign reaction media, and nonhazardous as well as nontoxic reagents if possible [6, 39, 176]. Thus, it is considered to be necessary to develop various environmentally friendly techniques in nanobiotechnology, namely, introduce non-covalent CNT functionalization approaches, exploiting mild reaction conditions and nonhazardous chemicals [115].

Non-covalent functionalization approaches are based on van der Waals and $\pi-\pi$ interactions and adsorption or wrapping of polynuclear aromatic molecules, surfactants, polymers, and biomolecules [36, 38, 46, 80, 145, 171, 182]. After the non-covalent functionalization, structure and electronic network of CNTs remain unaffected [203]. Non-covalent functionalization of CNTs is preferable in a number of approaches to maintain their important spectroscopy properties, such as near-infrared (NIR) absorption features, photoluminescence, and Raman scattering [53, 75, 128, 146]. In non-covalent functionalization approaches to initiate the interaction process between CNT surface and corresponding domains of functionalizing molecules, ultrasound treatment is widely used [32]. Ultrasonication plays a critical role in debundling of CNTs. Besides, under sonication molecules used for functionalization such as proteins, DNA, etc. are suggested to change their conformation with subsequent opening of hydrophobic sites responsible for interactions with nanotube sidewalls [79, 120, 179]. Therewith, ultrasound treatment may cause open ends and sidewall defect appearance together with shortening of CNTs, enabling increased efficiency of non-covalent molecule binding and cell penetrating [11, 54, 80, 89, 91, 141, 154].

Non-covalent functionalization can be used to disperse CNTs in water environments and to adjust their interactions with living cells. It can also be the platform for further attachment of molecules to the surface of dispersed CNTs [62]. Among currently used functionalizing molecules are R-pyrene-ω-aminooxy-functionalized PEG, pyrene, and phospholipids, bound to different surfactant polymers based upon poly(γ-glutamic acid) and poly(maleic anhydride-alt-1-octadecene), pyrenecarboxylic acid, pyro-pheophorbide, porphyrin derivatives, succinimidyl ester of 1-pyrenebutanoic acid, glycodendrimers [21, 30, 62, 81, 139, 159, 182], etc. A simple and nondestructive method for nanotube dispersing in aqueous media is based on non-covalent interactions between amphiphilic molecules and nanotube surfaces: Hydrophilic parts of such molecules interact with the solvent and hydrophobic parts are adsorbed onto the nanotube surface, thus solubilizing CNTs and preventing them from the aggregation into bundles and ropes [80]. Surfactants such as sodium dodecyl sulfate, sodium dodecane-1-sulfonate, sodium 4-dodecyl benzenesulfonate, tetraalkylammonium bromide, hexadecyl(trimethyl)azanium bromide, cetyltrimethyl ammoniumbromide, Triton, Pluronic, etc. are used for this aim

[36, 41, 68, 129, 164, 174, 175]. Surfactant-assisted dispersion of MWCNTs in aqueous media was shown to be strongly diameter dependent [36]. Not only hydrophobic interactions but Coulomb interactions and Lewis acid–base complexation were found to play a key role in surfactant-assisted dispersing of MWCNTs. While suspensions of CNTs can be obtained with plenty of different surfactants, only few are both nontoxic for living cells and able to withstand a variety of different conditions without the presence of surfactant excess [53].

20.3.2.1 Non-Covalent Functionalization Using Biomolecules

Functionalization of CNTs with the assistance of biological molecules remarkably improves the water dispersibility, biocompatibility, and functionality of end product and provides "greener" solution for nanobiotechnology [83]. The most promising molecules for non-covalent CNTs surface functionalization are proteins [79, 121, 179], carbohydrates [51, 189, 200], and nucleic acids [44, 108, 120]. Presence of aromatic regions and both hydrophilic and hydrophobic sites allows the interactions of these molecules with hydrophobic CNT surface one the one hand and with aqueous environment on the other hand. Supramolecular binding of aromatic molecules can be achieved by π–π stacking of those molecules onto the polyaromatic surface of CNTs [103]. This results in the formation of stably dispersed tubes with opened sites for further attachment of target molecules.

Proteins are natural polyampholytes containing both hydrophobic and hydrophilic domains [80, 121]. Among proteins used for the non-covalent CNT functionalization are lysozyme, bovine serum albumin (BSA), hydrophobins, hemoglobin, myoglobin, ovalbumin, trypsin, glucose oxidase, synthetic oligopeptides, histone, streptavidin, and self-assembling peptide amphiphiles [7, 9, 79, 80, 90, 111, 121, 179, 207]. The behavior of CNT dispersion by water-soluble proteins was found to be related to their unfolding and refolding process [111]. Presence of aromatic amino acids strongly determines the ability of proteins to disperse CNTs in water since π–π stacking interactions between aromatic residues of a peptide and the graphitic surface of CNTs play an important role in peptide-based dispersion of tubes [207].

Nucleic acids could be attached to carbon nanotubes non-covalently by adsorption [23, 56, 206, 205]. Compared to other polymers used, DNA offers the advantage of defined length and sequence, high dispersion efficiency, and well-developed chemistries for further functionalization of the DNA–CNT hybrid through either covalent or non-covalent functionalization [206]. In comparison with single-stranded DNA (ssDNA) molecules which are highly efficient to disperse CNTs in water [120, 206], double-stranded DNA (dsDNA) molecules are less costly and easier to obtain from natural sources [185].

The mechanism on the nucleic acids wrapping on CNTs is thought to be driven by van der Waals and π–π stacking interactions, the entropy loss due to the confinement of the DNA backbone, and electronic interactions between DNA and CNTs [109]. Molecular dynamic simulations of DNA adsorption on an SWCNT in an aqueous environment show that DNA binds to the external surface of SWCNT on a time scale of a few hundred picoseconds [202]. The adsorption process appears to have negligible

effect on the internal stacking structure of the DNA molecule but significantly affects the A-to-B form conversion of A-DNA. Results of another computational study show that siRNA strongly binds to SWCNT surface via unzipping its base pairs and the propensity of unzipping increases with the increase in SWCNT diameter [152].

In another study, numerous structural changes in DNA that might be interpreted as A–B conformation transitions and stabilization of structure in some DNA fragments were detected in DNA–SWCNT complexes [42]. DNA–CNT interaction model in this case was viewed to be similar to that in chromosomes during DNA assembling by histones. Wrapping of CNTs by ssDNA was found to be sequence dependent. A systematic search of the ssDNA library selected a guanine and thymine sequence d(GT)*n* ($n = 10$–45) that self-assembled into a helical structure around individual nanotubes in a way that made the properties of the DNA–CNT hybrid dependent on tube diameter and electronic properties [173, 205]. It was shown that bound to SWCNT ssDNA probes d(GT)*n* ($n = 30$) were stable against enzymatic cleavage and interference from nucleic-acid-binding proteins [181]. Nanotube-modified DNA probe, which targets a specific mRNA inside living cells, has increased self-delivery capability and intracellular biostability when compared to free DNA probes. Compactness and selectivity of DNA wrapping around SWCNTs were found to be dependent on the length of the DNA sequence, and by increasing the strand length, both the degree of compactness of the wrapping around the nanotube and the diameter selectivity decreased [177, 190]. The nucleobase dependence of CNT–DNA hybrid stability was found to decrease as G > C > A > T [3]. While hydrophobic π-stacking is suggested to be the main driving force for the CNT–DNA complex formation, other factors such as the electrostatic interaction between the phosphate backbone and the aqueous environment, base stacking within the single-stranded polymer, and geometric and stereochemical limitations might also influence stability features [11].

Non-covalent approaches are sometimes viewed to provide metastable immobilization of DNA onto the surface of CNTs. It was reported that the migration of DNA linked covalently to CNTs was retarded in gel electrophoresis but non-covalent interactions between DNA and CNTs did not completely prevent migration [44]. On the one hand, exploiting CNTs for the DNA delivery into cells with subsequent release of DNA inside the cell requires non-covalent attachment of DNA. On the other hand, for CNT separation, self-assembly, and other approaches covalent irreversible attachment of DNA onto the nanotube surface is of principal importance.

Polysaccharides and other molecules used for non-covalent CNT functionalization are chitosan and its derivatives, schizophyllan and curdlan, alginic and hyaluronic acid, N-acetylgalactosamine-linked polymers, modified single- and double-tailed phospholipids, phospholipid-dextran conjugates, and amino acids [22, 48, 51–53, 58, 77, 101, 116, 126, 170, 186, 189]. In a study of non-covalent CNTs functionalization using biomolecules, the dispersing efficiency and stability of product appeared to be high when the following agents were used: dsDNA and its monomers—deoxyribonucleoside triphosphates (dNTPs), BSA, vitreous humor extract, adenosine-triphosphate-Na (ATP-Na), and sodium humate [15, 16]. Spermidine, L-proline, and peptone displayed negligible dispersing activity obviously due to the lack of responsible sites. Functionalized CNTs were able to deliver DNA into plant protoplasts and walled cells exhibiting eligible toxicity levels.

20.4 CNTs in Genetic Engineering

Direct and indirect physical biotransformation processes commonly suffer from instability of the gene in the environment, deletion of the gene due to the high energy impact, poor penetration, and reproducibility [143]. Nanotechnology is expected to provide numerous benefits when utilized in biotransformation: (1) comparatively faster mode of gene transfer, (2) DNA is protected due to bonding or encapsulation and effectively transformed in controlled manner, (3) the probability of energy-induced DNA-damage-related gene mutation is strongly reduced, and (4) nanotechnology approaches are also easily combined with physical methods leading to effective and improved gene transfer [27, 143].

Having a number of favorable cell-entering properties improved by introducing well-designed chemical and physical modifications, CNTs are already reported to be efficient as gene carriers in a number of studies on bacterial and mammalian cells [17, 100, 112, 127, 131, 142, 148, 160, 167, 195]. In plants, being more resistant for foreign genetic information penetration, reports indicate that CNTs with different molecular cargoes can enter plant protoplasts and walled plant cells [106, 154, 155].

20.4.1 CNT-Mediated Transformation of Bacterial and Mammalian Cells

A plasmid delivery system based on water-dispersible MWCNTs that can simultaneously target the bacterial surface and deliver plasmids into the *Escherichia coli* cells is reported in Rojas-Chapana et al. [148]. The described approach was based on the electroporation technique and presented higher efficiency, miniaturization, and reduction of the amount of plasmid required for efficient transformation. In this case, CNTs were viewed to create temporary membrane disruptions of increased permeability that facilitate plasmid delivery into the cells. The latter could be attributed to CNTs acting as transient dipoles allowing nanoscale cell targeting and gentle electroporation. Results of another study indicated an increase in the transformation capacity of the naturally transformable *Neisseria meningitidis* in different concentrations of MWCNTs when compared with negative control without nanotubes [112]. This was supposed to take place due to interactions between bacterial DNA and subsequent protection CNT-binded DNA from DNAse action. Using CNTs for the transformation of *E. coli* based on the Yoshida effect [193] dramatically enhanced transformation efficiency [167]. Another improvement of *E. coli* transformation technique using MWCNTs was reported in Raffa et al. [142].

Efficient molecular delivery technique for mammalian cells, named nanotube spearing, based on the penetration of nickel-embedded nanotubes into cell membranes by magnetic field driving is described in Cai et al. [17]. Authors reported high transduction efficiency in Bal17 B-lymphoma, ex vivo B cells, and primary

neurons. Ammonium-functionalized SWCNTs and MWCNTs were used for the transformation of mammalian HeLa cells resulting in increased gene expression [131]. Different functionalized CNT types—ammonium-functionalized SWCNT and MWCNTs, lysine-functionalized SWCNTs—exhibited the ability to transfect the mammalian A549 cell line [160]. DNA immobilized onto the surface of MWCNTs that have been functionalized with PEI exhibited total inhibition of the migration in gel electrophoresis [100]. At the same time, PEI-grafted MWCNTs showed transfection efficiency for the delivery of DNA into mammalian 293 cells that was similar to or higher than that of PEI. This report indicates the presence of intracellular mechanism of DNA detachment from CNTs, allowing release and expression of transgene sequence.

Study of the capability of different cationic polymer-grafted (PEI, PAA) MWCNTs to efficiently complex and transfer plasmids revealed high DNA-binding capacity of polymer-grafted CNTs in gel migration studies and improvement in transgene expression in A549 mammalian cells when transformed with obtained conjugates [127]. An efficient molecular delivery technique based on the transportation of PEI-modified MWCNTs into 293 T cells is reported in Yu et al. [195]. Generally, in used approaches CNTs formed supramolecular complexes with plasmid DNA through interactions with anchoring residues on CNT surface. These complexes were obviously able to bind to, and penetrate within, cells. Nanotubes when used in appropriate concentrations exhibited low cytotoxicity and often provided increased levels of transgene expression in comparison to conventional methods.

20.4.2 CNTs Interactions with Living Cells

The uptake of CNTs or their conjugates by the cells is suggested to occur by phagocytosis (only in animal cells), including incomplete phagocytosis [31, 33, 92] or endocytosis [74–76, 106], which is in contrast to an insertion and diffusion pathway [31, 92, 107, 130, 131, 160]. CNTs have been found inside the cells in both direct imaging experiments using electron microscope and spectroscopy and indirect fluorescent microscopy studies [33, 84, 93, 106, 131, 135, 136, 141]. However, the data about the exact mechanism of CNT penetration into cells is still lacking. Experimental efforts aimed to distinguish active and passive uptake exploit changes of temperature [75, 88, 106, 196] and addition of selective chemical agents that inhibit active uptake [106, 141] to compare process-passing features under various conditions. Biological membranes may undergo several energy-consuming processes such as endocytosis [113] or phase transitions [192]. Properties of CNTs might allow direct penetration of the cell membrane through needle-like process [89, 91]. It is suggested to be quite difficult to identify a unique translocation mechanism and discard all other possibilities by studying a particular biological system [134].

Endocytosis was identified when SWCNTs (< 1000-nm length) were used as intracellular transporters for proteins and DNA [74–76]. Results of calculating the energy cost associated with the spontaneous insertion of a CNT into a model phospholipid bilayer (piercing through the membrane induced only by thermal motion) indirectly supported endocytosis-mediated translocation mechanisms [134]. In contrast, results of another extensive computational study of short (5-nm length) pristine and functionalized SWCNTs uptake by phospholipid bilayer models support the hypothesis of a direct translocation of the nanotubes through the phospholipid membrane [89]. In the mentioned study, the insertion of nanotubes within the bilayer is considered as a "nanoneedle"-like process. This result is in good correspondence with experimental data obtained earlier and indicates that short and amino-functionalized nanotubes (few hundreds of nanometer in length) act as "nanoneedles" able to passively penetrate the cell membrane of mammalian cells [91]. Preferential uptake of CNTs by energy-independent pathways was also reported for < 1000-nm-long MWCNTs [141] and 200-nm-long DNA-wrapped SWCNTs [11]. Length-dependent uptake is supposed to be a general phenomenon; however, the exact threshold is expected to vary with cell type [11]. Passive diffusion of peptide-functionalized SWCNTs through the cell membrane was also reported in Pantarotto et al. [130]. It was shown that amino-functionalized SWCNTs and MWCNTs possess a capacity to be taken up by mammalian (3T6, 3T3, HeLa, Jurkat human T-lymphoma, MOD-K) and prokaryotic (*Cryptococcus neoformans, Saccharomyces cerevisiae,* and *E. coli*) cells and to traffic through the different intracellular barriers by energy-independent mechanisms [88]. Authors suggested that the cylindrical shape and high aspect ratio of CNTs can allow their penetration through the plasma membrane, similar to a "nanosyringe."

20.4.2.1 CNTs Plant Cell Entering

In plants, protoplasts are often used to investigate the CNT cell-penetrating mechanism. Since the cell wall in protoplasts is enzymatically destructed, the only barrier for CNTs cell penetrating is the cell membrane [118]. In the study [154], an endosome-escaping MWCNTs uptake model taking place in protoplasts of *Catharanthus roseus* was identified. Oxidized MWCNTs with the fluorescent probe passively passed through the cell membrane without entrapment into the degrading endosomal organelles. This phenomenon was viewed to be of great practical value for the design endosomes escaping nano-transporters for plant cells based on MWCNTs. Moreover, the size-dependent translocation of MWCNTs into cellular structures including the nucleus and plastids was reported. Short MWCNTs (< 100 nm) were observed to target specific cellular substructures including the nucleus, plastids, and vacuoles. However, protoplast-based techniques are often time consuming and associated with decreased cell viability. A promising approach to circumvent the complete removal of cell wall is suggested to be the strategy of cellulase (an enzyme that catalyzes cellulose hydrolysis) immobilization onto CNT surface. Cup-stacked CNTs with immobilized cellulase on their tips and walls were designed to induce local lesions

in the plant cell wall, through which nanotubes could transport into the interior of the cell [155]. Modified tubes were able to penetrate the thick cellulosic cell wall.

SWCNTs were shown to enter arabidopsis (*Arabidopsis thaliana*) mesophyll protoplasts and walled cells by nonenergy-dependent pathway with subsequent penetrating nucleus, chloroplast, vacuole, and mitochondria [196]. The involved mechanism is supposed to be one kind of nanoscale capillary function and rely on van der Waals and hydrophobic forces. Non-covalently functionalized MWCNTs were able to deliver DNA into tobacco (*Nicotiana tabacum*) BY-2 suspension cells, *N. tabacum* leaf mesophyll cells, and protoplasts. This suggests the involvement of the intracellular DNA from tube-detachment mechanism together with the DNA escape from enzyme cleavage. Efficiency of CNT-plasmid DNA conjugate penetration into protoplasts was reported higher than that of BY-2 and mesophyll walled cells [15, 16]. Another study on fluorescein isothiocyanate (FITC)-labeled SWCNTs ($<$ 500-nm length) uptake by *N. tabacum* BY-2 suspension cells revealed the temperature and endocytosis-inhibitor pretreatment dependence of the uptake process suggesting the involvement of endocytosis [106]. Further investigations showed the difference in the distribution of SWCNT–FITC and SWCNT–DNA–FITC complexes in the cell. The former was observed in the vacuolar region and the latter in the cytoplasmic strands. Serag with coauthors [153] revealed that the trafficking of SWCNTs through various subcellular membranes of the plant cell might be facilitated or inhibited by attaching a suitable functional tag and controlling medium components. These findings may offer a background for the controlled uptake and the subcellular distribution of CNTs in plant cells and provide a key strategy to promote their cellular elimination to minimize toxicity.

20.4.3 Challenges to Solve

On the one hand, factors impeding biotechnological manipulation of CNTs are associated with their physical and chemical nature, namely, entangled bundles formation, low water dispersibility, inert properties of pristine CNTs, etc. Recent advances in CNT synthesis and surface modification approaches meet the above challenges to a great extent tailoring improved possibilities for extended applications. On the other hand, issues resulting from the CNT use might be summarized as not fully understood interaction mechanisms with living cells/organisms, lack of data concerning CNTs toxicity, environmental fate, and biodegradation. Numerous studies are carried out for getting more information on these topics. However, the results are often controversial due to the great number of changing parameters involved in explored phenomena.

Pristine CNTs usually possess a variety of length distribution and structures within the same sample [80]. It is also known that the methods of production of CNTs generate impurities such as byproduct carbonaceous species and residues from the transition metal catalysts. In biological applications, these impurities have been considered to be one of the key parameters for causing the toxicities to cells/tissues

[99]. Moreover, CNTs are weakly dispersed in all solvents due to strong van der Waals interactions [80]. In this frame, CNTs undergo chemical functionalization to enhance dispersibility in various solvents and to produce novel hybrid materials potentially suitable for biotechnological applications [9, 145]. Besides, in the design of CNT-based intracellular delivery approaches, cell membrane and plant cell walls may represent a strong protective barrier [37]. Although one of the CNTs' unique properties is the ability to penetrate cell membrane and wall, much attention is to be paid on the advancements in this field. For the fundamental studies, getting direct microscopic information regarding the interaction of nano-objects with phospholipid layers at the molecular level is also of great importance [134].

Localization, traffic, and toxicity of SWCNTs and MWCNTs to plants recently were studied on the organism level for onion (*Allium cepa*), cucumber (*Cucumis sativus*), cabbage (*Brassica oleracea*), carrot (*Daucus carota*), lettuce (*Lactuca sativa*), tomato (*Solanum lycopersicum*), radish (*Raphanus sativus*), rape (*Brassica napus*), rye grass (*Lolium perenne*), corn (*Zea mays*), zucchini (*Cucurbita pepo*), rice (*Oryza sativa*), alfalfa (*Medicago sativa*), wheat (*Triticum aestivum*), freshwater green algae (*Pseudokirchneriella subcapitata*) [18, 84–86, 97, 98, 114, 162, 194], etc. Cell responses were investigated on rice suspension cells, arabidopsis suspension, mesophyll cells and protoplasts [99, 157, 166, 168, 196], etc. Various studies of the CNT impacts on plant metabolism and cell viability revealed the enhanced seed germination, root elongation, improved plant growth, slight responses, delayed flowering, growth retardation, apoptosis, and necrosis. Controversial results are viewed to appear due to differences in properties of used CNTs, doses, plant species, and other conditions involved [119]. In particular, toxic effects of CNTs might be attributed to above-mentioned parameters such as the amounts and types of metal impurities, the degree and kind of aggregation in produced CNTs, physical characteristics, the type and role of functionalizing agents, and a combination of two or more of the these characteristics [194].

Research on CNTs eco-toxicity, aggregation, and transport has been conducted in recent years to provide information on their impact and fate in the environment [82, 132, 201]. Concerning the fate of CNTs after cell/organism entering, data on mechanisms for their elimination or degradation are lacking. Some studies show in vivo bio-defunctionalization of CNTs [191], biodegradation by enzymes horseradish peroxidase and neutrophil myeloperoxidase [5, 70, 149, 204] and bacterial community (*Burkholderia kururiensis, Delftia acidovorans, Stenotrophomonas maltophilia*) [201].

20.4.4 Plant Genetic Transformation: Limitations of Existing Methods

Currently used plant gene transfer technologies can be subdivided into physical methods (electroporation, particle bombardment, micro-injection, etc.), direct gene transfer techniques (protoplast fusion, transfection), gene transfer using plasma

Table 20.1 Limitations of conventional genetic transformation methods [143]

Methods	Limitations
Physical methods	
Electroporation	Frequency of stable transformation is low (0.001 or less)
	Normally, the transformed DNA is extensively rearranged leading to mitotic and meiotic instability
	Can be only used with protoplasts
	Probability of deletion is high
	Application is limited to only few species
Microprojectile/Particle bombardment/Biolistic	The transformed DNA is highly rearranged leading to mitotic and meiotic instability
	Amenable tissue culture/regeneration systems cannot completely be eliminated
	The transformed cell survival rate is decreased because of high membrane damage
Microinjection	Not suitable for small cells or tissues
	Infrequent gene transfer method in plant biotransformation
	Efficiency is low
	Suitable for large animal cells
Temperature-mediated gene transfer	Only used for experimental purpose
	Infrequent use
	Only be adopted with protoplast
	Slow and less efficient process
	With the intention for rapid biotransformation, enhanced temperature damages the nucleic acid and cells
Coprecipitation	Wall-less cells are amenable to biotransformation through coprecipitation
	Mitotic and meiotic instability may occur
Micromanipulation	Little use for stable transformation of plants
	Other limitations similar to biolistic method
Chemical Methods	Damage of cellular components and gene itself
	Is only applicable in case of protoplasts
	The regeneration of transformed protoplasts is very difficult, which lowers the transformation frequency
Biological methods	
Agrobacterium-mediated transformation	Host range is often limited to dicot plants
	With vulnerable plants, accessible culture systems must be adapted
	Chances of transgene silencing
	Poor gene transfer efficiency
	Limitation to carry limited size base pair
Virus-mediated transformation	Nonselectivity
	Slow process
	Low DNA-size-carrying capacity

membrane destabilizing/precipitating agents (chemicals that facilitate the gene transfer through the cell membrane, for example, PEG, polyvinyl alcohol, dextran, dimethyl sulfoxide, etc.), and natural means of gene transfer such as the use of *Agrobacterium* species [20, 35, 59, 65, 67, 71, 87, 95, 110, 122, 143, 144, 150, 158]. Efficiency of these conventional methods is often compromised due to the damage of the DNA and cells resulted from the application of excessive energy in physical and chemicals in chemical methods, host range limitations, complexity, time consumption (Table 20.1) [27, 143, 155], etc. In this frame, exploiting CNTs for the design of novel plant transformation approach holds a great promise. Unique properties of these carbon nanomaterials are viewed to be suitable for overcoming the number of existing limitations. Numerous studies on the ability of CNTs to transport target molecules pose an important background for further developments in this field.

20.5 Conclusions

CNTs are novel and promising for plant biotechnology nanomaterials having a range of advantageous properties anticipating successful applications in this field. Improvements in the properties control, applicability, biocompatibility, and safety of CNTs with tailored characteristics are primary issues of current studies. These efforts meet toward investigating CNT interactions with living organisms, detecting factors governing the efficiency of the practical outcome of CNT-based approaches. On the one hand, a general issue is the relatively good biocompatibility of carbon, which decreases when carbon materials are used in nano-form. On the other hand, nanosizing provides significant increase in functionality and widens the carbon material applications range to a huge extent. Together with advances in tailoring of nanostructures having controlled properties, this provides promising possibilities to meet urgent practical challenges.

For the development of CNT-based novel genetic transformation approaches, efforts are underway to overcome negligible CNTs water dispersibility, enhance their cell-penetrating ability, improve trafficking control, and minimize toxicity. Biomolecules, in particular DNA and proteins, might be attached to CNT surface non-covalently. This approach is viewed to hold a great promise as it does not change the structure of CNTs significantly as well as does not affect biological properties of loaded molecules. It also allows stable water dispersing, demonstrates high product biocompatibility, and suggests easy intracellular release of loaded molecules. Moreover, it provides "green," simple, and less time-consuming technology. Generally, CNT-based strategies in plant transformation if well designed are viewed to have a number of advantages in comparison with existing methods.

References

1. Ago H, Petritsch K, Shaffer MSP et al (1999) Composites of carbon nanotubes and conjugated polymers for photovoltaic devices. Adv Mater 11:1281–1285
2. Ajayan PM (1999) Nanotubes from carbon. Chem Rev 99:1787–1799
3. Albertorio F, Hughes ME, Golovchenko JA, Branton D (2009) Base dependent DNA-carbon nanotube interactions: activation enthalpies and assembly-disassembly control. Nanotechnology 20(39):395101
4. Ali-Boucetta H, Al-Jamal KT, McCarthy D et al (2008) Multiwalled carbon nanotube-doxorubicin supramolecular complexes for cancer therapeutics. Chem Commun 4:459–461
5. Allen BL, Kotchey GP, Chen YN et al (2009) Mechanistic investigations of horseradish peroxidase-catalyzed degradation of single-walled carbon nanotubes. J Am Chem Soc 131:17194–17205
6. Anastas P, Warner J (1998) Green chemistry: theory and practice. Oxford University, USA
7. Arnold MS, Guler MO, Hersam MC, Stupp SI (2005) Encapsulation of carbon nanotubes by self-assembling peptide amphiphiles. Langmuir 21:4705–4709
8. Baddour CE, Briens C (2005) Carbon nanotube synthesis: a review. Inter J Chem React Eng 3:3–20
9. Balavoine F, Schultz P, Richard C et al (1999) Helical crystallization of proteins on carbon nanotubes: a first step towards the development of new biosensors. Angew Chem Int Ed 38(13–14):1912–1915
10. Bandow S, Rao AM, Williams KA et al (1997) Purification of single-wall carbon nanotubes by microfiltration. J Phys Chem B 101:8839–8842
11. Becker ML, Fagan JA, Gallant ND et al (2007) Length dependent uptake of DNA wrapped single wall carbon nanotubes. Adv Mater 19:939–945
12. Bekyarova E, Ni Y, Malarkey EB et al (2005) Applications of carbon nanotubes in biotechnology. J Biomed Nanotechnol 1(1):3–17
13. Bhirde A, Patel V, Gavard J et al (2009) Targeted killing of cancer cells in vivo and in vitro with EGF-directed carbon nanotube-based drug delivery. ACS Nano 3:307–316
14. Buhro WE, Colvin VL (2003) Semiconductor nanocrystals—shape matters. Nat Mater 2(3):138–139
15. Burlaka OM, Pirko YV, Yemets AI, Blume YB (2011) Carbon nanotubes and their applications in plants genetic transformation (In Ukrainian). Nanostruct Mater Sci 2:84–101
16. Burlaka OM, Pirko YV, Yemets AI, Blume YB (2012) Functionalized carbon nanotubes for the delivery of biomolecules into plant cells. In: Abstracts of plant biology congress FESPB/EPSO, 29 July–3 August 2012, Freiburg, Germany
17. Cai D, Mataraza J, Qin Z et al (2005) Highly efficient molecular delivery into mammalian cells using carbon nanotube spearing. Nat Methods 2(6):449–454
18. Canas JE, Long M, Nations S et al (2008) Effects of functionalized and non-functionalized single-walled carbon nanotubes on root elongation of select crop species. Environ Toxicol Chem 27:1922–1931
19. Cao Q, Rogers JA (2008) Random networks and aligned arrays of single-walled carbon nanotubes for electronic device applications. Nano Res 1:259–272
20. Cha TS, Chen CF, Yee W et al (2011) Cinnamic acid, coumarin and vanillin: alternative phenolic compounds for efficient *Agrobacterium*-mediated transformation of the unicellular green alga, *Nannochloropsis* sp. J Microbiol Methods 84:430–434
21. Chen RJ, Zhang Y, Wang D, Dai H (2001) Noncovalent sidewall functionalization of single-walled carbon nanotubes for protein immobilization. J Am Chem Soc 123:3838–3839
22. Chen X, Tam UC, Czlapinski JL et al (2006) Interfacing carbon nanotubes with living cells. J Am Chem Soc 128:6292–6293
23. Chen Y, Liu H, Ye T, Kim J, Mao C (2007) DNA-directed assembly of single-wall carbon nanotubes. J Am Chem Soc 129:8696–8697

24. Chen JY, Chen SY, Zhao XR et al (2008a) Functionalized single-walled carbon nanotubes as rationally designed vehicles for tumor-targeted drug delivery. J Am Chem Soc 130:16778–16785
25. Chen X, Chen J, Deng C et al (2008) Amperometric glucose biosensor based on boron-doped carbon nanotubes modified electrode. Talanta 76:763–767
26. Chen JL, Zhu ZH, Ma Q et al (2009) Effects of pre-treatment in air microwave plasma on the structure of CNTs and the activity of Ru/CNTs catalysts for ammonia decomposition. Catal Today 148(1–2):97–102
27. Chen ZY, Liang K, Qiu RX, Luo LP (2011) Ultrasound- and liposome microbubble-mediated targeted gene transfer to cardiomyocytes in vivo accompanied by polyethylenimine. Ultrasound Med 30:1247–1258
28. Chen J, Chen Q, Ma Q (2012) Influence of surface functionalization via chemical oxidation on the properties of carbon nanotubes. J Colloid Interface Sci 370(1):32–38
29. Cheng J (2008) Biocompatibility and properties of carbon nanotubes in the biological systems. Dissertation, City University of Hong Kong
30. Cheng F, Zhang S, Adronov A et al (2006) Triply fused ZnII-porphyrin oligomers: synthesis, properties, and supramolecular interactions with singlewalled carbon nanotubes (SWNTs). Chem Eur J 12(23):6062–6070
31. Cheng C, Muller KH, Koziol KK et al (2009) Toxicity and imaging of multi-walled carbon nanotubes in human macrophage cells. Biomaterials 30:4152–4160
32. Cheng Q, Debnath S, Gregan E, Byrne HJ (2010) Ultrasound-assisted SWNTs dispersion: effects of sonication parameters and solvent. J Phys Chem C 114:8821–8827
33. Cherukuri P, Bachilo SM, Litovsky SH, Weisman RB (2004) Near-infrared fluorescence microscopy of single-walled carbon nanotubes in phagocytic cells. J Am Chem Soc 126:15638–15639
34. Chiang YC, Lin WH, Chang YC (2011) The influence of treatment duration on multi-walled carbon nanotubes functionalized by H_2SO_4/HNO_3 oxidation. Appl Surf Sci 257:2401–2410
35. Chowrira GM, Akella V, Fuerst PE, Lurquin PF (1996) Transgenic grain legumes obtained by in planta electroporation-mediated gene transfer. Mol Biotechnol 5:85–96
36. Clark MD, Subramanian S, Krishnamoorti R (2011) Understanding surfactant aided aqueous dispersion of multi-walled carbon nanotubes. J Colloid Interface Sci 354(1):144–151
37. Cooper GM, Hausman RE (2009) The cell: a molecular approach, 5th ed. Sinauer Associates Inc, Sunderland
38. D'Souza F, Chitta R, Sandanayaka ASD et al (2007) Supramolecular carbon nanotube-fullerene donor-acceptor hybrids for photoinduced electron transfer. J Am Chem Soc 129:15865–15871
39. Dahl JA, Maddux BLS, Hutchison JE (2007) Toward greener nanosynthesis. Chem Rev 107:2228–2269
40. Dillon AC, Jones KM, Bekkedahl TA et al (1997) Storage of hydrogen in single-walled carbon nanotubes. Nature 386:377–379
41. Ding K, Hu B, Xie Y et al (2009) A simple route to coat mesoporous SiO2 layer on carbon nanotubes. J Mater Chem 19:3725–3731
42. Dovbeshko GI, Repnytska OP, Obraztsova ED et al (2003) Study of DNA interaction with carbon nanotubes. Semicond Phys Quantum Electron Optoelectron 6(1):105–108
43. Dresselhaus MS, Dresselhaus G, Eklund PC (1996) Science of fullerenes and carbon nanotubes. Academic Press, San Diego
44. Dwyer C, Guthold M, Falvo M et al (2002) DNA-functionalized single-walled carbon nanotubes. Nanotechnology 13:601–604
45. Ebbesen T, Ajatan A, Hiura H, Tanigaki K (1994) Purification of carbon nanotubes. Nature 367:519–520
46. Ehli C, Rahman GMA, Jux N et al (2006) Interactions in single wall carbon nanotubes/pyrene/porphyrin nanohybrids. J Am Chem Soc 128:11222–11231
47. Etxeberria E, Gonzalez P, Baroja-Fernandez E, Pozueta-Romero J (2006) Fluid phase endocytic uptake of artificial nano-spheresand fluorescent quantum dots by sycamore cultured cells. Plant Signal Behav 1:196–200

48. Feazell RP, Nakayama-Ratchford N, Dai H, Lippard SJ (2007) Soluble single-walled carbon nanotubes as longboat delivery systems for Platinum(IV) anticancer drug design. J Am Chem Soc 129(27):8438–8439
49. Fennimore AM, Yuzvinsky TD, Han W-Q et al (2003) Rotational actuators based on carbon nanotubes. Nature 424:408–410
50. Fouad M, Kaji N, Jabasini M et al (2008) Nanotechnology meets plant biotechnology: carbon nanotubes deliver DNA and incorporate into the plant cell structure. In: Abstracts of 12th international conference on miniaturized systems for chemistry and life sciences, San Diego, California, USA, 12–16 October, 2008
51. Gandra N, Chiu PL, Li W et al (2009) Photosensitized singlet oxygen production upon two-photon excitation of single-walled carbon nanotubes and their functionalized analogs. J Phys Chem 113:5182–5185
52. Georgakilas V, Tagmatarchis N, Pantarotto D et al (2002) Amino acid functionalisation of water soluble carbon nanotubes. Chem Commun 24:3050–3051
53. Goodwin AP, Tabakman SM, Welsher K et al (2009) Phospholipid-dextran with a single coupling point: a useful amphiphile for functionalization of nanomaterials. J Am Chem Soc 131:289–296
54. Guo Z, Sadler PJ, Tsang SC (1998) Immobilization and visualization of DNA and proteins on carbon nanotubes. Adv Mater 10(9):701–703
55. Hamon MA, Itkis ME, Niyogi S et al (2001) Effect of the rehybridization on the electronic structure of single-walled carbon nanotubes. J Am Chem Soc 123:11292–11293
56. Han X, Li Y, Deng Z (2007) DNA-wrapped single walled carbon nanotubes as rigid templates for assembling linear gold nanoparticle arrays. Adv Mater 19:1518–1522
57. Harutyunyan AR, Pradhan BK, Chang J et al (2002) Purification of single-wall carbon nanotubes by selective microwave heating of catalyst particles. J Phys Chem B 106:8671–8675
58. Hasegawa T, Fujisawa T, Numata M et al (2004) Single-walled carbon nanotubes acquire a specific lectin-affinity through supramolecular wrapping with lactose-appended schizophyllan. Chem Commun 19:2150–2151
59. Hayashimoto A, Li Z, Murai N (1990) A polyethylene glycol-mediated protoplast transformation system for production of fertile transgenic rice plants. Plant Physiol 93:857–863
60. Hernadi K, Siska A, Thien-Nga L et al (2001) Reactivity of different kinds of carbon during oxidative purification of catalytically prepared carbon nanotubes. Solid State Ionics 141:203–209
61. Herrero MA, Toma FM, Al-Jamal KT et al (2009) Synthesis and characterization of a carbon nanotube-dendron series for efficient siRNA delivery. J Am Chem Soc 131:9843–9848
62. Holder PG, Francis MB (2007) Integration of a self-assembling protein scaffold with water-soluble single-walled carbon nanotubes. Angew Chem Int Ed 46:4370–4373
63. Hu Y, Guo C (2011) Carbon nanotubes and carbon nanotubes/metal oxide heterostructures: synthesis, characterization and electrochemical property. In: Naraghi M (ed) Carbon nanotubes—growth and applications. InTech, Croatia, pp 3–34
64. Iijima S (1991) Helical microtubules of graphitic carbon. Nature 354:56
65. Ito H, Fukuda Y, Murata K, Kimura A (1983) Transformation of intact yeast cells treated with alkali cations. J Bacteriol 153:163–168
66. Javey A, Guo J, Wang Q, Lundstrom M, Dai HJ (2003) Ballistic carbon nanotube field-effect transistors. Nature 424:654–657
67. Jiang Z, Berg H (1995) Increase of protoplast electrofusion supported by dextran fractions. Bioelectrochem Bioenerg 38:383–387
68. Jiang W, Yu B, Liu W, Hao J (2007) Carbon nanotubes incorporated within lyotropic hexagonal liquid crystal formed in room-temperature ionic liquids. Langmuir 23:8549–8553
69. Joshi PP, Merchant SA, Wang Y, Schmidtke DW (2005) Amperometric biosensors based on redox polymer-carbon nanotube-enzyme composites. Anal Chem 77:3183–3188
70. Kagan VE, Konduru NV, Feng WH et al (2010) Carbon nanotubes degraded by neutrophil myeloperoxidase induce less pulmonary inflammation. Nat Nanotechnol 5:354–359

71. Kakkar A, Verma VK (2011) Agrobacterium mediated biotransformation. J Appl Pharm Sci 1(7):29–35
72. Kam NWS, Dai H (2005) Carbon nanotubes as intracellular protein transporters: generality and biological functionality. J Am Chem Soc 127:6021–6026
73. Kam NWS, Dai H (2006) Single-walled carbon nanotubes for transport and delivery of biological cargos. Phys Stat Sol 243:3561–3566
74. Kam NWS, Jessop TC, Wender PA, Dai HJ (2004) Nanotube molecular transporters: internalization of carbon nanotube-protein conjugates into mammalian cells. J Am Chem Soc 126:6850–6851
75. Kam NWS, O'Connell M, Wisdom JA, Dai HJ (2005) Carbon nanotubes as multifunctional biological transporters and near-infrared agents for selective cancer cell destruction. Proc Natl Acad Sci U S A 102:11600–11605
76. Kam NWS, Liu ZA, Dai HJ (2006) Carbon nanotubes as intracellular transporters for proteins and DNA: an investigation of the uptake mechanism and pathway. Angew Chem Int Ed 45:577–581
77. Kang B, Yu D, Chang S et al (2008) Intracellular uptake, trafficking and subcellular distribution of folate conjugated single walled carbon nanotubes within living cells. Nanotechnology 19(37):375103–375111
78. Kang Y, Liu YC, Wang Q et al (2009) On the spontaneous encapsulation of proteins in carbon nanotubes. Biomaterials 30:2807–2815
79. Karajanagi SS, Yang H, Asuri P et al (2006) Protein-assisted solubilization of single-walled carbon nanotubes. Langmuir 22(4):1392–1395
80. Karousis N, Tagmatarchis N, Tasis D (2010) Current progress on the chemical modification of carbon nanotubes. Chem Rev 110(9):5366–5397
81. Kavakka JS, Heikkinen S, Kilpelainen I et al (2007) Noncovalent attachment of pyropheophorbide a to a carbon nanotube. J Chem Commun 5:519–521
82. Kennedy AJ, Hull MS, Steevens JA et al (2008) Factors influencing the partitioning and toxicity of nanotubes in the aquatic environment. Environ Toxicol Chem 27:1932–1941
83. Kharisov BI, Kharissova OV, Gutierre HL, Mendez UO (2009) Recent advances on the soluble carbon nanotubes. Ind Eng Chem Res 48:572–590
84. Khodakovskaya M, Dervishi E, Mahmood M et al (2009) Carbon nanotubes are able to penetrate plant seed coat and dramatically affect seed germination and plant growth. ACS Nano 3:3221–3227
85. Khodakovskaya M, de Silva K, Nedosekin D et al (2011) Complex genetic, photothermal, and photoacoustic analysis of nanoparticle-plant interactions. Proc Natl Acad Sci U S A 108:1028–1033
86. Khodakovskaya MV, de Silva K, Biris AS et al (2012) Carbon nanotubes induce growth enhancement of tobacco cells. ACS Nano 6(3):2128–2135
87. Klee H, Horsch R, Rogers S (1987) Agrobacterium-mediated plant transformation and its further applications to plant biology. Ann Rev Plant Physiol 38:467–486
88. Kostarelos K, Lacerda L, Pastorin G et al (2007) A cellular uptake of functionalized carbon nanotubes is independent of functional group and cell type. Nat Nanotech 2:108–113
89. Kraszewski S, Bianco A, Tarek M, Ramseyer C (2012) Insertion of short amino-functionalized single-walled carbon nanotubes into phospholipid bilayer occurs by passive diffusion. PLoS One 7(7):40703. doi:10.1371/journal.pone.0040703
90. Kurppa K, Jiang H, Szilvay GR et al (2007) Controlled hybrid nanostructures via protein mediated noncovalent functionalization of carbon nanotubes. Angew Chem Int Ed 46:6446–6449
91. Lacerda L, Raffa S, Prato M et al (2007) Cell-penetrating CNTs for delivery of therapeutics. Nano Today 2:38–43
92. Lacerda L, Russier J, Pastorin G et al (2012) Translocation mechanisms of chemically functionalised carbon nanotubes across plasma membranes. Biomaterials 33:3334–3343
93. Lamprecht C, Liashkovich I, Neves V et al (2009) AFM imaging of functionalized carbon nanotubes on biological membranes. Nanotechnology 20:434001

94. Lay CL, Liu HQ, Tan HR, Liu Y (2010) Delivery of paclitaxel by physically loading onto poly(ethylene glycol) PEG-graft-carbon nanotubes for potent cancer therapeutics. Nanotechnology 21(6):065101–065111
95. Lazzeri PA (1995) Stable transformation of barley via direct DNA uptake. Electroporation- and PEG-mediated protoplast transformation. Methods Mol Biol 49:95–106
96. Li G, Xu H, Huang W et al (2008) A pyrrole quinoline quinone glucose dehydrogenase biosensor based on screen-printed carbon paste electrodes modified by carbon nanotubes. Meas Sci Technol 19:065203
97. Lin D, Xing B (2007) Phytotoxicity of nanoparticles: inhibition of seed germination and root growth. Environ Pollut 150:243–250
98. Lin S, Reppert J, Hu Q et al (2009a) Uptake, translocation, and transmission of carbon nanomaterials in rice plants. Small 5(10):1128–1132
99. Lin C, Fugetsu B, Su Y, Watari F (2009) Studies on toxicity of multiwalled carbon nanotubes on Arabidopsis T87 suspension cells. J Hazard Mater 30:578–583
100. Liu Y, Wu DC, Zhang WD et al (2005) Polyethylenimine-grafted multiwalled carbon nanotubes for secure non-covalent immobilization and efficient delivery of DNA. Angew Chem Int Edn 44(30):4782–4785
101. Liu Y, Liang P, Zhang H-Y, Guo D-S (2006) Cation-controlled aqueous dispersions of alginic-acid-wrapped multi-walled carbon nanotubes. Small 2:874–878
102. Liu Z, Winters M, Holodniy M, Dai HJ (2007a) siRNA delivery into human T cells and primary cells with carbon-nanotube transporters. Angew Chem Int Edn 46:2023–2027
103. Liu Z, Sun X, Nakayama N, Dai H (2007) Supramolecular chemistry on water-soluble carbon nanotubes for drug loading and delivery. ACS Nano 1:50–56
104. Liu Z, Chen K, Davis C et al (2008) Drug delivery with carbon nanotubes for in vivo cancer treatment. Cancer Res 68:6652–6660
105. Liu Z, Tabakman S, Welsher K, Dai H (2009a) Carbon nanotubes in biology and medicine: in vitro and in vivo detection, imaging and drug delivery. Nano Res 2:85–120
106. Liu Q, Chen B, Wang Q et al (2009) Carbon nanotubes as molecular transporters for walled plant cells. Nano Lett 9(3):1007–1010
107. Lu Q, Moore JM, Huang G et al (2004) RNA polymer translocation with single-walled carbon nanotubes. Nano Lett 4:2473–2477
108. Lu G, Maragakis P, Kaxiras E (2005) Carbon nanotube interaction with DNA. Nano Lett 5(5):897–900
109. Lu F, Gu L, Meziani MJ et al (2009) Advances in bioapplications of carbon nanotubes. Adv Mater 21:139–152
110. Lurquin PF (1997) Gene transfer by electroporation. Mol Biotechnol 7:5–35
111. Matsuura K, Saito T, Okazaki T et al (2006) Selectivity of water-soluble proteins in single-walled carbon nanotube dispersions. Chem Phys Lett 429:497–502
112. Mattos IB, Alves DA, Hollanda LM et al (2011) Effects of multi-walled carbon nanotubes (MWCNT) under Neisseria meningitides transformation process. J Nanobiotechnol 9:53
113. Miaczynska M, Stenmark H (2008) Mechanisms and functions of endocytosis. J Cell Biol 180:7–11
114. Miralles P, Johnson E, Church TL, Harris AT (2012) Multiwalled carbon nanotubes in alfalfa and wheat: toxicology and uptake. J R Soc Interface 9(77):3514–3527
115. Mohanpuria P, Rana N, Yadav S (2008) Biosynthesis of nanoparticles: technological concepts and future applications. J Nanopart Res 10:507–517
116. Moulton SE, Maugey M, Poulin P, Wallace GG (2007) Liquid crystal behavior of single-walled carbon nanotubes dispersed in biological hyaluronic acid solutions. J Am Chem Soc 129:9452–9457
117. Murugesan S, Myers K, Subramanian V (2011) Amino-functionalized and acid treated multi-walled carbon nanotubes as supports for electrochemical oxidation of formic acid. Appl Catal B 103:266–274
118. Nagy JI, Maliga P (1976) Callus induction and plant regeneration from mesophyll protoplasts of *Nicotiana sylvestris*. Pflanzenphysiol 78:453–544

119. Nair R, Varghese SH, Nair BG et al (2010) Nanoparticulate material delivery to plants. Plant Sci 179:154–163
120. Nakashima N, Okuzono S, Murakami H et al (2003) DNA dissolves single-walled carbon nanotubes in water. Chem Lett 32(5):456–457
121. Nepal D, Geckeler KE (2007) Proteins and carbon nanotubes: close encounter in water. Small 3:1259–1265
122. Neuhaus G, Spangenberg G (1990) Plant transformation by microinjection techniques. Physiol Plant 79:213–217
123. Nguyen CV, Delzeit L, Cassell AM et al (2002) Preparation of nucleic acid functionalized carbon nanotube arrays. Nano Lett 2:1079–1081
124. Niyogi S, Hu H, Hamon MA et al (2001) Chromatographic purification of soluble single-walled carbon nanotubes (s-SWNTs). J Am Chem Soc 123:733–734
125. Niyogi S, Hamon MA, Hu H et al (2002) Chemistry of single-walled carbon nanotubes. Acc Chem Res 35:1105–1113
126. Numata M, Sugikawa K, Kaneko K, Shinkai S (2008) Creation of hierarchical carbon nanotube assemblies through alternative packing of complementary semi-artificial b-1,3-glucan/carbon nanotube composites. Chem Eur J 14:2398–2404
127. Nunes A, Amsharov N, Guo C et al (2010) Hybrid polymer-grafted multiwalled carbon nanotubes for in vitro gene delivery. Small 6(20):2281–2291
128. O'Connell MJ, Bachilo SM, Huffman CB et al (2002) Band gap fluorescence from individual single-walled carbon nanotubes. Science 297:593–596
129. Ogoshi T, Inagaki A, Yamagishi T-A, Nakamoto Y (2008) Defection-selective solubilization and chemically-responsive solubility switching of single-walled carbon nanotubes with cucurbit[7]uril. Chem Commun 19:2245–2247
130. Pantarotto D, Briand JP, Prato M, Bianco A (2004a) Translocation of bioactive peptides across cell membranes by carbon nanotubes. Chem Commun 1:16–17
131. Pantarotto D, Singh R, McCarthy D et al (2004) Functionalized carbon nanotubes for plasmid DNA gene delivery. Angew Chem Int Ed 43:5242–5246
132. Petersen EJ, Zhang LW, Mattison NT et al (2011) Potential release pathways, environmental fate, and ecological risks of carbon nanotubes. Environ Sci Technol 45:9837–9856
133. Podesta JE, Al-Jamal KT, Herrero MA et al (2009) Antitumor activity and prolonged survival by carbon-nanotube-mediated therapeutic siRNA silencing in a human lung xenograft model. Small 5:1176–1185
134. Pogodin S, Baulin VA (2010) Can a carbon nanotube pierce through a phospholipid bilayer? ACS Nano 4(9):5293–5300
135. Porter AE, Gass M, Muller K et al (2007) Direct imaging of single-walled carbon nanotubes in cells. Nature Nanotech 2:713–717
136. Porter AE, Gass M, Bendall JS et al (2009) Uptake of noncytotoxic acid-treated single-walled carbon nanotubes into the cytoplasm of human macrophage cells. ACS Nano 3:1485–1492
137. Potrykus I (1990) Gene transfer to cereals: an assessment. BioTechnology 8:535–542
138. Prato M, Kostarelos K, Bianco A (2008) Functionalized carbon nanotubes in drug design and discovery. Acc Chem Res 41:60–68
139. Prencipe G, Tabakman SM, Welsher K et al (2009) PEG-branched polymer for functionalization of nanomaterials with ultralong blood circulation. J Am Chem Soc 131:4783–4787
140. Qi P, Vermesh O, Grecu M et al (2003) Toward large arrays of multiplex functionalized carbon nanotube sensors for highly sensitive and selective molecular detection. Nano Lett 3:347–351
141. Raffa V, Ciofani G, Nitodas S et al (2008) Can the properties of carbon nanotubes influence their internalization by living cells? Carbon 46:1600–1610
142. Raffa V, Vittorio O, Costa M et al (2012) Multiwalled carbon nanotube antennas induce effective plasmid dna transfection of bacterial cells. J Nanoneurosci 2(1):56–62
143. Rafsanjani MSO, Alvari A, Samim M et al (2012) Application of novel nanotechnology strategies in plant biotransformation: a contemporary overview. Recent Pat Biotechnol 6:69–79

144. Rakoczy-Trojanowska M (2002) Alternative methods of plant transformation—a short review. Cell Mol Biol Lett 7:849–858
145. Ramos-Perez V, Cifuentes A, Coronas N et al (2013) Modification of carbon nanotubes for gene delivery vectors. In: Bergese P, Hamad-Schifferli K (eds) Nanomaterial interfaces in biology: methods and protocols. Methods in molecular biology, vol 1025. Springer Science, New York, pp 261–269
146. Rao AM, Richter E, Bandow S et al (1997) Diameter-selective Raman scattering from vibrational modes in carbon nanotubes. Science 275:187–191
147. Rinzler A, Liu J, Dai H et al (1998) Large-scale purification of single-wall carbon nanotubes: process, product, and characterization. Appl Phys A 67:29–37
148. Rojas-Chapana J, Troszczynska J, Firkowska I et al (2005) Multi-walled carbon nanotubes for plasmid delivery into *E. coli* cells. Lab Chip 5:536–539
149. Russier J, Menard-Moyon C, Venturelli E et al (2011) Oxidative biodegradation of singleand multi-walled carbon nanotubes. Nanoscale 3:893–896
150. Ruzin SE, McCarthy SC (1986) The effect of chemical facilitators on the frequency of electrofusion of tobacco mesophyll protoplast. Plant Cell Rep 5:342–345
151. Sanchez-Pomales G, Pagan-Miranda C, Santiago-Rodriguez L, Cabrera CR (2010) DNA-wrapped carbon nanotubes: from synthesis to applications. In: Marulanda JM (ed) Carbon nanotubes. InTech, Vukovar, pp 721–748
152. Santosh M, Panigrahi S, Bhattacharyya D et al (2012) Unzipping and binding of small interfering RNA with single walled carbon nanotube: a platform for small interfering RNA delivery. J Chem Phys 136:065106
153. Serag MF, Kaji N, Venturelli E et al (2011a) Functional platform for controlled subcellular distribution of carbon nanotubes. ACS Nano 5(11):9264–9270
154. Serag MF, Kaji N, Gaillard C et al (2011) Trafficking and subcellular localization of multiwalled carbon nanotubes in plant cells. ACS Nano 5(1):493–499
155. Serag MF, Kaji N, Tokeshiac M, Baba Y (2012) Introducing carbon nanotubes into living walled plant cells through cellulase-induced nanoholes. RSC Adv 2:398–400
156. Shelimov KB, Esenaliev RO, Rinzler AG et al (1998) Purification of single-wall carbon nanotubes by ultrasonically assisted filtration. Chem Phys Lett 282:429–434
157. Shen C-X, Zhang Q-F, Li J et al (2010) Induction of programmed cell death in arabidopsis and rice by single-wall carbon nanotubes. Am J Bot 97(10):1602–1609
158. Shrawat AK, Good AG (2011) Agrobacterium tumefaciens-mediated genetic transformation of cereals using immature embryos. Methods Mol Biol 710:355–372
159. Simmons TJ, Bult J, Hashim DP et al (2009) Noncovalent functionalization as an alternative to oxidative acid treatment of single wall carbon nanotubes with applications for polymer composites. ACS Nano 3:865–870
160. Singh R, Pantarotto D, McCarthy D et al (2005) Binding and condensation of plasmid DNA onto functionalized carbon nanotubes: toward the construction of nanotube-based gene delivery vectors. J Am Chem Soc 127:4388–4396
161. Solis-Fernandez P, Paredes JI, Cosio A et al (2010) A comparison between physically and chemically driven etching in the oxidation of graphite surfaces. J Colloid Interface Sci 344:451–459
162. Stampoulis D, Sinha SK, White JC (2009) Assay-dependent phytotoxicity of nanoparticles to plants. Environ Sci Technol 43:9473–9479
163. Star A, Tu E, Niemann J, Gabriel JCP et al (2006) Label-free detection of DNA hybridization using carbon nanotube network field-effect transistors. Proc Natl Acad Sci U S A 103:921–926
164. Suri A, Chakraborty AK, Coleman KS (2008) A facile, solvent-free, noncovalent, and nondisruptive route to functionalize single-wall carbon nanotubes using tertiary phosphines. Chem Mater 20:1705–1709
165. Takagi H, Soneda Y, Hatori H et al (2007) Effects of nitric acid and heat treatment on hydrogen adsorption of single-walled carbon nanotubes. Aust J Chem 60:519–523
166. Tan X-M, Fugetsu B (2007) Multi-walled carbon-nanotubes interact with cultured rice cells: evidence of a self-defense response. J Biomed Nanotechnol 3:285–288

167. Tan H, Fu L, Seno M (2010) Optimization of bacterial plasmid transformation using nanomaterials based on the Yoshida effect. Int J Mol Sci 11:4962–4972
168. Tan X-M, Lin C, Fugetsu B (2009) Studies on toxicity of multi-walled carbon nanotubes on suspension rice cells. Carbon 47:3479–3487
169. Tasis D, Tagmatarchis N, Bianco A, Prato M (2006) Chemistry of carbon nanotubes. Chem Rev 106:1105–1136
170. Tasis D, Papagelis K, Douroumis D et al (2008) Diameter-selective solubilization of carbon nanotubes by lipid micelles. J Nanosci Nanotechnol 8:420–423
171. Tomonari Y, Murakami H, Nakashima N (2006) Solubilization of single-walled carbon nanotubes using polycyclic aromatic ammonium amphiphiles in water-strategy for the design of solubilizers with high performance. Chem Eur J 12:4027–4034
172. Torney F, Trewyn BG, Lin VSY, Wang K (2007) Mesoporous silica nanoparticles deliver DNA and chemicals into plants. Nat Nanotechnol 2:295–300
173. Tu X, Zheng MA (2008) DNA-based approach to the carbon nanotube sorting problem. Nano Res 1:185–194
174. Tu W, Lei J, Ju H (2009) Functionalization of carbon nanotubes with water-insoluble porphyrin in ionic liquid: direct electrochemistry and highly sensitive amperometric biosensing for trichloroacetic acid. Chem Eur J 15:779–784
175. Vaisman L, Wagner HD, Marom G (2006) The role of surfactants in dispersion of carbon nanotubes. Adv Colloid Interface Sci 128–130:37–46
176. Virkutyte J, Varma RS (2011) Green synthesis of metal nanoparticles: biodegradable polymers and enzymes in stabilization and surface functionalization. Chem Sci 2:837–846
177. Vogel SR, Müller K, Plutowski U et al (2007) DNA-carbon nanotube interactions and nanostructuring based on DNA. Phys Stat Sol (b) 244:4026–4029
178. Welsher K, Liu Z, Sherlock SP et al (2009) A route to brightly fluorescent carbon nanotubes for nearinfrared imaging in mice. Nat Nanotechnol 4(11):773–780
179. Witus LS, Rocha JD, Yuwono VM et al (2007) Peptides that non-covalently functionalize single-walled carbon nanotubes to give controlled solubility characteristics. J Mater Chem 17:1909–1915
180. Wong SS, Joselevich E, Woolley AT et al (1998) Covalently functionalized nanotubes as nanometre- sized probes in chemistry and biology. Nature 394:52–55
181. Wu Y, Phillips JA, Liu H et al (2008a) Carbon nanotubes protect DNA strands during cellular delivery. ACS Nano 2(10):2023–2028
182. Wu P, Chen X, Hu N et al (2008) Biocompatible carbon nanotubes generated by functionalization with glycodendrimers. Angew Chem Int Ed Engl 4(27):5022–5025
183. Xie X, Goodell B, Qian Y et al (2009) A method for producing carbon nanotubes directly from plant materials. For Prod J 59(1–2):26–28
184. Xiong HF, Motchelaho MAM, Moyo M et al (2011) Correlating the preparation and performance of cobalt catalysts supported on carbon nanotubes and carbon spheres in the Fischer-Tropsch synthesis. J Catal 278:26–40
185. Xu Y, Pehrsson PE, Chen L et al (2007) Double-stranded DNA single-walled carbon nanotube hybrids for optical hydrogen peroxide and glucose sensing. J Phys Chem C 111:8638–8643
186. Yan LY, Poon YF, Chan-Park MB et al (2008) Individually dispersing single-walled carbon nanotubes with water-soluble chitosan derivatives. J Phys Chem C 112:7579
187. Yang W, Thordarson P, Gooding JJ et al (2007) Carbon nanotubes for biological and biomedical applications. Nanotechnology 18:412001
188. Yang D, Guo GQ, Hu JH et al (2008a) Hydrothermal treatment to prepare hydroxyl group modified multi-walled carbon nanotubes. J Mater Chem 18:350–354
189. Yang Q, Shuai L, Pan X (2008) Synthesis of fluorescent chitosan and its application in noncovalent functionalization of carbon nanotubes. Biomacromolecules 9:3422–9326
190. Yang QH, Wang Q, Gale N et al (2009) Loosening the DNA wrapping around single-walled carbon nanotubes by increasing the strand length. Nanotechnology 20:195603
191. Yang S-T, Wang H, Meziani MJ et al (2009) Bio-defunctionalization of functionalized single-walled carbon nanotubes in mice. Biomacromolecules 10(7):2009–2012

192. Yeagle PL (ed) (2005) The structure of biological membranes, 2nd ed. CRC, Boca Raton
193. Yoshida N, Ikeda T, Yoshida T (2001) Chrysotile asbestos fibers mediate transformation of Escherichia coli by exogenous plasmid DNA. FEMS Microbiol Lett 195:133–137
194. Youn S, Wang R, Gao J et al (2012) Mitigation of the impact of single-walled carbon nanotubes on a freshwater green algae: *Pseudokirchneriella subcapitata*. Nanotoxicology 6(2):161–172
195. Yu B-Z, Ma J-F, Li W-X (2009) Polyethylenimine-modified multiwalled carbon nanotubes for plasmid DNA gene delivery. Nat Preced: hdl:10101/npre.2009.2753.1
196. Yuan H, Hu S, Huang P et al (2011) Single walled carbon nanotubes exhibit dual-phase regulation to exposed arabidopsis mesophyll cells. Nanoscale Res Lett 6:44
197. Yun Y, Dong Z, Shanov V et al (2007) Nanotube electrodes and biosensors. Nano Today 2:30–37
198. Zhang M, Li J (2009) Carbon nanotube in different shapes. Mater Today 12(6):12–18
199. Zhang ZH, Yang XY, Zhang Y et al (2006) Delivery of telomerase reverse transcriptase small interfering RNA in complex with positively charged single-walled carbon nanotubes suppresses tumor growth. Clin Cancer Res 12:4933–4939
200. Zhang J, Wang Q, Wang L, Wang A (2007) Manipulated dispersion of carbon nanotubes with derivatives of chitosan. Carbon 45:1917–1920
201. Zhang L, Petersen EJ, Habteselassie MY et al (2013) Degradation of multiwall carbon nanotubes by bacteria. Environ Pollut 181:335–339
202. Zhao X, Johnson JK (2007) Simulation of adsorption of DNA on carbon nanotubes. J Am Chem Soc 129:10438–10445
203. Zhao Y-L, Stoddart JF (2009) Noncovalent functionalization of single-walled carbon nanotubes. Acc Chem Res 42:1161–1171
204. Zhao Y, Allen BL, Star A (2011) Enzymatic degradation of multiwalled carbon nanotubes. J Phys Chem A 115:9536–9544
205. Zheng M, Jagota A, Strano MS et al (2003a) Structure-based carbon nanotube sorting by sequence-dependent DNA assembly. Science 302:1545–1548
206. Zheng M, Jagota A, Semke ED et al (2003) DNA assisted dispersion and separation of carbon nanotubes. Nat Mater 2:338–342
207. Zorbas V, Smith AL, Xie H et al (2005) Importance of aromatic content for peptide/single-walled carbon nanotube interactions. J Am Chem Soc 127:12323–12328

Chapter 21
Platinum Nanoparticles with Adsorptive Layer of *Chlorella vulgaris* Polysaccharides Inactivate Tumor Cells of Ascitic Ehrlich Carcinoma, Ovarian Cancer and Leukemia

V. R. Estrela-Llopis, A. V. Chevichalova, N. A. Tregubova, E. D. Shishko and P. M. Litvin

21.1 Background

Over the past 20 years, there has been an intensive development of investigations of gold and silver nanoparticles (NP) for applications in biology and medicine—for increase of biodetection sensitivity [1], for intensification of physiotherapeutic treatment (photodynamic, photothermal, and radiotherapy [2–7]), as well as at targeted delivery of drugs [8, 9]. Such applications are connected with resonance plasmonic properties of gold and silver NP (biodetection) [10] and with the prevailing opinion about nontoxicity of gold as a precious metal [8, 11].

The review [12, 2008] notes that there are practically no studies on the use of platinum NP. This fact is surprising, since chemotherapy widely uses platinum ion complexes with various organic compounds, cisplatin, for example. Increased toxic side effects of such drugs may have caused a delay in the corresponding studies on the application of nanoplatinum. However, acad. K.B. Yatsimirskii noted in his monograph [13] that the neutral platinum Pt (0) is not toxic in contrast to the ionic forms. The recent years' investigations show that nanoplatinum particles can inactivate the cancer cells.

Mechanisms of toxic action of platinum NP had been studied in papers [14, 15]. For example, authors [14] show that platinum NP act as an oxidizing agent for

V. R. Estrela-Llopis (✉) · A. V. Chevichalova
F. D. Ovcharenko Institute of Biocolloid Chemistry, Ukrainian National Academy of Sciences, 42 Vernadsky Avenue, Kyiv 03680, Ukraine
e-mail: victorio.estrela@gmail.com

N. A. Tregubova · E. D. Shishko
R. E. Kavetsky Institute of Experimental Pathology, Oncology and Radiobiology, Ukrainian National Academy of Sciences, 45 Vasilkovska Str., Kyiv, Ukraine
e-mail: 4evi4alova@gmail.com

P. M. Litvin
V. E. Lashkarev Institute of Semiconductor Physics, Ukrainian National Academy of Sciences, 41 Avenue of Science, Kyiv 03028, Ukraine
e-mail: plyt2007@gmail.com

O. Fesenko, L. Yatsenko (eds.), *Nanocomposites, Nanophotonics, Nanobiotechnology, and Applications,* Springer Proceedings in Physics 156,
DOI 10.1007/978-3-319-06611-0_21,

mitochondrial coenzyme nicotinamide adenine dinucleotide due to their catalytic properties. This affects the ATP synthesis and consequently the vital functions of the cell. The study also shows that in the acidic medium of phagosomes (where platinum NP are concentrated in a result of phagocytosis), free platinum ions are released from the particle surface, and these ions are also cytotoxic. The paper [15] shows that the influence of such ions result in the violation of proliferation, mitosis, and development of apoptosis of glioblastoma U251 and lung fibroblasts IMR-90 cells. This effect is explained by DNA damage of such cells by releasing active oxygen forms (O_2^- and H_2O_2) under the influence of platinum ions. It should be noted that in this work platinum NP stabilized by polyvinyl alcohol were used.

In our work, we apply polysaccharides (PS) of the microalgae *Chlorella vulgaris* strain LARG-3 (Institute of BiophysicsSD of RAS, Krasnoyarsk city, Russia) to stabilize platinum NP. This choice is due to the effective practice of PS application for cancer therapy.

Anticancer properties of PS were confirmed in a number of studies [16–21]. Thus, authors of [16] have shown that high-molecular *Chlorella's* PS stimulate the synthesis of cytokines and II-6, IL-10, INF-γ, necrosis factor of TNF-α cells and the proliferation of splenocytes. The acid polysaccharide ChlonA of microalgae *Chlorella pirenoidosa* stimulates the phagocytic activity of the reticuloendothelial system (of rats) and increases immunity [17]. High-molecular anionic polysaccharide hyaluronan of the extracellular matrix inhibits process of metastasis and decreases the multidrug resistance of cancer cells [18]. When developing the method of synthesis gold single-platelet nanocrystals–nanoprisms, based on the use of PS *Chlorellavulgaris* strain LARG-3 as a reducing stabilizer, we found that these PS have an average molecular weight of 500 kDa and are of an anionic nature [19].

The influence of fungi PS on the activation of the immune system is also established [20]. Glynco biloba PS activate apoptosis and inhibition of proliferation of gastric cancer cells [21]. Healing properties of *Chlorella* and its extracts have been widely used in oriental medicine [22].

PS and phagocytosis. PS amplify the penetration of NP into the cell based on the known mechanism of phagocytosis. Thus, in 1978 it was shown that the anionic high-molecular polyelectrolytes penetrate and act on Sarcoma-180 cells [23] better than cationic and neutral polymers. The paper [24] shows that the polyanions cause reorientation of phospholipids in the membrane which facilitates its deformation and stimulates phagocytosis of the NP covered with adsorbing layer of such polyanions. PS can be degraded in the acidic medium of the phagosomes. This effect creates the possibility of the direct action of the drug NP covered with PS [24].

Carbohydrate (polysaccharide) targeting [25]—scientific direction in the field of drug delivery, which effectively develops in recent years is similar to subject of our work. Here, PS are used as ligands for the creation of saccharide-modified drugs. This direction is based on the particular features of the glycolysis process during the development of malignant tumors. It is known [26] that tumor cells utilize glucose at a much faster rate, even under anaerobic conditions, than the cells of the healthy tissue—the tumor is a kind of a "trap" for glucose. The monograph [27] indicates that the glycolytic phenotype is almost a universal phenomenon of human tumors.

Therefore, we can assume that cancer cells and tumors accumulate and assimilate glyco-target nanocarriers according to the mechanisms that determine their characteristic elevated level of glucose uptake. These glyco-target carriers include objects of our research—platinum NP modified by the adsorption layer of *Chlorella's* PS.

The purpose of our work is to synthesize and investigate the possibility to use such nanocomposites in cancer therapy. The expediency of the presented in article researches are validated by quoted in the review mechanisms of cytotoxic effect on cancer cells of nanoplatinum and polysaccharides (independently), as well as stimulating effect of the PS on phagocytosis.

21.2 Methods

Namalwa lines cells of blood cancer were grown in an RPMI 1640 (SIGMA) medium with an addition of 10 % of fetal bovine serum. In these experiments, we used the suspension of cells in the nutrient medium.

Cells of human ovarian cancer of A2780 line were grown in an ISCOV (SIGMA-ALDRICH) medium with addition of 10 % fetal calf serum (FCS) at 37 °C.

Isolation of lymphocytes from the venous blood of a healthy human was performed based on standard techniques of centrifugation of blood in a defined density gradient for the lymphocytes separation from erythrocytes and other normal blood elements [28]. Such cells are generally considered a healthy analogue (control) of blood cancer cells. Comparison of rates of aggregation of healthy lymphocytes with NP PtPS with the analogous effect for the leukemia cells will establish the selectivity of such aggregation.

PS Chlorella vulgaris LARG-3 were precipitated with acetone from the culture medium of *Chlorella* cells (at a 2:1 ratio), evaporated previously at 70 °C up to tenfold decrease in volume. PS were separated by centrifugation, the acetone residues were removed by means of evaporation. The resulting product was dissolved in distillate and dialyzed against bidistillate. The concentration of the PS was determined by the phenol-sulfuric method [29].

Platinum NP stabilized by adsorptive layer of PS (NP PtPS) were obtained by restoring of platinum from 1 mM solution of $HPtCl_6 \cdot 3H_2O$ by ascorbic acid and the solution of PS supplemented after 15–20 min of stirring of the above mixture until a PS final concentration of 30 mg/dm^3 was obtained in the mixture. This concentration of PS is determined from an experiment that includes the study of the adsorption isotherm of PS on platinum NP and changes of electrokinetic zeta potential of the particles as a result of such adsorption (Fig. 21.1).

Here, dashed lines mark optimum range of PS concentration (20 ÷ 50 mgPS/dm^3) to get platinum NP PtPS with adsorption of PS close to saturation on the surface of platinum's NP-Gmax = 0.35 gPS/gPt.

Distribution of platinum NP and bioconjugates of NP PtPS by the size was investigated by atomic force microscopy (scanning probe microscope Dimension 3000,

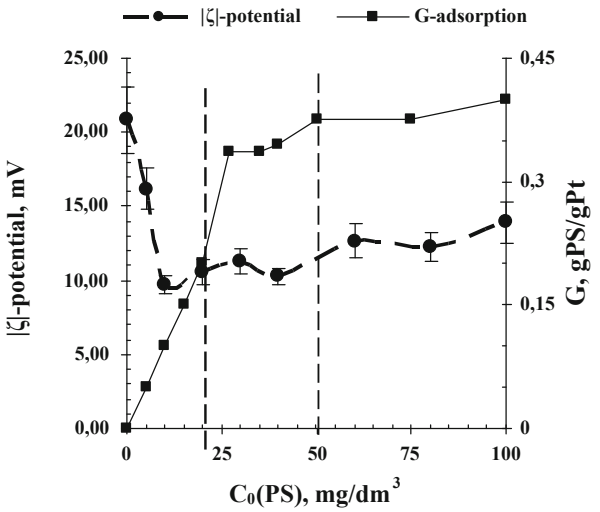

Fig. 21.1 Adsorption of polysaccharides (G) on the surface of platinum nanoparticles decreases its zeta potential (ζ).

BRUKER/VEECO)—Fig. 21.2. A comparison of Fig. 21.2a and 21.2b shows that the adsorption of PS increases the average size of platinum particles from 18 to 38 nm.

Micrographs of platinum NP, with and without an adsorptive layer, were obtained by transmission electronic microscopy (TEM) and are shown in Fig. 21.2c and 21.2d, respectively. The gray shell around the electron-dense particles (Fig. 21.2d) corresponds to the adsorption layer of PS. Particle sizes on the micrographs are comparable to the size of the same particles, as defined by AFM (compare Fig. 21.2a, 21.2b and 21.2c, 21.2d).

Determination of IC50 for NP Pt and NP PtPS. The half maximal inhibitory concentration (IC50) index is used for investigating the effectiveness of pharmaceutical preparations in the in vitro experiments. IC50 is the concentration of the drug, when during a fixed time at least half of the cancer cells die in the in vitro experiment. Mixing and exposure of cancer cells with platinum sols were carried out on a standard cell with 96 wells. In each hole, 1 cm^3 of A2780 cell suspension with a concentration of 5×10^4 cm^{-3} per nutrient medium ISCOV was placed, where they remained for 48 h in the monolayer form. To get mixtures with different concentrations of NP Pt and NP PtPS, the initial sol was diluted multiple times with nutrient medium and mixed with the cells in each well. The incubation of cells with NP was 24 h. After completion of the exposure, the mixture of cells and particles was moved from the well in the Goryaev chamber, the dead cells were isolated by staining with a solution of 0.2 % trypan blue. Then, the number of living cells in the chamber and their percentage compared to the concentration of live cells in control wells, where NP were not added, were counted in three replications.

The efficacy of heterocoagulation was determined by the difference between the initial concentration of platinum nanoparticles in a mixture with the cells and (after 1 hour exposure) concentration of these particles in the supernatant, after separation of aggregates of cells with particles by centrifugation [30].

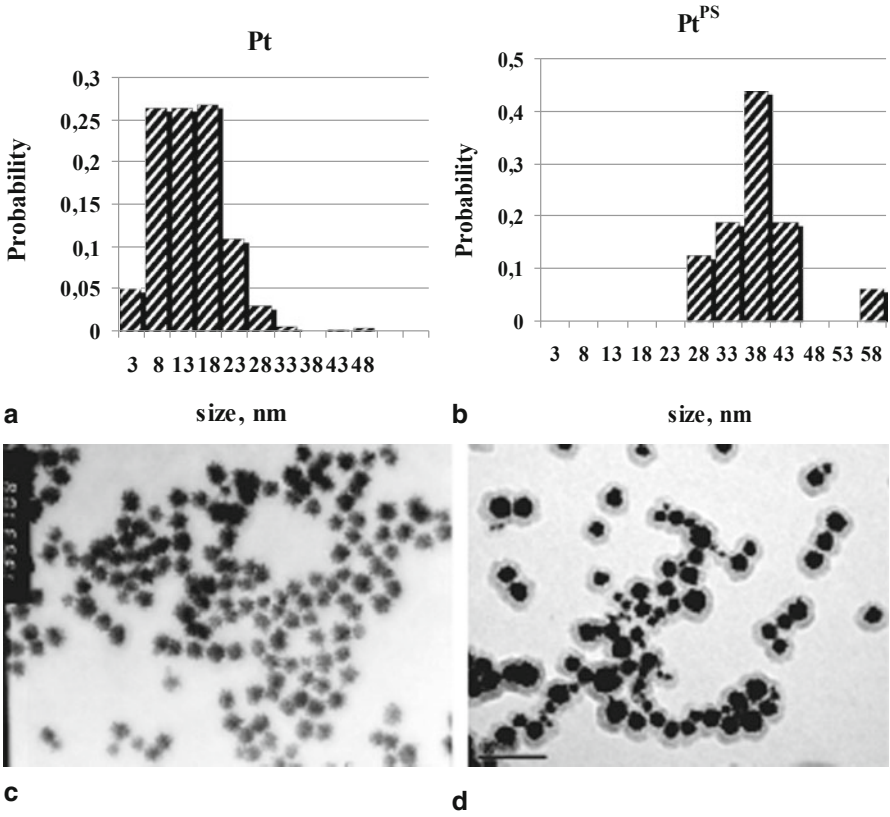

Fig. 21.2 Distribution of NP Pt (**a**) and NP PtPS (**b**) particles according to the size, as indicated in the AFM and TEM micrograph of these particles, respectively— × 133,010 (**c**), and × 202,311 (**d**)

Contents of NP PtPS not aggregated with cells were analyzed for platinum content by atomic absorption spectroscopy method—AAS-5M (Sumy city, Ukraine).

Kinetics of cytotoxic effect is a gradual decrease of live cells concentration (increase in the dead cells percentage) as a result of contact with the NP PtPS. Control sample of cancer cells suspension (0.2 ml) was sampled at defined time intervals of contact. The concentration of dead cells in such a sample was counted in the Goryaev chamber by the use of trypan blue dye (light microscopy—LYUMAM P-1 LOMO).

Electron microscope investigations of NP Pt and PtPS were conducted on the electron microscope TEM-125K (Sumy city, Ukraine). TEM (JEM-1230 ≪ JEOL ≫, Japan) was used also for cytomorphological study of the A2780 line human ovarian cancer cells. The ultrastructure of *Namalva* leukemia cells and healthy blood lymphocytes was studied on the analytical electron microscope JEM1500FXII (JEOL, Japan). Ultrafine sections of the cells were obtained from cell suspension previously fixed by glutaraldehyde and osmium tetroxide and then immobilized in polymerized

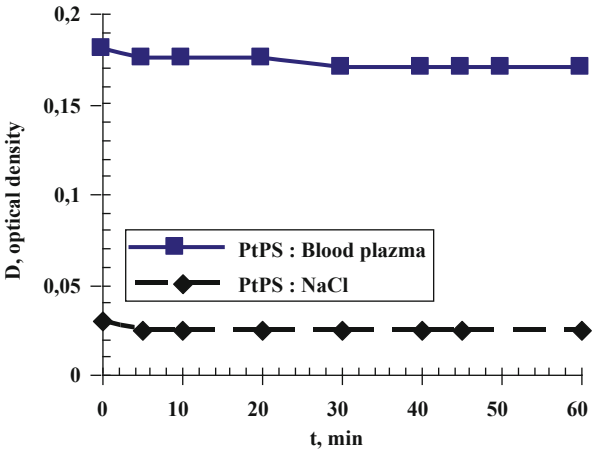

Fig. 21.3 Kinetics of aggregation of nanoparticles PtPS in blood plasma and normal saline (0.9 % NaCl) solutions.s.o PS = 4 mg/dm^3

epoxy according to known methods of preparation of biological samples for electron microscopy [27].

21.3 Results and Discussion

Influence of medium composition on the stability of NP PtPS. Aggregative stability is one of the basic conditions of successful application of any form of medical nanodrugs that are injected via blood. Therefore, we had studied the kinetics of NP PtPS stability in normal saline and blood plasma solutions in advance (in the ratio of sol to medium—1:19)—Fig. 21.3.

The constancy of the optical density over time suggests that the observable system is stable. Unlike saline, blood plasma contains up to 7 % of various proteins. A slight decrease in the optical density curve ($\Delta = 0.01$) for NP PtPS in plasma may have appeared due to the adsorption of proteins (interaction between amino groups of proteins and carboxyl/hydroxyl groups of PS)—Fig. 21.3. So, stability of NP PtPS in plasma may be argued in favor of protective effect of PS towards adsorption of plasma proteins on NP PtPS. Stability of NP PtPS in saline and blood plasma determines the possibility of preparing the relevant drugs for intravenous injection.

Presented here fact of the NP PtPS aggregative stability in biological fluids is important for confirmation by accuracy of the presented below research results of heterocoagulation of particles with cells. If in this process, the NP are not coagulated and do not form large aggregates (see Fig. 21.3), this result eliminates the artifacts (when determining the heterocoagulation effectiveness—colloid uptake) as a result of the simultaneous sedimentation during centrifugation the getero-aggregates of particles and tumor cells with particles gomo-aggregates.

Mutual stability of the PtPS particles during their heterocoagulation with cells is also confirmed by the TEM micrograph in Fig. 21.9b, which shows that during the

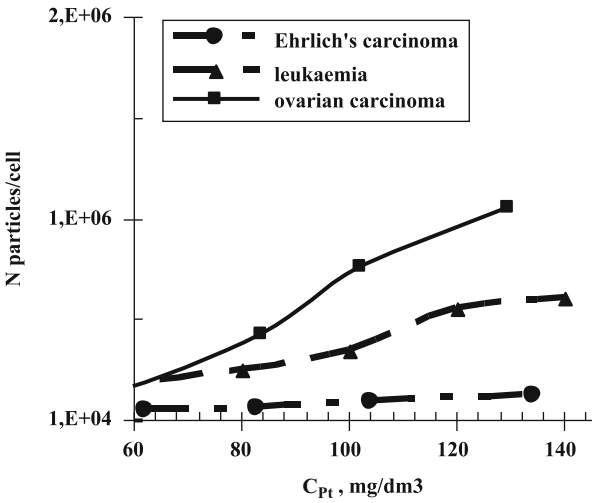

Fig. 21.4 Effect of the concentration of nanoparticles PtPS on their heterocoagulation with cancer cells ($C_{cell} = 470{,}000/cm^3$)

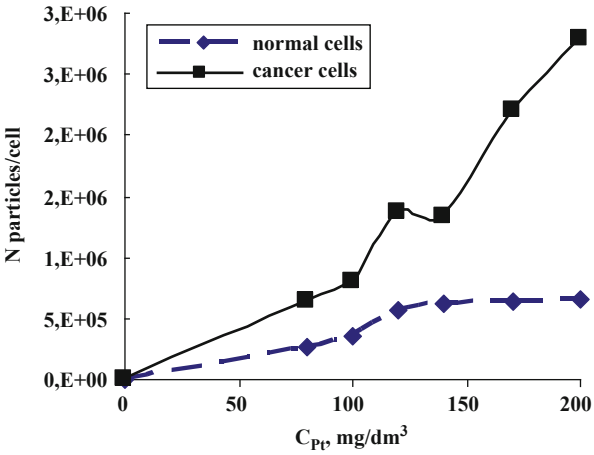

Fig. 21.5 Selectivity of NP PtPS heterocoagulation with cancer leukemia and healthy lymphocytes cells. The influence of particles concentration on quantity of nanoparticles NP PtPS, aggregated with one cell ($Ccell = 470,000/cm^3$)

concentration of particles near the surface of the tumor cell the particles with each other are not coagulated.

Efficiency of the aggregation of PtPS NP with cancer cells of different carcinogenesis (Ehrlich carcinoma, ovarian cancer—A2780 line, blood cancer—Namalwa line) was studied based on the heterocoagulation research (colloid uptake) and the corresponding kinetics of the cytotoxic effect. The results are shown in Fig. 21.4.

As can be seen from the data presented, the cancer cells are actively aggregated with NP PtPS. Aggregation of these NP with human ovarian cancer cells is higher as compared to cells of Ehrlich carcinoma and leukemia.

Selectivity of NP PtPS aggregation with cancerous and similar healthy cells. To determine the selectivity of NP PtPS aggregation with leukemia cells as compared to healthy lymphocytes, we investigated their heterocoagulation.

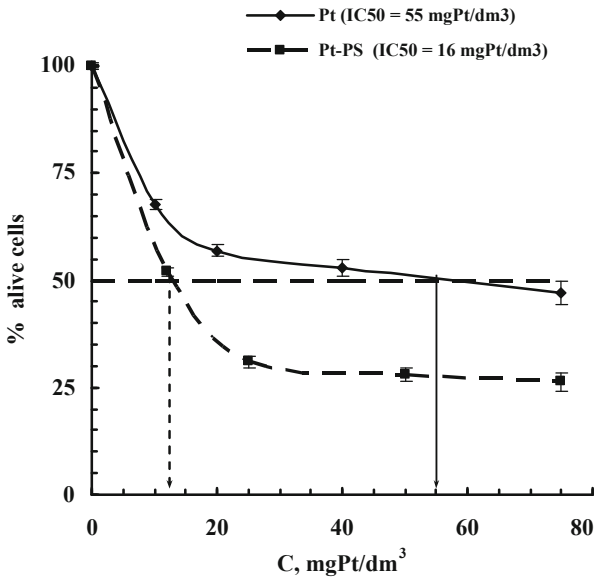

Fig. 21.6 IC50 value for platinum nanoparticles refined in accordance with the trend of the experimental curve.

Results of the investigation of NP PtPS aggregation with Namalwa line cancer cells or with healthy lymphocytes (Fig. 21.5) show that platinum NP modified by PS selectively interact with such cells—their aggregation with cancer cells (the number N of particles aggregated with a single cell) is much higher than with healthy cells.

One of the methods of investigating the toxic effect of the drug for the cells is based on the determination of the IC50 index. Figure 21.6 shows the particle concentration dependence of the percentage of intact (live) A2780 cells after the same contact time of cells with the platinum NP and the same particles but coated by the adsorption layer of Chlorella's PS.

As can be seen from the data presented, the modification of platinum NP by adsorption of PS on their surface greatly enhances the toxic effect of nanoplatinum.Efficiency of the toxic effects of NP PtPS is markedly higher than NP Pt—in the first case, a half of cells die at a concentration of NP PtPS equal to 16 mg/dm^3 and in the second, at a concentration of NP Pt equal to 55 mg/dm^3. Thus, an adsorption layer of PS on the surface of platinum NP reduces the value IC50, more than three times. The reasons for this effect may be related to the above-noted factors of the PS toxic impact on the cancer cells and the ability of polysaccharide, as an anionic polyelectrolyte, to intensify phagocytosis.

Kinetics of the cytotoxic effect. We have studied the kinetics of the toxic effect of NP PtPS on Ehrlich carcinoma cells, ovarian cancer, and lymphoma cells and, for comparison with the latter—on healthy (N) lymphocytes. Kinetics study is based on the determination of the percentage of live and dead cells depending on the time of their contact with the NP. The results are shown in Fig. 21.7.

The data presented in Fig. 21.7 show that during the first hour of contact more than 50 % of ovarian carcinoma cells and Ehrlich carcinoma cells die and

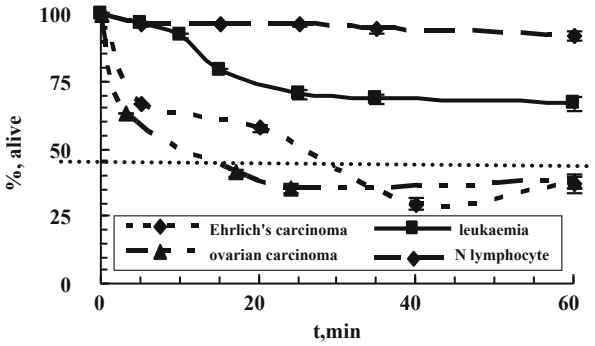

Fig. 21.7 Kinetics of the cytotoxic effect of PtPS NP on Ehrlich carcinoma cells, ovarian cancer, lymphoma cells, and healthy (N) lymphocytes ($C_{cell} = 470{,}000/cm^3$, $C_{Pt} = 80\,mg/dm^3$)

approximately 25 % of lymphoma cells die, while healthy cells retained their vital activity (only 5 % of such cells die within an hour of contact). This result confirms the data presented in Fig. 21.6 about the selectivity of toxic action of PtPS NP on cancer but not healthy cells.

Cytomorphological changes in the ultrastructure of cells under the influence of PtPS NP were investigated by transmission electron microscopy. The influence of platinum NP with adsorption layer of PS on A2780 cells culture after 30 min of exposure resulted in changes in its ultrastructure that can be associated with the processes of the activation of proteolytic enzyme system. So, a host of small lipid granules, lysosomes, secondary lysosappearedomes and vacuoles, containing electron-dense polydisperse material, appeared in the cytoplasm—Fig. 21.8b. The cell nucleus of such cells is deformed, eccentrically located in the cytoplasm (Fig. 21.8b) or segmented (Fig. 21.8c)—compared with microphotos Fig. 21.8a of the initial ovarian cancer cell, cultured at standard conditions without NP.

The result of the effect of NP PtPS on lymphoma Namalwa cells is shown on TEM microphotographs in Fig. 21.9. Standard ultrastructure of Namalwa cells is presented in Fig. 21.9. The process of the concentration of the single, nonaggregated particles near the surface (in the microenvironment) of such cell can be seen on microphoto Fig. 21.9b.

As shown in Fig. 21.9c, after an hour of contact with NP PtPS, the ultrastructure of some cancer cells is damaged, the nucleus and outer membrane get deformed, phagosomes are formed (compared with the initial Namalwa cell structure—Fig. 21.9a), while other cells demonstrate full defragmentation into separate apoptotic bodies (Fig. 21.9c).

21.4 Conclusions

We suggest a new "green" method of the synthesis of platinum nanoparticles, which is based on the use of polysaccharides of *Chlorella vulgaris* microalgae as a reducing stabilizer. With the use of the methods of investigation of the aggregation intensity

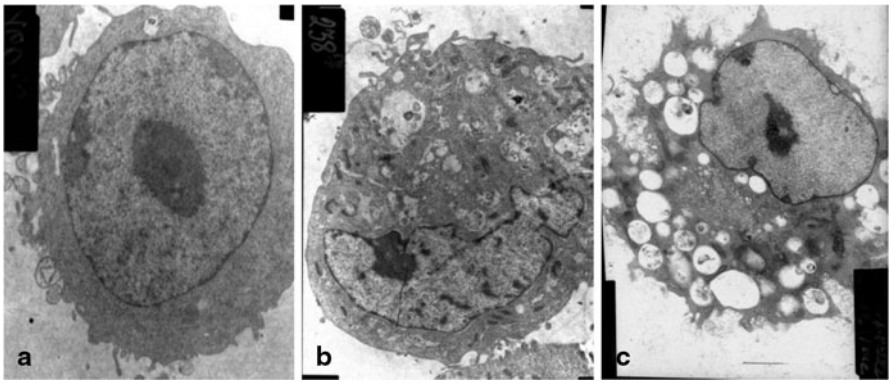

Fig. 21.8 Change in an ultrastructure of ovarian cancer cells A2780 after 30 min contact time with PtPS

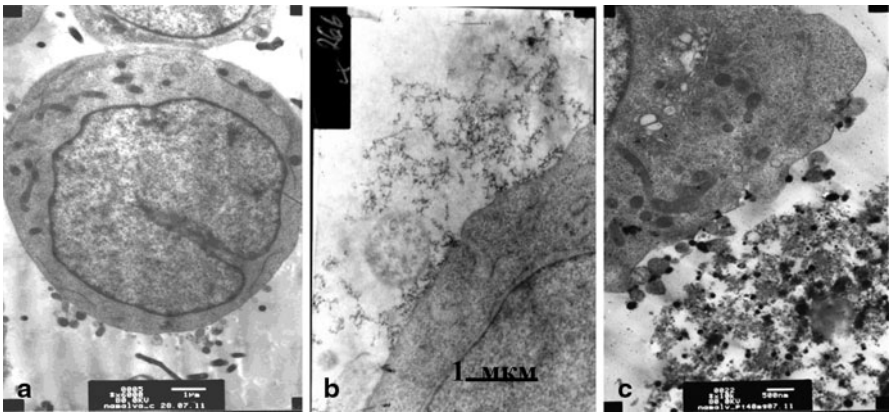

Fig. 21.9 Disintegration of the ultrastructure of leukemia cells by NP PtPS

and the kinetics of cytotoxic effect, we have studied the impact of platinum NP with the adsorption layer of *Chlorella vulgaris* PS on cancerous cells of various origins (Ehrlich carcinoma, ovarian cancer, lymphoma) and on healthy lymphocytes, and proved toxic effect of such NP on tumor cells. It was shown that PS adsorbed on the surface of the NP reduce the toxic dose of platinum NP more than three times. It was found that NP PtPS selectively inactivate the cancer cells while preserving the viability of healthy cells (a pair of *βsneoplastic lymphocyte—Namalwa line* and healthy *lymphocyte* cells). Bioconjugates of platinum NP with PS may be the useful basis for the development of new nanoplatinum-based drugs for cancer therapy.

References

1. Dykman L, Khlebtsov N (2012) Gold nanoparticles in biomedical applications: recent advances and perspectives. Chem Soc Rev 41:2256–2282
2. Gamaleja N, Lesnyak G, Prokopenko I (2007) Photobiology and photomedicine 7:67 (rus).
3. Huang X, Prashant K, El-Sayed IH, El-Sayed MA (2007) Gold nanoparticles and nanorods in medicine: from cancer diagnostics to photothermaltherapy. Nanomedicine 2(5):681–693
4. Krutyakov Y, Kudrinskiy A, Olenin A, Lisichkin G (2008) Synthesis and properties of silver nanoparticles: advances and prospects. Russ Chem Rev 77(3):233–257
5. Dreaden EC, Alkilany AM, Huang X, Murphy CJ, El-Sayed MA (2012) The golden age: gold nanoparticles for biomedicine. Chem Soc Rev 41:2740–2779
6. Jain PK, Huang X, El-Sayed IH, El-Sayed MA (2007) Review of some interesting surface plasmon resonance-enhanced properties of noble metal nanoparticles and their applications to biosystems. Plasmonics 2:107–111
7. Khlebtsov BN, Zharov VP, Melnikov AG, Tuchin VV, Khlebtsov NG (2006) Optical amplification of photothermal therapy with gold nanoparticles and nanoclusters. Nanotechnology 17(20):5167–5179
8. Pissuwan D, Niidome T, Cortie MB (2011) The forthcoming applications of gold nanoparticles in drug and gene delivery systems. J Controlled Release 149:65–71
9. Shi J, Xiao Z, Kamaly N, Farokhzad OC (2011) Self-assembled targeted nanoparticles. Acc Chem Res 44(10):1123–1134
10. Abalde-Cela S, Aldeanueva-Potel P, Mateo-Mateo C et al (2010) Surface-enhanced Raman scattering biomedical application of plasmonic colloidal particles. J Royal Soc Interface 7: 435–450
11. Vigderman L, Zubarev ER (2012) Therapeutic platforms based on gold nanoparticles and their covalent conjugates with drug molecules. Adv Drug Deliv Rev 65:663–676 (1 Rev)
12. Bhattacharya R, Mukherjee P (2008) Biological properties of "naked" metal nanoparticles. Adv Drug Delivery Rev 60:1289–1306
13. Yatsimirskii KB (1976) Problems of bioneorganicheskoy chemistry. Moscow: Mir
14. Hikosaka K et al (2008) Platinum nanoparticles have an activity similar to mitochondrial NADH: ubiquinone oxidoreductase. Colloids Surf B 66:195–200
15. Asharani PV, Xinyi N, Hande M, Valiyaveettil S (2010) DNA damage and p53-mediated growth arrest in human cells treated with platinum nanoparticles. Nanomedicine 5(1):51
16. Kralovec JA (2005) Chlorella composition having high molecular weight polysaccharides and polysaccharide complexes. Patent US No. 6974576 (13.12.2005)
17. Komiyama A, Umezawa I (1985) Acidic polysaccharide CH-1 isolated from Chlorella pyrenoidosa and the use thereof. Patent US No. 4533548 (06.08.1985)
18. Misra S, Toole BP, Ghatak S (2006) Hyaluronan constitutively regulates activation of multiple receptor tyrosine kinases in epithelial and carcinoma cells. J Bio Chem 281(46):34936
19. Estrela-Llopis VR, Borodinova TI, Yurkova IN (2010) Extracellular biomineralization and synthesis of gold and platinum nano- and microcrystals in polysaccharide aqueous solutions, Chap. 12. In Starov V (ed) Nanoscience: colloidal and interfacial aspects. CRC Press, Boca Raton, pp 307–368
20. Daba AS, Ezeronye OU (2003) Anti-cancer effect of polysaccharides isolated from higher basidiomycetes mushrooms. Afr J Biotechnol 2(12):672–678
21. Xu AH, Chen HS, Sun BC, Xiang XR, Chu YF, Zhai F, Jia LC (2003) Therapeutic mechanism of ginkgo biloba exocarp polysaccharides on gastric cancer. World J Gastroenterol 9(11): 2424–2427
22. ABEILLE'DOR COMPANY (Singapore) http://www.abdchlorella.com/index.php/chlorella-facts/
23. Hodnett EM, Amirmoazzami J, Tai JTH (1978) Anionic polymers and biological activities: effects of some new polycarboxylic acids on the ascitic sarcoma 180 of mice. J Med Chem 21:7

24. Yessine MA, Leroux JC (2004) Membrane-destabilizing polyanions: interaction with lipid bilayers and endosomal escape of biomacromolecules. Adv Drug Deliv Rev 56:999–1021
25. Yu W, Zhang N, Li C (2009) Saccharide modified pharmaceutical nanocarriers for targeted drug and gene delivery. Curr Pharm Des 15(32):3826–3836
26. Shapot VS (1975) Biochemical aspects of tumor growth.Moscow: Medicine, 304 (rus)
27. Osinski S, Vaupel P (2009) Microphysiology of tumors. Kiev: Naukovadumka, 108 (rus)
28. Hayat MA (2000) Principles and techniques of electron microscopy: biological applications. Cambridge University Press, Cambridge, p 543
29. Du Bois M., Gilles KA, Hamilton JK, Rebers PA, Smith F (1956) Colorimetric method for determination of sugars and related substances. Anal Chem 28(3):350
30. Estrela-Llopis VR et al (2009) Investigation of coagulation gold and platinum nanoparticles and nanostructures in blood plasma and their interaction with transformed cells of certain tumorigenesis to be used in oncology therapy. Report on research work No. 0107U007693 (rus)

Part IV
Applications

Chapter 22
Biosensors Based on Urease Adsorbed on Nickel, Platinum, and Gold Conductometric Transducers Modified with Silicalite and Nanozeolites

Ivan S. Kucherenko, Oleksandr O. Soldatkin, Berna Ozansoy Kasap, Burcu Akata Kurç, Volodymir G. Melnyk, Lyudmila M. Semenycheva, Sergei V. Dzyadevych and Alexei P. Soldatkin

22.1 Introduction

Biosensors are important analytical tools capable of providing rapid, sensitive, selective, and cheap analysis of concentration of certain substances in liquid or vapor samples. They are composed of a physical transducer (usually electrode) and a biological recognition element (mostly enzymes) immobilized in the active region of transducer [1]. Immobilization of biological molecules onto the surface of transducer is an important stage in biosensor preparation because it can significantly influence the biosensor's analytical characteristics. Conventional methods of immobilization have some disadvantages, in particular bad reproducibility of biosensor preparation, so the development of new methods of enzyme immobilization is an actual challenge [2].

I. S. Kucherenko(✉) · O. O. Soldatkin · S. V. Dzyadevych · A. P. Soldatkin
Laboratory of Biomolecular Electronics, Institute of Molecular Biology and Genetics, National Academy of Sciences of Ukraine, Zabolotnogo Street 150, Kyiv 03143, Ukraine

I. S. Kucherenko
Institute of Biology, Taras Shevchenko National University of Kyiv, Volodymyrska Street 64, Kyiv 01601, Ukraine
e-mail: kucherenko.i.s@gmail.com

O. O. Soldatkin · S. V. Dzyadevych · A. P. Soldatkin
Institute of High Technologies, Taras Shevchenko National University of Kyiv, Volodymyrska Street 64, Kyiv 01601, Ukraine
e-mail: alex_sold@yahoo.com

B. O. Kasap · B. A. Kurç
Central Laboratory, Middle East Technical University, Ankara 06531, Turkey
e-mail: bernaozansoy@gmail.com

B. A. Kurç
Micro and Nanotechnology Department, Middle East Technical University, Ankara 06531, Turkey
e-mail: akata@metu.edu.tr

O. Fesenko, L. Yatsenko (eds.), *Nanocomposites, Nanophotonics, Nanobiotechnology, and Applications,* Springer Proceedings in Physics 156,
DOI 10.1007/978-3-319-06611-0_22,

Recent advances in material science allow the synthesis of microsized and nanosized silica-aluminum particles, which are perspective carriers of biological molecules. Modification of the transducer active regions with such particles and further enzyme adsorption onto modified surfaces can be a promising approach in the development of biosensors [3]. In our work, we used three kinds of particles as adsorbents: silicalite, nanozeolite L, and nanozeolite Beta (BEA).

Silicalites are porous micro- and nanoparticles with a crystal lattice formed by silicon and oxygen atoms. They belong to zeolites, but differ from other zeolites in the absence of aluminum atoms in silicalite structure. Their crystals contain numerous channels (and thus silicalites have a large surface area) which makes them good adsorbents. The presence of hydroxyl groups as well as hydrophilic and hydrophobic sites on the silicalite surface enables numerous interactions between enzyme and microparticle [4]. In particular, silicalite has been reported as an adsorbent of lipase and bovine serum albumin [5, 6].

Nanosized zeolites (nanozeolites) are an interesting group of zeolites which includes particles with the size of crystals < 1000 nm (often < 200 nm). Their structure resembles a structure of larger zeolites, but nanozeolites are characterized by larger external surface area and smaller accumulates of crystals [7, 8].

In our work, we examined a possibility of the creation of conductometric biosensors using silicalite and nanozeolites L and Beta as carriers of enzyme urease. Conductometric transducers with nickel, gold, and platinum interdigitated electrodes were chosen for comparison. This study is an extension of our previous work devoted to investigation of analytical characteristics of biosensors with gold transducers modified with silicalite using drop coating [9]. In this work presented, we explored urease-based biosensors for urea determination, in which three kinds of nanoparticles and electrodes made of three different metals were used. The urease-based biosensor was chosen as a subject under investigation because urease is quite stable an enzyme and can undergo numerous immobilization procedures; furthermore, such biosensors are applied in medicine for the measurement of urea in blood or dialysate, and can be potentially applied in agro-food chemistry (e.g., high urea concentration in milk can be an indicator of its artificial origin) and environmental monitoring for detecting heavy metals [10, 11].

V. G. Melnyk · L. M. Semenycheva
Department of Electrical and Magnetic Measurements, Institute of Electrodynamics, National Academy of Sciences of Ukraine, Peremohy Av. 56, Kyiv 03680, Ukraine
e-mail: melnik@ied.org.ua

L. M. Semenycheva
e-mail: ttmelnyk@gmail.com

S. V. Dzyadevych
e-mail: dzyad@yahoo.com

A. P. Soldatkin
e-mail:a_soldatkin@yahoo.com

22.2 Experimental

22.2.1 Materials

In this work, enzyme urease (EC 3.5.1.5), activity 66.3 U/mg, was from Fluka (Switzerland); glycerol, bovine serum albumin (BSA, fraction V), and urea were from Sigma-Aldrich Chemie (Germany). Potassium-phosphate buffer (KH_2PO_4-K_2HPO_4) was of domestic production. Other inorganic substances were of analytical grade.

Silicalites and zeolites were synthesized in the Middle East Technical University (Ankara, Turkey).

22.2.1.1 Synthesis Procedure of Nanozeolite Beta

The molar composition of the nanozeolite Beta is 0.25 Al_2O_3:25 SiO_2:490 H_2O:9 TEAOH. Silica source was tetraethoxy silane (TEOS; 98 %, Aldrich). Aluminum isopropoxide (98 %, Aldrich), tetraethylammonium hydroxide (TEAOH; 20 wt. % in water, Aldrich), and doubly distilled water were used as the other reactants. Aging was continued under static conditions for 4 h with clear solution. The crystallization was completed within 17 days in Teflon-lined autoclaves under static conditions at 100 °C. The product was separated by centrifugation, washed with distilled water, and dried at 40 °C [12]. Approximate particle size of nanozeolite Beta was 60 nm.

22.2.1.2 Synthesis Procedure of Nanozeolite L

The molar composition of the nanozeolite L is 0.08Al_2O_3:1SiO_2:0.5K_2O:10H_2O. Aluminum powder is dissolved in KOH solution [13]. Colloidal silica (Ludox HS-40, Dupont) was then added under vigorous stirring, and the gel was stirred at room temperature for 5 min. The crystallization continued for 6 days in Teflon-lined autoclaves under static conditions at 170 °C. Approximate particle size of nanozeolite L was 60 nm.

22.2.1.3 Synthesis Procedure of Silicalite

The optimized molar composition of the gel used for synthesis of silicalite-1 is 1 tetrapropylammonium hydroxide (TPAOH):4TEOS:350H_2O. By hydrolyzing TEOS with TPAOH solution, a clear homogeneous solution was obtained at room temperature after 6 h of stirring. The crystallization occurred at 125 °C after 1 day. By centrifugation, the unreacted material was removed and silicalite-1 was obtained. Approximate particle size of silicalite was 400 nm.

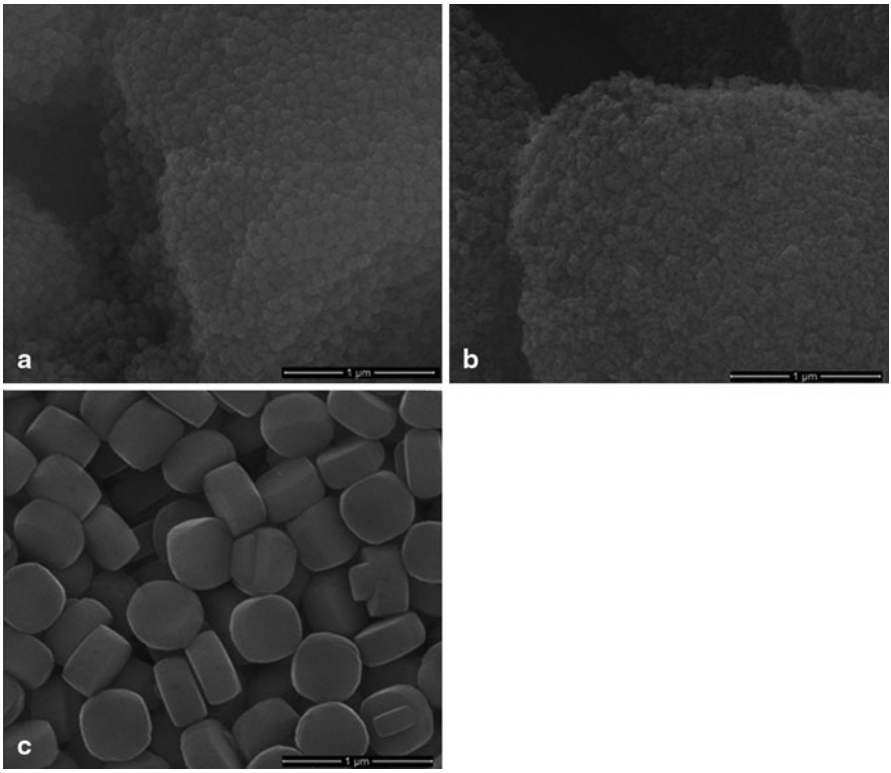

Fig. 22.1 The scanning electron microscopy images of synthesized zeolites, **a** Nanozeolite Beta. **b** Nanozeolite L. **c** Silicalite

22.2.1.4 Characterization of Zeolites

The resulting samples were characterized by powder X-ray diffraction (XRD) using Ni-filtered Cu-$K\alpha$ radiation in a Philips PW 1729. Scanning electron microscopy (SEM) analyses were performed after AuPb coating in a 400 Quanta FEI. The energy-dispersive X-ray spectroscopy (EDX) analyses of the all samples were carried out utilizing a Phoenix EDAX X-ray analyzer equipped with Sapphire super ultrathin window detector attached to the Hitachi S. 4700 FE-SEM. The nitrogen adsorption/desorption experiments were carried out using NOVA 3000 series (Quantachrome Instruments) instrument. The surface areas of the samples were obtained by Multipoint BET, while pore size and pore volumes were obtained by Saito-Foley (SF) and t-plot methods. Sample preparation method includes outgassing samples under vacuum at 300 K for 4 h before analysis.

The morphologies of the produced zeolites can be seen in Fig. 22.1.

According to the X-ray diffraction data presented in Fig. 22.2, all three samples exhibited characteristic diffraction lines of their structures. In Table 22.1, Si/Al ratios,

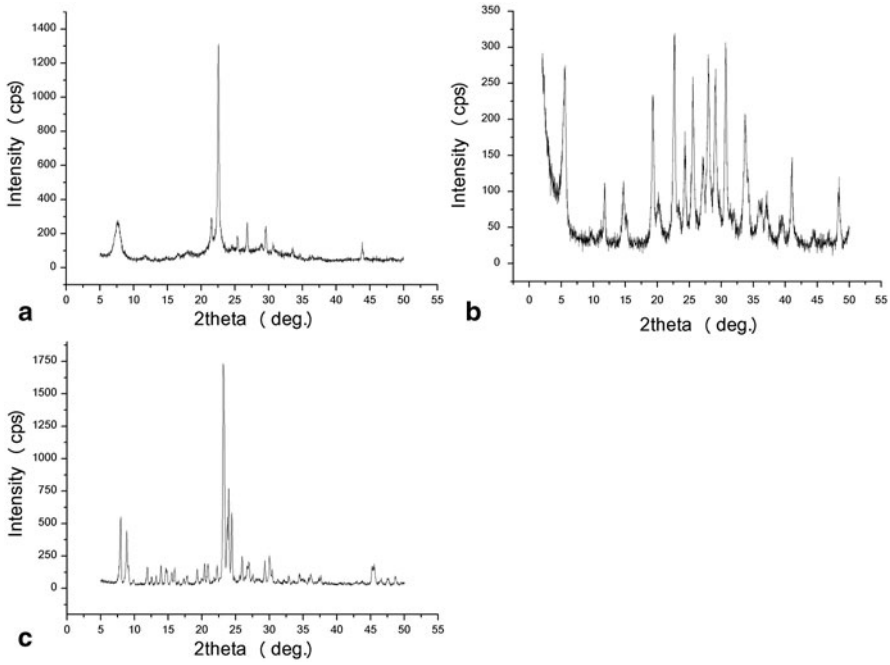

Fig. 22.2 XRD spectrum of synthesized zeolites. **a** Nanozeolite Beta. **b** Nanozeolite L. **c** Silicalite

Table 22.1 Characteristics of zeolites

Sample name	Si/Al[a]	Part size (nm)[b]	Pore size (nm)[c]	S_{ext} (m^2/g)[d]	S_{total} (m^2/g)[e]	Pore volume (cc/g)
Nanozeolite Beta	26.54	∼60	0.43	190	472	0.20
Nanozeolite L	0.97	∼60	0.40	197	419	0.18
Silicalite	No Al.	∼400	0.45	52	185	0.08

[a]Measured by EDX
[b]Measured by SEM
[c]Measured by Saito-Foley (SF) Method
[d]Measured by t-plot method
[e]Measured by BET

particle sizes, pore sizes, external and total surface area, and micro- and mesopore volumes are given.

22.2.2 Conductometric Transducers

In this work, we used conductometric transducers composed of two pairs of interdigitated electrodes deposited onto a ceramic support. Transducers were intended to

operate in a differential mode of measurements: Biorecognition element (enzymes) was placed on one pair of electrodes, and reference element (inert protein) on another. We compared electrodes made from different metals: gold, platinum, and nickel.

Gold transducers were manufactured in V. Lashkaryov Institute of Semiconductor Physics of National Academy of Science of Ukraine (Kyiv, Ukraine) in accordance with our recommendations. They were 5 × 30 mm in size, sensitive area of each electrode pair was about 1.0 × 1.5 mm. The width of each digit as well as interdigital space was 20 μm. A photograph and microphotographs of these transducers can be found in [14].

Platinum conductometric transducers were fabricated at the Institute of Chemo- and Biosensorics (Munster, Germany). Two pairs of Pt (150-nm thick) interdigitated electrodes were made by the lift-off process on the Pyrex glass substrate. The Ti intermediate layer of 50 nm thickness was used to improve adhesion of Pt to substrate. Central part of the sensor chip was passivated by Si_3N_4 layer to define the electrode's working area. Both the digit's width and the interdigital distance were 10 μm, and their length was about 1 mm. Thus, the sensitive part of each electrode was about 1 mm^2. A photograph of these transducers can be found in [15].

Nickel transducers were 5 × 30 mm in size and consisted of two identical pairs of nickel interdigitated electrodes deposited onto a ceramic support. The electrodes were deposited onto the support by thermo vacuum sputtering of titanium (adhesion layer) and nickel. The dimensions of sensitive area of each electrode pair were about 1.5 × 2 mm. The width of each interdigital space and each digit was 50 μm. The SEM image of the active region of nickel transducer is shown in Fig. 22.3a.

22.2.3 Modification of Transducers with Silicalite and Zeolites

We used two procedures of transducers modification with silicalite and zeolites. The first procedure (spin coating) was more complicated and was used to cover the transducer surface with silicalite and nanozeolites Beta and L. Other procedure (drop coating) was simpler and was used for silicalite only. These procedures did not influence the transducer's working parameters.

In literature, for the organized assembly of zeolite microcrystals with sizes between 500 nm and 12 μm on glass substrates, direct attachment method, rubbing of the zeolites on the surface with a finger, was first used by Yoon et al. [16]. They claimed that due to the hydrogen bonds between the surface hydroxyl groups of bare zeolite crystals and bare glass substrates, high-quality silicalite monolayers were formed. In addition to that, usage of poly(ethyleneimine) (PEI) between zeolite and glasswork as a hydrogen-bonding mediator also can be used in the direct attachment method for increasing the binding strength of hydrogen bonds between microcrystals and substrates.

In our study, PEI was used as a layer between zeolite and electrode surface. Mucasol (1/6 v/v in distilled water) was used to change the surface hydrophility and improve homogeneity of zeolite layer.

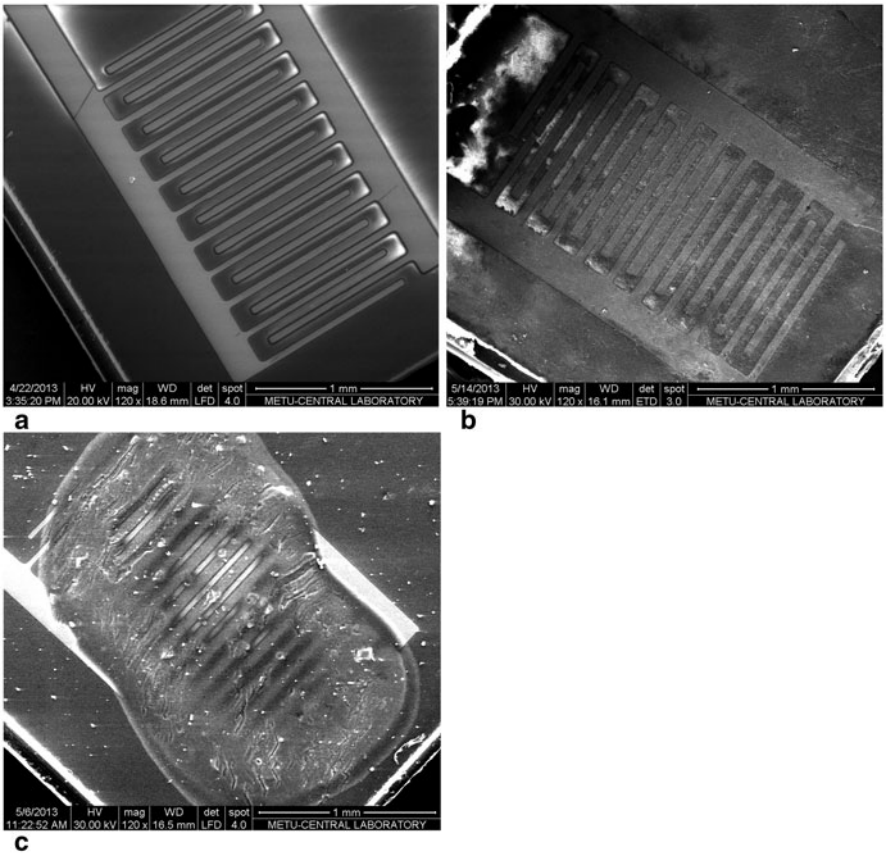

Fig. 22.3 Active regions of conductometric interdigitated electrodes: bare electrodes (**a**) and electrodes covered with silicalite using spin coating (**b**) and drop coating (**c**) SEM images

Electrode surfaces were dip coated with mucasol for 15 min, rinsed with copious amount of distilled water, and dried under air. Mucasol is an alkaline high-performance universal detergent containing phosphoric acid and tripotassium salt trihydrate. For the formation of homogeneous layers of PEI, both dip-coating and spin-coating techniques had been tried. Since spin coating gave more homogeneous layers, it was continued to be used. The effect of PEI solvent type (such as hot water and ethanol), PEI concentration (0.5 , 1, 3 %), spin-coating time (3000 rpm 15 s, 7 s), and calcination temperature after direct attachment of zeolites (100, 90, 50 °C) were investigated. The obtained monolayers were checked by using optic microscope. The suitable conditions for zeolite monolayer production were chosen as spin coating with 0.5 % PEI in ethanol at 3000 rpm for 15 s and 100 °C calcination temperature for 30 min.

SEM photos of the transducers modified with zeolites by such procedure are shown in Figs. 22.3b and 22.4.

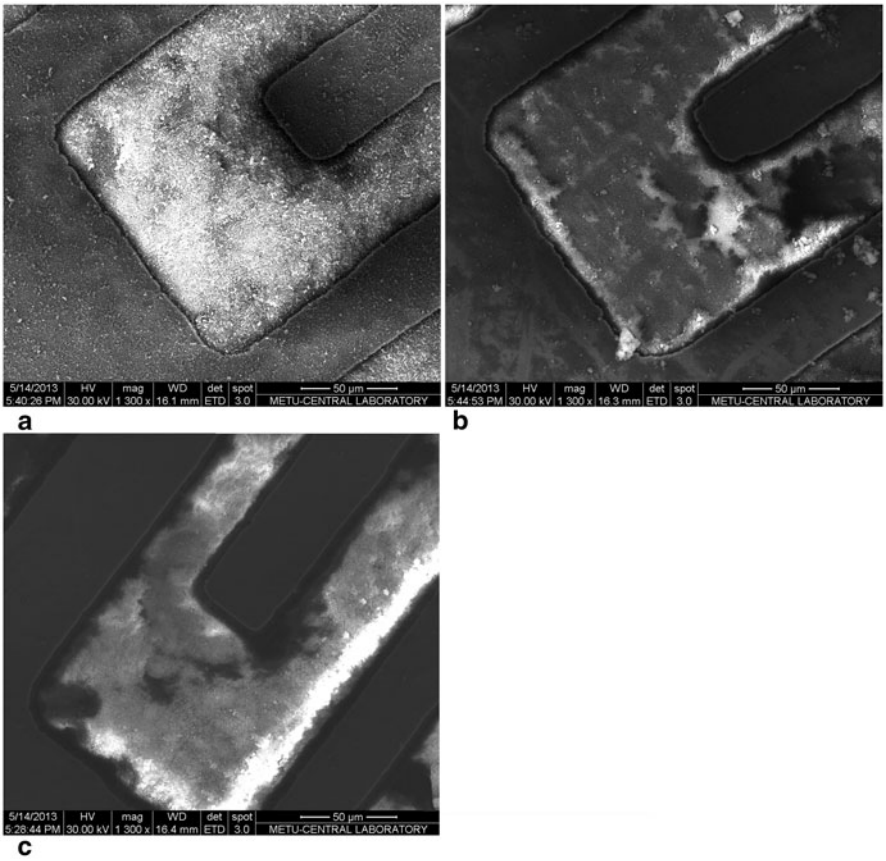

Fig. 22.4 Conductometric nickel interdigitated electrodes covered by spin coating with particles of silicalite (**a**), nanozeolite Beta (**b**), and nanozeolite L (**c**) SEM images

In case of drop coating, 10 % (w/w) silicalite suspension in 5 mM phosphate buffer, pH 7.4, was used. This suspension was ultrasonicated for at least 20 min, then 0.2 µl of suspension was deposited onto the active zone of each pair of electrodes; afterwards they were heated at 200 °C for 3 min. The procedure resulted in coating transducer surface with an unordered layer of silicalite particles (Fig. 22.3c).

22.2.4 Preparation of Bioselective Elements

To prepare biorecognition elements by urease adsorption, we used the transducers previously coated with different zeolite particles (see Sect. 2.3). The same immobilization procedure was used for transducers covered by both spin coating and drop coating. 0.15 µl of 5 % urease solution in 20 mM phosphate buffer, pH 7.4, was

deposited onto one pair of electrodes while the same amount of 5 % BSA in analogous buffer was deposited onto another (reference) pair of electrodes; then the transducers underwent complete air-drying for 20 min at room temperature. Neither glutaraldehyde nor other auxiliary compounds were used. Next, the transducers were submerged into the working buffer for 10–15 min to wash off the unbounded enzyme. After the experiments, surfaces of transducers were freed from zeolite particles and adsorbed urease using ethanol-wetted cotton.

22.2.5 Measurement Procedure

Conductometric transducers were connected to the portative device for conductometric measurements (9.5 × 2.5 × 13.5 cm) that was made in the Institute of Electrodynamics of National Academy of Sciences of Ukraine (Kiev, Ukraine). This device applied sinusoidal potential with a frequency of 36.5 kHz and amplitude of 14 mV, avoiding such effects as faradaic processes, double-layer charging, and polarization of the microelectrodes. The nonspecific changes in the output signal induced by the fluctuations of temperature, medium pH, etc. were decreased due to the usage of differential mode of measurement: Conductivity of solution measured by reference pair of electrodes was subtracted from the conductivity measured by pair of electrodes with biorecognition element. Illumination and temperature variations had practically no influence on the biosensor characteristics. The measurements were carried out in a glass cell filled with phosphate buffer (volume 2 ml), under vigorous magnetic stirring.

Measurements were carried out at room temperature in continuously stirred 5 mM phosphate buffer solution, pH 7.4, in an open 2-ml cell. The substrate concentrations in the cell were varied by adding different aliquots of the stock solutions (100 and 500 mM). All experiments were repeated three times. The data in the figures are either mean of three repeated results of the experiment or mean ± standard deviation (SD).

22.3 Results and Discussion

22.3.1 Biosensors Based on Nickel Transducers Covered with Nanoparticles by Spin coating

At the first stage of research, we covered nickel transducers with either silicalite or nanozeolite L or nanozeolite Beta using spin coating (Figs. 22.3b and 22.4). As seen from the images, a rather uniform layer of particles was formed; this layer was slightly different on the nickel electrode (darker parts of images) and on the ceramic support (brighter parts). It was not an ideal monolayer; in some places, there were two or three layers of particles. However, no aggregation of the particles was observed on the transducer surface.

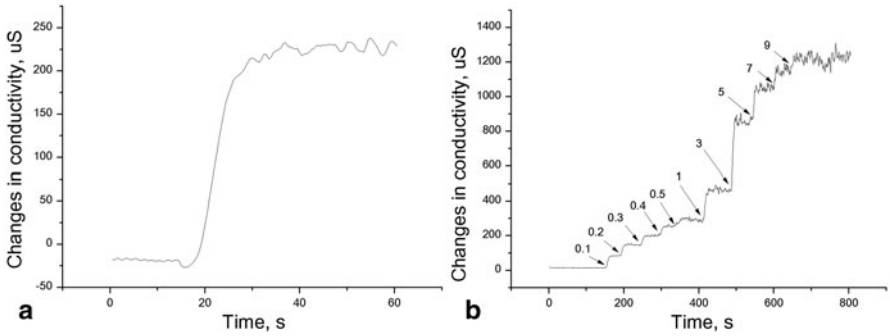

Fig. 22.5 Typical responses of a biosensor, based on urease adsorbed on nanozeolite Beta, to 0.5 mM of urea (**a**) and to successive additions of urea (**b**). Concentration of urea (in mM) is given on the plot. Nickel transducer was covered with nanoparticles using spin coating

Typical responses of the biosensor, based on urease adsorbed on nanozeolite Beta, to addition of 0.5 mM of urea and to the successive additions of urea are shown in Fig. 22.5. The biosensors with other nanoparticles showed similar responses, that is why they are not presented. As seen, the biosensor was characterized by fast performance (steady-state response was obtained in 1 min). The signal noise increased with increasing urea concentration, so the biosensor accuracy decreased at the urea concentrations above 5 mM.

22.3.1.1 Analytical Characteristics of Biosensors Containing Silicalite and Nanozeolites Beta and L

The calibration curves of urea determination for the biosensors with silicalite and nanozeolites Beta and L are shown in Fig. 22.6. As can be seen, they are very similar, which means that the near-electrode layer of nanoparticles adsorbed the same amount of enzyme. The linear concentration range was 10 μM–1 mM (simple scale) and 0.5–4 mM (logarithmic scale). The biosensors sensitivity to urea was from 350 to 430 μS/mM. All the biosensors had the detection limit in the range of 5–10 μM.

22.3.1.2 Reproducibility of Biosensor Responses

Reproducibility of biosensor responses (i.e., reproducibility of urea determination) was examined during continuous operation for several hours. We measured the responses to the same urea concentration (0.5 mM) during one working day with 10-min intervals, the sensor being kept in the constantly stirred buffer all the time between the measurements; no decrease in responses was observed (Fig. 22.7). An error (relative SD, R.S.D.) of urea measurement was about 3–8 % for the biosensors using silicalite and 6–8 % for those with nanozeolite L and nanozeolite Beta (it should be noted that the samplers used in this work had an error of addition of about 1–1.5 %,

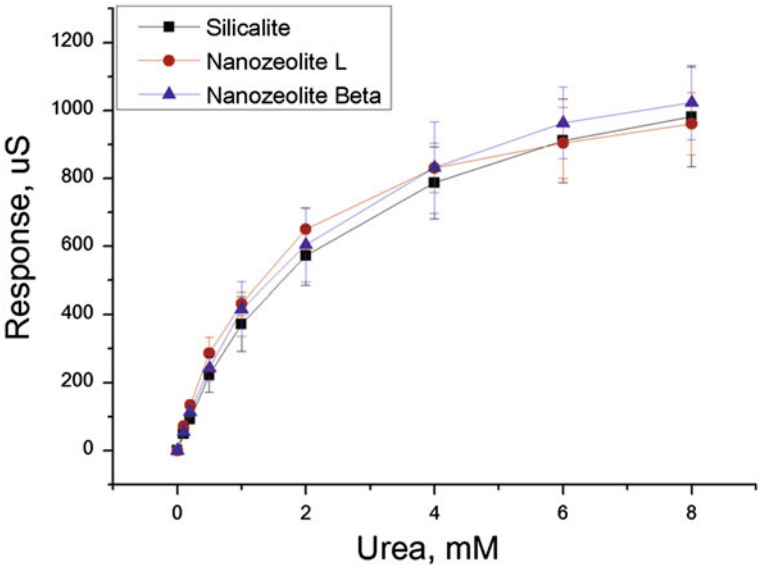

Fig. 22.6 Calibration curves for urea determination. Urease was adsorbed on nickel transducers spin coated with silicalite and nanozeolites Beta and L

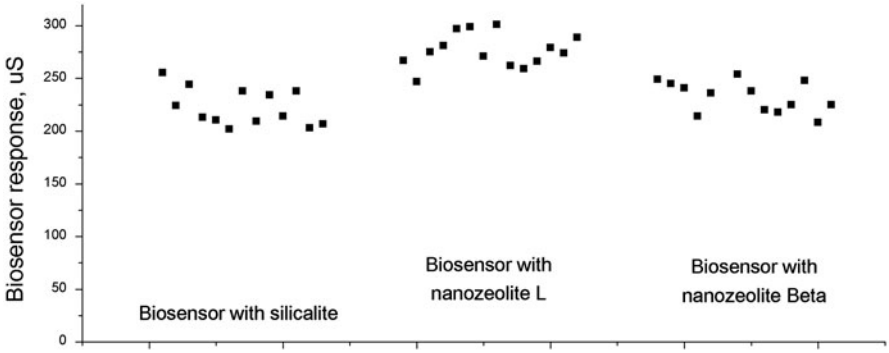

Fig. 22.7 Reproducibility of biosensor responses to 0.5 mM of urea obtained during continuous operation. Urease was adsorbed on nickel transducers covered with silicalite and nanozeolites Beta and L using spin coating

which amounted to about 30 % of the measurement error). Thus, the accuracy of urea determination was not very good as compared with the biosensors based on direct analysis of substrate, which usually have signal reproducibility of about 2–4 %.

However, the biosensors demonstrated good reproducibility of preparation: R.S.D. of responses of different biosensors was 12–15 %.

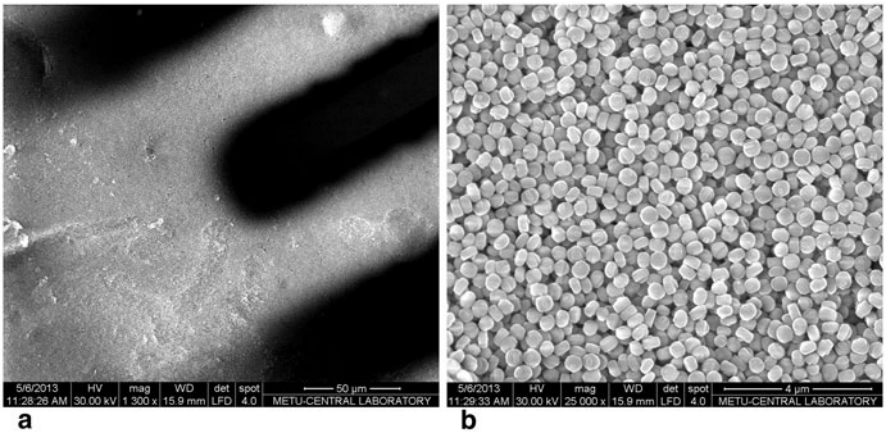

Fig. 22.8 Conductometric interdigitated nickel electrodes covered with silicalite using drop coating (SEM images with different magnification)

22.3.2 Biosensors Based on Nickel, Gold, and Platinum Transducers Covered with Silicalite Using Drop Coating

22.3.2.1 SEM Images and Responses of the Biosensors with Nickel Electrodes

At the next stage of our work, we used another method of applying nanoparticles on the transducer surface— drop coating (described in Sect. 2.3). Nickel transducers were modified only with silicalite because this variant demonstrated the best reproducibility of responses in the previous part of the work (other analytical characteristics were almost the same for biosensors with silicalite and nano-Beta and nano-L zeolites). SEM images of the transducers modified with silicalite using drop coating are shown in Figs. 22.3c and 22.8 (in Fig. 22.8, nickel electrodes are black, while ceramic support is white; this effect is caused by specific settings of SEM). As seen, a rather thick layer of nanoparticles was formed; this layer fully covered the transducer active region.

Biosensors were obtained by adsorption of urease on such transducers; typical responses of the biosensors (Fig. 22.9a and 22.9b) were quite quick (steady-state response was obtained in 1.5–2 min) but a bit slower than in case of spin coating (see Fig. 22.5). This was surely caused by a thicker layer of silicalite on the transducer surface which slowed the substance's diffusion in the near-electrode layer of working buffer. The signal noise increased with increasing concentration of urea, but not as significantly as in case of spin coating (see Sect. 3.1.1).

Next, reproducibility of the biosensor preparation was studied. Several identical bare transducers were covered with silicalite by drop coating, and urease was adsorbed on them. Two to three responses to 0.5 mM of urea were measured using each obtained biosensor. Then, urease and silicalite were removed from the transducers

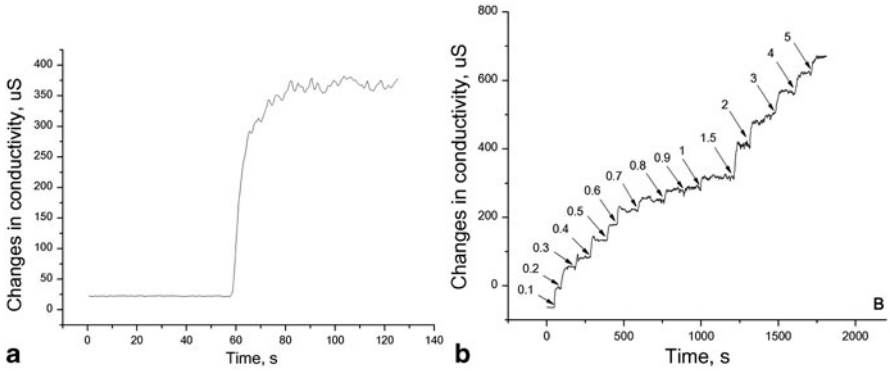

Fig. 22.9 Typical responses of biosensors based on urease adsorbed on transducers with nickel electrodes covered with silicalite using drop coating. Urea concentration—0.5 mM (**a**) or is given (in mM) on the plot (**b**)

Table 22.2 Analytical characteristics of biosensors based on urease adsorbed on transducers with nickel, gold, and platinum electrodes covered with silicalite using drop coating. Noise was measured as a standard deviation of signals obtained during 25 s (50 points)

Biosensor characteristic	Type of electrode		
	Nickel	Gold	Platinum
Sensitivity to urea, μS/mM	500–800	1100–1500	700–1000
Linear range, mM	From 0.003 to 0.6–1	From 0.002 to 0.6–0.8	From 0.003 to 1
Limit of urea detection, μM	1.5–3	1–2	2
Noise of the baseline, μS	0.4–0.8	0.6–0.9	0.5–0.8
Noise of the response (to 0.5 mM of urea), μS	5–9	5–7	3–6

surface with ethanol-wetted cotton, and the entire procedure was repeated. R.S.D. of responses of different biosensors was 20–30 %, which is worse than in case of biosensors with spin coating. This difference occurred because layers of nanoparticles formed by spin coating were much more uniform and reproducible than those formed by drop coating.

Other characteristics of the biosensors are presented in Table 22.2. As seen, modification of nickel transducers with silicalite by drop coating ensured better characteristics of the biosensor (except for the reproducibility of biosensor preparation) than spin coating. In addition, the procedure of drop coating was much easier than spin coating. For these reasons, only drop coating was used in further work.

22.3.2.2 Analytical Characteristics of Biosensors with Nickel, Gold, and Platinum Electrodes

Generally, electrodes from noble metals have better conductive properties than those from conventional metals [17]. However, the noble metals are very expensive. Therefore, at the next stage, we carried out a comparative study of the biosensors with

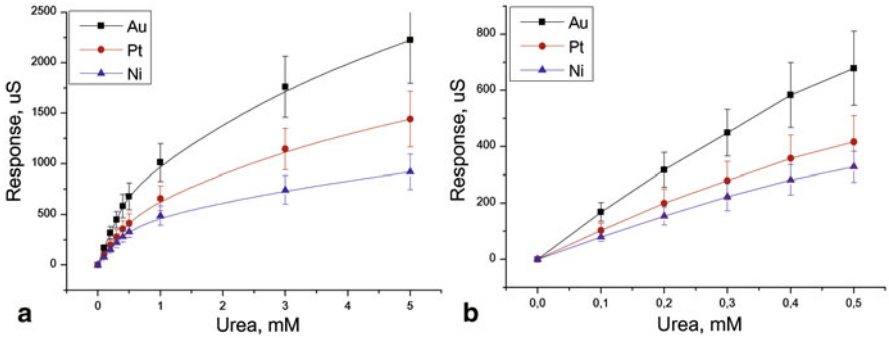

Fig. 22.10 Calibration curves for urea determination (**a** total concentration range, **b** linear range) obtained with biosensors based on urease adsorbed on nickel, gold, and platinum transducers covered with silicalite using drop coating

gold and platinum electrodes, on the one hand, and those with nickel electrodes on the other. In all biosensors, the same method of silicalite placement (drop coating) and similar immobilization method (adsorption) were used.

The silicalite layer formed on the surface of gold/platinum transducers was similar to that formed on nickel transducers (see Figs. 22.3 and 22.8), so SEM images here are not given. The responses of biosensors with gold/platinum transducers also differed very slightly from those of nickel transducers.

The calibration curves for urea determination are shown in Fig. 22.10 and detailed analytical characteristics in Table 22.2. As expected, sensitivity of biosensors with gold and platinum electrodes was higher than that with nickel electrodes; however, other parameters were almost the same.

22.3.2.3 Reproducibility of Biosensor Responses

Next, reproducibility of biosensor responses during several hours of continuous operation was examined (Fig. 22.11). Procedure was the same as in case of silicalite spin coating. R.S.D. of urea measurement was 3.5–5 % for biosensors with nickel electrodes, 2–4 % with gold electrodes, and 2–7 % with platinum electrodes. During a day, no decrease in biosensor responses was observed, but in some cases, first responses after immobilization were higher due to the leakage of enzyme or silicalite; thus, it was required to wash transducers carefully after urease adsorption. Accuracy of urea determination by these biosensors was better than in case of spin coating, and close to that of biosensors based on covalently immobilized enzymes.

22.3.2.4 Operational Stability of the Biosensors and Reproducibility of Biosensors Preparation

Generally, adsorbed enzymes are bound to the adsorbent by relatively weak electrostatic and hydrophobic bonds. For this reason, gradual washout of enzymes is a

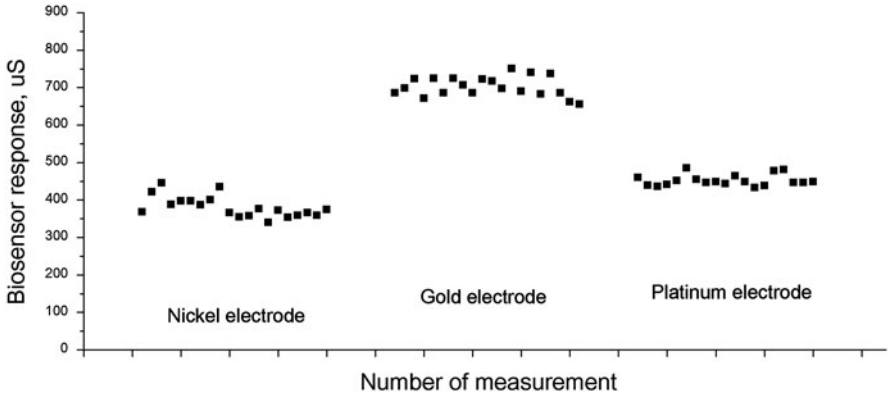

Fig. 22.11 Reproducibility of biosensor responses to 0.5 mM of urea obtained during continuous operation. Urease was adsorbed on transducers with nickel, gold, and platinum electrodes with silicalite drop coating

common disadvantage of the biosensors based on adsorbed enzymes. Therefore, it was important to examine operational stability of such biosensors. During the experiment, 10–15 responses of the freshly made biosensors to 0.5 mM of urea were obtained one after another, and then the transducers with adsorbed urease were stored dry at +4 °C until next day. During one cycle of measurements (2 h), no significant decrease in biosensor responses was observed; however, after 20-h storage, very significant drop of responses was revealed in biosensors with nickel electrodes, and smaller drop with gold and platinum electrodes (Fig. 22.12). Transducers were stored in the same conditions, so the difference in operational stability is caused by different silicalite adhesion to the transducers surface: The worst adhesion was observed for nickel electrodes, and the best for platinum ones. By operational stability, the biosensors developed were comparable with other biosensors based on adsorbed urease but were inferior to the biosensors based on covalently immobilized urease [11]. Therefore, it seems reasonable to speculate about storage conditions (for example, transducers can be stored dry at − 20 °C or at + 4 °C in the working buffer); however, this is beyond the frame of our present work.

22.4 Conclusions

In this work, we developed conductometric biosensors based on urease, adsorbed on transducers modified with silicalite and nanozeolites Beta and L. There was no significant difference between biosensors with nickel transducers modified with all three particles; however, biosensors with silicalite had better reproducibility of responses. Two procedures for transducers modification with silicalite were evaluated; drop coating appeared to be more perspective due to its simplicity and better characteristics of obtained biosensors. Nevertheless, biosensors using spin coating had better

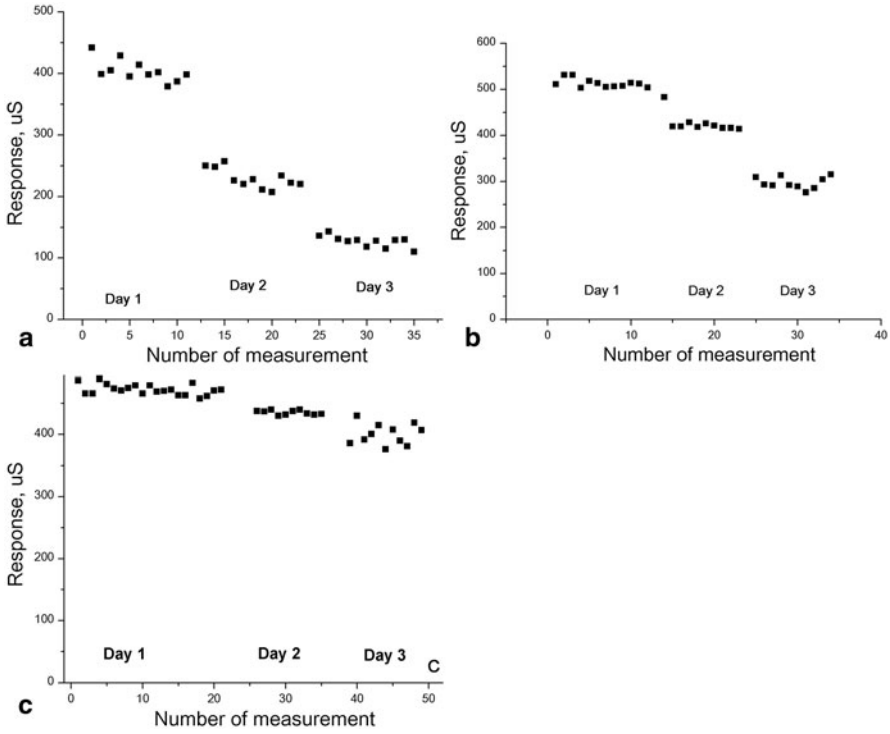

Fig. 22.12 Operational stability of biosensors during 3 days. Urease was adsorbed on transducers with nickel (**a**), gold (**b**), and platinum (**c**) electrodes drop-coated with silicalite

reproducibility of preparation. Transducers with gold and platinum electrodes were modified with silicalite by drop coating and were compared with nickel electrodes; the biosensors with gold electrodes showed twice as high sensitivity to urea as the biosensors with nickel electrodes; platinum electrodes were 1.5 times more sensitive than nickel electrodes. Operational stability of the biosensors based on transducers with platinum electrodes was the best, the worst stability was observed in case of biosensors with nickel electrodes; other analytical characteristics were the best for biosensors with gold electrodes. In general, our work showed that transducers modified with nanoparticles can be successfully used for biosensor creation.

Acknowledgments The authors gratefully acknowledge the financial support of this study by Project European IRSES-318524-NANODEV. Furthermore, this study was partly supported by NASU in the frame of Scientific and Technical Program "Sensor devices for medical-ecological and industrial purposes: metrology and trial performance."

References

1. Trevenot DR, Toth K, Durst RA, Wilson GS (1999) Electrochemical biosensors: recommended definitions and classification. Pure Appl Chem 71:2333–2348
2. Teles FRR, Fonseca LP (2008) Applications of polymers for biomolecule immobilization in electrochemical biosensors. Mater Sci Eng C 28:1530–1543
3. Hasanzadeh M, Shadjou N, Eskandani M, Guardia M (2012) Mesoporous silica-based materials for use in electrochemical enzyme nanobiosensors. Trends Anal Chem 40:106–118
4. Ashtekar S, Hastings JJ, Barrie PJ, Gladden LF (2000) Quantification of the number of silanol groups in silicalite and mesoporous MCM-41: Use of Ft-Raman spectroscopy. Spectrosc Lett 33:569–584. doi:10.1080/00387010009350140
5. Macario A, Katovic A, Giordano G, Forni L, Carloni F, Filippini A, Setti L (2005) Immobilization of lipase on microporous and mesoporous materials: studies of the support surfaces. Stud Surf Sci Catal 155:381–394
6. Tavolaro A, Tavolaro P, Drioli E (2007) Zeolite inorganic supports for BSA immobilization: comparative study of several zeolite crystals and composite membranes. Colloids Surf B 55:67–76
7. Willis RR, Benin AI (2007) Toward commercialization of nanozeolites. Stud Surf Sci Catal 170:242–249
8. Tosheva L, Valtchev VP (2005) Nanozeolites:synthesis, crystallization mechanism, and applications. Chem Mater 17:2494–2513
9. Kucherenko IS, Soldatkin OO, Kasap BO, Ozturk S, Akata B, Soldatkin AP, Dzyadevych S (2012) Elaboration of urease adsorption on silicalite for biosensor creation. Electroanalysis 24:1380–1385
10. Bayramoglu G, Yalcin E, Arıca MY (2005) Immobilization of urease via adsorption onto l-histidine-Ni(II) complexed poly(HEMA-MAH) microspheres: preparation and characterization. Process Biochem 40:3505–3513
11. Singh M, Verma N, Kumar Garg A, Redhu N (2008) Urea biosensors. Sens Actuators B 134:345–351
12. Prokešová P, Mintova S, Čejka J, Bein T (2003) Preparation of nanosized micro/mesoporous composites via simultaneous synthesis of Beta/MCM-48 phases. Microporous Mesoporous Mater 64:165–174
13. Larlus O, Valtchev VP (2004) Crystal morphology control of LTL-Type zeolite crystals. Chem Mater 16(17):3381–3389
14. Soldatkin OO, Peshkova VM, Saiapina OY, Kucherenko IS, Dudchenko OY, Melnyk VG, Vasylenko OD, Semenycheva LM, Soldatkin AP, Dzyadevych S (2013) Development of conductometric biosensor array for simultaneous determination of maltose, lactose, sucrose and glucose. Talanta 115:200–207
15. Dzyadevych SV, Soldatkin AP, Arkhypova VN, El'skaya AV, Chovelon JM, Georgiou CA, Martelet C, Jaffrezic-Renault N (2005) Early-warning electrochemical biosensor system for environmental monitoring based on enzyme inhibition. Sens Actuators B 105:81–87. doi:10.1016/j.snb.2004.02.039
16. Lee JS, Kim JH, Lee YJ, Jeong NC, Yoon KB (2007) Manual assembly of microcrystal monolayers on substrates. Angew Chem Int Ed 46:3087–3090. doi:10.1002/anie.200604367
17. Dzyadevych SV, Arkhypova VN, Soldatkin AP, El'skaya AV, Martelet C, Jaffrezic-Renault N (2008) Conductometric enzyme biosensors. In: Marks RS (ed) Handbook of biosensors and biochips. Wiley-Interscience, New York, pp 379–394. doi:10.1002/9780470061565hbb037

Chapter 23
Magnetic Properties of Nanoparticle $RMnO_3$ (R = Pr, Nd, and Tb) Compounds

Wiesława Bażela, Andrzej Szytuła, Stanisław Baran, Bogusław Penc, Marcin Dul, Ryszard Duraj, Zinaiida Kravchenko, Eduard Zubov, Konstantin Dyakonov, Jens-Uwe Hoffmann, Tommy Hofmann, Andreas Hoser and Volodymyr Dyakonov

23.1 Introduction

The manganese perovskites with the general formula $AMnO_3$, where A = La, a rare earth metal or Ca, Sr, etc., are subject of intensive investigations of their magnetic and electric properties. Structural and magnetic properties of these compounds are sensitive to both the manganese valence and internal (chemical) factors. The interest in the manganite has been renewed with the discovery of colossal magnetoresistance, magnetocaloric response, and multiferroic behavior. Recently, the investigations concentrate on the influence of the grain size on their properties. The model for an interpretation of the magnetic properties of the nanoparticle compounds is based on the ratio of ideal inner core and nonmagnetic surface, i.e., on the surface/volume ratio [1].

For $RMnO_3$ (R = rare earth elements) compounds, the critical temperature of the magnetic ordering, which indicates change of magnetic interactions, decreases with increasing number of 4 f electrons (see Fig. 1 in [2]).

W. Bażela (✉) · M. Dul · R. Duraj
Institute of Physics, Cracow University of Technology, Podchorążych 1,
30–084 Kraków, Poland, Tel.: +48 12 6370666
e-mail: wbazela@pk.edu.pl

M. Dul
e-mail: dulmarcin@gmail.com

R. Duraj
e-mail: puduraj@cyf-kr.edu.pl

A. Szytuła · S. Baran · B. Penc
M. Smoluchowski Institute of Physics, Jagiellonian University,
Reymonta 4, 30–059 Kraków, Poland
e-mail: andrzej.szytula@uj.edu.pl

S. Baran
e-mail: stanislaw.baran@uj.edu.pl

B. Penc
e-mail: boguslaw.penc@uj.edu.pl

O. Fesenko, L. Yatsenko (eds.), *Nanocomposites, Nanophotonics, Nanobiotechnology, and Applications,* Springer Proceedings in Physics 156,
DOI 10.1007/978-3-319-06611-0_23,

In this work, the influence of the grain size on the structural and magnetic properties of $RMnO_3$ (R = Pr, Nd, and Tb) compounds is analyzed. The results obtained for the nanoparticle samples are compared with the data for adequate bulk materials.

23.2 Experimental Details

The investigated nanoparticle compounds were obtained by a sol–gel technique described in [3, 4]. The obtained products were annealed at different temperatures between 800 and 900 °C.

The crystal structure of the samples was studied by room temperature X-ray powder diffraction (XRD) method using a Philips PW-3710 X'PERT diffractometer with CuK_α radiation. The data were analyzed using the Rietveld-type refinement program FullProf [5].

X-ray diffraction analysis has been carried out after each annealing step. Analysis of both the full XRD patterns and individual reflections reveals that the reflex profiles broaden out as the particles size is reduced.

The grain size, *d,* was determined using the Scherrer relation $d = \lambda/B \cos\theta$ [6]. Here, $\lambda = 1.54178$ Å is the X-ray wavelength, θ the corresponding angle of Bragg diffraction, and B the difference between the half-widths of a Bragg reflection of the nano-powder and a standard sample. The standard sample of Si powder with the size of 10 μm was used to calibrate the intrinsic width associated with equipment. The particle size was calculated using the experimental X-ray diffraction pattern and the following relation:

$$B = \beta - \beta_{0,}$$

Z. Kravchenko · E. Zubov · V. Dyakonov
A. A. Galkin Donetsk Physico-Technical Institute, National Academy of Sciences of Ukraine, R. Luxembourg Str. 72, 83114 Donetsk, Ukraine
e-mail: zubov@fti.dn.ua

E. Zubov
e-mail: zubov@fti.dn.ua

V. Dyakonov
Institute of Physics, PAS, 02–68 Al. Lotników 32/46, Warszawa, Poland
e-mail: dyakon@ifpan.edu.pl

K. Dyakonov
A. F. Ioffe Physico-Technical Institute RAN, Politekhnicheskaja 26, 194021 St.-Petersburg, Russia
e-mail: k.dyakonov@mail.ioffe.ru

J.-U. Hoffmann · T. Hofmann · A. Hoser
Helmholtz-ZentrumBerlin für Materialien und Energie GmbH, Hahn-Meitner Platz 1, 14 109 Berlin, Germany
e-mail: hoffmann-j@helmholtz-berlin.de

T. Hofmann
tommy.hofmann@helmholtz-berlin.de

A. Hoser
hoser@helmholtz-berlin.de

where β is the half-width of the Bragg reflex of investigated sample and β_0 the similar value for the Si powder.

The magnetic measurements were carried out using a vibrating sample magnetometer (VSM) and ac measurement system (ACMS) options of the Quantum Design PPMS platform. Three types of dc measurement were performed:

- The zero filed cooled (ZFC) and field cooled (FC) magnetic susceptibility curves at applied field of $H = 50$ Oe at low temperatures
- Scanning from 1.9 K up to 300 K in a magnetic field of 1 kOe
- Magnetization curves in the field up to 90 kOe at selected temperatures

The ac magnetic susceptibility ($\chi_{ac} = \chi' + i\chi''$, where χ' and χ'' are the real and imaginary components, respectively) was measured versus frequency between 10 Hz and 10 kHz in the external magnetic field equal to 2 Oe.

The neutron diffractograms were obtained over a temperature range of 1.5–50 K using the E6 diffractometer installed at the BERII reactor (Helmholtz-Zentrum Berlin) with the incident neutron wavelength of 2.447 Å. The data were analyzed using the FullProf program [5].

23.3 Results

23.3.1 Crystal Structure

The room temperature X-ray diffraction data and neutron diffraction data at low temperatures indicate that all the nano-samples are homogeneous and single phase with an orthorhombic crystal structure described by the Pnma space group. In this structure, the R (Pr, Nd, or Tb) and O1 atoms occupy the 4(c) site: *x*, ¼, *z*; Mn atoms are in 4(b) site: 0, 0, ½; and O2 atoms are in the 8(d) site: *x, y, z*. The analysis of the diffractograms obtained for the different nano-samples indicates that the fitted structural parameters differ slightly on those for the bulk samples. The data from the X-ray diffraction measurements are listed in Table 1 in [3] and Table 1 in [4].These data confirm that the nano-samples have the similar crystal structure that bulk one. The unit cell volume values reported for the nanoparticle samples are slightly less (about of 1 %) than the value for bulk materials (see Table 23.1).

From the X-ray diffraction data, the grain sizes of the investigated samples were also determined (see Table 23.1). For all the samples, these values are < 100 nm fulfilling condition that they are nanoparticles.

23.3.2 Magnetic Properties

23.3.2.1 $PrMnO_3$ and $NdMnO_3$

Figure 23.1 presents the results of dc magnetic studies of the $NdMnO_3$ nanoparticle samples. Similar dependence is observed for $PrMnO_3$. Temperature dependences of

Table 23.1 Particle size $< d_{XRD} >$ and unit cell volume V of the $RMnO_3$ (R = Pr, Nd, Tb) nano-powders calculated using the Scherrer relation (d_{XRD} in nm, V in nm^3)

Sample		$< d_{XRD} >$	$V(nm)^3$
$PrMnO_3$	800 °C	66	231.80(2)
	900 °C	85	232.88(2)
	Bulk	245	234.65(6)
$NdMnO_3$	800 °C	56	231.56(2)
	850 °C	70	232.14(6)
	900 °C	89	232.88(7)
	Bulk	250	234.60(2)
$TbMnO_3$	800 °C	45	227.52(4)
	900 °C	70	227.90(5)
	Bulk	255	229.37(1)

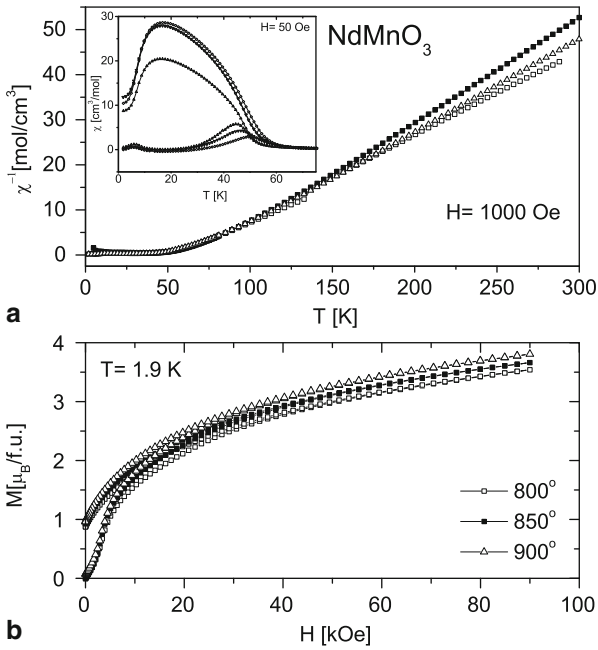

Fig. 23.1 $NdMnO_3$. **a** Temperature dependences of the inverse susceptibility for nano-samples. *Inset* shows the magnetic susceptibilities as a function of temperature. *Lower* and *upper curves* correspond to ZFC and FC susceptibilities, respectively. **b** Magnetization isotherms at 1.9 K

the ZFC and FC magnetic susceptibilities indicate a strong difference between these values which indicate a strong influence of the domain walls. The ZFC curves have the maxima near 45 and 6 K. The ZFC and FC curves are separated below 60 K. The FC curves have maxima near 17.5 K. The critical temperatures of the magnetic ordering are less than those of bulk material (see Table 23.2).

Above 125 K, the reciprocal magnetic susceptibilities obey the Curie–Weiss law: $\chi = C/(T - \theta_p)$, where C is the Curie–Weiss constant and θ_p the Curie–Weiss temperature.

The magnetic field dependences of magnetization also indicate a decrease of magnetization with decreasing values of the grain size. The magnetic dc data for these compounds are summarized in Table 23.2. Presented results suggest that:

Table 23.2 Magnetic data for the $RMnO_3$ (R = Pr, Nd, and Tb) compounds from magnetometric measurements; the critical temperatures of magnetic ordering in the Mn and R sublattices (T_{Mn}, T_R), the paramagnetic Curie–Weiss temperature (θ_p), experimental values of the magnetic moments effective, and in ordered state (μ_{eff}, μ)

Compound	T_{Mn}(K)	T_R(K)	θ_p(K)	$\mu_{eff}(\mu_B)$	$\mu(\mu_B)$
$PrMnO_3$					
Nano 800 °C	50		81	6.4	3.3
Nano 900 °C	56	15	88	6.4	3.6
Bulk	74	10	104	6.5	3.9
$NdMnO_3$					
Nano-800 °C	50	7	58	6.1	3.7
Nano-850 °C	55	9	62	6.1	3.8
Nano-900 °C	55	10	67	6.2	4.0
Bulk	70	11	68	6.2	4.2
$TbMnO_3$					
Nano-800 °C	41.7	7.1	− 29	10.6	3.5
Nano-850 °C	41.7	7.4	− 30	10.7	3.65
Bulk	42.5	9.2	− 26.5	10.9	4.14

- The effective magnetic moment values do not depend on the preparation of the samples and are larger than the values calculated from the relation of $\mu_{eff} = [(\mu_{eff}^{R})^2 + (\mu_{eff}^{Mn})^2]^{1/2}$, where μ_{eff} is equal to 3.58 μ_B (R = Pr) and 3.62 μ_B (R = Nd) and $\mu_{eff}^{Mn} = 4.90\mu_B$. The theoretical values of the effective magnetic moments are equal to 6.07 μ_B ($PrMnO_3$) and 6.09 μ_B ($NdMnO_3$).
- Positive values of the Curie–Weiss temperatures indicate that the ferromagnetic interactions are predominant.
- The magnetic moment values at $T = 1.9$ K and $H = 90$ kOe are less than the theoretical values for ferromagnetic order which are equal to 7.2 μ_B ($PrMnO_3$) and 7.27 μ_B ($NdMnO_3$), respectively. This fact and the absence of saturation at $H = 90$ kOe indicate the complex character of magnetic ordering.

The influence of the grain size on the magnetic properties is clearly visible on ac curves. In Figs. 23.2 and 23.3, the temperature and frequency dependences of the imaginary part of the ac magnetic susceptibility for $PrMnO_3$ and $NdMnO_3$ are shown. For the bulk $PrMnO_3$ sample, the sharp maximum is observed at 70 K. The nonzero values of the imaginary part indicate the existence of magnetic order with the ferromagnetic components. The maxima in $\chi''(T)$ for the $PrMnO_3$ nano-samples are broad and are shifted down to low temperatures with a decrease of both annealing temperature and grain size. For samples annealed at 800 °C, the change of the maximum with changing frequency f indicates the existence of the relaxation process. This dependence is described by the semiempirical parameter $K = \Delta T / [T\Delta(\log f)]$, where T is the temperature of maximum, ΔT the change of this temperature with changing frequency. The K parameter fitted to experimental data was obtained equal to 0.0214 for the sample annealed at 800 °C. This value is typical for the spin-glass system. On the contrary, the $\chi''(T)$ curves for the nano-sample annealed at 900 °C do not depend on the frequency as well as in bulk sample.

The $\chi''(T)$ dependence for the $NdMnO_3$ nano-sample annealed at 800 °C (see Fig. 23.3) exhibits two sharp maxima at 40 and 7 K corresponding to the critical

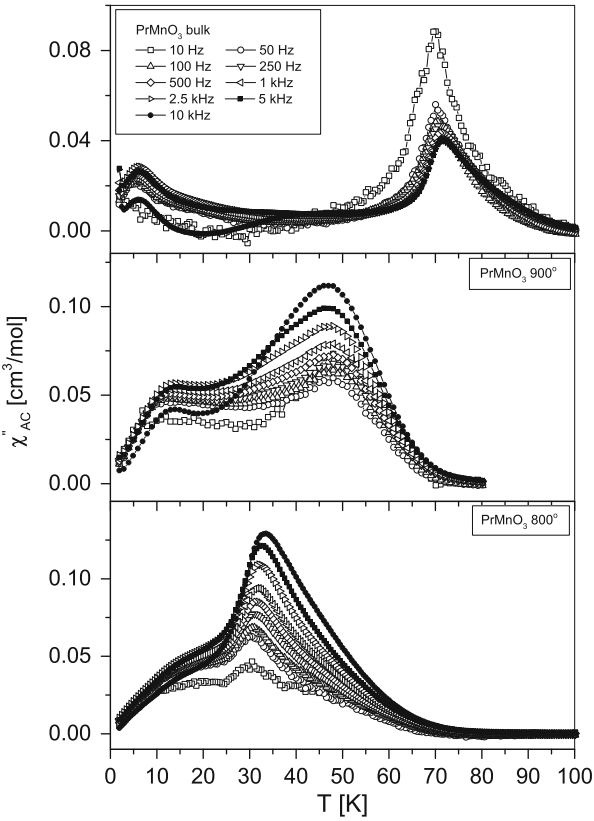

Fig. 23.2 Temperature and frequency dependences of the imaginary χ''_{ac} component of ac susceptibility for the bulk and nanoparticle $PrMnO_3$ samples

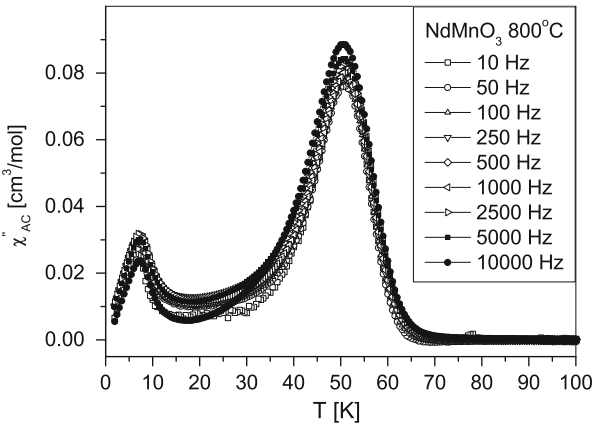

Fig. 23.3 Temperature and frequency dependences of the imaginary χ''_{ac} component of ac susceptibility for the nano 800 °C $NdMnO_3$ sample

temperature of the Mn and Nd moments ordering, respectively. Nonzero χ'' value indicates that the ordering has ferromagnetic component.

23.3.2.2 $TbMnO_3$

Low temperature dependence of the dc magnetic susceptibility for $TbMnO_3$ has the maxima corresponding to the Nèel temperature of the Tb sublattice. The results of magnetic measurements performed over a wide range of temperatures and external magnetic fields summarized in Table 23.2 show that

- The negative value of the paramagnetic Curie temperature suggests that the antiferromagnetic interactions are dominant.
- The effective magnetic moments are close to the theoretical value of 10.88 μ_B/formula unit.
- The Nèel temperature connected with the Tb sublattice ordering and equal to 9.2 K for bulk material is less than the values for the nanoparticle samples equal to 7.1 and 7.4 K. The magnetic ordering in the Mn sublattice is manifested by the deviation from the Curie–Weiss law near 40 K.
- The magnetization curves confirm that the antiferromagnetic order is dominant. With increasing magnetic field values, the metamagnetic phase transition in the Tb sublattice was observed at low temperatures. The magnetization does not achieve saturation in magnetic field up to 50 kOe and decreases with decreasing sintering temperature. The average magnetic moments per formula unit at 2 K and 50 kOe are equal to 3.50 μ_B and 3.65 μ_B for the nano 800 and 850 °C samples, respectively. These values are less than those for both polycrystalline sample (4.14 μ_B) and free ions (13.0 μ_B).

23.3.3 Neutron Diffraction

In order to explain microscopic properties of the above discussed nanoparticle samples, the neutron diffraction experiments have been performed.

In the crystal unit cell, the atoms are in the following positions:

- R (Pr, Nd or Tb) atoms in R1 (x, ¼, z), R2 (½ $-x$, ¾, ½ $+z$), R3. ($-x$, ¾, $-z$), and R4 (½ $+x$, ¼, ½ $-z$),
- Mn atoms: Mn1 (0, 0, ½), Mn2 (½, 0, 0), Mn3 (0, ½, ½), and Mn4 (½, ½, 0).

The possible magnetic modes in the R and Mn sublattices of $RMnO_3$ for $\mathbf{k = 0}$ with the Pnma space group are presented in. [7]. The analysis based on the Bertaut method provides three antiferromagnetic modes: $\mathbf{A} = m_1 - m_2 - m_3 + m_4$, $\mathbf{C} = m_1 + m_2 - m_3 - m_4$ and $\mathbf{G} = m_1 - m_2 + m_3 - m_4$ and one ferromagnetic mode: $\mathbf{F} = m_1 + m_2 + m_3 + m_4$.

23.3.3.1 $PrMnO_3$ and $NdMnO_3$

In the neutron diffraction patterns measured at low temperatures, the peaks of the magnetic origin are indexed based on the crystal unit cell ($k = 0$). For both compounds, the magnetic unit cell coincides with the chemical one. The analysis of the neutron diffraction data indicate

- The absence of the peaks corresponding to the long-range magnetic ordering in the $PrMnO_3$ sample annealed at 800 °C at temperatures down to $T = 1.5$ K.
- The peaks of the magnetic origin in the Mn sublattice of the $PrMnO_3$ sample annealed at 900 °C corresponding to the noncollinear magnetic structure of C_xF_y-type with the following components of the magnetic moment: $\mu_x = 0.74(3)\ \mu_B$, $\mu_y = 1.23(3)\ \mu_B$ and total moment equal to $1.44(3)\ \mu_B$.
- Similar magnetic structure observed for the bulk $PrMnO_3$ sample with the magnetic moment components equal to $\mu_x = 1.96(5)\ \mu_B$, $\mu_y = 1.53(6)\ \mu_B$ and the total moment equal to $2.49(5)\ \mu_B$ [8].
- The C_xF_y-type structure in the Mn sublattice and the F_y-type structure in the Nd sublattice in the nano-size $NdMnO_3$ sample with the following values of the magnetic moment components and total magnetic moment:
  - For 900 °C: $\mu_x = 1.97(5)\ \mu_B$, $\mu_y = 1.23(6)\ \mu_B$ and $\mu_{total} = 2.32(5)\ \mu_B$ for the Mn sublattice and $\mu_{total} = 1.57(11)\ \mu_B$ for the Nd sublattice.
  - For 850°C: $\mu_x = 1.54(2)\ \mu_B$, $\mu_y = 1.44(6)\ \mu_B$ and $\mu_{total} = 2.11(6)\ \mu_B$ for the Mn sublattice and $0.7(3)\ \mu_B$ for the Nd sublattices [8].

A similar magnetic structure is observed in the bulk $NdMnO_3$ sample with $\mu_x = 2.89(3)\ \mu_B$, $\mu_y = 1.44(18)\ \mu_B$ and $\mu_{tot} = 3.28(8)\ \mu_B$ for Mn sublattice and $1.24(18)\ \mu_B$ for the Nd sublattice [9].

In both nano-size $NdMnO_3$ samples, the magnetic ordering in the Mn sublattice is stable down to 60 K.

23.3.3.2 $TbMnO_3$

The low-angle neutron diffraction patterns measured at different temperatures for the bulk and nano particle samples obtained at 800 and 850 °C are shown in Fig. 23.4. Below 46 K, the additional peaks of the magnetic origin connected with the Mn sublattice are observed. These peaks can be indexed by the wave vector $\mathbf{k} = (k_x, 0, 0)$.

A numerical analysis of the intensities of magnetic peaks indicates that the magnetic order in the Mn sublattice is described by the C_x mode. The Mn-moments are parallel to the c-axis and form a collinear incommensurate structure.

At low temperatures, the additional peaks connected with the Tb moments ordering are observed. The positions of these peaks are described by the wave vector $\mathbf{k} = (k_x, 0, 0)$ with different values of k_x (see Table 23.3). The magnetic order is noncollinear described by the F_yA_z mode. The wave vectors and total magnetic moments values are listed in Table 23.3 and summarized below:

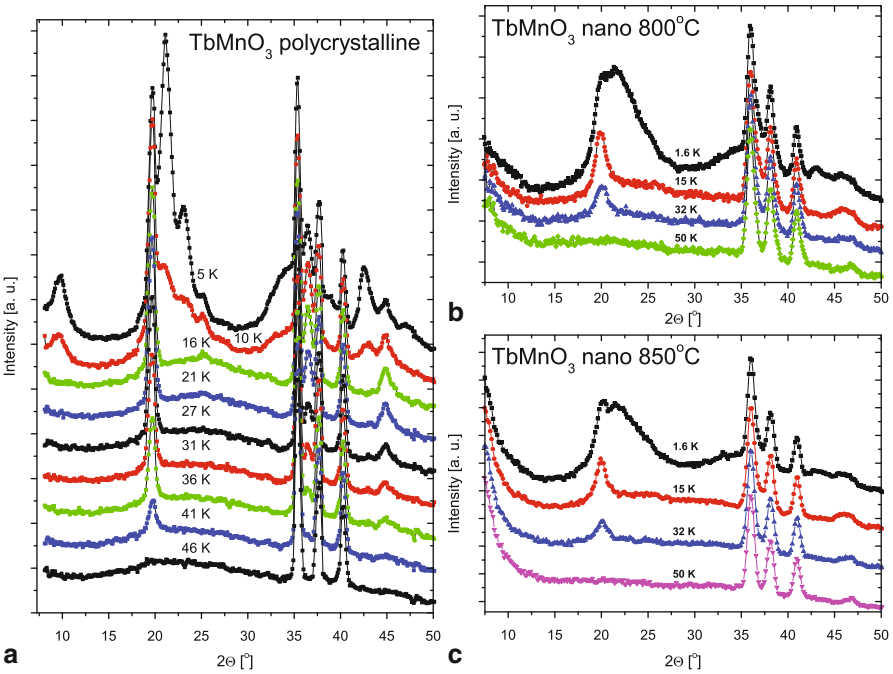

Fig. 23.4 The low-angle neutron diffraction patterns for **a** bulk- and **b** and **c** nano- $TbMnO_3$ samples measured at different temperatures. (Reproduced from [10])

Table 23.3 Magnetic structure parameters for the $TbMnO_3$ samples from the neutron diffraction data; μ_{Mn}—magnetic moment of Mn atom, k_x —component of the wave vector. Lower row data for the Tb sublattice

T(K)	Nano-800 °C		Nano-850 °C		Bulk	
[K]	$\mu_{Mn}(\mu_B)$	k_x	$\mu_{Mn}(\mu_B)$	k_x	$\mu_{Mn}(\mu_B)$	k_x
32	1.60(12)	0.326(4)	1.35(15)	0.326(5)	2.88(3)	0.2821(1)
15	2.29(8)	0.312(2)	2.08(10)	0.315(2)	3.84(3)	0.282(1)
1.6	2.94(2)	0.31292)	3.03(4)	0.328(2)	4.10(2)	0.281(1)
Tb sub.	3.68(11)[a]	0.443(5)[a]	4.43(7)[a]	0.451(3)[a]	6.55(5)[b]	0.432(1)[b]

[a]Data at 1.6 K
[b]Data at 5 K

- The values of k_x component for both (Mn and Tb) sublattices are larger than those for nano-samples.
- The magnetic moment values of the Mn and Tb sublattices are less than those for nano-samples.
- The broadening magnetic peak suggests the cluster-like character of the magnetic ordering in the Tb sublattice [10].

23.4 Discussion

Data presented in this work indicate that the magnetic properties of the nanoparticle samples strongly depend on the grain size values. This manifests itself in the decrease of the values of both magnetic moments in ordered state and magnetic ordering temperature with decreasing grain size.

The decrease of magnetic moments are detected in ordered state, while in the paramagnetic one the effective magnetic moment values determined are close to the free R^{3+} and Mn^{3+} ions values. This is in good agreement with the model for the nanoparticles based on an ideal inner core and nonmagnetic surface shell [1]. The thickness of the magnetically dead layer (t) can be estimated by assuming that it has the zero magnetization and using the following equation [11]:

$$\mu_S = \frac{\mu(\text{bulk})(D-2t)^3}{D^3},$$

where μ_S and μ(bulk) are the magnetic moments of the nanoparticle and bulk materials, D is the size of the nano-crystalline sample.

Based on the Mn magnetic moments experimentally determined from neutron diffraction data, the thickness of nonmagnetic shell calculated using the above formula is equal to 7.1(4) nm in $PrMnO_3$ (900 °C) and 4.6(5) nm in $NdMnO_3$ (for both nanoparticle samples) and 4.0(5) and 4.9(5) nm in $TbMnO_3$ annealed at 800 and 900 °C, respectively. The calculations using the magnetization data yield the smaller thickness values, namely, 3.6(2) and 2.2(2) nm in $PrMnO_3$ annealed at 800 and 900 °C, respectively, 2.9(2) and 3.0(3) nm in $NdMnO_3$ annealed at 850 and 900 °C and 2.9(3) and 2.5(2) nm in $TbMnO_3$ annealed at 800 and 900 °C, respectively. These results are in good agreement with data determined from the magnetization data for some manganites [1, 11]. Comparison between the thickness values found from magnetization and neutron diffraction data indicates that the external magnetic field causes the increase of a magnetically dead layer.

Data presented indicate that the Mn moments form the collinear structure described by either the C_x-mode in $TbMnO_3$ or noncollinear C_xF_y-mode in $RMnO_3$ (R = Pr, Nd). The interactions between the Mn moments are based on the exchange integrals discussed by Bertaut [12]. Analysis of the interactions for the orthorhombic manganites with magnetic structure described by the propagation vector $\mathbf{k} = (k_x, 0, 0)$ leads to the following dependence between k_x and exchange integrals—$\cos(\pi k_x) \approx (2J'' - J')$ [13] where J' is the exchange integral in the a–c plane and J' is the integral along the b-axis. The results of the inelastic neutron scattering for the bulk $TbMnO_3$ sample give a positive value of $J' \approx 0.15(1)$ meV and negative one of $J'' \approx -0.31(2)$ meV [14]. An increase of the k_x component observed in the nanoparticle $TbMnO_3$ samples indicates the decrease of these integrals values. The general conclusion which implies from this work is that the magnetic properties strongly change with decreasing grain size.

References

1. López-Quintela MA, Hueso LE, Rivas J, Rivadulla F (2003) Intergranular magnetoresistance in nanomanganites. Nanotechnology 14:212. doi:10.1088/0957-4484/14/2/322
2. Kimura T, Ishihara S, Shintarni H, Arima T, Takahaski KT, Ishizaka K, Tokura Y (2003) Distorted perovskite with eg1 configuration as a frustrated spin system. Phys Rev B 68:060403. doi:10.1103/PhysRevB.68.060403
3. Dyakonov V, Bażela W, Duraj R, Dul M, Kravchenko Z, Zubow E, Dyakonov K, Baran S, Szytuła A, Szymczak H (2013) Grain size effect on magnetic properties of $REMnO_3$ (RE=Pr,Nd). Low Temp Phys 39:452. doi:10.1063/1.4801432
4. Dyakonov V, Szytuła A, Szymczak R, Zubov E, Szewczyk A, Kravchenko Z, Bażela W, Dyakonov K, Zarzycki A, Varyukhin V, Szymczak H (2012) Phase transitions in $TbMnO_3$ manganites. Low Temp Phys 38:216. doi:10.1063/1.3691530
5. Rodriguez-Carvajal J (1993) Recent advances in magnetic structure determination by neutron powder diffraction. Phys B: Condens Matter 192:55. doi:10.1016/0921-4526(93)90108-I
6. Cullity BD (1978) Elements of X-ray diffraction. Addison-Wesley, Reading
7. Bertaut EF (1968) Representation analysis of magnetic structures. Acta Crystallogr Sect A 24:217. doi:10.1107/S0567739468000306
8. Baran S, Dyakonov V, Hofmann T, Hoser A, Penc B, Kravchenko Z, Szytuła A (2013) Neutron diffraction studies of nanoparticle $RMnO_3$ compounds (R=Pr, Nd). J Magn Magn Mater 344:68. doi:10.1-16/j.jmmm.2013.05.014
9. Muñoz A, Alonso JA, Martinez-Lopez MJ, Fernandez-Diaz MT (2000) Magnetic structure evolutions of $NdMnO_3$ derived from neutron diffraction data. J Phys: Condens Matter 12:1361
10. Bażela W, Dul M, Dyakonov V, Gondek Ł, Hoser A, Hofmann J-U, Penc B, Szytuła A, Kravchenko Z, Nosalev I, Zarzycki A (2012) Magnetic and neutron diffraction studies of the polycrystalline and nanoparticle $TbMnO_3$. Acta Physi Pol A 122:384
11. Balcells L, Fontcuberta J, Martínez B, Obradors X (1998) High-field magnetoresistance at interfaces in manganese perovskites. Phys Rev B 58:R14697. doi:10.1103/PhysRevB.58.R14697
12. Bertaut EF (1963) Spin configurations of ionic structures: theory and practice. In: Rado GT, Shul H (eds) Magnetism, a treatise on modern theory and materials, vol III. Academic Press, New York, p 149
13. Brinks HW, Rodriguez-Carvajal J, Fjellåg H, Kjakshus A, Hauback BC (2001) Crystal and magnetic structure of orthorhombic $HoMnO_3$. Phys Rev B 63:094411. doi:10.1103/PhysRevB.63.094411
14. Senff D, Link P, Hradil K, Hiess A, Regnault LP, Sidis Y, Aliouane N, Argyrion DN, Braden M (2007) Magnetic excitations in multiferroic $TbMnO_3$: evidence for a hybridized soft mode. Phys Rev Lett 98:137206. doi:10.1103/PhysRevLett. 98.137206

Chapter 24
Technological Approaches for Growth of Silicon Nanowire Arrays

Anatoly Druzhinin, Anatoly Evtukh, Ihor Ostrovskii, Yuriy Khoverko, Stepan Nichkalo and Stanislav Dvornytskyi

24.1 Introduction

The growth of highly ordered, aligned, nanometer-sized structures has recently attracted great attention because of their potential application in various functional devices. Processes based on self-organizational materials are very attractive because their possibility provides an opportunity to form the nanostructures that are difficult to achieve with conventional methods. One-dimensional nanostructures, such as semiconductor nanowires, are promising for use as a component base in nanoelectronic devices. On their basis, the field effect transistors (FETs) [1], bipolar transistors [2], light-emitting diodes (LEDs) [3], and solar cells [4] have been developed. As the unique transport, electrical, optical, and other properties of nanowires are determined by the size and morphology, the current study of their technological growth conditions and their formation kinetics and investigation of electrical properties are urgent [5].

This chapter presents the experimental results on growth of Si nanowires by low-pressure chemical vapor deposition (LPCVD) in open system, formation of nanowires by wet etching, and formation of ordered porous alumina oxide matrix for further growth of aligned silicon nanowires. The developed technologies can help to solve the problem of the formation of silicon nanowires with given size and location on the substrate.

S. Nichkalo (✉) · A. Druzhinin · I. Ostrovskii · Y. Khoverko · S. Dvornytskyi
Lviv Polytechnic National University, 79013,
S. Bandera Str., 12, Lviv, Ukraine
e-mail: nichkalo@gmail.com

A. Evtukh
V.E. Lashkaryov Institute of Semiconductor Physics NAS of Ukraine,
Kyiv, Ukraine

O. Fesenko, L. Yatsenko (eds.), *Nanocomposites, Nanophotonics, Nanobiotechnology, and Applications,* Springer Proceedings in Physics 156,
DOI 10.1007/978-3-319-06611-0_24,

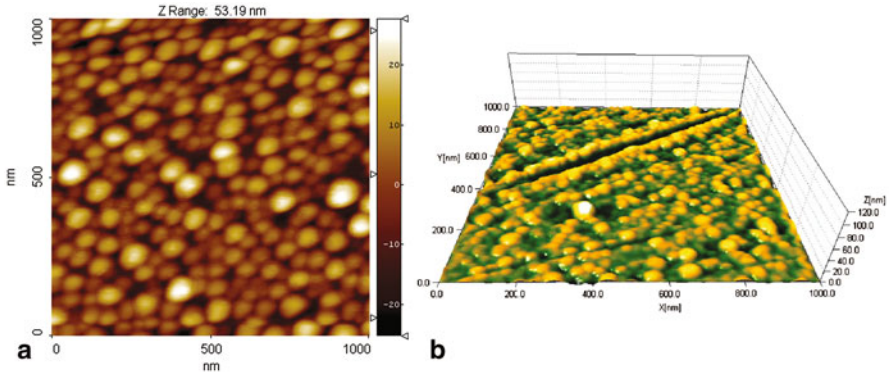

Fig. 24.1 Typical AFM images of Si substrate with Au films that are coagulated into Si-Au nanodrops after annealing at temperature $T = 600\,^{\circ}\mathrm{C}$. **a** Au film thickness $d \approx 9$ nm. **b** Au film thickness $d \approx 4$–5 nm

24.2 Experimental Procedure and Results of LPCVD Growth

To obtain the Si nanowires, two technologies have been used, namely LPCVD and wet chemical etching of silicon. At first, gold films with different thicknesses ranging from 4 to 10 nm were deposited on Si (100) substrates. Atomic force microscopy (AFM) images showed the films were quite uniform. After temperature annealing of Si substrates at 600 °C, Au films coagulated into nanodrops (Fig. 24.1). As can be seen, the average diameter of Si-Au droplets strongly depends on the thickness of initial Au films and decreases from 100 to 40 nm with a decrease in Au film thickness from 9 to 4 nm.

At the next step, Si-Au drops were used as nucleation centers and catalysts for Si nanowires growth. For the growth of ordered nanowire array, the template with Au cells has been used and Si nanowires were grown in each cell (Fig. 24.2a). Figure 24.2b shows that Si nanowires have a small size distribution and the average diameter is about 60 nm. The experimental results demonstrated that the average nanowire's diameter depends on the diameter of coagulated Si-Au nanodrops (Fig. 24.1), the diameter of which depends on the thickness of deposited gold film. The increase in growth time leads to an increase in the nanowire diameter. In addition, during 5-min nanowire growth, the formation of pedestals with an average diameter of about 60 nm on Si substrate with the thickness of Au film about 10 nm was revealed. The increase of growth time to 10 min led to formation of pedestals with larger diameter (about 100 nm).

24.2.1 The Analysis of Radial Nanowires Growth

According to time-dependent theory of combined nanowire growth by vapor–liquid–solid (VLS) technique, the process of Si nucleation could be described with taking into account kinetic processes such as:

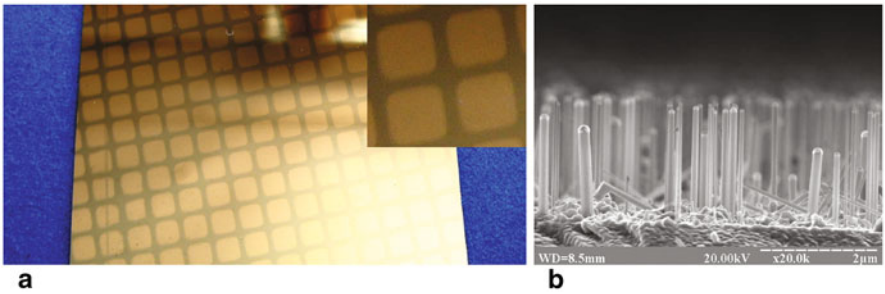

Fig. 24.2 **a** Optical image of Si substrate with Au cells template formed by vacuum deposition. **b** SEM image of ordered Si nanowire array grown at $T = 580$ °C for $t = 5$ min

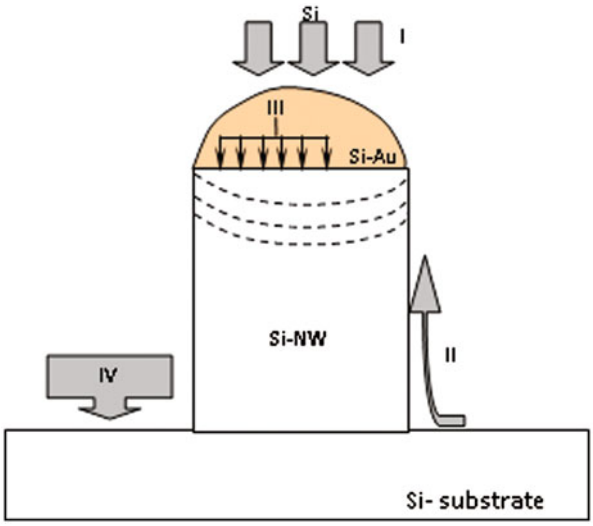

Fig. 24.3 Scheme of Si nanowire growth formation followed by IV kinetic processes

1. Adsorption and desorption onto the droplet surface
2. Diffusion flow into droplet which is the sum of the particle flows exhausted directly on lateral faces and those which have migrated from the substrate surface
3. Layer growth from liquid solution on the liquid–crystal interface under the droplet, taking finite size of side into account
4. Growth onto nonactivated substrate surface

The schematic view of individual nanowire formation with aforementioned processes is depicted in Fig. 24.3.

The amount of semiconductor material particles in droplet N changes in time because of the above-mentioned processes. In consideration of all contributions, we

have the following equation [6]:

$$\frac{2\pi R^2}{\Omega_l}\frac{dR}{dt} = \pi R^2 \frac{V}{\Omega_S} - 2\pi R^2 \frac{r_l C_{eq}}{\tau_l}(\zeta + 1) - \pi R^2 \frac{V_L}{\Omega_S} + \frac{\pi R^2 V}{\Omega_S}\frac{R_*}{R}, \tag{24.1}$$

where R is the droplet radius (hemisphere shaped), Ω_l the volume occupied by the catalyst and semiconductor atoms in liquid phase, Ω_s the volume occupied by the catalyst and semiconductor atoms in solid phase, V the deposition rate of gas flow, r_l the interparticle spacing in gas phase, ζ the supersaturation, V_L the flow of atoms from liquid to solid phase, C_{eq} the equilibrium concentration of the solution, and R_* the collecting radius of adatoms.

Supersaturation $\zeta = C/C_{eq} - 1 = x/x_{eq} - 1$, where $x = N/(N_{Au} + N)$ the concentration of semiconductor material in the solution, N the amount of semiconductor material particles in the droplet, $x_{eq} = C_{eq}\Omega_l$ percentage equilibrium concentration at growth temperature T.

Under the assumption of steady-state crystal growth:

$$dR/dt \approx V \tag{24.2}$$

$$R_* \sim \lambda_s \tag{24.3}$$

where λ_s is the effective deposition diffusion distance onto Si substrate surface.

Equation (24.1) in consideration of (24.2), (24.3):

$$\frac{2V}{\Omega_l} = \frac{V}{\Omega_S} - \frac{2r_l C_{eq}}{\tau_l}(\zeta + 1) - \frac{V_L}{\Omega_S} + \frac{V R_*}{\Omega_S R}. \tag{24.4}$$

It has been assumed that, first, the droplet is a hemisphere, and second, the catalyst and semiconductor atoms occupy the same volume in liquid phase Ω_l. It follows from this that the droplet size could be expressed from the next equation: $\Omega_{drop} = (2/3)\pi R^3 = (N_{Au} + N)\,\Omega_l$.

From the experimental results, it was estimated the mean radius ($R \sim 50$ nm) and the size of the droplet:

$$\Omega_{drop} = (2/3)\pi R^3 = (2/3) \cdot 3,14 \cdot \left(50 \cdot 10^{-9}\right)^3 = 25 \cdot 10^{-2} cm^{-3}$$

Input information: $\Omega_l \approx 3 \cdot 10^{-23} cm^3; \Omega_s \approx 2 \cdot 10^{-23} cm^3; r_l \approx 100\,nm; V_L \approx 1\,nm/sec; \tau_l \approx 4\,sec$

$$V\left(\frac{R_*}{\Omega_S R} - \frac{2}{\Omega_l} + \frac{1}{\Omega_S}\right) = \frac{2r_l C_{eq}}{\tau_l}(\zeta + 1) + \frac{V_L}{\Omega_S}. \tag{24.5}$$

Reducing eq. (24.4) with all input information to eq. (24.5), we have obtained the next deposition rate of gas flow (radial growth rate) $V \sim 1.8$ nm/min. This value means that in a 10-min growth process, the whisker should be increased to 18 nm in diameter. Therewith the supersaturation value is about $\zeta = 0.33$.

Suggesting that nanowire growth rate is directly proportional to the supersaturation,

$$V = b \cdot \zeta^2, \tag{24.6}$$

where b is the kinetic crystallization coefficient, it is possible to estimate its value. In this case, the kinetic crystallization coefficient is about $\sim 3 \times 10^{-6}$ cm/sec. These findings (supersaturation, radial growth rate, kinetic coefficients) are in good agreement with literary data [7, 8].

24.3 Experimental Procedure and Results of Chemical Etching

Additionally, another technology for formation of Si nanowires has been used, which is the chemical etching method that includes the using of Si-Au droplets as the masks. Chemical etching process was carried out in solution (12 ml of 48 % HF + 0.103 M of $AgNO_3$) for $t = 15$ min, $t = 30$ min, $t = 45$ min, followed by rinsing in HNO_3 acid and drying. It was determined that the etching during $t = 30$ min is most acceptable for formation of Si nanowires. As a result, the vertically aligned silicon nanowires were formed on Si substrate.

To realize the growth of regular silicon nanowires, the ordered porous alumina matrix was formed by electrochemical oxidation of aluminum in acid–aqueous electrolyte. Along with the oxidation process, there is also the partial etching of aluminum. The size and distance between pores are proportional to the anodization voltage and depends on the type of acid. The faster the aluminum is dissolved, the smaller the diameter of pores: 5–30 nm for sulfuric acid, 40–60 nm for oxalic acid, and 80–130 nm for phosphoric acid. In all cases, there is a very thin oxide layer at the bottom of the pores. The diameter of the pores, D_p and the distance between the pores, D_{int} are proportional to anodization voltage. In other words, $D_p = k_1 U$ and $D_{int} = k_2 U$, where $k_1 \sim 1.29$ nm/V and $k_2 \sim 2.5$ nm/V [9].

To form the ordered long pores, a two-step anodization process has been used in our experiments. Before anodization, the sample was developed in 5% NaOH solution at 60 °C and neutralized with 50% solution of nitric acid and then the electrical voltage was applied to anodization cell. At the first stage, the porous alumina was formed in 0.3 M oxalic acid water solution at a voltage of 40 V and the temperature of 0 °C for 2 h. Then all porous aluminum oxide was removed in the mixture of 0.2 M H_2CrO_4 and 0.4 M H_3PO_4 acids at 60 °C for 5 min. Then the anodization process was repeated until there was a sharp decline in current. As a result, the aluminum oxide matrix with pore diameter of $\sim$ 50 nm was obtained (Fig. 24.4). Most orderliness is achieved at the voltage of about 40 V, and it improves with the increase of the first-stage anodization time and the acid concentration. The surface density of pores depends on anodization currents [10, 11]:

$$n = n_0 J^{-\alpha}, \tag{24.7}$$

where n_0 and α are the constants that depend on acids in solution: $n_0 = 5,79 \times 10^9$, 112×10^9, 176×10^9 cm^{-2}, and $\alpha = 0.68$, 0.72, 0.335 for the acids H_3PO_4, $H_2C_2O_4$, and H_2SO_4, respectively.

Thus, the formation of porous alumina matrix enables to grow the vertically aligned silicon nanowires arrays of given size and in the strictly defined area.

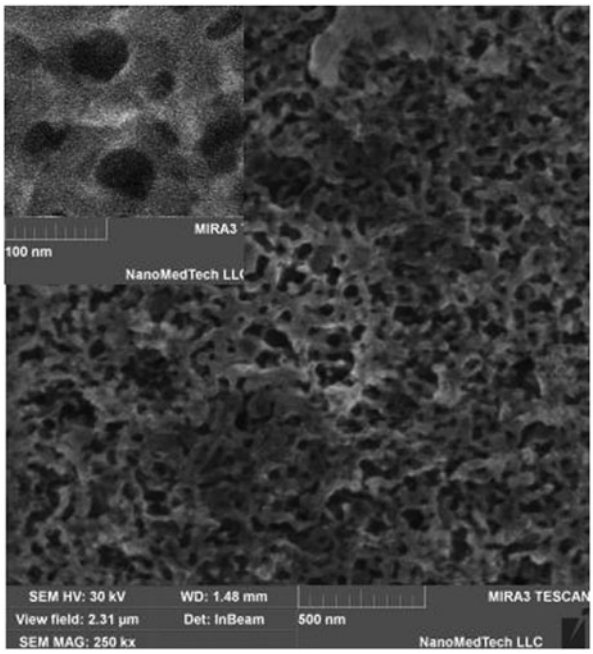

Fig. 24.4 SEM image of porous alumina matrix

24.4 Conclusions

The peculiarities of Si nanowire formation by both LPCVD technology and chemical etching through mask have been investigated. The Si-Au drops were used in both cases. It was shown that Si nanowires grown by LPCVD have small distribution of the lateral size and the average diameter was about 60 nm. It has been shown that the diameter of nanowires depends on the size of Si-Au nanodrops, the larger drops, the higher diameter. The increase in the growth time led to increase in nanowires diameter. The formation of pedestal on the bottom of nanowires has been revealed. The theoretical analysis of radial nanowire growth and comparison with experimental results allowed determining some important parameters of the process, namely the radial growth rate, vapor supersaturation, and kinetic coefficient. It was shown that using of Si-Au droplets as the mask during chemical etching of Si might help to obtain vertically aligned silicon nanowires. The alumina formation process by anodization has been investigated and porous alumina matrix with average diameter of the pores of 50 nm has been obtained. The latter technique can be used for growth of ordered vertically aligned silicon nanowires combined by LPCVD technology.

References

1. Greytak AB, Lauhon LJ, Gudiksen MS, Lieber CM (2004) Growth and transport properties of complementary germanium nanowire field-effect transistors. Appl Phys Lett 84:4176–4178
2. Cui Y, Lieber CM (2001) Functional nanoscale electronic devices assembled using silicon nanowire building blocks. Science 291(5505):851–853
3. Dubrovskii VG, Cirlin GE, Ustinov VM (2009) Semiconductor nanowires: Synthesis, properties and applications. Semiconductors 43(12):1585–1628
4. Peng KQ, Xu Y, Wu Y, Yan YJ, Lee ST, Zhu J (2005) Aligned single-crystalline Si nanowire arrays for photovoltaic applications. Small 1:1062–1067
5. Wang N, Cai Y, Zhang RQ (2008) Growth of nanowires. Mater Sci Eng R 60:1–51
6. Dubrovskii VG, Sibirev NV, Cirlin GE, Harmand JC, Ustinov VM (2006) Theoretical analysis of the vapor-liquid-solid mechanism of nanowire growth during molecular beam epitaxy. Phys Rev 73:021603–021612
7. Givargizov EI (1977) Growth of needle-like and plate crystals from vapour. Nauka, Moscow
8. Kashchiev D (2006) Dependence of the growth rate of nanowires on the nanowire diameter. Cryst Growth Des 16:1154–1156
9. Wade TL, Cojocaru CS, Wegrowe J-E, Pribat D (2008) Nanoporous alumina templates for nanowire electron devices. In: Rahman F (ed) Nanostructures in electronics and photonics. Pan Stanford Publishing Pvt. Ltd., Singapore, pp 42–84
10. Belov AN, Gavrilov SA, Shevyakov VI (2006) Peculiarities of nanostructured anodic alumina formation. Rus Nanotechnol 1–2:223–227 (in Russian).
11. Patermarakis G, Moussoutzanis K (2002) Interpretation of the promoting effect of sulphate salt additives on the development of non-uniform pitted porous anodic Al_2O_3 films in H_2SO_4 electrolyte by a transport phenomenon analysis theory. Corros Sci 44:1737–1753

Chapter 25
Influence of Physical Parameters on the Transconductance g_m of Channel for the Component Submicron

M. Draidi, M. Zaabat and A. Boudine

- Transconductance variation g_m according to the gate length L and voltage V_{ds}.
- Transconductance variation g_m according to the resistance R_s and voltage V_{ds}.

25.1 Introduction

Transistors with GaAs metal-semiconductor field effect (MESFET) are widely used in microwave and digital applications due to their superior characteristics at high frequencies [2, 5].

The simulation of nonlinear circuits based on GaAs requires the use of a precision MESFET model, if predicted circuit performance and completion are closely correlated. In the industry, it usually starts with a computer simulation of the device or circuit manufacture. The development or improvement of new channels of components requires means for modeling, realization, and characterization [1, 5].

It is therefore very important to predetermine the characteristics of the component, physical modeling being one of its main applications. Depending on the application chosen and taken into account, the complexity of the operation of a transistor gate field-effect submicron, optimization of the component according to the geometrical and physical parameters is only possible by the experimental approach [1, 4].

It is imperative to understand the phenomenon exists, and the variation of a single-parameter technology may be able to have various effects on the characteristics and possibilities of the field effect transistor. Those are not easy to analyze without an accurate determination of internal parameters that govern [2, 3].

M. Draidi (✉) · M. Zaabat · A. Boudine
Faculty of Exact Sciences and Natural and Life Sciences, Active Devices and Materials Laboratory, Larbi Ben M'hidi University, Oum El Bouaghi 04000, Algeria
e-mail: Mourad.Draidi@gmail.com

M. Draidi
Tel.: +2136 62 62 79 19

O. Fesenko, L. Yatsenko (eds.), *Nanocomposites, Nanophotonics, Nanobiotechnology, and Applications,* Springer Proceedings in Physics 156,
DOI 10.1007/978-3-319-06611-0_25,

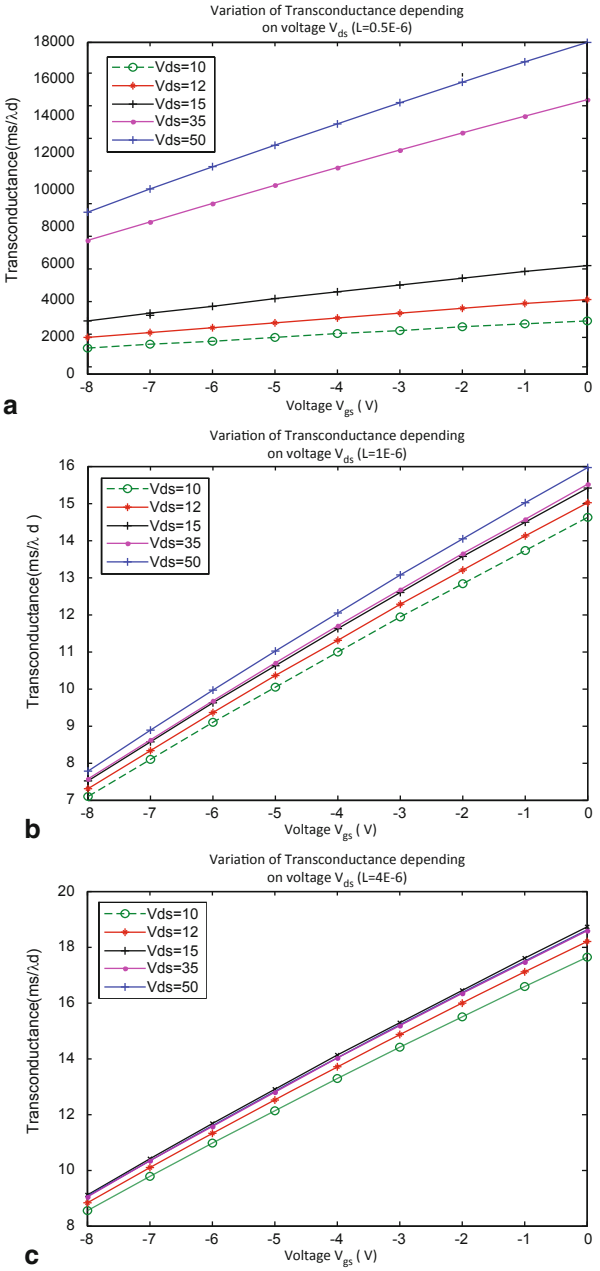

Fig. 25.1 Variation of transconductance g_m depending on the gate length L and voltage V_{ds} (we take $R_s = 100\ \Omega$)

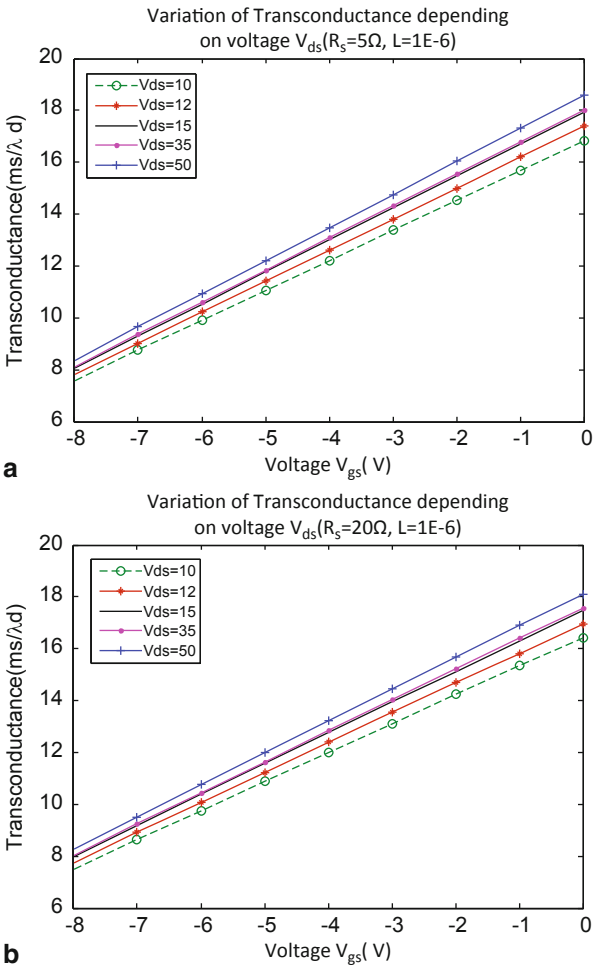

Fig. 25.2 Variation of the transconductance g_m according to the resistance R_s and the voltage V_{ds} (we take L = 1E-6)

The component designer must know the influence of technological parameters, so that it may consider their influence on the behavior of the device. Especially, when it comes to circuits monolithic microwave integrated [4, 6].

Calculation of the transconductance g_m

The expression of the transconductance is given by the equation:

$$g_m = \left.\frac{\Delta I_{ds}}{\Delta V_{gs}}\right|_{V_{ds}=Cte}$$

We see that the value of the channel transconductance decreases with increasing width of the gate, which confirms the phenomenon of electrons over speed in the channel for submicron components (Figs. 25.1 and 25.2).

We note that the influence of the source parasitic resistance value R_s on the transconductance is minimal.

25.2 Conclusion

The results are in agreement with the literature under the same conditions, the method is applicable for all other geometries.

The Poisson equation can have an analytical formula for the depopulated area and the voltage, therefore having a better accuracy in the calculation of other parameters.

References

1. Benghalia A, Ahmadpanah M, Baudrand H (Aug 1988) Accurate two-dimensional approach for capacitance calculation in microcoplanar MES transmission lines. Electron Lett 24(16):996–998
2. Enokit T, Sugitani S, Yamane Y (1990) IEEE Trans Electron Devices 37, p 935–941
3. Golio MJ, Golio JRC (1991) IEEE trans. Microw Theory Tech 39:142–146
4. Horio K, Yamada T (April 1999) Two dimensional analysis of surface state effects on turn-on characteristics in GaAs MESFET's. IEEE Trans. Electron Devices ED-46; no. 4
5. Kennis P, Faucon L (June 1981) Rigorous analysis of planar MIS transmission lines. Electron Lett 17(13):454–456
6. Lepaul S (1996) Contribution a la modélisation numérique des composants électroniques aux dimensions nanométriques. Thèse de doctorat, Université de Paris VI

Chapter 26
Structural, Optical, and Photocatalytic Properties of Quasi-One-Dimensional Nanocrystalline ZnO, ZnOC:nC Composites, and C-doped ZnO

E. V. Shalaeva, O. I. Gyrdasova, V. N. Krasilnikov, M. A. Melkozerova, I. V. Baklanova and L. Yu. Buldakova

26.1 General

Zinc oxide with a wurtzite structure belongs to a group of advanced functional materials because it possesses a unique set of properties. Its most important property is high photocatalytic activity in low-temperature oxidation reactions of toxic and colored organic compounds dissolved in water [1–6]. The action of oxide semiconductor photocatalysts is based on the generation of free carriers (electrons and holes) under exciting radiation, which take part in redox reactions on the oxide surface [7]. The photocatalytic activity can be increased first of all by creating a high specific surface area and a high concentration of native structural defects, which raises the specific concentration of sorption and oxidation centers on the catalyst surface [8–10]. There are numerous original researches and reviews devoted to various synthesis methods of nanosized ZnO materials having a high specific surface area [11–17]. Another way for improving the photocatalytic properties of wide-band-gap semiconductors is modification of the electron-energy spectrum of oxides. The results of first-principle quantum chemical calculations show that restructuring of the electron-energy spectrum and reduction of the optical gap can occur owing to native structural defects such as oxygen vacancies of ZnO [18–19]. The effects of electron-energy-spectrum restructuring and photocatalytic activity enhancement induced by oxygen vacancies have been confirmed experimentally for nanostructured ZnO [20]. Reduction of recombination processes of generated electron–hole pairs also increases the photocatalytic activity [7]. The combination of the above methods for improving the photocatalytic activity seems promising for the development of ZnO-based photocatalysts. Nobel metal/ZnO nanocomposites exhibit very high cat-

E. V. Shalaeva (✉) · O. I. Gyrdasova · V. N. Krasilnikov · M. A. Melkozerova · I. V. Baklanova · L. Yu. Buldakova
Institute of Solid State Chemistry UB RAS, 91, Pervomaiskaya str.,
Ekaterinburg, Russian Federation 620990
e-mail: shalaeva@ihim.uran.ru

O. I. Gyrdasova
e-mail: gyrdasova@ihim.uran.ru

O. Fesenko, L. Yatsenko (eds.), *Nanocomposites, Nanophotonics, Nanobiotechnology, and Applications,* Springer Proceedings in Physics 156,
DOI 10.1007/978-3-319-06611-0_26,

alytic photoactivity not only because they have high specific area but also because of improved charge transfer through metal particles and reduced recombination rate of hole–electron pairs [21, 22]. In its turn, doping of zinc oxide, for example with 3d metals, leads to restructuring of the electron-energy spectrum and consequently to increased photoactivity and extending photoresponse of ZnO from the ultraviolet (UV) to the visible spectral region [23–29]. The effect of 3d-metal doping on the photocatalytic properties is more pronounced for nanosized ZnO materials.

Recently, nanosized Zn–O–C materials have attracted increasing attention for a wide range of possible applications among the environment-friendly photocatalysts [30–38]. The growth of photocatalytic activity has been reliably demonstrated for ZnO:nC composites, where carbon forms individual phases including graphene layers [35–37] and C_{60} molecules [39]. The main mechanism of photocatalytic activity growth for ZnO:nC composites is attributed to the reduction of recombination processes of electron–hole pairs owing to graphene layers or thin carbon layers on the ZnO surface [38]. For ZnO with monolayer coverage of C_{60}, the hybridization of C_{60} with semiconductor is considered to play an important role in the enhancement of photocatalytic activity [39]. Some ZnO/graphene composites are found to exhibit the increased light absorption intensity in UV and visible light as compared with the pure ZnO particles [35–37]. The reduction of the optical gap is associated with the optical absorption properties of the ZnO/graphene composite. However, ab-initio electron structure calculations show that restructuring of the electron-energy spectrum and optical-gap narrowing can take place owing to carbon doping of ZnO [40–42]. So, synthesis and comparative research of structural and optical properties of ZnO:nC composites and C-doped ZnO phases in nanostructured state is of much interest for catalytic applications.

Nanostructured doped zinc oxide can be produced by wet chemical synthesis, a technologically simple and power-efficient method. The various wet chemical routes have been applied for the preparation of ZnO with different morphologies: nanowires [16, 43, 44], nanobelts [45], nanotubes [46–49], nanosheets [50], and nanospheres [51]. These products are usually single crystalline. However, the polycrystalline catalysts are more functional due to the higher specific surface area. Few techniques allow obtaining polycrystalline quasi-one-dimensional ZnO [52–54]. We shall consider the possibilities of the precursor method worked out by the authors [55, 56] for the synthesis of quasi-one-dimensional nanostructured aggregates ZnO and Zn–O–C. Using transmission electron microscopy (TEM), Raman spectroscopy, and EPR spectroscopy methods, we shall demonstrate that the aggregates Zn–O–C have either a ZnOC:nC composite or a C-doped ZnO single-phase structure depending on heat treatment conditions and that all the aggregates exhibit a tubular morphology and a nanocrystalline structure with a high specific surface area and a high concentration of singly charged oxygen vacancies. The results of examination of the photocatalytic properties of the synthesized aggregates will be reported. We shall show that the photocatalytic activity for the hydroquinone oxidation reaction increases in the series: the reference ZnO powder, quasi-one-dimensional ZnO, and quasi-one-dimensional aggregates C-doped ZnO. This tendency correlates with the reduction of the optical gap width. As a result of our studies, we have arrived at an important conclusion

that thermal treatment of ZnO:nC composites allows one to produce C-doped ZnO with high catalytic activity. This increasing photoactivity of C-doped ZnO aggregates is achieved by the optimal specific surface area and electron-energy spectrum restructuring owing to the presence of singly charged oxygen vacancies and carbon dissolved in the ZnO lattice.

26.2 Synthesis of Quasi-One-Dimensional Aggregates ZnO and Zn–O–C by the Precursor Method

26.2.1 Synthesis and Characterization of Precursor Organometallic Compounds of Zinc

To synthesize quasi-one-dimensional ZnO aggregates, we use the organometallic glicolate complexes as precursors. In some works including our studies, it was shown that during heating these compounds turn into oxides inheriting the shape of the precursor particles and crystals [55–57]. We studied preliminarily which shapes of particles various zinc glicolate complexes can have and under which synthesis conditions these complexes are formed [27].

The method for synthesis of zinc glicolate complexes is based on hydrothermal treatment of alkoxides in ethylene glycol, which is taken in excess and is used both as a solvent and as a reagent for synthesis. For synthesis of glicolate complexes, we used zinc formate $Zn(HCOO)_2{\cdot}2H_2O$ and ethylene glycol $HOCH_2CH_2OH$. Synthesis was carried out at three different temperatures, 50, 100, and 150 °C, for 12 h while mixing. The solid reaction products were separated from the liquid phase by vacuum filtration, washed with dehydrated acetone, and dried at 40 °C to remove acetone. The products were placed in weighing bottles to prevent the effect of atmospheric moisture. Zinc formates necessary for the experiments were synthesized by the action of formic acid on zinc oxide:

$$ZnO + 2HCOOH + H_2O = Zn(HCOO)_2 \cdot 2H_2O. \tag{26.1}$$

The interaction of the formate $Zn(HCOO)_2{\cdot}2H_2O$ with ethylene glycol was found to depend essentially on the temperature of synthesis. The stages of chemical interaction at the three temperatures of synthesis, 50, 100 and 150 °C, can be described by the following reactions:

$$Zn(HCOO)_2 \cdot 2H_2O + HOCH_2CH_2OH \rightarrow Zn(HCOO)_2(HOCH_2CH_2OH) + 2H_2O\uparrow, \tag{26.2}$$

$$Zn(HCOO)_2\,(HOCH_2CH_2OH) \rightarrow Zn(HCOO)(OCH_2CH_2O)_{1/2} + 1/2HOCH_2CH_2OH + HCOOH\uparrow, \text{ and} \tag{26.3}$$

$$\mathrm{Zn(HCOO)\,(OCH_2CH_2O)_{1/2} + 1/2HOCH_2CH_2OH \rightarrow Zn(OCH_2CH_2O)} \quad (26.4)$$
$$+ \mathrm{HCOOH} \uparrow .$$

As is seen from Eq. 26.2, at the first stage of the interaction at a temperature of 50 °C the solvate $Zn(HCOO)_2(HOCH_2CH_2OH)$ is formed as a result of substitution of one molecule of ethylene glycol for two molecules of water in the zinc formate. At a temperature of 100 °C, the solvate $Zn(HCOO)_2(HOCH_2CH_2OH)$ dissolves in ethylene glycol forming a homogeneous colorless solution, from which crystals of zinc formate glicolate of the composition $Zn(HCOO)(OCH_2CH_2O)_{1/2}$ or $Zn_2(HCOO)_2(OCH_2CH_2O)$ precipitate (Eq. 3). Since the formate ion is displaced from formate glycolate and is removed from the solution in the form of formic acid, at 150 °C and above, $Zn(HCOO)(OCH_2CH_2O)_{1/2}$ changes into completely substituted zinc glicolate of the composition $Zn(OCH_2CH_2O)$ (Eq. 4). All the three organometallic complexes of zinc (solvates, formate glicolates, formates) are identified by X-ray diffraction and infrared (IR) spectroscopy as individual phases [27]. Therefore, we established that various organometallic complexes of zinc can be formed as a result of the interaction of ethylene glycol and zinc formate, and the temperature of the process was the main factor determining the degree of ligand substitution of the formate group in $Zn(HCOO)_2 \cdot 2H_2O$.

The most remarkable result is the diverse morphology of the organometallic zinc complexes. The solvate $Zn(HCOO)_2(HOCH_2CH_2OH)$ is a colorless substance having the shape of rhombic plates with refractive indices $Ng = 1.519$ and $Np = 1.492$. The formate glicolate $Zn(HCOO)(OCH_2CH_2O)_{1/2}$ is crystallized in the form of colorless thin fibers characterized by very high water absorbency. At rapid heating of oversaturated solution of $Zn(HCOO)(OCH_2CH_2O)_{1/2}$ in ethylene glycol, it can be crystallized in the form of bars with refractive indices $Ng = 1.609$, $Np = 1.543$, and $\Delta Ng - Np = 0.066$. The zinc glicolate $Zn(OCH_2CH_2O)$ forms colorless crystals shaped as distorted octahedra with very imperfect cleavage and refractive indices $Ng = 1.581$, $Nm = 1.564$, $Np = 1.548$, and $\Delta Ng - Np = 0.033$. Figure 26.1 demonstrates scanning electron microscopy images (SEM) of $Zn(HCOO)(OCH_2CH_2O)_{1/2}$ formate glicolate fibers and octahedral particles of glicolate $Zn(OCH_2CH_2O)$.

Let us consider the results of the investigation of the process and products of thermolysis of organometallic zinc complexes synthesized by the hydrothermal method.

26.2.2 Thermolysis Products of Organometallic Zinc Compounds

For the synthesis of ZnO and Zn–O–C, we have examined two alternative routes of organometallic complex thermolysis: thermolysis in air and, in order to prevent carbon removal and to obtain Zn–O–C aggregates, thermolysis in inert He atmosphere.

Thermal decomposition of fibrous formate glicolate $Zn(HCOO)(OCH_2CH_2O)_{1/2}$ in air is an exothermic process occurring in two main stages in the temperature

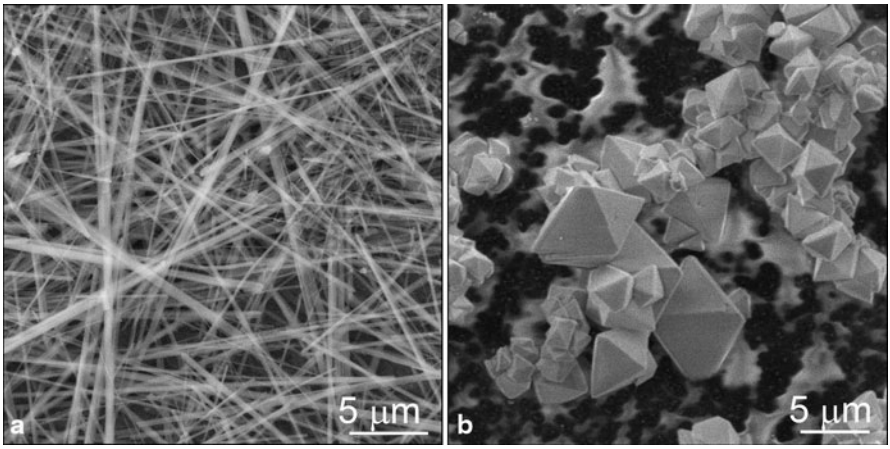

Fig. 26.1 SEM images of organometallic precursors. **a** $Zn(HCOO)(OCH_2CH_2O)_{1/2}$ fibers. **b** $Zn(OCH_2CH_2O)$ octahedral particles

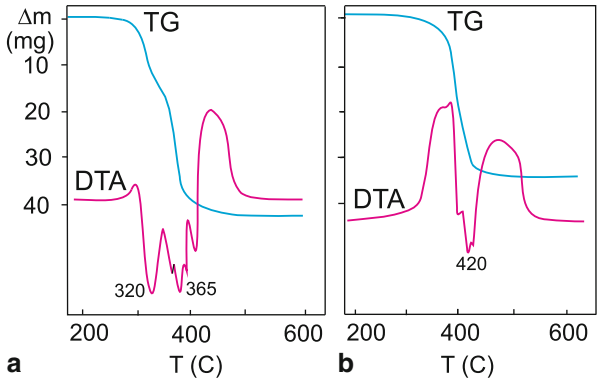

Fig. 26.2 TG and corresponding DTA curves for **a** zinc formate glycolate $Zn(HCOO)(OCH_2CH_2O)_{1/2}$ and **b** zinc formate $Zn(OCH_2CH_2O)$

intervals 300–390 °C and 400–450 °C (Fig. 26.2a). Upon thermal treatment, the particles of the formed zinc oxide acquire the fibrous shape of the precursor crystals (Fig. 26.3a). According to chemical and thermogravimetric analysis data, the content of carbon in the product of thermolysis of formate glicolate in air is 10 wt. % at 350 °C, about 0.5 wt. % at 450 °C, and < 0.1 wt. % at 500 °C. The X-ray analysis shows that the product of thermolysis at 450 °C is identified as zinc oxide with a wurtzite structure (Sp.G. $P6_3mc$) and lattice parameters $a = 0.3249$ nm and $c = 0.5207$ nm (Fig. 26.4a). Thermolysis of glicolate $Zn(OCH_2CH_2O)$ is a one-stage exothermic process (Fig. 26.2b). As in the case of thermolysis of formate glicolate, the particles of the thermolysis product (zinc oxide) acquire the form of the precursor (Fig. 26.3b).

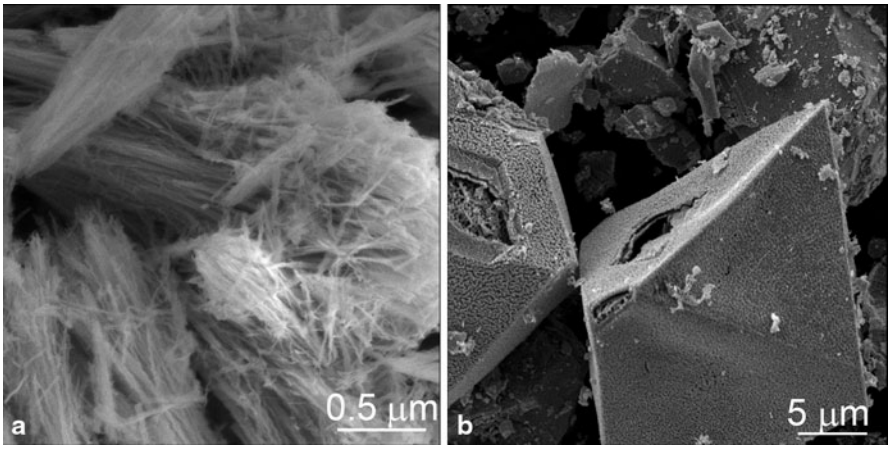

Fig. 26.3 SEM images of the thermolysis products of **a** zinc formate glycolate Zn(HCOO)$(OCH_2CH_2O)_{1/2}$ and **b** zinc formate $Zn(OCH_2CH_2O)$. Thermolysis is carried out in air

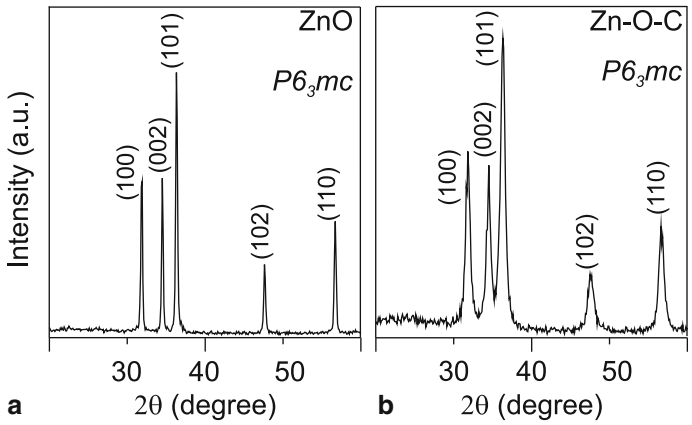

Fig. 26.4 X-ray powder diffraction patterns for the thermolysis products of zinc formate glycolate annealed **a** in air at 450 °C and **b** in He atmosphere at 500 °C

The thermolysis product of formate glicolates in inert atmosphere at 500°C also has a quasi-one-dimensional morphology (Fig. 26.5a). According to X-ray analysis, the product has a wurtzite structure and the degree of the crystalline phase dispersion is higher than that for the zinc oxide obtained by thermolysis in air. (Fig. 26.4b). The elemental and thermogravimetric analyses reveal that the aggregates produced by thermolysis in inert atmosphere contain 7.5 wt. % carbon including 6.8 wt.% free carbon and 0.7 wt. % carbon bound in the structure of ZnO.

Thus, the interaction of ethylene glycol and zinc formate during hydrothermal synthesis makes it possible to obtain various organometallic zinc complexes with

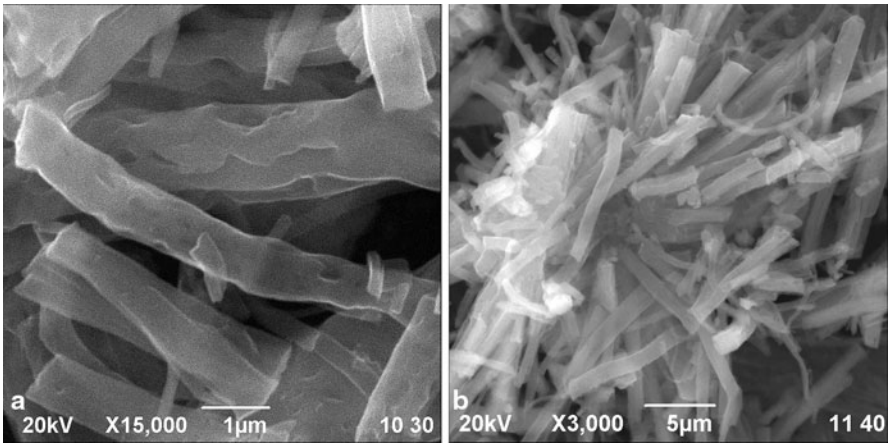

Fig. 26.5 SEM images of the thermolysis products of zinc formate glycolate annealed **a** in He atmosphere at 500 °C and **b** in He atmosphere at 500 °C and then boiled in formic acid

different crystal morphology: solvates $Zn(HCOO)_2(HOCH_2CH_2OH)$ in the form of thin rhombic plates, formate glicolates $Zn(HCOO)(OCH_2CH_2O)$ shaped as thin fiber crystals, and glicolates $Zn(OCH_2CH_2O)$ having the form of octahedral particles. The thermolysis products inherit the shape of the organic precursor particles for all types of complexes. The quasi-one-dimensional aggregates are produced by thermolysis of formate glicolate complexes; namely, the zinc oxide ZnO is obtained during thermal treatment in air and Zn–O–C aggregates are formed by thermal treatment in inert He atmosphere.

26.3 Structural Properties of ZnO and Zn–O–C Quasi-One-Dimensional Aggregates: TEM and Spectroscopic Investigation

26.3.1 Morphology and Microstructure of ZnO and Zn–O–C Aggregates. Composites and Single-Phase Structures

According to the SEM data, the thermal decomposition products of zinc formate glicolate have a quasi-one-dimensional morphology (Fig. 26.5a). What are the microstructure and native defects of these aggregates and how do the structural characteristics change depending on the primary synthesis and thermolysis conditions? How will these characteristics finally affect the optical and photocatalytic properties of the aggregates? To answer these questions, we used TEM, Raman spectroscopy, and EPR spectroscopy methods.

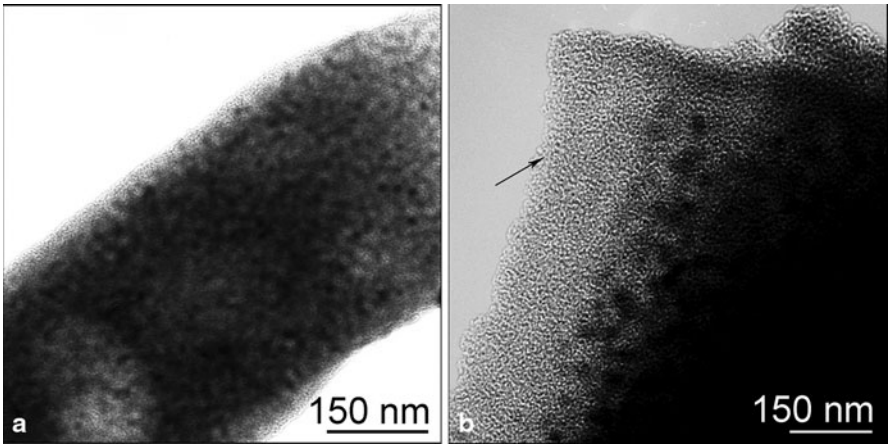

Fig. 26.6 Bright-field TEM images of Zn–O–C quasi-one-dimensional scrolls synthesized by thermolysis in He atmosphere at 500 °C. **a** Overview. **b** Edge of unwrapped scroll. The *arrow* shows the area with amorphous structure

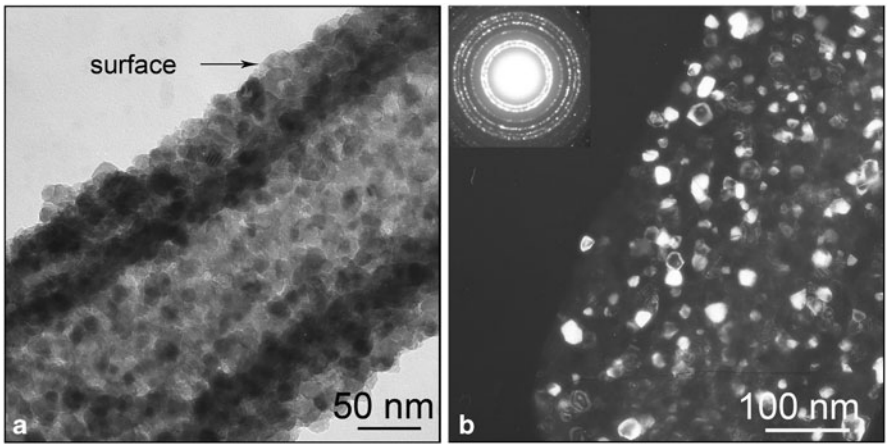

Fig. 26.7 Quasi-one-dimensional ZnO aggregate with tubular morphology and nanocrystalline structure. **a** Bright-field TEM image showing nanoscale surface roughness. **b** Dark-field TEM image taken with $(100)_{ZnO}$ and $(101)_{ZnO}$ reflections and microdiffraction pattern of individual aggregate (*inset*)

Figure 26.6 displays TEM images from individual quasi-one-dimensional aggregate Zn–O–C obtained by thermolysis of formate glicolate in He atmosphere at 550 °C. For comparison, we present our data for quasi-one-dimensional aggregate ZnO [58]—the thermal decomposition of formate glicolate in air at 500 °C (Fig. 26.7).The bright-field TEM images show that the aggregates Zn–O–C are usually scrolls. The scroll morphology is also found for quasi-one-dimensional ZnO, but generally they have tubular morphology (Fig. 26.7).

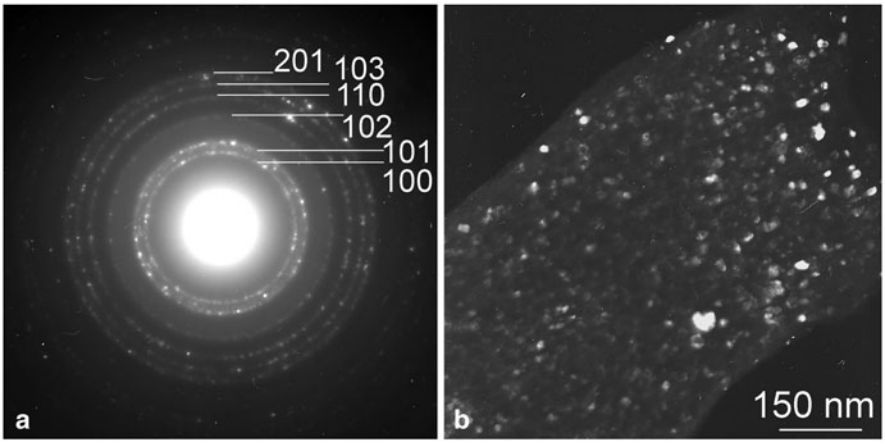

Fig. 26.8 Quasi-one-dimensional Zn–O–C aggregate with nanocrystalline zinc oxide. **a** Microdiffraction pattern of individual aggregate. **b** Dark-field TEM image taken with $(100)_{ZnO}$ and $(101)_{ZnO}$ reflections

The Debye-Scherrer rings of electron diffraction patterns without texture signs (Figs. 26.7a, 26.8a) show that the individual quasi-one-dimensional aggregates ZnO and Zn–O–C contain a nanoscale nonoriented crystalline phase. The whole system of reflections is indexed in the hexagonal cell with parameters $a = 0.323$ nm and $c = 0.520$ nm, which corresponds to the wurtzite structure of zinc oxide and agrees with the X-ray diffraction data. The dark-field TEM images taken in the $(100)_{ZnO}$- and $(101)_{ZnO}$- type reflections confirm that the ZnO-based crystalline phase is nanosized (Fig. 26.8b). For quasi-one-dimensional aggregates Zn–O–C, the average size of the crystallites is 10–15 nm and they have a higher degree of dispersion compared with ZnO aggregates. The average size of the crystallites for ZnO aggregates is of the order of 20 nm.

It should be noticed that the bright-field TEM images of quasi-one-dimensional Zn–O–C exhibit diffraction contrast typical of amorphous phases (Fig. 26.6). The chemical analysis data suggest that the quasi-one-dimensional aggregates contain amorphous carbon. It was not possible to identify the diffuse halos of the amorphous phase on the microdiffraction patterns in the presence of the Debye rings of nanodispersed zinc oxide. However, according to the Raman spectra, the observed amorphous phase is a carbon-containing phase. Along with the vibrational spectrum of ZnO including the bands to 1160 cm^{-1} [59], the Raman spectrum recorded at room temperature also contains two intensive lines in the high-frequency region (Fig. 26.9). These are the lines "D" and "G" typical of hydrogenated amorphous carbon annealed at 600 °C [60, 61]. An active graphite "G" band associated with E_{2g} vibrational mode of sp^2 bonded atoms is located at around 1599 cm^{-1}. The "D" band that represents a zone-edge A_{1g} mode due to disorder is located at 1357 cm^{-1}. Therefore, the quasi-one-dimensional aggregates Zn–O–C produced by thermolysis

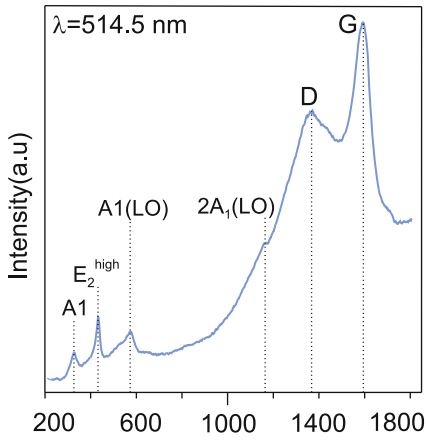

Fig. 26.9 Raman spectra of Zn–O–C aggregates synthesized by thermolysis in He atmosphere at 500 °C. The series of Raman modes of ZnO are indicated: 327.5 ($A1$), 432.5 (E_2^{high}), 575.1 ($A1(LO)$), 1159.5 cm^{-1} ($2A_1(LO)$). Peaks D and G typical of hydrogenated amorphous carbon are observed

in He atmosphere do not have a monophase structure but a composite amorphous-crystalline structure, where the amorphous carbon matrix contains nanodispersed crystallites of zinc oxide. These composite aggregates will be further denoted by ZnOC:nC. Note that the quasi-one-dimensional morphology of the amorphous carbon matrix remains if the aggregates ZnOC:nC are boiled in formic acid and zinc oxide is dissolved (Fig. 26.5b).

Tubular and scroll-like morphology, as well as the nanocrystalline structure of the oxide phase in Zn–O–C and Zn–O aggregates, will result in nanoscale surface roughness (Fig. 26.7a) and a high specific surface area. For Zn–O aggregates, the value of specific surface area is estimated to be $\sim$ 30–40 m^2/g.

The examination of the structure of quasi-one-dimensional ZnO and Zn–O–C by high-resolution electron microscopy (HREM) made it possible to obtain a more detailed notion about their structure. The HREM pictures exhibit large regions with the $(100)_{ZnO}$ lattice image; their sizes are much greater than the sizes of nanocrystallites (Fig. 26.10). Therefore, these regions are monocrystalline ultrathin layers of zinc oxide and they have preferred orientation in the quasi-one-dimensional composites. As is seen, the $(100)_{ZnO}$ plane is parallel to the long axis of the quasi-one-dimensional aggregate and accordingly the $(001)_{ZnO}$- type plane is perpendicular to this axis. Thus, the c axis of ZnO layer coincides with the axis of preferable growth of the organic precursor crystal.

The data obtained show that there are several stages of zinc oxide growth during thermolysis of formate glicolate crystals. The basic stage is the nonoriented nucleation and growth of zinc oxide, whereas at temperatures $\sim$ 500–600 °C, oriented nucleation and growth of crystalline zinc oxide usually take place during hydrothermal and precursor synthesis [44, 50]. The reasons for this should be searched for in the peculiarities of the organic precursor decomposition. As we have established, the decomposition of the formate glicolate precursor at low temperatures (350 °C) in air gives rise to nanodispersed or X-ray-amorphous black products. Nanodispersed carbon phases and, possibly, carbon–hydrogen polymeric products impede epitaxially

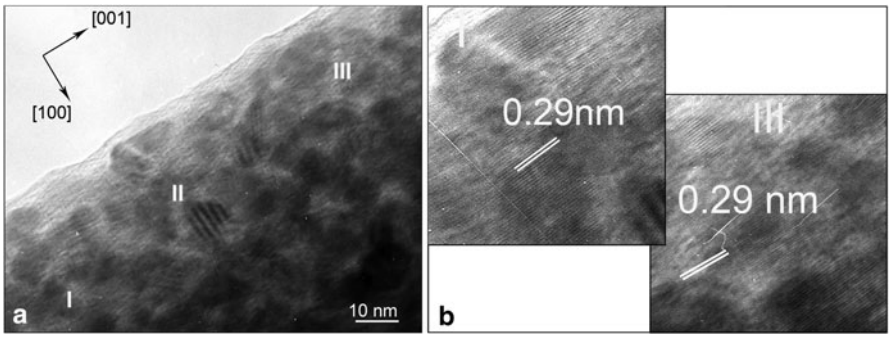

Fig. 26.10 ZnO epitaxially oriented ultrathin layer on the surface of quasi-one-dimensional Zn–O–C aggregate. **a** $(100)_{ZnO}$ lattice image of extended area. **b** $(100)_{ZnO}$ lattice image of marked regions *I* and *III*. The $[001]_{ZnO}$ direction of layer is parallel to the elongated axis of quasi-one-dimensional aggregate

oriented growth of zinc oxide. As follows from the TG curves, the process of removal of hydrocarbon products of thermolysis continues up to ~ 450°C (Fig. 26.2a). Consequently, epitaxially oriented growth of ZnO monolayer may occur only at the final stages of thermolysis. In addition, we find no signs of textured growth of ZnO nanocrystallites, but an epitaxially oriented ultrathin layer is observed on the aggregate surface. So, this fact should be obviously attributed to preferable removal of volatile carbon–hydrogen products only from one of the surfaces of the tubular aggregate.

Thus, the nanocrystalline structure of quasi-one-dimensional ZnO and Zn–O–C is due to the peculiarities of thermolysis of the formate glicolate complex and a high temperature of thermal decomposition is crucial. This conclusion is in agreement with the results of a series of works [54, 44]. The nanocrystalline structure of tubular zinc oxide was obtained by the authors [54] during thermolysis of a precursor synthesized from a solution of zinc acetate and ethylene glycol. Thermolysis of zinc hydroacetate at 300 °C results in a monocrystalline structure of the quasi-one-dimensional aggregates [44].

The nanocrystalline structure of the quasi-one-dimensional aggregates turns out to be resistant to annealing temperature variation from 450 to 550 °C and to variation of formate glicolate formation temperature in the range from 80 to 100 °C, as well as to doping of the metal sublattice of zinc oxide [62–65]. The quasi-one-dimensional aggregates sometimes have a textured microcrystalline structure (Fig. 26.11) when the storage conditions of the hygroscopic precursor Zn(Me) are not fulfilled. In this case, the quasi-one-dimensional aggregates become unstable and during ultrasonic dispersion they destroy and the individual zinc oxide nanocrystals of anisotropic shape are formed (Fig. 26.11b).

Further, let us consider the structural characteristics of Zn–O–C aggregates, which were exposed to additional isothermal annealing in air to optimize the content of free carbon. The Raman spectroscopy data (Fig. 26.12) demonstrate that with an increase

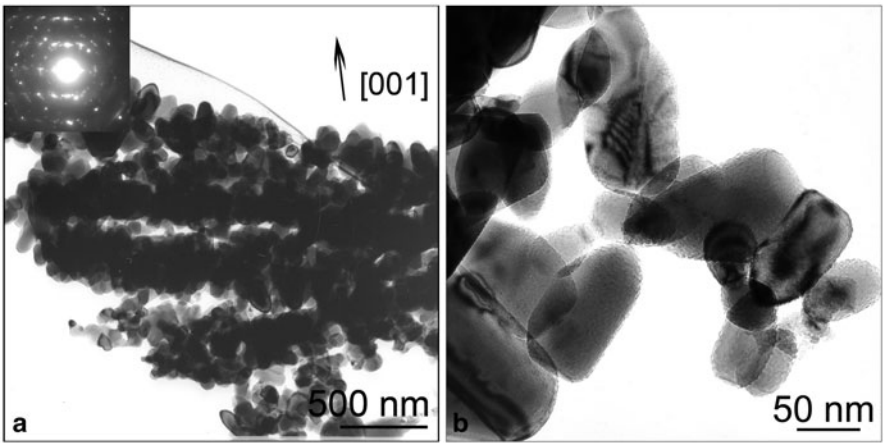

Fig. 26.11 Bright-field TEM images of $Zn_{0.95}Mn_{0.05}$ aggregates with textured structure. **a** Fragment of quasi-one-dimensional aggregate where all Zn(Mn)O crystallites are oriented along $[001]_{ZnO}$ axis. **b** Zn(Mn)O nanocrystallites of anisotropic shape elongated along $[001]_{ZnO}$

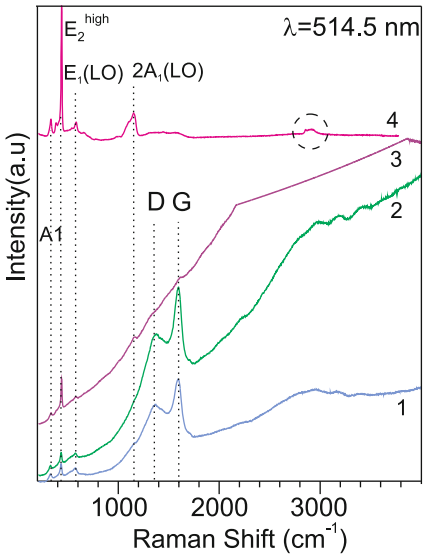

Fig. 26.12 Raman spectra of Zn–O–C aggregates in initial state (1) and annealed at temperatures: 2—300 °C, 3—400 °C, 4—550 °C. The orange–red emission line near 2900 cm^{-1} (604.7 nm) is marked by a *circle*

in the annealing temperature the intensity of the ZnO vibration bands grows and the contributions from both components "G" and "D" of amorphous carbon become smaller. In the temperature range 400–450 °C, the spectrum changes appreciably. The intensities of the "D" and "G" bands from the carbon phase decrease considerably and the background grows due to greater photoluminescence overshadow of the Raman spectrum. At 550 °C, the Raman spectrum exhibits no lines of the carbon phases, including graphene (Fig. 26.12). Both vibration bands "G" and "D" are observed

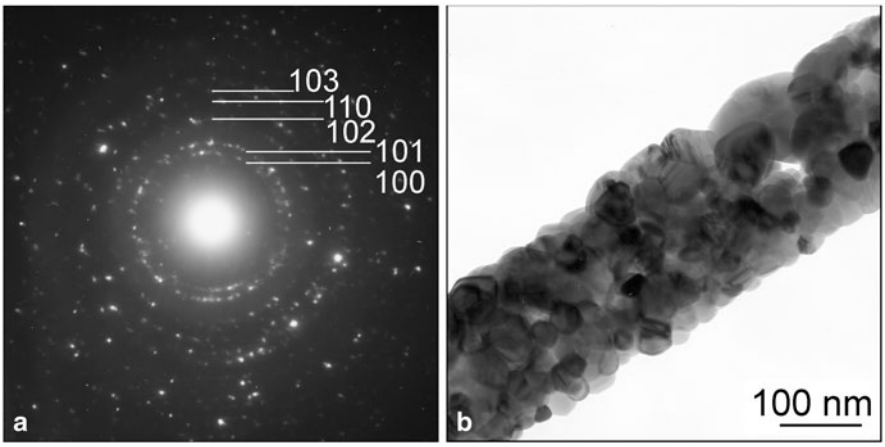

Fig. 26.13 Quasi-one-dimensional tubular C-doped ZnO aggregate with nanocrystalline structure. **a** Microdiffraction pattern. **b** Bright-field TEM image

on the Raman spectra of graphene [36, 35]. Besides, at this temperature, orange-red emission near 2900 cm^{-1} (604.7 nm) is registered distinctly in the high-frequency region. At lower temperatures, this line is shaded by photoluminecence. The orange-red emission is due to the transition between levels of charged oxygen vacancies in the gap and excited holes in the valence band of imperfect zinc oxide [66, 67]. As the temperature is raised further to 1000 °C, the emission lines disappear completely.

From the Raman spectroscopy data it is evident that the Zn–O–C aggregates annealed at 550 °C contain no carbon phases. The carbon content in these aggregates is ~ 0.15 wt. %. All carbon in the aggregates is bound and these Zn–O–C aggregates can be considered as C-doped ZnO. As follows from first-principle calculations [41, 42] and examination of electrophysical properties [68], carbon is preferably localized in the Zn sublattice. TEM data for quasi-one-dimensional C-doped ZnO agree completely with the results of Raman spectroscopy. The microdiffraction patterns and electron-microscopic images show that the quasi-one-dimensional aggregates annealed at 550 °C have a monophase nanocrystalline structure, often with tubular morphology (Fig. 26.13). The amorphous phase is absent and the sizes of C-doped ZnO crystallites are much greater than those for zinc oxide in the ZnOC:nC composites. The average crystallite sizes of the C-doped ZnO phase are 35–40 nm, which will lead to lower values of specific surface area for C-doped ZnO aggregates as compared with ZnOC:nC ones.

As we have found, the distinguishing feature of both types of quasi-one-dimensional aggregates ZnO and Zn–O–C produced by thermolysis of formate glicolate crystals is the nanocrystalline structure. The monocrystalline ultrathin ZnO layer, which is epitaxially oriented relative to the organometallic substrate, is formed only at late stages of thermolysis. Such structure of the quasi-one-dimensional aggregates results in high values of specific surface area. The high specific surface area

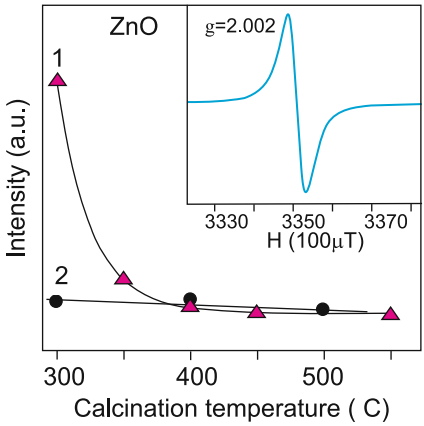

Fig. 26.14 The intensity of the EPR-signal with $g = 2.002$ versus the annealing temperature for Zn–O–C aggregates synthesized by thermolysis in He atmosphere (*1*) and for Zn–O aggregates synthesized by thermolysis in air (*2*). EPR-spectrum is shown in the *inset*

of these aggregates should be accompanied by high concentrations of native point defects of the oxide surface, which are very important for photocatalytic properties. In the next paragraph, we shall discuss our results of EPR spectroscopy study of native ZnO defects in quasi-one-dimensional aggregates.

26.3.2 Native ZnO Defects: EPR Spectroscopy

As regards photocatalytic properties, of particular interest is the examination of such native point defects in ZnO as vacancies or interstitial atoms. These defects serve as additional oxidizing centers or sorption centers on the surface [8–10] promoting photocatalytic reactions. Moreover, native ZnO point defects, including surface defects, contribute extra energy levels in the band gap [18–19]. As a result, the photocatalytic activity can increase and photoresponse of catalyst can be extended to visible light. Singly charged point defects belong to this type of defects.

The EPR spectroscopy method was used to study singly charged point defects in quasi-one-dimensional aggregates ZnO and Zn–O–C [58]. The EPR spectra of the ZnO samples produced during thermolysis both in inert atmosphere and in air contain a narrow symmetrical line of Lorentzian shape ($\Delta H = 4.5 \pm 0.2$ G). The value of the *g*-factor is close to the spin-only value and is equal to 2.002 ± 0.001. The width and position of this signal are constant and depend neither on the method of precursor decomposition nor on the subsequent heat treatment conditions. Figure 26.14 presents the relative intensity of the spectral lines versus the temperature of annealing in air. The most intensive signal was registered in the spectrum of the product of thermolysis in helium (inset in Fig. 26.14). During subsequent annealing of this sample at temperatures 300–600 °C the signal decreases and after annealing at 700 °C it disappears completely. A similar dependence is observed also for the ZnO sample produced by thermolysis in air.

The EPR signal with the g-factor equal to 2.00 is usually observed on the spectra of photoexcited ZnO monocrystals [69] and powders subjected to mechanical treatment [70]. In the absence of excitation, a signal with the g-factor of 1.96 is usually registered in the zinc oxide at room temperature. The information as to which type of defects in ZnO these signals may belong to was very contradictory at first [71]. The high-field EPR signal with $g = 1.96$ was associated with singly charged vacancies V_O^+ [72]. In later works, this signal was assigned to electrons on donor energy levels due to impurities, while the low-field EPR signal with $g = 2.00$ was attributed to oxygen vacancies [19]. In some works, the EPR signal with $g = 2.00$ is also ascribed to interstitial oxygen ions O_i^- [73] and singly charged zinc vacancies V_{Zn}^-[74]. At present, numerous theoretical and experimental studies yielded a great amount of information showing that this line is referred to singly charged oxygen vacancies [18, 19].

The observed dependence between the EPR signal intensity and the composition of the gaseous medium during annealing indicates that the line with $g = 2.002$ belongs exactly to oxygen vacancy V_O^+. The most oxygen-deficient product is formed during decomposition of the precursor in inert atmosphere. Besides, no signals were observed in the EPR spectra of ZnO used for sample preparation. Therefore, this line cannot be attributed to impurities in the initial reagent. The number of paramagnetic centers V_O^+ in 1 mol of zinc oxide produced by thermolysis of formate glicolate in helium is 1.06×10^{20} particles. Upon annealing in air, the degree of imperfection in the anionic sublattice decreases, which manifests itself in the reduction of the EPR signal intensity.

According to the first-principle calculation results, the singly charged vacancies V_O^+in ZnO have a high formation energy and are not stable under thermodynamic equilibrium conditions [19]. To produce them in the amount sufficient for detection by the EPR method, the system should be excited for example by UV radiation. We attribute the existence of stable V_O^+ vacancies in quasi-one-dimensional aggregates ZnO and Zn–O–C to the stabilizing effect of the nonequilibrium imperfect surface formed as a result of thermolysis. As was noted above, high-temperature annealing (above 700 °C) results in the absence of the EPR signal that takes place due to the formation of a coarse crystalline structure and healing of point defects.

The high concentration of singly charged oxygen vacancies stabilized on the surface of ZnO and Zn–O–C aggregates, as well as the presence of dissolved carbon should be accompanied by the appearance of extra energy levels in the band gap [40–41]. So, in the Raman spectra we observed orange-red emission associated with transitions between the energy level of charged oxygen vacancy and the energy level of excited holes in the valence band of the C-doped ZnO (Fig. 26.12). Therefore, the optical characteristics of these materials will also differ appreciably from those of reference zinc oxide.

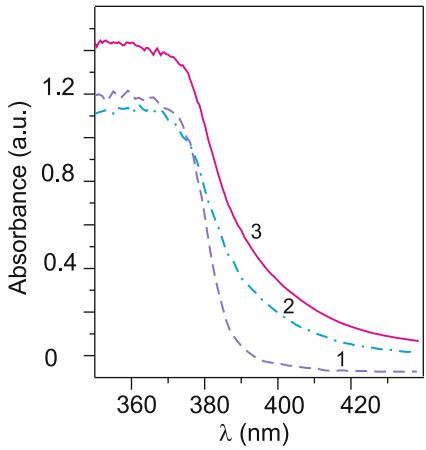

Fig. 26.15 UV-visible spectra of the reference ZnO (*1*), quasi-one-dimensional ZnO aggregates (*2*), and quasi-one-dimensional C-doped ZnO aggregates (*3*)

26.4 Optical Properties of ZnO, ZnO:nC Composites, and C-doped ZnO

The optical absorption spectrum in the UV and visible regions for quasi-one-dimensional ZnO is depicted in Fig. 26.15. The absorption spectra of C-doped ZnO aggregates and of reference zinc oxide are given for comparison. Noteworthy is the shift of the optical absorption edge to the lower-energy region (red shift) for nanocrystalline ZnO and C-doped ZnO with tubular quasi-one-dimensional morphology. For nanocrystalline phases ZnO and C-doped ZnO, on the contrary, a blue shift of the optical absorption edge could be expected, which is due to quantum size effects and phonon confinement model [75–79]. However, the effect of these factors on the optical band gap width in ZnO becomes most evident in materials with individual crystallite sizes not larger than 10 nm [76–78]. As was shown above, the average crystallite size of ZnO synthesized by the authors is 15–20 nm, while that for C-doped ZnO phase annealed at 550 °C is 35 nm. In this case, the blue-shift effect is not pronounced. The observed red shift of the optical absorption edge is the effect associated first of all with the point structural defects detected in this study, namely, with singly charged oxygen vacancies V_O^+. These defects are not found in standard sample ZnO. The red shift correlates with the appearance of optical density at energies lower than the optical absorption edge of ZnO owing to extra energy levels in the band gap. These energy levels are due to singly charged vacancies V_O^+ [18–19]. In the presence of carbon in ZnO phase, the red shift is even more noticeable than for quasi-one-dimensional ZnO. According to EPR spectroscopy data, the concentrations of singly charged vacancies in ZnO and C-doped ZnO are similar, but for quasi-one-dimensional C-ZnO this concentration is slightly smaller. An additional red shift to the low-energy region can emerge owing to energy levels of dissolved carbon in the band gap. These energy levels, as evidenced by the first-principle calculations, arise for carbon-doped zinc oxide [40–42].

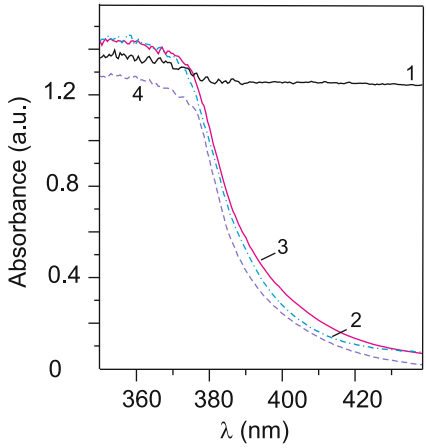

Fig. 26.16 UV-visible spectra for the quasi-one-dimensional Zn–O–C aggregates synthesized by thermolysis in He atmosphere (*1*) and then annealed at 400 °C (*2*), 550 °C (*3*), and 650 °C (*4*)

Let us consider further how the optical absorption characteristics for Zn–O–C aggregates change depending on the annealing conditions. The optical absorption spectra of Zn–O–C aggregates synthesized by thermolysis in helium atmosphere and annealed at different temperatures, 400, 550, and 650 °C, are displayed in Fig. 26.16. The spectrum of quasi-one-dimensional Zn–O–C produced by thermolysis in helium atmosphere exhibits no optical absorption edge of zinc oxide. The samples annealed in air up to 300 °C have analogous absorption spectra. The intrinsic optical properties of the oxide phase are shaded by the presence of a large amount of amorphous carbon. The spectra of the samples annealed at 400 °C contain an optical absorption edge of ZnO in the UV region. When the annealing temperature is raised to 550 °C, the absorption edge exhibits a red shift to the visible region, which is indicative of additional optical density at energies lower than that of the fundamental absorption edge of ZnO. The Raman spectroscopy data (Fig. 26.12) show that at these temperatures the C-doped ZnO single phase is formed and the carbon phases disappear. Finally, at the annealing temperature of 650 °C, the absorption edge shifts again to the UV region. The content of bound carbon in these aggregates is minimal and amounts to 0.12 wt. % as evidenced by the chemical analysis data. The concentration of singly charged oxygen vacancies determined by EPR spectroscopy also decreases.

As expected, the examination of optical absorption of quasi-one-dimensional aggregates ZnO and C-doped ZnO with nanocrystalline structure reveals that the optical absorption edges shift to the low-energy region (red shift), which correlates with the high concentration of singly charged oxygen vacancies and dissolved carbon. The aggregates ZnO and C-doped ZnO with nanocrystalline structure and modified optical characteristics exhibiting a red shift of the optical absorption edge are obviously of interest as photocatalysts. The results of photocatalytic tests of the synthesized quasi-one-dimensional aggregates ZnO and Zn–O–C are reported in the next paragraph.

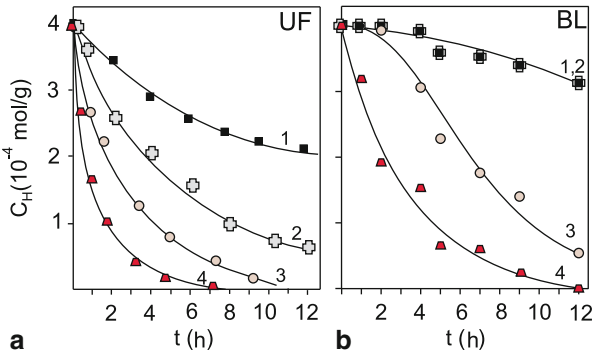

Fig. 26.17 The kinetics of catalytic oxidation of hydroquinone under ultraviolet (**a**) and visible (**b**) light without catalyst (*1*) and with catalysts: the reference ZnO (*2*), quasi-one-dimensional ZnO (*3*), and quasi-one-dimensional C-doped ZnO (*4*)

26.5 Photocatalytic Activity of ZnO and Zn–O–C Quasi-One-Dimensional Aggregates

The photocatalytic properties of the synthesized quasi-one-dimensional aggregates Zn–O and Zn–O–C have been examined using hydroquinone oxidation reaction in water as an example. The kinetic dependences of hydroquinone oxidation under UV and blue light are displayed in Fig. 26.17. It is seen that the hydroquinone oxidation rate increases in the series of reactions: (1) without catalyst, (2) with ZnO reference catalyst, (3) with ZnO quasi-one-dimensional catalyst, and (4) with C-doped ZnO quasi-one-dimensional catalyst. The growth of the photocatalytic activity completely agrees with the tendency of optical-gap-width reduction in the considered series of catalysts (Fig. 26.15). Earlier, we observed an analogous correlation for metal-doped quasi-one-dimensional aggregates Zn(Me)O [65]. We ascribe the maximal photocatalytic activity of C-doped ZnO to electron-energy spectrum restructuring owing to carbon impurity states in the band gap. As a result, the optical gap of C-doped ZnO becomes smaller as compared with that of ZnO. In some works, the catalytic activity of Zn–O–C powders is increased by lowering the recombination rate of photoexcited electron–hole pairs owing to thin graphite-like or graphene layers coating ZnO particles [39]. The increase in the photocatalytic activity, which we observed for quasi-one-dimensional aggregates Zn–O–C annealed at 550 °C, cannot be connected with this effect. The absence of carbon phases (even in the form of graphene monolayers) is confirmed by Raman (Fig. 26.12) and optical absorption spectra (Fig. 26.16).

As follows from the obtained results, the variation of the energy spectrum of electrons due to carbon impurity in band gap has a more essential effect on the photocatalytic activity of C-doped ZnO than the reduction of the specific surface area. As was shown above, the quasi-one-dimensional C-doped ZnO aggregates have crystallites of larger sizes as well as smaller concentrations of charged oxygen vacancies than quasi-one-dimensional aggregates ZnO.

Figure 26.18 shows the degree of conversion for the reaction of hydroquinone oxidation with the use of quasi-one-dimensional catalysts Zn–O–C annealed at different temperatures. The dependence has an extreme character with a maximum at 500–550 °C, where the degree of conversion is 90–91 %. At these temperatures, C-doped

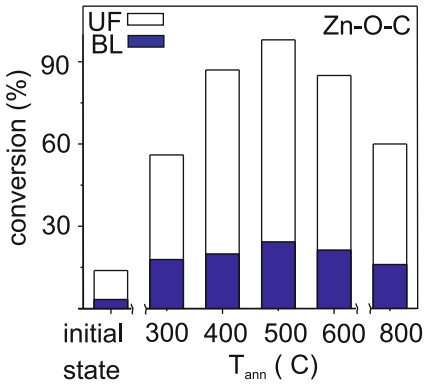

Fig. 26.18 Oxidative conversion of hydroquinone with Zn–O–C catalysts versus the annealing temperature of Zn–O–C aggregates

ZnO phase with carbon concentration of 0.15 wt. % is formed. As the annealing temperature is raised above 600 °C, the concentration of carbon impurities and singly charged vacancies in the C–ZnO aggregates lowers. In the electron-energy spectrum, the contributions from the carbon impurity states and singly charged vacancies states decrease and a blue shift of the optical absorption edge is observed. The specific surface area of the quasi-one-dimensional aggregates becomes smaller too. As a result, at a temperature higher than 600 °C the catalytic activity drops abruptly.

In conclusion, the developed method of precursor synthesis from formate glicolate complexes of zinc allows obtaining quasi-one-dimensional aggregates ZnO and Zn–O–C with the nanocrystalline structure of zinc oxide and with a high concentration of native structural defects—singly charged oxygen vacancies. The composite structure of Zn–O–C aggregates (ZnO in amorphous carbon) can be transferred to the C-doped ZnOC phase as a result of thermal annealing. Temperature treatment of the composites ZnO:nC provides optimal values of the specific surface area and restructuring of the electron-energy spectrum with reduction of the optical gap width owing to the presence of singly charged oxygen vacancies and dissolved carbon in the zinc oxide lattice. The photocatalytic activity grows in the series: the reference ZnO, quasi-one-dimensional aggregates ZnO, and quasi-one-dimensional C-doped ZnO aggregates.

Acknowledgments This work was supported by the Russian Foundation for Basic Research (project 12−03-00453-a). The authors are also grateful to the Ural Branch of RAS for the support of this study through the regional programs (12-U-3−1009).

References

1. French SA, Sokol AA, Bromley ST, Richard C et al (2001) From CO_2 to methanol by hybrid QM/MM embedding. Angew Chem Int Ed Engl 40:4437–4440
2. Byrappa K, Subramani AK, Ananda S et al (2006) Photocatalytic degradation of rhodamine B dye using hydrothermally synthesized ZnO. Bull Mater Sci 29:433–438

3. Chen C, Liu J, Liu P, Yu B (2011) Investigation of photocatalytic degragation of methyl orange by using nano-sized ZnO catalysts. Adv Chem Eng Sci 1:9–14. doi:10.4236/aces.2011.11.11002
4. Anandan S, Vinu A, Mori T, Gokulakrishnan N, Srinivasu P et al (2007) Photocatalytic degradation of 2,4,6-trichlorophenol using lanthanum doped ZnO in aqueous suspension. Catal Commun 8:1377–1382. doi:10.1016/j.catcom.2006.12.001
5. Yassıtepe E, Yatmaz HC, Öztürk C et al (2008) Photocatalytic efficiency of ZnO plates in degradation of Azo dye solutions. J Photochem Photobiol A 198(1):1–6. doi:10.1016/j.jphotochem.2008.02.007
6. Yu JG, Yu XX (2008) Hydrothermal synthesis and photocatalytic activity of zinc oxide hollow spheres. Environ Sci Technol 42:4902–4907. doi:10.1021/es800036n
7. Fox MA, Dubay MT (1993) Heterogeneous photocatalysis. Chem Rev 93:341–357
8. Wang J, Liu P, Fu X et al (2009) Relationship between oxygen defects and the photocatalytic property of ZnO nanocrystals in nafion membranes. Langmuir 25:1218–1223
9. Strunk J, Kähler K, Xia X, Muhler M (2009) The surface chemistry of ZnO nanoparticles applied as heterogeneous catalysts in methanol synthesis. Surf Sci 603:1776–1783
10. Polarz S, Strunk J, Ischenko V, Maurits WE et al (2006) On the role of oxygen defects in the catalytic performance of zinc oxide. Angew Chem Int Ed Engl 45:2965–2969
11. Fan Z, Lu JG (2005) Zinc oxide nanostructures: synthesis and properties. J Nanosci Nanotech 5(10):1561–1573
12. Shulin JI, Changhui Y (2008) Synthesis, growth mechanism, and applications of zinc oxide nanomaterials. J Mater Sci Technol 24(4):457–472
13. Wang X, Song J, Wang ZL (2007) Nanowire and nanobelt arrays of zinc oxide from synthesis to properties and to novel devices. J Mater Res 17:711–720
14. Suzuki K, Inoguchi M, Kageyama K et al (2009) Well-crystallized zinc oxide quantum dots with narrow size distribution. J Nanopart Res 11:1349–1360. doi:10.1007/s11051- 008-9521x
15. Li S, Zhang X, Yan B, Yu T (2009) Growth mechanism and diameter control of well-aligned small-diameter ZnO nanowire arrays synthesized by a catalyst-free thermal evaporation method. Nanotechnology. doi:10.1088/0957-4484/20/49/495604
16. Kawano T, Uchiyama H, Kiguchi T et al (2009) Epitaxial growth of winding ZnO nanowires on a single-crystalline substrate. J Ceram Soc Jpn 117(3):255–257
17. Sakamoto N, Ishizuka S, Wakiya N, Suzuki H (2009) Shape controlled ZnO nanoparticle prepared by microwave irradiation method. J Ceram Soc Jpn 117(9):961–963
18. Kohan AF, Ceder G, Morgan D, Van de Walle CG (2000) First-principles study of native point defects in ZnO. Phys Rev B 61:15019–15027
19. Janotti A, Van de Walle CG (2007) Native point defects in ZnO. Phys Rev B 76:165202–165224
20. Ansari SA, KhanMM KalathilSh (2013) Oxygen vacancy induced band gap narrowing of ZnO. Nanoscale 5:9238–9246
21. Henglein A (1989) Small-particle research: physicochemical properties of extremely small colloidal metal and semiconductor particles. Chem Rev 89:1861–1873
22. Zhou G, Deng J (2007) Preparation and photocatalytic performance of Ag/ZnO nanocomposites. Mater Sci Semicond Process 10:90–96
23. Xiao Q, Zhang J, Xiao C, Tan X (2007) Photocatalytic decolorization of methylene blue over $Zn_{1-x}Co_xO$ under visible light irradiation. Mater Sci Eng B 142:121–125
24. Ekambaram S, Iikubo Y, Kudo A (2007) Combustion synthesis and photocatalytic properties of transition metal-incorporated ZnO. J Alloy Compd 433:237–240
25. Abdollahi Y, Abdullah AH, Zainal Z, Yusof NA (2011) Synthesis and characterization of manganese doped ZnO nanoparticles. Int J Basic Appl Sci 11(4):62–69
26. Slama R, Ghribi F, Houas A et al (2011) Visible photocatalytic properties of vanadium doped zinc oxide aerogel nanopowder. Thin Solid Films 519:5792–5795
27. Krasil'nikov VN, Gyrdasova OI, Buldakova LY, Yanchenko MY (2011) Synthesis and photocatalytic properties of low-dimensional cobalt-doped zinc oxide with different crystal shapes. Russ J Inorg Chem 56(2):145–151

28. Zhang D, Zeng F (2012) Visible light-activated cadmium-doped ZnO nanostructured photocatalyst for the treatment of methylene blue dye. J Mater Sci 47:2155–2161
29. Li L, Wang W, Liu H, Liu X, Song Q, Ren S (2009) First principles calculations of electronic band structure and optical properties of Cr-doped ZnO. J Phys Chem C 113:8460–8464
30. Sobana N, Swaminathan M (2007) Combination effect of ZnO and activated carbon for solar assisted photocatalytic degradation of Direct Blue 53. Sol Energy Mater Sol Cells 91:727–734
31. Byrappa K, Subramani AK, Ananda S et al (2006) Impregnation of ZnO onto activated carbon under hydrothermal conditions and its photocatalytic properties. J Mater Sci 41:1355–1362
32. Sobana N, Muruganandam M, Swaminathan M (2008) Characterization of Ac-ZnO catalyst and its photocatalytic activity on 4-acetylphenol degradation. Catal Commun 9:262–268
33. Pulido Melian E, Gonzalez Diaz O, Dona Rodriguez JM et al (2009) ZnO activation by using activated carbon as a support: characterization and photoreactivity. Appl Catal A Gen 364: 174–181
34. Yong-Jin HT, Worsley MA, Baumann TF, Satcher JH (2011) Synthesis of ZnO coated activated carbon aerogel by simple sol-gel route. J Mater Chem 21:330–333
35. Liu X, Pan L, Zhao Q, Lv T, Zhu G et al (2012) UV-assisted photocatalytic synthesis of ZnO-reduced graphene oxide composites with enhanced photocatalytic activity in reduction of Cr(IV). Chem Eng J 183:238–243
36. Liu Y, Hu Y, Zhou M, Qian H, Hu X (2012) Microwave-assisted non-aqueous route to deposit well-dispersed ZnO nanocrystals on reduced graphene oxide sheets with improved photoactivity for the decolorization of dyes under visible light. Appl Catal B Environ 125:425–431
37. Li X, Wang Q, Zhao Y, Wu W, Chen J, Meng H (2013) Green synthesis and photocatalytic performances for ZnO-reduced graphene oxide nanocomposites. J Colloid Interface Sci 411:69–75
38. Yu H-F, Chou H-Y (2013) Preparation and characterization of dispersive carbon-coupling ZnO photocatalysts. Powder Technol 233:201–207
39. Fu H, Xu T, Zhu S, Zhu Y (2008) Photocorrosion inhibition and enhancement of photocatalytic activity for ZnO via hybridization with C60. Environ Sci Technol 42:8064–8069
40. Kim D, Hong J (2010) Magnetic property of carbon doped ZnO and X-ray magnetic circular dichroism: a first principles study. J Korean Phys Soc 56(5):1446–1450
41. Sanjeev KN, Markus EG, Sung S et al (2012) Anisotropic ferromagnetism in carbon-doped zinc oxide from first-principles studies. Phys Rev B. doi:10.1103/PhysRevB.86.054441
42. Mishra DK, Mohapatra J, Sharma MK, Chattarjee R (2013) Carbon doped ZnO: synthesis, characterization and interpretation. J Magn Magn Mater 329:146–152
43. Deng Y, Wang G, Li N, Guo L (2009) Synthesis and red-shift photoluminescence of single-crystalline ZnO nanowires. J Lumin 129:55–58
44. Lin C-C, Li Y-Y (2009) Synthesis nanowires by thermal decomposition of zinc acetate dehydrate. Mater Chem Phys 113:334–337
45. Zhang Y, Zhu F, Zhang J, Xia L (2008) Converting layered zinc acetate nanobelts to one-dimensional structured ZnO nanoparticle aggregates and their photocatalytic activity. Nanoscale Res Lett 3:201–204
46. Vayssieres L, Keis K, Hagfeldt A, Lindquist S-E (2001) Three-dimensional array of highly oriented crystalline microtubes. Chem Mater 13(2):4395–4398
47. Shen L, Bao N, Yanagisawa K et al (2007) Organic molecule-assisted hydrothermal self-assembly of sized-controlled tubular ZnO nanostructures. J Phys Chem C 111:7280–7287
48. Yu Q, Fu W, Yu C, Yang H et al (2007) Fabrication and optical properties of large-scale ZnO nanotube budles via a simple solution route. J Phys Chem C 111:17521–17526
49. Brahma S, Rao KJ, Srinivasarao S (2010) Rapid growth of nanotubes and nanorods of wurtzite ZnO through microwave-radiation of metalorganic complex of zinc and a surfactant in solution. Bull Mater Sci 33(2):89–95
50. Liu J, Guo Z, Meng F et al (2009) Novel porous single-crystalline ZnO nanosheets fabricated by annealing $ZnS(en)_{0.5}$ (en = ethylenediamine) precursor. Application in a gas sensor for indoor air contaminant detection. Nanotechnology. doi:10.1088/0957-4484/20/12/125501

51. Zhu J, Liu H, Liu X, Wang X et al (2009) A convenient method for preparing shape-controlled ZnO nanocrystals in a polyol/water mixture system without surfactants. J Wuhan Univ Technol-Mater Sci Ed 24(1):30–33. doi:10.1007/s111595 - 009-1030-y
52. Zhang J, Sun L, Liao C, Yan C (2002) A simple route towards tubular ZnO. Chem Commun. doi:10.1039/B108863G
53. Li L, Pan S, Dou X, Zhu Y, Huang X et al (2007) Direct electrodeposition of ZnO nanotube arrays in anodic alumina membranes. J Phys Chem C 111:7288–7291
54. Zhang J, Zhu P, Li Z, Chen J et al (2008) Fabrication of polycrystalline tubular ZnO via a modified ultrasonically assisted two-step polyol process and characterization of the nanotubes. Nanotechnology. doi:10.1088/0957-4484/19/16/165605
55. Krasil'nikov VN, Shtin AP, Gyrdasova OI, Polyakov EV, Shveikin GP (2008) Synthesis and properties of titanium glycolate $Ti(OCH_2CH2O)_2$. Russ J Inorg Chem 53(7):1065–1069
56. Krasil'nikov VN, Shtin AP, Gyrdasova OI, Baklanova IV, Perelyaeva LA (2008) The titanium and vanadyl glycolates as precursors of titanium and vanadium oxide for high dispersed and nanosized extended objects. Nanotechnol Russ 3(1–2):109–113
57. Jiang X, Wang Y, Herricks T, Xia Y (2004) Ethylene-glycol-mediated synthesis of metal oxide nanowires. J Mater Chem 14:695–703
58. Melkozerova MA, Krasil'nikov VN, Gyrdasova OI, Zabolotskaya EV, Shalaeva EV, Samigullina RF (2012) Nature of defects in nanocrystalline zinc oxide with particles of tubular morphology. Theor Exp Chem 48(3):149–152
59. Yang B, Kumar A, Upia N, Feng P, Katiyar RS (2010) Low-temperature synthesis and Raman scattering of Mn-doped ZnO nanopowders. J Raman Spectrosc 41:88–92
60. Ferrari AC, Robertson J (2001) Resonant Raman spectroscopy of disordered, amorphous, and diamondlike carbon. Phys Rev B. doi:10.1103/PhysRevB.64.075414
61. Chu PK, Li L (2006) Characterization of amorphous and nanocrystalline carbon films. Mater Chem Phys 96:253–277
62. Gysdasova OI, Krasil'nikov VN, Shalaeva EV, Buldakova LY, Yanchenko MY, Bamburov VG (2010) Synthesis, microstructure, and photocatalytic characteristic of quasi-one-dimensional zinc oxide doped with d-elements. Dokl Chem 434(1):211–213
63. Gyrdasova OI, Krasilnikov VN, Shalaeva EV, Kuznetsov MV, Tyutynnik AP (2012) Synthesis and structure of quasi-one-dimensional zinc oxide doped with manganese. Russ J Inorg Chem 57(1):72–78
64. Gyrdasova OI, Krasil'nikov VN, Melkozerova MA, Shalaeva EV, Zabolotskaya EV et al (2012) Synthesis, microstructure, and native defects of photoactive $Zn_{1-x}Cu_xO$ solid solutions ($0 \leq x \leq 0.1$) with tubular aggregates. Dokl Chem 447:258–261
65. Melkozerova MA, Krasil'nikov VN, Gyrdasova OI, Shalaeva EV, Baklanova IV et al (2013) Effect of doping with 3d elements (Co, Ni, Cu) on the intrinsic defect structure and photocatalytic properties of nanostructured ZnO with tubular morphology of aggregates. Phys Solid State 55(12):2459–2465
66. Kang HS, Kim JW, Lim SH, Chang HW, Kim GH et al (2006) Investigation on the variation of green, yellow, and orange emission properties of ZnO thin film. Superlattices Microstruct 39:193–201
67. Iza DC, Muoz-Rojas D, Quanxi J, Swartzentruber B, MacManus-Driscoll JL (2012) Tunning of defects in ZnO nanorod arrays used in bulk heterojunction solar cells. Nanoscale Res Lett. doi:10.1186/1556-276X-7- 655
68. Park JW, Kim DH, Choi S-H, Lee M, Lim D (2010) The role of carbon in ZnO. J Korean Phys Soc 57(6):1482–1485
69. Vlasenko LS (2009) Point defects in ZnO: electron paramagnetic resonance study. Phys B 404:4774–4778
70. Jakes P, Erdem E (2011) Finite size effects in ZnO nanoparticles: an electron paramagnetic resonance (EPR) analysis. Phys Status Solidi RRL 5(2):56–58
71. Vlasenko LS (2010) Magnetic resonance studies of intrinsic defects in ZnO: oxygen vacancy. Appl Magn Reson 39:103–111

72. Kasai PH (1963) Electron spin resonance studies of donor and acceptors in ZnO. Phys Rev 130(3):989–995
73. Pöppl A, Völkel G (1991) ESR and photo-ESR investigations of zinc vacancies and interstitial oxygen ions in undoped ZnO ceramics. Phys Status Solidi A 125:571–581
74. Galland D, Herve A (1974) Temperature dependence of the ESR spectrum of the zinc vacancy in ZnO. Solid State Commun 14(10):953–956
75. Ekimov AI, Efros AL, Onushchenko AA (1985) Quantum size effect in semiconductor microcrystals. Solid State Commun 56:921–924
76. Lin K-F, Cheng H-M, Hsu H-C, Lin L-J, Hsieh W-F (2005) Band gap variation of size-controlled ZnO quantum dots synthesized by sol-gel method. Chem Phys Lett 409:208–211
77. Savarimuthu PA, Lee LI, Kim JK (2007) Tuning optical band gap of vertically aligned ZnO nanowire arrays grown by homoepitaxial electrodeposition. Appl Phys Lett 90:103107–103109
78. Lu JG, Ye ZZ, Zhang YZ, Liang QL, Fujita S et al (2006) Self-assembled ZnO quantum dots with tunable optical properties. Appl Phys Lett 89:023122–023124
79. Soosen SM, Koshy J, Chandran A, George KC (2010) Optical phonon confinement in ZnO nanorods and nanotubes. Indian J Pure Appl Phys 48:703–708

Chapter 27
Two-Dimensional Spin-FET Transistor

A. Boudine, L. Kalla, K. Benhizia, M. Zaabat and A. Benaboud

27.1 Introduction

The electrons are not only characterized by their electrical charge but also by their spin magnetic moment. Up to the late 1990s, the electronics had virtually ignored the electron spin (except Pauli's law that two electrons cannot be in the same energy state with equal spin orientation). Since then, spin electronics, or magneto-electronics [1], has grown increasingly and rapidly. In this section, we will see how it is possible to introduce the concepts of magneto-electronic components in a semiconductor. An immediate benefit of this approach is a much reduced switching voltage. Spin–orbit (SO) interactions in technologically important semiconductors are typically weak and weakly sensitive to external potentials [2]. As a result, a large swing in the gate potential (few volts) is often required to turn a short channel spin-polarized field effect transistor (spin-FET) of the traditional type on or off [1]. That results in considerable dynamic energy dissipation during switching. In contrast, our strategy is to modulate transmission resonances (Ramsauer and Fano-type resonances) that occur in the channel of traditional spin-FETs [3, 4] with a gate potential. Since the resonance widths (in energy) are very small, a few millivolts change in the gate potential can take the device from on-resonance to off-resonance and switch it on or off. This approach results in a very small switching voltage (a few millivolts instead of the few volts required in traditional spin-FETs) resulting in much reduced dynamic energy dissipation [4].

A. Boudine (✉) · L. Kalla · M. Zaabat · A. Benaboud
Active Devices and Materials Laboratory, Faculty of Exact Sciences and Nature and Life Sciences, Larbi Ben M'hidi University, 04000 Oum El Bouaghi, Algeria
e-mail: a_boudine@hotmail.com

K. Benhizia
Université Constantine 1, Route Ain El Bey, 25017 Constantine, Algérie

O. Fesenko, L. Yatsenko (eds.), *Nanocomposites, Nanophotonics, Nanobiotechnology, and Applications,* Springer Proceedings in Physics 156,
DOI 10.1007/978-3-319-06611-0_27,

27.2 Spintronic

The spin electronics, or "spintronics" [2] is a new research theme has been booming since the late 1980s. The first structures studied in this area are made of ferromagnetic metal multilayers, separated by insulators or "tunnels" or by nonmagnetic metal films. Their operating principles are related to a property of ferromagnetic metals on the spin of electrons: They inject or collect preferentially carriers whose spin is polarized along the direction of their magnetic moment. Such devices are already used industrially as magnetic field sensors for read heads of hard disks or are expected to be soon in the case of magnetic random access memory.

During the past 4 years, groups working in the field of semiconductor components were also interested in properties related to the spin of the electron [5]. Indeed, recent studies have shown that it is possible to act on the spin of charge carriers and use this quantity to modify the electrical and optical structures in semiconductors.

27.2.1 Spintronics in Semiconductors (Spin-FET)

In semiconductors, the control of the spin of the carriers, in addition to their charges, may give rise to a new generation of electronic devices [6]. This idea was born of a new concept device that can benefit from the manipulation of spin to create a new feature. It is the case of the Datta and Das transistor, whose its structure will be briefly described [7].

This concept was proposed in 1990 and named spin-FET "rotation spin transistor." This device looks at first sight like the classical field-effect transistor, as illustrated in Fig. 27.1, and has a current source, a drain, and a channel with a conductance controllable via a gate voltage Vg; however, comparison stops there. The spin transistor is based on spin-selective contacts, that is to say the capability of injecting or collecting a given spin orientation. The injection and the collection of spin-polarized current is carried by ferromagnetic electrodes (Fe, for example).

To modulate the drain current, Datta and Das proposed to control the rotation of the "bundle" of spin in the channel using the SO Rashba coupling to be a function of the voltage applied to the gate [3]. The drain current reaches a maximum value when the spin orientation is parallel to the magnetization of the electrodes and injection manifold. It reaches a minimum value when they are opposed. This concept also implies a transistor-coherent transmission, i.e., without loss of spin between the injector (source) and collector (drain). Under this proposal, the channel where the propagation of spin takes place must be a two-dimensional electron gas system (2 DEG) to take advantage of the high mobility allowing a coherent propagation. This 2-DEG channel can be obtained in a transistor structure with modulation doping (MODFET)-type InGaAs/InAlAs [8].

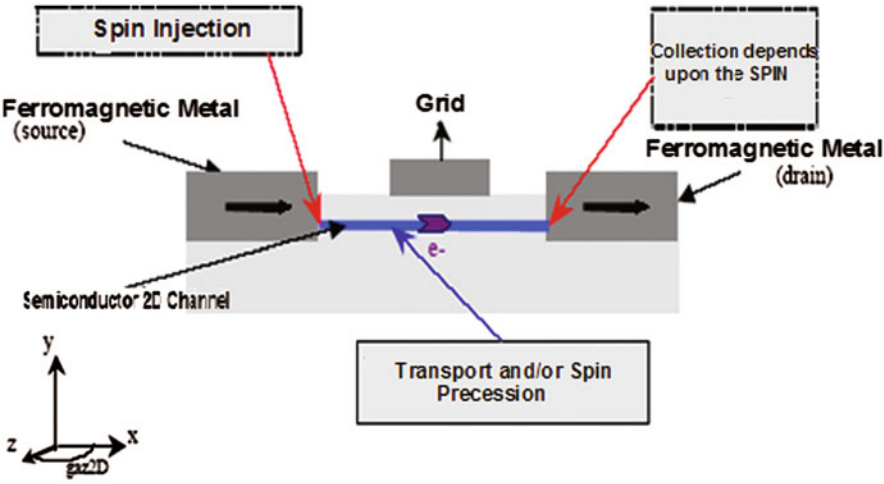

Fig. 27.1 Schematic diagram of the transistor with spin precession (spin-FET)

27.3 Quantum Wire Model

27.3.1 Drain Current Variations

The expression of the drain current in a spin-FET in our model is given by the following equation:

$$I_D = q\frac{E_y}{V_C}\mu(E_y)E_x\frac{1+P_0\cos\left(E_yL/V_R\right)}{1+P_0}, \tag{27.1}$$

where the parameter V_C, equal to $q/(2\varepsilon_0\varepsilon_{SC}W)$, is uniform to the voltage. It may be noted that the term E_y/V_C in this expression represents the density in the grid controlled by accumulated electrons in the channel. The parameter μ denotes the electron mobility and thus μE_x represents the speed of electrons. The mobility μ varies with the intensity of confinement in the channel. It means with the field E_y, the ratio $(1+P_0\cos\left(E_yL/V_R\right))/(1+P_0)$ reflects the analysis of spin at the drain. This ratio varies periodically, with period $E_{y0} = 2\pi V_R/L$. Its amplitude depends on the spin polarization P_0. We initially consider the mobility constant and we study the derivative g of I_D/μ function of E_y:

$$g(u) = \frac{qE_X}{V_C}\frac{1+P_0(\cos\left(u\right)-u\sin\left(u\right))}{1+P_0}, \tag{27.2}$$

where u is a dimensionless parameter equal to E_yL/V_R; except in V_C, the function $g(u)$ does not depend on parameters characterizing the quantum wire transistor. The variations of g give the information on the transconductance of the spin-FET.

27.4 Quantum Two-Dimensional Model

In the ideal situation where spin (or its projection along a direction) is conserved, spin current is simply defined as the difference between the currents of electrons in the two spin states. This concept has served well in early studies of spin-dependent transport effects in metals.

27.4.1 Theoretical Approach

In semiconductor spintronic structures, where spin is carried by electrons and/or holes, the spin dynamics is controlled by magnetic interactions. Some of these are surveyed below.

27.4.1.1 Interaction with an External Magnetic Field

An external magnetic field $\vec{B}$ exerts a torque on a magnetic dipole and the magnetic potential energy is given by the Zeeman term

$$U = \frac{g^* \mu_B}{2} \vec{\sigma} \cdot \vec{B}, \tag{27.3}$$

where g^* is the effective g-factor and $\vec{\sigma}$ represents a vector of the Pauli spin matrices, used in the quantum-mechanical treatment of spin ½ (see [9]). The interaction (3) leads to the spin precession around the external magnetic field. This interaction is important in all systems where a magnetic field is present. Moreover, fluctuations of $\vec{B}$ could lead to noise contributing to spin relaxation.

27.4.1.2 SO Interaction

The SO interaction arises as a result of the magnetic moment of the spin coupling to its orbital degree of freedom. It is actually a relativistic effect, which was first found in the emission spectra of hydrogen. An electron moving in an electric field sees, in its rest frame, an effective magnetic field. This field, which is dependent on the orbital motion of the electron, interacts with the electron's magnetic moment.

The Hamiltonian describing SO interaction, derived from the four-component Dirac equation, has the form

$$H_{SO} = \frac{\hbar^2}{4m^2c^2} (\vec{\nabla} \times V) \cdot \vec{\sigma}, \tag{27.4}$$

where m is the free electron mass, $\vec{p}$ is the momentum operator, and is the gradient of the potential energy, proportional to the electric field acting on the electron. When

dealing with crystal structures, the SO interaction, Eq. 27.4, accounts for symmetry properties of materials. Here, we emphasize two specific mechanisms that are considered to be important for spintronics applications. The Dresselhaus SO interaction [1] appears as a result of the asymmetry present in certain crystal lattices, e.g., the zinc blende structures. For a 2DEG in semiconductor heterostructures with an appropriate growth geometry, the Dresselhaus SO interaction is of the form

$$H_D = \frac{\beta}{\hbar}(\sigma_x p_x - \sigma_z p_z). \tag{27.5}$$

Here, β is the coupling constant.

The Rashba SO interaction [3] arises due to the asymmetry associated with the confinement potential and is of interest because of the ability to electrically control the strength of this interaction. The latter is utilized, for instance, in the Datta–Das spin transistor [7, 10]. The Hamiltonian for the Rashba interaction is written [3] as

$$H_R = \frac{\alpha}{\hbar}(\sigma_x p_z - \sigma_z p_x), \tag{27.6}$$

where α is the coupling constant. Other possible sources of SO interactions are nonmagnetic impurities, phonons [14], sample inhomogeneity, surfaces, and interfaces. In some situations, these could play a role in spin transport and spin relaxation dynamics.

27.4.2 Model

Consider the two-dimensional channel of a spin-FET in the x-y plane with current flowing in the x-direction. An electron's wave vector components in the channel are designated as kx and kz, while the total wave vector is designated as kt. Note that $k^2 = k_X^2 + k_Z^2$.

The gate terminal induces an electric field in the y-direction, which causes Rashba interaction. The Hamiltonian operator describing an electron in the channel is

$$H = \frac{p_x^2 + p_z^2}{2m^*}[\mathrm{I}] + \alpha[V_G](\sigma_x p_z - \sigma_z p_x), \tag{27.7}$$

where the p-s are the momentum operators, the σ-s are the Pauli spin matrices and [**I**] is the 2×2 identity matrix. Since this Hamiltonian is invariant in both x and z coordinates, the wave functions in the channel are plane wave states $e^{i(k_x x + k_z)}$. Diagonalization of the Hamiltonian yields the eigenenergies and the eigenspinors in the two spin-split bands in the two-dimensional channel:

$$\begin{aligned} E_d &= \frac{\hbar^2 k^2}{2m^*} + \alpha\,[V_G]\,k \quad \text{(lower band)} \\ E_u &= \frac{\hbar^2 k^2}{2m^*} - \alpha\,[V_G]\,k \quad \text{(upper band)} \end{aligned} \tag{27.8}$$

and

$$[\Psi]_l = \begin{bmatrix} \sin\theta \\ \cos\theta \end{bmatrix} \quad \text{(lower band)}$$
$$[\Psi]_u = \begin{bmatrix} -\cos\theta \\ \sin\theta \end{bmatrix} \quad \text{(upper band)} \tag{27.9}$$

where $\theta = (1/2)arctan\ (k_z/k_x)$.

Now if we also assume that the spin injection efficiency at the source is 100 % and the electron for an energy E have two different waves for $k_X^{(1)}$ and $k_X^{(2)}$ (corresponding to the two values of k), the corresponding spinor at the drain end will be:

$$[\Psi]_{drain} = C_1 \begin{bmatrix} \sin\theta \\ \cos\theta \end{bmatrix} e^{i\left(k_X^{(1)}L + k_z W\right)} + C_2 \begin{bmatrix} -\cos\theta \\ \sin\theta \end{bmatrix} e^{i\left(k_X^{(2)}L + k_z W\right)}$$
$$= e^{ik_z W} \begin{bmatrix} \sin\left(\theta + \dfrac{\pi}{4}\right) \sin\theta e^{ik_X^{(1)}L} + \cos\left(\theta + \pi/4\right) \cos\theta e^{ik_X^{(2)}L} \\ \sin\left(\theta + \dfrac{\pi}{4}\right) \cos\theta e^{ik_X^{(1)}L} - \cos\left(\theta + \pi/4\right) \sin\theta e^{ik_X^{(2)}L} \end{bmatrix} \tag{27.10}$$

where L is the channel length (distance between source and drain contacts) and W is the transverse displacement of the electron as it traverses the channel.

Then the transmission's factor is given by:

$$|T|^2 = \cos^4\left(\theta + \frac{\pi}{4}\right) \left| 1 + \tan^4\left(\theta + \frac{\pi}{4}\right) e^{i\left(k_X^{(1)} - k_X^{(2)}\right)L} \right|^2. \tag{27.11}$$

The current density in the channel of the spin-FET (assuming ballistic transport) is given by the Tsu–Esaki formula:

$$J = \frac{q}{W_y} \int_0^\infty \frac{1}{h} dE \int \frac{dk_Z}{\pi} |T|^2 [f(E) - F(E + qV_{SD})], \tag{27.12}$$

where q is the electronic charge, W_y is the thickness of the channel (in the y-direction), V_{SD} is the source-to-drain bias voltage, and $f(E)$ is the electron occupation probability at energy E in the contacts. Since the contacts are at local thermodynamic equilibrium, these probabilities are given by the Fermi–Dirac factor.

In the linear regime, the expression of the drain current reduces to

$$J = \frac{q^2 V_{SD}}{W_y} \int_0^\infty \frac{1}{h} dE \int \frac{dk_Z}{\pi} |T|^2 \left[-\frac{\partial f\ (E)}{\partial E} \right]. \tag{27.13}$$

This yields that the channel conductance G is

$$G = \frac{I_{SD}}{V_{SD}} = \frac{q^2 W_z}{\pi h} \int_0^\infty dE \int dk_Z |T|^2 \left[-\frac{\partial f\ (E)}{\partial E} \right]. \tag{27.14}$$

27.5 Conclusion

In this work, we studied the transport of two-dimensional spin-polarized in SpinFET, we have established a relation giving the expression of the source–drain current as a function of the parameters of the semiconductor used, and the electric field across the control grid and polarization of injected spins, and then we have calculated the associated transconductance G. This model is based on semiclassical considerations with the holders of spin injected with ballistic trajectories inside the conduction channel.

References

1. Prinz GA (1995) Spin-polarized transport. Phys Today 48:58
2. Prinz GA (1999) Magnetoelectronics applications. J Magn Magn Mater 200(1–3):57–68
3. Rashba EI (1960) Properties of semiconductors with an extremum loop, I/Cyclotron and combinational resonance in a magnetic field perpendicular to the plane of the loop. Sov Phys Solid State 2:1109
4. Thibaut W (2000) Etude du transport d'électrons polarisés en spin dans les hétéro-structures métal ferromagnétique/semi-conducteur pour l'obtention de nouveaux composants électroniques Thèse de doctorat soutenance en
5. Bournel A (2000) Magnéto électronique dans des dispositifs à semi-conducteurs. Ann Phys Fr 25(1):1–176
6. Wolf SA et al (2001) Spintronics: a spin-based electronics vision for the future. Science 294:1488
7. Datta S, Das B (1990) Electronic analog of the electro—optic modulator. Appl Phys Lett 56(7):665
8. Das B, Miller DC, Datta S (1989) Evidence for spin splitting in InxGa1-xAs/In0.52Al0.48As heterostructures as B®0. Phys Rev B 39(2):1411
9. Landau LD, Lifshitz EM (1997) Quantum mechanics. Butterworth-Heinemann, Oxford
10. Bychkov Y, Rashba EI (1984) Oscillatory effects and the magnetic susceptibility of carriers in inversion layers. J Phys C 17:6039–6045

Chapter 28
Future Strain Properties of Multilayer Film Materials

Serhyi I. Protsenko, Larysa V. Odnodvorets and Ivan Yu. Protsenko

28.1 Introduction

Electrophysical properties of thin-film materials (resistivity, thermal resistance coefficient, strain coefficients) differ significantly from those of bulk samples (wires, plates, massive condensates) due to their thickness, crystal structure, elemental composition, concentration and type of defects and others. Electrophysical properties are very sensitive to changes in film thickness and size of crystallites, the concentration of impurity atoms and defects of crystal structure and the effect of external fields (deformation, magnetic field intensity, temperature, etc.). As is well known (see, for example, [46]), these factors cause a number of structural, phase size and concentration effects. As our attention is focused on size effects (SE) in strain in single- and multilayer films, we note that they are further classified into external (scattering of electric current at the external surfaces of the films and interfaces) and internal SE (scattering of current at the grain boundaries). Strain effect occurs when compressing or stretching of the bulk or film conductor [27]. The essence of physical processes at strain effect reduced to changes on the microscopic level (increasing or decreasing lattice parameter) or macroscopic and microscopic levels at grain boundaries or interface (rotate and resize grains, the appearance of localized energy levels, changes in the concentration and type of defects, the dependence of deformation [21, 36] parameter of specularity, coefficient of scattering (transition) at grain boundaries and interface).

Although that strain effect was discovered by W. Thomson (Kelvin) in 1856, a systematic study of this phenomenon began in 1930. A single stimulus for this was the first production samples of wire-strain sensors by E. Simmons and L. Rouge, A. Columbani, P. Toure, R. Parker and A. Krinsky, B.Verma (see, for example, [27]), G. Witt and T. Coutts (see, for example [53]), G. Kuczynski [20], Z. Meiksin and R. Hudzynski [28], and others made significant contribution to the study of strain

S. I. Protsenko (✉) · L. V. Odnodvorets · I. Yu. Protsenko
Department of Applied Physics, Sumy State University,
Rymskyi-Korsakov Str., 2, 40007 Sumy, Ukraine
e-mail: protsenko@aph.sumdu.edu.ua

O. Fesenko, L. Yatsenko (eds.), *Nanocomposites, Nanophotonics, Nanobiotechnology, and Applications,* Springer Proceedings in Physics 156,
DOI 10.1007/978-3-319-06611-0_28,

effect in bulk and film materials in the years 1950–1970. All these studies, except for works by Z. Meiksin et al., were experimental in character and mainly of practical orientation. The end of 1970 and 1980 were marked with intense theoretical studies of SE in the strain of single-layer metal films by F. Warkusz [52] and C. Tellier, A. Tosser and C. Pichard (generalization of a large number of publications, see in the monograph; [46]) and the beginning of similar studies on the example of two-layer films in the works of F. Khater and M. El-Hiti [17, 18]. Testing of these theoretical models has been made in works by I. Protsenko et al. (see, for example, [7]). In addition, development of improved experimental methods of measuring gauge factor (GF; [54]) made it possible to get new results for single- and two-layer film systems.

The transition from two-layer films to multilayers from the experimental point of view is under no difficult methodical character; but, in terms of constructing theoretical semiclassical models, similar works proposed [17, 46, 52] that this transition involves certain difficulties which, in fact, were not resolved at that time.

Semiclassical a model based on the concept of deformation effects in the electro carry parameters of was developed [21]. This model gives good correspondence with experimental results.

28.2 Theoretical Models of the Strain Effect in Single- and Multilayer Films

Systematic studies of SE in strained film materials began in 1960, and the task of Z. Meiksin and R. Hudzynski ([28], see also [33]) was an attempt to reconcile experimental results, known at that time, about the longitudinal strain coefficient (γ_l) with theoretical conception. Their theoretical model was based on the famous theory of SE in electrical conductivity of monocrystalline plates by Fuchs-Sondheimer. The authors [28] analysed five different ranges of thickness and structure state of films:

- Thick films (thickness $d > 600\,\text{nm}$)
- Homogeneous continuous films ($20\,\text{nm} < d < 600\,\text{nm}$)
- Thin films of filamentary structure ($10\,\text{nm} < d < 20\,\text{nm}$)
- The films with islands which are contacted ($d = 10\,\text{nm}$)
- Discontinuous tunnel-bound island films ($d < 10\,\text{nm}$)

Note that for us, the greatest interest are the first two cases, since the other three relate to discontinuous or island films, which are almost not considered in our work. In case of thick films, we deal effectively with bulk samples and therefore values for γ_l are obtained based on these formulas:

$$R = \rho\frac{l}{ad}, \ln R = \ln\rho + \ln l - \ln a - \ln d,$$
$$\gamma_l = \frac{d\ln\lambda_0}{d\varepsilon_l} - \frac{d\ln\rho}{d\varepsilon_l} + 1 + 2\mu, \tag{28.1}$$

where R and ρ are resistance and resistivity; l and a are length and width of the sample; $d\varepsilon_l = d\ln l \equiv \frac{dl}{l}$ is the longitudinal deformation; $\frac{d\ln\rho}{d\varepsilon_l} = \gamma_l^{\rho}$ is the strain coefficient note across resistivity; $\mu = -\frac{d\ln a}{d\ln l} \cong -\frac{d\ln d}{d\ln l}$ is the Poisson coefficient.

γ_l^{ρ} can submit as:

$$\frac{d\ln\rho}{d\varepsilon_l} \cong -\frac{d\ln\lambda_0}{d\varepsilon_l} - \frac{d\ln n}{d\varepsilon_l} = \eta_{\lambda_0 l} + \eta_{nl}, \tag{28.2}$$

where λ_0 and n are the mean free path of electrons (MFPE) and their concentration and $\eta_{\lambda_0 l}$, η_{nl} are deformation coefficients for MFPE and electron concentration.

According to Kuszynski [20], wave number of electrons on the Fermi surface $k\prime$ at relatively small deformations can be expressed as:

$k' \cong (1 - \beta\varepsilon_l)$ or $\ln k' \cong -\beta\varepsilon_l$,

where β is the coefficient the order of unity.

Thus, given $n = 2\pi k'$, the value for γ_l^{ρ} is to be represented in the form

$$\gamma_l^{\rho} \cong -\frac{d\ln\lambda_0}{d\varepsilon_l} + \beta, \tag{28.3}$$

where, according to Mayadas and Shatzkes [26], $\beta \cong -1$ if at the deformation $dn > 0$ (compression of the sample or increase in the number of interactions between electrons with increase in the length of the sample) or $\beta \cong +1$ if at the deformation $dn < 0$ (tensile of sample or decrease in the number of interactions between electrons). The value $\eta_{\lambda_0 l} < 0$ when the deformation leads to increase of MFPE and $\eta_{\lambda_0 l} > 0$ when the deformation leads to decrease of MFPE.

In case of homogeneous continuous films [28], the size ratio for strain coefficient can be written as:

$$\gamma_l = \gamma_{0ll} - \frac{\mathrm{Y}(k)}{\mathrm{Z}(k)}(\eta_{\lambda_0 l} - \mu), \tag{28.4}$$

where $\mathrm{Y}(k) = \frac{3}{8}\left[k^{-1} + 2k\left(1 - \frac{1}{4}k^2\right)B(k) + \left(\frac{1}{2}k^2 - \frac{1}{2}k - 1 - k^{-1}\right)e^{-k}\right]$ and $\mathrm{Z}(k) = \frac{\rho}{\rho_0} = \left[1 + \frac{3}{4}k\left(1 - \frac{1}{12}k^2\right)B(k) - \frac{3}{8}k^{-1}\left(1 - e^{-k}\right) - \left(\frac{5}{8} + \frac{1}{16}k - \frac{1}{16}k^2\right)e^{-k}\right]$ —the function of Fuchs. $k = \frac{d}{\lambda_0}$, the reduced thickness, and $B(k) = \int_K^{\infty}\left(\frac{e^{-g}}{g}\right)dg$, the integral exponent (g, variable value).

Since the ratio $\frac{\mathrm{Y}(k)}{\mathrm{Z}(k)}$ is always greater than zero, the ratio between γ_l and γ_{l0} completely determined the sign of value $(\eta_{\lambda_0 l} - \mu)$: if $(\eta_{\lambda_0 l} - \mu) > 0$, γ_l will always be less than γ_{l0} and vice versa. Thus, dependence $\gamma_l(d)$ is monotonically with increasing thickness near the bottom or top to the asymptotic value γ_{l0}. According to data [36, 42]), $\gamma_l > \gamma_{l0}$ for films Sc ($\eta_{\lambda_0 l}$ can accept values from − 3.02 to − 4.04) and Cr ($\eta_{\lambda_0 l}$ can accept values from − 3.04 to − 9.17) and for invar alloy films (Fig. 28.1). Note that similar results are also an example of two-component permalloy films received authors [16]. Great contribution to the development of theoretical models has been made by C. Tellier–A. Tosser–C. Pichard (TTP) which was generalized in a monograph [46]. In a series of works, along with the effect of Fuchs-Sondheimer

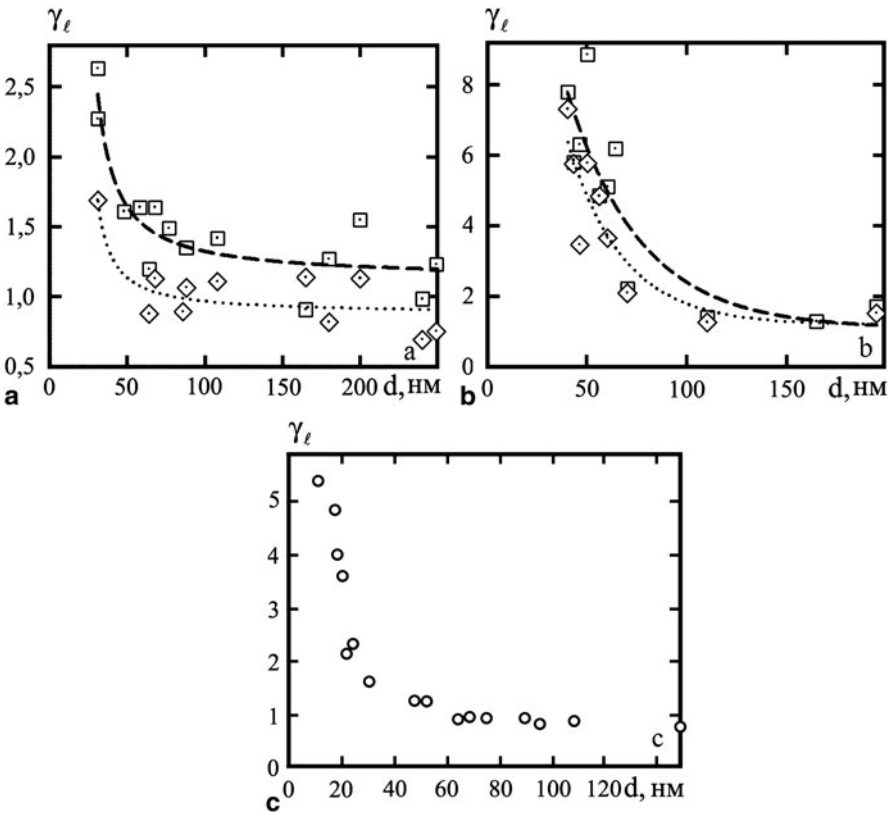

Fig. 28.1 Size dependence γ_l for Sc (**a**) and Cr (**b**) [36] and invar alloy films (**c**) [42]. Number of deformation cycles: ⊡: III and ⊖: IV

(external SE), the internal SE was first taken into account by A. Mayadas and M. Shatzkes [26]. They proposed the model of effective MFPE, linearized ratio and three-dimensional model to qualitatively analyse the basic conformity to the law of internal and external SE and also to calculate the main parameters of electroconductivity and strain effect. In the case of polycrystalline film model, effective MFPE does not restrict on the ratio between λ_0 and the average crystallite size (L).

Based on MS for conductivity (σ),

$$\sigma = \sigma_0[f(\alpha) - A(k, p, \alpha)], \tag{28.5}$$

where p is the parameter of specular reflection from external surface film, $f(\alpha) = 1 - \frac{3}{2}\alpha + 3\alpha^2 - 3\alpha^3 \ln(1 + \alpha^{-1})$ is the function of grain boundary scattering of electrons ($\alpha = \frac{\lambda_0}{L}\frac{R}{1-R}$, where R is the parameter of scattering electron on grain boundary), $A(k, p, \alpha) = \frac{6}{\pi k} \geq (1 - p) \int_0^{2\pi} d\Phi \int_1^{\infty} dt \frac{\cos^2\Phi}{H^2(t,\Phi)} \left(\frac{1}{t^3} - \frac{1}{t^5}\right) \frac{1-\exp[-ktH(t,\Phi)]}{1-p\exp[-ktH(t,\Phi)]}$,

$H(t,\Phi) = 1+2(\cos\Phi)^{-1}(1-t^{-2})^{-\frac{1}{2}}, t = \frac{1}{\cos\Theta}$ (Θ is the angle between velocity vector of electron and axis z), and TTP of ratio was obtained for γ_l in approaching of effective MFPE.

After differentiation, $\ln\sigma$ (ratio 28.5) by strain ε_l was obtained:

$$\gamma_l = \gamma_{ol}^{\rho} + [f(\alpha) - A(k,p,\alpha)]^{-1}\left\{(\eta_{\lambda_{0l}} + \beta)X - \left(1 + \mu_f \cdot \frac{1-\mu_s}{1-\mu_{fl}}\right)Y'\right\} + 1 + \mu_s + \mu_{fl}\frac{1-\mu_s}{1-\mu_{fl}}, \tag{28.6}$$

where μ_s and μ_{fl} are Poisson coefficients for substrate and film, and X and $Y\hat{E}^I$ are known functions [8]. We emphasize that the ratio for transfer strain coefficient γ_t has a similar mathematical structure.

Some limiting cases of formula (28.6) are given, which allow to conduct qualitative analysis of SE in strain. At the complete absence of diffuse scattering of electrons (p = 1), formula (28.6) is simplified to the form:

$$\gamma_l|_{p=1} \cong 1 + \mu_s + \mu_{fl}\frac{1-\mu_s}{1-\mu_{fl}} + (1+\eta_{\lambda_0 l})\left[1 + \frac{\alpha\frac{df(\alpha)}{d\alpha}}{f(\alpha)}\right], \tag{28.6a}$$

where the multiplier $1+\frac{\alpha\frac{df(\alpha)}{d\alpha}}{f(\alpha)} \cong f(\alpha) \equiv \frac{\rho_0}{\rho_g}$ (ρ_0 is the resistivity of the bulk sample).

When $\mu_f = \mu_S$ and $d \to \infty$ with Eq. (28.6a), we can get the ratio for γ_{gl}, where the index "g" indicates grain boundary scattering of electrons

$$\gamma_{gl} \approx 1 + 2\mu_f + (1+\eta_{\lambda_0 l})f(\alpha) \tag{28.6b}$$

and at the L i– $d \to \infty$ the equation given is similar to (28.1):

$$\gamma_l \approx \eta_{\lambda_0 l} + 2(1+\mu_f).$$

The calculated graphs based on the Eqs. (28.6) and (28.6b) is shown in Fig. 28.2.

The physical sense of the graph for Fig. 28.2a is understood because it illustrates the usual SE for strain coefficient of polycrystalline films. In addition, the graph in Fig. 28.2b has no physical sense because of the uncertainty parameter α, which depends on both on L i R. The next step in the development of the theory of SE for strain coefficient is a linearization model TTP [46]:

$$\gamma_l = (\eta_{\lambda_0 l}+1)f(\alpha) - \lambda_0(1-p)[(\eta_{\lambda_0 l}+1)f(\alpha)H(\alpha) - (1-\mu\prime)U(\alpha)]\cdot d^{-1}, \tag{28.7}$$

where $H(\alpha)$ and $U(\alpha)$ are known tabulated functions.

If the dependence (28.7) in the linearized coordinates presented in coordinates $\gamma_l \cdot d$ versus d, then the angular coefficient can be calculated $(\eta_{\lambda_0 l}+1)f(\alpha)$ and then of the intercept on the axis $\gamma_l \cdot d$– value $\lambda_0(1-p)$.

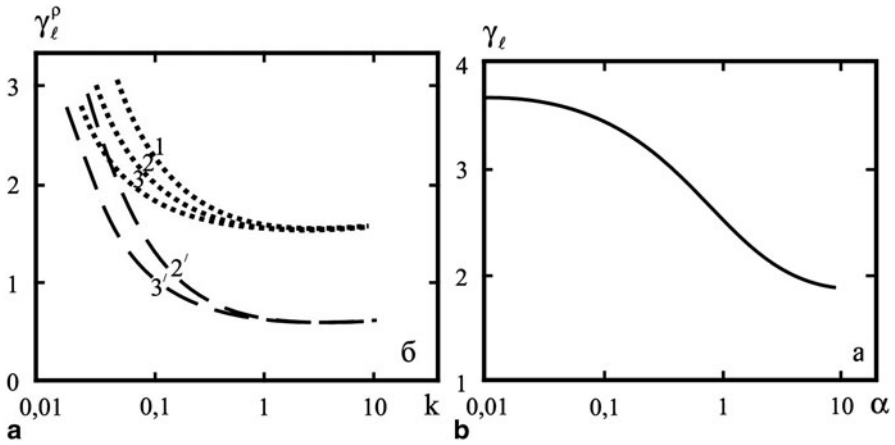

Fig. 28.2 γ_l^ρ versus reduced thickness (**a**) and γ_l versus grain boundary scattering parameter (**b**) for polycrystalline films: **a**: $\eta_{\lambda_0 l} = 1.15$; $\mu_S = 0.40$; $\mu_f = 0.38$; *1*—$p = 0$; $\alpha = 0.25$; *2*—$p = 0.25$; $\alpha = 0.25$; *3*—$p = 0.50$; $\alpha = 0.25$; *2'*—$p = 0.25$; $\alpha = 2$; *3'*—$p = 0.50$; $\alpha = 2$; **b**: $p = 1$; $\mu_S = 0.25$; $\mu_f = 0.40$ [46]

For coefficient γ_l, authors (Teiller and Tosser [46]) have obtained the equation:

$$\gamma_l = (\eta_{\lambda_0 l} + 1) - \eta_{\lambda_0 l} \frac{F'(\nu_x) + G'(\nu_y) + G'(\alpha')}{M(\nu_x, \nu_y, \alpha')} + \frac{\mu_s G'(\nu_y) - F'(\nu_x) + \mu' G^-(\alpha')}{M(\nu_x, \nu_y, \alpha')} + (1 + 2\mu_f), \tag{28.8}$$

which adopted the following notation:

$$M(\nu_x, \nu_y, \lambda_z') = F^{-1}(\nu_x) + G^{-1}(\nu_y) + G^{-1}(\nu_z') - 2 \equiv \frac{\rho_g}{\rho_0} = \frac{1}{f(\alpha)};$$

$$F'(\nu_x) = \nu_x \frac{dF(\nu_x)}{d\nu_x} F^{-1}(\nu_x), \quad G'(\nu_y) = \nu_y \frac{dG(\nu_y)}{d\nu_y} G^{-1}(\nu_y),$$

$$G'(\nu_z{}') = \nu_z{}^- \frac{dG(\nu_z{}')}{d\nu_z{}'} G^{-2}(\nu_z{}'); \; F(\nu_x) = 3\nu_x \left[\frac{1}{2} - \nu_x + \nu_x^2 \ln(1 + \nu_x^{-1})\right];$$

$$G(\nu_{y,z}) = \frac{3}{2}\nu_{x,y}\left[\nu_{y,z} - \frac{1}{2} + (1 - \nu_{y,z}^2)\ln(1 + \nu_{y,z}^{-1})\right], \; \nu_x = \frac{L_x}{\lambda_0}\left(\ln\frac{1}{r}\right)^{-1},$$

$$\nu_{y,z} = \frac{L_{y,z}}{\lambda_0}\left(\ln\frac{1}{r}\right)^{-1}, \; \nu_z' = \mu^{-1} + \nu_z^{-1}, \; \mu = \frac{d}{\lambda_0}\left(\ln\frac{1}{p}\right)^{-1},$$

$$\mu' = \mu_f \frac{1 - \mu_S}{1 - \mu_f} \cong \mu_f,$$

where r is the transmission coefficient at the grain boundary and μ' is the reduced Poisson coefficient.

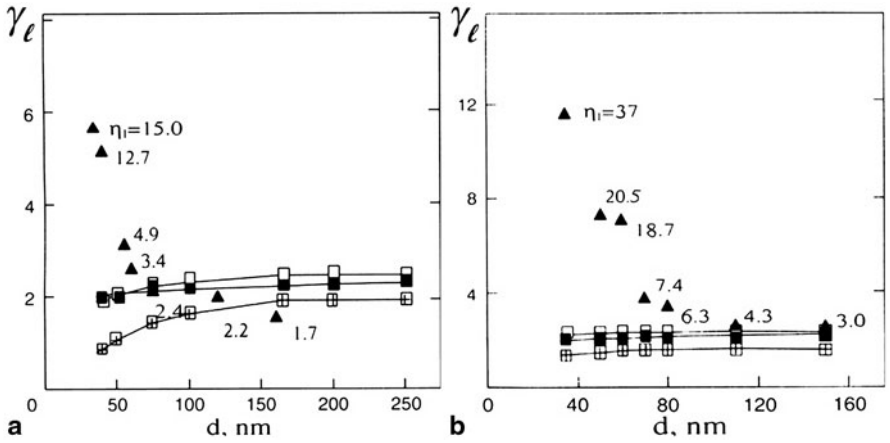

Fig. 28.3 Strain coefficient versus thickness films Cr (**a**) and Cu (**b**). ■: obtained using the calculated ρ/ρ_0 value; □: using the experimental ρ/ρ_0 value; ⊞ using the experimental ρ/ρ_g value; ▲ – experimental plot. The numbers presented in the vicinity of point ▲ are the calculated value of the deformation coefficient $\eta_{\lambda_0 l}$ obtained using the experimental ρ/ρ_0 value [7]

Experimental data for Cr and Cu films and calculate data based on the three-dimensional model (Eq. (28.8)) in Fig. 28.3 are presented in the work by Chornous et al. [7]. As is evident, the poorest correspondence is found when the value $M(\nu_x, \nu_y, \nu_z') = \frac{\rho}{\rho_0}$ is theoretically calculated. This allows the conclusion that the deformation coefficient of the MFPE is a size-dependent parameter of electroconductivity (Fig. 28.3).

It can be accounted for by the MFPE depending on the film thickness. The poor agreement of the three-dimensional model with the experimental results under relatively small thickness is due to the theory when $\eta_{\lambda_0 l} = \text{const}$. The idea of size dependence of the given parameter versus film thickness and grain size cannot bring about objections even for the consideration that many different physical quantities also dependent on the film thickness. Thus, the three-dimensional model for strain coefficient is at satisfactory agreement with the experimental results at the additional hypothesis on the size dependence of deformation coefficient of MFPE versus film thickness.

Systematic theoretical investigations of strain effect of two-layer films and multilayers were established in the works by F. Khater and M. El-Hiti [17, 18] for monocrystalline and I.Protsenko, L.Odnodvorets and A.Chornous [37] for polycrystalline films. These authors show that two-layer films can simulate parallel wiring of point contacts. The fact that all theoretical models give good agreement with experimental results demonstrates compliance with real film samples providing parallel connection.

Thus, according to Khater and El-Hiti [17, 18] and Protsenko et al. [37], we can write:

$$\frac{1}{R} = \frac{a}{l}[\sigma_{01} F_1(d_1, \lambda_{01}, p_1^*, r_1)d_1 + \sigma_{02} F_2(d_2, \lambda_{02}, p_2^*, r_2)d_2], \tag{28.9}$$

where p_i^* is the effective parameter of specularity ($p_1^* = \frac{p_1+p_{12}}{2}$, $p_2^* = \frac{p_{20}+p_{12}}{2}$, where p_1, p_{12} and p_{20} are the parameters of specularity at the boundary film/substrate, interface and film/vacuum, respectively).

After evident transformations of equation (28.9)

$$\frac{dR}{R} = -(d\ln d_1 + d\ln \sigma_{01} + d\ln F_1)A_1 - (d\ln d_2 + d\ln \sigma_{01} + d\ln F_2)$$
$$A_2 - (\ln a - d\ln l),$$

where $A_i = \frac{d_i \sigma_{0i} F_i}{d_1 \sigma_{01} F_1 + d_2 \sigma_{02} F_2} = \frac{d_i \sigma_i}{d_1 \sigma_1 + d_2 \sigma_2}$ and $d\ln l = d\varepsilon_l$, we obtain

$$\gamma_l = A_1 \left(1 + \eta_{\lambda_{01} l} + \mu_1' - \frac{d\ln F_1}{d\ln l}\right) + A_2 \left(1 + \eta_{\lambda_{02} l} + \mu_2' - \frac{d\ln F_2}{d\ln l}\right) + 1 + \mu_s, \tag{28.10}$$

where $\frac{d\ln \sigma_0}{d\ln l} = -(1 + \eta_{\lambda_0 l})$.

Since $\frac{d\ln F_i}{d\ln l} = \frac{d\ln F_i}{d\ln k_i}(\eta_{\lambda_{0i} l} - \mu_i') + \frac{d\ln F_i}{d\ln k_i}(\eta_{\lambda_{0i} l} - \mu_k')\frac{d\ln k_i}{d\ln k_k}$ and $\frac{d\ln F_i}{d\ln k_i} = 1 - \frac{\beta_i}{\beta_{0i}}$, $\frac{d\ln k_i}{d\ln k_k} = \frac{\beta_{0i}}{\beta_{0k}}$ (β is the thermal resistance coefficient (TRC); *i*–, $k = 1, 2$ and $i \neq k$), after substitutions in the previous equation, taking into account that

$$\gamma_l = A_1 \left\{(\gamma_{01l} + \mu_1') + \left(1 - \frac{\beta_1}{\beta_{01}}\right)\left[(1 - \gamma_{01l}^{\rho} + \mu_1') + (1 - \gamma_{02l}^{\rho} + \mu_2')\frac{\beta_{01}}{\beta_{02}}\right]\right\}$$
$$+ A_2 \left\{(\gamma_{02l} + \mu_2') + \left(1 - \frac{\beta_2}{\beta_{02}}\right)\left[(1 - \gamma_{02l}^{\rho} + \mu_2') + (1 - \gamma_{01l}^{\rho} + \mu_1')\frac{\beta_{02}}{\beta_{01}}\right]\right\}$$
$$+ 1 + \mu_s. \tag{28.11}$$

Since this equation corresponds poorly to experimental data, the authors [21] proposed a semiclassical model, which included the dependence from deformation (ε_l) not only for MFPE but also *p, r* and *Q* (transition parameter of interface) parameters. Derivative functions by Fuchs in Eq. (28.10), for example F_1, may be written as:

$$\frac{d\ln F_1}{d\ln l} = \frac{d\ln F_1(k_1, m_1, p_1^*, r_1)}{d\ln l} = \left(\frac{d\ln F_1}{d\ln k_1}\frac{d\ln k_1}{d\ln l} + \frac{d\ln F_1}{d\ln m_1}\frac{d\ln m_1}{d\ln l}\right)$$
$$+ \left(\frac{d\ln F_1}{d\ln k_1}\frac{d\ln k_1}{d\ln l}\frac{d\ln k_2}{d\ln l} + \frac{d\ln F_1}{d\ln m_1}\frac{d\ln m_1}{d\ln m_2}\frac{d\ln m_2}{d\ln l}\right)$$
$$+ \left(\frac{d\ln F_1}{d\ln k_1}\frac{d\ln k_1}{d\ln p_1^*}\frac{d\ln p_1^*}{d\ln l} + \frac{d\ln F_1}{d\ln k_1}\frac{d\ln k_1}{d\ln Q}\frac{d\ln Q}{d\ln l}\right)$$
$$+ \left(\frac{d\ln F_1}{d\ln k_1}\frac{d\ln k_1}{d\ln k_2}\frac{d\ln k_2}{d\ln p_2^*}\frac{d\ln p_2^*}{d\ln l} + \frac{d\ln F_1}{d\ln k_1}\frac{d\ln k_1}{d\ln k_2}\frac{d\ln k_2}{d\ln Q}\frac{d\ln Q}{d\ln l}\right), \tag{28.12}$$

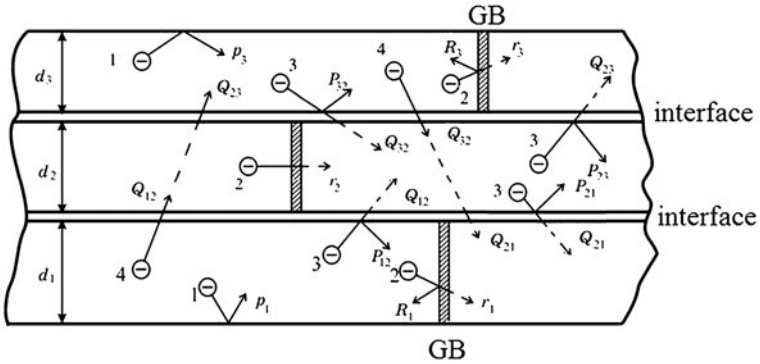

Fig. 28.4 Scheme of scattering and interlayer electron transitions: *1, 1″*—surface scattering; *2, 2′, 2″*—grain boundary scattering (GB, in general case $r_1 \neq r_2 \neq r_3$); *3, 3′, 3″*—scattering and transition on interface [21]

where $m_i = \frac{L_i}{\lambda_{0i}}$ is the reduced mean size of crystalline.

From Eq. (28.10) and ratio (28.11), the authors [21] proposed an equation for γ_l multilayer with the arbitrary amount of layers, which takes into account the surface and grain boundary scattering of electrons more correctly. In the case when electric properties of *i*–layer are stipulated by electrons *i*-layer and *(i± 1)*-layer, which possible by the implementation of conditions: $\lambda_{01} \cong d_1 + d_2$, $\lambda_{02} \cong d_2 + \frac{d_1+d_3}{2}$ and $\lambda_{03} \cong d_3 + d_2$ (electron transitions, which corresponding to this situation, are shown schematically in Fig. 28.4.) for three-layer equation for γ_l has the form:

$$\begin{aligned}
\gamma_l = {} & A_1 \left\{ \left(\gamma^{\rho}_{01l} + \mu_1{}'\right) - \left(1 - \frac{\beta_1}{\beta_{01}}\right) \left[\left(2\gamma^{\rho}_{01l} - 1 - \mu_1{}' - \eta_{p1l} \frac{d\ln k_1}{d\ln p_1} - \eta_{Q1l} \frac{d\ln k_1}{d\ln Q_1} - \eta_{r1l} \frac{d\ln m_1}{d\ln r_1}\right) \right.\right. \\
& \left.\left. + \left(\gamma^{\rho}_{02l} - 1 - \mu_2{}' - \eta_{p2l} \frac{d\ln k_2}{d\ln p_2} - \eta_{Q2l} \frac{d\ln k_2}{d\ln Q_2} - \eta_{r2l} \frac{d\ln m_2}{d\ln r_2}\right) \frac{\beta_{01}}{\beta_{02}} \right] \right\} \\
& + A_2 \left\{ \left(\gamma^{\rho}_{02l} + \mu_1{}'\right) - \left(1 - \frac{\beta_2}{\beta_{02}}\right) \left[\left(2\gamma^{\rho}_{02l} - 1 - \mu_2{}' - \eta_{p2l} \frac{d\ln k_2}{d\ln p_2} - \eta_{Q2l} \frac{d\ln k_2}{d\ln Q_2} - \eta_{r2l} \frac{d\ln m_2}{d\ln r_2}\right) \right.\right. \\
& \left.\left. + \left(\gamma^{\rho}_{03l} - 1 - \mu_3{}' - \eta_{p3l} \frac{d\ln k_3}{d\ln p_3} - \eta_{Q3l} \frac{d\ln k_3}{d\ln Q_3} - \eta_{r3l} \frac{d\ln m_3}{d\ln r_3}\right) \frac{\beta_{02}}{\beta_{03}} \right] \right\} \\
& + A_3 \left\{ \left(\gamma^{\rho}_{03l} + \mu_3{}'\right) - \left(1 - \frac{\beta_3}{\beta_{03}}\right) \left[\left(2\gamma^{\rho}_{03l} - 1 - \mu_3{}' - \eta_{p3l} \frac{d\ln k_3}{d\ln p_3} - \eta_{Q3l} \frac{d\ln k_3}{d\ln Q_3} - \eta_{r3l} \frac{d\ln m_1}{d\ln r_3}\right) \right.\right. \\
& \left.\left. + \left(\gamma^{\rho}_{02l} - 1 - \mu_2{}' - \eta_{p2l} \frac{d\ln k_2}{d\ln p_2} - \eta_{Q2l} \frac{d\ln k_2}{d\ln Q_2} - \eta_{r2l} \frac{d\ln m_2}{d\ln r_2}\right) \frac{\beta_{03}}{\beta_{02}} \right] \right\} + 1 + \mu_s, \qquad (28.13)
\end{aligned}$$

where it is considered that $Q_1 = Q_{12} = Q_{21}$, $Q_2 = Q_{21} = Q_{23}$ and $Q_3 = Q_{32} = Q_{23}$; $Q_{13} = \frac{Q_{12}+Q_{23}}{2}$ and $Q_{31} = \frac{Q_{12}+Q_{23}}{2}$.

We note that Eq. (28.13) can be relatively easily compared with experimental data, since its right side are values and parameters that can be calculated on the basis of experimental results for single-layer films. To do this, for all single-layer films, which consist of the three-layer system, we need the size dependence of TRC in both static deformations (for example, $\varepsilon_{l1} = 0$ and $\varepsilon_{l2} = 1.0\%$) and the constant of average grain size. These data together can be calculated with parameters such as

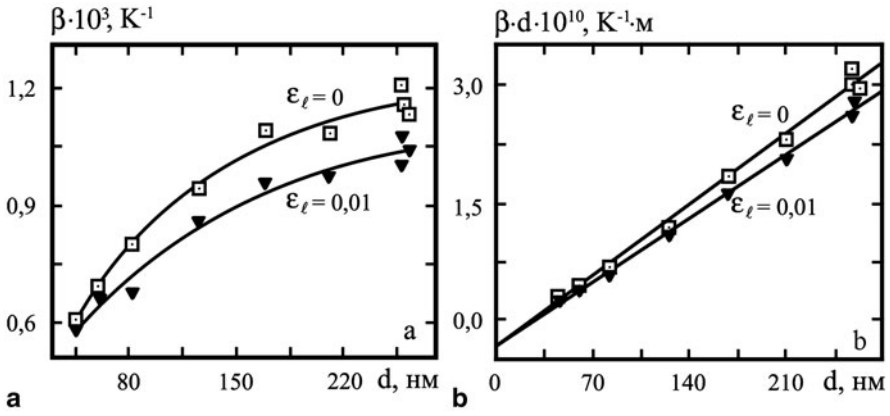

Fig. 28.5 β versus d (**a**) and $\beta \cdot d$ versus d (**b**) for non-deformed ($\varepsilon_l = 0$) and deformed ($\varepsilon_l = 0,01$) Sc films [36]

$p, r, \lambda_0, \eta_{\lambda 0 l}, \eta_{pl}, \eta_{rl}, \frac{d\ln k}{d\ln p}$ and $\frac{d\ln r}{d\ln m}$ (for more details, see [32]) using the linearized ratio and model of isotropic scattering TTP [46]:

$$\beta \cdot d \cong \beta_g \cdot d - \beta_g \cdot \lambda_0 (1 - p) H(\alpha), \tag{28.14}$$

where $H(\alpha)$, as in Eq. (28.7), is known with the tabulated function,

$$\beta^{-1} \cdot d \cong \beta_g^{-1} \cdot d + \frac{3}{8} \cdot \beta_0^{-1} \lambda_0 \ln\left(\frac{1}{p}\right). \tag{28.15}$$

$$\beta_g{}^{-1} \cdot \beta_0 \cong 1 + 1{,}45 \cdot \frac{\lambda_0}{L} \ln\left(\frac{1}{r}\right), \quad \frac{R}{1 - R} \cong 0{,}97 \ln\left(\frac{1}{r}\right).$$

Example of size dependence for films in Sc coordinates $\beta - d$ and $\beta \cdot d - d$ are presented in Fig. 28.5. Based on these dependences for films Cr, Sc and Cu electrocarry parameters (Table 28.1, Fig. 28.6) were calculated, which were used for testing the theoretical model (28.13) for three-layer films based on Cr, Sc and Cu.

Results of testing are presented in Table 28.2. These data show that in the model (28.13) taking into account the deformation effects correctly makes it possible to forecast strain properties not only for three-layer film systems but also multilayers. But along with this it should be noted that the correspondence of experimental and calculated results in the case of three-layer films of Cu/Cr/Cu is 25–27 % and in case of double-layer films $[Ni(25)/V(25)]_n/S$ ($n = 1$–3) is 27–31 % [32]. This difference is related to the fact that Eq. (28.9) is obtained under the assumption that there is preservation of identity of the individual layers. These film systems are impossible to realize, even in the absence of bulk diffusion or limitations (such a situation occurs in the samples based on Cr, Cu and Sc and Cu and V), as much grain-boundary diffusion causes mixing of elements (see, for example, [40]). As a result of diffusion processes in the process of condensation or heat treatment solid solutions (ss) can

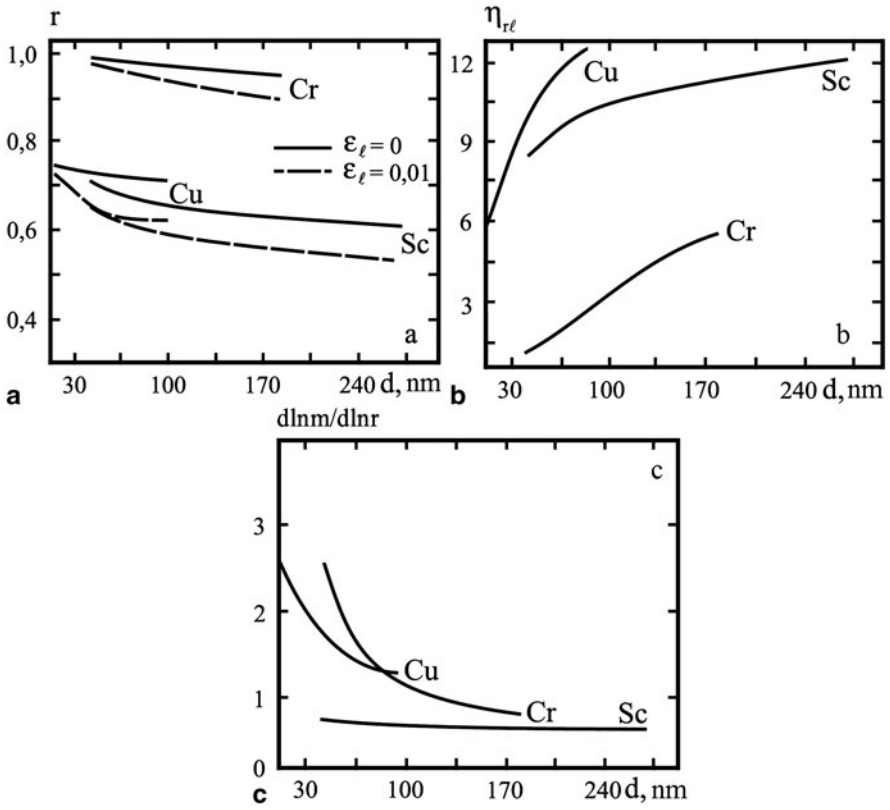

Fig. 28.6 Value of coefficients r (**a**), η_{rl} (**b**) and $\frac{d\ln m}{d\ln r}$ (**c**) for Cr, Sc and Cu films

be formed with unlimited or limited or intermetallic solubility [5]. Naturally, these processes lead to a change of parameters r, η_{rl}, Q and $\frac{d\ln m}{d\ln r}$ both aside increases and decreases. Trying to take into account the influence of diffusion processes on the conductivity of two-layer polycrystalline films was carried out by the authors [8]. But the obtained value includes many different options that are not always possible to determine experimentally or calculated.

The second factor that causes some discrepancy of experimental and calculated data for GF is associated with the nanostructure of individual layers. This is not to withstand the stringent requirement ($L = c\text{const}$) model of isotropic scattering and, consequently, the parameters λ_0, p and r are calculated accurately.

In conclusion, this section should emphasize the following. Model (28.13) allows us to understand the physical processes in multilayers on a microscopic level, but it is difficult to forecast strain properties on the basis of this model. From this perspective, there is a more efficient use of macroscopic models.

Table 28.1 Electrocarry parameters and strain characteristics at the $T = 300$ K

Electrocarry parameters		Strain characteristics		
$\varepsilon_l = 0\%$	$\varepsilon_l = 1\%$	$\eta_{\lambda_0 l}$	η_{pl}	$\frac{d\ln k}{d\ln p}$
Cr				
$p = 0.105$	$p = 0.056$			
$\lambda_0(1-p) = 56.1$ nm	$\lambda_0(1-p) = 64.6$ nm			
$\lambda_0 = 62.7$ nm	$\lambda_0 = 68.4$ nm	− 9.17	46.55	0.048
$\frac{\beta_g}{\beta_0(\varepsilon=0)} = 0.95$	$\frac{\beta_g}{\beta_0(\varepsilon=0)} = 0.90$			
Sc				
$p = 0.144$	$p = 0.181$			
$\lambda_0(1-p) = 138$ nm	$\lambda_0(1-p) = 156.9$ nm			
$\lambda_0 = 161.3$ nm	$\lambda_0 = 166.2$ nm	− 3.02	− 25.52	− 0.174
$\frac{\beta_g}{\beta_0(\varepsilon=0)} = 0.34$	$\frac{\beta_g}{\beta_0(\varepsilon=0)} = 0.30$			
Cu				
$p = 0.193$	$p = 0.125$			
$\lambda_0(1-p) = 33$ nm	$\lambda_0(1-p) = 34.5$ nm			
$\lambda_0 = 40.9$ nm	$\lambda_0 = 39.4$ nm	12.20	3.67	− 0.382
$\frac{\beta_g}{\beta_0(\varepsilon=0)} = 0.78$	$\frac{\beta_g}{\beta_0(\varepsilon=0)} = 0.70$			

Table 28.2 Comparison of the experimental and calculated data

Film system (thickness, nm)	Gauge factor, γ_l		
	Experiment	Calculated by model (28.13)	$\frac{\gamma_l^{\exp} - \gamma_l^{calt}}{\gamma_l^{\exp}}$
Cr(70)/Cu(45)/Sc(55)/Substrate	17.0	17.6	− 0.03
Cr(55)/Cu(120)/Sc(250)/S	7.5	8.3	− 0.10
Cu(25)/Cr(80)/Cu(50)/S	9.5	7.1	+ 0.25
Cu(120)/Sc(70)/Cr(75)/S	7.8	9.3	− 0.19
Cu(140)/Cr(65)/Sc(200)/S	8.2	7.1	+ 0.13
Cu(140)/Cr(80)/Cu(75)/S	7.0	5.1	+ 0.27

In the case of systems that contain individual separate layers ("biplate" film system type), formed by a thin transitional layer of solid solution at the interface or around the volume of the sample, ratio for γ_l are as follows [32, 38]:

$$\gamma_l^{\rho} = \gamma_{l1}^{\rho} + \gamma_{l2}^{\rho} - \frac{d_1\mu_1 + d_2\mu_2}{d_1 + d_2} - \frac{\gamma_{l1}^{\rho}\rho_1 d_2 - \rho_1 d_2\mu_2 + \gamma_{l2}^{\rho}\rho_2 d_1 - \rho_2 d_1\mu_1}{\rho_1 d_2 + \rho_2 d_1}, \tag{28.16}$$

$$\begin{aligned}\gamma_l^{\rho} \cong\ & \gamma_{l1}^{\rho} + \gamma_{lss}^{\rho} + \gamma_{l2}^{\rho} \\ & - \frac{(d_1 - d_1'')(\gamma_{lss}^{\rho}\rho_{ss}\rho_2 + \gamma_{l2}^{\rho}\rho_{ss}\rho_2) + (d_2 - d_2'')(\gamma_{lss}^{\rho}\rho_{ss}\rho_1 + \gamma_{l1}^{\rho}\rho_{ss}\rho_1)}{(d_1 - d_1'')\rho_{ss}\rho_2 + (d_2 - d_2'')\rho_{ss}\rho_1 + (d_1'' + d_2'')\rho_1\rho_2} \\ & + \frac{(d_1'' + d_2'')(\gamma_{l1}^{\rho}\rho_1\rho_2 + \gamma_{l2}^{\rho}\rho_1\rho_2)}{(d_1 - d_1'')\rho_{ss}\rho_2 + (d_2 - d_2'')\rho_{ss}\rho_1 + (d_1'' + d_2'')\rho_1\rho_2},\end{aligned}$$

where ρ_{ss} is the resistivity of solid solution and d_1'' and d_2'' are the thickness of layer ss under interface on first and secondary layers.

$$\gamma_l^{\rho} = \frac{\gamma_{l1}^{\rho}\rho_1 c_1 + \rho_1 c_1 \gamma_{l1}^{c} + \gamma_{l2}^{\rho}\rho_2 c_2 + \rho_2 c_2 \gamma_{l2}^{c}}{c_1\rho_1 + c_2\rho_2} \cong \frac{\gamma_{l1}^{\rho}}{1 + \frac{c_2\rho_2}{c_1\rho_1}} + \frac{\gamma_{l2}^{\rho}}{1 + \frac{c_1\rho_1}{c_2\rho_2}}, \quad (28.17)$$

where $\gamma_{li}^{c} = \frac{d\ln c_i}{d\ln l}$ is the relative change in concentration of the i-element at deformation.

28.3 Strain Properties in Range Elastic and Plastic Deformation

Unique physical and mechanical properties of nanocrystalline bulk and nanodimensional and nanocrystalline film samples are of great scientific interest. Investigations of the mechanical properties of fibrous crystals (the so-called "whiskers") preceded this increased interest. In these materials were revealed a wide range of the elastic deformation, which was about percents (for example, 3.8 % (Cu, Cr) and 4.9 % (Fe)) exceeding some 100 times the range for monocrystals; high coercitivity and hardness were only 15 % less than the theoretical value.

During the investigation of bulk and film nanocrystalline materials, great attention was paid to the study of their mechanical properties and the mechanism of plastic deformation [10, 11, 30, 34]. In this work was shown that the initial stage of the plastic deformation of bulk nanocrystalline materials is conditioned by the microslippage along the grain boundaries and cannot be described within the classical dislocation mechanism. The authors performed the investigations of the deformation mechanism by the stretching of Cu bulk samples (the nanograin size is 40–60 nm) and of $Fe_{73.5}CuNb_3Si_{13.5}B_9$ alloy (10 nm) directly in the electron microscope column. They concluded that in this case the deformation is mainly realized due to the nanograin rotation (rotational deformation modes) and the defect interaction in the boundaries and the near-boundary zones. The authors [22, 23] carried out "in situ" investigations of the mechanical properties and deformation mechanism by the example of thin Al films of micron thickness. It was established as well that the mechanical characteristics of free films and bulk samples are considerably different that is explained by the local decrease in the grain thickness with the appearance of the internal stresses as a result of dislocation localization inside their volume. Measurements of the Young's modulus for multi-layer film system based on two-layer nanodimensional Cu/Ni fragments of the thickness from 1.6 to 12 nm are carried out in Cammarata et al. [4]. Obtained value of the Young's modulus E of the multi-layer system was from 1.02 to 1.10 of the calculated value $E = c_1E_1 + c_2E_2$, where c_1 and c_2 are the concentrations of Cu and Ni atoms in separate fragments.

The authors [10] obtained the diagrams of the deformation of the coarse-grained (grain size is more than 1.5 μm) and fine-grained (grain size is less than 0.5 μm) Au films in the thickness range 0.2–2 μm. It was established that in the first case the mechanical properties do not substantially differ from those of bulk samples, except

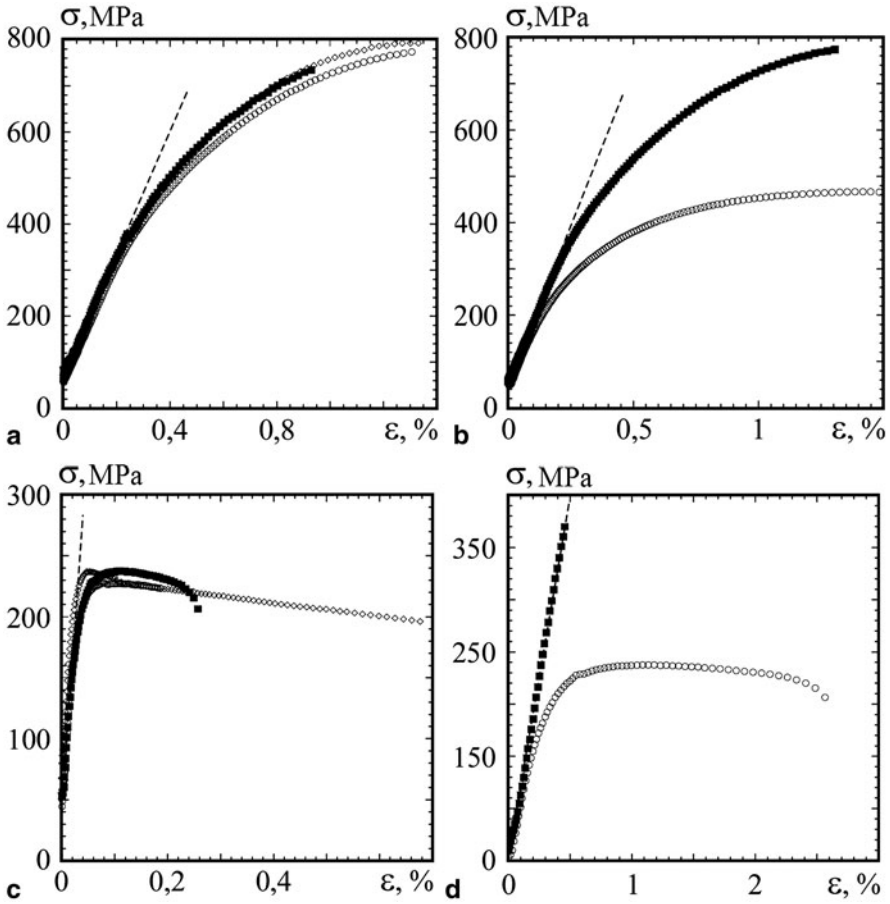

Fig. 28.7 Diagrams of the deformation for Cu (**a, b**) and Al (**c, d**) films of the thickness of 0.2 (■) and 1.0 (o) μm. Film width, μm: 5 (□), 10 (■) and 20 (o). (From [11])

for the low film plasticity. The strong dependence of the mechanical properties on the deformation velocity was observed in the case of the fine-grained samples.

Systematic investigations of the size effect in the plasticity of submicron (thickness is from 0.2 to 1 μm) Cu, Al and Au films are presented [11]. Obtained deformation diagrams (Fig. 28.7) allowed to determine the Young's modulus and establish new features of the mechanical properties.

Thus, for example, in Cu film when the thickness decreases from 1 to 0.2 μm the liquid limits increase from 160 to 345 MPa, and in Al films of the thickness of 0.2 μm, the plasticity is not observed at all and their brittle failure occurs at a stress of 375 MPa. Transition from elastic-to-plastic deformation takes place at the longitudinal deformation $\varepsilon_{ltr} \cong 0.25\%$ (Al films), $0.1 - 0.2\,\%$ (Cu films) and $0.05 - 0.15\,\%$ (Au films) that corresponds to the same value obtained by the authors [15] by the example of Pd films (Fig. 28.8) of the thickness of 4 μm ($\varepsilon_{ltr} \cong 0.25\%$)

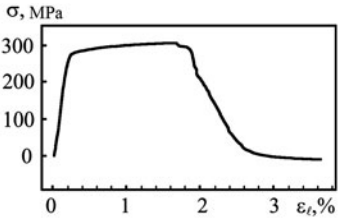

Fig. 28.8 Diagram of the deformation for Pd film with a thickness of 4 μm [15]

and of multi-layer film heterostructure based on Mo and Cu with the thickness of the separate layers up to 15 nm ($\varepsilon_{ltr} \cong 0.235\%$). In particular, the author [29] has studied the mechanical properties (limits of elasticity, ε_{tr}, and hardness, σ_m, and the Young's modulus) depending on the thickness using epitaxial, polycrystalline oriented and quasi-amorphous Au film of the thickness of 50−1500 nm. It was established that $\varepsilon_{tr} \leq 1\%$ and σ_m and E do not have a precise correlation with the film thickness, although in both cases their general tendency to decrease with the increase in the thickness when the dependences pass through the maximum is observed. The author notes a significant increase in σ_m in comparison with bulk samples: 20−48 MPa (films), 10–15 MPa (annealed samples of bulk Au) and 20–30 MPa ("whiskers"). At the same time, the Young's modulus has a smaller value in comparison with bulk monocrystals: 4–8 GPa (films) and 4.2–11.4 GPa (bulk monocrystals)

The authors [22] by the example of Al and Al, 1.5 %Ti films obtained the diagrams of the deformation and established that $\varepsilon_{tr} \cong 0.17$ and 0.30 %.

The work [48] presented data of other authors according to which $\varepsilon_{tr} = 0.17$–0.30 % for Ti–(48–51)%Ni films and for Cu films by ion deposition method $\varepsilon_{tr} \cong 0.40$ % ($d \cong 0.5$–1.5 μm) and by magnetron deposition method $\varepsilon_{tr} \cong 0.1$–0.3 % ($d \cong 1.5$–2.5 μm). In film materials, the grain-boundary electron scattering [3, 32] makes a substantial contribution to the gauge factor, that is conditioned the value of γ_l up to some tens of units [39]. Authors of the work [48] obtained single- and two-layer films (thickness of the separate layers is from 10 to 80 nm) by the thermal evaporation method in the vacuum chamber with pressure of the residual gases of 10^{-4} Pa on the polystyrene substrate, which was beforehand prepared by contact pads [39].

We have to especially note that high adhesion of metal films to polystyrene leads to measuring the strain properties on the system film/substrate. In this case, since the elasticity limit of metal films ε_{ltr} is less than 2 %, all measurements were performed in the conditions of elastically or plastically deformed film and elastically deformed substrate. They were guided by the results [4, 10, 11, 15] while determining the value of ε_{ltr} by the indirect method (using the dependence of the resistance R on ε_l).

Investigation of the strain properties was carried out using the developed automated system (Fig. 28.9) that gave the possibility to realize many deformation "stress-strain" cycles under static and dynamic conditions at the deformation speed from 0 to 0.1 %/s. Hardware of this system consists of the frequency meter; 8-channel 16-bit sigma-delta ADC ADAM-4018 by which the sample resistance is measured; relay module ADAM-4068 (which is the source of the driving voltage of the electric motor); USB RS232/422/485 interface converter ADAM-4561; asynchronous

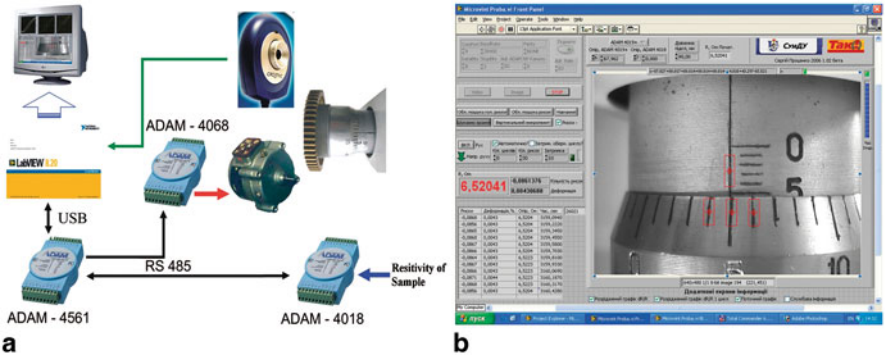

Fig. 28.9 Structural representation of the automated system (**a**) and interface of the developed software (**b**). Dependences of $\Delta R/R_i$, obtained during VIII–XI deformation cycles (Fig. 28.10a) under different deformations

capacitor motor and webcams of Creative Labs. The experiment control and result processing were performed based on the software developed in LabVIEW 8.50 using the machine vision module LabVIEW Vision Development Module 8.2 [39].

In Figs. 28.10 and 28.11, there are examples of different deformation dependences for Cu/Cr/S and Fe/Cr/S two-layer films, which show change of resistance and the value of the momentary coefficient of longitudinal GF: $\gamma_{lM} = \frac{1}{R_i} \cdot \frac{\Delta R_i}{\Delta \varepsilon_{li}}$, depending on ε_l, is to be correlated with the type of deformation.

Linear character of R and $\Delta R/R_i$ dependences on ε_l within the interval up to 1 % for II–VII deformation cycles can be explained by elastic (up to $\varepsilon_l \cong 0.25\%$) or quasi-elastic (within $\varepsilon_l = 0.25$–0.90 % interval) deformation of Cr film. Sharp distinction of the deformation cycle I from the other cycles can be explained by different relaxation processes, which take place there (such as partial turn of grains, microplastic deformation, reallocation and motion of imperfections of crystalline structure and foreign atoms, etc.). When increasing the longitudinal deformation up to 2 %, we transit to the range of plastic deformation as can be inferred from the nonlinear dependences of R and $\Delta R/R_i$ on ε_l.

Figure 28.10 [39] shows that there occurs a peculiar stabilization of microdeformation processes when a large amount of deformation cycles takes place (non-elasticity effect in polycrystals), and this fact lets us find a certain analogy with thermal stabilization of resistive properties of film materials.

Relatively large rate of increase of resistance under deformation may be an indirect proof for this assertion. In view of the fact that $\overline{\gamma_l}$ in the range of plastic deformation has relatively large values for both systems, we focus our attention on a certain contradiction between this result and the data for bulk samples. In the range of plastic deformation of bulk electrical resistance strain gauge, the relation between γ_{0l} and the coefficient of longitudinal GF is expressed by the Eq. (28.1). Based on the investigated strain effect in range elastic and plastic deformation, the calculated values of ε_{ltr} for double-layer systems are presented in the Table 28.3. The value of ε_{ltr} corresponds to the maximum on the dependence γ_{lM} versus ε_l (Fig. 28.10b-d and Fig. 28.11).

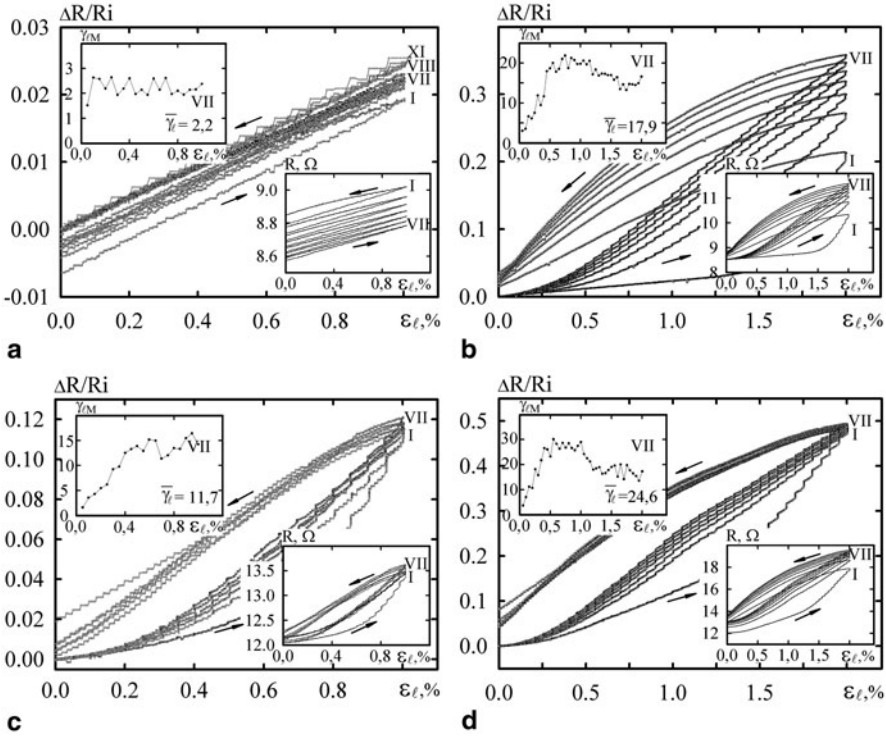

Fig. 28.10 Dependences of R, $\Delta R/R$ and γ_{lM} on ε_l for Cu(20)/Cr(14)/S film systems (**a, b**) and Cu(20)/Cr(30)/S (**c, d**). Index "i" is the mark of initial value of R; i is the number of $\Delta\varepsilon$ interval and $\overline{\gamma_l}$ is the mean value of GF [39]. The speeds (1 % per $\tau = 140$, 67, 30 and 20 s, respectively). Let us draw the conclusion about weak dependence of $\overline{\gamma_l}$ on deformation speed: $\overline{\gamma_l}$ 2.30 when $\tau = 140$ s and 2.50 when $\tau = 20$ s. Transition from elastic deformation to plastic deformation exerts much more influence on the GF value than the change of the deformation speed. At the same time, the proximity of γ_{lM} and $\overline{\gamma_l}$ values and similar character of the dependences of $\Delta R/R_i$ and γ_{lM} for Fe/Cr/S film system (Fig. 28.11) allows one to assert that in this case the plastic deformation takes place starting with $\varepsilon_l \cong 0.4$

At the elastic deformation, the grain-boundary slippage takes place according to which the first term in Eq. (28.1) is to be equal to zero, and, when $\mu \cong 0.5$, $\gamma_{0l} \cong 2$. The data we obtained for the film samples allow to conclude that there is a significant contribution (more than 10 units) of grain-boundary electron scattering to the total GF value. Size dependences of $\overline{\gamma_l}$ on the thickness of one of the layers, when thickness of the other layer is specified, which are represented in Fig. 28.12, indicate that $\overline{\gamma_l} \cong 2$ most probably takes place in the range of elastic deformation. The results obtained for the range of elastic deformation are in agreement with the calculated results obtained from the macroscopic model for the "binary plate"-type film system (Eq. (28.16)). It should be noted that experimentally obtained results for the Fe/Cr/S system do not agree (agree with an accuracy of 30–40 %) with Eq. (28.16), as in this case where the results were obtained not for a two-layer film system but for a one-layer two-component film, phase composition of which represents a solid solution

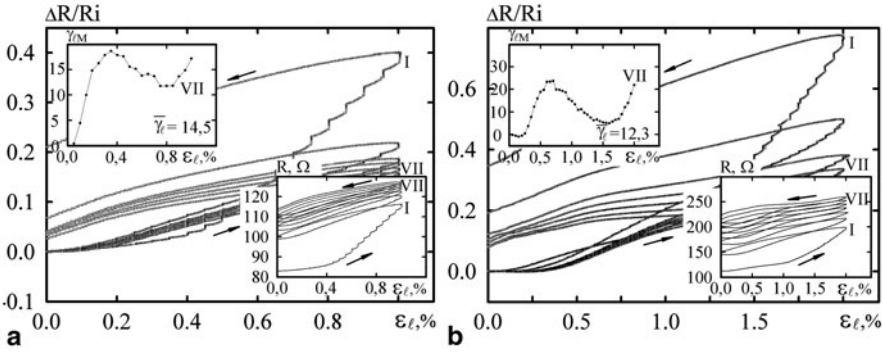

Fig. 28.11 Dependences of R, $\Delta R/R$ and γ_{lM} on ε_l for Fe(21)/Cr(31)/S film system in range $\Delta\varepsilon_1 =$ 0–1 % (**a**) and $\Delta\varepsilon_2 = 0$–2 % (**b**) [39]

Table 28.3 Values of ε_{ltr} for different double-layer film systems

Film systems	Fe/Cr		Cu/Cr		Pd/Fe
	Fe(20)/ Cr(30)/S	Fe(40)/ Cr (30)/S	Cu(20)/ Cr(20)/S	Cu(20)/ Cr(35)/S	Pd(10)/ Fe(20)/S
ε_{ltr}, %	0.40	0.30	0.40	0.25	0.50

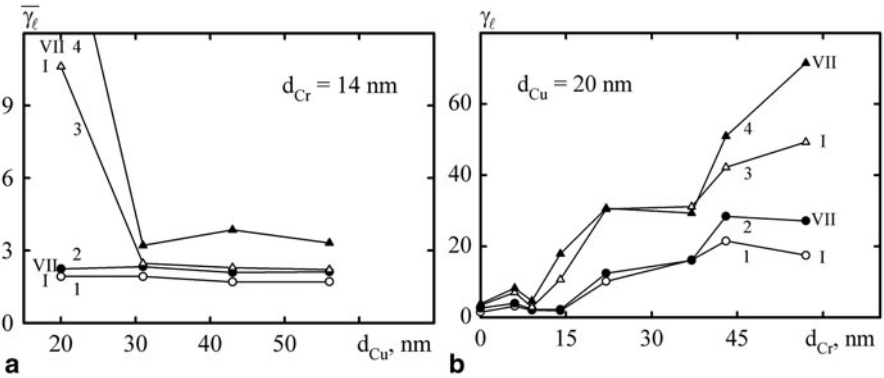

Fig. 28.12 Size dependences of $\overline{\gamma_l}$ for Cu/Cr(14)/S (**a**) and Cu(20)/Cr/S film systems (**b**): *1, 2*—$\Delta\varepsilon_l = 1$ %; *3, 4*—$\Delta\varepsilon_l = 2$ % [39]

(α-Fe, Cr). Such a conclusion is proved well by experimental results for Fe/Cr good agreement (agree with an accuracy 15–20 %) with calculations made according to the Eq. (28.17) for film alloy.

The effect of abnormal increase of momental longitudinal strain coefficient γ_{li} under the deformation ε_l can be explained [49] with nonlinear deformation processes. To establish conditions for the appearance of the maximum in dependence γ_{li} versus ε_l, we use equation, i.e. extremum condition.

After derivation of Eq. (28.16) and assuming that $\frac{\partial \mu_k}{\partial \varepsilon_l} \approx 0$ and $\left(\frac{d_1\mu_1+d_2\mu_2}{d_1+d_2}\right)$ have relatively small size (order unit), the extremum condition can be rewritten as:

$$\frac{1}{\rho_1}\frac{\partial^2\rho_1}{\partial\varepsilon_l^2}+\frac{1}{\rho_2}\frac{\partial^2\rho_2}{\partial\varepsilon_l^2}\cong\frac{\gamma_{li1}^{\rho}}{\rho_1}+\frac{\gamma_{li2}^{\rho}}{\rho_2}+\frac{\frac{\partial\gamma_{li1}^{\rho}}{\partial\varepsilon_l}\rho_1d_2+\frac{\partial\gamma_{li2}^{\rho}}{\partial\varepsilon_l}\rho_2d_1}{\rho_1d_2+\rho_2d_1}+\frac{\gamma_{li1}^{\rho}\rho_1d_2(\gamma_{li1}^{\rho}-2\mu_2)+\gamma_{li2}^{\rho}\rho_2d_1(\gamma_{li2}^{\rho}-2\mu_1)}{\rho_1d_2+\rho_2d_1}. \quad (28.18)$$

Assuming Poisson's coefficient, depending on the deformation, i.e. $\frac{\partial \mu_k}{\partial \varepsilon_l} \neq 0$, we obtain an equation that is very similar to (28.18). Both of them take the following form:

$$\rho_2\frac{\partial^2\rho_1}{\partial\varepsilon_l^2}+\rho_1\frac{\partial^2\rho_2}{\partial\varepsilon_l^2}\cong\gamma_{li1}^{\rho}\rho_2+\gamma_{li2}^{\rho}\rho_1, \quad (28.19)$$

if we consider that $\gamma_{li}^{\rho}/\rho \sim 10^7\text{Ohm}^{-1}\text{m}^{-1}$, $\gamma_{li}^{\rho}\cdot d/(d_1+d_2) \sim 10$ and $\gamma_{li}^{\rho}\cdot\rho d \sim 10^{-4}\text{Ohm m}^2$.

After derivation Eq. (28.17) and assuming that value $\frac{\partial \ln c_i}{\partial \varepsilon} = 0$, we obtain the extremum condition similar to (28.19):

$$\frac{1}{\rho_1}\frac{\partial^2\rho_1}{\partial\varepsilon_l^2}+\frac{1}{\rho_2}\frac{\partial^2\rho_2}{\partial\varepsilon_l^2}\cong\gamma_{li1}^{\rho}C_1+\gamma_{li2}^{\rho}C_2. \quad (28.20)$$

Equations (28.19) and (28.20) can be written as follows:

$$\frac{\partial^2\rho_1}{\partial\varepsilon_l^2}\cong\frac{\rho_1}{\rho_2}\left(\gamma_{li2}^{\rho}-\frac{\partial^2\rho_2}{\partial\varepsilon_l^2}\right)+\gamma_{li1}^{\rho}=C_1 \text{ and } \frac{\partial^2\rho_1}{\partial\varepsilon_l^2}\cong\rho_1\left(\gamma_{li11}^{\rho}+\gamma_{li22}^{\rho}-\frac{1}{\rho_2}\frac{\partial^2\rho_2}{\partial\varepsilon_l^2}\right)=C_2, \quad (28.21)$$

at the condition that ρ_2 slightly depends on the deformation. Analysis of ratio (28.21) makes it possible to conclude, that if

$\frac{\rho_1}{\rho_2}\cdot\left|\frac{\partial^2\rho_2}{\partial\varepsilon_l^2}\right| > \frac{\rho_1}{\rho_2}\gamma_{li2}^{\rho}+\gamma_{li1}^{\rho}$ or $\frac{\rho_1}{\rho_2}\cdot\left|\frac{\partial^2\rho_2}{\partial\varepsilon_l^2}\right| > \rho_1(\gamma_{li1}^{\rho}c_1+\gamma_{li2}^{\rho}c_2)$ in dependence γ_{li} versus ε_l may be place maximum $\left(\frac{\partial^2\rho_1}{\partial\varepsilon_l^2}<0\right)$. Under this condition, the dependence of the resistivity on the deformation is nonlinear:

$\rho(\varepsilon_l)=\frac{1}{2}C_1\varepsilon_l^2+A_1\varepsilon_l+B_1$ ("biplate" film system type),

$\rho(\varepsilon_l)=\frac{1}{2}C_2\varepsilon_l^2+A_2\varepsilon_l+B_2$ (system where solid solutions are formed),

where $A_k=(\partial\rho/\partial\varepsilon_l)_{\varepsilon_l\to0}$ is the sensitivity of the resistivity to strain at $\varepsilon_l\approx0$; $B_k=\rho(0)$ is the initial resistivity value.

A similar conclusion we get in the analysis of the two limiting cases $\rho_1 \gg \rho_2$ and $\rho_1 \ll \rho_2$. We also analysed the influence of different electron scattering mechanisms on the tensoresistive properties in terms of the Eq. (28.7) using the results

Table 28.4 Parameters electrocarry at elastic and plastic strain

Film systems	Elastic strain $\Delta\varepsilon_l = 0-(\Delta\varepsilon_{ltr}-0.1)$,%					Plastic strain $\Delta\varepsilon_l = 0-(\Delta\varepsilon_{ltr}+0.1)$,%				
	γ_l	λ_0, nm	λ_g, nm	$\Delta\lambda_g$, nm	R	γ_l	λ_0, nm	λ_g, nm	$\Delta\lambda_g$, nm	R
Fe(20)/Cr(30)	3.4	94	42	−1.0	0.36	5.6	87	40	−3.4	0.38
Fe(50)/Cr(30)	3.9			−1.1	0.40	10.7			−3.2	0.41

for Fe/Cr film system as an example. The value λ_0 and $\lambda_g = \lambda_0 \cdot f(\alpha)$ in the diffuse approximation ($p=0$), $\Delta\lambda_g$ under strain and R in range of elastic and plastic deformation were presented on the Table 28.4 [3].

It follows from these data that grain-boundary and volume scatterings are primary mechanisms responsible for the strain sensitivity of the films (as can be judged from large $\Delta\lambda_g$ and R). Remarkably, the character of electron grain-boundary scattering does not depend on the straining mechanism, since the difference between R in the elastically and plastically strained films is within the experimental error.

Our investigations show that film systems of Cu and Cr or Fe and Cr can be used as sensitive elements of strain sensors. If we compare the γ value of the above-mentioned film systems with one of different film materials as sensitive elements of strain sensors, we can state that in certain cases Cu/Cr and Fe/Cr two-layer films have an advantage with respect to the $\overline{\gamma_l}$ value. Thus (see for example [39]), in Ta oxynitride films, which have been analysed as high-temperature sensors, $\overline{\gamma_l} \cong 3.0-3.5$ units; in diamond polycrystalline films $\overline{\gamma_l} \cong 40-50$ units; in TaN_x films ($x = 0.04-0.20$), $\overline{\gamma_l}$ varies from 3.4 ($x \cong 0.04$) to 6 ($x \cong 0.12$) units, and after $TaN_{0.08}$ film annealing from 870 up to 1270 K, value of $\overline{\gamma_l}$ reduces from 4.25 to 4.05 units; in Si nanocrystalline films, $\overline{\gamma_l} = 10-25$ (p-type) and $\overline{\gamma_l} = -(10-20)$ units (n–type).

Therefore, our results are, up to some degree, in good agreement with the reported results in the literature for the strain sensitivity requirements.

Our investigations show that the strain at which the elastic–plastic transition takes place depends on the film thickness and decreases monotonically with increasing thickness. In double-layer Fe/Cr films, the grain-boundary scattering of electrons is equally effective under elastic and plastic strains, since the respective grain-boundary scattering coefficients (about 0.4) coincide within the experimental error. Electron scattering in the volume and at the boundaries of grains leads to a 30 % decrease in the MFPE.

28.4 Temperature Dependence of the Strain Coefficient

The temperature dependence can be analysed based on the definition of the coefficient of thermal strain coefficient $\beta_{\gamma l} = \frac{1}{\gamma_l} \cdot \frac{\partial \gamma_l}{\partial T}$ and ratio for $\gamma_l = \frac{1}{R} \cdot \left(\frac{\partial R}{\partial \varepsilon_l}\right)_T$. Then the

ratio for β_{γ_l} can be represented as follows:

$$\beta_{\gamma_l}=\left[\frac{1}{R}\left(\frac{\partial R}{\partial \varepsilon_l}\right)_T\right]^{-1}\cdot\left[\frac{\partial}{\partial T}\left(\frac{1}{R}\cdot\frac{\partial R}{\partial \varepsilon_l}\right)_T\right]_{\varepsilon_l}=-\beta+\frac{1}{R}\cdot\frac{\partial}{\partial T}\left(\frac{\partial R}{\partial \varepsilon_l}\right)_T. \quad (28.22)$$

After substituting ratio (28.1) to (28.22), we may obtain:

$$\beta_{\gamma_l}=\frac{\gamma_l-1-2\mu_f}{\gamma_l}\left(-\beta+\frac{1}{\gamma_l-1-2\mu_f}\cdot\frac{1}{\rho}\cdot\frac{\partial^2\rho}{\partial\varepsilon_l\partial T}\right), \quad (28.23)$$

the condition $\gamma_l >> 1$ is simplified to the form:

$$\beta_{\gamma_l}=-\beta+\frac{1}{\gamma_l\rho}\cdot\frac{\partial^2\rho}{\partial\varepsilon_l\partial T}. \quad (28.23a)$$

In case $\frac{\partial^2\rho}{\partial\varepsilon_l\partial T}=0$, ratio (28.23) is simplified to the form

$$\beta_{\gamma_l}\cong-\beta \quad (28.23b)$$

in accordance with the conclusion [53].

Note that the second term in ratio (28.23) and (28.23a) may be of the same order as β (for example $\gamma_l\sim 1$, $\rho\sim 10^{-6}-10^{-7}$ Ohm.m and $\frac{\partial^2\rho}{\partial\varepsilon_l\partial T}\sim 10^{-9}-10^{-10}$ Ohm m K^{-1}), and therefore the ratio (28.23b) not performed. In the analysis of (28.23a) we limit to two cases: $\beta > 0$ (polycrystalline films and $\beta < 0$ (nanocrystalline or amorphous films). In the first case, $\beta_{\gamma_l} > 0$ provided that $\beta<\frac{1}{\gamma_l\rho}\cdot\frac{\partial^2\rho}{\partial\varepsilon_l\partial T}$ and $\frac{\partial^2\rho}{\partial\varepsilon_l\partial T}>0$.

In this case, γ_l will increase with increasing temperature, possibly by law [47] $\gamma_l=C_1+C_2T$, where C_1 and C_2 are constants.

This conclusion is confirmed by the example of polycrystalline films of Cr, V and film alloys (Co-Ni) and (Ni-Ag; Table 28.5). In the second case, when $\beta < 0$ and $\frac{\partial^2\rho}{\partial\varepsilon_l\partial T}>0$, though possible less stringent conditions:

$$\left|\frac{1}{\gamma_l\rho}\cdot\frac{\partial^2\rho}{\partial\varepsilon_l\partial T}\right|<\beta \text{ i } \frac{\partial^2\rho}{\partial\varepsilon_l\partial T}<0,$$

when the value will also be greater than zero.

This occurs in case of nanocrystalline Mo i W films (Table 28.5).

In this case, we will have a negative value if $\beta_\gamma < 0$ at conditions

$$\left|\frac{1}{\gamma_l\rho}\cdot\frac{\partial^2\rho}{\partial\varepsilon_l\partial T}\right|<|\beta| \text{ at the } \frac{\partial^2\rho}{\partial\varepsilon_l\partial T}<0.$$

This is obviously the case with poly- and monocrystalline films of In, thick films RuO_2 + glass and WO_3+RuO_2 + glass and nichrome wires (Table 28.5). These data again confirm the conclusion that the ratio (28.23b is performed. We obtained a correlation between the values γ_l and β for TaN-Cu nanocomposites with different content of Cu [12]. Thus, at Cu concentration from 15 to 50 at.% γ_l increases from 1.83 to 4.50 units and β increases from -0.8×10^{-3} to $+2.18\times10^{-3}$ K^{-1}, i.e. γ_l increases with increasing temperature. Similar data is known for multilayer Cu/Fe [1].

Table 28.5 Temperature characteristics of strain sensors [31]

Sensitive element of strain sensor	$\beta \times 10^3$, K^{-1}	$\beta_{\gamma 1} \times 10^3$, K^{-1}	$\frac{\partial^2 \rho}{\partial \varepsilon_1 \partial T} \cdot 10^9$, Ohm m K^{-1}
Polycrystalline film Cr	0.65	5.00	4.0
-″-	0.70	6.00	4.5
Polycrystalline film V	0.23	0.28	7.0
Polycrystalline film Co-Ni	–	0.13–0.26	–
Film alloys Ni_xAg_{1-x}			
x = 35 %	0.84	2.70	17.0
x = 45 %	0.81	3.10	12.5
x = 50 %	0.75	3.30	11.8
Nanocrystalline films Mo	−0.09	9.90	11.4
Nanocrystalline films W	−0.20	4.00	16.0
Mono- and polycrystalline in films	–	− (0.45–0.70)	–
Thick films:			
RuO_2 + glass	–	− 0.22	
$WO_3 + RuO_2$ + glass	–	− 0.51	
Multilayer Cu/Fe	–	7.02–7.64	–

28.5 Magnetodeformation Effect

Question about dependence of the strain coefficient of film and bulk materials versus the value of magnetic field (the magneto-deformation effect) is among the little-studied ones, though it is a subject of current interest. Thus, the authors' [55] investigations of magnetic field influence on the GF of amorphous metal alloys were based on Fe and B basis and determined its very essential influence on their values. Authors explain the obtained results by the Young modulus change under magnetic field action (the so-called ΔE effect). The authors [51] carried out theoretical and experimental study of the magneto-deformation effect on the example of diamond films with *p*-type conduction. It was established that in the range of deformation $\Delta\varepsilon = 2 \times 10^{-5} - 10^{-4}$ on magnetic film $B = 3$ T, the value of GF decreases to 10 % that is connected with the deformation-induced change of valence band and with the influence of magnetoresistance effect.

Quantitative characteristic of magneto-deformation effect may be the magnetic coefficient of strain coefficient, the methodological basis of whose introduction can be the same as for the thermal coefficient of strain coefficient (ratio (28.18)), that is,

$$\beta^k_{\gamma_{lB}} = \frac{1}{\gamma_l}\left(\frac{\partial \gamma_l}{\partial B}\right)_{\varepsilon l}, \tag{28.24}$$

where index "*k*" corresponds to the longitudinal, transverse or perpendicular geometry measuring.

Using Eqs. (28.1) and (28.24) for $\beta_{\gamma l B}$, we get [35]:

$$\beta^k_{\gamma_{lB}} = \frac{1}{\gamma_l}\frac{\partial}{\partial B}\left(\frac{1}{\rho}\frac{\partial \rho}{\partial \varepsilon_l} + 1 + 2\mu_f\right)^k = \frac{1}{\gamma_l}\left(-\frac{1}{\rho^2}\frac{\partial \rho}{\partial B}\cdot\frac{\partial \rho}{\partial \varepsilon_l} + \frac{1}{\rho}\frac{\partial^2 \rho}{\partial \varepsilon_l \partial B}\right)^k. \tag{28.25}$$

We assume that in film samples the weak magnetostriction effect takes place, and therefore μ_f does not practically depend on the magnetic field. Ratio (28.25) is transformed to the following form:

$$\beta_{\gamma_l B}^k = \frac{1}{\gamma_l}\left(-\beta_B \cdot \frac{1}{\rho}\frac{\partial \rho}{\partial \varepsilon_l} + \frac{1}{\rho}\frac{\partial^2 \rho}{\partial \varepsilon_l \partial B}\right)^k$$
$$= \frac{\gamma_l - 1 - 2\mu_f}{\gamma_l}\left(-\beta_B + \frac{1}{\gamma_l - 1 - 2\mu_f} \cdot \frac{1}{\rho}\frac{\partial^2 \rho}{\partial \varepsilon_l \partial B}\right)^k, \tag{28.26}$$

which provided γ_l and $\gamma_t \geq 10$ simplified to the form

$$\beta_{\gamma_l B}^k \cong -\beta_B^k + \left(\frac{1}{\gamma_l \rho} \cdot \frac{\partial^2 \rho}{\partial \varepsilon_l \partial B}\right)^k, \tag{28.26a}$$

in relation (28.26a) into account Eq. (28.1) and through $\beta_B^k = \frac{1}{\rho}\frac{\partial \rho}{\partial B}$ is the magnetic resistance coefficient.

The simplified ratio (28.26a) allows to qualitatively analyse the field dependence γ_l (such analysis for γ_t has not principled difference). In case $\beta_B^k < 0$, γ_l increases in magnetic field), if $\left(\frac{\partial^2 \rho}{\partial \varepsilon_l \partial B}\right)^k > 0$ or $\left(\frac{\partial \rho}{\partial \varepsilon}\right)^k > \left|\frac{\partial \rho}{\partial B}\right|^k$.

Probably, this case takes place in double-layer films on Cr and Fe basis, for which the value of γ_l in magnetic field is by 3–6 % more than 0.1 T [45].

If $|\beta_B|^k < \left|\frac{\partial^2 \rho}{\partial \varepsilon_l \partial B}\right|^k$ value of γ_l decreases in the external magnetic field, as it takes place in diamond films [51] or metal alloys [55] under relatively strong fields. In case, when $\beta_B^k > 0$, the value of $\beta_{\gamma_l B}^k > 0$ at the condition $|\beta_B|^k < \left|\frac{\partial^2 \rho}{\partial \varepsilon_l \partial B}\right|^k$ and $\left(\frac{\partial^2 \rho}{\partial \varepsilon_l \partial B}\right)^k < 0$. At the same time, under conditions $\left(\frac{\partial^2 \rho}{\partial \varepsilon_l \partial B}\right)^k > 0$ and $\left(\frac{\partial^2 \rho}{\partial \varepsilon_l \partial B}\right)^k > |\beta_B|^k$ the value γ_l increases in the external magnetic field, although these experimental results are unknown.

A similar analysis of magneto-deformation effect in the double-layer films systems is made in the work of Makukha et al. [25] at the used ratio (28.16). The ratio for $\beta_{\gamma_l B}^k$ has the form:

$$\beta_{\gamma l B}^k = \beta_{\gamma_1 B}^k \cdot \gamma_1 + \beta_{\gamma_2 B}^k \cdot \gamma_2 - \frac{\gamma_1 \rho_1 d_2 (\beta_{\gamma_1 B} + \beta_{\rho_1 B}) + \gamma_2 \rho_2 d_1 (\beta_{\gamma_2 B} + \beta_{\rho_2 B})}{(\rho_1 d_2 + \rho_2 d_1)}$$
$$+ \frac{\beta_{\rho_1 B} \rho_1 d_2 \mu_2 + \beta_{\rho_2 B} \rho_2 d_1 \mu_1}{(\rho_1 d_2 + \rho_2 d_1)} + \frac{(\beta_{\rho_1 B} \rho_1 d_2 + \beta_{\rho_1 B} \rho_2 d_1)(\gamma_2 \rho_2 d_1 + \gamma_2 \rho_2 d_1)}{(\rho_1 d_2 + \rho_2 d_1)^2}$$
$$- \frac{(\beta_{\rho_1 B} \rho_1 d_2 + \beta_{\rho_1 B} \rho_2 d_1)(\gamma_2 \rho_2 d_1 + \gamma_2 \rho_2 d_1)}{(\rho_1 d_2 + \rho_2 d_1)^2} - \frac{(\beta_{\rho_1 B} \rho_1 d_2 + \beta_{\rho_2 B} \rho_2 d_1)(\rho_1 d_2 \mu_2 + \rho_2 d_1 \mu_1)}{(\rho_1 d_2 + \rho_2 d_1)^2},$$

where

$$\beta_{\rho B}^k \cong \left[\left(\frac{\partial \rho_1}{\partial B}\rho_2(d_1 + d_2) + \frac{\partial \rho_2}{\partial B}\rho_1(d_1 + d_2)\right)(\rho_1 d_2 + \rho_2 d_1) - \rho_1 \rho_2 (d_1 + d_2)\left(\frac{\partial \rho_1}{\partial B}d_2 + \frac{\partial \rho_2}{\partial B}d_1\right)\right]^{-1}$$
$$\cong \left[\rho_1 \rho_2 (d_1 + d_2)(\rho_1 d_2 + \rho_2 d_1)\right]^{-1}$$

$$\cong \frac{\beta_{\rho B_1}\rho_2 d_1 + \beta_{\rho B2}\rho_1 d_2}{\rho_1 d_2 + \rho_2 d_1},$$

where $\beta^k_{\rho B} = \left(\frac{1}{\rho}\cdot\frac{\partial\rho}{\partial B}\right)^k$ is the magnetic coefficient of resistivity.

Ratio for $\beta^k_{\gamma lB}$ greatly simplifies in two limiting cases:

at $d_2 << d_1$, $\beta^k_{\gamma lB} \cong \beta^k_{\gamma_1 B}\gamma_1 + \beta^k_{\rho_2 B}\mu_1$; and at $d_2 >> d_1$, $\beta^k_{\gamma lB} \cong \beta^k_{\gamma_2 B}\gamma_2 + \beta^k_{\rho_1 B}\mu_2$.

As with single-layer films, these limiting cases follow the conditions under which GF increases or decreases in the external magnetic field:

if $\beta_{\gamma_1 B} > 0^k$ and $\beta^k_{\rho_2 B} > 0$ or $\beta^k_{\gamma_1 B} > 0$, then $\beta^k_{\rho_2 B} < 0$, but $\beta^k_{\gamma_1 B} > \left|\beta^k_{\rho_2 B}\right|$;

if $\beta^k_{\gamma_1 B} < 0$ and necessarily $\beta^k_{\gamma_1 B} > 0$ or $\beta^k_{\gamma_1 B} > 0$ and $\beta^k_{\rho_2 B} > \left|\beta^k_{\gamma 1 B}\right|$.

The analysis allows the prediction of magneto-deformation properties of single- and double-layer films.

We have analysed the classical model for strain coefficient of single-layer films and phenomenological models for two-and multilayer thin-film systems. Despite the fact that the classical models have been developed for multilayer films (see, for example, [9]), we prefer the phenomenological models because they allow prediction of strain properties. Also note that in recent years extensive research was conducted on strain properties of heterogeneous plastic materials, which have higher values of GF. For example, in films based on RuO_2 and Si, Pb and Al (Table 28.5; [14]) or in films of Ni: a-C: H [19], GF value varies within 10–20 units. This may be an incentive for their use as sensing elements of sensors with non-electrical quantities.

28.6 Conclusion

In conclusion, we would like to focus on two little-known problems associated with the limit value strain coefficient [41] and the new strain effect we proposed and studied in the magneto-optical properties [6].

Classical theory of strain effect in bulk samples was developed and in the most general form longitudinal strain coefficient is written as:

$$\gamma = \frac{d\ln R}{d\varepsilon} = \frac{d\ln\rho}{d\varepsilon} + (1 + \mu + \mu') \cong \frac{d\ln\rho}{d\varepsilon} + (1 + 2\mu). \tag{28.27}$$

Considering that the $\frac{d\ln\Theta_D}{d\ln V} = \gamma$ (Θ_D is the Debye temperature for film,

V is the volume, γ is the Gruneisen constant), ratio (28.27) can be rewritten as:

$$\gamma_l^{\rho} = 1 + 2\gamma(1 - 2\mu_f) = 1 + \eta_{\lambda_0 l},$$

and converted to the form:

$$\gamma_l = 1 + (2\gamma - 4\mu_f\gamma) + (1 + 2\mu_f). \tag{28.28}$$

From ratio (28.28), it follows that $\gamma_l^b = \lim\gamma_l = 2(1 + 2\mu_f) \cong 3$ (although for the condition $\gamma_l^{\rho} = 0$ the value is $\gamma_l^b = 2$). The authors [44] have analysed this issue

for thin films in the framework of the Fuch-Sondgeimer (FS) in the limiting case of small thicknesses ($\frac{d}{\lambda} << 1$, d is the film thickness). They got the value for γ_l provided at the condition $\rho \sim \lambda_0^{-1} n^{-\frac{3}{2}}$:

$$\gamma_l = 2\left(\frac{5}{6} + \mu_f\right) + (2\gamma - 4\gamma\mu_f) \tag{28.29}$$

that $\mu_f = 0.5$ gives the value $\gamma_l^b = 2.7$.

We have considered [41] the other limiting cases of FS models, namely $\frac{d}{\lambda_0} >> 1$, where size dependence ρ has the form:

$$\rho/\rho_0 + \frac{3}{8}\frac{\lambda_0(1-p)}{d},$$

but a ratio for γ_l is written as:

$$\gamma_l \cong 1 + 2\gamma - 2\mu - 4\mu\gamma\left(1 - \frac{3}{8}\frac{\lambda}{d}(1-p)\right) + (1 + 2\mu_f) \cong 2 + (2\gamma - 4\mu_f\gamma), \tag{28.30}$$

that $\mu_f = 0.5$ carried to $\gamma_l^b = 2$ (here taken into account that $\frac{\lambda}{d} << 1$ and that $p \cong 0.1 - 0.2$).

The authors [13] on the basis of a more general ratio model FS received the equation:

$$\gamma_l^\rho \cong 2\mu\gamma\left(1 - \frac{\beta}{\beta}\right) \cong (0.5 - 0.8)\gamma,$$

where for $\gamma_l^b \cong 2 + (0.5 - 0.8)\gamma \cong 3.0 - 3.6$ at the $\gamma = 2$ (β and β_0 are temperature coefficients of resistance film and bulk samples, respectively).

Numerical experimental results for the anomalous value γ_l are now known. First of all, it comes to the data of the works by Parker R.L. et al. (1963) and Tyschenko et al. [50], which are the values $\gamma_l < \gamma_l^b$ for films Au, Pd, Ni and Co (Parker R.L. et al. 1963). Calculated by ratio (28.29), which corresponds to the condition $d/\lambda_0 << 1$, the value μf for different values γ_l at the fixed values of Gruneisen constant (Fig. 28.13) indicate that anomaly small size γ_l occur at a value $\mu_f > 0.4$, i.e. in the quasi- and plastic deformation. Similar calculations are based on ratio (28.30). It corresponds to the conditions $d/\lambda_0 >> 1$ which are in very good agreement with calculations based on ratio (28.29). For example, if $\gamma_l = 3$ that $\mu_f = 0.25$ ($\gamma = 1$); 0.37 ($\gamma = 2$) and 0.41 ($\gamma = 3$). At the same time, the ratio of (28.3) is not consistent with calculations by ratios (28.29) and (28.30), since it corresponds to bulk samples.

Really, when you consider that the minimum wavelength phonons $\lambda_{\min} = 2a$ (a is the lattice parameter), then the strain Θ_D for the longitudinal phonon spectrum mode decreases the amount of:

$$\Delta\Theta_D^x = \frac{hv_{ph}}{2k_B} \cdot \left(\frac{1}{a \cdot (1 + \mu_f\varepsilon)} - \frac{1}{a}\right) = \frac{v_{ph}}{2k_B a} \cdot \left(\frac{\mu_f\varepsilon}{1 + \mu_f\varepsilon}\right)$$

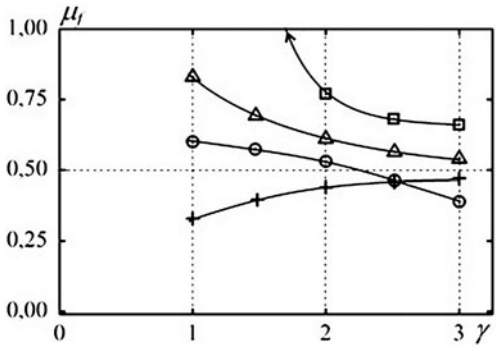

Fig. 28.13 Calculated values of μ_f based on ratio (28.4) for different values of γ and γ_l. Value $\gamma_l = 1$ (□); 2 (Δ); 2.5 (o) and 3 (+)

and slightly increases in the case of transverse oscillation modes:

$$\Delta\Theta_D^{y,z} = \frac{h\nu_{ph}}{2k_B a} \cdot \left(\frac{\mu_f \varepsilon}{1 - \mu_f \varepsilon}\right),$$

where ν_{ph} is the phase velocity and k_B is the Boltzmann constant.

It is known that in thin films or small particles we observe a decrease of Θ_D (see, for example, [43]), which increases the mean square displacement of atoms as $\overline{u^2} \sim \left(\frac{T}{\Theta_D}\right)^2$ [20, 43]. Increase in $\overline{u^2}$ determines some effective increase in $\mu_f = -\frac{d\ln d}{d\ln l}$. Qualitative considerations indicate that the longitudinal deformation film value Θ_D will also generally decrease, although strain causes a slight increase. Thus, in all film materials the value of μ_f must be somewhat overpriced compared to that in bulk samples.

Another mechanism of an increase $\mu_f{}'$ is associated with some reduction in thickness $\Delta d'$ due to diffusion of surface atoms at grain boundaries, which during deformation $\Delta\varepsilon_{l,t} > 0$ width will increase. The smoothing relief of film surface will cause an additional contribution $\Delta\mu_f{}'$ in value $\mu_f{}'$.

The analysis in the macroscopic approach can qualitatively explain the physical nature of boundary parameter γ_l^b and cause anomalous small values γ_l. Clearly, macroscopic analysis indicates only the cause of this effect or discloses these microscopic processes that lead to small sensitivity to strain specific resistance at a relatively large value of it. Obviously, the change in mechanical properties μ_f, γ and temperature Θ_D cause somehow a reduction of the size of the coefficients r and Q and limiting value λ_0. Because of this perspective, the problem has a large complexity, and we have limited ourselves only to qualitative analysis.

The second problem, which was discussed above, involves the use of thin-film materials. Effectiveness of nanodimensional thin-film materials as sensitive elements of temperature, pressure, strain, magnetic field and others sensors make it possible to develop a concept of multi-sensors, including sensors, strain and magnetic field; the principle of the latter may be based on magneto-strain effect.

The principle of operation of these sensors is based on the strain effects of electric resistance (R) film (see, for example, [31, 39, 41] or giant magnetoresistance (GMR;

B. [2, 24]). As a kind of strain effect can be seen magneto-strain effect when the strain coefficient measured in the presence of an external magnetic field (B). Phenomenological theory of this effect in single-layer films and multilayers are proposed in the works by Protsenko S.I. [35] and Makukha Z.M. et al. [25].

As previously indicated, the quantitative characteristic of strain effect is the strain coefficient, defined by the relation:

$$\gamma_{l,t}^{R} = \frac{d\ln R}{d\ln \varepsilon_{l,t}} = \frac{1}{R} \cdot \frac{\Delta R}{\Delta \varepsilon_{l,t}}.$$

Similar strain coefficients for GMR and magneto-strain effect can be defined as follows:

$$\gamma_{l,t}^{GMR} = \frac{1}{GMR} \cdot \frac{\Delta GMR}{\Delta \varepsilon_{l,t}} \text{ and } \beta_{\gamma_{l,t}B} = \frac{1}{\gamma_{l,t}} \cdot \left(\frac{\Delta \gamma_{l,t}}{\Delta B}\right)_{\varepsilon_{l,t}}. \tag{28.31}$$

The quantitative characteristic magneto-optic Kerr effect (MOKE) on a strain coefficient is as follows:

$$\gamma_{l,t} = \frac{1}{\Theta_0} \cdot \frac{\Delta \Theta}{\Delta \varepsilon_{l,t}}, \tag{28.32}$$

where Θ_0 is the angle of the rotation of polarization plane at the $\varepsilon = 0$, $\Delta\Theta = \Theta_{\varepsilon_{l,t}} - \Theta_0$ ($\varphi_{\varepsilon_{l,t}}$ is the angle of rotation the polarization plane with $\varepsilon_{l,t} \neq 0$).

Experimental studies on MOKE [6] performed in an external magnetic field during strain to 10 % allowed to carry out research both in elastic (up 0.5 %) and plastic (in the range of 0.5–10 %) strain. The strain was carried out when its direction and the direction of the magnetic field lines are parallel (we denote the index "l") or perpendicular (index "t"), respectively. Note that this indexing is to a large extent arbitrary and has the same meaning as in the case of strain effect (Eq. (28.32)). It deals with a variety of measurement geometries of MOKE.

Based on dependencies $\Theta_\varepsilon/\Theta_0$ versus ε and Eq. (28.32), it can be represented as follows:

$$\gamma_{l,t}^{MOKE} = \frac{1}{\Delta \varepsilon_{l,t}} \cdot \left(\frac{\Theta_\varepsilon}{\Theta_0} - 1\right), \tag{28.33}$$

coefficients γ_l^{MOKE} were calculated, the value of which increases with increasing common concentration of Fe atoms. At the same time, γ_t^{MOKE} does not depend on the value of ε_t, the common concentration of Fe atoms.

Coefficient γ_l^{MOKE} varies in range from 8 (for Fe (32)/Pt (3)/S) to 2.5 units (for Fe (32)/Pt(10)/S) and from 3 (for multilayers [Fe(3)/Pt(3)]$_8$/S) to 1.2 units (for multilayers [Fe(3)/Pt(10)]$_8$/S). Coefficient $\gamma_t \cong (4.0 - 4.5)$ units for all investigated two-layer films and multilayers. As hysteretic dependences, presented in Fig. 28.2, we explain the different characteristics of the interaction of electromagnetic waves with electron gas at the l- or t-geometry measurement of MOKE.

Acknowledgements The work was carried out with financial support from the Ministry of Education and Science of Ukraine.

References

1. Alalykin SS, Alalykin AS, Danilov AA, Krylov PN (2007) Tenzorezistivnye svoistva nanorazmernykh multisloinykh structure Cu/Fe. Bulletin University of Udmurtia 4:84–87
2. Anwarzai B, Ac V, Luby S, Majkova E, Sendera R (2010) Pseudo spin-valve on plastic substrate as sensing elements of mechanical strain. Vacuum 84:108–110
3. Buryk PI, Velykodnyi DV, Odnodvorets LV, Protsenko IYu, Tkach OP (2011) Tensoresistive effect in thin metal films in the range of elastic and plastic strain. Tech Phys 56(2):232–237
4. Cammarata RC, Schlesinger TE, Kim C, Qadri SB, Edelstein S (1990) Nanoindentation study of the mechanical properties of copper-nickel multilayered thin films. Appl Phys Lett 59(9):1862–1864.
5. Cheshko IV, Protsenko IYu (2009) Formuvannya metastabil'nykh tverdykh rozchyniv u plivkovykh systemakh na osnove Co i Cu, Ag ta Au. Metallofiz Noveishie Technol 31(7):963–967
6. Cheshko IV, Makukha ZM, Odnodvorets LV, Shumakova MO, Velykodnyi DV, Protsenko IYu (2013) Strain effect on magneto-optical and magnetic properties of film system based on Fe and Pt. Univ J Mater Sci 1(2):13–17
7. Chornous AM, Opanasyuk NM, Pogrebnjak AD, Protsenko IYu (2000) Experimental test of a three-dimensional model for electrophysical properties of metal films. Jpn J Appl Phys 39(12B):L1320–L1323
8. Dekhtyaruk L, Pazukha I, Protsenko S, Cheshko I (2006) Conductivity of single-crystal and polycrystalline bilayer metal films under the conditions of interdiffusion. Phys Solid State 48(10):1831–1843
9. Dekhtyaruk LV, Protsenko IYu, Chornous AM (2007) Transportni rozmirni effecty u dvosharovykh polikrystakichnykh plivkakh. Usp Fiz Met 8(1):21–64
10. Emery RD, Povirk GL (2003) Tensile behavior of free-standing gold films. Part I. Coarse-graines films. Acta Mater 51:2067–2078
11. Espinosa HD, Prorok BC, Peng B (2004) Plasticity size effects in free-standing submicron polycrystalline FCC films subjected to pure tension. J Mech Phys Solids 52:667–689
12. Fu B, Gao L (2006) Tantalum nitride/copper nanocomposite with zero temperature coefficient of resistance. Scripta Mater 55:521–524.
13. Ghodgaokard AM, Ramani K (1980) Computation of the strain coefficient of resistivity in thin metallic films. Phys Stat Sol A 60(1):C99–C109
14. Hrovat M, Belavic D, Samardzija Z, Holc J (2001) A characterization of thick film resistors for strain gauge applications. J Mater Sci 36:2679–2689
15. Ievlev VM, Belonogov EK, Maksimenko AA, Agapov BL, Shkatov VV (2006) Substructura i prochnost' condensirovannykh plenok palladiya. Deformatsiya i razrushenie materialov. V.1. MGIU, Moskow, pp 468–471
16. Jen SU, Wu TC, Liu CH (2003) Piezoresistance characteristics of some magnetic and non-magnetic metal films. J Magn Magnet Mat 256:54–62
17. Khater F, El-Hiti M (1988a) Strain coefficients of electrical resistance of double-layer thin metallic films. Phys Stat Sol A 108(1):241–249
18. Khater F, El-Hiti M (1988b) Temperature coefficient of the strain coefficient of electrical resistivity of double-layer thin metallic films. Phys Stat Sol A 109(2):517–523
19. Koppert R, Goettel D, Freitag-Weber O, Shultes G (2009) Nickel containing diamond like carbon thin films. Solid State Sci 11:1797–1800
20. Kuczynski GC (1954) Effect of elastic strain on the electrical resistance of metals. Phys Rev 94(1):61–64
21. Lasyuchenko O, Odnodvorets L, Protsenko I (2000) Microscopic theory of tensosensibility of multilayer polycrystalline films. Cryst Res Technol 35(3):329–332
22. Lee H-J, Cornella G, Bravman JC (2000) Stress relaxation of free-standing aluminum beams for microelectromechanical systems applications. Appl Phys Lett 76(23):3415–3417
23. Lee HJ, Zhang P, Bravman JC (2003) Tensile failure by grain thinning in micromachined aluminum thin films. Appl Phys 93:1443–1451

24. Luby S, Anwarzai B, Aĉ V, Majkova E, Senderak R (2012) Pseudo spin-valve with different spacer thickness as sensing elements of mechanical strain. Vacuum 86:718–720
25. Makukha ZM, Protsenko SI, Odnodvorets LV, Protsenko IYu (2012) Magneto-strain effect in double-layer film systems. J Nano Electron Phys 4(2) Part II. doi:02043-1-02043-3
26. Mayadas AF, Shatzkes M (1970) Electrical resistivity model for polycrystalline films: the case of arbitrary reflection at external surfaces. Phys Rev B1(4):1382–1389
27. Meiksin ZH (1975) Discontinuous and cermet films. Physics of thin films, vol 8. Academic, New York, pp 99–168
28. Meiksin ZH, Hudzinski RA (1967) A theoretical study of the effect of elastic strain on the electrical resistance of thin metal films. J Appl Phys 38(11):4490–4494
29. Neugebauer CA (1960) Tensile properties of thin, evaporated gold films. J Appl Phys 31(6):1096–1101
30. Noskova NI, Volkova EI (2001) In situ study of deformation of nanocrystalline copper. Phys Metals Metallography 91(6):629–635
31. Odnodvorets LV, Protsenko SI, Chornous AM, Protsenko IYu (2007) Effect tenzochutlyvosti v metalevykh plivkovykh materialakh. Usp Fiz Met 8(2):109–156
32. Odnodvorets L, Protsenko S, Synashenko O, Velykodnyi D Protsenko I (2009) Electrophysical properties of Ni/V and Cr/Fe multilayer films. Cryst Res Technol 44(1):74–81
33. Parker RL, Krinsky A (1963) Electrical resistance-strain characteristics of thin evaporated metal films. J Appl Phys 34(9):2700–2708
34. Pozdnyakov VA, Glezer AM (2002) Structural mechanisms of plastic deformation in nanocrystalline materials. Phys Solid State 44(4):732–737
35. Protsenko SI (2009) Magnetodeformation effect in thin metal films. J Nano Electron Phys 1(2):5–7
36. Protsenko SI, Chornous AM (2003) Doslidgennya i prognoz tenzorezystyvnykh vlastyvostei plivkovykh system na osnovi Cr, Cu i Sc. Metallophyzika i noveishie technologii 25(5):587–601
37. Protsenko IYu, Odnodvorets LV, Chornous AM (1999) Electroconductivity and tensosensibility of multilayer films. Met Phys Adv Tech 18:47–59
38. Protsenko SI, Cheshko IV, Velykodnyi DV, Pazukha IM, Odnodvorets LV, Protsenko IYu, Synashenko OV (2007) Structurno-fazovyi stan, stabil'nist' interfeisiv ta electrofizychni vlastyvosti dvosharovykh plivkovykh system. Usp Fiz Met 8(4):247–278
39. Protsenko SI, Velykodnyi DV, Kheraj VA, Desai MS, Panchal CJ, Protsenko IYu (2009) Electrophysical properties of Cu/Cr and Fe/Cr film systems within elastic and plastic deformation range. J Mater Sci 44(18):4905–4910
40. Protsenko SI, Synashenko OV, Zabila Y, Marzalek M (2011) Diffusion processes in nanoscale two-layer film systems based on Fe and Cu or Fe and Cr. J Surf Invest 5(4):787–790
41. Protsenko IYu, Odnodvorets LV, Tyschenko KV, Shumakova MO (2013) Features strain properties anomalous small of strain coefficient. J Mech Eng Technol 1(1):34–39
42. Rajanna K, Nayak MM (2000) Strain sensitivity and temperature behavior of invar alloy films. Mat Sci Eng B B77:288–292
43. Sadaiyandi K (2009) Size dependent Debye temperature and mean square displacements of nanocrystalline Au, Ag and Al. Mater Chem Phys 115:703–706
44. Sharma BK, Jain N, Srivastava R (1983) Strain coefficient of resistivity in thin metallic films. Helvetica Phys Acta 56:1093–1097
45. Synashenko OV, Tkach OP, Buryk IP, Odnodvorets LV, Protsenko SI, Shumakova NI (2009) Magnetoresistive properties of multilayer nanodimensional film systems. Probl Atomic Sci Technol 6:169–174
46. Tellier CR, Tosser AJ (1982) Size effects in thin films. ESPS, Amsterdam, 309 p
47. Tillier CR (1985) Effect of defect structure on the electrical conduction mechanism in metallic thin films. J Mater Sci 20(6):1901–1919
48. Tkach OP, Odnodvorets LV, Protsenko SI, Velykodnyi DV, Tyschenko KV, Protsenko IYu (2010) Mechanical properties of micron and nanodimensional metal films. J Nano Electron Phys 2(1):22–29

49. Tyschenko KV, Odnodvorets LV, Protsenko IYu (2012) Peculiarities of deformation dependence of the strain coefficient in metal films. Pramana—J Phys (in press)
50. Tyschenko KV, Pazukha IM, Shabelnyk TM, Protsenko IYu (2013) Electrophysical properties on nanocrystalline platinum thin films. J Nano Electron Phys 5(1) doi:01029-1-01029-5
51. Wang WL, Liao KJ, Hu CG (2003) Study on piezoresistive effect of diamond films under magnetic field. Sens Actuators A 108:55–58
52. Warkusz F (1980) Electrical and mechanical properties of thin metal films: size effects. Progr Surf Sci 10(3):287–382
53. Witt GR (1974) Some effect of strain and temperature on the resistance of thin gold-glass cermet films. Thin Solid Films 22:133–156
54. Zabila EO, Protsenko IYu (2005) Method of studying the tensoresistive properties of chrome films at relatively small and large deformations. Ukr J Phys 50(7):727–734
55. Zakharenko NI, Semen'ko MP (2007) Vliyanie magnitnogo polya na tensoresistivnyi effect v amorphnykh splavakh na osnovi zheleza. Phys Metals Metallography 104(2):150–154

Chapter 29
Kinetics of Nonequilibrium Transition in Spin-Crossover Compounds

Iurii Gudyma, Cristian Enachescu and Artur Maksymov

29.1 Introduction

The development of contemporaneous field of information technologies requires new type of materials able to satisfy the increasing need of data storage capacity and recording rate. A solution to avoid large energy consumption for achieving high recording rate and large storage capacities of information devices is the development of finite systems of nanoscopic size. In this context, molecular magnets based on spin state interconversion are promising perspectives for practical applications. Remarkable representatives of such kind of materials are spin-crossover compounds, which are magnetic bistable coordination compounds characterized by two states with different spin configuration: low-spin (LS) diamagnetic state, stable at low temperatures and high-spin (HS) paramagnetic state, stable at high temperature and sometimes metastable at low temperatures, as we discuss later. The interconversion of spin configuration from one state to another occurs during the action of external physical fields such as magnetic field, temperature, light irradiation, pressure etc.

For the first time the interconversion of two spin states as a result of variation in temperature was observed in the works of Cambi and coworkers in the 1930s by studying the unusual magnetism of iron (III) derivatives of various dithiocarbamates [1, 2]. Their works focused on the study of magnetism of various derivatives of iron (II) and iron (III) and it was found that in these naturally existing systems, the spin states were very sensitive to the character of the axial ligands. The intermediate values of the magnetic moment observed in the experiments were interpreted as a

Iu. Gudyma (✉) · A. Maksymov
Chernivtsi National University, Kotsubynski Str., Nr. 2, Chernivtsi 58012, Ukraine
e-mail: yugudyma@gmail.com

C. Enachescu
Alexandru Ioan Cuza University of Iasi, Bulevardul Carol I, Nr. 11, Iasi 700506, Romania
e-mail: cristian.enachescu@uaic.ro

O. Fesenko, L. Yatsenko (eds.), *Nanocomposites, Nanophotonics, Nanobiotechnology, and Applications,* Springer Proceedings in Physics 156,
DOI 10.1007/978-3-319-06611-0_29,

bonding of different nature that was supposed to be partially ionic and partially covalent. In the 1950s, Orgel proposed another explanation of the anomalous magnetic behavior observed 20 years earlier, relying on an equilibrium between two iron (III) species with different number of unpaired electron [3]. A few years later, Busch and coworkers reported for the first time the spin-crossover phenomenon in the synthetic six-coordinated Co (II) complexes [4, 5]. Subsequent studies of spin transition in a synthetic iron (II)-based spin-crossover have been performed by König and Madeja in the 1967s [6]. They realized extensive magnetic and Mössbauer spectroscopic studies on these complexes and gave the explanation of the nature of spin transition in some of the first iron (II) spin-crossover complexes. The possibility of spin transition in artificial systems plays a pivotal role for synthesizing the spin-crossover compounds with necessary properties. In 1982, McGarvey and Lawthers found that for some ferrous and ferric ion-based spin-crossover complexes in solution, the system could be transferred into HS state by pulsed laser excitation of LS state [7]. The discovery of McGarvey et al. was followed by the observation of Decurtins at al. [8] that at cryogenic temperatures, solid iron (II) spin-crossover systems can be quantitatively trapped in the HS state by light monochromatic irradiation. At small temperatures the so formed HS state has virtually infinite lifetime, thus the state is metastable. This effect is known as light-induced excited spin-state trapping (LIESST). After 30 years from this discovery, one can say that it was a crucial point for the subsequent development of studies on spin-crossover complexes, as well as for the perspective applications of spin-crossover compounds. The studies of spin-crossover nanoparticles are of fundamental interest with relevance to the technological applications of functional miniaturized materials, such as thin films, nanopatterns, and nanoparticles. However, the pertinent questions concerning individual SCO nano-objects and their interactions with the surroundings are not entirely explored [9, 10, 11].

As a result of numerous experimental and theoretical works on molecular magnets the main features of the compounds in which the change of spin configuration of system states occurs have been determined. The fundamental consideration of the occurrence of spin crossover in terms of ligand field theory, for iron(II) in particular, was given by Hauser in [12]. In the framework of ligand field consideration the spin-crossover materials are referred as belonging to the class of inorganic complexes with $d^4 - d^7$ electronic configuration and transition metal ion central situated in the ligand field with octahedral symmetry [12, 13, 14, 15].

Due to strong manifestation of the properties specific for the spin-crossover materials, such as cooperative effects, gradual changes of spin-configuration and other, the practical application of six-coordinated, in particular iron(II), spin-crossover compounds as materials of information technology is more suitable in comparison with other spin-crossover complexes. This opportunity lies in the possibility of simple transition between the LS and HS states of iron(II) based compounds under external perturbations (change of temperature, application of pressure, by light irradiation or by pulsed magnetic field supported by a lot of reasonable features such as stability over successive cycles, low addressing power, short addressing time since the transition is purely electronic in nature (nanosecond scale), and a hysteresis effect when the transition between the two states is accompanied by cooperative effects [14]). These

properties offer the good prospects for application the spin crossover (SCO) phenomenon in molecular electronics, data storage, display devices, nonlinear optics, photomagnetism, and other [14, 15, 16].

The present chapter is organized as follows: in the second section we analyze the effects occurring at intramolecular level during spin transition. In particular, we describe the degeneracy of spin states and effects related with light irradiation of the sample. The third section is devoted to some theoretical considerations for describing the spin crossover effects. We shall discuss two basic approaches: the microscopic Ising-like description of spin-crossover materials with elastic interactions between the species and macroscopic one, based on dynamical studies of phenomenological characteristics, in particular magnetic moment related to the fraction of HS molecules (denoted here as n_H). In the fourth section is considered the stochastic dynamics of spin-crossover compounds arising from the interaction of the system with environment. The behaviour of spin-crossover system driven by colored noise is described in the fifth section. Here, the escape time is studied from metastable state of spin-crossover compounds by varying the parameters of control field and noise.

29.2 The Spin-Crossover Phenomenon

As mentioned earlier, the transition between the states of spin-crossover compounds may be caused in the main by the action of temperature, light irradiation, pressure, or (very strong) magnetic fields. It leads to drastic change of the spin-crossover material properties determined by the electron distribution on the sublevels of d-orbital for LS and HS states. Soon after the synthesis of first spin-crossover compounds showing a thermal hysteresis, researchers from several fields (inorganic chemistry, physical chemistry, solid state physics, theoretical chemistry) began the search for their practical application. By the mid-1980s, the interest to study intersystem crossing phenomena between the HS and LS state started to decrease due to some disadvantages of temperature-induced interconversion relying on slow transition rate and difficulties to its control. Thereby, the interest for potential application of spin-crossover compounds as ultrafast data storage and recording system diminished.

For understanding the mechanism of the interconversion between LS and HS configuration we must consider the structural features of spin-crossover complexes and the way of populating the high-energy levels. For this purpose, we examine ferrous based compounds as they are the most widely used.

For the free iron(II) ion, the five nondegenerate levels of its d orbitals are filled up according to Hund's rule in such a way that four electrons are unpaired and only two of them compose one pair. In perfectly octahedral coordination complexes the action of crystal field, created by nonmetallic ligand environment, on metal ion provokes the splitting of its d-orbital into a subset of three orbitals d_x, d_y, d_z, and which are basis of the irreducible representation t_{2g} sublevel, and a subset of two orbitals d_{x1}, d_{y1} which are the basis to the irreducible representation e_g sublevel (Fig. 29.1) [12]. The LS configuration is characterized by a large energy difference

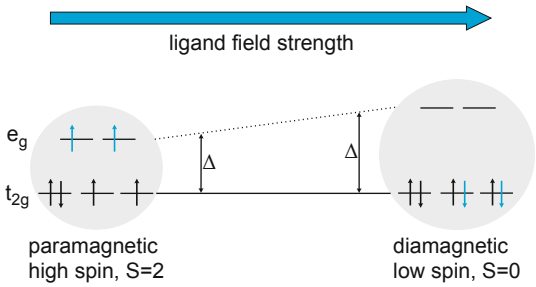

Fig. 29.1 The illustration of electron distribution on d-orbital of iron(II) spin-crossover complexes

between metastable ${}^5T_{2g}$ and ground state ${}^1A_{1g}$, thus the strength of electron-electron repulsion is not enough to populate e_g sublevel. In this case, according to Hund's rule, the d-electrons will nicely pair up in the t_{2g} sublevel, resulting in a diamagnetic low-spin ground state due to spins compensation. In the neighborhood of transition point, the energy difference between ${}^5T_{2g}$ and ${}^1A_{1g}$ states decreases, leading to the equilibrium between ligand field strength and electron-electron repulsion. In this case, according to the same Hund's rule, the d-electrons will enter the t_{2g} and e_g orbitals, but the spins are not compensated, which leads to a resultant magnetic moment. For LS configuration, the metal-ligand bounds are stronger and shorter due to electron absence on e_g sublevels, whereas for HS, the situation is opposite. For this reason, on the macroscopic scale, the spin transition is accompanied by changes in the volume of spin-crossover materials.

The transition caused by the external controlling physical fields, accompanied by sharp transition curve related with the drastic change of the properties of spin-crossover materials, distinguish the occurrence of first order phase transition. The state diagrams of spin-crossover compounds and the environment influence on phase transition have been extensively discussed in several papers [12, 17, 18, 19].

From the practical point of view to consider the light-induced interconversion is more preferable, based on LIESST effect consisting in trapping of the excited spin states. This effect may be observed for solid state spin-crossover at low temperature. The schematic representation of LIESST effect is illustrated in Fig. 29.2. The mechanism of realization of this effect is the following: as a result of absorption light quanta, the electrons are transferred into intermediate allowed states ${}^1T_{1g}$ and ${}^1T_{2g}$. The electrons from these short-lived states quickly relax back into ground states and also into intermediate triplet states ${}^3T_{2g}$ and ${}^3T_{1g}$, from which the transition occurs in the ground state as well as in the metastable HS state ${}^5T_{2g}$. Taking into account that transitions ${}^1A_{1g} \rightarrow {}^3T_{1g}$ and ${}^1A_{1g} \rightarrow {}^3T_{2g}$ are forbidden, the nonequilibrium population of metastable ${}^5T_{2g}$ state follows. The metastability of HS state may be explained by the appearance of energy barrier trough lengthening of metal-ligand bound and small energy difference between the states. At low temperatures, HS metastable states formed in this way practically do not decay, therefore for the interconversion back into ground LS state we need to irradiate the pattern with an appropriate wavelength (usually red or infrared). This effect is well known as reverse LIESST effect. The reverse LIESST effect is initiated by an allowed ${}^5T_{2g} \rightarrow {}^5E_g$ transition, where the

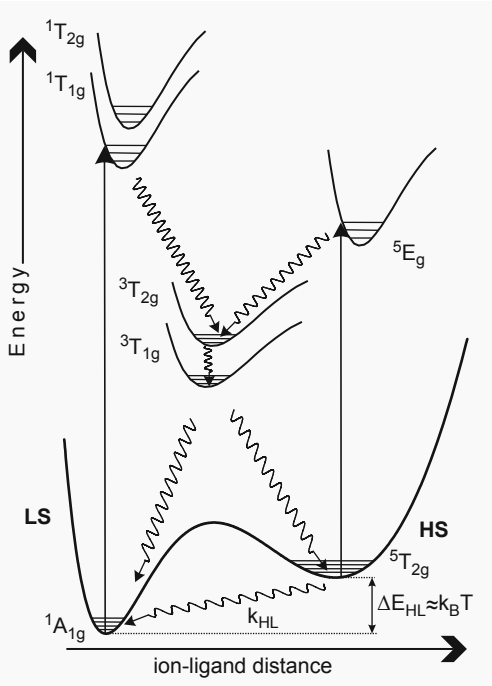

Fig. 29.2 The schematic representation light induced spin transition for iron(II) based complexes

energy value of the level ^5E_g is close to the energy value of the triplet levels ^3T which lead to it population. The last step of the reverse LIESST is transition from triplet intermediate states ^3T to ground state $^1A_{1g}$, but due to forbiddance of such transition not all HS states undergo the interconversion, which are shown in the work [13]. The light induced transition is very fast (about few femtoseconds [20, 21]) and is characterized by high quantum yield.

The metastable state obtained by photoexcitation relaxes towards the fundamental state by a nonradiative process [22, 23]. At low temperature it acts as a tunneling process, more or less slow according to the height of the energy barrier. At higher temperature (typically above 40 K) this process is thermally activated and can be described by an Arrhenius-type law. At room temperature, it is in general very fast, with life a time of the order 10^{-9} to 10^{-12} s. The relaxation is monoexponential for low intermolecular interactions (Fig. 29.3a) and becomes self-accelerated in the cooperativity case (Fig. 29.3c) [24]. For some compounds, in which both direct and reverse LIESST are efficient, it is possible to observe both HS-LS and LS-HS relaxation, that converge to the same state (Fig. 29.3b).

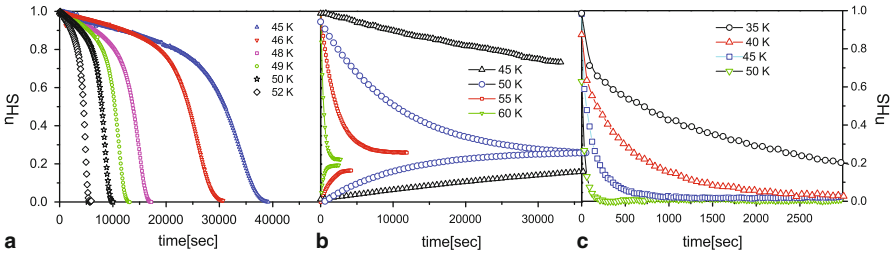

Fig. 29.3 The relaxation in iron (II)-based complex with low intermolecular interactions (**a**) and with cooperative interaction (**b**) and (**c**)

29.3 The Theoretical Models of Spin-Crossover Compounds

Several theoretical models have been elaborated for describing the behaviour of spin-crossover compounds. The approaches for studying spin-crossover transition may be divided into two main groups: models that are explored in a microscopic approach based on Ising-like description [25, 26, 27] and macroscopic phenomenological models giving a good description of macroscopic system parameters [28, 29, 30]. Both approaches present advantages and disadvantages and several relationships between them have been previously discussed and are presented in the papers [26, 27, 31].

In the framework of microscopic model, it is easier to understand the processes that determine the phase state of the spin transition, and the mechanism which leads to bistable behavior of the system. Taking into account that spin-crossover molecules are the structural units of such system, the microscopic approach is very convenient for describing the intermolecular processes occurring in materials. But as real materials contain a large number of molecules for microscopic examination of the system it would be necessary to make some approximation which would reduce the accuracy of system description.

Contrariwise, in the macroscopic approach realised by using simple mathematical tools, it is possible to describe the dynamics of spin-crossover system through the dependencies of its phenomenological parameters on external physical field perturbation [28]. In this case, it is easy to include the external driving forces in the kinetic equations, but now is impossible to give the information about microscopic processes [17, 18, 19, 32].

29.3.1 The Macroscopic Phenomenological Model

For studying spin-crossover transition with optical control parameter, it is more convenient to use the phenomenological model, which is based on competing processes between photoexcitation and relaxation of HS molecules [28]. In the simplest case, if

we neglect the interaction of spin-crossover molecules, the general kinetic equation describing the system evolution including the action of light intensity is as follows:

$$\frac{dn_H}{d\hat{t}} = I_0\omega n_L(\hat{t}) - k_{HL}(T)n_H(\hat{t}) + k_{LH}(T)n_L(\hat{t}). \tag{29.1}$$

Here I_0 is intensity of light irradiation, ω is product of absorption cross-section with the quantum yield of the system, k_{HL} is the rate of spontaneous transition from LS to HS state at constant temperature T, k_{LH} the rate of spontaneous transition from LS to HS state, and n_H and n_L is the fraction of molecules in HS and LS states. The first term in Eq. (29.1) $I_0\omega n_L(\hat{t})$ describes the induced photoexcitation of LS molecules due to absorption of light quanta, the second term $k_{HL}(T)n_H(\hat{t})$ represents the spontaneous relaxation of HS molecules, and the third term $k_{LH}(T)n_L(\hat{t})$ describes the spontaneous transition from LS to HS state.

The dynamics of spin-crossover compounds without photoexcitation may be described by the Eq. (29.1) where the $I_0\omega n_L(\hat{t}) = 0$. It corresponds to the spontaneous thermal equilibrium [33]. The temperature dependencies for this regime may be obtained from detailed balance equation of the next form:

$$\frac{n_H}{n_L} = \frac{k_{LH}(T)}{k_{HL}(T)}. \tag{29.2}$$

We focus our attention on light induced dynamics of spin-crossover compounds. Because the probability of spontaneous transition is much less in comparison with photoinduced transition, i.e. $k_{LS}n_H(\hat{t}) << I_0\omega n_L(\hat{t})$, hereinafter the spontaneous LS $\rightarrow$ HS transition described by $k_{LH}(T)n_L(\hat{t})$ is not taken into account.

At the system steady state, where the fractions of HS and LS molecules are the same, by neglecting the spontaneous transition from LS to HS state, which may provoke minor system disordering, the equilibrium states of the spin-crossover system may be found from the next relation followed from detailed balance in the system:

$$\frac{n_H}{n_L} = \frac{I_0\omega}{k_{HL}(T)}. \tag{29.3}$$

It must be noted that the photoexcitation at low temperature is characterized by very high quantum yield (near to 1), which is considered constant, unlike the relaxation process which is self-accelerated due to suppression of potential barrier related with depopulation of HS system state [34]. Such cooperative relaxation is observed in thermal activation regime implying the high temperatures and in regime with low temperature.

The relaxation in systems with strong intermolecular interaction depends on the states of neighborhood molecules. In this case, the decay of system states an arbitrary temperature may be described by exponential dependence of relaxation rate on HS fraction in the following way [24]

$$k_{HL}(T, n_H) = k_{HL}^{\infty} n_H \exp\left[-\frac{E_a(n_H)}{k_B T}\right], \tag{29.4}$$

where the thermal activation energy of the molecule for HS → LS relaxation is

$$E_a(n_H) = E_a(0) + \alpha k_B T n_H.$$

Here k_{HL}^{∞} is high temperature asymptotic of the relaxation rates at the end of the process ($T \to \infty$), k_B is Boltzmann constant, T is temperature, $\alpha(T)$ is self-acceleration factor (in the thermal activation regime it is written $\alpha = 2zJ/(k_B T)$, where z is the number of interacting neighbours, J is the intermolecular interaction parameter). For the simplicity the initial activation energy is equalized to zero $E_a(0) = 0$.

Therefore the macroscopic master equation of light-induced system with dimensionless quantities, obtained by substitution $t = k_{HL}^{\infty} n_H \hat{t}$ and considering that $n_L = (1 - n_H)$, is written [17]:

$$\frac{n_H}{dt} = \beta(1 - n_H) - n_H \exp[-\alpha n_H] = f_{exc} - f_{rel}. \tag{29.5}$$

Here the control parameter is $\beta = I_0 \omega / k_{HL}^{\infty}$; the photoexcitation term is $f_{exc} = \beta(1 - n_H)$ and the relaxation one is $f_{rel} = n_H \exp[-\alpha n_H]$. The stationary solutions of Eq. (29.5) give the description of system steady states.

29.3.2 The Ising-Like Model and its Relation with Mechanoelastic Model

Using phenomenological interaction parameters, acting similarly for all molecules in a sample, the subsequent mean-field models have been able to reproduce successfully several of the characteristic features of SC compounds, such as the occurrence of a thermal hysteresis and its dependence on the strength of intermolecular interaction, the shift of the thermal transition towards higher temperatures when applying external pressure, the sigmoidal shape of relaxation curves, or the light induced bistability. However, these rather simple models do not distinguish between short range and long range interactions and therefore do not allow an advanced analysis of experimental curves, nor are they able to explain how the effect of the individual switch of molecules spreads through the entire solid. In addition, these models cannot be applied for the study of size effects in nanoparticulate spin-crossover systems. Therefore more accurate models were necessary. The simplest theoretical model for studying the phase transition in the magnetic materials on microscopic level taking into account the intermolecular interaction is the Ising model [25, 26, 27, 35]. In the spin-crossover Ising-like model the LS and HS states are described by a fictitious variable s, which takes the values -1 for LS state and $+1$ for HS one. In general case, the Ising-like Hamiltonian for spin-crossover system with short-range and long-range interaction is described by the next equation:

$$H = -J \sum_{ij} s_i s_j - \Delta_{eff} \sum_i s_i, \tag{29.6}$$

where $\Delta_{eff} = (1/2)k_B T \ln(g_H/g_L) - \Delta + G\langle s\rangle$ is effective "magnetic field", $\langle s\rangle = m$ is fictitious magnetization, J and G describe short-range and long-range interaction respectively, 2Δ is the energy difference between HS and LS states for an individual spin-crossover molecule, g_H/g_L is degeneracy ratio of each states, T is temperature. For the spin-crossover compounds Δ_{eff} cannot be zero. The ratio g_H/g_L may take large value (around some thousand) due to consideration of degeneracy and density of vibrational levels in each states.

In the paper [36] the authors investigate the dynamical properties of the $1D$ Ising-like Hamiltonian taking into account interactions in the spin-crossover system, in order to predict its static and dynamic behavior. For this purpose, they used the dynamic Glauber approach for the Ising-like model [37], where the spins are assumed to interact with the thermal bath, which causes them to flip randomly in time. The mean-field version of the two-level dynamic problem led to the same phenomenological formula for the sigmoidal relaxation [26, 27, 31]. The treatment of Huang [38, 39] for the Ising models with correlations, which lies in usage of the Bethe-Peierls method to solve the Glauber problem for $1D$ Ising systems under a magnetic field, made possible the analysis of Ising-like system which combines short- and long-range interactions [36]. The influence of finite-size effects on properties of stationary state together with transient process of a bistable system with long range interaction was studied in [40], where the Husimi–Temperlay model with infinite range interaction was adopted.

The spin-crossover phenomenon is supported by changes of metal-ligand bounds length which influence very much on the properties of coordination complexes. The distance variation between metal ion and ligand environment leads to the development of short-range and long-range interaction with pronounced cooperative effects between the spin-crossover molecules.

While Ising-like models can reproduce several features of SC behavior, the physical meaning of the interaction parameters is not clear as it does not take into account the distortions created by the different sizes of molecules. These distortions are precisely the origin of intermolecular interactions; therefore Ising-like models are not expected to reproduce correctly the same state molecule cluster spreading during the transition, the new class of elastic model has been therefore developed.

Recently, several papers proposed elastic models based on a ball and string concept (i) for a linear chain described by an atom-phonon coupling model [41], (ii) for two-dimensional systems using molecular dynamics [42], and (iii) for 3D systems using Monte Carlo Metropolis methods [43]. In these models the elastic interactions are seen as an internal pressure, and consequently the effective interaction is proportional to the fraction of molecules in HS state. The simulation of hysteresis loops for a system of molecules in a finite $2D$ hexagonal lattice connected by springs and subjected to external pressure was carried out in [44], thereby considering distributions of transition temperatures similar to the Preisach model [45] as suggested by the FORC diagram method [46].

In the mechanoelastic model as described in previous papers [47, 48, 49, 50], the spin crossover units occupy the vertices of a triangular tiling, composing a planar

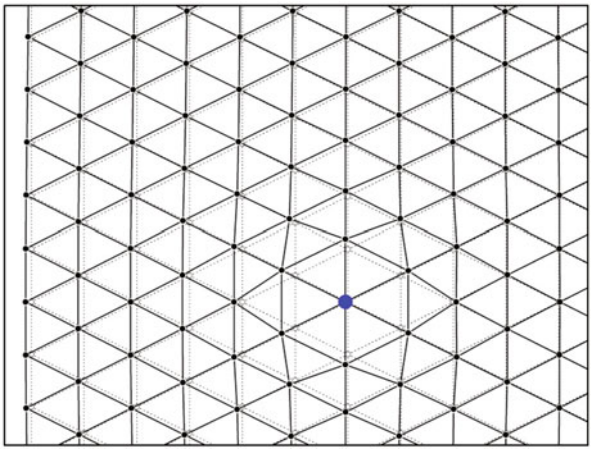

Fig. 29.4 The triangular network of particles connected with springs. In the initial state all the molecules are in the LS state (*open circles*). When a molecule switches its state to HS (*blue full circle*), all the other molecules (*small circles*) change their positions. The lattice becomes then distorted: the distortions are bigger in the vicinity of switched molecule (*short range effect*), but they are present even in remote parts of the system (*long range effect*)

lattice with open boundaries (Fig. 29.4). The molecules are linked by springs, whose elastic constant simulates the elastic interactions responsible for the cooperative phenomena for which spin crossover compounds are renowned. In the system with all molecules either in the HS or in the LS state, respectively, the springs are neither elongated nor compressed and therefore no external elastic forces act on individual molecules. If a molecule changes its state, then it will change its radius and therefore its neighboring springs will instantaneously change their lengths. The resulting elastic forces will determine the progressive motion of all the molecules in the system, which stops when all of them have reached a new mechanical equilibrium.

From a computational point of view, it is difficult to find the equilibrium positions of all molecules in the system by solving equilibrium equations (especially for large systems). Therefore, it was considered instead that each molecule has a damped oscillatory-type motion. Then, the new equilibrium positions are simply found by solving a system of coupled differential equations for all molecules in the system

$$\begin{cases} m\dfrac{d^2x_i}{dt^2} = F_{xi} - \mu\dfrac{dx_i}{dt}, \\ m\dfrac{d^2y_i}{dt^2} = F_{yi} - \mu\dfrac{dy_i}{dt} \end{cases} \tag{29.7}$$

until the maximum change in position of any molecule between two consecutive steps is smaller than a given threshold value. The following notations have been used: x_i, y_i are the Cartesian coordinates of molecule i, μ is the damping constant, and F_{xi}, F_{yi} are the components of the instantaneous force $\overrightarrow{F_i}$ acting on molecule i given by the sum of the forces from the neighbouring springs:

$$\begin{aligned} F_{i,x} &= \sum_{\text{neighbors springs}} k \cdot \delta r_{ij,x}, \\ F_{i,y} &= \sum_{\text{neighbors springs}} k \cdot \delta r_{ij,y}, \end{aligned} \tag{29.8}$$

where k is the spring constant, and $\delta \overrightarrow{r}_{ij}$ is the deviation of the neighbour spring j from its unstressed value. This approach allows the simulations of systems containing more than 100,000 molecules. The new equilibrium state corresponds to the new state of minimum elastic energy.

It is worth noticing that in the mechanoleastic model, due to the triangular symmetry, the problem of interactions is simplified with the use of a single interaction parameter, namely the elastic spring constant, from which all other parameters considered in the above-mentioned models follow. The mechanoelastic model has been first elaborated for describing HS-LS relaxation. It was subsequently adapted for the study of thermal hysteresis of photophysical processes including the phenomenon of a light induced hysteresis, for the investigation of the clusters evolution during the transition and for the analysis of the role of impurities in diluted spin crossover complexes.

29.3.3 *The Spin-Crossover System Dynamics in Framework of Mechanoelastic Model*

The evolution of the whole system is simulated by a Monte Carlo procedure based either on transition probabilities (Arrhenius approach), or on system Hamiltonians (Metropolis approach). In both cases, a Monte Carlo step is realized when all the molecules in the system have been checked once. In the Monte Carlo Metropolis approach [49], the following Hamiltonian is considered:

$$H = \frac{1}{2} \sum_i \left(\Delta_{eff} - k_B T \ln g \right) \sigma_i + \frac{k}{2} \sum_{i,j} d x_{ij}^2, \tag{29.9}$$

where the first term corresponds to the classical Hamiltonian used in the Ising-like system and the second term stands for the elastic energy $W_{elastic}$ calculated as the sum of energies for all the springs in the system. Accordingly, the Metropolis probability is written:

$$P = \exp\left(- \frac{(D - k_B T \ln g) \cdot \left(\sigma_i^{final} - \sigma_i^{initial} \right) + \kappa \cdot \left(W_{elastic}^{final} - W_{elastic}^{initial} \right)}{k_B T} \right), \tag{29.10}$$

where the final elastic energy corresponds to the new positions of molecules calculated considering that the switch has been produced.

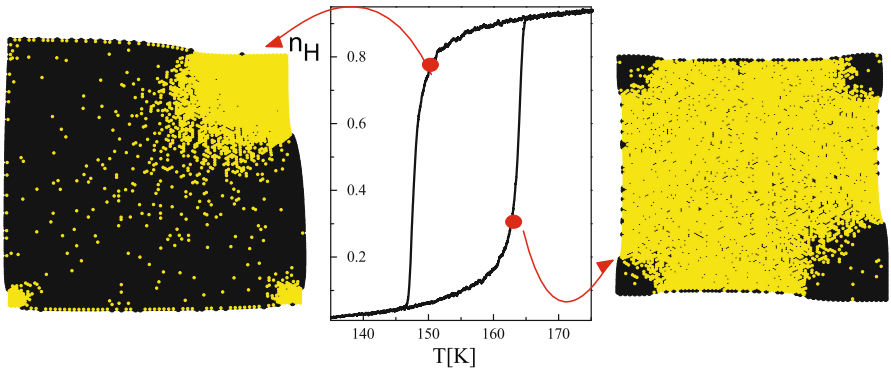

Fig. 29.5 Thermal hysteresis obtained in the framework of the mechanoelastic model, and snapshots of the system on both hysteresis branches when around 25 % of moelcules have swiched, *Black circles*: HS molecules, *Gray circles*: LS molecules. The parameters used in the model are: $\Delta H = 1100$ K, $\Delta S = 7$, $\Delta E = 400$ K, $\kappa = 2000$, $k = 1\ N/m$, $\mu = 1\ N \cdot s/m$

In the Arrhenius approach [50], the probability for a molecule to switch from one state to another depends on intrinsic parameters of the system, such as the activation energy, the HS-LS enthalpy difference and the degeneracy ratio and, particularly important in the present context, on local forces expressed in the form of a local pressure, which is proportional to the scalar sum of all the elongations and compression of the neighboring springs

$$P^i_{HS\to LS} = \frac{1}{\tau}\exp\left[-\frac{E_A - \kappa p_i}{k_B T}\right], \tag{29.11}$$

$$P^i_{LS\to HS} = \frac{1}{\tau}\exp\left[-\frac{2\Delta - k_B T \ln g}{k_B T}\right]\exp\left[-\frac{E_A - \kappa p_i}{k_B T}\right], \tag{29.12}$$

where E_A is the effective activation energy, τ a constant scaling factor, chosen so that the above probabilities are well below unity at any temperature, and κ a constant that establishes the extent to which the local pressure p_i influences the relaxation.

The local pressure is simply defined as:

$$p_i = \sum_{\text{neighbors springs}} k \cdot \delta r_{ij}. \tag{29.13}$$

By the definition of the local pressure, there is a relatively high probability for a HS molecule to switch to the LS state, if it is enclosed by compressed springs, while the similar probability of a molecule enclosed by elongated springs is low.

The simulation of the thermal hysteresis loop in the framework of the mechanoelastic model is presented in the Fig 29.5. Strong interaction, expressed by large spring constant values, results in formation of clusters which spread starting from corners in hexagonal and rectangular systems, or from edges in circular systems.

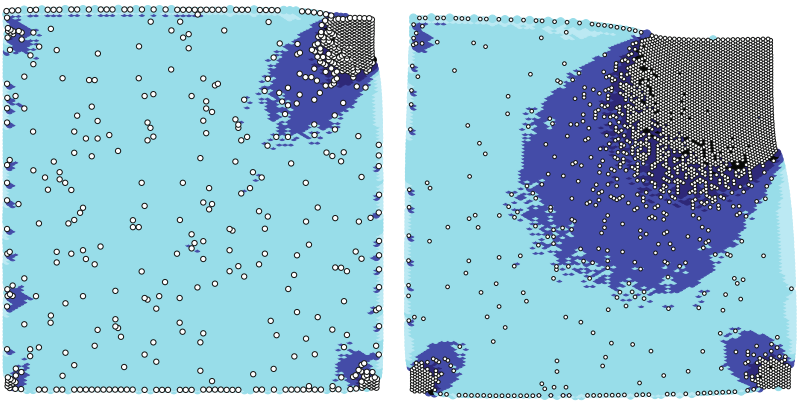

Fig. 29.6 Snapshots of the local pressure for two situations of the system during thermal HS-LS transition: LS molecules: open circles. The colour of HS molecules is linked to their local pressure: a higher pressure corresponds to a darker molecule

In Fig. 29.6 we have represented the local pressure diagram for two situations during the HS-LS transition: a small fraction of LS molecules (left) and an intermediate fraction of LS molecules (right). At the very beginning of the transition, the HS molecules switch randomly, as the local pressure is the same for all the molecules in the system. After a while, the switch of several HS molecules determines the rearrangement of all the molecules in the system and consequently the change of the local pressures. A careful analysis of Fig. 29.6 left reveals the reasons of cluster growth from corners: the local pressure on HS molecules situated inside the sample stays approximately constant while for the HS molecules situated near the newly switched LS molecules around corners it dramatically increases. According to Eq. (29.12) the HS molecules subjected to a higher local pressure will have a higher probability to switch. The subsequent evolution of the system is suggested by Fig. 29.6 right: the four clusters are joining and the last molecules to switch are those situated near the middle of each sides of the rectangle.

In order to study the LIESST effect, we have to consider an additional probability for a molecules to be switched from LS to HS state by light. At any time, the probability for a given molecule to switch from the HS to the LS state, $P^i_{HS\to LS}$, depends on the temperature and on the forces acting on the molecule from its neighbors, while under the assumption that the intersystem crossing probabilities of LIESST do not depend upon the HS fraction, the probability for a molecule to switch from the LS to the HS state, $P^i_{LS\to HS}$, is constant and is related to the intensity of irradiation as in the low temperature region the probability for a thermal LS to HS transition is negligible:

$$P^i_{HS\to LS} = \frac{1}{\tau}\exp\left[-\frac{E_A - \kappa p_i}{k_B T}\right], \tag{29.14}$$

$$P^i_{LS\to HS} = I, \tag{29.15}$$

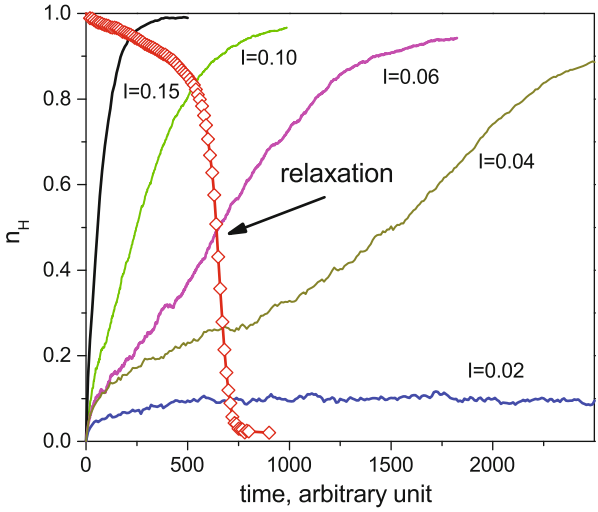

Fig. 29.7 Photoexcitation curves in presence of relaxation at $T = 50$ K for various values of intensity I. The sigmoidal shapes of the photoexcitation curve for lower values of intensity are the effect of the competition between relaxation and photoexcitation. The relaxation curve in dark is also shown for comparison. The used parameters are: $\Delta H = 1100$ K, $T = 50$ K, $\kappa = 2000$, $k = 1\ N/m$, $\mu = 1\ N \cdot s/m$

where I is a term proportional to the irradiation intensity and the absorption cross section at the irradiation wavelength, and the other variables have the same significance as previously mentioned.

Photoexcitation curves calculated for different light intensities are presented in Fig. 29.7, together with a typical relaxation curve (implying $I = 0$ and fully HS initial state). The photoexcitation curves are close to single exponential if the intensity is comparatively higher relative to the relaxation rate. The photoexcitation time is in this case directly proportional to the light intensity and the final metastable state obtained is closed to saturation. If the light intensity decreases, then the role played by relaxation becomes significant: the sample cannot anymore be saturated and a steady state establishes for lower values of high spin states. For even lower intensity values of the light, the photoexcitation curve changes into a sigmoidal S-shape. This shape is obtained here not because of some possible cooperative effects intrinsic to the photoexcitation [51] or due to some variations of the quantum efficiency with the HS fraction [52], as the photoexcitation is obviously linear here, but it can be simply understood only on the basis of the self-accelerated character of the cooperative HS-LS relaxation, as mentioned above. As in the classical mean field approach, the maximum effect of the relaxation is observed for a low n_H value, where the relaxation rate is maximum; and once the photoexcitation surpasses this value, it becomes faster.

If the irradiation intensity is lower than a threshold value, then the excitation is not sufficiently fast to overcome the relaxation, so the photoexcitation levels off at a steady state value of the n_H close to zero.

29.4 The Behavior of Noise Driven Spin-Crossover Complexes

The dynamic properties of a multilevel system can be described through a master equation, i.e., an evolution equation written in terms of transition rates. The macroscopic master equation can be written in the following form in the mean field approach, neglecting the bulk absorption and considering the photoexcitation linear:

$$\frac{dn_H}{dt} = \beta(1 - n_H) - n_H \exp(-\alpha n_H) \equiv f(n_H), \tag{29.16}$$

where $f(n_H)$ is the external applied force which describes the deterministic dynamics of the system.

The system dynamics described by the rate Eq. (29.16) can be analyzed in the framework of dynamic potential based on Lyapunov functions [17, 53]. In this way, the system is described by the equation

$$\frac{dn_H}{dt} = -\frac{dU(n_H)}{dn_H}, \tag{29.17}$$

where $U(n_H) = -\int_0^{n_H} f(x)dx$ is nonequilibrium (dynamic) potential. Equation (29.17) describes the system evolution representing the balance between photoexcitation and relaxation. This equation gives the complete description of deterministic system dynamics in hydrodynamic approximation.

Since

$$\frac{dU(n_H)}{dt} = --\frac{dU(n_H)}{dn_H}\frac{dn_H}{dt} = -\left[\frac{dF(n_H)}{dn_H}\right]^2 < 0, \tag{29.18}$$

$n_H(t)$ tries to minimize the potential $U(n_H)$ until $dU(n_H)/dt$ reaches zero. This gives us the right to designate the term $U(n_H)$ as the Lyapunov function or the nonequilibrium potential. An inequality (29.18) represents the evolution of the system, i.e., approaching that of the steady states. The locations of system extrema may be found from the following expression:

$$\frac{dU(n_H)}{dn_H} = 0. \tag{29.19}$$

By analogy with the first-order transition phenomena, the local minimum of $U(n_H)$ can be associated with the metastable state of the system, while the global minimum corresponds to the stable state. Therefore, the nonequilibrium potential is similar to the free energy in equilibrium phenomena, but still its conception is inapplicable for the nonequilibrium systems.

For appropriate values of light intensity and relaxation rate, a bistability under light is observed, a direct consequence of the sigmoidal shape of relaxation curves and of S-shape of photoexcitation curve. Depending of the initial configuration of the system, one of the two steady states is obtained: the lower one if we start from the purely LS state and the higher one if we start from the purely HS state. If the

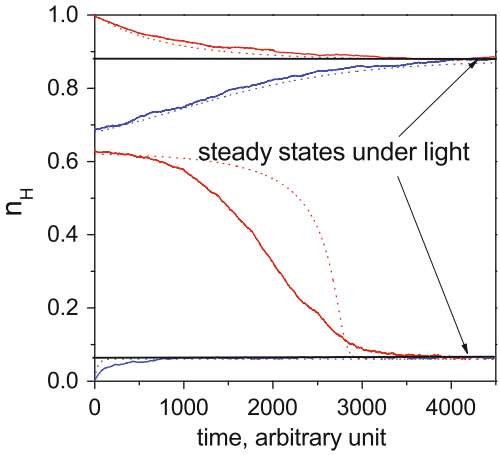

Fig. 29.8 Bistability at low temperature: depending on the starting point, one of the two steady states can be obtained. Here the system steady states are indicated by the *solid horizontal lines*

initial state of the system is in between the two steady states, then the system directs towards one of these states, depending on if the departure point is below or above the bifurcation point. In the Fig. 29.8, we present the relaxation curves of the system obtained by numerical calculation carried out by Monte Carlo (solid curves) and second order Runge–Kutta type method (dashed curves). The transient regimes in Fig. 29.8 represent the evolution of the system, i.e., the approaching to the one of the steady states which correspond to local and global minima of system dynamic potential. The relaxation curves obtained by both methods for different initial states show good agreement.

All real systems in contact with environment incur the fluctuation of system phenomenological variable, which describes their states in phase space. The external fluctuating forces may be crucial for spin-crossover nanomaterials, especially in critical dynamics. This means that we have to consider the effect of a randomly varying external field on the photoinduced reactions. The dynamic of such system may be described as its contact with heat bath [17, 18, 54, 55]. The successful attempts to describe the dynamics of a system being in contact with an environment playing a role of the heat bath, are based on the concept of the Langevin equation. Such approach may be used for any system in that each process has, in fact, its time scale. Then, all degrees of freedom can be decomposed into slow and fast degrees of freedoms. One selects some relevant degrees of freedom and treats the rest as a bath in form of additive noise. The system has then two distinct mechanisms for time evolution–regular motion and random or disorganized motion. The random forces induced by environment are correlated on a very small time scale compared to the characteristic relaxation time for the system, around a locally stable state. Thereby the evolution of spin-crossover system perturbed by noise can be described by a one-variable nonlinear Langevin equation, written in terms of transition rates:

$$\frac{dn_H}{dt} = f(n_H) + \xi(t), \tag{29.20}$$

where $\xi(t)$ indicates the noise induced by the environment. The Langevin Eq. (29.20) with additive noise term $\xi(t)$ describes the dynamics of a system in the presence of an interaction with environment (similar to model A in critical phenomena, see [56, 57]). This kinetic equation simulates the system dynamics as a motion of Brownian particle in the phase space. The stability of the high-spin states in spin-crossover compounds with respect to the influence of the external thermal white noise has been studied in [17]. The detailed theoretical analysis of the non-linear kinetics in spin-crossover solids under cross-correlated noises was provided in the paper [18].

An idealized treatment assumes the random force in Eq. (29.20) $\xi(t)$ as a white Gaussian noise with zero means and a zero-ranged correlation functions

$$\left\langle \xi(t)\xi(t')\right\rangle = 2\varepsilon^2\delta(t'-t), \tag{29.21}$$

where ε is noise strength.

In general the noise represents the hierarchical coupling of the system to the heat bath. In terms of generalized functions, the Gaussian white noise is a derivative of the Wiener process. Therefore, one can show that the Fokker–Plank equivalent of Eq. (29.20) in Stratonovichs interpretation, defining the evolution of the system transition probability, is given in [58]

$$\frac{\partial P(n_H,t)}{\partial t} = -\frac{\partial}{\partial n_H}\left[f(n_H)P(n_H,t)\right] + \varepsilon^2\frac{\partial^2}{\partial n_H^2}P(n_H,t), \tag{29.22}$$

where $P(n_H,t)$ is the probability distribution function, defined so that the value $P(n_H,t)n_H dt$ is the probability to find a diffusive particle in the position n_H at time t. In the case of the natural or instantly reflected boundary condition the probability flux does not exist. The steady state solution of Eq. (29.22) is easily found to be

$$P_{st}(n_H) = N\cdot\exp\left(\int_0^{n_H}\frac{f(y)}{\varepsilon}dy\right), \tag{29.23}$$

where N is normalization constant obtained from the condition

$$N\cdot\int_0^1 P_{st}(n_H)dn_H = 1.$$

The simplest way to analyze the stochastic dynamics of the system expressed by Eq. (29.20) is to describes it by stationary probability function in the Boltzmann–Gibbs as follow

$$P_{st}(n_H) \simeq \exp\left[-U(n_H)/\varepsilon\right]. \tag{29.24}$$

The extremes of the potential $U(n_H)$ correspond to the stationary fixed points of system dynamics. For a bistable system, the probability distribution has two maxima which correspond to the steady states. Figure 29.9 presents the stationary probability distribution, plotted from Eq. (29.24) and obtained from numerical calculations of the

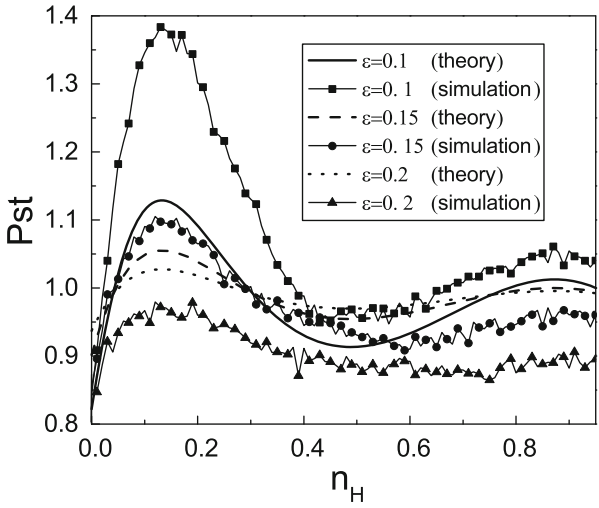

Fig. 29.9 The analytical and numerical stationary probability distribution for different values of additive noise

set of random trajectories (29.20) carried out by the modified second-order Runge–Kutta type method [59] as follows

$$\begin{aligned} y(t) &= n_H(t) + f(n_H(t))\Delta t + \sqrt{\Delta t}\varepsilon u(t), \\ x(t+\Delta t) &= x(t) + \frac{\Delta t}{2}\left[f(x(t)) + f(y(t))\right] + \frac{\sqrt{\Delta t}}{2}\varepsilon u(t). \end{aligned} \tag{29.25}$$

Here $u(t)$ is Gaussian random variable with zero mean value and variance equal to 1. The curves exhibit that with the increase of additive noise intensity, the flattening of stationary probability distribution is observed, indicating the suppression of the potential barrier between the states. Such noise action is undesirable because it leads to indistinguishability of the system states, which means in practice the loss of information in a real memory cell.

Due to the influence of the environment on system control parameters in more rigorous approach it is composed of deterministic and stochastic parts $\beta(t) = \beta + \eta(t)$. In this case the Eq. (29.20) gives the following form

$$\frac{dn_H}{dt} = f(n_H) + g(n_H)\eta(t) + \xi(t). \tag{29.26}$$

Here $\eta(t)$ is stochastic process representing the Gaussian white multiplicative noise. In this case $g(n_H) = (1 - n_H)$ is multiplicative noise amplitude. In contrast to the system with additive noise here, the multiplicative noise depends on system variable (here n_H). It leads to a situation where small deviations in the photoexcitation intensity may lead to a large fluctuation of HS fraction production. In the simplest case the statistical conditions for multiplicative noise are following:

$$\begin{aligned} \langle \eta(t) \rangle &= 0, \\ \left\langle \eta(t)\eta(t') \right\rangle &= 2\sigma\delta(t-t'), \\ \left\langle \eta(t)\xi(t') \right\rangle \equiv \left\langle \xi(t)\eta(t') \right\rangle &= 2\chi\sigma\varepsilon\delta(t-t'). \end{aligned} \tag{29.27}$$

Here σ is the multiplicative noise intensity and χ is the degree of cross-correlation between additive and multiplicative noises. It arises from common origin of the noises which is of the thermal nature.

The stochastic differential Eq. (29.26) has no direct analytical solution but it may be analyzed by corresponding Fokker–Plank equation. The most convenient way to analyze the Eq. (29.26) which contains two noise terms is to reduce it to the equivalent dynamical equation with one multiplicative noise with effective amplitude [60, 61]. The resulting kinetic equation is:

$$\frac{dn_H}{dt} = f(n_H) + G(n_H)\Xi(t), \tag{29.28}$$

where the stochastic process $\Xi(t)$ obeys the simplest conditions $\langle \Xi \rangle = 0$ and $\left\langle \Xi(t)\Xi(t') \right\rangle = 2\delta(t - t')$. The effective amplitude $G(n_H)$ is then:

$$G(n_H) = \left[\sigma^2 g^2(n_H) + 2\chi\sigma\varepsilon g(n_H) + \varepsilon^2\right]^{1/2}.$$

From stationary solution of Fokker–Plank equations [62, 63] which corresponds to macroscopic kinetic equation (29.28) we found the stationary probability distribution of system states

$$P_{st}(n_H) = N \exp\left[-V_{FP}(n_H)\right], \tag{29.29}$$

where $V_{FP}(n_H)$ is stochastic Fokker–Plank potential. For the system dynamics with two noise terms it may be found in the following form

$$V_{FP}(n_H) = -\int_0^{n_H} \frac{f(x) - G(x)\frac{\partial G(x)}{\partial t}}{G^2(x)} dx. \tag{29.30}$$

The changes of probability distribution by variation of multiplicative noise intensity and cross-correlation coefficient between the noises are shown in the Fig. 29.10. The curves exhibit that the increase of the intensity of multiplicative noise cardinally changes the shape of stationary probability distribution. In this case noise promotes transition between system states. Analyzing the dependencies of the stationary probability distribution on the degree of correlation between the noises, it is easy to see that the increase of correlation amplifies the multiplicative noise action (this fact may be observed from the asymmetrization of stationary probability distribution, as illustrated in Fig. 29.10b).

Based on the approach developed in our papers [17, 18, 32, 64, 19, 40, 31] the noise-induced optical bistability and state transitions in spin-crossover solids with delayed feedback was studied [65]. Especially the mean first passage time (MFPT) of the transition from the LS state to the HS one as the function of the noise intensity was found. In this work the MFPT exhibits a maximum and the noise-enhanced stability is observed. However, the MFPT decreases with increase of the delayed feedback intensity, thus the delayed feedback accelerates the conversion from the LS state to the HS state.

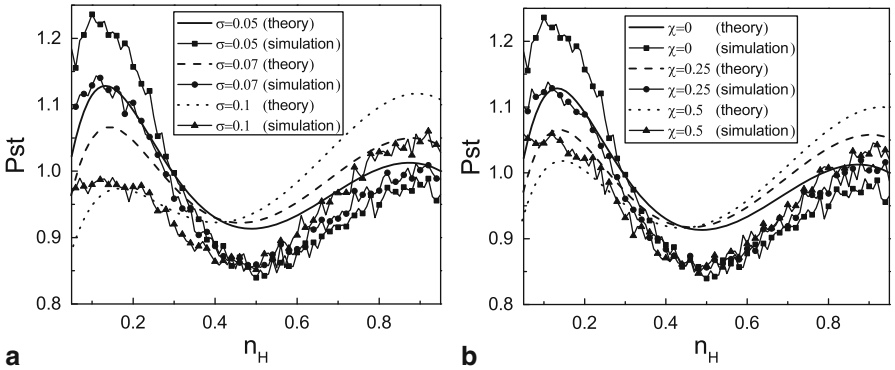

Fig. 29.10 The analytical and numerical stationary probability distribution for different values of multiplicative noises (**a**) and the degree of correlation (**b**) (in **a**, $\chi = 0$, $\varepsilon = 0.1$; in **b**, $\sigma = 0.05$; $\varepsilon = 0.1$)

29.5 Time of Escape from Metastable State Driven by Color Noise Action

As it was mentioned in the previous section the presence of a noise term can modify in an unexpected way the behavior of the corresponding deterministic (noiseless) equation; therefore it must be described at least in Langevin approach. In a recent paper [17] we have studied the stability of the high-spin states in spin-crossover compounds with respect to the influence of the external thermal white noise. Subsequently in the paper [18], the state diagrams of the spin-crossover system have been built for the interplay between parametric and additive noise using the concept of a Gaussian white noise with zero correlation time.

But a real noise has a finite (perhaps small, but not zero) correlation time. In this case, the hypothesis of white noise, although suitable for a general description of the process, does not explore all the possibilities of a real noise. Thus the spin-crossover system should be explored under the influence of colored noise. The simplest representation of colored noise is the Ornstein–Uhlenbeck stochastic process. It is an example of Gaussian process with nonzero correlation time τ meaning that values of the noise at different times are not independent random variables. The system dynamics driven by Ornstein–Uhlenbeck (OU) noise $\xi_{OU}(t)$ in general may be described by the similar for white noise action Langevin equation (29.20) by substituting $\xi(t)$ with $\xi_{OU}(t)$. The main difference from the white noise case refers to the autocorrelation function of noise term. In this case for OU noise it is defined as follows

$$\left\langle \xi_{OU}(t)\xi_{OU}(t')\right\rangle = \frac{D^2}{\tau}\exp\left(\frac{t-t'}{\tau}\right), \tag{29.31}$$

where τ describing the time-scale and D is noise intensity.

In this case the system dynamics with colored noise action is no longer Markovian process which makes its solution impossible without some approximations. The main

approach proposed by Hänggi et al. [66, 67] and later developed by Gudyma et al. for spin-crossover system [32] refers to the system description with colored noise by two-dimensional Markovian process driven by Gaussian white noise. The system dynamics with colored noise is the following

$$\frac{dn_H}{dt} = f(n_H) + \xi_{OU}(t), \tag{29.32}$$

$$\frac{d\xi_{OU}(t)}{dt} = -\frac{\xi_{OU}(t)}{\tau} + \frac{D}{\tau}\varepsilon(t). \tag{29.33}$$

For the concerned system, the noise intensity D indicates the amplitude of the instantaneous fluctuations during the change of the HS fraction. These fluctuations represent the cumulative effects of many weakly coupled environmental degrees of freedom. In Eq. (29.32) $\varepsilon(t)$ is the white Gaussian stochastic processes with zero mean and correlation function

$$\left\langle \varepsilon(t)\varepsilon(t') \right\rangle = 2\delta(t - t').$$

The kinetic equation for two-dimensional Markovian process may be obtained by derivation of Eq. (29.32) and subsequent replacement of $d\xi_{OU}/dt$ by right part of Eq. (29.33) following the condition that $\xi_{OU}(t) = dn_H/dt - f(n_H)$. As a result we obtain the kinetic equation in the next form

$$\ddot{n}_H + \dot{n}_H \tau^{-1} \left[\left(1 - \tau \frac{df(n_H)}{dn_H} \right) - f(n_H) \right] = \frac{D}{\tau}\varepsilon(t). \tag{29.34}$$

The dot over the functions means the derivative with respect of t.

Neglecting the velocity variations (i.e., $\ddot{n}_H = 0$) we found that the non-Markovian flow in combined Eqs. (29.32), (29.33) may be approximated by a one-dimensional Markovian process. According to a "unified colored-noise approximation" [67], a set of Eqs. (29.32) and (29.33) reduces to an equation that is linear in $\dot{n}_H$, but nonlinear in n_H. On the new time scale $s = t\tau^{-1/2}$ the result is a stochastic differential equation with a multiplicative Markovian noise

$$\dot{n}_H = f(n_H)\gamma^{-1}(n_H, \tau) + g(n_H)\varepsilon(s). \tag{29.35}$$

Here the nonlinear damping is $\gamma(n_H, \tau) = \tau^{-1/2} - \tau^{1/2} f'(n_H)$ and the noise amplitude function is $g(n_H) = D\tau^{-1/4}\gamma^{-1}(n_H, \tau)$. The correlation of noise term $\varepsilon(s)$ is the same as for $\varepsilon(t)$.

The Fokker–Plank equivalent of the Stratonovich Eq. (29.35), is given

$$\begin{aligned} \frac{\partial P(n_H, s)}{\partial s} = &- \frac{\partial}{\partial n_H} \left[f(n_H)\gamma^{-1}(n_H, \tau) P(n_H, s) \right] \\ &+ \frac{\partial}{\partial n_H} \left[g(n_H, \tau) \frac{\partial}{\partial n_H} \left[g(n_H, \tau) \right] P(n_H, s) \right]. \end{aligned} \tag{29.36}$$

The stationary solution of this equation for the colored noise action takes the form:

$$P_{st}(n_H, \tau) = N \exp \left[\int_0^{n_H} \frac{f(y) - g(y)g'(y)}{g^2(y)} \right] \simeq \exp \left[V_{FP}(n_H, \tau) \right]. \tag{29.37}$$

The extremes of effective potential (29.37) correspond to the stationary fixed points of the noise-sustained dynamics.

Due to interaction of spin-crossover system with environment it can leave the potential minimum well via thermal activation over the barrier. The problem of escape from a metastable state is important for many scientific areas such as the theory of diffusion in solids, the dynamics in nonlinear optics, chemical kinetics, transport in biomolecules, electron transport in semiconductors, and many others. In general, the escape time problem may refer not only to the decay of metastable state driven by thermal fluctuations, but also to the systems characterized by nonthermal steady states which may exhibit competing states of local stability.

One of the first studies of the influence of colored noise on the escape rate from the potential well of bistable system was carried out by Hänggi et al. in [68, 69]. The estimation of transition possibility of the system from metastable state to stable and vice versa through escape time ratio in the presence of noise was studied in the paper [70]. The problem of the decay of metastable state in the presence of noise has been previously studied by a mean first passage time technique. For a stochastic process $n_H(t)$ with values in a some state space, the mean first-passage time (MFPT) $T(n_H)$ may be interpreted as the average time elapsed until the process starting out at point n_H leaves a prescribed domain $(a; b)$ of state space for the first time. Using the Fokker–Planck formalism for stochastic differential equation the mean first passage time can be obtained, in a Kramers-like approximation [63, 71] from the expression

$$T(n_H) = \int_{n_H}^{b} \frac{dy}{\psi(y)} \int_{a}^{y} \frac{\psi(z)}{g^2(z)} dz, \tag{29.38}$$

where

$$\psi(z) = \exp\left[\int_0^z \frac{2\gamma^{-1}(x,\tau) f(x)}{g^2(x)} dx\right].$$

The evolution of the system starts at the initial point a and reaches the final point b. Here, a is meant to represent the local minimum of the potential V_{FP} which is associated to the metastable state whereas b is the inflection point which coincides with local maximum of system potential indicating the exiting of the system from metastable state. Using the concept of the MFPT with a reflecting boundary condition at a and an absorbing boundary condition at b and replacing $a \to \infty$, $b \to n_H$ and $n_H \to a$ in the integral (29.38), we obtain the time of escape from metastable state

$$T(a \to n_H) = \int_{a}^{n_H} \frac{dy}{\psi(y)} \int_{-\infty}^{y} \frac{\psi(z)}{g^2(z)} dz. \tag{29.39}$$

The expression (29.39) determines the average time spent by the system in the a to n_H interval. If the barrier is high ($V_{FP}(b,\tau) >> D^2$), then the term $\psi(z)$ has a minimum value at the point b, therefore the integral $\int_{-\infty}^{y} \psi(z)/g^2(z)dz$ is practically independent of n_H and is considered as having a constant value. The main contribution to the integrals (29.39) in this case is

$$T(a \to n_H) \simeq \left\{\int_{-\infty}^{b} \frac{\psi(z)}{g^2(z)} dz\right\} \int_{a}^{n_H} \frac{dy}{\psi(y)}. \tag{29.40}$$

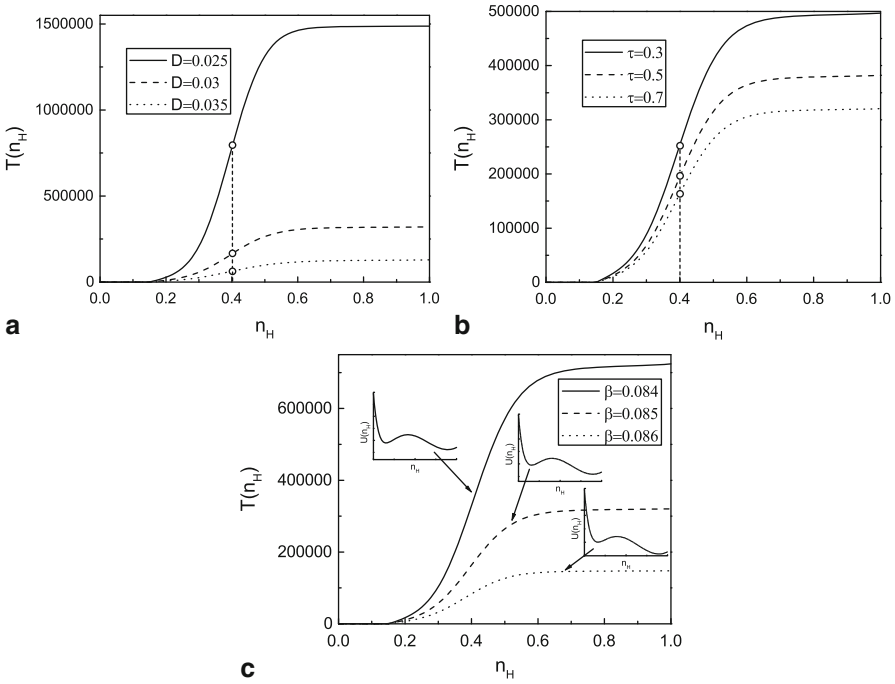

Fig. 29.11 The time $T(a \rightarrow n_H)$ as a functions of: **a** The noise intensity for fixed values of $\beta = 0.085$ and $\tau = 0.7$; **b** the correlation time for fixed values of $\beta = 0.085$ and $D = 0.3$; **c** the intensity of light for fixed values of $\tau = 0.7$ and $D = 0.3$

The first influence of the colored noise effect on the escape rate in a bistable well potential has been detected by Hänggi et al. [68].

We have analyzed the results for the time of escape out of a potential as functions of the noise intensity D, the correlation time τ, and the light intensity β for different cases, together with the dependence of initial and final points with these parameters. The results are shown in the Fig. 29.11.

Figure 29.11a shows the results for this time obtained from the simulations for the parameters indicated in the caption. The time (29.40) increases monotonically as n_H increases, but it decreases when increasing noise intensity. In Fig. 29.11b the results for the time of escape from metastable state for spin-crossover system as function of the correlation time at $\beta = 0.085$ and $D = 0.3$ are displayed. Empty circles in Figs. 29.11a, b are inflection points for given values of D and τ which correspond to the spinodal point b of the dynamic potential (29.30) and represent the border between the paramagnetic metastable and the diamagnetic stable states. The transition from one state to the other leads to dramatic change, not only of magnetic but of all system properties. From the plots we notice that the increase of correlation time leads to decreasing the mean first passage time.

Numerical results for the time of escape over potential barrier $T(a \to n_H)$ (29.40) are plotted in Fig. 29.11c at various light intensities β for constant correlation time τ and noise D. Qualitative changes in the shape of the effective potential are displayed on the insets of Fig. 29.11c for values of dimensionless correlation time $\tau = 0.7$ and noise intensity $D = 0.3$. Light intensity increasing effectively depresses the barrier height between metastable and stable states and causes decreasing the time of escape $T(a \to n_H)$ because the barrier height determines the rate at which the system escapes from the metastable well. In general, decreasing of the potential barrier height between metastable and ground states of the system yields the shorter escape time.

29.6 Conclusion

The spin-crossover compounds have great perspectives as functional materials of information technology field, therefore the researchers continue to approach them vigorously. The behaviour of spin-crossover compounds were studied using two main approaches: microscopic approaches based on modified Ising-like model and macroscopic phenomenological approaches based on kinetic equation describing the dynamics of fractions of high-spin molecules, giving better understanding of physical processes taking place at microscopic and macroscopic levels during the occurrence of phase transition. We focus our attention on the bistable properties of spin-crossover compounds able to be determined in the framework of each model depending on internal and environmental parameters including its hierarchical coupling. The mechanoelastic microscopic model is useful for the study of the influence of elastic interactions between spin-crossover sites and cooperative effects in the materials. Also, we calculated the photoexcitation curves of spin-crossover system in presence of relaxation. The obtained S-shape of the curves is related with self-accelerated character of cooperative HS-LS relaxation.

The behavior of noise driven spin-crossover system was studied by dynamic stochastic potential in terms of Lyapunov functions, obtained from macroscopic kinetic equation in Langevin approach. The statistical description of additive and multiplicative noise action on the spin-crossover compounds was given as a stationary solution of corresponding Fokker–Planck equation in general describing the evolution probability of system states. One can see that the shape of stationary probability distribution is strongly influenced by the degree of correlation between multiplicative and additive noises. Correlation amplifies the action of the multiplicative noise whereas the action of additive noise intensity leads to the flattening of the stationary probability distribution. The statistical approach provided in this work make possible the calculation of system coupling with heat bath.

Based on a simple phenomenological model describing photoexcitation and relaxation in spin-crossover compounds, we have examined the response of the spin-crossover system on influence of realistic (colored) noise as an action of heat bath. Within the mean first passage time technique and Kramers-like approximation the

time of escape from metastable state were obtained. It was found that the time of escape from metastable state decreased with the increase of noise intensity and correlation time. The obtained results are practically important for optically switchable and recording devices.

Acknowledgements Research of Iu. G. and A. M. was supported in part by the an Erasmus Mundus mobility program EMERGE, co-financed by the European Commission in the framework of the Erasmus Mundus programme. Iu. G. and A. M. thank the scientific group of Prof. Alexandru Stancu for the hospitality at the Alexandru Ioan Cuza University of Iasi while this work was in progress.

References

1. Cambi L, Szegö L (1931) Ber Deutsch Chem Ges 64:167
2. Cambi L, Malatesta L (1937) Ber Deutsch Chem Ges 70:2067
3. Orgel L (1956) in 10 ème Conseil de Chimie. Bruxelles, p 289
4. Figgins PE, Busch HD (1960) J Am Chem Soc 82:820
5. Robinson MA, Curry JD, Busch DH (1963) Inorg Chem 2:1178
6. König E, Madeja K (1966) Chem Comm 3:61
7. McGarvey J, Lawthers I, Chem J (1982) Chem Commun 1982:906
8. Decurtins S, Gütlich P, Köhler C, Spiering H (1984) Chem Phys Lett 105:1
9. Veen R van der, Kwon OH, Tissot A, Hauser A, Zewail AH (2013) Nat Chem 5:395
10. Bousseksou A, Molnár G, Salmon L, Nicolazzi W (2011) Chem Soc Rev 40:3313
11. Félix G, Abdul-Kader K, Mahfoud T, Gural'skiy I, Nicolazzi W, Salmon L, Molnár G Bousseksou A (2011) Surface plasmons reveal spin crossover in nanometric layers J Am Chem Soc 133:15342
12. Gütlich P, Goodwin H (eds) (2004) Spin crossover in transition metal compounds I. Topics in current chemistry, vol 233. Springer, Berlin
13. Gütlich P, Goodwin H (eds) (2004) Spin crossover in transition metal compounds II. Topics in current chemistry, vol 234. Springer, Berlin
14. Gütlich P, Goodwin H (eds) (2004) Spin crossover in transition metal compounds III. Topics in current chemistry, vol 235. Springer, Berlin
15. Halcrow M (ed) (2013) Spin-crossover materials properties and applications. Wiley, Chichester
16. Kahn O, Martinez C (1998) Spin-transition polymers:from molecular materials toward memory devices. Science 279:44–48
17. Gudyma Yu, Semenko O (2004) Nonequilibrium kinetics in spin-crossover compounds. Phys Status Solidi B 241:370–376
18. Gudyma IV, Maksymov A (2010) Theoretical analysis of the states of spin-crossover solids under cross-correlated noises. Physica B 405:2534–2537
19. Gudyma Iu, Maksymov A (2011) High spin metastable state relaxation of spin-crossover solids driven by white noise. J Phys Chem Solids 72:73–77
20. Collet E, Buron-Lecointe M, Cailleau H (2006) X-ray diffraction investigation of the nature and the mechanism of photoinduced phase transition in molecular materials. J Phys Soc Jpn 75:011002
21. Lorenc M, Hébert J, Moisan N, Trzop E, Servol M, Buron-Le Cointe M, Cailleau H, Boillot ML, Pontecorvo E, Wulff M, Koshihara S, Collet E (2009) Successive dynamical steps of photoinduced switching of a molecular Fe(III) spin-crossover material by time-resolved X-ray diffraction. Phys Rev Lett 103:028301
22. Hauser A (1986) Reversibility of light-induced excited spin state trapping in the $Fe(ptz)_6(BF_4)_2$ and the $Zn_{1-x}Fe_x(ptz)_6(BF_4)_2$ spin-crossover systems Chem Phys Lett 124:543–548

23. Gütlich P, Hauser A, Spiering H (1994) Thermal and optical switching of iron(II) complexes. Angew Chem Int Ed 33:2024–2054
24. Hauser A (1992) Cooperative effects on the HS→LS relaxation in the $[Fe(ptz)_6](BF_4)_2$ spin-crossover system. Chem Phys Lett 192:65–70
25. Wajnflasz J (1970) Etude de la transition „Low Spin" – „High Spin" dans les complexes octaédriques d'ion de transition. Phys Stat Sol 40:537–545
26. Boukheddaden K, Shteto I, Hoô B, Varret F (2000) Dynamical model for spin-crossover solids I. Relaxation effects in the mean-field approach. Phys Rev B 62:14796–14805
27. Boukheddaden K, Shteto I, Hoô B, Varret F (2000) Dynamical model for spin-crossover solids II. Static and dynamic effects of light in the mean-field approach. Phys Rev B 62:14806–14817
28. Desaix A, Roubeau O, Jeftic J, Haasnoot JG, Boukheddaden K, Codjovi E, Linarès J, Noguès M, Varret F (1998) Light-induced bistability in spin transition solids leading to thermal and optical hysteresis. Eur Phys J B 6:183–193
29. Varret F, Boukheddaden K, Chong C, Goujon A, Gillon B, Jeftic J, Hauser A (2007) Light-induced phase separation in the $[Fe(ptz)_6](BF_4)_2$ spin-crossover single crystal. Europhys Lett 77:30007
30. Varret F, Bleuzen A, Boukheddaden K, Bousseksou A, Codjovi E, Enachescu C, Goujon A, Linares J, Menendez N, Verdaguer M (2002) Examples of molecular switching in inorganic solids, due to temperature, light, pressure, and magnetic field. Pure Appl Chem 74:2159–2168
31. Gudyma IuV, Maksymov AIu (2012) Optical induced switching in spin-crossover compounds: microscopic and macroscopic models and its relationship. Appl Opt 51:C55–C61
32. Gudyma Iu, Maksymov A, Enachescu C (2010) Decay of a metastable high-spin state in spin-crossover compounds: mean first passage time analysis. Eur Phys J B 78:167–172
33. Varret F, Boukheddaden K, Codjovi E, Maurin I, Tokoro H, Ohkoshi S, Hashimoto K (2005) Light-induced thermal hysteresis and intensity thresholds in molecular switcheable solids, by mean-field macroscopic master equation approach: Discussion of the experimental data obtained for Co -Fe Prussian Blue Analogues. Polyhedron 24:2857–2863
34. Enachescu C, Constant-Machado H, Codjovi E, Linares J, Boukheddaden K, Varret F (2001) Direct access to the photo-excitation and relaxation terms in photo-switchable solids: non-linear aspects. J Phys Chem Solids 62:1409–1422
35. Bousseksou A, Nasser J, Linares J, Boukheddaden K, Varret F (1992) Ising-like model for the two-step spin-crossove. J Phys I France 2:1381–1403
36. Boukheddaden K, Linares J, Spiering H, Varret F (2000) One-dimensional Ising-like systems: an analytical investigation of the static and dynamic properties, applied to spin-crossover relaxation. Eur Phys J B 15:317–326
37. Glauber RJ (1963) Time-dependent statistics of the Ising model. J Math Phys 4:294–307
38. Huang H (1973)Time-dependent statistics of the Ising model in a magnetic field. Phys Rev A 8:2553–2556
39. Huang H (1974) Dynamics of the Ising model. Phys Lett A 48:2553–2556
40. Gudyma Iu, Maksymov A, Miyashita S (2011) Noise effects in a finite-size Ising-like model. Phys Rev E 84:031126
41. Nasser JA (2005) Diluted spin conversion compounds behaviours in the atom-phonon coupling model: case of not too large dilution. Eur Phys J B 48:19–27
42. Nishino M, Boukheddaden K, Konishi Y, Miyashita S (2007) Simple two-dimensional model for the elastic origin of cooperativity among spin states of spin-crossover complexes. Phys Rev Lett 98:247203
43. Konishi Y, Tokoro H, Nishino M, Miyashita S (2008) Monte Carlo simulation of pressure-induced phase transitions in spin-crossover materials. Phys Rev Lett 100:067206
44. Stoleriu L, Enachescu C, Stancu A, Hauser A (2008) Elastic model for complex hysteretic processes in molecular magnets. IEEE Trans Magn 44:3052–3055
45. Enachescu C, Machado H, Menendez N, Codjovi E, Linares J, Varret F, Stancu A (2001) Static and light induced hysteresis in spin-crossover compounds: experimental data and application of Preisach-type models. Physica B 306:155–160

46. Enachescu C, Tanasa R, Stancu A, Varret F, Linares J, Codjovi E (2005) First-order reversal curves analysis of rate-dependent hysteresis: The example of light-induced thermal hysteresis in a spin-crossover solid. Phys Rev B 72:054413
47. Enachescu C, Stoleriu L, Stancu A (2009) Model for elastic relaxation phenomena in finite 2D hexagonal molecular lattices. Phys Rev Lett 102:257204
48. Enachescu C, Nishino M, Miyashita S, Hauser A, Stancu A, Stoleriu L (2010) Cluster evolution in spin crossover systems observed in the frame of a mechano-elastic model. Europhys Lett 91:27003
49. Enachescu C, Nishino M, Miyashita L, Stoleriu S, Stancu A (2012) Monte Carlo Metropolis study of cluster evolution in spin-crossover solids within the framework of a mechanoelastic model. Phys Rev B 86:054114
50. Chakraborty P, Enachescu C, Hauser A (2013) Analysis of the experimental data for pure and diluted $[FexZn_{1-x}(bbtr)_3](ClO_4)_2$ spin-crossover solids in the framework of a mechanoelastic model. Eur J Inorg Chem 2013:770–780
51. Koshino K, Ogawa T (2000) Theory of the photoinduced spin-state transitions in spin-crossover complexes. J Lumin 87–89:642–645
52. Enachescu C, Oetliker U, Hauser A (2002) Photoexcitation in the spin-crossover compound $[Fe(pic)_3]Cl_2 \cdot EtOH(pic = 2 - Picolylamine)$. J Phys Chem B 106:9540–9545
53. Chong C, Varret F, Boukheddaden K (2010) Evolution of self-organized spin domains under light in single-crystalline. Phys Rev B 81:014104
54. Gudyma IuV, Semenko OM (2007) Noise-induced coupling and phase transition in initially homogeneous bistable system. Physica A 386:47–53
55. Gudyma AIu, Gudyma IuV (2010) Noise-induced collective regimes of complex system in contact with a random reservoir. Physica A 389:667–672
56. Hohenberg PC, Halperin BI (1977) Theory of dynamic critical phenomena. Rev Mod Phys 49:435–479
57. Ma Sk (2000) Modern theory of critical phenomena. Perseus Books, New York
58. Klyatskin V (2000) Dynamics of stochastic systems. Elsevier Science, Amsterdam
59. San Miguel M, Toral R (2000) Stochastic effects in Physical systems. In: Tirapegui E, Martínez J, Tiemann R (eds) Instabilities and nonequilibrium structures VI. Kluwer Academic, Dordrecht, pp 35–130
60. Wu D, Cao L, Ke S (1994) Bistable kinetic model driven by correlated noises: steady-state analysis. Phys Rev E 50:2496–2502
61. Gudyma Yu, Ivans'kii B (2006) Behavior of asymmetric bistable system under influence of cross-correlated noises. Mod Phys Lett B 20:1233–1239
62. Risken H (1989) The Fokker-Planck equation: methods of solution and applications. Springer, Berlin
63. Gardiner C (1986) Handbook of stochastic methods. Springer, Berlin
64. Gudyma Iu, Maksymov A (2010) Nonlinear stochastic relaxation dynamics in spin-crossover solid-state compounds. Semiconductor Physics, Quantum Electronics and Optoelectronics 13:357–362
65. Sang X, Zeng CH, Wang H (2013) Noise-induced optical bistability and state transitions in spin-crossover solids with delayed feedback. Eur Phys J B 86:229
66. Jung P, Hänggi P (1987) Dynamical systems: a unified colored-noise approximation. Phys Rev A 35:4464–4466
67. Hänggi P, Jung P (1995) Colored noise in dynamical systems. Adv Chem Phys 89:239–326
68. Hänggi P, Marchesoni F, Grigolini P (1984) Bistable flow driven by coloured Gaussian noise: AvCritical study. Z Phys B 56:333–339
69. Hänggi P (1986) Escape from a metastable state. J Stat Phys 42:105–148
70. Gudyma Iu, Maksymov A, Dimian M (2013) Stochastic kinetics of photoinduced phase transitions in spin-crossover solids. Phys Rev E 88:042111
71. Hänggi P, Talkner P, Borkovec M (1990) Reaction-rate theory: fifty years after Kramers. Rev Mod Phys 62:251–341

Index

O. Fesenko, L. Yatsenko (eds.), *Nanocomposites, Nanophotonics, Nanobiotechnology, and Applications,* Springer Proceedings in Physics 156,
DOI 10.1007/978-3-319-06611-0,